

***The emplacement and deformation of high-temperature tuffs:
a structural analysis of the Grey's Landing ignimbrite, Snake
River Plain, Idaho***

Graham Douglas Michael Andrews

submitted for the degree of Doctor of Philosophy (Ph. D.)

Department of Geology

Faculty of Science

University of Leicester

January 2006

***The emplacement and deformation of high-temperature tuffs:
a structural analysis of the Grey's Landing ignimbrite, Snake
River Plain, Idaho***

Graham Douglas Michael Andrews

submitted for the degree of Doctor of Philosophy (Ph. D.)

Department of Geology

Faculty of Science

University of Leicester

January 2006

The emplacement and deformation of high-temperature tuffs: a structural analysis of the Grey's Landing ignimbrite, Snake River Plain, Idaho

Graham Andrews

The Grey's Landing ignimbrite is an exceptionally well-preserved and well-exposed lava-like ignimbrite in the Snake River Plain volcanic province of southern Idaho, USA. High-grade tuffs are typically intensely welded and rheomorphic, preserving evidence of syn- and post-depositional ductile flow. The Grey's Landing ignimbrite underwent two distinct phases of rheomorphism: (1) syn-depositional welding and rheomorphism as the deposit aggraded, producing a penetrative, mylonite-like L > S fabric including sheath folds, a strong elongation lineation, and shear-sense indicators; and (2) post-depositional, *en masse*, gravity-driven flow of parts of the deposit down palaeo-slopes, producing a fold-dominated deformation characterised by large-scale folds of the upper surface of the ignimbrite. Thermal and rheological modelling suggest that the original magma was hot (~ 950 °C), volatile-rich (≤ 5 wt % fluorine), and low viscosity ($\geq 10^6$ Pa.s⁻¹). Syn-depositional rheomorphism had a strain rate of $\sim 10^{-5}$ s⁻¹ and deformed ignimbrite with a viscosity similar to the original magma. Post-depositional rheomorphism was limited to 6 months at the upper surface and ≤ 16 years in the centre of the thickest ignimbrite, at a strain rate of $\sim 10^{-6}$ s⁻¹.

Preface

This thesis is the culmination of four years research into the emplacement of rheomorphic ignimbrites, a rare form of pyroclastic density current deposit. This work stems from an on-going research program at the University of Leicester into the transport of pyroclastic density currents and the deposition of ignimbrites, including work on Tenerife, Gran Canaria, and in the United Kingdom and United States of America. The Leicester group, led by Dr. Michael Branney, has maintained an interest in rheomorphic ignimbrites since the early 1990s, furthered by this project and accompanying research in Idaho; and a future project on Pantelleria, Italy.

During the course of this study, I made four trips to Idaho, totalling 28 weeks, during which field observations were made, and structural data collected. Field observations were recorded with the aid of field notebooks, field maps, and photographs. Samples collected were returned to Leicester for optical and geochemical analysis. I benefited greatly from being part of a group of geologists examining stratigraphic problems, and eruption and emplacement processes in the Snake River Plain, led informally by Dr Bill Bonnicksen. Their logistical and intellectual support remain key to our on-going research in southern Idaho.

This thesis is divided into six chapters beginning with a review of concepts from structural geology and physical volcanology relevant to this study. Chapter 2 describes the stratigraphy of the Rogerson Formation, including the Grey's Landing ignimbrite, and sets out the importance of high-grade ignimbrites in the Yellowstone-Snake River volcanic province. Chapter 3 is a structural analysis of the Grey's Landing ignimbrite and forms the core of this thesis. It describes the fabric elements present, and the orientation, style and timing of rheomorphic deformation. Finally, it interprets the structural assemblages described, and attempts to conceptualise the processes that led to their formation. Chapter 4 attempts to constrain the rheological evolution of the Grey's Landing ignimbrite before, during, and after rheomorphism, using petrological and geochemical data, and thermal and rheological modelling. This constrains the eruption temperature, cooling rate, viscosity, and duration of rheomorphism. Chapter 5 compares and contrasts the results of Chapters 3 and 4 with established conceptual models for the emplacement of rheomorphic ignimbrites, and attempts to provide better constraints to those models. Chapter 6 summarises the

conclusions and outcomes of this research, and provides recommendations for future work. The thesis includes four accompanying appendices of geochemical data, and a copy of a field-guide to the field area.

Table of contents

Chapter 1 - Rheomorphism in ignimbrites: a review

| | |
|---|------|
| Introduction | 1-1 |
| Ductile deformation in shear zones | 1-2 |
| Fundamental concepts in structural geology | 1-2 |
| Fabrics and structures in tectonic shear zones | 1-4 |
| Ductile shear in non-particulate gravity currents | 1-9 |
| Welding and rheomorphism in ignimbrites: a review | 1-14 |
| Pyroclastic density currents and ignimbrites | 1-14 |
| Welding in tuffs: compaction versus agglutination | 1-15 |
| Physical controls on welding | 1-17 |
| Welding in high-grade tuffs | 1-21 |
| Rheomorphism in tuffs | 1-22 |

Chapter 2 – The Rogerson Formation and its relation to the Yellowstone – Snake River Plain volcanic province

| | |
|---|------|
| Introduction | 2-1 |
| Regional setting – Miocene to Recent volcanism in the intermontane northwest USA | 2-2 |
| Introduction | 2-2 |
| The Yellowstone – Columbia River ‘mega’-volcanic province | 2-2 |
| Miocene explosive and effusive rhyolitic volcanism in Idaho | 2-10 |
| The Rogerson Formation and the Rogerson Graben | 2-13 |
| Stratigraphy of the Rogerson Graben – the Rogerson Formation | 2-13 |
| Late Miocene to Holocene evolution of the Rogerson Graben | 2-26 |
| Eruption history | 2-28 |
| Discussion | 2-30 |
| The tectono-stratigraphic significance of the Rogerson Formation – correlations with neighbouring successions | 2-30 |
| Snake River-type volcanism: voluminous lavas and lava-like ignimbrites | 2-31 |
| Initial conclusions | 2-34 |

Chapter 3 – Evolution of structure within the Grey’s Landing ignimbrite

| | |
|---|------|
| Introduction | 3-1 |
| The Grey’s Landing ignimbrite: general anatomy | 3-2 |
| Ignimbrite distribution and thickness variations | 3-2 |
| The ‘thin’ ignimbrite facies | 3-2 |
| The ‘thick’ ignimbrite facies | 3-3 |
| Fabric elements and kinematic criteria in the Grey’s Landing ignimbrite | 3-3 |
| Planar fabric elements | 3-3 |
| Linear fabric elements | 3-11 |
| Kinematic criteria | 3-16 |
| Structure within the thin ignimbrite facies | 3-21 |
| General anatomy | 3-21 |
| Description of structures | 3-21 |
| Initial interpretation | 3-24 |
| Provisional conclusions | 3-26 |
| Structure within the thick ignimbrite facies | 3-26 |
| General anatomy | 3-26 |
| Description of structures | 3-27 |
| Initial interpretations | 3-38 |
| Provisional conclusions | 3-45 |
| Transitions between structural domains | 3-46 |
| Overview | 3-46 |
| Description | 3-46 |
| Interpretation | 3-48 |
| Summary | 3-48 |

Chapter 4 – Constraints on the rheological evolution

| | |
|--|-----|
| Introduction | 4-1 |
| Objective | 4-1 |
| Chapter outline | 4-2 |
| Background: rheological control on volcanic processes | 4-2 |
| Measuring ‘effective’ viscosity: a holistic methodology | 4-2 |
| Background: temporal trends of physical parameters | 4-6 |
| Physical constraints on the viscosity of the Grey’s Landing ignimbrite | 4-9 |
| Geochemical data | 4-9 |

| | |
|---|------|
| Pre-eruptive temperature: estimates from geothermometry | 4-15 |
| Viscometry | 4-19 |
| Indications of low viscosity | 4-19 |
| Viscometry – empirical modelling | 4-19 |
| Viscometry – fluid dynamics | 4-20 |
| Viscometry – relationship with shear stress and strain rate | 4-21 |
| Strain rates and shear stresses | 4-25 |
| Discussion | 4-26 |
| Chapter 5 – Discussion | |
| Syn-depositional welding and rheomorphism | 5-1 |
| Review of evidence | 5-1 |
| Pre-existing conceptual models | 5-2 |
| Syn-depositional welding and rheomorphism in the Grey’s Landing ignimbrite | 5-9 |
| Post-depositional rheomorphism | 5-10 |
| Review of evidence | 5-10 |
| Conceptual models | 5-11 |
| Post-depositional rheomorphism in the Grey’s Landing ignimbrite | 5-13 |
| Summary | 5-13 |
| Chapter 6 – Conclusions, implications of the study, and future work | |
| Emplacement history | 6-1 |
| Achievements | 6-2 |
| Further work | 6-3 |
| Appendices | |
| References | |

Acknowledgements

Acknowledgements:

I would like to take this opportunity to thank my supervisors Drs Steve Temperley and Bill Bonnicksen, Profs Mike McCurry and Martha Godchaux, especially Dr Mike Branney, for their continued assistance, advice, encouragement and dedication to me during the last four years. Without their support I would not have survived or enjoyed my research. My appreciation also goes to my thesis examiners, and all the staff and my fellow post-graduates in the Department of Geology at the University of Leicester. Special thanks to Mr Rob Wilson, Drs Mike Norry, Dickson Cunningham, Lawrence Coogan, Tiff Barry and Richard England, and Profs Andy Saunders and Mike Lovell. Thanks also to Drs Curtis Manley, Alan Whittington, Ian Alsop and Craig White.

Special thanks goes to my field assistants Karen Colclough, David Baines, Steven Rippington, and most importantly Sarah Brown; and to the plethora of friendly, helpful and charming people I met in Idaho, especially Mr and Mrs Walker Tolman of Twin Falls, Idaho, and Mrs Melissa Neiers and Mrs Sarah McCurry of Pocatello, Idaho.

Finally, I wish to express my love and gratitude to my parents who have never criticised my choice of career, or been anything else than 110% supportive.

Thank you all



Chapter 1:

Rheomorphism in ignimbrites: a review

Introduction

Rheomorphic tuffs are welded volcanic deposits deformed by ductile flow during or immediately after emplacement. As will be shown, rheomorphism is the penultimate stage of six key stages in the formation of a rheomorphic tuff: magma chamber processes, eruption, transport, deposition, welding, rheomorphism; and any residual static cooling. Rheomorphic ignimbrites are a common and important component in many volcanic successions, moreover, they have been identified in nearly all volcano-tectonic settings: intra-continental (e.g., Snake River Plain, Idaho; Bonnicksen and Citron, 1982), intra-oceanic (e.g., Mogán and Fataga Formations, Gran Canaria; Schmincke, 1974), rifted continental margin (e.g., Paraná volcanic province, Brazil; Kirstein et al., 2001), and continental arc (e.g., Bad Step Tuff, England; Branney et al., 1992). They have good preservation potential, much better than non-welded pyroclastic successions, and are known from the Palaeoproterozoic (e.g., Bijli rhyolites, India; Mukhopadhyay et al., 2001) to the Holocene (e.g., Green Tuff, Pantelleria, Italy; Mahood and Hildreth, 1986).

The study of rheomorphic ignimbrites encompasses two fields of geology that are often, and wrongly, thought of as distinct and separate: physical volcanology and structural geology. This thesis is the first work on rheomorphic tuffs where modern structural geology techniques have been applied to investigate the emplacement of a rheomorphic ignimbrite, since the work Chapin and Lowell (1979) and Wolff and Wright (1981).

This chapter reviews the concepts and techniques of structural geology established by workers investigating exhumed deep crustal shear zones (e.g., Ramsay, 1967; Cobbold and Quinquis, 1980; Ramsay and Huber, 1983; 1987; Passchier and Trouw, 1996) and then introduces the application of these techniques to ice and

salt glaciers (namakiers), sedimentary slumps and lavas, and finally to rheomorphism in tuffs.

Ductile deformation in shear zones

Anisotropic deformation within ductile portions of the lithosphere is characterised by development of ductile shear zones which are planar zones of high finite strain surrounded by rocks showing lower finite strain (e.g., Ramsay, 1980; Ramsay and Huber, 1987). Exhumed mylonite zones and their field relations, structures, and microfabrics can reveal the history of non-coaxial, ductile deformation in rocks, and have provided the primary data to allow physical and numerical modelling of the deformation.

Fundamental concepts in structural geology

This section summarizes some fundamental concepts concerning ductile shear zones that form the basis of the main part of this study (Chapter 3).

Stress and strain

Rocks are deformed as a physical response of changes in the externally applied stresses. Stress is a pair of equal and opposite forces acting on a unit area of a body, and is governed by Newton's Third Law of Motion. Stress equals force (e.g., gravity) divided by the area of the surface on which it acts. Normal stresses act perpendicular to a surface while shear stresses act parallel to that surface; by convention positive normal stress acts inwards (compressive) and positive shear stress is dextral (right lateral). Three principal normal stresses can be defined (Fig. 1-1a) acting on the surfaces of a cube (σ_1 , σ_2 , and σ_3). If $\sigma_1 = \sigma_2 = \sigma_3$ the stress is described as hydrostatic (i.e. like a liquid) and the only possible deformation is volume change. If the principal normal stresses are different ($\sigma_1 \geq \sigma_2 \geq \sigma_3$) the resultant will involve shape change and possibly volume change.

Volume change, shape change and rotation in response to an applied stress are forms of strain (Fig. 1-1b). Strain can be homogeneous throughout a body or heterogeneous: during homogeneous strain, straight and parallel lines remain straight and parallel, whereas, during heterogeneous strain they become curved

and non-parallel (Fig. 1-1c). Although heterogeneous strain is almost impossible to understand in its entirety, complex heterogeneous strains often break down into smaller domains of calculable homogeneous strain. Within shear zones strain may be distributed homogeneously (i.e. strain equal throughout) if the zone margins are planar and parallel, or heterogeneously (strain unequal throughout) if the margins anastomose, curve or are non-parallel.

Types of strain

Strain can be characterised and measured in terms of angular change, the change in the length of a line, volume change, etc (Ramsay, 1967; Ramsay and Huber, 1983). Therefore, *a priori* knowledge of the original lengths and angular relationships of an object is required for a strain analysis. Natural strain markers (objects with predictable original shapes) are typically abundant (e.g., fossils with bilateral symmetry) and folded layers can be conceptually ‘unfolded’ to reveal their original length.

Strain is described by the magnitudes and orientations of the three principal strains, X, Y, and Z, parallel to the respective maximum, intermediate and minimum elongation axes of a hypothetical ellipsoid (Fig. 1-2a). If the orientation of the principal strains remains constant through increments of a progressive deformation, the strain is described as being non-rotational or coaxial, often called ‘pure shear’ (Fig. 1-2b). Strain that rotates the principal strain axes is described as non-coaxial, or more commonly, ‘general strain’; ‘simple shear’ is a specific $K = 1$ ellipsoid undergoing non-coaxial distortion (Fig. 1-2b). Natural deformation usually encompasses both coaxial and non-coaxial end members. Non-coaxial strain is typical of ductile shear zones and mylonites, where there are abundant asymmetric structures, including kinematic criteria, that reflect the rotational nature of the deformation.

Three special types of homogeneous strain can be distinguished by particular ratios of the principal strains and the corresponding strain ellipses (Fig. 1-3). (1) Prolate strain ($X > Y = Z$) where stretching is uniform in the X direction (Fig. 1-3a), and (2) oblate strain ($X = Y > Z$) where shortening is uniform in the Z

direction (Fig. 1-3b). (3) In plane strain intermediate axis remains unchanged ($X > Y = 1 > Z$), X is stretched and Z is shortened (Fig. 1-3c). Variations in the shape of the strain ellipsoid are summarized on the Flinn diagram where flattening and stretching dominated fields are established (Fig. 1-3d).

Strain through time: incremental and finite strain

Any deformed body exhibits a final strain state (finite strain) after passing through a series of earlier deformed states (incremental or infinitesimal strain, e.g., Fig. 1-2b). This process is termed progressive deformation (Ramsay, 1967). Usually, only the finite strain of a body can be examined and measured, however, sometimes it is possible to identify structures that have exhibit different strain histories (e.g., vesicles of different relative ages exhibit different degrees of deformation) throughout a deformed unit. These can help to reconstruct the deformation of different parts of a body through time, thereby establishing the deformation history.

Fabrics and structures in tectonic shear zones

Exhumed deep crustal ductile shear zones are characterised by small grain size, well-developed planar and linear fabrics, and the presence of fabric elements with monoclinic shape symmetry (Passchier and Trouw, 1996). Mylonites are the exhumed deep crustal ductile shear zones. They are, like many geo-materials, crystalline or granular solids that deform at the crystal / grain scale by a number of distinct mechanisms (e.g., grain boundary sliding, dislocation creep; see Passchier and Trouw, 1996 and references therein). Many contain porphyroclasts, clasts distinctly larger than the groundmass commonly interpreted to be remnants or resistant grains from the protolith (Passchier and Trouw, 1996). Porphyroclasts are commonly wrapped by fabric elements, and commonly show evidence for having been rotated, indicative of non-coaxial strain. The fabric and structural elements within mylonites, and other ductily deformed geo-materials, can be divided into four broad and non-generic groups (Fig. 1-4): (1) planar fabrics (e.g., axial planar cleavages), (2) linear fabrics (e.g., lineations); (3) kinematic indicators (e.g., rotated porphyroclasts), and (4) folds (e.g., sheath folds).

Planar fabrics

Planar fabrics are any penetrative planar features that exist within a rock. They may result from physical variations within the rock (e.g., bedding) or they may be subtle (e.g., colour-banding). Two types of planar fabric may exist in a deformed rock: (1) initially planar structures (e.g., bedding; Fig. 1-5a), and (2) planar fabrics commonly characteristic of oblate strain (S-tectonites) and plane strain deformation (L=S tectonites; Ramsay, 1967). Planar fabrics may be mechanically isotropic and respond passively to strain, or they may be anisotropic and control the distribution, scale and style of structural fabric elements.

Primary planar fabrics, S_0 , (*sensu* Passchier and Trouw, 1996) are the surfaces folded during the first-phase of deformation (D_1). Secondary planar fabrics (S_n ; *sensu* Passchier and Trouw, 1996) are those produced by deformation and therefore, they cross-cut or parallel S_0 foliations (Fig. 1-5a). Tectonites, including mylonites, often include more than one set of cross-cutting secondary foliations that are inferred to develop contemporaneously during progressive deformation (Passchier and Trouw, 1996). The most common types of S_n foliation observed are axial planar cleavage (Fig. 1-5a) and crenulation cleavage (Fig. 1-5b). Fold-axial-cleavage develops where elements (usually phyllosilicate minerals, e.g., micas, chlorite) re-orientate or grow in parallelism with the principal flattening plane (YZ) perpendicular to the shortening direction (principal strain Z). Crenulation cleavage forms when an earlier close-spaced foliation is folded at a small-scale.

Both primary and secondary planar fabrics may be transposed into parallelism during intense and sustained non-coaxial strain (Twiss and Moores, 1992; Ham and Bell, 2004). During prolonged progressive deformation, isoclinal folds of the primary foliation are dismembered, forming rootless fold hinges. These are, in turn, assimilated into the dominant foliation to form intrafolial folds (Fig. 1-4).

Linear fabrics

Any fabric that can be described as a visible (e.g., stretched clasts) or cryptic (e.g., magnetic fabric; Knight and Walker, 1988) line is a linear fabric, and they are

typical of prolate (L-tectonites) and plane strain (L=S tectonites) deformation. They are usually developed on planar fabric surfaces (Fig. 1-4) and they can be penetrative or surficial (Twiss and Moores, 1992). Lineations in L- and L=S tectonites include three types; mineral, discrete and constructed. Mineral lineations are formed by linear arrays of mineral grains (e.g., quartz rods in gneisses). Discrete lineations are formed by the stretching of pre-tectonic objects, for example sedimentary clasts (Fig. 1-5c), fossils, reduction spots and vesicles; they form the principal elements in defining the transport trend during deformation (Cloos, 1957) and are assumed to be parallel to the maximum principal strain axis (X), and therefore they are the most important structures to record from a mylonite. Constructed lineations form as a result of deformation, for example fold hinges, slickenlines, and intersection lineations where two foliations intersect.

Kinematic criteria

The sense of shear during non-coaxial deformation, usually equating to the actual transport direction, may be recorded by kinematic criteria in which various fabric and structural elements (e.g., folds, shear bands, rotated porphyroclasts; Fig. 1-4) develop asymmetry (Hammer and Passchier, 1991; Passchier and Trouw, 1996). The most commonly used kinematic indicators are microscopic fabrics or inclusions within a ductile-deformed matrix, examined in thin sections cut normal to the Y axis and parallel to the stretching direction, X, established from a stretching lineation. Kinematic indicators can be divided into two types: (1) rotational (e.g., rotated porphyroclasts, Passchier and Simpson, 1986; asymmetric boudins, Goscombe and Passchier, 2003) and (2) irrotational (e.g., shear bands; Passchier and Trouw, 1996).

Rotated porphyroclasts are the most commonly used shear sense indicators in tectonites (Passchier and Simpson, 1986; Samanta et al., 2002). They are commonly mantled by grain aggregates (mantled porphyroclasts, *sensu* Passchier and Trouw, 1996) that form asymmetric wings in diametrically opposite low strain zones around the porphyroclast (Fig. 1-6). σ -type objects (Fig. 1-6a) are

characterized by deflection of planar fabrics around a porphyroclast without the planar fabric itself being folded. In contrast, δ -type objects (Fig. 1-6b) are characterized by asymmetric drag folds in the low strain zones around porphyroclasts that have a vergence associated with the rotation of the porphyroclast (Samanta, 2002).

Folds

Folds develop where planar fabrics (e.g. bedding, foliation) undergo ductile shortening (Fig. 1-4), and they occur at all scales from microscopic to hundreds of kilometres. They are of value to geologists because they form in most deformation regimes and have recognisable geometrical and spatial associations with other structures so that, for example, small-scale folds are instructive in interpreting folds too large to be exposed in a single section. Fold type and style reflect both the physical conditions (e.g., stress, temperature and pressure) and the mechanical properties of the rock (competence, layer thickness) during folding. Understanding the significance of fold geometry in conjunction with foliations, lineations and kinematic criteria, is a key to understanding the conditions of deformation.

Description and classification of folds

Many folds are complex three-dimensional structures that can only be described using a number of criteria (Ramsay, 1967). A full discourse on the classification of folds is beyond the scope of this chapter, and is covered elsewhere (e.g., Ramsay and Huber, 1983; Twiss and Moores, 1992). Here, I just review fold morphology, geometry and style associated with non-coaxial deformations.

In the case of folded layers, small-scale complexity can be ignored by reducing quantification of the fold to five easily measurable criteria: hinge, axial plane, interlimb angle, wavelength and amplitude (Fig. 1-7a). The scale, attitude and orientation of a fold are fully described by these five criteria, so that any fold can be described uniquely. Interlimb angle is particularly useful as it is an gauge of

the total shortening a folded body has experienced: the lower the interlimb angle the greater the shortening.

Ramsay (1967) identified five classes of fold style. The most important classes are 1B (parallel folds) and 2 (similar folds; Fig. 1-7b), readily distinguished from each other by the thickness ratio between their respective hinges and limbs. In class 1B folds the thickness of the folded layer remains constant, whereas, in class 2 folds there is significant hinge thickening and limb thinning.

Similar style folds - folding typical of non-coaxial deformation

Whereas parallel folds are common in strongly anisotropic layered sequences, similar folds are dominant in passive-shear regimes or heterogeneous strain where the rock body is, or is close to, isotropic (i.e. low competency contrast) and the rocks are comparatively weak (Ramsay, 1967). This is only possible in a regime where the foliation is passive and has zero mechanical strength, so it is no surprise that similar style folds are typical of ductile shear zones and mylonites (Carreras et al., 2005), and other near-isotropic and weak materials, such as, salt and water ice. Hinge thickening and limb thinning are achieved by ductile movement (flow) towards the hinge, of material during heterogeneous strain. In this scenario the hinge is a zone of comparatively low strain, whereas the limbs undergo the greatest strain.

Progressive shearing attenuates the limbs of isoclinal, similar-style folds producing an intrafolial fabric and rootless folds (Figs 1-4 and 1-5d). Sheath folds are a special type of similar-style fold characteristic of very high non-coaxial strain within a ductile regime (Cobbold and Quinquis, 1980; Skjernaa, 1989; Fig. 1-4). They have the shape of tapering tubes (Fig. 1-4; i.e. test-tubes, bullets, condoms) in three dimensions, and eye structures when exposed in the YZ plane (Fig. 1-5e), and characteristically parallel the maximum principal stretching direction and lineation (Ridley, 1986). Oblique folds (Fig. 1-4) are sheath-like but only close in one direction but, again, trend parallel or sub-parallel to the stretching direction (Smith, 2000b). Whatever the orientation of fold axes during

nucleation, they will tend to be transposed into parallelism during progressive non-coaxial deformation.

Three mechanisms for the formation of sheath and sheath-like folds have been proposed (Fig. 1-8): (1) transposition of the fold axes, (2) nucleation around flow perturbations, and (3) differential shear between deformation cells. The transposition of fold axes by passive hinge rotation during progressive non-coaxial shear (Fig. 1-8a) is frequently interpreted to be the cause of sheath folds in ductile shear zones and orogenic belts, especially where a continuum of fold axes from perpendicular to transport direction parallel (e.g., Ghosh and Sengupta, 1987; Mies, 1991; Alsop, 1992; Ghosh et al., 1999; Carreras et al., 2005). Typically, sheath folds formed in this way are laterally extensive along the strike of the fold axial surface. Sheath fold nucleation around porphyroclasts ('flow perturbations') has been demonstrated from field and experimental evidence (Fig. 1-8b), irrespective of whether or not they be mm-scale crystal fragments or cm-scale boudins (Marques and Cobbold, 1995; Rosas et al., 2002). Typically, such sheath folds are single and distinct, and do not exist as part of a larger folded surface. Differential shear between discrete volumes ('cells') in shear zones encourages flow perturbations (Alsop and Holdsworth, 2002; Fig. 1-8c). Adjacent cells of surging and slackening flow evolve within the shear zone, giving rise to sheath fold closures up-transport direction (culminations) and down-transport (depressions) respectively (Alsop and Holdsworth, 2002). As with transposition of fold axes, differential shear between cells produces laterally extensive sheath folds and axial planar surfaces.

Ductile shear in non-particulate gravity currents

Non-particulate gravity currents are coherent deforming masses of material moving under the influence of gravity, for example, down a slope. Geological examples include ice glaciers, salt glaciers (namakiers), sedimentary slumps and lavas. The ductile flow processes and structures in deep crustal ductile shear zones are also characteristic of non-particulate gravity currents (Fig. 1-9a), and have some similarities with rheomorphic ignimbrites. They are low viscosity,

their deformation is rapid, they are gravity driven, they have a free surface, they are incompetent and mechanically isotropic, and they share several morphological characteristics.

Silicic lavas

Lavas are emplaced by lava flows, which are non-particulate gravity currents erupted during effusive (non-explosive) volcanism (Cas and Wright, 1987; Griffiths, 2000). Although structural investigations of lavas are limited (e.g., Fink, 1980; Smith, 2002), observations of moving contemporary lava flows provide us with an opportunity to observe the flow mechanisms and learn about flow rates and timescales.

Silicic lavas typically exhibit surface structures termed ogives (Fig. 1-9), circumferential, ridges and trenches produced by compression of the distal, and often lobate, end of the lava (Fig. 1-9b and d). Analysis of ogive wavelength in silicic lavas by comparison with festoon folds (ropey structure) on basalt pāhoehoe lavas, allows estimation of lava viscosity and strain rate (Fink, 1980; Gregg et al., 1998). Ogives may result from a combination of upper surface buckle-style folds, and fold and thrust ‘ramps’ that root in a basal shear zone (Fig. 1-9a). Buckle folds are produced by layer parallel shortening of the competent upper surface, the upper surface gradually becomes more competent during prolonged cooling and degassing. Alternatively, any generally sourceward dipping inclined structure within silicic lavas is often referred as ‘ramp structure. They may be thrusts rooting into a basal shear zone where distal decelerating lava is overridden by material supplied from up-flow, or they may be deep-rooted similar-style folds partitioned between thrusts (Fig. 1-10); either way, they are analogous to imbricate fans.

Small-scale structures in silicic lavas are typically related to deformation of flow-banding (S_0) or vesicles (Castro and Cashman, 1999). Most silicic lava flows are texturally heterogeneous, composed of mm-scale to m-scale layers of glassy rhyolite intercalated with pumiceous layers of different competence. Flow-banding is a penetrative planar fabric caused by ductile deformation of the lava,

and is often folded. It results from several different processes during magma ascent, eruption and emplacement (Castro and Cashman, 1999; Manga, 2005), including repeated autobrecciation and reannealing during flow (e.g., Smith, 1996; Tuffen et al., 2003; Gonnermann and Manga, 2005), mingling of different melt compositions (e.g., Leat and Schmincke, 1993; Seaman, 1995; De Rosa et al., 1996; Perugini et al., 2004), variation in microlite concentration (Manga, 2005), welding and syn-welding shearing in clastogenic lavas (e.g., Gottsmann and Dingwell, 2001; Soriano et al., 2002; Furukawa and Kamata, 2004), and vesiculation (e.g., Hausback, 1987; Fig. 1-11).

The interiors of silicic lavas often display folded and boudinaged flow-banding, rotated porphyroclasts and preferred crystal orientations. Where flow-banding is mechanically isotropic (i.e. passive) similar-style folds dominate, however, progressive heterogeneous non-coaxial shear may modify, refold and transpose early-formed folds and produce sheath folds. In contrast to crustal ductile deformation, axial planar cleavage is not developed at any stage due to a lack of phyllosilicate minerals. However, stretching lineations are common, and form by layer-parallel stretching in parts of the lava flow that are extending, as is recorded by boudinage of competent layers (Castro and Cashman, 1999; Smith, 2002). Rotated porphyroclasts form from phenocrysts, lithic clasts and mingled blebs of magma (Fig. 1-12). Rotational shear-sense indicators in lavas were first described by Cummings (1964) who incorrectly envisaged eddies developing down-current of an inclusion (Fig. 1-12a). Rotated phenocrysts and lithic lapilli in rhyolite lavas are analogous to those in ductile shear zones (Vernon, 1987; Fig. 1-12b) and have been applied to interpret the emplacement directions of ancient lavas (e.g., Christiansen and Lipman, 1966). Blebs on mingled magma may also act as kinematic criteria if there is sufficient competency contrast between the bleb and the surrounding lava flow (Fig. 1-12c).

The majority of structural studies of silicic lavas have concentrated on extensively outcropping Holocene examples (e.g., Big Obsidian Flow, Oregon and the Rocche Rosse, Lipari), but they are often not well exposed in three dimensions. In contrast, ancient silicic lavas provide extensive cross-sections but are often buried,

and commonly they are thoroughly recrystallised destroying small-scale structures defined by flow-banding.

Glaciers and namakiers

Glaciers and namakiers are non-particulate gravity currents transporting crystalline ice or salt down-slope. The deposits from glaciers and namakiers do not fully record temporal or spatial variations, or style of deformation within the current, and therefore the currents themselves must be examined. Planar fabrics are often difficult to identify in glaciers and namakiers, for example, bedding is usually identified by colour-banding (Talbot et al., 2000; Talbot and Aftabi, 2004) or layers of rock debris (e.g., tephra, Ximenis, 2000). Secondary planar fabrics are abundant but often difficult to interpret; they include dilational surfaces (e.g. crevasses), normal faults, and thrust faults; and axial planar cleavages and basal shear zones with mylonitic fabrics. It is not clear how these planar fabrics form and deform during progressive deformation during flow of the current, for example, Figure 1-13a shows the transposition of an unspecified sub-horizontal planar fabric (assumed to be bedding, S_0) into a steep fabric parallel to the flow direction and valley sides, without describing any folding that may have occurred at the same time (Hambrey and Lawson, 2000; Hambrey et al., 2005). In contrast, Figure 1-13b depicts the spatial distribution of structures perpendicular to the flow direction of the glacier, features include crevasses at the head and compressional fold-thrust ridges ('ogives'; Fig. 1-9c) at the distal end (Goodsell et al., 2002; Hambrey and Glasser, 2003; Talbot and Aftabi, 2004). However, no attempt is made to relate the transition from extensional to compressional strain, nor to account for the change from ductile (sheath folds) to brittle (thrust faults) behaviour.

Because they deform at much faster rates than deep crustal shear zones, direct measurement is possible and provides useful models for deformation rates (Hambrey and Lawson, 2000). However, structural analysis of glaciers and namakiers is typically limited to examination of the upper surface of currents due to the lack of vertical exposure surfaces incised into the current, and to cross-

sections through the distal terminations; therefore the three dimensional evolution of structure from the head region (i.e. accumulation zone or vent) is often poorly constrained. Consequently, present studies of glaciers and namakiers do not provide many useful insights into the three dimensional evolution of ductile structures within non-particulate currents and their deposits.

Soft-sediment slumps

Soft-sediment slumps are laterally displaced and deformed sediment masses bound by shear planes (Stow, 1986), whereas, soft-sediment slides are essentially allochthonous and non-deformed masses bound by shear planes (Martinsen, 1994). Slumps of non-lithified or weakly-lithified sediment are common in many tectonically unstable sedimentary basins, especially where de-watering is inhibited by rapid sedimentation. Slumped sediments are typically massive and isotropic, reducing competency contrasts within the mass (Strachan, 2002). Multiple generations of folds, secondary planar fabrics, linear fabrics, and extensional and thrust faults have been reported, and interpreted as the products of rapid but progressive, non-coaxial deformation during slumping (e.g., Gill, 1979; Tobisch, 1984; Elliot and Williams, 1988; Martinsen and Bakken, 1990; Patterson and Tobisch, 1993; Smith, 2000). During progressive deformation upright buckle-style folds formed by coaxial layer parallel shortening are rotated and modified in a non-coaxial regime (Farrell, 1984; Smith, 2000). Originally buckle-style folds (class 1B) become curvilinear, similar-style (class 2) isoclinal and recumbent folds and sheath folds (e.g., Martinsen, 1994), where the S_0 fabric is transposed by an axial planar cleavage and flattening fabric (Tobisch, 1984). However, as with glaciers and namakiers, reported case studies do have access to significant three dimensional exposure; most ancient slumps are exposed in two dimensions within a larger sedimentary sequence (e.g., Gill, 1979; Smith, 2000; Fig. 1-14), and modern marine and lacustrine slumps are inaccessible and have only been investigated by side-scan sonar imaging of their upper surfaces and seismic profiling (e.g., Piper et al., 1999; Schnellmann et al., 2005; Fig. 1-14).

Summary

Although studies of non-particulate gravity currents have concentrated on active currents (e.g., glaciers) or recently emplaced currents (e.g., Holocene silicic lavas) there is undoubtedly value in examining and assessing work carried out in these types of currents, however, it is apparent that some are of only limited value as analogues for rheomorphism in tuffs. The major problem with many studies is that they do not reveal the internal structure of the non-particulate gravity current in question (e.g., due to lack of incised outcrops), rather they focus on the external structure, for example, surface ogive folds. In contrast, it is possible that insights into the emplacement of rheomorphic ignimbrites (this study) may highlight some problems with emplacement models for other non-particulate gravity currents, and help resolve and clarify other models.

Welding and rheomorphism in ignimbrites: a review

Rheomorphic ignimbrites are welded and deformed by ductile flow during and immediately after deposition. Emplacement of rheomorphic ignimbrite is composed of six overlapping stages summarised in Figure 1-15: (1) pre-eruption processes within the magma chamber, (2) eruption, (3) transport, (4) deposition, (5) welding, and (6) rheomorphism; and finally any residual static cooling. I will briefly address pyroclastic density currents and their deposits before concentrating on the welding process, the physical controls on welding, and finally rheomorphism.

Pyroclastic density currents and ignimbrites

Pyroclastic density currents are hazardous and ground-hugging, particulate gravity currents of pyroclasts, magmatic gases, admixed air, that travel through less dense media (i.e. air and / or water) (*sensu* Branney and Kokelaar, 2002). They can transport thousands of cubic kilometres of hot pyroclasts and debris, hundreds of kilometres from source in periods of seconds to hours. An ignimbrite-forming eruption is one of Nature's most impressive and devastating phenomena and even members of the general public are aware of the dangers of pyroclastic density currents from past eruptions including the AD79 eruption at Vesuvius, the 1902

eruption at Mt. Pelée, and the 1980 eruption at Mt. St. Helens. However, our understanding of the processes involved in eruption, transport and deposition remains incomplete. Observation and analysis of ‘real’ pyroclastic density currents is hampered by their dangerous and transient nature. Therefore, understanding must be gleaned from examination of their deposits and conceptual-, analogue-, and numerical-modelling.

Pyroclastic density current deposits, ‘ignimbrites’ are rich in pumiceous ash shards (i.e. bubble wall and cusped) and pumice. They are typically predominantly massive or poorly stratified, and very poorly sorted with pumice and lithic lapilli supported in an ash matrix (Fig. 1-16). They commonly include subordinate well-stratified facies, and may be unconsolidated or lithified. They characteristically form low-profile sheets that inundate topography, with marked increases in thickness in palaeotopographic lows (e.g., palaeo-valleys) where their upper surfaces are usually flat and gently inclined by $< 4^\circ$. Thin parts of ignimbrites may also partly drape topographic highs (Walker, 1983; Branney and Kokelaar, 2002).

Welding in tuffs: compaction versus agglutination

Welding in tuffs is the process by which hot ash particles and pumice lapilli anneal together by variable degrees of ductile deformation, and reduction of the pore space in the deposit (Smith, 1960b), the hot deformation producing a characteristic sub-horizontal eutaxitic fabric (Fig. 1-17). Welded deposits, both ignimbrites (Ross and Smith, 1961) and fall deposits (Sparks and Wright, 1979), are lithified and mechanically stronger than non-welded deposits and are less easily eroded. Many ignimbrites have vertical zonal variations in welding intensity that have been attributed to vertical variations in compaction (load strain) and cooling rate (Smith, 1960b). However, despite nearly 50 years of theoretical, experimental and field investigation, the timing of welding and some of the physical controls are still poorly understood.

Two end-member types of welding have been proposed: (1) load welding, and (2) aggregation welding (Freundt, 1999). Many studies assume that hot pyroclasts

are compacted by the load of the overlying deposit as the ignimbrite cools *in situ* (Fig. 1-18; Friedman et al., 1963; Ragan and Sheridan, 1972; Riehle, 1973; Sparks and Wright, 1979; Riehle et al., 1995; Streck and Grunder, 1995; Quane and Russell, 2005a; Grunder et al., 2005; Sheridan and Wang, 2005). For example, many ignimbrites show most intense welding one quarter or one third of the way up from the base, away from more rapidly cooled margins and where the burial load was highest. This conceptual model has been applied predominantly to moderately welded ignimbrites (e.g., Bandelier and Bishop Tuffs and other extensive ignimbrites in the Western US) to account for the vertical welding zonation and flattening profiles exhibited by fiamme (Smith, 1960b; Peterson, 1979; Fig. 1-17), and it has been modelled (e.g., Ragan and Sheridan, 1972; Riehle, 1973; Riehle et al., 1995; Quane and Russell, 2005b; Russell and Quane, 2005; Sheridan and Wang, 2005). This conceptual model of welding is termed ‘load welding’ by Freundt (1999).

However, load welding probably does not account for all welding in tuffs. Field evidence shows that many, often thin (≤ 10 m thick), tuffs are intensely welded to their upper and lower surfaces (e.g., ignimbrite ‘P1’, Freundt and Schmincke, 1995); and are occasionally ‘lava-like’, where they resemble silicic lavas (e.g., ignimbrite ‘TL’, Sumner and Branney, 2002). Intense welding is often accompanied by extensive rheomorphism and vesiculation (Mahood, 1974; Branney et al., 1992), the preservation of spherical particles (‘globules’) interpreted to be magma droplets (Hay et al., 1979; Milner et al., 1992), and thorough devitrification; both suggesting unusually high emplacement temperatures and prolonged cooling (Schminke, 1974). Experimental evidence shows that hot pyroclastic particles in a dilute pyroclastic density current will rapidly aggregate with each other within the current, and then rapidly agglutinate with an underlying deposit (Freundt, 1998). The low viscosity of particles, their ‘stickiness’ and ‘plasticity’, is critical to their ability to aggregate and agglutinate; it has been suggested that pyroclast particle viscosity is so low that they have no effective strength, and therefore flatten and weld instantaneously in the absence of a load strain (e.g., Branney and Kokelaar, 1992; Freundt, 1998; 1999; Capaccioni

and Cuccoli, 2005). This conceptual model of welding is termed ‘aggregation welding’ by Freundt (1999).

Physical controls on welding

Because the rate and intensity of welding are dependent on the rheology of pyroclasts, it is important to address the physical controls that encourage low pyroclast viscosity and high pyroclast temperature. Rheology is the qualitative measure of the behaviour of a material during deformation, for example whether a rock responds by brittle fracture or by ductile flow in response to an applied strain and strain rate (Webb and Dingwell, 1990). Liquids are typically more likely to flow than solids, moreover different liquids have different rheologies, for example, water and molasses. Two sets of criteria control the rheology of pyroclasts during welding: (1) the physical properties of the silicate melt, ‘pre-eruption’ effects; and (2) changes in the physical properties of the pyroclasts during eruption, transport, deposition and residual static cooling, ‘post-eruption’ effects. The physical properties of the melt are pre-eruptive controls on the melt within the magma chamber, and can be considered as controlling the rheology of the starting material. Post-eruption effects, usually cooling and de-gassing during transport, progressively and often heterogeneously change the rheology of the pyroclasts.

The glass transition (T_g) is a kinetic boundary between a liquid-like (viscous) and solid-like (elastic) mechanical response to an applied stress (e.g., Giordano et al., 2005). Above T_g glassy particles will deform viscously permitting welding; below T_g , the glass behaves elastically and will not weld. T_g exhibits a temperature-dependence on composition (viscosity is lower at T_g in peralkaline melts), volatile composition (e.g., H₂O), and cooling rate (Fig. 1-19a); and is represented by a time-temperature curve rather than a single temperature (Dingwell and Webb, 1990; Giordano et al., 2005). Passing through T_g will stop welding, either by rapid cooling (e.g., quenching) or rapidly increasing the applied strain rate (see discussion in Giordano et al., 2005). Minimum values for T_g have been experimentally determined and provide lower temperature limits for rapid

and intense welding of ignimbrite at $\geq 400^{\circ}\text{C}$, and timescales of the order of 10s of seconds to 10s of minutes (Giordano et al., 2000; 2005).

Viscosity

Whereas the rheology of a material is dependent on the applied strain and strain rate, and therefore can not be uniquely measured, the viscosity of that material can be. Viscosity is the measure of the ability of a material to resist ductile deformation; for a given applied strain (e.g., gravity), a low viscosity material (e.g., water) will flow easily, whereas a highly viscous material (e.g., ice) will flow much more slowly. Magma viscosity is thought to reflect the degree of silicate polymer development in the melt; for example, a thoroughly polymerised magma will have a very high viscosity, and will not flow easily (Webb and Dingwell, 1990). The length and abundance of silicate polymers is controlled by five, interacting, physical and chemical properties: (1) temperature, (2) melt composition, (3) dissolved volatile content and composition, (4) crystal content, and (5) vesicularity (Dingwell, 1998). Welding is only likely to occur below a maximum viscosity, above which pyroclasts will not deform and adhere to each other.

Temperature

The viscosity of silicate melts is inversely proportional to the temperature (McBirney and Murase, 1984; Fig. 1-19b). This is attributed to the break-down of silicate polymers at progressively higher temperatures, such that, above the liquidus temperature of a particular melt composition (e.g., a rhyolite), there are no interlocking polymers and the viscosity is at a minimum (Bottinga, 1994). Furthermore, above the liquidus temperature the relationship between viscosity and temperature is linear (Newtonian), below the liquidus the relationship progressively becomes highly non-linear (non-Newtonian). Temperature has the strongest control on viscosity in silicate magmas.

Melt composition

It is widely reported that mafic and / or peralkaline magmas generally exhibit lower viscosities than metaluminous rhyolites over a given temperature range

(e.g., McBirney and Murase, 1984; Dingwell et al., 1985; Dingwell and Hess, 1998; Giordano et al., 2005; Fig. 1-19b). Polymerisation is encouraged by a equal ratio of SiO₂ and Al₂O₃ ‘framework’ molecules, and ‘framework-linking’ high field strength elements (e.g., Na and K; Mahood, 1984). This typically results in peralkaline rhyolites (‘phonolites’; Na + K > Al) and peraluminous rhyolites (Na + K < Al) having lower viscosities than metaluminous rhyolites (Na + K = Al), in turn; rhyolites typically have higher viscosities than basalts.

Volatile compositions and concentrations

Dissolved volatiles have a profound effect on the viscosity of magmas, especially in evolved silicic compositions which are comparatively rich in volatiles (Persikov et al., 1990). For a given temperature and melt composition, the addition of dissolved volatiles to a melt will significantly lower its viscosity, for example, addition of 2 mol. % H₂O will decrease the viscosity of a silicate melt by ~4 orders of magnitude (Shaw 1972; Giordano et al., 2004; Fig. 1-19c). The volatile species present are important as only H₂O, F and Cl have been demonstrated to have significant effects on the viscosity of rhyolite melts (Lange, 1992; Stevenson et al., 1998). Moreover, the concentration of dissolved volatiles, itself a function of their solubility governed by pressure and temperature (Lange and Carmichael, 1991), also has significant effect (Friedman et al., 1963; Shaw, 1963).

Water (H₂O) is the most abundant and important volcanic volatile species effecting magma viscosity, however, the viscosity of erupted silicates rarely exceeds 10⁷ poises (Scaillet et al., 1998). In general, the addition of ~2 wt.% H₂O will reduce the viscosity of an evolved silicate liquid (e.g., a rhyolite) by approximately 3 log units (e.g., Friedman et al., 1963; Shaw, 1963; Lange, 1992, Stevenson et al., 1998; Fig. 1-19c). This relationship reflects the intake of water as hydroxyl (OH⁻) molecules into the developing polymer at the expense of framework-linking ions, and subsequently the incorporation of molecular H₂O beyond 5 wt.% (Lange, 1992). The effect of H₂O on magma viscosity is

enhanced by the presence of F and Cl (Stevenson et al., 1998; Lange, 1992), though H₂O has a much greater individual effect (Giordano et al., 2004).

Fluorine (F⁻) is most soluble (≤ 8 wt.%) at low pressures (< 5 kbars) and is likely to stay dissolved in the liquid much longer than H₂O (e.g., Dingwell and Mysen, 1985; Dingwell, 1989; Carroll and Webster, 1990; Giordano et al., 2004), therefore it continues to have an effect in otherwise thoroughly de-gassed sub-liquidus melts (Lange, 1991; Fig. 1-19d). F⁻ is an effective de-polymerizing agent because it breaks Al₂O₃ framework molecules and forms AlF and GaF molecules that prevent the incorporation of framework-linking ions (Dingwell et al., 1985). Chlorine (Cl⁻) has a similar, though weaker, effect by removing Na⁺ framework-linking ions as NaCl (halite) molecules (Carroll and Webster, 1990).

Crystal content

Because most magmas have temperatures often below their liquidus ‘real’ liquids must be considered as a coupled liquid-crystal system. Crystal content correlates positively with viscosity, independent of temperature (McBirney and Murase, 1984), for example, a 20% increase in crystal volume fraction produces a half log unit increase in viscosity (Lejeune and Richet, 1995; Fig. 1-20a). At 40% crystal content there is a major increase in viscosity due to the onset of inter-crystal interferences (Stevenson et al., 1996), at contents $\geq 70\%$ melts have a brittle rheology as they behave like solids.

Vesicularity

The presence of bubbles can significantly effect the bulk viscosity of an evolved liquid in a similar way to the presence of crystals (Bagdassarov and Dingwell, 1992; 1993; Stein and Spera, 1992; Manga et al., 1998; Manga and Loewenberg, 2001; Fig. 1-20b). Vesicularity is proportional to viscosity, and at low temperatures magmatic emulsions show non-Newtonian behaviour at very low bubble fractions ($\phi < 0.03$ vol.%; McBirney and Murase, 1984).

Emplacement temperature

The emplacement temperature is assumed to be equal to, or somewhat less, than the magmatic temperature, which can be estimated from mineral-phase equilibria (e.g., Fe – Ti oxide geothermometry), and is effected by cooling during transport (Thomas and Sparks, 1992), for example, by the admixing of cold air into the pyroclastic density current (Freundt, 1998; 1999). Published magmatic temperatures for rhyolites range from ~1150°C (Chapeco volcanic field, Paraná, Brazil; Kirstein et al., 2001) to ~660°C (Ammonia Tanks member, south-west Nevada volcanic field; Bindeman and Valley, 2003), and estimated emplacement temperatures range from ~950°C to ~100°C (Hildreth, 1983; Manley, 1992; Voight and Davis, 2000; Keating, 2005). Estimates of temperature loss during transport of pyroclasts from a specific eruption vary from 100°C to 150°C (Riehle et al., 1995; Sheridan and Wang, 2005), suggesting that a pyroclastic density current erupted well above the optimal welding temperature will deposit an ignimbrite that is also above this value, and therefore will readily weld. Furthermore, the range of eruption and emplacement temperatures reported corresponds positively with the range in welding intensities exhibited by different deposits.

Welding in high-grade tuffs

The concept of ‘ignimbrite grade’ is qualitative assessment of the degree of welding a unit has undergone (Walker (1983), and its categories generally approximate a the range of pyroclast rheologies from fluidal (very low viscosity) to brittle solids (very high viscosity). The ‘ignimbrite grade continuum’ provides a conceptual framework linking the genesis of different grades of welded tuff, and demonstrates the variation in physical properties, eruptive and welding processes, and lithofacies between different grades (Table 1-1; Branney and Kokelaar, 1992). Five grade categories have been established: (1) fountain-fed lavas, (2) extremely high-grade, (3) high-grade, (4) intermediate-grade, and (5) low-grade.

The hottest pyroclasts will be liquid and coalesce on deposition in a similar way to Hawaiian-style fire-fountains (e.g., fire-fountain fed lava flows, Capaccioni and

Cuccoli, 2005), and proximal agglutinate spatter deposits (e.g., the Badlands Rhyolite vent, Manley, 1996a). Extremely high-grade tuffs (e.g., the Bad Step Tuff, Branney et al., 1992) are intensely welded, lava-like and rheomorphic throughout and may contain globules (Hay et al., 1979), and typically lack fiamme and a eutaxitic fabric. They are thought to weld predominantly by aggregation-welding. High-grade tuffs (e.g., the Green Tuff, Mahood and Hildreth, 1986) are welded throughout, with intensely welded and rheomorphic zones, and they typically contain fiamme and exhibit a eutaxitic fabric. They are thought to weld by a combination of load-welding and aggregation-welding, with aggregation-welding dominant in intensely welded zones. Intermediate-grade tuffs (e.g., the Bishop Tuff, Wilson and Hildreth, 1997) are composed of non-welded upper and lower parts and a central welded zone, where they are characteristically pumice and fiamme-rich in respective zones. Intermediate-grade tuffs are typical of load-welding, and thermal and mechanical models of load-welding have been based on observations from these types of deposit (e.g., Smith and Bailey, 1966; Sheridan and Ragan, 1976; Peterson, 1979; Streck and Grunder, 1995; Wilson and Hildreth, 2003; Grunder et al., 2005; Quane and Russell, 2005a). Low-grade tuffs are non-welded, and may be totally non-consolidated or weakly lithified (sintered) by post-depositional cementation by vapour-phase crystallization.

Rheomorphism in tuffs

Rheomorphism is the hot-state ductile flow of welded tuff during or immediately after deposition, and was first described in terms of a process by Schmincke and Swanson (1967). That rheomorphism occurs during the emplacement of high-grade and extremely high-grade tuffs is irrefutable, however aspects such as the timing of rheomorphism relative to deposition and welding, and the deformation styles remain uncertain.

It has been suggested for extremely high-grade tuffs and some high-grade tuffs, that aggregation-welding is accompanied by rheomorphic flow, so called ‘syn-depositional’ or ‘primary’ welding (Branney and Kokelaar, 1992; Freundt, 1998).

Three mechanisms are thought to combine to make the freshly deposited and welding mass flow: (1) gravity, if deposited on a slope; (2) lateral momentum of aggrading pyroclasts; and (3) shearing by an over-passing pyroclastic density current, loosely analogous to the generation of waves by the fetch of wind on the sea surface. Syn-depositional rheomorphism is supported by field evidence: (1) the development of pervasive, small (relative to deposit thickness) folds and sheath folds, interpreted to have formed in narrow shear zones (e.g., Branney et al., 2004b). (2) The variation in linear fabric and sheath fold axes orientation with height through deposits, interpreted to record repeated switching of the flow direction during emplacement (e.g., Branney et al., 2004b). (3) The pervasiveness of rheomorphic structures in rapidly chilled proximal spatter deposits, that have been interpreted to record brief periods of intense rheomorphic flow (e.g., Furukawa and Kamata, 2004). (4) The pervasiveness of rheomorphic structures (e.g., folded planar fabrics and linear fabrics) throughout the deposit, from bottom to top (e.g., Pioli and Rosi, 2005).

Syn-depositional rheomorphism is incompatible with load-welding, because load-welding requires time for the deposit thickness to increase, thereby increasing the load, and the gradual deformation of pyroclasts to create a welded mass. In contrast, post-depositional and post-welding, ‘secondary’, rheomorphism has been proposed, wherein *in situ* load-welding is followed (rather than accompanied) by gravity-driven rheomorphic flow of the deposit *en masse* (Wolff and Wright, 1981b). This can be envisaged as flow in a similar style to that of a silicic lava. Secondary rheomorphism is characterized by large folds that deform a significant thickness ($\leq 100\%$) of the deposit, these may be accompanied by thrusts and form ramp structures (e.g., Leat and Schmincke, 1993) similar to those in silicic lavas. Primary and secondary rheomorphism are not necessarily mutually exclusive, instead, it is likely that some deposits may experience both types of rheomorphism (e.g., ignimbrite ‘TL’, Sumner and Branney, 2002). Moreover, secondary flow of an extremely high-grade tuff that has undergone syn-depositional rheomorphism would be expected to produce complex refolded folds and interference patterns, as the primary rheomorphic fabric was deformed.

Fabrics and structures produced by rheomorphism in ignimbrites

Rheomorphic ignimbrites are characterised by the presence of a wide range of fabrics and deformation structures, some of which are similar to those in silicic lavas: (1) planar fabrics, (2) linear fabrics, (3) kinematic criteria, and (4) folds (Fig. 1-21). Rheomorphic ignimbrite typically exhibit pervasive and penetrative planar fabrics that may be defined by a eutaxitic fabric (Fig. 1-22; e.g. Schmincke and Swanson, 1967; Wolff and Wright, 1981b; Sumner and Branney, 2002), compositional-banding (e.g. Kobberger and Schmincke, 1999), imbricated fiamme (Schmincke and Swanson, 1967; Fig. 1-21), or vesiculated parting surfaces (e.g. Chapin and Lowell, 1979; Pioli and Rosi, 2005). Linear fabrics are common, and are often defined by a combination of stretched vesicles (e.g. Pioli and Rosi, 2005), stretched fiamme (Figs 1-21 and 22; e.g. Schmincke and Swanson, 1967; Sumner and Branney, 2002), and elongation lineations developed in the tuff matrix (e.g. Chapin and Lowell, 1979; Sumner and Branney, 2002). Kinematic criteria are often abundant, typically as rotated porphyroclasts including crystals and lithic clasts (e.g. Schmincke and Swanson, 1967). Finally, folds are abundant in rheomorphic ignimbrites deforming the pervasive planar fabric (Fig. 1-21). They are commonly heterogeneously distributed, cm- to m-scale and similar-style, and can occur in numerous different orientations and attitudes (e.g. Schmincke and Swanson, 1967; Chapin and Lowell, 1979; Wolff and Wright, 1981b; Branney et al., 1992; Pioli and Rosi, 2005). Sheath folds are common (Branney et al., 2004b) and are interpreted to have formed by progressive non-coaxial shear of originally cylindrical folds.

Some rheomorphic tuffs contain a great enough variety and abundance of fabrics and structures to enable a structural analysis to be carried out. The Grey's Landing ignimbrite, Twin Falls County, Idaho, USA, is one such deposit; combining a diverse range of planar and linear fabrics, kinematic criteria and folds in an exceptionally well-exposed and laterally extensive sheet. The remainder of this thesis will concentrate on the process of emplacement of the Grey's Landing ignimbrite.

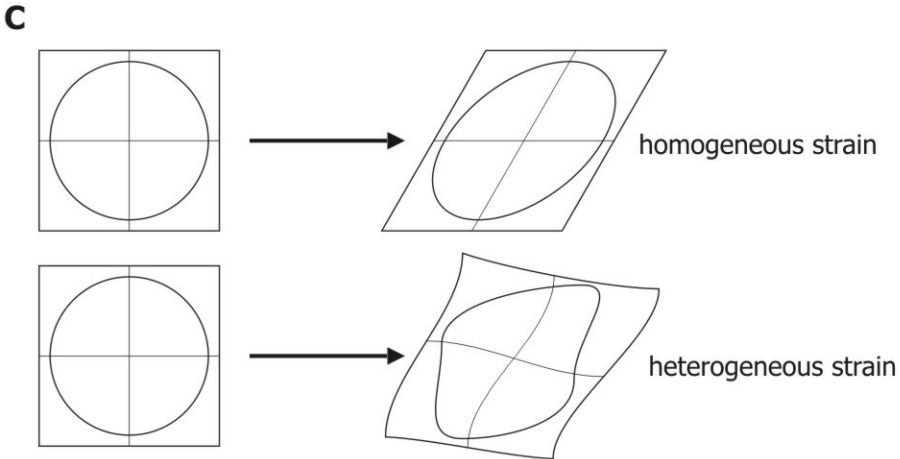
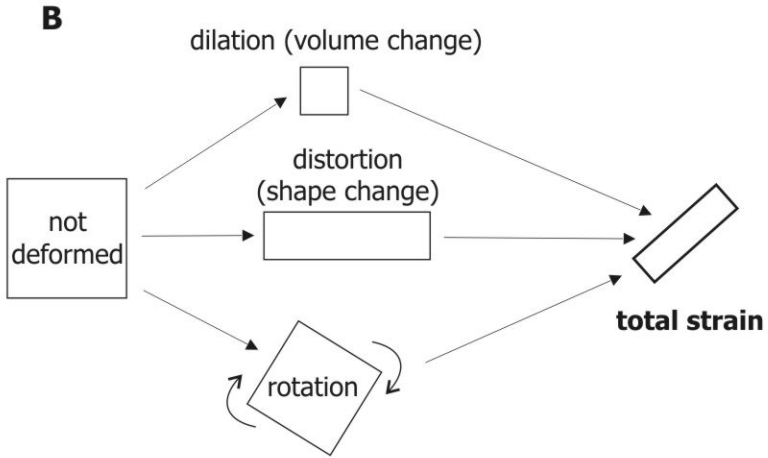
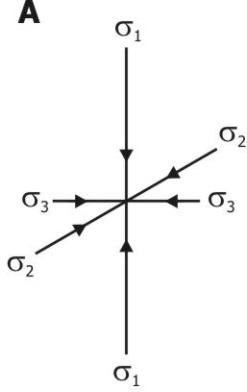


Fig. 1-1. Stress and strain. (A) the stress axial cross where the orientation and magnitudes of the three principal normal stresses are represented. (B) components of total strain (Park, 1989). (C) homogeneous and heterogeneous strain (Park, 1989). Note how heterogeneous strain causes straight and parallel lines to become curved and non-parallel, unlike homogeneous strain.

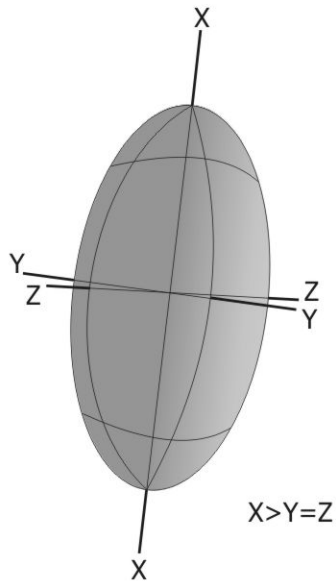
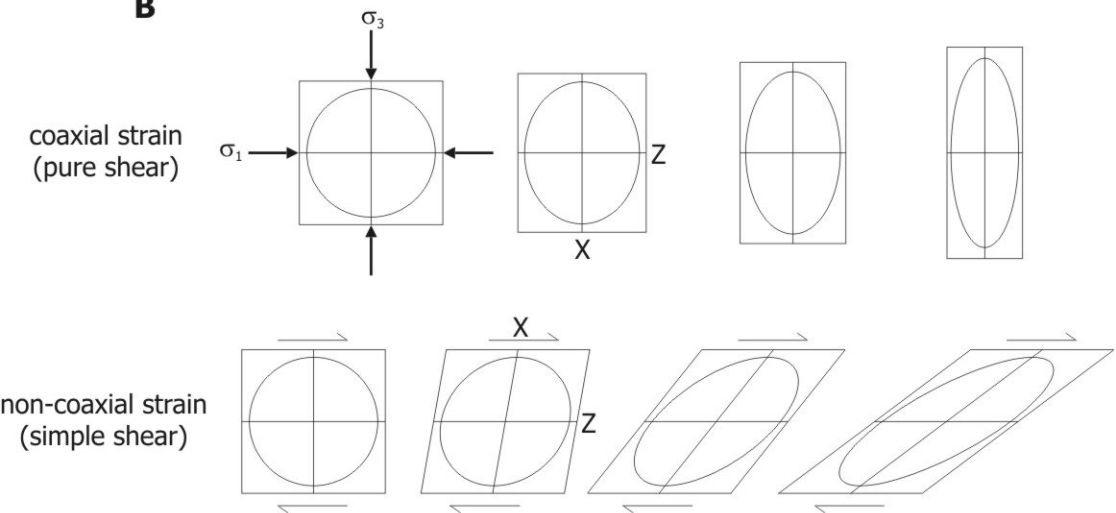
A**B**

Fig. 1-2. Strain (A) the three dimensional strain ellipsoid showing the principal strains $X > Y = Z$. (B) Progressive deformation in two dimensions during homogeneous coaxial (top) and non-coaxial (bottom) strains. Note how under both strain states, X lengthens while Z shortens.

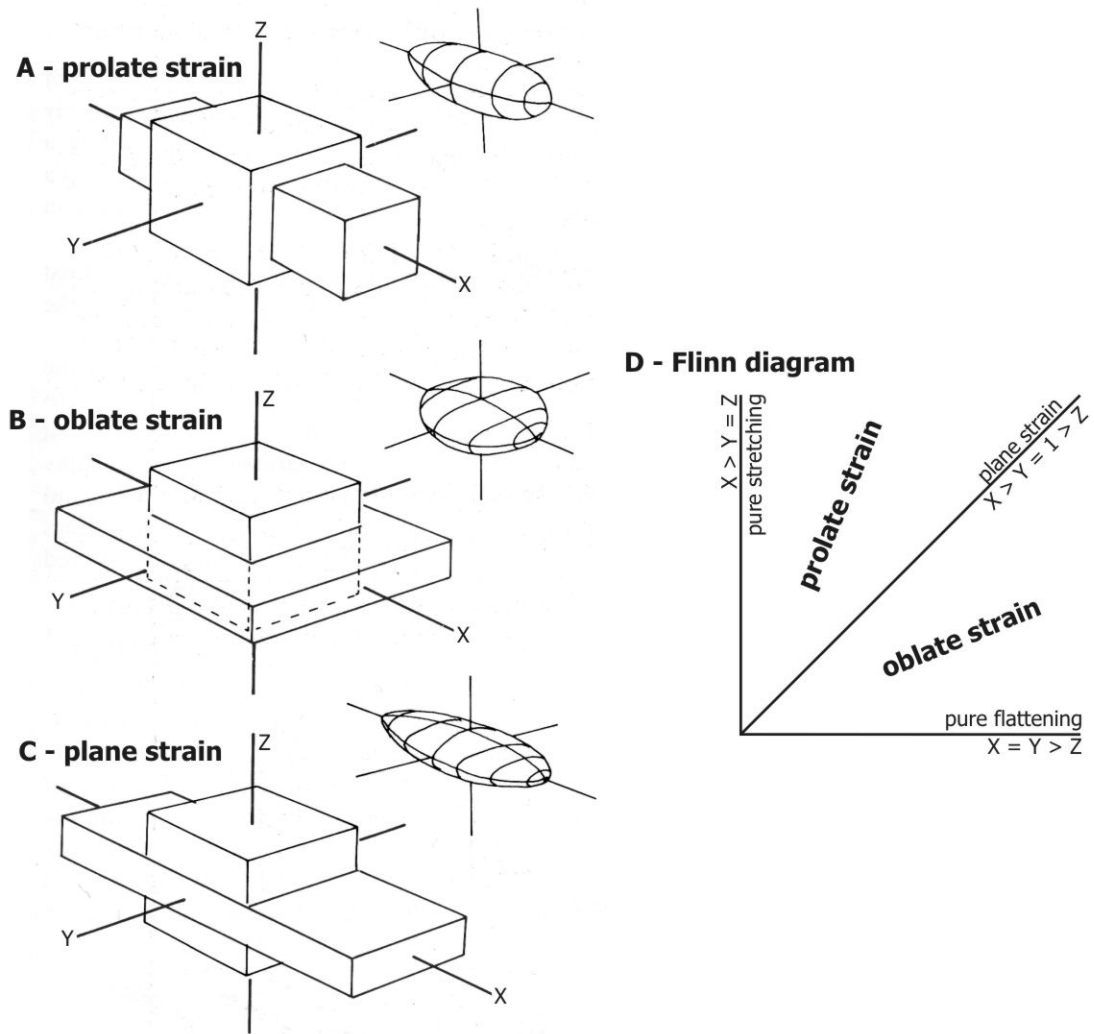


Fig. 1-3. Types of strain. (A) prolate strain (pure stretching). (B) oblate strain (pure flattening). (C) plane strain. (D) Flinn diagram showing relationship between prolate, oblate and plane strain. Adapted from Park (1989).

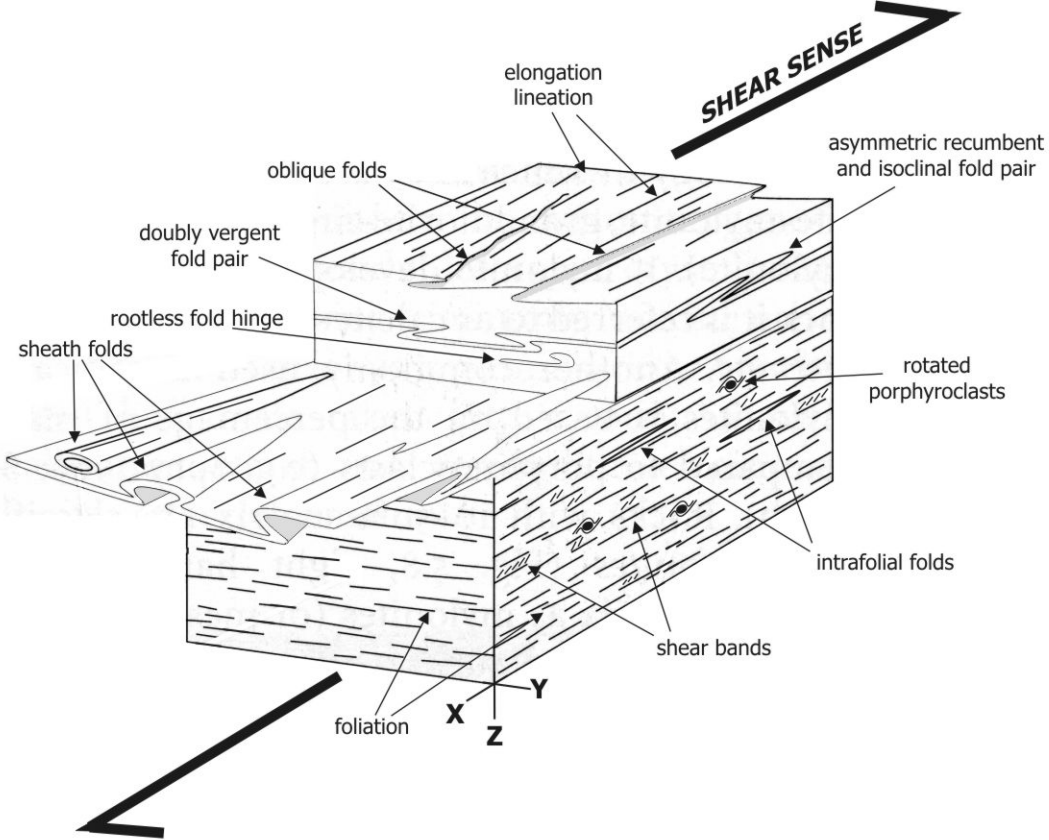


Fig. 1-4. Ductile shear zones. Schematic diagram showing the geometry of structures within a ductile shear zone or mylonite zone. Adapted from Passchier & Trouw (1996).

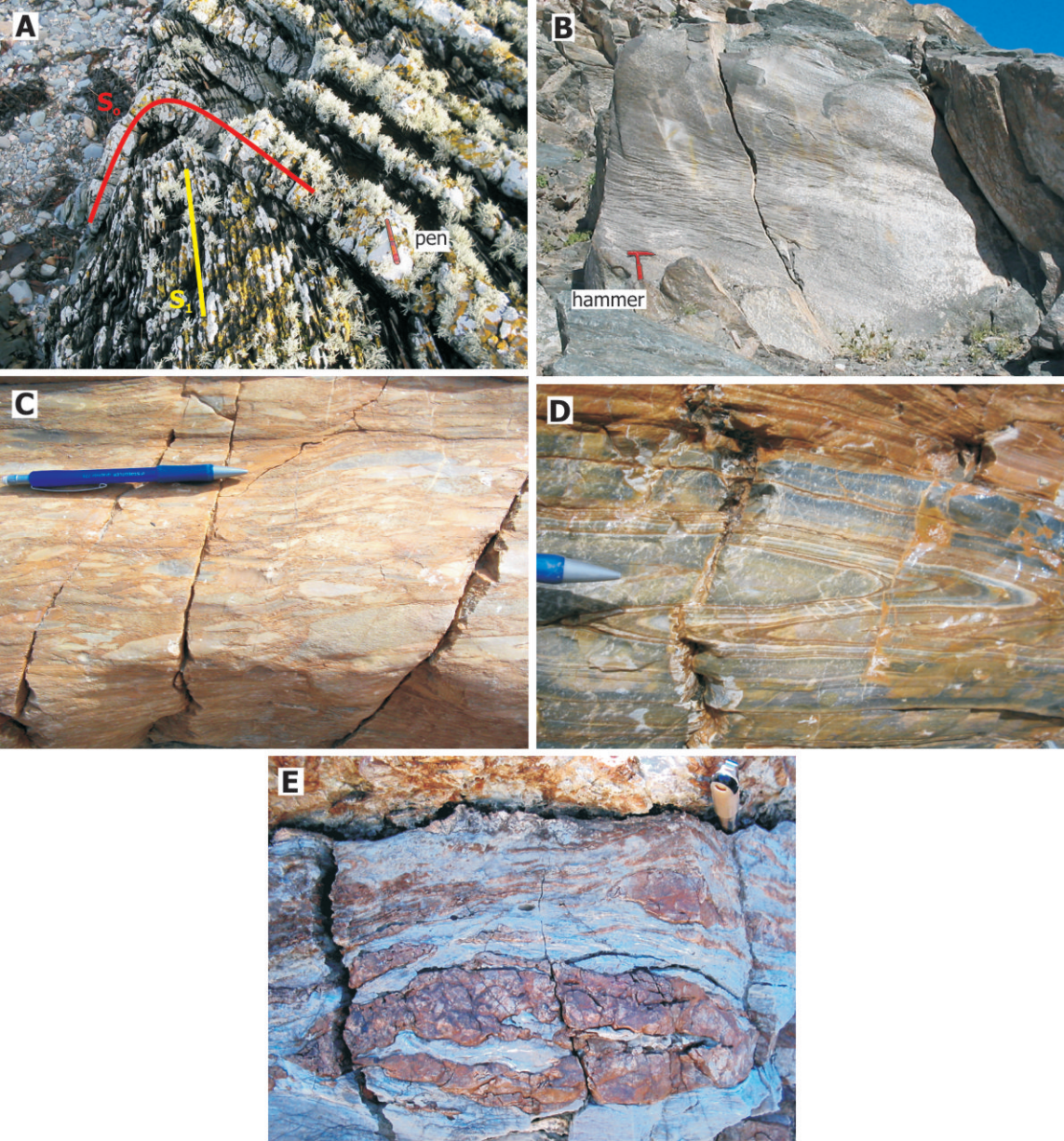


Fig. 1-5. Fabrics and structures in tectonic shear zones. (A) Vertical S_1 axial planar cleavage in folded S_0 turbiditic sandstones and shales, Kearney Group, Kearney Point, County Down, Northern Ireland. (B) Crenulation cleavage developed on in the hinge of a recumbent F_2 fold, folding S_1 axial planar cleavage, Orocopia schist, Orocopia Mountains, California. (C) Stretching lineation (parallel to pen) formed by the stretching of carbonate clasts in the Noonday Dolomite Formation, Mosaic Canyon, Death Valley, California. (D) Intrafolial fold within a transposed foliation. Noonday Dolomite Formation. (E) Eye structure viewed down the X axis (parallel to pen in top right). Calc-silicate mylonite in the upper shear zone of the Buckskin Mountains metamorphic core complex, Arizona.

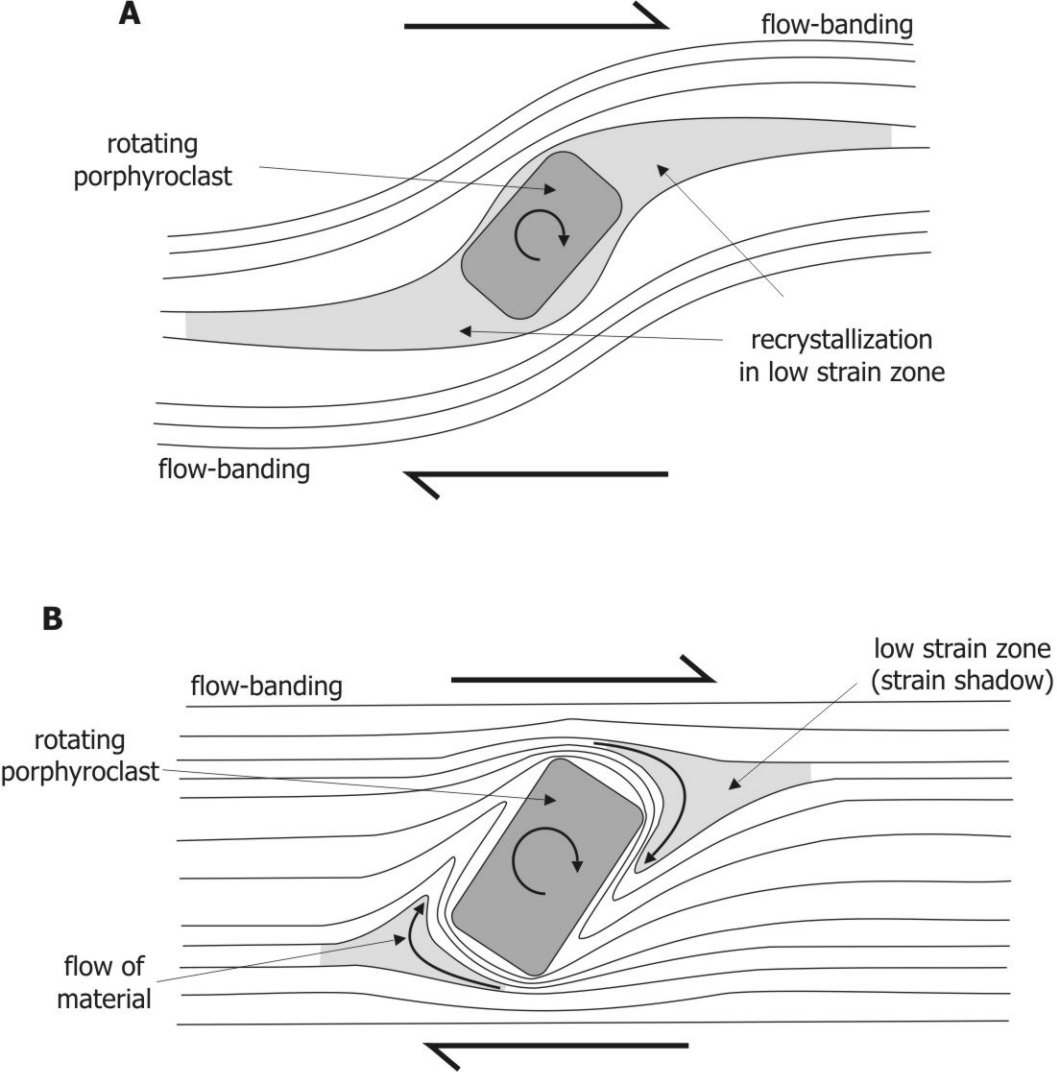


Fig. 1-6. Rotational shear sense indicators. Schematic diagrams showing (A) a σ -type porphyroblast, and (B) a δ -type porphyroblast, within a dextral shear regime; (adapted from Passchier & Trouw, 1996).

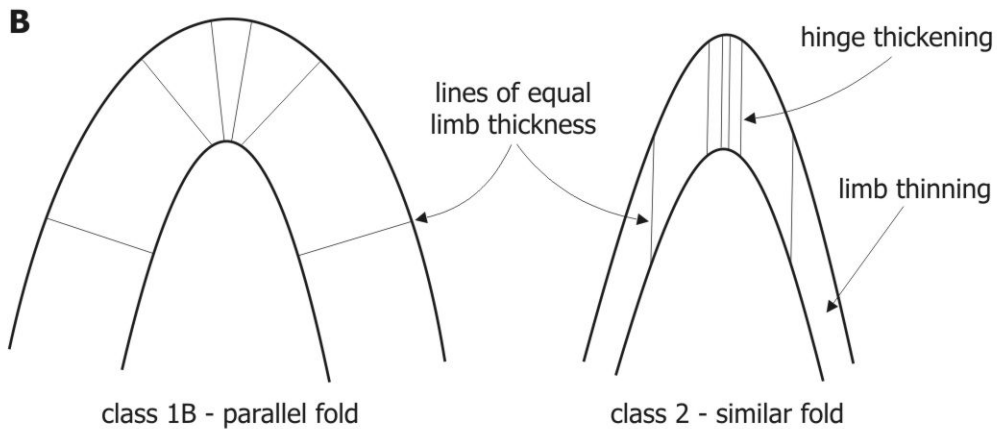
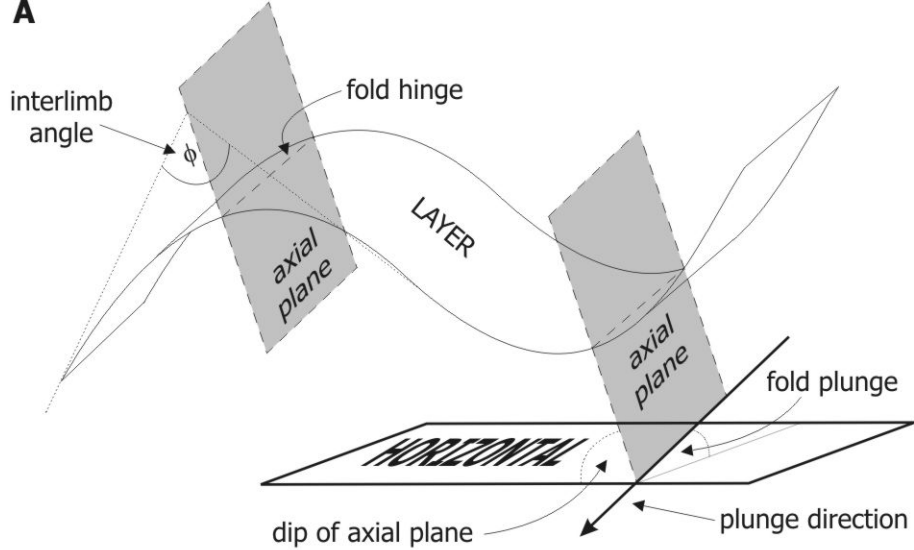


Fig. 1-7. Fold morphology. (A) the minimum morphological characteristics required to describe a fold. (B) fold classes based on differences in the curvature of adjacent folded surfaces, and thickness variation about the fold axis (Ramsey, 1967).

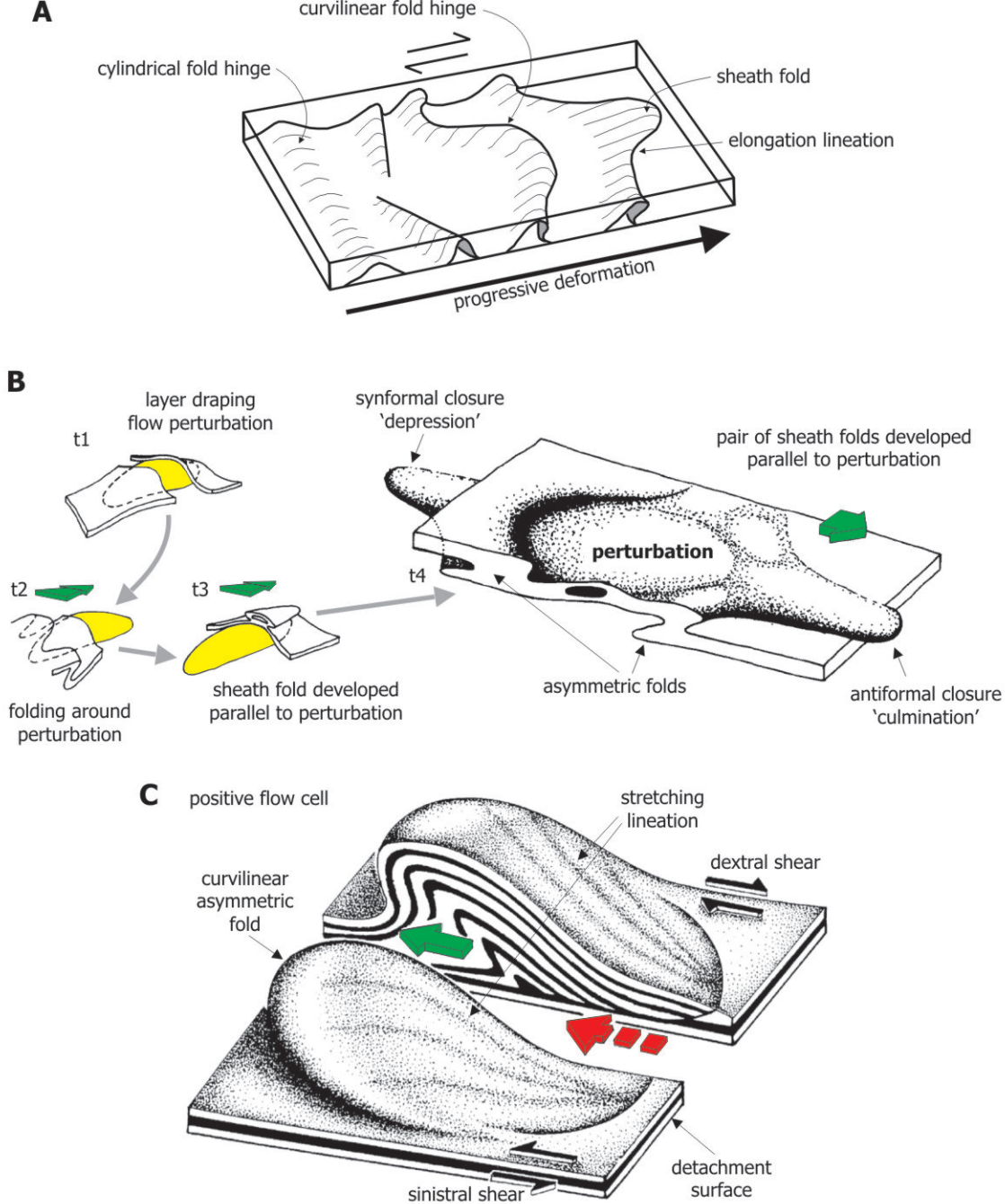


Fig. 1-8. Mechanisms for the development of sheath folds. (A) rotation and stretching of an initially cylindrical fold during progressive, non-coaxial deformation. (B) heterogeneous stretching and folding of a layer around a rigid perturbation, during non-coaxial deformation (modified from Marques & Cobbold, 1995; and Rosas et al., 2002). (C) formation of a sheath fold by differential shear surrounding a positive flow cell (modified from Alsop & Holdsworth, 2002).

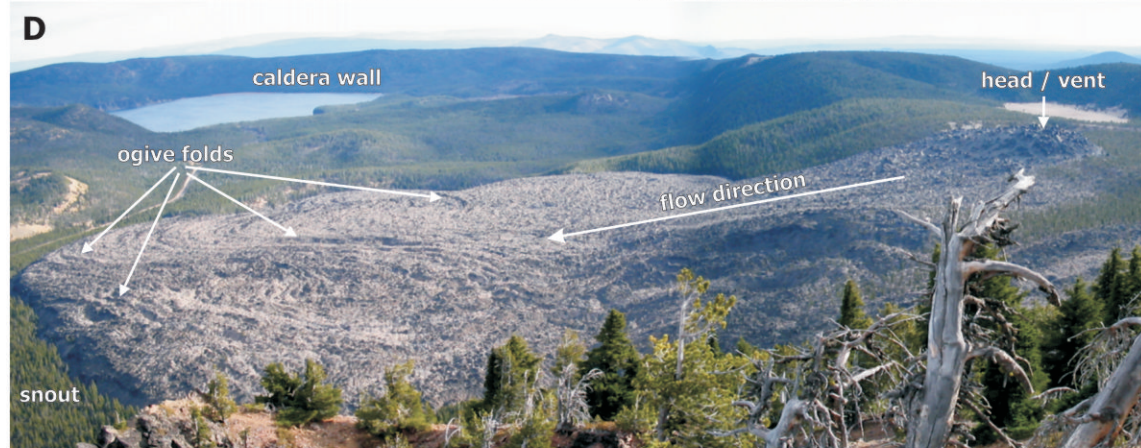
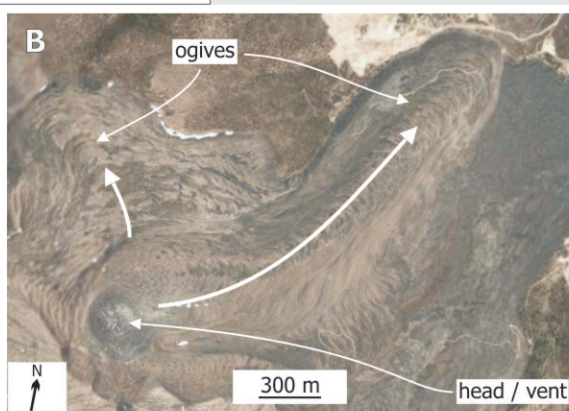
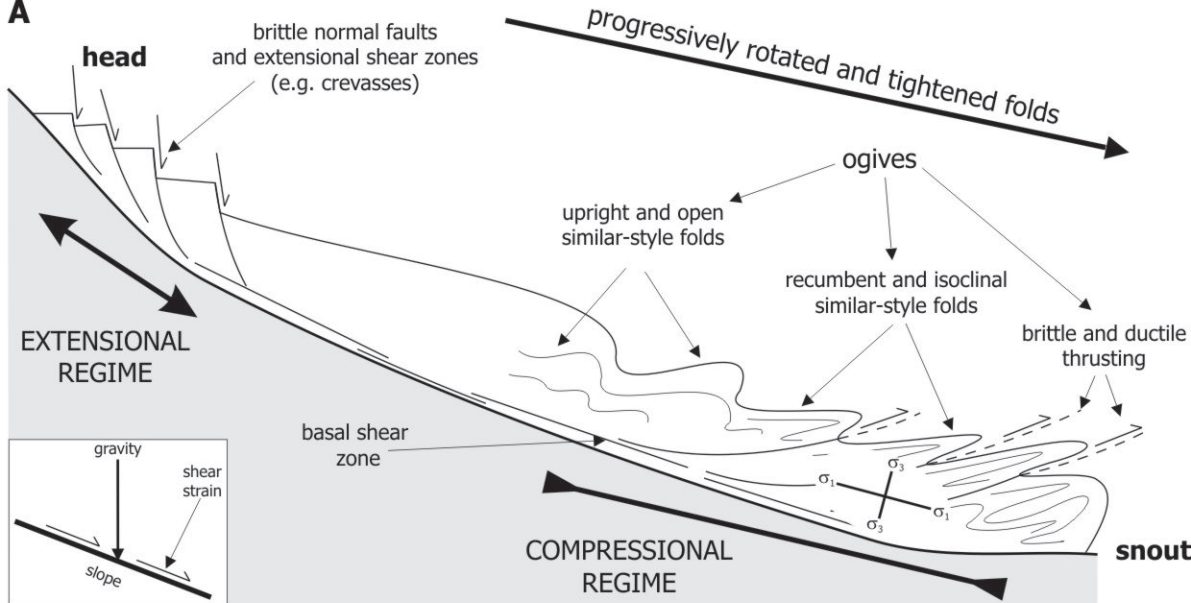


Fig. 1-9. Non-particulate gravity currents. (A) Conceptual cross-section (flow parallel) showing the association of major ductile and brittle structures within a typical non-particulate gravity current and the local strain orientation. Not to scale. Note the concentration of brittle structures at the surface and ductile structures within the current. (B) True colour Landsat 7 image of part of the Big Glass obsidian flow, Medicine Lake Highland, California, showing regularly-spaced (30 m) surface ogive structures convex away from the vent. © Google Earth™ 2005; © Image 2005 EarthSat™. (C) False colour Landsat 7 image of an un-named namakier at Shah Gheyb, 75 km ENE of Lar, Zagros Mountains, southern Iran, showing regularly-spaced (80 m) circumferential ogives. © Google Earth™ 2005; © Image 2005 EarthSat™. (D) panoramic view of the Big Obsidian Flow, Newberry Crater, Oregon, looking east. Note the vent area to the right high on the caldera margin, and the broad flat snout with ogive folds.

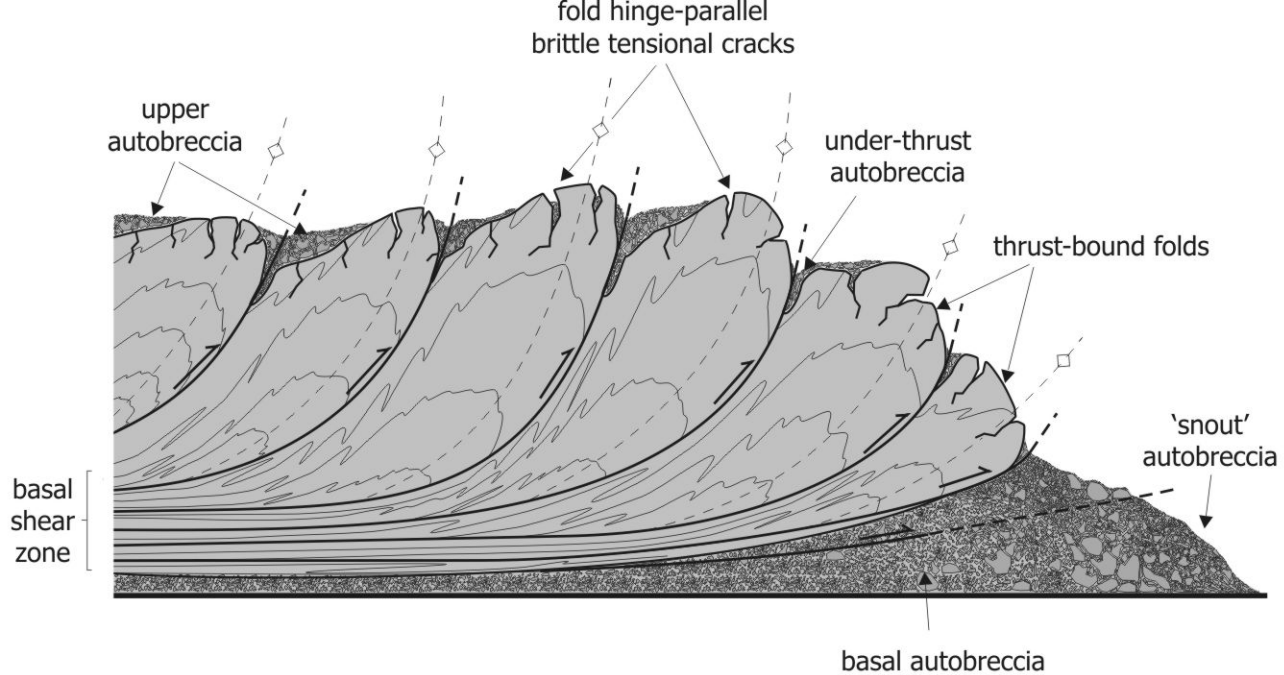


Fig. 1-10. Schematic cross-section through the snout of a silicic lava showing the nature of ramp structures. Ramps, separated by brittle thrusts, form circumferential ogives in plan view.

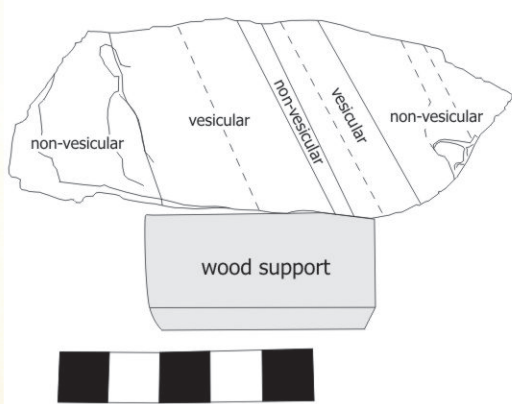


Fig. 1-11. Hand specimen and interpretive sketch showing flow-banding defined by variations in vesicle concentration. Rhyolitic obsidian (pitchstone), Judd's Dykes, Isle of Arran, Firth of Clyde, Scotland.

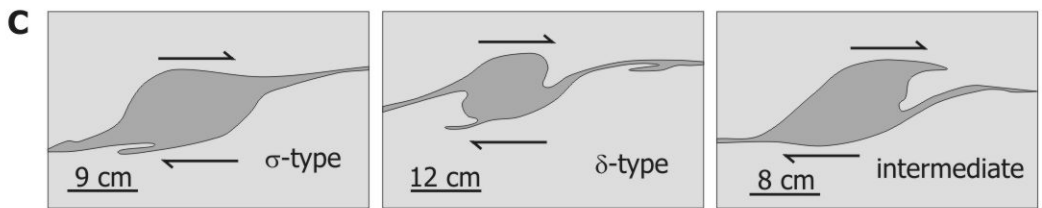
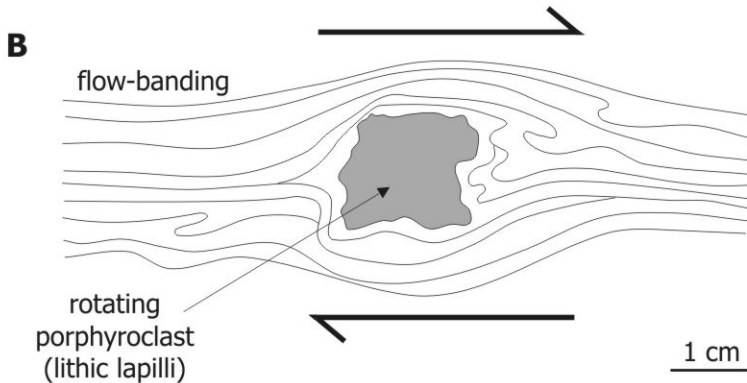
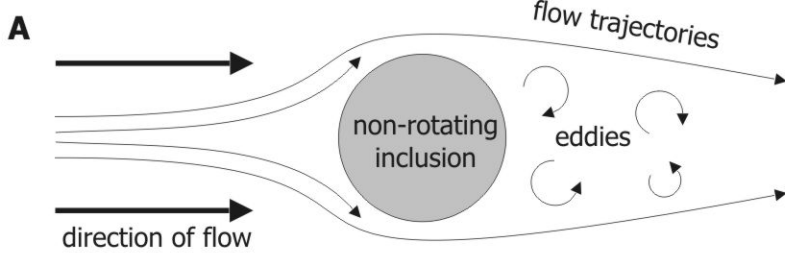


Fig. 1-12. Kinematic indicators in lavas. (A) Porphyroclasts as shear sense indicators as proposed by Cummings (1964). Modified after Cummings (1964), not to scale. (B) δ -type porphyroclast in flow-banded rhyolite lava (Christiansen & Lipman, 1966). (C) Three shapes of mingled-magma blebs (Ventura, 1998); σ -type, δ -type and intermediate σ/δ -type.

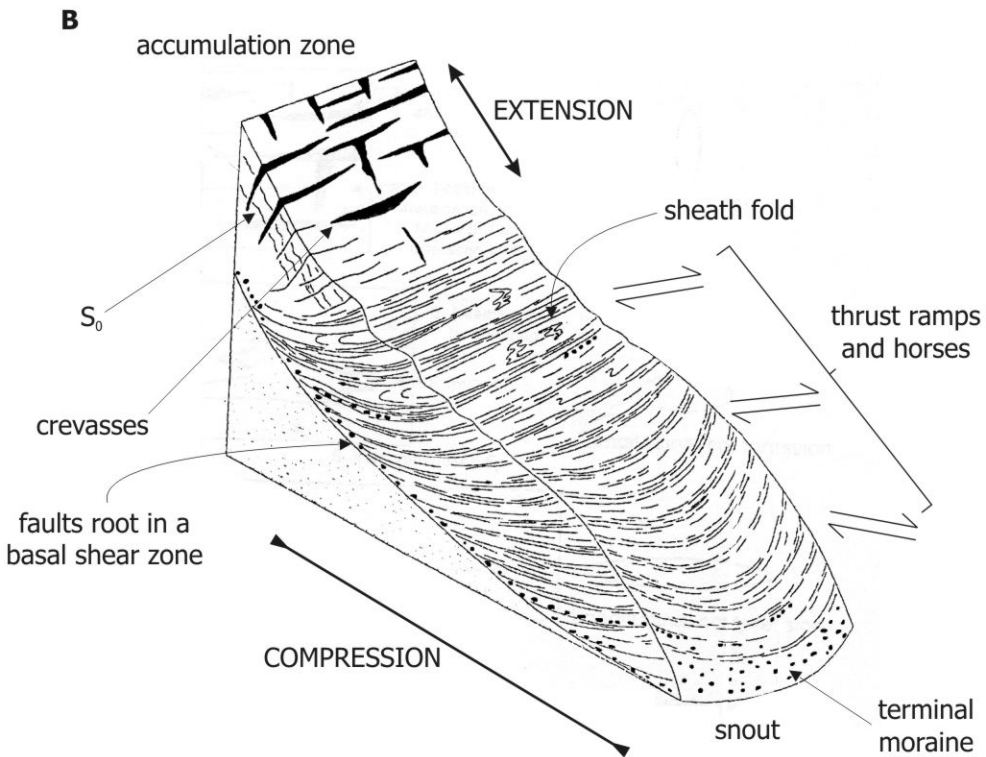
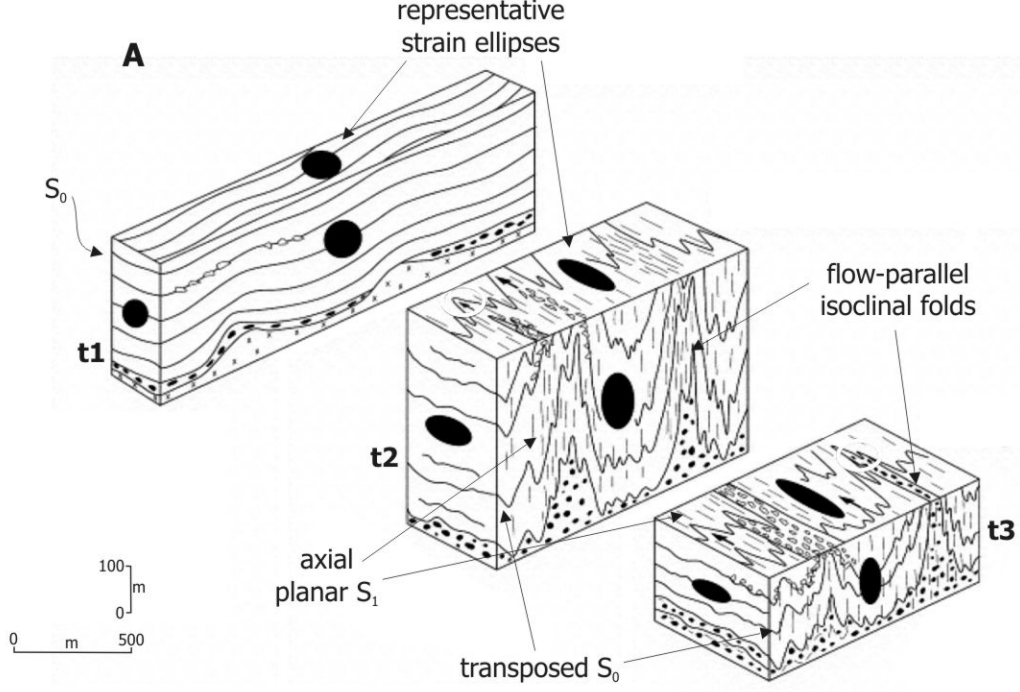


Fig. 1-13. Ice glaciers - incompatible longitudinal sections. (A) schematic time-slice cross-sections through a laterally constricted glacier showing the development of a transposed originally planar fabric and the formation of vertical isoclinal folds and axial planar cleavage (modified from Hambrey and Glasser, 2003). (B) schematic representation of the spatial distribution of extensional (crevasses) and compressional (sheath folds and thrust ramps) structures in an ideal glacier (modified from Goodsell et al., 2002). Note that the folded and thrust planar fabric is not specified, nor is a basal shear zone indicated in the original.

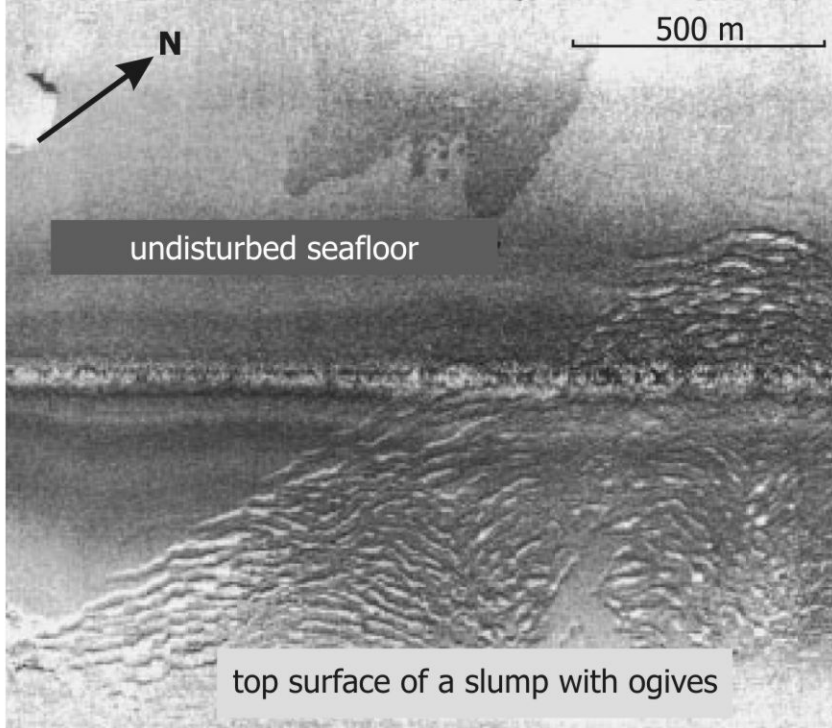


Fig. 1-14. Sedimentary slumps. Sidescan sonar image of the top surface of a slump deposit at the Grand Banks, North Atlantic, south of Newfoundland, Canada. Note the uneven surface disrupted by ogives, relative to the even seafloor. Modified from Piper et al. (1999).

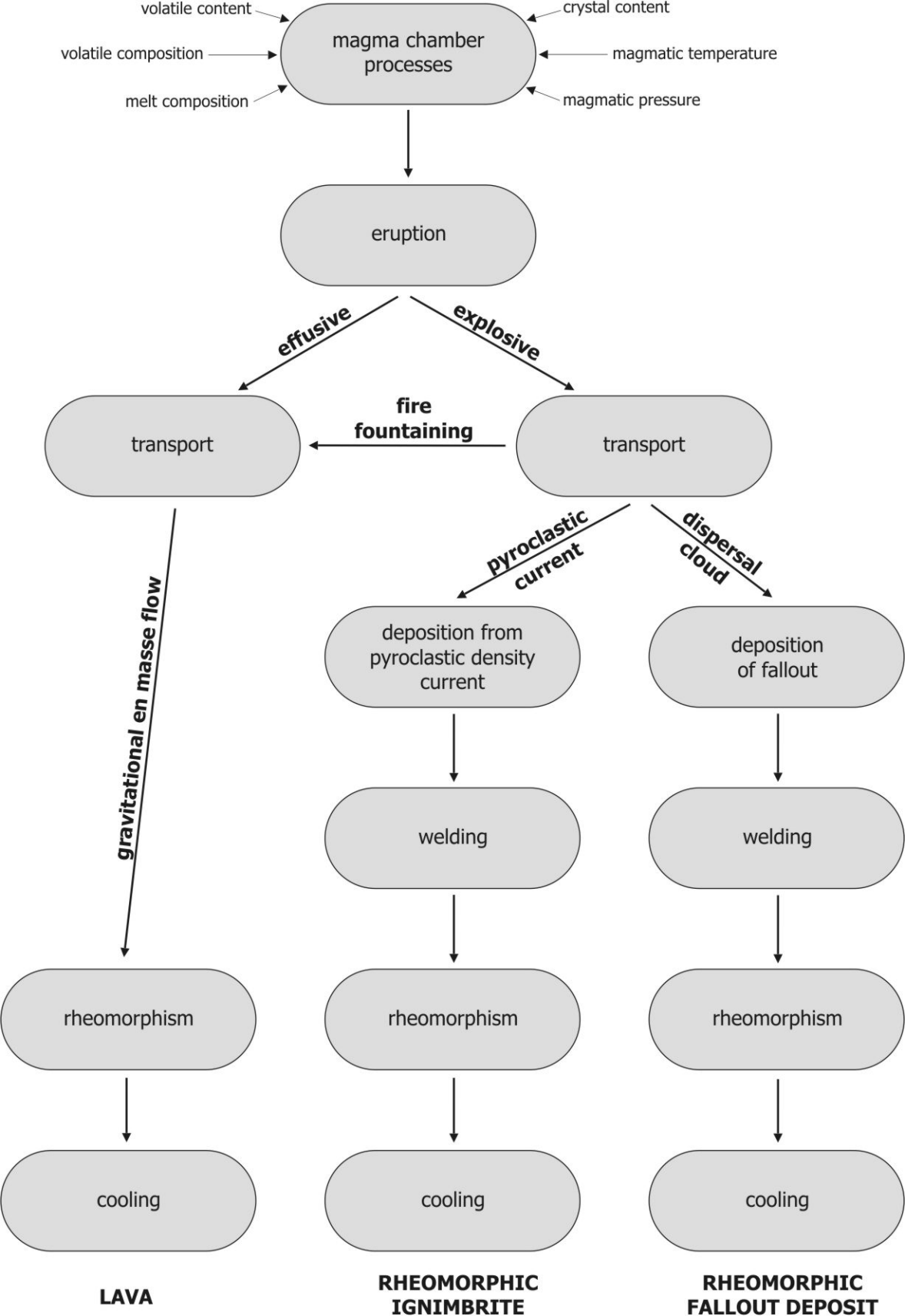


Fig. 1-15. Simplified flow-diagram demonstrating the seven key stages of the formation of rheomorphic tuffs. Note that lavas and rheomorphic tuffs may all be formed from the same ideal magma chamber.

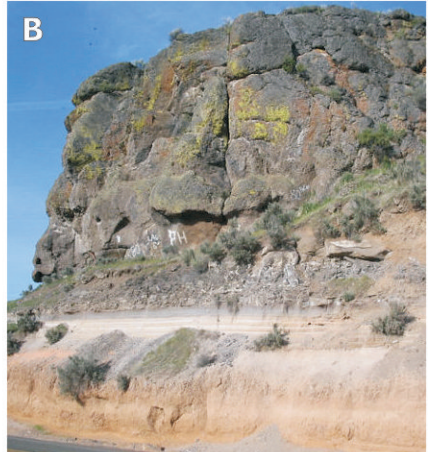


Fig. 1-16. (A) Eutaxitic fabric of obsidian blocks in the base of the moderately-welded Arico ignimbrite (~4 m thick), Tenerife. (B) Massive, intensely-welded Rattlesnake Tuff (~12 m thick) lying on a non-welded fall deposit; Burns, Oregon. (C) Columnar-jointed, massive, moderately-welded Bandelier Tuff (half-way up slope); Jemez Canyon, Jemez Mountains, New Mexico. Note how the Bandelier Tuff thickens from left to right, into a palaeo-valley developed in the orange-red Abo Sandstone Formation.

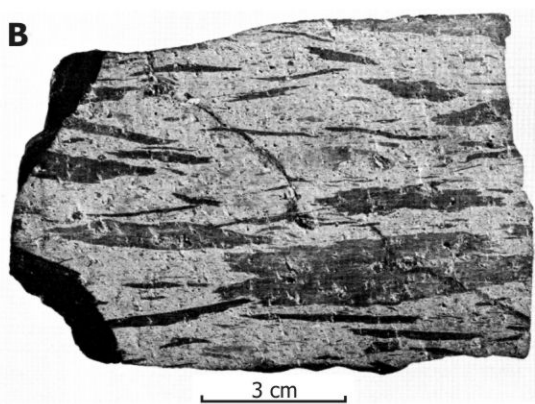
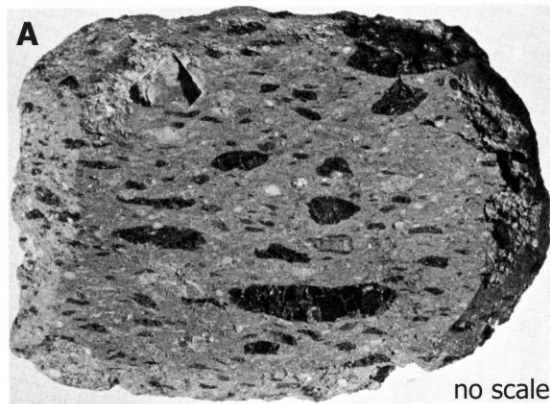


Fig. 1-17. Samples of eutaxitic welded tuff. (A) Bandelier Tuff, Jemez Springs, New Mexico (Ross & Smith, 1961, p. 4). (B) Un-named tuff, Guerrero, Mexico (Ross & Smith, 1961, p. 29). Note the characteristic 'flame'-ended fiamme in the lower sample.

dynamic and turbulent pyroclastic density current

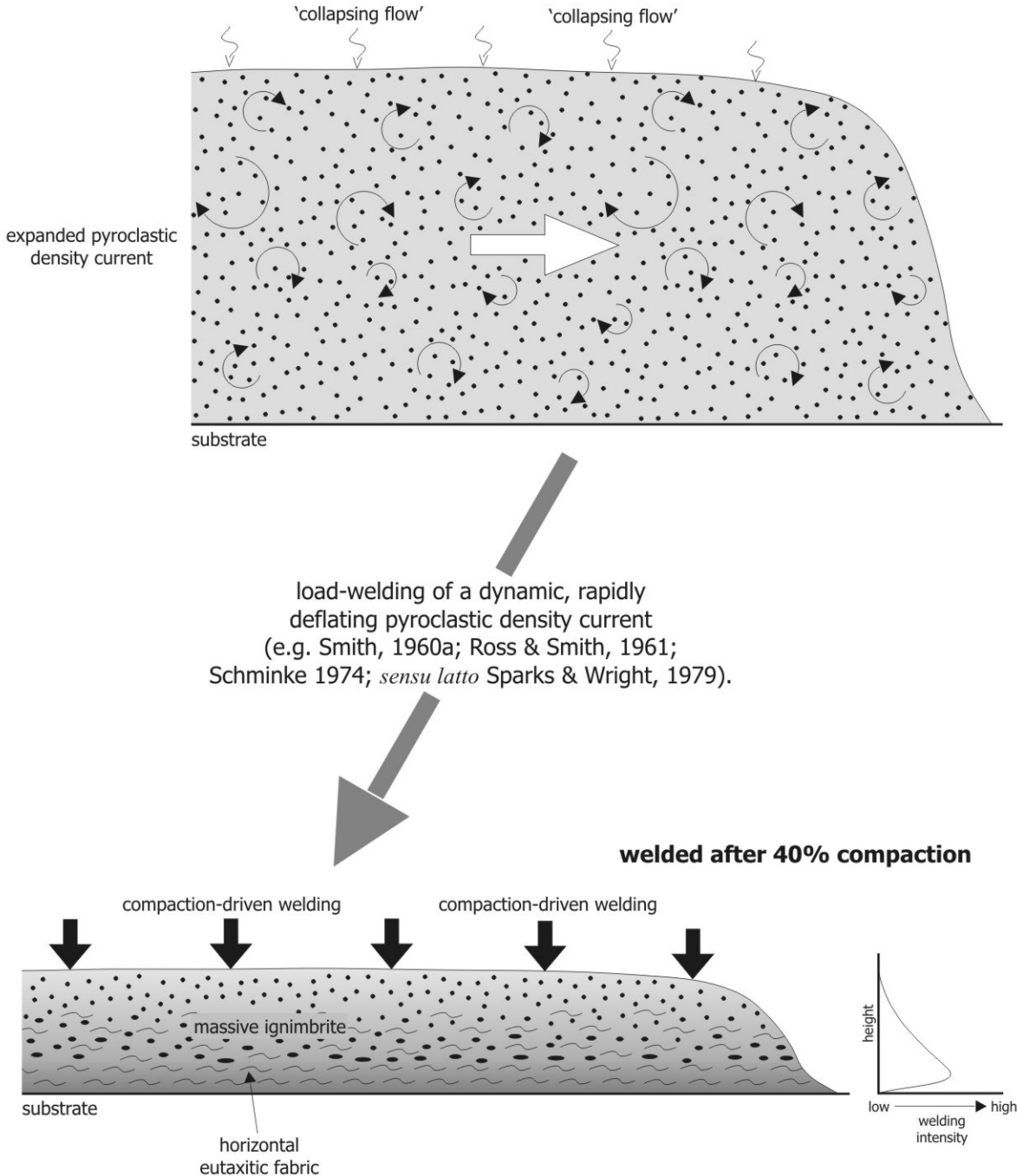


Fig. 1-18. Schematic representation of load-driven welding. A representative welding profile (bottom right) demonstrates the greatest strain (based on flattening of pumice / fiamme) in the lower-central part of the deposit.

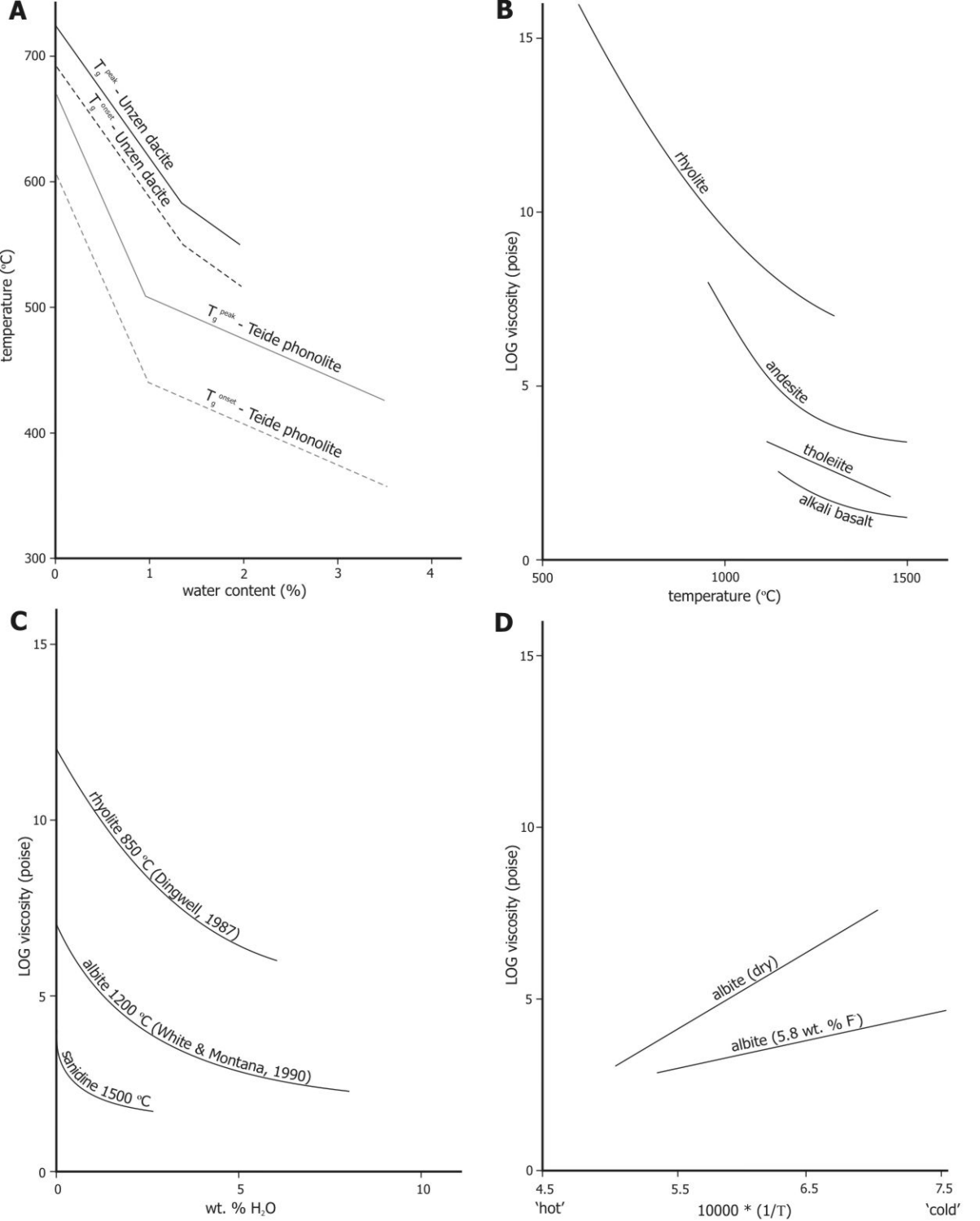


Fig. 1-19. (A) Variation of experimentally determined T_g with water content in a phonolite (Teide, Tenerife) and a dacite (Unzen, Japan). Modified from Giordano et al. (2005). T_g^{onset} is the lower end of the T_g temperature range, below which the glass behaves rigidly. T_g^{peak} is the upper end of the T_g temperature range, above which the glass behaves as a liquid. (B) Experimentally estimated viscosities of common magma types (Murase & McBirney, 1973; McBirney & Murase, 1984). (C) Compilation of experimental data, showing the influence of H_2O on melt viscosity (Lange, 1992). Sanidine data from Shaw (1963). (D) Compilation of experimental data, showing the influence of F^- on melt viscosity, modified from Lange (1992). Dry albite data from Urbain et al. (1982), albite with 5.8 wt. % F^- from Dingwell et al. (1985). Note the inverse temperature scale.

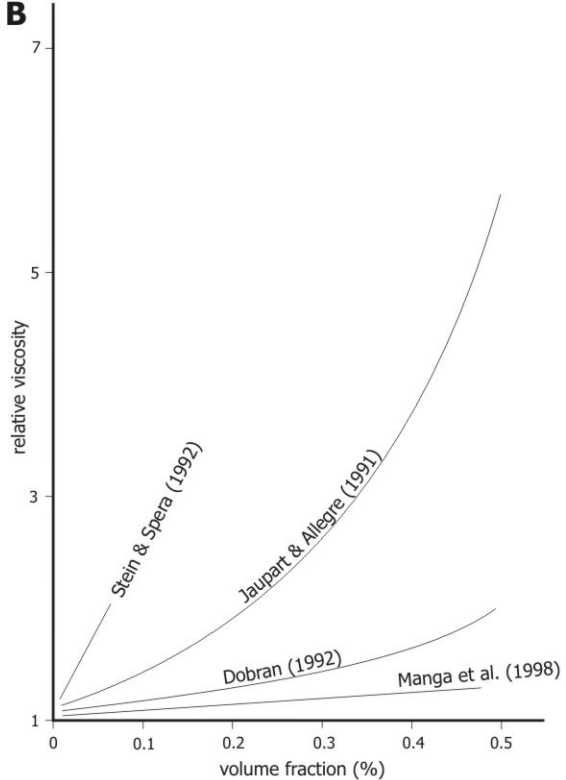
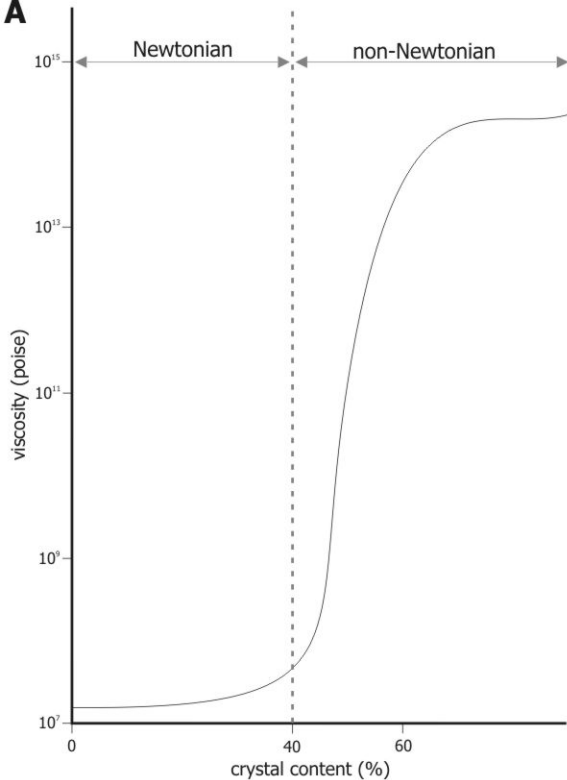


Fig. 1-20. (A) The influence of crystal content on melt viscosity (Lejeune & Richet, 1995). (B) The influence of vesicle volume fraction on silicate melt viscosity (Manga et al., 1998).

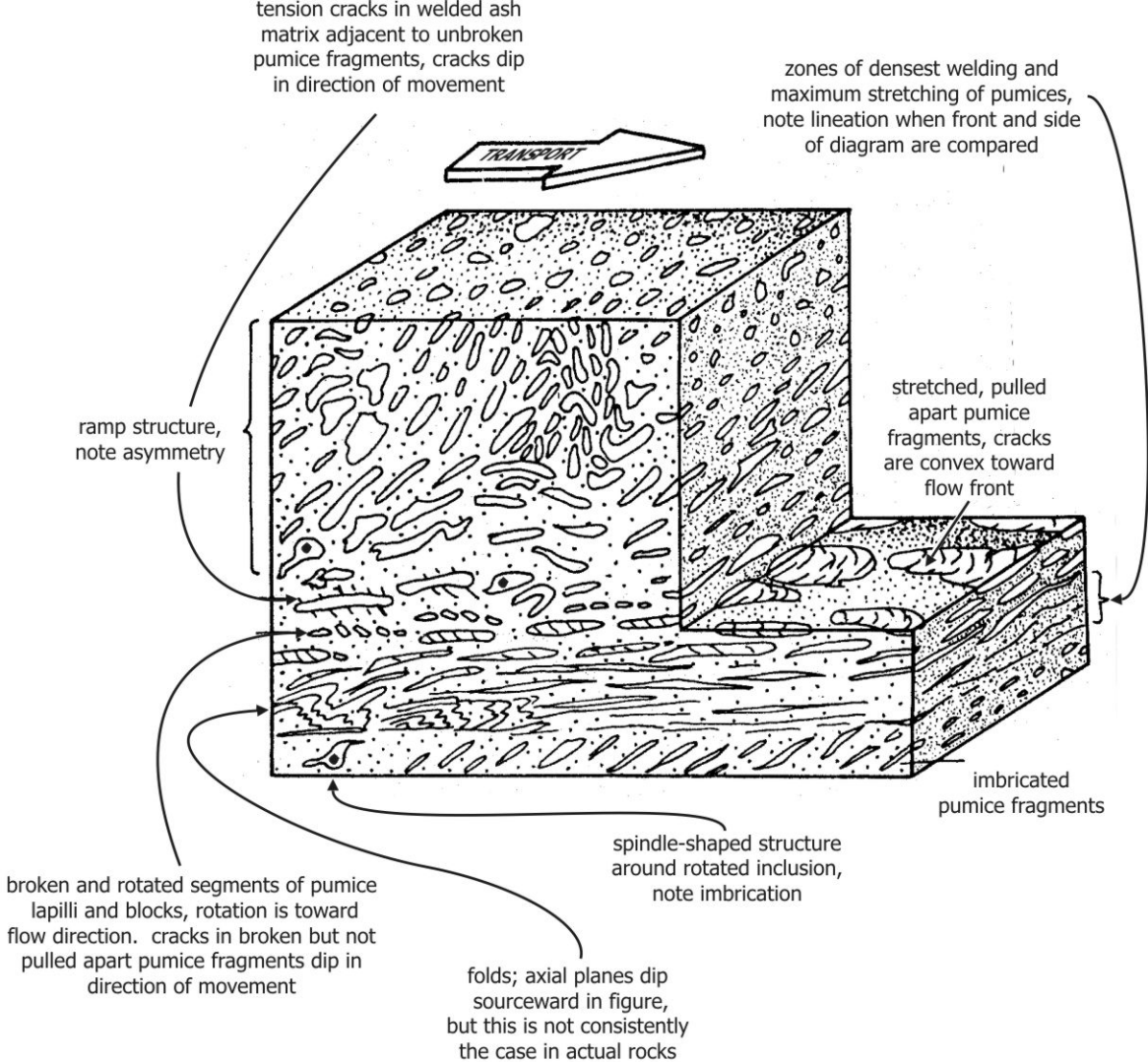


Fig. 1-21. Schematic block diagram showing flowage structures in a single rheomorphic tuff from Gran Canaria, Schmincke & Swanson (1967).

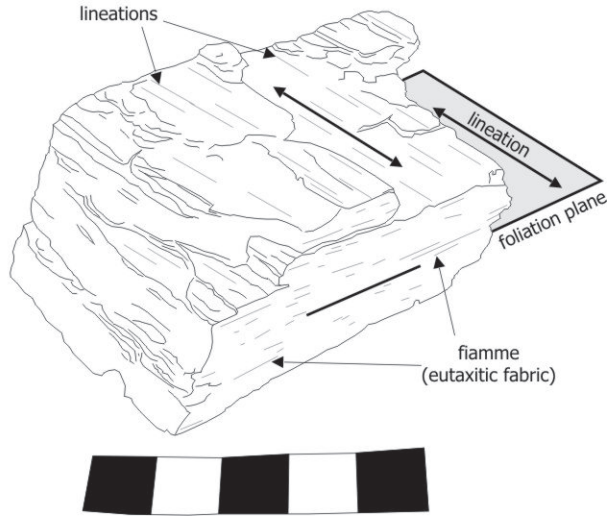


Fig. 1-22. Planar and linear fabrics. Photo and sketch interpretation of foliated and lineated (L/S tectonite) rheomorphic ignimbrite 'D', Mogan Formation, Gran Canaria, Spain. Scale bar 5 cm.

Chapter 2:

The Rogerson Formation and its relation to the Yellowstone – Snake River Plain volcanic province

Introduction

The late – Miocene Rogerson Formation (new name) is a previously not described formation within the Yellowstone – Snake River Plain volcanic province (Fig. 2-1). The Rogerson Formation records the emplacement of several high-grade rhyolitic ignimbrites erupted from eruptive centres in south-central and southwestern Idaho. It is thought to record the transition of volcanic activity from the Bruneau – Jarbidge area to the Twin Falls area because of the migration of the Yellowstone hot-spot and contemporaneous extension forming the West Snake River Plain graben. It is probably the western-most, and oldest, graben-fill succession adjacent to the southern margin of the Yellowstone – Snake River Plain volcanic province identified so far.

The Rogerson Formation is atypical of volcanic successions in most other volcanic provinces because of the preponderance of high- and extremely high-grade ignimbrites. Two of the ignimbrites are lava-like and rheomorphic. The formation also includes massive and bedded, non-welded volcanoclastic deposits with intercalated palaeosols, but pumice-fall deposits are sparse and pumice-rich ignimbrites typical of Plinian-style volcanism are absent. The physical volcanology of the Rogerson Formation is, however, typical of many ignimbrite successions in the central and southwestern Snake River Plain.

Regional setting – Miocene to Present volcanism in the intermontane northwest USA

Introduction

The Yellowstone – Snake River Plain volcanic province is widely acknowledged as the ‘text-book’ example of a continental hot-spot track (e.g., Morgan, 1971; Hall, 1996), forming an integral part of the youngest, largest, and best exposed continental large igneous province (LIP) on Earth. Recent advances in the understanding of Yellowstone – Snake River Plain volcanic province have concentrated on three distinct aspects: (1) the causes of asthenospheric melting: mantle plume or lithospheric extension; (2) the inception of magmatism and the relationships between neighbouring and contemporary volcanic provinces (e.g., Carlson et al., 2005); and (3) investigating the nature of the present-day Yellowstone thermal anomaly, especially with reference to the mantle-plume paradigm (e.g., Humphreys et al., 2000; Christiansen et al., 2002).

The Yellowstone – Columbia River ‘mega’-volcanic province

Several voluminous Neogene volcanic provinces in the intermontane United States (southern Idaho, northern Nevada, eastern Oregon, eastern Washington, and western Wyoming) are considered to make up the Yellowstone – Columbia River volcanic ‘mega-province’ (Fig. 2-1). This large area (~ 300,000 km²) is dominated by extensive high plains (≥ 2 km elevation) and trap-topography (e.g., Steens Mountain, Oregon; Mount Bennett Hills, Idaho; Fig. 2-1) incised by deep (≤ 1500 m) river-canyons (e.g., Hell’s Canyon, Idaho – Oregon border). It forms part of a north – south trending band of Cenozoic magmatism throughout the western Cordillera and Basin and Range province of the North American continent (Pierce and Morgan, 1992), from the central Mexican Sierra Madre Occidental to central British Columbia (Hooper et al., 2002).

The total volume of erupted material within the Yellowstone - Columbia River mega-province, since its inception at ~16.6 Ma (Camp and Ross, 2004), is \geq

350,000 km³ ($\geq 300,000$ km³ of basalt and $\geq 50,000$ km³ of rhyolite), with significant tephra deposits deposited across the western and central regions of the United States (e.g., Fleck et al., 1998; Rose et al., 2003; Sarna-Wojcicki et al., 2005). It is composed of five subordinate volcanic provinces (Camp and Ross, 2004; Fig. 2-1), in order of decreasing volume: (1) the Columbia River – Oregon flood basalts (e.g., Reidel et al., 1989; Hooper et al., 2002; Camp et al., 2003); (2) the Yellowstone – Snake River Plain (e.g., Pierce and Morgan, 1992; Pierce et al., 2000; 2002); (3) Oregon High Lava Plains (e.g., Jordan et al., 2004; Pierce et al., 2000; 2002); (4) the West Snake River Plain graben (e.g., Bonnicksen and Godchaux, 2002; Clemens and Wood, 2002); (5) the northern Nevada rift (e.g., Zoback et al., 1994; Colgan et al., 2004). All these provinces appear genetically linked based upon several common characteristics: 1) inception of anorogenic, bimodal (basalt and rhyolite) volcanism in the Idaho – Nevada – Oregon border area between 16.6 Ma and 16 Ma; 2) volcanic centres radiating away from a locus in the Idaho – Nevada – Oregon border region (Fig. 2-1); and 3) they contain voluminous (≥ 100 km³) and high-temperature (≥ 1000 °C) lavas and / or ignimbrites.

Geologic history of the Yellowstone – Columbia River ‘mega’-volcanic province: a summary

The formation and evolution of the mega-province is now widely thought to reflect the influence of a thermal anomaly (hot-spot) under the Idaho – Nevada – Oregon border region from 16.6 Ma, and the passage of the North American plate over it to its present location beneath the Yellowstone Plateau (Matthews and Anderson, 1973; Smith et al., 1974; 1977). The locus of rhyolitic, and subsequently, basaltic volcanism in the Yellowstone – Snake River Plain volcanic province has migrated north-eastwards through the last 16 Ma.

The tectono-stratigraphic history has been collated in Table 2-1, where I have attempted to summarise the volcanic, sedimentary, and tectonic evolution as it pertains to specific regions within the Yellowstone – Columbia River ‘mega’-province (e.g., central Oregon). This shows inception of volcanism in a narrow

temporal and spatial interval. Furthermore, it shows the gradual divergence of volcanism away from the Idaho – Nevada – Oregon border area forming the Yellowstone – Snake River Plain (NE-trending) and Oregon High Lava Plains (NW-trending). Finally, it shows the general pattern of voluminous rhyolite volcanism followed by basalt lava effusion and contemporaneous sedimentation.

Pre-Miocene basement and structure

The basement structure of the intermontane region is the result of three major tectonic events in the Phanerozoic: (1) rifting of the western margin of the Archean Wyoming shield and surrounding Proterozoic platform (Wyoming craton; Fig. 2-2a), during the Lower Palaeozoic (Dickinson, 2002). (2) Oceanic terranes were accreted during the Upper Palaeozoic and Mesozoic and intruded by Cordilleran-type granite batholiths (e.g., the Idaho batholith; Fig. 2-2a) at an active continental arc-margin (the Sevier orogeny; late Jurassic - early Cretaceous); and (3) Cenozoic post-orogenic collapse of the Sevier – Laramide orogen, and back-arc magmatism and extension across the Basin and Range taphrogen (Fig. 2-2a; Dickinson, 2002; Rahl et al., 2002). The rifted western margin of the Wyoming craton to which Mesozoic terranes accreted, is recorded by variations in $^{87}\text{Sr}/^{86}\text{Sr}$ ratio in Miocene volcanic rocks; those erupted through Archean basement have ratios ≥ 0.706 , those erupted through Mesozoic terranes have ratios ≤ 0.704 (Pierce and Morgan, 1992).

In northern Idaho and eastern Washington the 0.704 and 0.706 isopleths (Fig. 2.2a) are adjacent, N – S trending, and parallel, suggesting a rapid thickening of the lithosphere from thin (≤ 25 km) accreted terranes to thick (≥ 50 km) craton. The Idaho – Nevada – Oregon border region is in a ≤ 300 km wide zone between the N – S trending 0.704 and 0.706 isopleths (Fig. 2.2a), and is interpreted to overlie attenuated Proterozoic lithosphere and accreted Lower Palaeozoic terranes. The transition from thin to thick lithosphere is inferred to be gradual because the 0.704 and 0.706 isopleths are widely spaced (Pierce and Morgan, 1992; Hughes and McCurry, 2002).

16.6 – 15.0 Ma

Volcanism began at 16.6 Ma in the Idaho – Nevada – Oregon border area; characterised by inferred lithospheric doming (Pierce and Morgan, 2002) and stretching (e.g., the Northern Nevada rift; Zoback et al., 1994), peralkaline caldera-forming rhyolite eruptions at McDermitt, NV (Rytuba and McKee, 1984), the development of small bimodal volcanic fields (e.g., Santa Rosa – Calico; Brueseke et al., *in prep.*), and voluminous basalt effusions (e.g., at Steens Mountain, OR; Camp et al., 2003). Pre-existing N – S trending crustal weaknesses related to former Mesozoic terrane accretion were exploited by rifting (e.g., the Idaho – Oregon rift; Cummings et al., 2000) and mafic dyke intrusion (e.g., Jourdan et al., 2006) which fed the most voluminous eruptions of the Columbia River flood basalts (Grande Ronde and Imnaha Formations; Reidel et al., 1989) in the Idaho – Oregon – Washington border area ($\geq 200,000 \text{ km}^3$ in 1.1 Ma; Hooper et al., 2002).

The paroxysmal phase of the Yellowstone – Columbia River mega-volcanic province (Table 2-1) is inferred by many to be the result of a mantle plume-head impacting the base of the lithosphere (Brandon and Goles, 1988; Pierce and Morgan, 1992; 2002). Pre-existing weaknesses in the lithosphere allowed the rapid emplacement of primitive mafic magmas, some of which were erupted as flood basalts, whereas others melted and hybridized with sialic crust before being erupted as rhyolite. Rapidly emplaced and voluminous flood basalts, peralkaline silicic volcanics, lithospheric doming, rifting, and radial magmatic and mineralization trends are characteristic of other areally extensive intra-continental igneous provinces (e.g., the East African rift system, Ebinger and Sleep, 1998), especially the early phases. Presently, no ‘non-plume’ models (e.g., subducting – slab models, Beucler et al., 1999; local mantle anomaly models, Christiansen et al., 2002) can account for the relatively sudden initiation of voluminous volcanism across such a large region, and widespread lithospheric doming and stretching: the only unifying model invokes a mantle plume impacting the base of the North American lithosphere at the Idaho – Nevada – Oregon border at ~ 16.6 Ma.

15.0 – 10.0 Ma

This phase saw the development of two time-transgressive volcanic trends radiating away from the McDermitt area (the Yellowstone – Snake River Plain and Oregon High Lava Plains volcanic provinces), and the initiation of rifting to form the West Snake River Plain graben (Fig. 2-2c). Volcanism continued on the Columbia River plateau (e.g., Wanapum Formation; Martin, 1989) and in the Idaho – Oregon graben, though much smaller volumes were erupted. Volcanism in the Yellowstone – Snake River Plain (Pierce and Morgan, 1992; Hughes and McCurry, 2002) and Oregon High Lava Plains (Jordan et al., 2002) volcanic provinces and the West Snake River Plain graben (Woods and Clemens, 2002) was voluminous and bimodal. Rhyolitic high-grade ignimbrites (e.g., the Devine Canyon Tuff; Greene, 1973) and extensive lavas are typical (e.g., the Jump Creek lavas; Bonnicksen et al., 2004). Extensive volcanic products are thought to derive from three areas loosely termed ‘eruptive centres’ by Bonnicksen (1982a) developed in southwestern Idaho: (1) the Owyhee – Humboldt centre (Brueseke et al., 2004; encompassing the Juniper Mountain volcanic field, Manley and McIntosh, 2002) between ~ 14.7 – 11.9 Ma; (2) the Bruneau – Jarbidge centre (Bonnicksen, 1982b) between ~ 12.7 – 8.0 Ma; and (3) the Twin Falls centre (McCurry et al., 1996) between ~ 10.9 – 7.6 Ma. In southern Oregon contemporaneous rhyolite volcanism was subordinate to the effusion of basalt lavas, whereas, rhyolite lavas in the West Snake River Plain graben were erupted, and at least initially, more important than basalts. The graben hosted large lakes, pre-cursors to the late Miocene Lake Idaho (Bonnicksen et al., 2002).

The Yellowstone – Snake River Plain volcanic province is interpreted as a hot-spot track formed by the passage of southern Idaho over the Yellowstone plume ‘neck’ (Pierce and Morgan, 2002). As before, although some plume-sourced basalt was erupted directly, much more was ponded, where it melted and hybridized with sialic crust, forming rhyolite. Oxygen isotope studies indicate the melting of vast volumes of the Cretaceous Idaho batholith (hydrated during the Eocene) under the West Snake River Plain graben, and parts of Bruneau – Jarbidge and Twin Falls centres (Boroughs et al., 2005; Fig. 2-2a), although other

isotopic systems suggest a more complex evolution (Leeman *pers. comm.*, 2005). The large number of rhyolite ignimbrite eruptions and lava effusions (≥ 50), and their large total volume ($\geq 10,000 \text{ km}^3$), between 11.7 – 10.0 Ma, has led Bonnicksen (2004) to describe the period as the ‘ignimbrite flare-up’, that he attributes to the combined Bruneau – Jarbidge and Twin Falls eruptive centres, and the West Snake River Plain graben as a continuous entity. The origin of the West Snake River Plain graben is unclear and several hypotheses have been proposed, including the most widely accepted (a symmetric rift opened around the stable Idaho batholith to accommodate extension in the adjacent Snake River Plain during passage over the hot-spot; e.g., Wood and Clemens, 2002). Less widely accepted hypotheses include: (1) the graben being an ‘aulacogen-like’ continental rift formed as a result of lithospheric doming around the impacting plume-head to the south (Shervais et al., 2002); and (2) a NW-trending extensional duplex related to pre-existing crustal shear zones in southeastern Oregon (Hooper et al., 2002).

The origin of the Oregon High Lava Plains (Fig. 2-2c) volcanic province is more contentious (see review by Jordan, 2005). The NNW-trend of the Oregon High Lava Plains is difficult to reconcile with the NNE-trend of the Yellowstone – Snake River Plain volcanic province (Fig. 2-2c); therefore, the same hot-spot can not, presently, be beneath both provinces. Several workers have used this observation as evidence against the presence of a single mantle-plume controlling volcanism across the region (e.g., back-arc extension, Carlson and Hart, 1987; propagating fault zone, Christiansen et al., 2002). However, they share many similarities (e.g. common spatial and temporal inception point; voluminous bimodal volcanism; association with Columbia River plateau flood basalts) and non-plume hypotheses cannot integrate the Oregon High Lava Plains volcanic province with adjacent and contemporaneous volcanism. In contrast, the conceptual framework provided by considering the Yellowstone – Columbia River ‘mega’-volcanic province offers a more elegant hypothesis (Fig. 2-3), where the plume-head spreads on impact with the base of the lithosphere and, initially, allows flow of mantle material in all directions, but preferentially along pre-

existing weaknesses (e.g., the Idaho – Oregon graben). As plate motion detached the thermal anomaly of the initial plume impact from the later rising plume, the sources of the Yellowstone – Snake River Plain volcanic province (plume-neck) and the Oregon High Lava Plains (remainder of plume-head) diverged (Jordan et al., 2004; Jordan, 2005).

10.0 – 4.0 Ma

Rhyolite volcanism waned after ~ 8.5 Ma, and was concentrated around the inferred Twin Falls, Picabo, and Heise eruptive centres in the Yellowstone – Snake River Plain province, and the Burns caldera complex in south-central Oregon (Fig. 2-1). Significant thicknesses of ignimbrite and fallout ashes were deposited in actively subsiding, approximately N – S trending, half-graben along the margins of the eastern Snake River Plain. Voluminous basalt lavas buried many parts of the southwestern Snake River Plain and West Snake River Plain graben, often in the presence of ‘Lake Idaho’ (Bonnichsen and Godchaux, 2002), which is a lake inferred from the widespread occurrence of lacustrine sedimentary rocks (e.g., the Chalk Hills Formation; Wood and Clemens, 2002) and significant thicknesses of basaltic hydromagmatic tephra and pillow lavas (e.g., Godchaux and Bonnichsen, 2002).

This period is inferred to record further waning of the Yellowstone plume as it passed under progressively thicker, and not previously weakened, Archean cratonic lithosphere (Leeman et al., 1985; Hughes and McCurry, 2002; Fig. 2.2a). The Heise eruptive centre is (like the Yellowstone plateau) interpreted as a complex of overlapping nested-calderas (e.g., Morgan and McIntosh, 2005). Eruptive centres in southwestern and south-central Idaho were buried by ≤ 1000 m of basalt lavas during contemporaneous subsidence inferred to be thermo-mechanical subsidence following the removal of the hot-spot from beneath (Brott et al., 1981; McQuarrie and Rodgers, 1998), but a significant part of the subsidence may have been caldera collapse (Branney et al., *pers. comm.*). Half-graben depocentres for ignimbrites and fallout ashes north and south of the Snake River Plain are inferred to be the result of pre-existing Basin and Range taphrogen

structures, reactivated by passage of the hot-spot and subsequent thermo-mechanical subsidence (Rodgers et al., 2002).

4.0 Ma – present

The most recent phase is characterised by Holocene eruptions at Newberry, OR (Fig. 2-2e; Jordan, 2005), and present-day geothermal activity at Yellowstone, WY, following three major caldera- and rhyolite ignimbrite-forming eruptions between 2.0 – 0.6 Ma (Christiansen, 2001). There were no significant rhyolite eruptions between 4.0 and 2.0 Ma (the ‘rhyolite eruption lull’ of Perkins and Nash, 2004). Minor basalt effusions have continued in the eastern Snake River Plain (e.g., Craters of the Moon, Kuntz et al., 2004), the Yellowstone caldera (Christiansen, 2001), and the Oregon High Lava Plains (Jordan, 2005). Recent seismicity and analysis of Quaternary fault motions identifies a parabolic-shaped area around the Yellowstone plateau, where the greatest number and greatest magnitude of earthquakes are located: the seismic parabola of Anders et al. (1989).

Volcanism is currently limited to geothermal activity, however, the Yellowstone plateau and the ‘seismic parabola’ area (Fig. 2.2e) are tectonically active, with frequent large-magnitude earthquakes ($\geq M = 7$; e.g., Hebgen Lake 1959, Borah Peak 1983). Large vertical motions on N – S trending faults are inferred from the age and thickness of basin-fills in graben and half-graben adjacent to the Yellowstone plateau (e.g., Teton Valley, WY). The eastern Snake River Plain is thought to be subsiding aseismically, with ductile stretching at shallower crustal levels than the adjacent parabola region, due to the enhanced geotherm and by the intrusion of mafic dykes and sills (Rodgers et al., 1990).

Miocene explosive and effusive rhyolitic volcanism in south-central Idaho

The Yellowstone – Snake River Plain volcanic province is characterised by bimodal eruptions of rhyolite lavas and ignimbrites, and basalt lavas. Rhyolites are typically time-transgressive, and successive volcanic centres young north-eastwards towards the Yellowstone plateau (Fig. 2-4) in contrast to basalts that show no relationship between age and location.

Time-transgressive rhyolitic eruptive centres

Loci of rhyolite volcanism (eruptive centres; Fig. 2-4) have been inferred along the Yellowstone hot-spot track in southern Idaho (Pierce and Morgan, 1992). Only the Yellowstone and Heise centres have a topographic expression, and they have been interpreted as being nested caldera complexes (e.g., Christiansen, 2001). Older centres are buried and any topographic expression is concealed. They are inferred to be nested caldera complexes infilled by voluminous intra-caldera tuffs and silicic lavas. They are buried beneath lacustrine deposits and basalt lavas, and most of our knowledge of these centres is derived from outflow sheets at the southern and northern margins of the Snake River Plain (e.g., the Cougar Point Tuff Formation) and from canyon-wall sections through some of the older centres (e.g., Owyhee canyon). There are significant gaps in our understanding of the volcanic stratigraphy, both temporally and spatially, and this hinders understanding of the temporal evolution of each centre and of the province as a whole. Until recently, the volcanic centres were inferred to be discrete and separated by country rock. This view is now changing and recent work (e.g., Andrews et al., *in press*; Bonnicksen et al., *in press*) around the inferred Bruneau – Jarbidge and Twin Falls centres (Fig. 2-4) suggests that the transition of volcanism from one centre to the next was complex, with contemporaneous volcanism in both centres and volcano-tectonic subsidence that affected both centres, and intervening and adjacent areas, including the Rogerson Graben. It is not clear to what extent volcanism in this area derived from two separate eruptive centres.

The Bruneau – Jarbidge eruptive centre (~ 12.7 – 8.0 Ma)

The Bruneau – Jarbidge eruptive centre (Fig. 2-4) is one of the best understood areas in the central Yellowstone – Snake River Plain volcanic province because of the extensive outflow sheets of the Cougar Point Tuff Formation (Bonnichsen and Citron, 1982; Cathey and Nash, 2004), and the preservation of topographic margins on the inferred southern and south-western boundaries (e.g., the Grasmere escarpment; Bonnichsen, 1982a). The evolution of the eruptive centre is summarised as follows: (1) explosive eruption of voluminous ($\geq 100 \text{ km}^3$), high-grade rhyolitic ignimbrites (the Cougar Point Tuff Formation), some of which were rheomorphic and lava-like (*sensu* Branney and Kokelaar, 1992), towards the north, south, south-west, and south-east (Fig. 2-4). (2) A $\leq 100 \text{ km}$ radius depression possibly formed by subsidence during ignimbrite eruptions (possibly a series of nested calderas) was gradually filled by voluminous ($\geq 50 \text{ km}^3$) rhyolite lavas erupted from inferred vents within and at the margins of the centre (e.g., the Dorsey Creek rhyolite; Bonnichsen, 1982b). (3) Rhyolitic volcanism was followed by lithospheric extension, extensive basalt lava effusion, and lacustrine sedimentation, which gradually buried the centre and obscured its shape (Bonnichsen, 1982a; Bonnichsen and Godchaux, 2002). (4) Incision by river canyons removed significant areas of the basalt lava cover and created canyon-wall sections through the rhyolite lavas and ignimbrites, however, a sub-rhyolite volcanic base has yet to be reached. Low-level geothermal activity is persistent along parts of the inferred eruptive centre margin, where faults (possibly caldera-bounding faults) channel warm ($\leq 100 \text{ }^\circ\text{C}$) water to the surface (e.g., Murphy Hot Springs, ID; Fig. 2-4).

The Bruneau – Jarbidge eruptive centre is characterised by high-temperature ($80^\circ\text{C} - 1000^\circ\text{C}$) rhyolites with sparse, anhydrous mineral assemblages including: plagioclase, sanidine, augite, pigeonite, hypersthene, fayalite, quartz, magnetite and ilmenite. Apatite and zircon are common accessory phases. Many calderas are characterised by pervasive metasomatism, alteration and intrusion, however, this has not been reported from the Bruneau – Jarbidge or Twin Falls centres

Cyclic magmatic trends have been reported within the Cougar Point Tuff Formation, and are inferred to result from episodic tapping of a long-lived and heterogeneous magma chamber (Cathey and Nash, 2004). Voluminous rhyolite lavas within the eruptive centre are very similar chemically to the Cougar Point Tuff Formation, suggesting the continuation of the same magma chamber despite the change to non-explosive activity (Cathey, 2005).

The Cougar Point Tuff Formation (Bonnichsen and Citron, 1982) is part of the vast, informal 'Idavada Volcanic Group' (Malde and Powers, 1962), and is composed of at least ten ignimbrites, some of which are made up of multiple sheets, and intercalated fallout tuffs. On erosion, the high-grade ignimbrites typically form steep cliff exposures separated by vegetated slopes (or benches) with little or no rock outcropping. This means that the stratigraphy of the Cougar Point Tuff Formation is incompletely exposed; perhaps as much as 50 % of the succession is not described because it forms vegetated slopes between the more welded units. The cumulative thickness and volume of all Cougar Point Tuff members conservatively is estimated to be 500 m thick, and at least several thousand cubic kilometres, all of which erupted in a little more than two million years (12.7 - 10.5 Ma), with recurrence intervals of roughly 200-300 ka (Bonnichsen et al., *in press*). Inclusion of the unknown volumes of dispersed fallout tephras, regionally correlative ignimbrites, and any thick, ponded intra-caldera fill, would significantly increase estimates of the cumulative volume of material erupted from the Bruneau - Jarbidge eruptive centre, perhaps by an order of magnitude.

The Twin Falls eruptive centre (~ 10.9 – 7.6 Ma)

The Twin Falls eruptive centre (Fig. 2-4; proposed by Pierce and Morgan, 1992) is even more speculative than the Bruneau – Jarbidge centre, as there is no extant topographic expression, no canyon incision within it, and is inferred predominantly from outflow ignimbrite sheets to the south of the inferred southern margin. Some ignimbrites (e.g., the Tuff of McMullan Creek; McCurry et al., 1996) in the Cassia Mountains are inferred to have been emplaced from the

north based on the trends of stretching lineations, and they appear to thicken towards the north (McCurry et al., 1996). The ignimbrites are morphologically, texturally, and compositionally similar to those inferred to have been erupted in the Bruneau – Jarbidge centre, though they are slightly less evolved and hotter (~ 1000 °C) (Hughes and McCurry, 2002). Ignimbrite eruptions are inferred to have been followed by voluminous, caldera-filling rhyolite lavas (e.g., the Shoshone Falls and Balanced Rock rhyolites) exposed in canyons and small ignimbrites (e.g., the Castleford Crossing ignimbrite) (Bonnichsen et al., 1989). Basalt lavas then buried the area (Bonnichsen and Godchaux, 2002).

The Rogerson Formation and the Rogerson Graben

The Rogerson Graben is a significant N – S trending basin in southern Twin Falls County, Idaho stretching south into Elko County, Nevada (Fig. 2-5). The graben is open to the north where it is buried by later basalt lavas, and to the south where it joins a wider basin stretching south from Jackpot, NV. It is bounded to the east and west by topographic highs made up of gently west-dipping rhyolite sheets that are onlapped and overstepped by members of the Rogerson Formation. The western margin is a prominent fault scarp (~ 700 m relief) exposing a section through twelve rhyolite sheets of the Brown’s Bench massif (Bonnichsen et al., *in press*).

Stratigraphy of the Rogerson Graben – the Rogerson Formation

The Rogerson Formation is a newly established stratigraphic unit within the pre-existing, and informal, Idavada Volcanic Group of Malde and Powers (1962). It is composed of five cliff-forming rhyolite sheets with poorly exposed intercalated rhyolitic volcanoclastic deposits (Fig. 2-6; Appendix 1), and is best exposed along the N – S trending Salmon Falls Creek Reservoir and US Highway 93. The formation has been identified within the Rogerson graben and along the southern margin of the Snake River Plain where it outcrops between older rhyolite sheets of the Brown’s Bench massif and younger basalt lavas (Fig. 2-5).

Pre-Rogerson Formation rocks

Pre-Rogerson Formation units are not exposed within the graben, where the Jackpot Member is the oldest unit observed. The Rabbit Springs, Brown's View and Grey's Landing members are observed to onlap and overstep pre-Rogerson Formation rhyolite sheets at the margins of the graben (Fig. 2-5), where they are angularly unconformable. Older sheets in the Brown's Bench massif are interpreted to be high-grade ignimbrites (Bonnichsen et al., *in press*) and a correlation between the uppermost units and the Jackpot Member cannot be ruled out at this time. I infer, tentatively, that the same succession of rhyolite sheets underlies the Rogerson Formation within the Rogerson Graben.

The Jackpot Member

Description

At its type locality at Salmon Falls Creek, 4.5 km south of Jackpot, Nevada (Fig. 2-5) the Jackpot Member is ≥ 75 m thick, although its base is not exposed (Fig. 2-7). It outcrops extensively (> 300 km²) in the south of the Rogerson Graben, where it is unconformably overlain by a thick, bedded volcanoclastic deposit and the Rabbit Springs Member (Fig. 2-6). It is readily distinguished from other members by its stratigraphic position, considerable thickness, lava-like appearance, internal stratigraphy, and the unique occurrence of myrmekitic intergrowths around sanidine crystals in thin section (Fig. 2-8a).

I subdivide the Jackpot Member into seven informal sub-units ('Jackpot 1 to 7', Fig. 2-7) that form prominent cliffs, based on different columnar joint patterns, lithophysae¹-rich layers, and topographic benches between each cliff. 'Jackpot 1 to 4' (Fig. 2-8b) are welded, generally devitrified (lithoidal²), lava-like, and lack eutaxitic fabrics. 'Jackpot 1 and 2' have well-developed, closely spaced, sub-horizontal joints (sheet-joints of Bonnichsen, 1982b), columnar joints and prominent upper lithophysae-rich layers that lack joints. 'Jackpot 3' lacks columnar joints and lithophysae, and sheet-joint surfaces have a linear fabric

¹ Lithophysae – devitrified nodule typically with a star-shaped cavity.

defined by orientated prolate vesicles and are deformed by open, upright folds. ‘Jackpot 4’ is a lava-like, sheet-jointed rhyolite similar to ‘Jackpot 1’, with some poorly developed columnar joints, and isolated lithophysae throughout its upper half especially concentrated in a 2 m-thick zone at the top.

‘Jackpot 5’ is 26 - 30 m thick, lava-like and flow-folded, with well developed columnar jointing, and well developed sheet-jointing in lower and central parts. The top 15 m show N or NE-trending upright, open folds on a scale of 1 m – 10 m with NW-SE elongation lineations (stretched vesicle; Fig. 2-5). Prolate vesicles have axial ratios of $\leq 10 : 1$ and trend parallel to the lineation. The uppermost 4 m are a perlitic vitrophyre³ with abundant lithophysae partly filled with pistachio-green chalcedony.

‘Jackpot 6’ (type locality: Sweetwater Lane, 2 km south of Jackpot, Fig. 2-5) is less intensely welded, more obviously pyroclastic than the other Jackpot sub-units and is characterized by the presence of abundant, equant obsidian lapilli (1 – 2 cm). It conformably overlies the upper vitrophyre of ‘Jackpot 5’. A strongly welded 20 cm-thick base grades up into a layer of weakly welded obsidian lapilli-tuff (≤ 2 m). This layer is truncated by an erosion surface overlain by lenses of cross-bedded, non-welded lapilli-tuff of similar composition. This in turn grades up into a 1.5 m thick layer of obsidian lapilli-tuff containing lenses of accretionary lapilli. The top of this layer is not seen.

‘Jackpot 7’ is an 8 m thick columnar-jointed, flow-banded and dominantly lava-like sheet, similar to the non-lithophysal parts of ‘Jackpot 1’ (Fig. 2-7). It is exposed widely across the southern Rogerson Graben, where it forms a prominent cap at the top of the Jackpot Member (Fig. 2-8c). It has well-developed sheet-joints and is thoroughly devitrified. Folds and vitrophyres have not been seen. Ragged quartz and sanidine concentrations, possibly crystal-bearing fiamme (≤ 8 cm long), occur in a 75 cm thick layer, 1.5 m from the base.

² Lithoidal – ‘rock-like’, thoroughly devitrified rhyolite, no remaining vitric rhyolite.

³ Vitrophyre – layer of glassy lava or ignimbrite, typically at the base and top.

Interpretation

Jackpot Member sub-units 1 – 5 and 7, resemble lavas because they are massive, intensely flow-banded and jointed (Fig. 2-7), and are devoid of pumice and lithic lapilli, fiamme, and sedimentary structures. However, I interpret them to be ignimbrites because: (1) they exhibit laterally persistent internal stratigraphies; (2) they lack autobreccias, at both the base and top of the member, or between sub-units 1 – 5; and (3) they are too thin to be lavas. Laterally persistent divisions between sub-units are defined by topographic breaks, changes in columnar joint size and spacing, the upper vitrophyre of Jackpot 5; and lithophysae-rich layers (Figs 2-7, 2-8b, 2-8c), which I interpret to record breaks in deposition, rapid cooling, and volatile de-gassing between emplacements. These divisions do not contain autobreccias, the presence of which is diagnostic of large-volume silicic lavas (Henry and Wolff, 1992; Bonnicksen and Kauffman, 1997; Sumner and Branney, 2002), and no silicic lavas known in the Snake River Plain volcanic province that lack them. Furthermore, silicic lavas in the region tend to be thick (≥ 50 m - ~ 300 m; Bonnicksen and Kauffman, 1997), and tend not to form distal feather edges, as ignimbrites typically do. I interpret NW – SE trending lineations to record emplacement from the Bruneau – Jarbidge area to the WNW (Figs 2-4 and 2-5).

‘Jackpot 6’ is the least intensely welded sub-unit and its pyroclastic origin is clearly shown by the presence of cross-stratification, lensoidal bedding, ash shards, obsidian lapilli, and accretionary lapilli. I interpret this sub-unit to be an ignimbrite deposited from a pyroclastic density current that was cooler than those that emplaced sub-units 1 – 5 and 7. I suggest that the base of sub-unit 6 welded when it was deposited on top of the still hot sub-unit 5. The absence of weathered surfaces, soils, exotic tephra layers or sediments and vitrophyres between sub-units suggests that it represents a single eruptive unit of seven rapidly emplaced ignimbrites, which in turn, welded, cooled and devitrified together as a simple cooling unit (Smith, 1960b).

I have established the Jackpot Member based on the field evidence available within the study area (Andrews et al., *in press*). However, contemporaneous investigations in the adjacent Brown's Bench massif (Fig. 2-5) have come to a different interpretation (Bonnichsen et al., *in press*). They report field evidence (appearance and thickness of Jackpot 7) and infer that it is a separate ignimbrite (their Brown's Bench Unit 8), possibly post-dating the Jackpot Member (their Brown's Bench Unit 7) by several tens of thousands of years. Further field investigations (e.g., identifying intervening palaeosols) and radiometric dating of the rhyolites in question is continuing, in an attempt to reconcile the two stratigraphies.

Undifferentiated volcanoclastic deposits

Description

Deposits of undifferentiated, bedded volcanoclastic rocks occur at two stratigraphic levels: (1) unconformably overlying the Jackpot Member; and (2) discordantly overlying the Rabbit Springs Member (Fig. 2-6). Both units consist of 2 – 10 cm thick layers of silt and sand-sized particles, with rare lenses of accretionary lapilli or ash-pellets, some rare rounded pumice lapilli, and intercalated thin palaeosols containing calcified rootlets. Individual layers are laterally continuous for ≥ 5 m; however, scour-structures, ripple laminations, low-angle cross-stratification (cross-set height ≤ 10 cm), normal graded bedding, and de-watering structures are common. Both units are typically buried by thick (≤ 40 cm) slopewash, and are locally bioturbated, making further examination difficult.

The lower bedded volcanoclastic unit unconformably overlies a buried landscape developed in Jackpot sub-units 5, 6, and 7 (Fig. 2-5), where the Jackpot Member has been extended (normal faults) to produce several 25– 30 m deep, NNE-trending, km-scale graben. This is best demonstrated immediately to the east of the Backwaters area (Figs 2-5 and 2-9a). In turn, the lower bedded volcanoclastics are conformably overlain by the Rabbit Springs Member, and the topmost 1 m is fused against the basal vitrophyre of the later unit (Figs 2-9a and 2-9b).

Interpretation

Both undifferentiated volcanoclastic units are interpreted as sequences of fallout ashes and related silt- and sand-grade epiclastic deposits. Normal graded bedding and de-watering structures are consistent with deposition of fallout ash into standing water and onto soft substrate, and the presence of ripples and erosional scours suggests that currents reworked the deposit (e.g., Nakayama and Yoshikawa, 1997). The presence of palaeosols with calcified rootlets within both sequences suggests periods of non-deposition, plant growth, and pedogenesis, either in shallow water or exposed at the surface. The sources of fallout ashes are unknown; however, significant thicknesses of distally and medially sourced fallout ashes are reported from basins throughout the Snake River Plain and adjacent regions (e.g., Perkins et al., 1995; Perkins and Nash, 2002).

The lower volcanoclastic unit fills and buries several graben developed in the Jackpot Member. I interpret that sustained fallout ash deposition occurred after, and possibly during, extension of the Jackpot Member and in the absence of contemporaneous ignimbrite emplacement. The early Rogerson Graben and smaller graben within it were probably host to small ephemeral lakes and short-lived (thin palaeosols) dry and vegetated high-stands.

The Rabbit Springs Member

Description

The Rabbit Springs Member (Fig. 2-6) unconformably overlies horsts developed in the Jackpot Member and conformably overlies undifferentiated volcanoclastic deposits (Figs 2-9a and 2-9b). It is an 8 - 12 m thick sheet with a minimum extent of 200 km², exposed across the central and eastern portion of the Rogerson Graben, where it is the lowest of several members that thin to a feather edge and pinch out eastwards against the Shoshone Hills graben-margin (Fig. 2-5). In the Backwaters area it is disrupted by a pair of contemporaneous normal faults (the member thickening from 9 m to 12 m) that deform the basal but not upper vitrophyre.

In the type locality of Backwaters, Idaho (Fig. 2-5) it is an 11 m thick tuff, with a lithoidal centre, and spherulitic and lithophysal upper and lower vitrophyres (Fig. 2-10). The basal vitrophyre is massive perlite, with a eutaxitic fabric of flattened Y-shaped ash shards, some of which wrap crystals (Fig. 2-9c). It is devoid of pumice lapilli and is characterized by an abundance of spherulites and lithophysae (≤ 8 cm across) some of which are filled with white chalcedony. The central lithoidal zone is thoroughly devitrified, with closely spaced sheet-joints, and relic pseudomorphs after spherulites within the matrix. This unit has yielded an $^{40}\text{Ar} - ^{39}\text{Ar}$ date of 10.37 ± 0.13 Ma (Bonnichsen et al, *in press*).

Interpretation

The Rabbit Springs Member is a high-grade, low aspect-ratio ignimbrite. The absence of elongation lineations, flow folds and autobreccias suggest it is not rheomorphic. I interpret this as a single ignimbrite emplacement unit because of its thinness, vitroclastic textures, and lack of internal breaks (e.g. autobreccias, intercalated fallout ashes or palaeosols). Furthermore, I interpret it as a simple cooling unit because of its simple welding profile (Smith, 1960b). Normal faults that partition thickness variations but do not deform the upper vitrophyre, are interpreted to be extensional growth faults (e.g., Childs et al., 2003) suggesting ignimbrite emplacement into an actively extending graben.

Undifferentiated volcanoclastic deposits

Description

The upper bedded volcanoclastic unit discordantly overlies the Rabbit Springs Member and thins rapidly to the eastern margin of the graben; however, the contact is not exposed. The sedimentary characteristics of the unit are nearly identical to the lower volcanoclastics (see above); however, at least three thick (≥ 1 m) palaeosols (containing calcified rootlets) are developed within the unit. Internal angular unconformities are recorded by planar erosion surfaces cutting palaeosols, and subsequent discordant burial by later volcanoclastics. This is best demonstrated immediately to the southeast of the Backwaters area (Figs 2-5 and

2-9a). The upper bedded volcanoclastics are conformably overlain by the Brown's View Member, although the contact is not exposed (Fig. 2-6).

Interpretation

The upper volcanoclastic unit appears to be discordant with the underlying Rabbit Springs Member and may be unconformable, although an erosion surface has not been observed. Major planar erosion surfaces, possibly flooding surfaces, cut palaeosols within the unit, which were then buried by onlapping and discordant (west-dipping) volcanoclastic packages, suggesting that the half-graben was contemporaneously extending, and that the graben-floor was often not horizontal. The presence of thick palaeosols suggests sustained periods of non-deposition, plant growth and pedogenesis, between major erosive events and subsequent deposition of fallout ash.

The Brown's View Member

Description

The Brown's View Member (type locality: Backwaters, Figs 2-5 and 2-11) is a 4 – 8 m thick, $\geq 400 \text{ km}^2$ sheet that is exposed intermittently across the central Rogerson Graben, where it conformably overlies undifferentiated volcanoclastic deposits. It is the oldest member exposed outside the Graben to the northwest (Fig. 2-5), where it onlaps and oversteps older lava-like rhyolites of the Brown's Bench massif ($10.22 \text{ Ma} \pm 0.09$ ($^{40}\text{Ar} - ^{39}\text{Ar}$); Bonnicksen and Godchaux, 2002).

A massive, chocolate-brown lithoidal centre ($\sim 1.5 \text{ m}$ thick) separates two sparsely spherulitic vitrophyres ($\leq 3 \text{ m}$ thick; Fig. 2-11). Both vitrophyres exhibit a $\leq \text{mm}$ -scale eutaxitic fabric (Fig. 2-9d), cusped shards, and crystal and lithic fragments. There are no pumice lapilli or fiamme. The massive upper vitrophyre contains isolated lithophysae (5 – 8 cm diameter) and passes up into a thin orange palaeosol ($\sim 20 \text{ cm}$ thick), with angular obsidian lapilli and small calcified rootlets. In contrast to the Rabbit Springs Member, the Brown's View Member contains less lithophysae and spherulites, and it lacks sheet-joints.

Interpretation

The Brown's View Member is a high-grade, low aspect-ratio ignimbrite. I interpret the presence of ubiquitous vitroclastic textures, the thinness of the sheet, the simple welding profile, and the absence of breaks (e.g. intercalated palaeosols, fallout ashes, sedimentary layers, and autobreccias) as evidence for a single emplacement unit, and simple cooling unit (e.g., Smith, 1960b).

The Backwaters Member

Description

The Backwaters Member (type locality: Backwaters, Fig. 2-5) is 8 - 15 m thick. It likely conformably overlies the Browns View Member (contact not well exposed) across the centre and north of Rogerson Graben (Fig. 2-5). It comprises at least two units (A and B on Fig. 2-12) separated by a palaeosol and erosion surface. Unit A is a ≥ 8 m thick layer of non-welded, massive tuff, containing lenses of sub-rounded to angular pumice lapilli and lithics supported by a tuff matrix, and is overlain by a 2 m thick palaeosol. The base of this unit is not exposed. Unit B is a 3 – 6 m thick, massive tuff containing lenses of sub-angular pumice lapilli and abundant calcified rootlets. It has an erosional base and the upper 4 m is host to a bioturbated palaeosol. Grass imprints are preserved on the upper surface of the palaeosol. The lower 2 m have been fused to black vitrophyre and the palaeosol baked, likely due to heat conducted downwards from the overlying Grey's Landing ignimbrite (Fig. 2-13a).

Interpretation

I interpret, tentatively, volcanoclastic units A and B of the Backwaters Member as non-welded ignimbrites because they are massive, poorly sorted, and contain sub-angular to sub-rounded pumice clasts. Furthermore, they appear to contain a substantial juvenile component where the glassy (and therefore possibly juvenile) ash matrix of unit B has been fused. The erosive base of unit B is also consistent with deposition from a pyroclastic density current. However, I can not rule out deposition from a debris flow (e.g., Smith, 1986; Palmer and Walton, 1990), an interpretation consistent with massive and poorly sorted deposits containing

rounded pumice lapilli. The presence of palaeosols indicates significant pauses in deposition, representing periods of eruptive repose.

The Grey's Landing Member

Description

The Grey's Landing Member (type locality: Grey's Landing, Idaho, Figs 2-5 and 2-13b) is a 5 to 65 m thick, rhyolite sheet comprising a stratified ashfall deposit and a lava-like ignimbrite with a lower vitrophyre, a thick lithoidal centre, and a thin upper vitrophyre locally overlain by a non-welded top (Fig. 2-12). The upper vitrophyre is eroded at the Type Section but is exposed elsewhere (e.g., Cedar Creek Reservoir, Fig. 2-5). In sections less than 5 m thick, the entire member is vitric.

The Grey's Landing Member unconformably overlies the Backwaters Member both within and outside the Rogerson Graben, and its full areal extent is estimated to be $\geq 400 \text{ km}^2$ (Fig. 2-5). It has a wedge-shaped form within the Rogerson Graben that thins to a feathered edge towards the east (Fig. 2-13c) and south. Outside the graben it onlaps and oversteps older lava-like rhyolites of the Brown's Bench massif, and drapes the palaeo-fault scarp of the Brown's Bench Fault (Cricket Creek; Fig. 2-5). This unit has yielded a K - Ar date of $7.62 \pm 0.4 \text{ Ma}$ (Hart and Aronson, 1983). It is overlain by late-Miocene and early-Pliocene basalt lavas in the north of the graben and in the adjoining Snake River Plain (Bonnichsen and Godchaux, 2002, Fig. 2-5).

An equally extensive, parallel-stratified ash layer, $\leq 1.5 \text{ m}$ thick, drapes the upper palaeosol of the Backwaters Member (Figs 2-12, 2-13d and 2-13e). Along Highway 93, (Fig. 2-5) the stratified ash sits on a $\sim 2 \text{ m}$ thick-bedded tephra succession in a local depression in the Backwaters Member, and contains a 3 cm thick Plinian pumice fall deposit. The stratified ash becomes progressively more fused and compacted under thicker ignimbrite (e.g., at Grey's Landing; Figs 2-13d and 2-13e).

The basal vitrophyre (Figs 2-12, 2-13d and 2-13e) is 1 – 3 m thick, massive and spherulitic (2 – 4 cm diameter), and conformably overlies the underlying stratified ash. Extensive, horizontal sheets (> 5 m long, ~ 6 cm thick) of devitrified rhyolite are found within the vitrophyre (Fig. 2-13d), with a lineation (~ E – W; Fig. 2-5) developed on their surfaces. Rare lithophysae (\leq 8 cm diameter) are concentrated in eutaxitic tuff in graben-flank sections (\leq 5 m). Vitroclastic textures are preserved in strain-shadows around rotated crystals, in an otherwise flow-banded and flow-folded, glassy matrix (Fig. 2-14a).

A red-brown lithoidal central zone is pervasively flow-banded and flow-folded, with dm- to 10 m scale flow-folds (Figs 2-14b – d), including sheath folds (e.g., Branney et al. 2004). Flow-folding scale and style define two deformation domains (Fig. 2-14c); a lower ‘flat’ domain of cm- to m-scale, recumbent isoclinal folds, and an upper ‘steep’ domain in which isoclinal folds are refolded by m- to 10 m scale upright folds. A penetrative lineation (Fig. 2-15a) is developed on some sheet-joint surfaces, especially in the less folded parts, and the orientation of lineations and parallel fold hinges varies with increasing height, as reported by Branney et al., (2004). ‘Dimple joints’ (Fig. 2-15b; Bonnicksen, 1982b), dominate the lower 10 m where sheet joints and flow-folds are absent. Vesicles (0.2 - 20 cm diameter) occur in the upper 20 m of the lithoidal zone. Some have risen buoyantly, intruding and deforming the flow-banding (Fig. 2-15c).

A dark grey, vitroclastic upper vitrophyre is flow-banded and flow-folded. It is perlitic and locally spherulitic (\leq 3 cm diameter) and lithophysal (\leq 4 cm diameter). It is best exposed at Salmon Dam and Cedar Creek Reservoir (Fig. 2-5); however, it has been removed at the type locality. It locally shows autobrecciation, with jigsaw-fit blocks \leq 0.5 m in diameter. At Salmon Dam and Cedar Creek Reservoir a massive to faintly stratified, aphyric, orange, sand-sized ash is preserved within 10 m scale synforms developed in the upper vitrophyre. Typically, the contact between welded vitrophyre and non-welded tephra is a breccia where angular clasts (\leq 10 cm diameter) of non-welded tephra are

supported by a matrix of non-welded and partly fused orange ash, which is progressively more fused towards the vitrophyre.

Interpretation

I interpret the basal stratified ash as a contemporaneous fallout ash, based on mantling of the substrate, very good sorting, laterally continuous lamination and thickness, as well as the absence of erosive features and internal truncations. I infer that the layers derive from the same eruption as that which emplaced the overlying ignimbrite because of the absence of an intercalated palaeosol or erosion surface.

Although the Grey's Landing Member is largely lava-like, I interpret it to be an ignimbrite on the basis of the vitroclastic and eutaxitic textures in the upper and lower vitrophyres, its low aspect ratio, and the widespread absence of a basal autobreccia. Flow folds and elongation lineations characterize rheomorphic deformation (e.g., Schmincke and Swanson, 1967; Chapin and Lowell, 1979; Wolff and Wright, 1981). Measurements of lineation-trends and rotation directions in crystals (Fig. 2-14a) suggest that, at least initially, the ignimbrite was emplaced from the east. I interpret the upper breccia to record *in situ* brecciation of welded ignimbrite in response to internal stress caused by rheomorphic flow while the upper part of the deposit started to cool and degas; in contrast to *en masse* flow like a lava (e.g., Henry and Wolff, 1992). I infer, tentatively, that the overlying aphyric, orange ash is a contemporaneous non-welded ignimbrite flow-unit because of its massive appearance, although I cannot rule out origin as a fall deposit. The origin of dimple-joints remains enigmatic; I interpret them to be a devitrification feature because they are only found in lithoidal rhyolite (e.g., Bonnicksen, 1982b), and suggest that each dimple may be a formed by a flattened spherulite, originally surrounded by vitric rhyolite that is now devitrified.

I interpret the basal stratified-fall deposit, lava-like ignimbrite and upper orange ash together as a simple cooling unit (e.g., Smith, 1960b), based on fusing of the upper and lower ash deposits by the ignimbrite and deformation of the upper ash. Therefore, the ignimbrite and both ashes are probably products of the same, single

eruptive event. More tentatively, I interpret the lava-like ignimbrite to be a single flow unit based on the absence of any evidence in the sheet for a flow hiatus, although it is possible that such evidence would have been obscured by rheomorphism.

The Coyote Creek Member

Description

The Coyote Creek Member (type locality: road-cut along Highway 93, 10 km south of Rogerson, Idaho, Fig. 2-5) is a 4 to 5 m thick, buff-brown, non-welded, massive, sand-sized ash, volcaniclastic layer (Fig. 2-16) that conformably overlies the Grey's Landing Member (Fig. 2-6), although it is poorly exposed and has a limited areal extent ($\sim 4 \text{ km}^2$). It is composed of poorly sorted silt- and sand-grade material, mainly glass shards. The upper surface is a thick palaeosol ($\leq 1.5 \text{ m}$), and the whole deposit is strongly bioturbated. Irregularly shaped ashy concretions ($\sim 5 \text{ cm}$ diameter) are common.

Interpretation

Although somewhat enigmatic in origin, I interpret, tentatively, the Coyote Canyon Member to be a non-welded ignimbrite based on the presence of juvenile ash and its massive appearance. However, once again I cannot rule out deposition from a volcaniclastic debris flow (e.g., Smith, 1986; Palmer and Walton, 1990).

The Sand Springs Member

Description

The Sand Springs Member (type locality: road-cut along Highway 93, 10 km south of Rogerson, Figs 2-5 and 2-6) is a $\geq 8 \text{ m}$ thick, dark-grey rhyolite that conformably overlies the soil at the top of the Coyote Canyon Member (Fig. 2-16). It is restricted to the eastern margin of the Rogerson Graben, covering $\sim 4 \text{ km}^2$. The basal 7 cm comprises a non-welded, parallel-stratified tuff. This grades up through massive, incipiently welded, moderately welded and then intensely welded, eutaxitic, vitric tuff. Vitroclastic textures (Fig. 2-15d) and small obsidian

lapilli (0.5 – 1 cm diameter) are ubiquitous throughout the deposit becoming progressively more flattened with increasing height.

Interpretation

The Sand Springs Member is clearly pyroclastic and welded, based on eutaxitic vitroclastic textures and progressively flattened obsidian lapilli, and I interpret it as an ignimbrite. It is a single emplacement unit and the simple welding profile suggests it is a simple cooling unit.

Post-Rogerson Formation rocks

The Rogerson Formation was partly buried by basalt lavas erupted from numerous fissures and low-profile vents that parallel the orientations of contemporaneous and younger faults. At Salmon Dam two basalt lavas (6.91 ± 0.66 Ma and 6.70 ± 0.63 Ma respectively; Bonnicksen and Godchaux, 2002) unconformably overlie the Grey's Landing Member (Fig. 2-5), where they cap and preserve the easily eroded upper vitrophyre and orange tuff. An ancestral Salmon Falls Creek Canyon was cut into the Grey's Landing Member through the basalt lava cover, and subsequently partly filled by an intra-canyon lava erupted from Salmon Butte (Bonnicksen and Godchaux, 2002). Following the cessation of volcanism, the Salmon Falls Creek cut a new canyon parallel to the previous one exposing the intra-canyon lavas.

Late - Miocene to Holocene evolution of the Rogerson Graben

The tectonic history of the graben has been established using the thickness distributions of ignimbrites, volcanoclastic sediments, and lavas; and cross-cutting relationships between stratigraphic members and faults; back as far as the emplacement of the Jackpot Member ($>> 10.37$ Ma), beyond which I have no stratigraphic or tectonic constraints. The evolution of the graben can be divided into three phases: (1) initiation; (2) syn-ignimbrite emplacement; and (3) post-ignimbrite emplacement.

Several small, NNE-trending graben ($\leq 10\%$ E - W extension) developed in the Jackpot Member and were infilled by undifferentiated volcanoclastic sediments (Figs 2-5 and 2-17). The status of the graben-bounding Brown's Bench fault at this time is unknown. However, the orientation and scale of the fault is consistent with major Basin and Range faults further south in central Nevada, suggesting that it is an inherited structure affecting both pre-Miocene basement and Snake River Plain volcanics.

The extending graben-floor (NNE-trending growth faults) was inundated by the west-thickening Rabbit Springs Member (Fig. 2-17), suggesting the Rogerson Graben was an asymmetric half-graben. Subsequent deposition of bedded volcanoclastic sediments was interspersed with repose periods (palaeosols), and graben-floor tilting and erosion (minor angular unconformities). The Brown's View, Backwaters and Grey's Landing Members thickened westward against, and buried, the Brown's Bench Fault (onlapping and overstepping older ignimbrites in the footwall; Figs 2-5 and 2-17). The relationship between the Coyote Creek and Sand Springs Members and graben formation is unknown.

Graben development has continued since the deposition of the Rogerson Formation, displacing late Miocene – Pliocene basalt lavas by 40 m and an accompanying northward propagation of the tip-point of the Brown's Bench Fault.

In summary, the Rogerson Formation and overlying lavas record ~ 10 Ma of episodic extension, graben-floor tilting, and scarp burial, related to the formation of the Rogerson Graben. The Rogerson Graben, therefore, shares many characteristics (e.g. rapid in-filling by ignimbrites, long repose periods, growth faults, prolonged extension) with basins along the margins of the Snake River Plain (e.g., the Oakley and Raft River basins, Idaho; Rodgers et al., 2002), and other volcanic provinces associated with extensional tectons (e.g., extensional arcs, Fackler-Adams and Busby, 1998). Basins adjacent to the eastern Snake River Plain have been interpreted to have formed through the localised reactivation of Basin and Range normal faults by the migration of the

Yellowstone hot-spot (Anders et al., 1989; Rodgers et al., 1990; 2002), and I infer the same scenario for the Rogerson Graben.

Eruption history

The Rogerson Formation is the product of prolonged, explosive rhyolitic volcanism in the central Snake River Plain. A history of ≥ 8 eruptions is recorded; the duration of which is unknown but may have been c. 11 – 7.5 Ma. The eruptive history of the Rogerson Formation, from oldest to youngest is as follows.

1. A rapid succession of pyroclastic flows entered the Rogerson Graben, possibly from a source near Bruneau - Jarbidge (Fig. 2-4; lineation data; Fig. 2-5) and deposited a voluminous, lava-like ignimbrite (Jackpot Member). A cooler phase of the eruption produced non-welded, traction cross-stratified tuffs with accretionary lapilli ('Jackpot 6') before a return to higher-temperature emplacement.
2. Several NNE-SSW trending graben developed (Fig. 2-5) forming local depocentres for fallout ashes probably erupted from the Bruneau – Jarbidge area, and reworked to form bedded volcanoclastic sediments. Periods of quiescence are recorded as soils.
3. Another ignimbrite eruption, possibly from Bruneau-Jarbidge, emplaced the welded Rabbit Springs Member (10.37 Ma \pm 0.13). Contemporaneous graben extension is indicated by growth faults in the ignimbrite.
4. Continued regional extension led to subsidence and westward tilting of the Rogerson Graben floor, while the basin accumulated non-welded rhyolitic ash and volcanoclastic sediment with several extended periods of soil formation.

5. The next major pyroclastic flow to enter the graben may have had a different magmatic source, possibly near Twin Falls. It deposited a single cooling unit, the eutaxitic Brown's View ignimbrite.
6. Following a repose period (soil horizon) further pyroclastic inundations deposited two, non-welded ignimbrites or debris-flow deposits (Backwaters Member) separated by another significant period of repose.
7. A large-volume, compositionally zoned, rhyolitic explosive eruption deposited a 1.5 m stratified ashfall layer and overlying 60 m thick rheomorphic ignimbrite (the Grey's Landing Member; ~ 7.62 Ma). The eruption may have been from the northeast (kinematic criteria indicate emplacement from the east; Fig. 2-5), near Twin Falls. The rheomorphic character of the ignimbrite reflects hot magmatic temperatures (925 °C – 1025 °C).
8. Following repose periods (palaeosols), further explosive eruptions deposited the non-welded Coyote Creek ignimbrite and the welded Sand Springs ignimbrite, possibly also from the north.
9. Extension of the Rogerson Graben by NNE- and NNW-trending normal faulting and the eruption of at least three late-Miocene basalt lavas (Fig. 2-5; Bonnicksen and Godchaux 2002).
10. Salmon Falls Creek incised a ≥ 50 m deep canyon into the basalt lavas and Grey's Landing ignimbrite (late Miocene, Bonnicksen and Godchaux 2002).
11. The creek was dammed by basalt lava from Salmon Butte (Salmon Dam, Fig. 2-5) and then subsequently re-incised (late Pliocene – Pleistocene, Bonnicksen and Godchaux 2002).

Discussion

The tectono-stratigraphic significance of the Rogerson Formation – correlations with neighbouring successions

I interpret the Rogerson Formation to record deposition of ignimbrites and fallout ashes from the Yellowstone – Snake River Plain volcanic province, into the Rogerson Graben. During the time represented by the Rogerson Formation the graben was actively extending and propagating northwards, becoming a major depo-centre no later than 10.37 Ma when the Rabbit Springs ignimbrite was emplaced. Of the several graben and half-graben developed along the margins of the Snake River Plain (e.g., Rodgers et al., 2002) the Rogerson Graben is the most westerly and contains the oldest graben-fill succession reported (Fig. 2-4).

Further examination of adjacent successions is required to better constrain the distributions, ages, and sources of members within the Rogerson Formation, however, I attempt to draw some preliminary conclusions regarding the stratigraphic significance of the formation. The Jackpot and Rabbit Springs (\leq 10.37 Ma) Members are characteristically sanidine and quartz-phyric; the presence of these crystal types is typical of members of the contemporaneous Cougar Point Tuff Formation (12.7 – 10.4 Ma) and associated ignimbrites and lavas erupted from the Bruneau – Jarbidge area (e.g., Bonnicksen, 1982a; 1982b; Cathey and Nash, 2004). Moreover, NW – SE trending lineations are consistent with emplacement from the Bruneau – Jarbidge area (Figs 2-4 and 2-5). In contrast, the Brown's View, Grey's Landing (7.62 Ma) and Sand Springs Members are devoid of sanidine and quartz, and the Grey's Landing ignimbrite preserves kinematic indicators suggesting emplacement from the east (Fig. 2-5); all criteria typical of eruptions from the Twin Falls area (10.9 – 8.6 Ma; McCurry et al., 1996; Wright et al., 2002).

Attempts to correlate between the established type areas for the Cougar Point Tuff Formation and the Cassia Mountains succession (e.g., Perkins et al., 1995) have been frustrated by lack of knowledge of the stratigraphy in intervening areas,

including the Rogerson Graben and Brown's Bench massif. The stratigraphy described above, and detailed reconnaissance of the Brown's Bench massif (Bonnichsen et al., *in press*), have begun to fill in that gap in the stratigraphic framework, and efforts continue. Provisionally, the Jackpot Member (sub-units 1 – 6) is likely to correlate with the 10.94 Ma (Ar/Ar) Tuff of Big Bluff (Perkins et al., 1995; McCurry et al., 1996) in the Cassia Mountains and 10.91 Ma (Ar/Ar) Brown's Bench Unit 7 (Bonnichsen et al., *in press*). All three units share very similar compositions, appearances, and general stratigraphic positions. Jackpot Member sub-unit 7 has been correlated with Brown's Bench Unit 8 based stratigraphic position, appearance and thickness (Bonnichsen et al., *in press*), furthermore, they suggest that these correlate with the 10.5 Ma (Ar/Ar) Tuff of Steer Basin in the Cassia Mountains (McCurry et al., 1996; Perkins and Nash, 2004). As discussed above (Jackpot Member description and interpretation; Andrews et al., *in press*), further investigations need to be completed before either of these correlations can be accepted, most importantly evidence of a significant time-gap between Jackpot sub-units 6 and 7 (e.g., an intervening palaeosol or sedimentary horizon) must be identified. Bonnichsen et al. (*in press*) have correlated, tentatively, two units within the Brown's Bench massif to members of the Cougar Point Tuff Formation, but at this time, no positive correlation has been established between the Jackpot Member and a specific Cougar Point Tuff member.

Snake River-type volcanism: voluminous lavas and lava-like ignimbrites

A new style of silicic volcanism?

As I have described (above) the Rogerson Formation (Fig. 2-6) is composed of two types of ignimbrite; extremely high- and high-grade, high temperature (≥ 800 °C) ignimbrite (e.g., the Grey's Landing Member; Fig. 2-18), and non-welded and poorly preserved ignimbrite (e.g., the Backwaters Member). Moreover, there is generally an absence of pumice lapilli and lithic lapilli, both within ignimbrites and fall deposits. The tephras preserved are overwhelmingly fine-grained ashes

(sand-sized ash shards). This association is typical of south-central Snake River Plain region, where, in addition to welding intensity, the lack of lapilli, and fine-grainsizes, voluminous silicic lavas ($> 10 \text{ km}^3$) are abundant (Fig. 2-18). This association is atypical of most silicic volcanic provinces (e.g., the Taupo volcanic zone, New Zealand, Graham et al., 1995; Tenerife, Canary Islands, Brown et al., 2003; the Neapolitan – Phlegrean volcanic region, Italy, Rolandi et al., 2003) where high-grade ignimbrites and voluminous silicic lavas are rare. Instead, small-volume ($< 10 \text{ km}^3$) silicic domes and coulees, and pumice-lapilli rich ignimbrites and fall deposits are characteristic (Fig. 2-18). However, the association of volcanic rocks observed in the south-central Snake River Plain (including the Rogerson Formation) is found in other regions (e.g., Etendeka – Parana, Bellieni et al., 1984; Trans-Pecos, TX, Henry et al., 1988; Yardea, Australia, Creaser and White, 1991), and has been identified as a distinctive style of silicic volcanism: Snake River-type distinct from ‘typical’ silicic volcanism.

Distinguishing voluminous lavas from lava-like ignimbrites

Investigations of lava-like rhyolites have inevitably led to discussion over their emplacement mechanism: (1) as a lava, flowing *en masse* from the vent; or (2) as an ignimbrite, deposited from a pyroclastic density current. We have interpreted each member as an ignimbrite based on several criteria: (1) unit form and thickness (e.g., Mukhopadhyay et al., 2001), (2) textures preserved in vitrophyre, and (3) the absence of autobreccias. Most rhyolite lavas in the Snake River Plain are thick ($\geq 50 - 300 \text{ m}$) and have aspect ratios $\leq 1:10^3$ (Fig. 2-19; Branney et al., *in prep.*). Moreover, they exhibit widespread basal and carapace autobreccias (e.g., Bonnicksen 1982b; Henry and Wolff 1992; Manley 1996a), and typically vitroclastic textures are rare and limited to where autobreccia has been entrained into the flowing lava (e.g., Manley 1996b). In contrast, lava-like ignimbrites are thin (typically $< 100 \text{ m}$ thick) and have aspect ratios of $\geq 1:10^3$ (Fig. 2-19). Vitroclastic textures are ubiquitous, although they may be obscured by rheomorphism and devitrification, and autobreccias are uncommon and often not widespread (e.g., Sumner and Branney 2002). Generally, the presence of abundant broken crystals (e.g., Fig. 2-15d) is characteristic of ignimbrites rather

than of lavas (e.g., Fisher and Schminke 1984; Allen and McPhie; 2003). Crystal breakage is driven by two independent processes. First, high velocity impacts between crystals and second, explosive decompression of melt inclusions within a crystal (Best and Christiansen 1997). However, crystal breakage can be limited in extremely high-grade ignimbrites (Branney and Kokelaar 1992; Branney et al. 1992; Henry and Wolff 1992).

Classification of rhyolite lavas

Voluminous silicic lavas are especially characteristic of Snake River-type volcanism and are very unusual in other volcanic provinces. ‘Typical’ rhyolite lavas are small ($< 10 \text{ km}^3$) and are usually domes or coulees (Fig. 2-18) and have aspect ratios (thickness over approximate diameter) less than $1:10^2$ (Fig. 2-19), and commonly less than $1:10^1$ (Walker, 1973). Data for the dimensions of Snake River-type silicic lavas were collated in this thesis (Fig. 2-19) and shows that they are much more voluminous ($> 10 \text{ km}^3 - \geq 1000 \text{ km}^3$) and have aspect ratios ($1:20 - < 1:10^3$) similar to some ignimbrites, and that they form a distinct field separate from ‘typical’ rhyolites. I infer that the huge volumes of Snake River-type lavas (similar to ignimbrites) indicate that they are effusions that drained large magma chambers, and that they are fundamentally different from small silicic domes that are the products of shallow intrusions and magma-filled conduits that broke the surface. Furthermore, the low aspect ratios of Snake River-type silicic lavas suggest they were erupted quickly and at high supra-solidus temperatures ($\geq 800 \text{ }^\circ\text{C}$; Henry and Wolff, 1992), allowing for rapid flow away from the vent before cooling led to significant increases in viscosity, and eventual cessation. In contrast, most silicic domes are extruded at sub-solidus temperatures and flow incredibly slowly, often deforming more by brittle deformation than by ductile flow.

Initial conclusions

1. The Rogerson Formation is a graben-filling sequence of five welded ignimbrites and associated volcanoclastic deposits, including non-welded ignimbrites, fallout ashes, and volcanoclastic sediments (Fig. 2-6). Two welded ignimbrites, the Jackpot and Grey's Landing Members, are lava-like and rheomorphic.
2. The Rogerson Formation is typical of Snake River-type volcanic successions, and is atypical of most silicic provinces elsewhere (Fig. 2-18). Snake River-type ignimbrites are characterised by high magmatic temperatures, lack of pumice and lithic lapilli or fiamme, intense welding (typically lava-like and rheomorphic), and very large volumes.
3. The Rogerson Formation may record the migration of the locus of volcanism across Southern Idaho following the track of the Yellowstone hotspot (Fig. 2-4). Furthermore, it may record contemporaneous basin development along reactivated faults coincident with lithospheric stretching around the hotspot locus and the adjacent Basin and Range taphrogen.

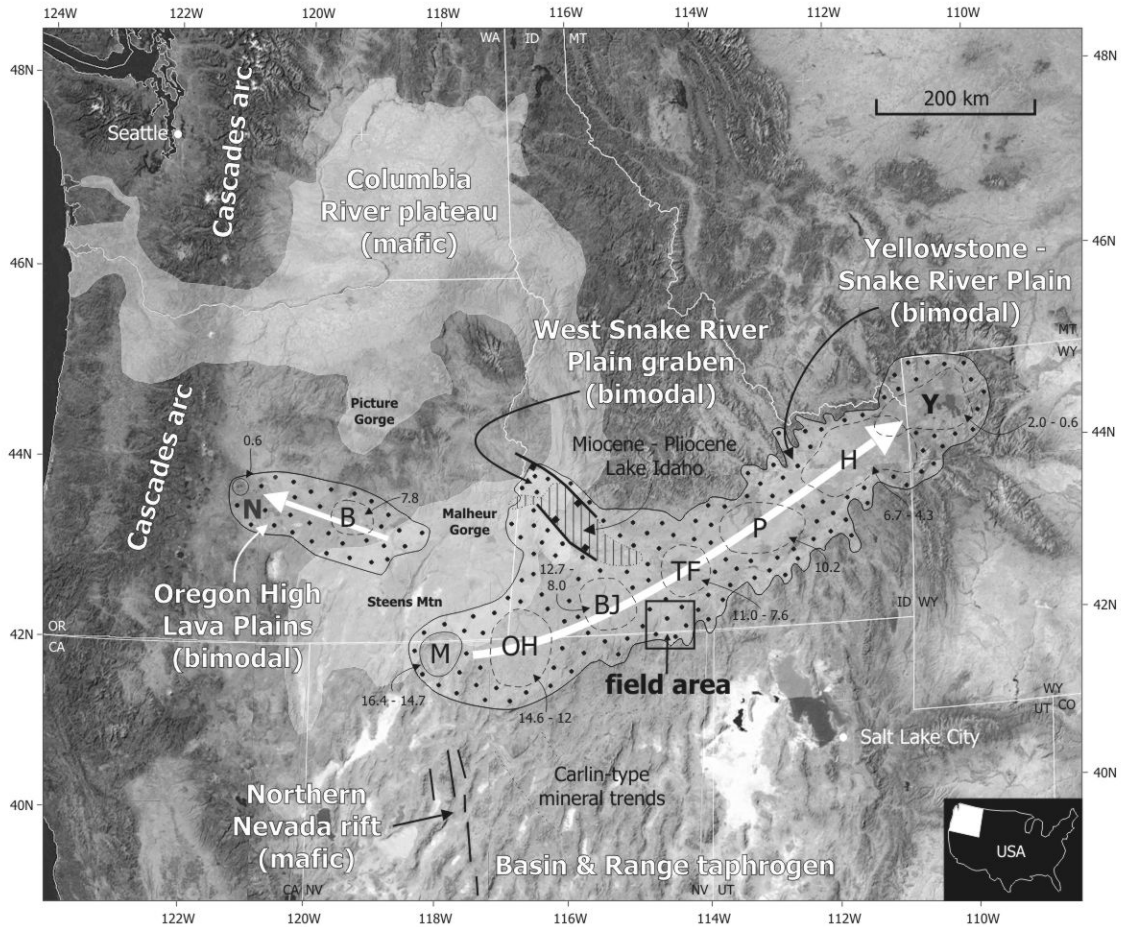


Fig. 2-1. The Columbia River - Yellowstone volcanic mega-province and subordinate volcanic provinces and fields in the intermontane north-west USA (inset). N = Newberry caldera, B = Burns caldera, M = McDermitt caldera, OH = Owyhee - Humboldt eruptive centre, BJ = Bruneau - Jarbidge eruptive centre, TF = Twin Falls eruptive centre, P = Picabo eruptive centre, H = Heise eruptive centre, Y = Yellowstone caldera field. Extent of Columbia River basalts (including the Steens Mountain, Malheur Gorge, and Picture Gorge basalts) taken from Camps & Ross (2004). Extent and ages of Oregon High Lava Plains taken from Christiansen and Yeats (1992) and Jordan et al. (2004). Extent and ages of Yellowstone - Snake River Plain volcanic province from Hughes and McCurry (2002), Wood and Clemens (2002), and Morgan and McIntosh (2005). Large white arrows represent the relative age progression of silicic caldera volcanism.

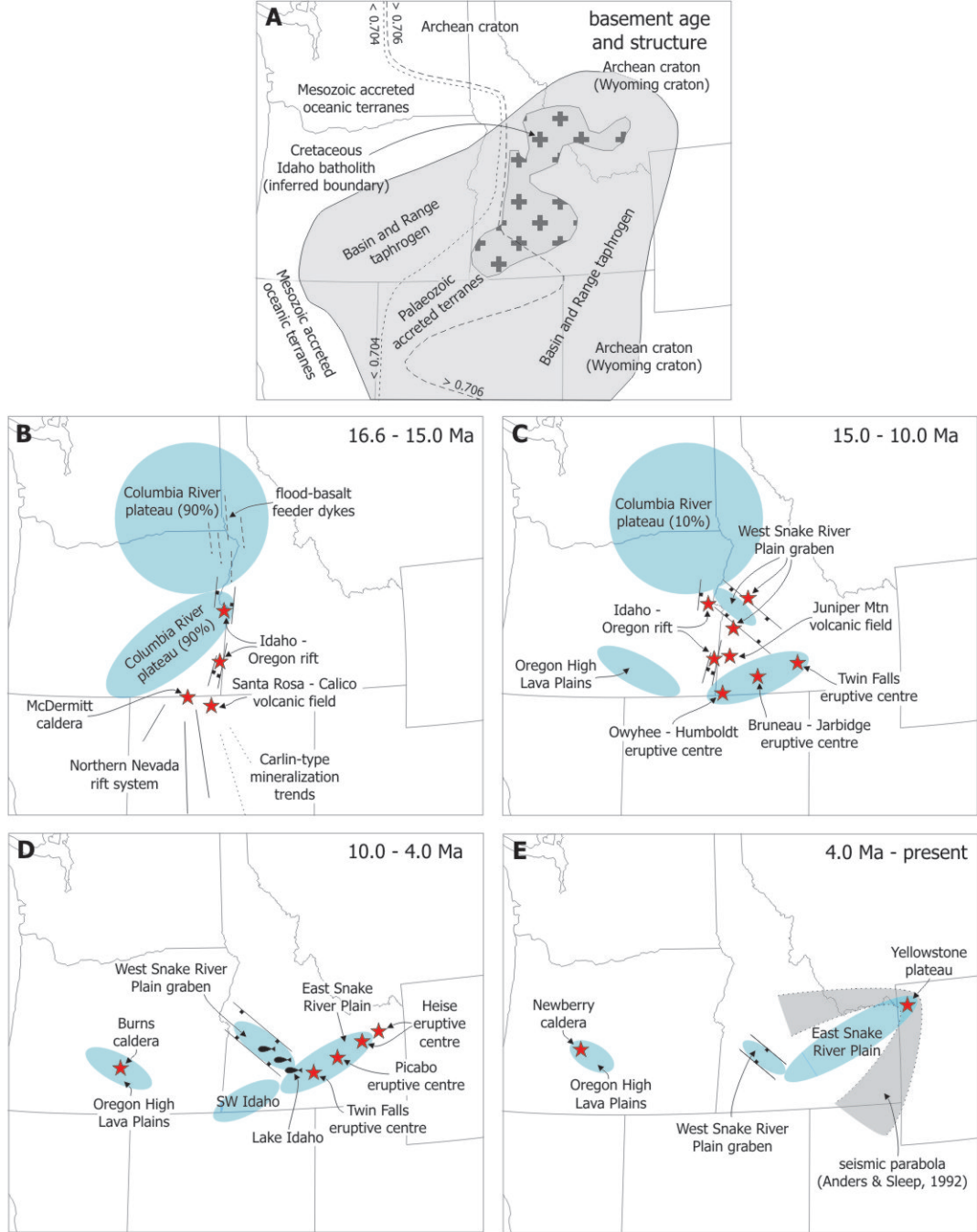


Fig. 2-2. The temporal and spatial evolution of the Yellowstone - Columbia River mega-volcanic province. Schematic geological maps for pre-volcanic basement and structure (A) and four phases of volcanism (B - E); displaying active basaltic volcanic fields (blue), rhyolite volcanic centres (red stars), and extensional regimes (grey). In map A, basement west of the $^{87}\text{Sr}/^{86}\text{Sr} = 0.704$ isopleth is 'thin' lithosphere (< 25 km) of accreted Mesozoic oceanic terranes, whereas basement east of the 0.706 isopleth is 'thick' Archean cratonic lithosphere (> 50 km) (Pierce & Morgan, 1992). Basement between the 0.704 and 0.706 isopleths is inferred to be 'intermediate thickness' lithosphere (~ 35 km), of attenuated Palaeozoic platform (Hughes & McCurry, 2002).

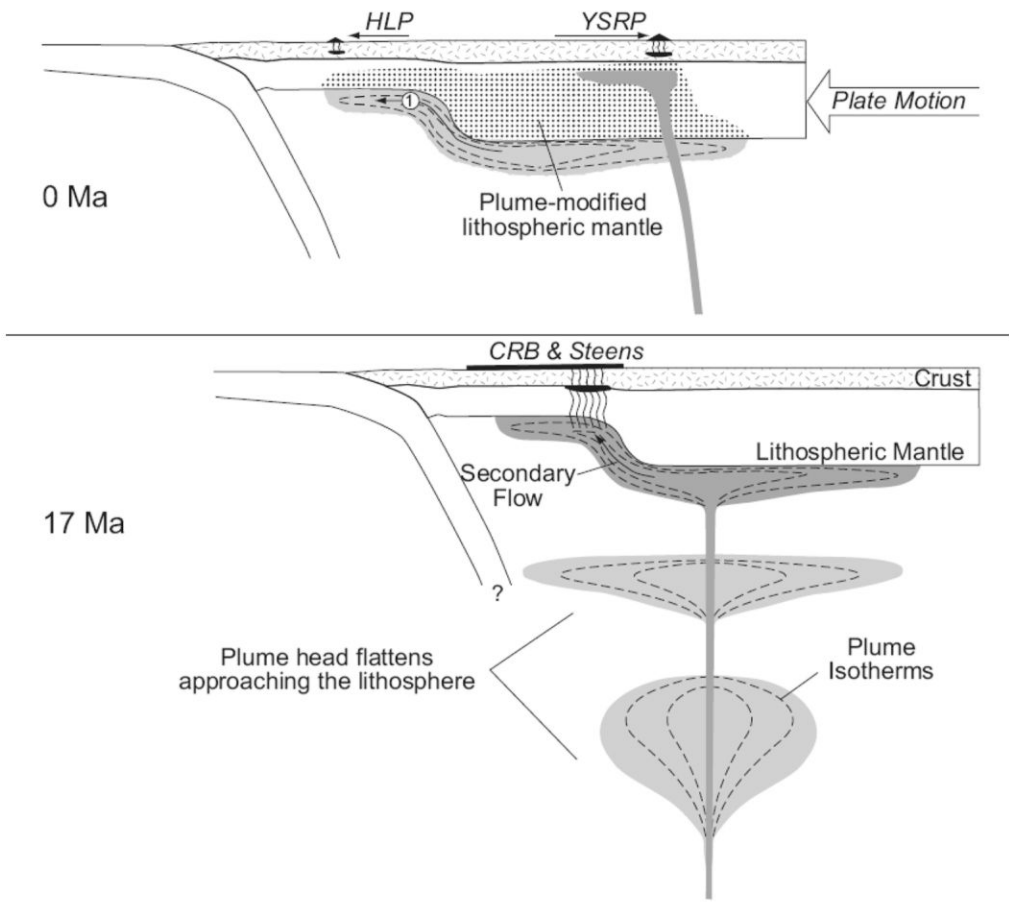


Fig. 2-3. Schematic cartoon of the divergence of active volcanism in the Yellowstone - Snake River Plain (YSRP) and Oregon High Lava Plains (HLP) volcanic provinces, following the impact of a mantle plume below a common inception point (modified from Jordan, 2005). At 17 Ma the rising mantle plume impacts the base of the lithosphere and flows along the base of the lithosphere until it comes to pre-existing weaknesses in the lithosphere allowing rapid tapping of hot asthenosphere, and flood basalt eruption. Present-day, the Oregon High Lava Plains are sustained by residual melt from the remaining plume head, whereas, the Yellowstone - Snake River Plain province is sustained an active, narrow conduit of rising asthenospheric mantle. 1 = westward flow of plume material on basal lithospheric topography.

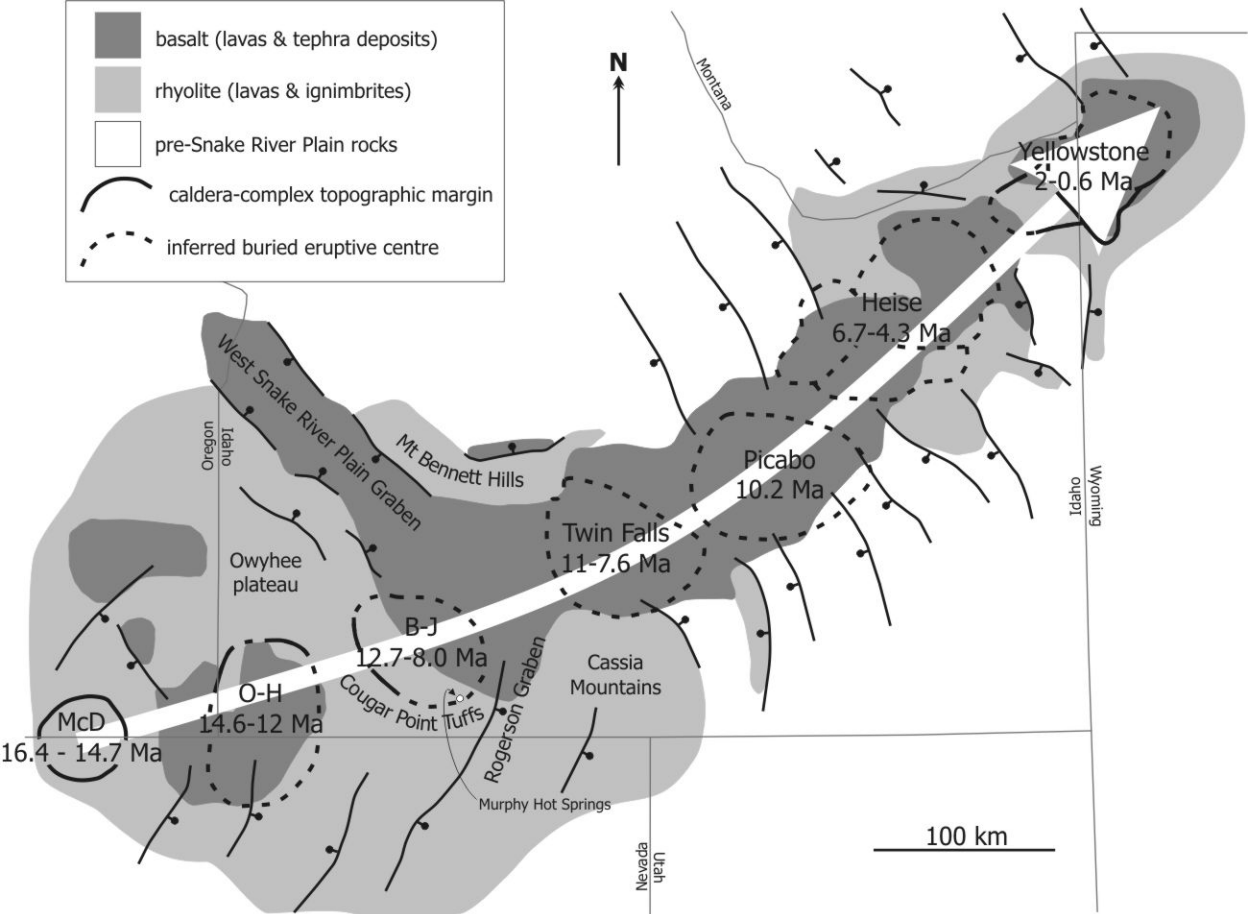


Fig. 2-4. Simplified geologic map of the Yellowstone - Snake River Plain volcanic province. Modified from Pierce and Morgan 1992; Hughes and McCurry 2002; and Rodgers et al. 2002. Age data taken from Hughes and McCurry 2002.

Rogerson Formation

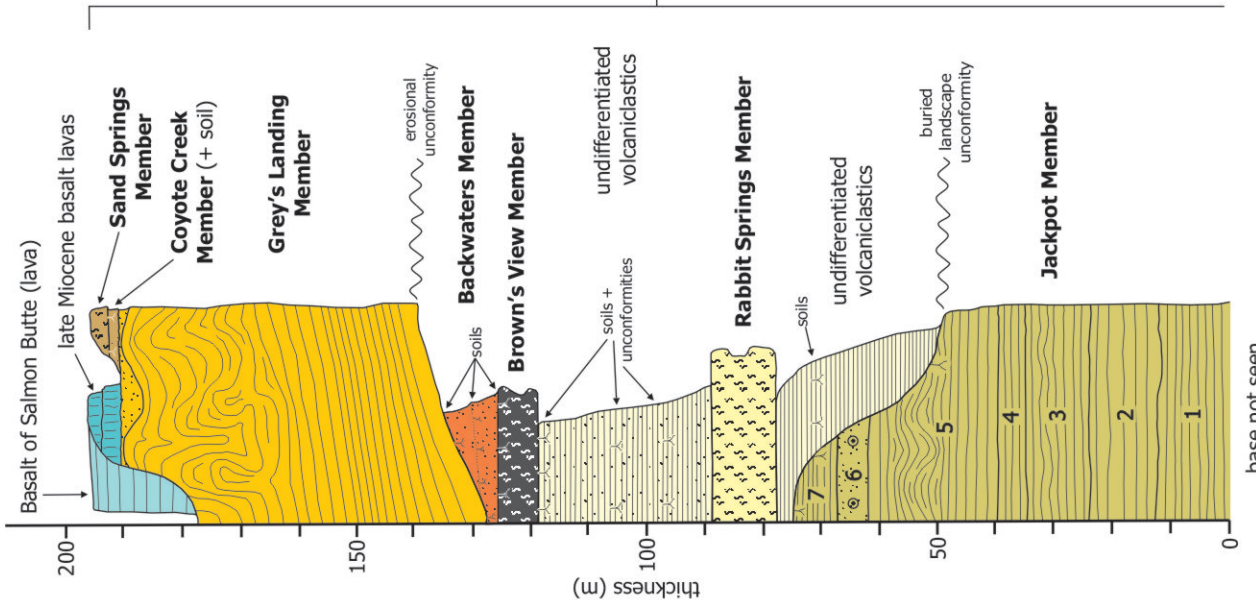


Fig. 2-6. General vertical section through the Rogerson Formation in the Rogerson Graben. Soils, erosion surfaces, and unconformities are marked. Details of lithofacies, welding grade, type locality, minimum volume, and crystal assemblage are given on the right. plag = plagioclase, sa = sanidine, pgt = pigeonite, aug = augite, qtz = quartz, mt = magnetite, il = ilmenite, zr = zircon, ap = apatite

| lithofacies and fabric | Type Locality UTM co-ordinates | min. volume (km ³) | estimated crystal content and max. Size (mm) | crystal assemblage |
|---|--------------------------------------|--------------------------------|--|--|
| high-grade, eutaxitic | HWY 93 620970 4660947 | > 0.25 | 10 - 15% 5 mm | plag, pgt, aug, mt, zr, ap |
| lava-like, rheomorphic, flow banded | Grey's Landing 687702 4667000 | >> 13 | 10 - 15% 3 mm | plag, pgt, aug, mt, zr, ap |
| high-grade, eutaxitic | Backwaters 685369 4659239 | > 1.25 | 10 - 15% 4 mm | plag, pgt, aug, mt, il, zr, ap |
| high-grade, eutaxitic | Backwaters 685369 4659239 | > 1.5 | 10 - 20% 6 mm | plag, sa, pgt, aug, qtz, mt, il, zr, ap |
| lava-like, flow banded, locally folded. Jackpot 6 non-welded | Salmon Falls Creek 691667 4646088 | >> 22.5 | 10 - 15% 4 mm | sa, plag, qtz, pgt, aug, mt, zr, ap |

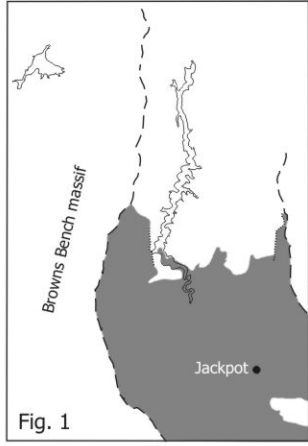
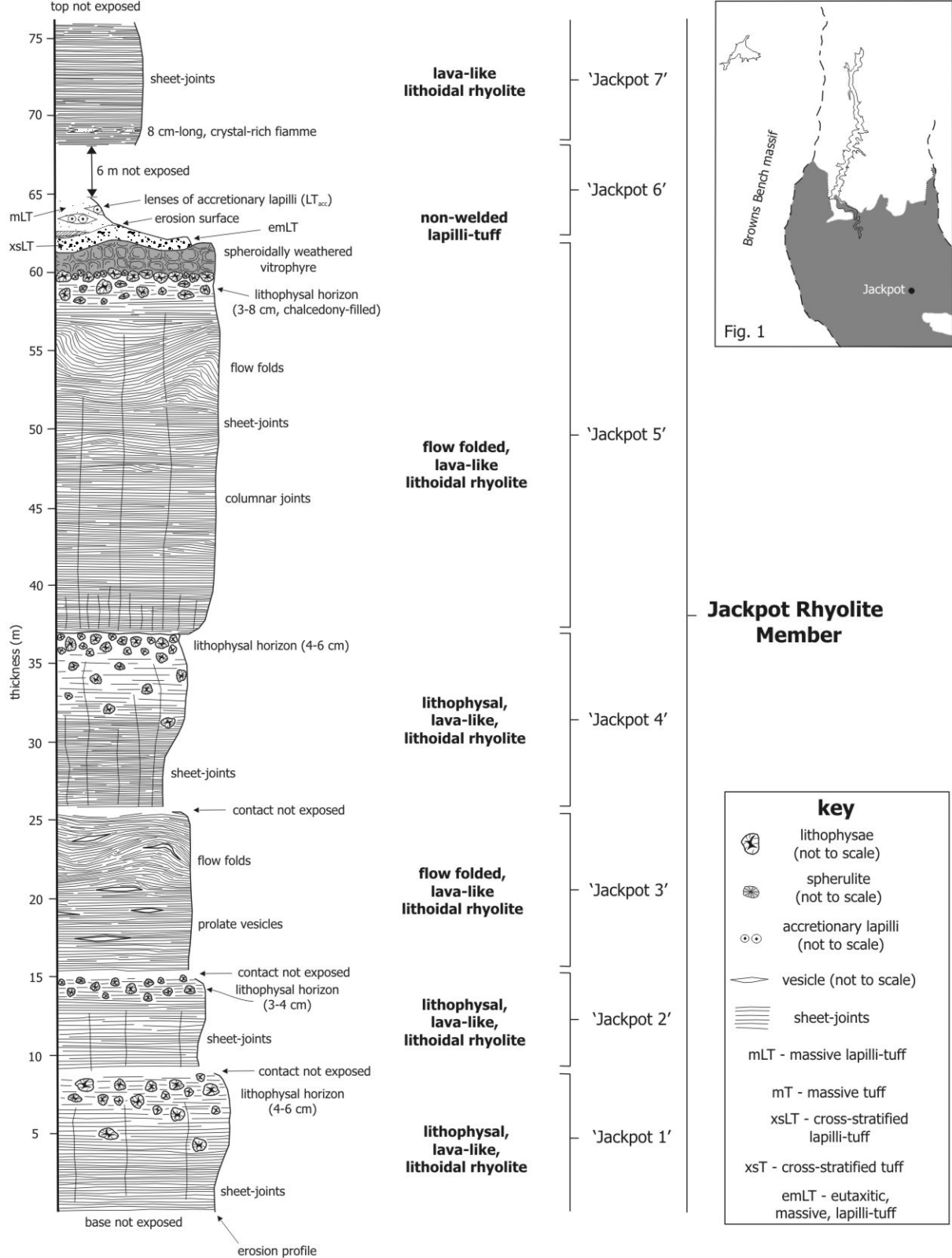


Fig. 2-7. Graphic log of the Jackpot Member, based upon sections at Salmon Falls Creek and Sweetwater Lane. Abbreviations on key follow Branney and Kokelaar, 2002. Inset shows the outcrop of the member.

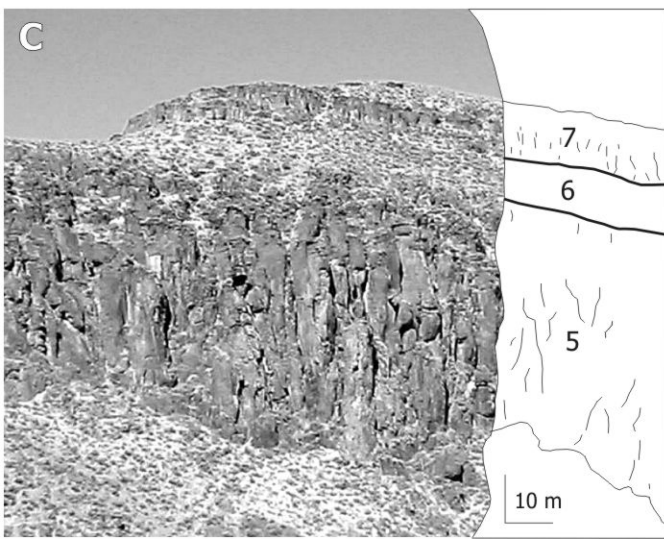
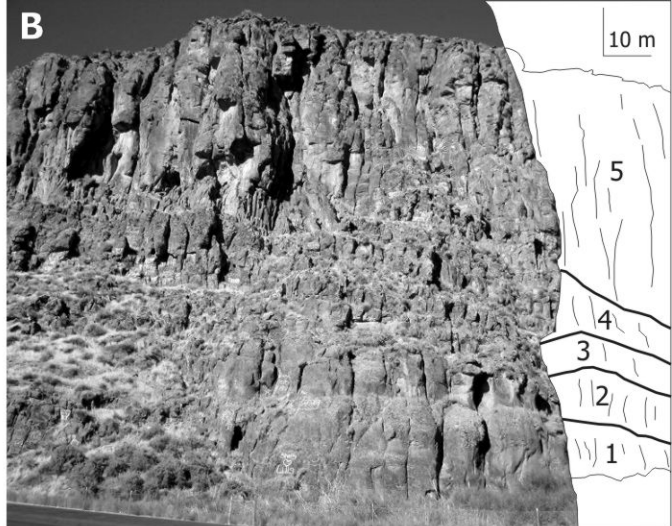
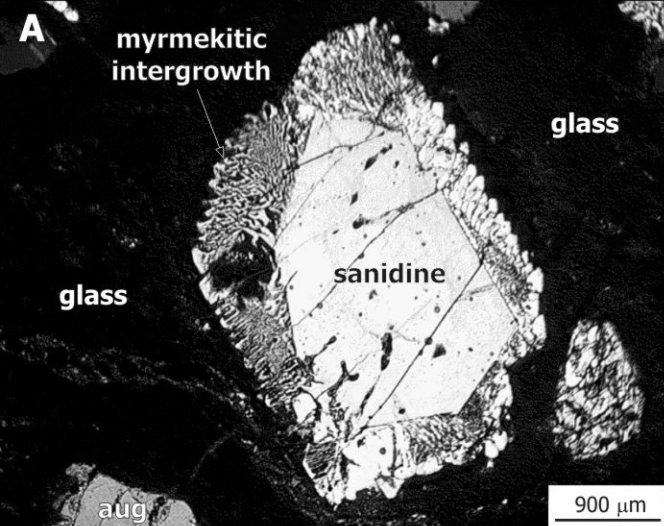


Fig. 2-8. The Jackpot Rhyolite Member. (A) Myrmekitic intergrowth of quartz and K-feldspar around an anhedral sanidine phenocryst, in isotropic glass matrix; crossed polars (PPL). (B) Lower part of the Jackpot Member at Salmon Falls Creek, showing subdivisions into 'Jackpot 1 - 5' by topographic benches and variations in columnar-jointing patterns. (C) Upper part of the Jackpot Member in escarpment immediately west of Jackpot, NV.

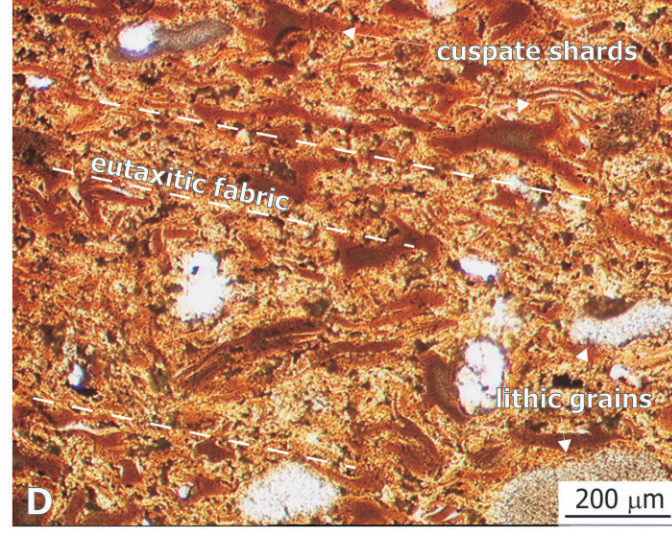
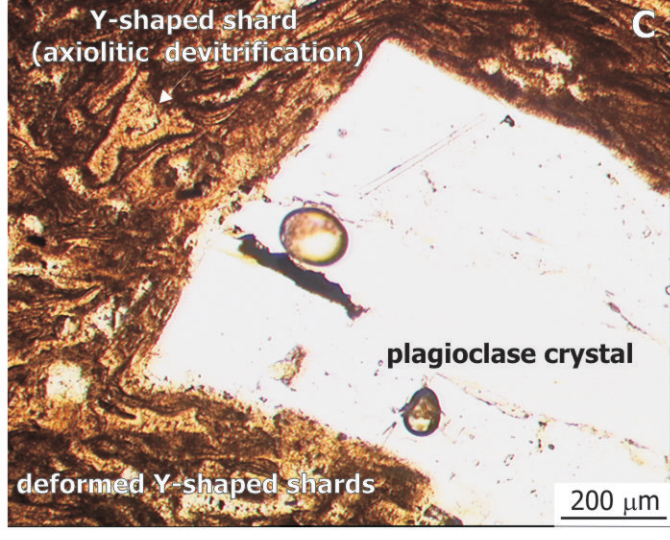
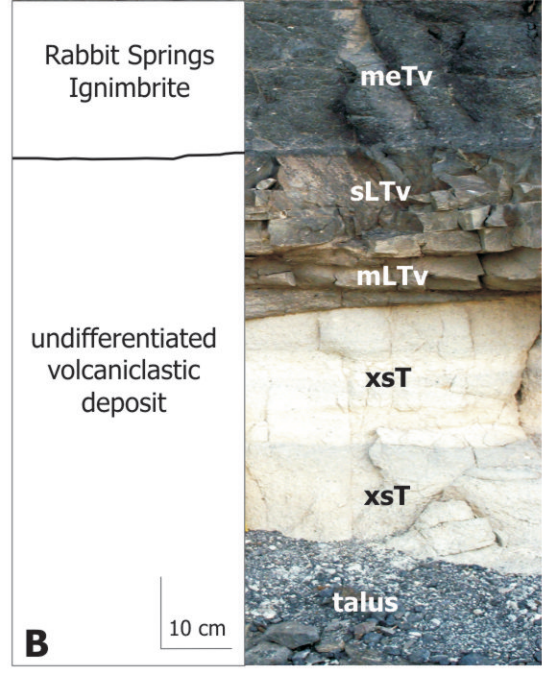
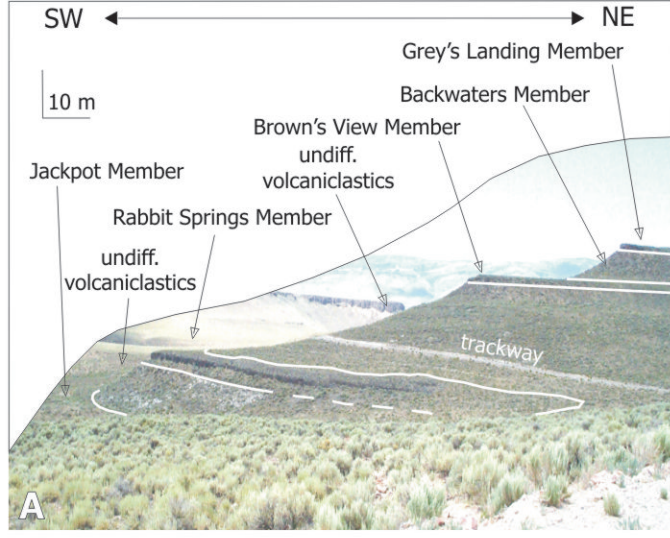
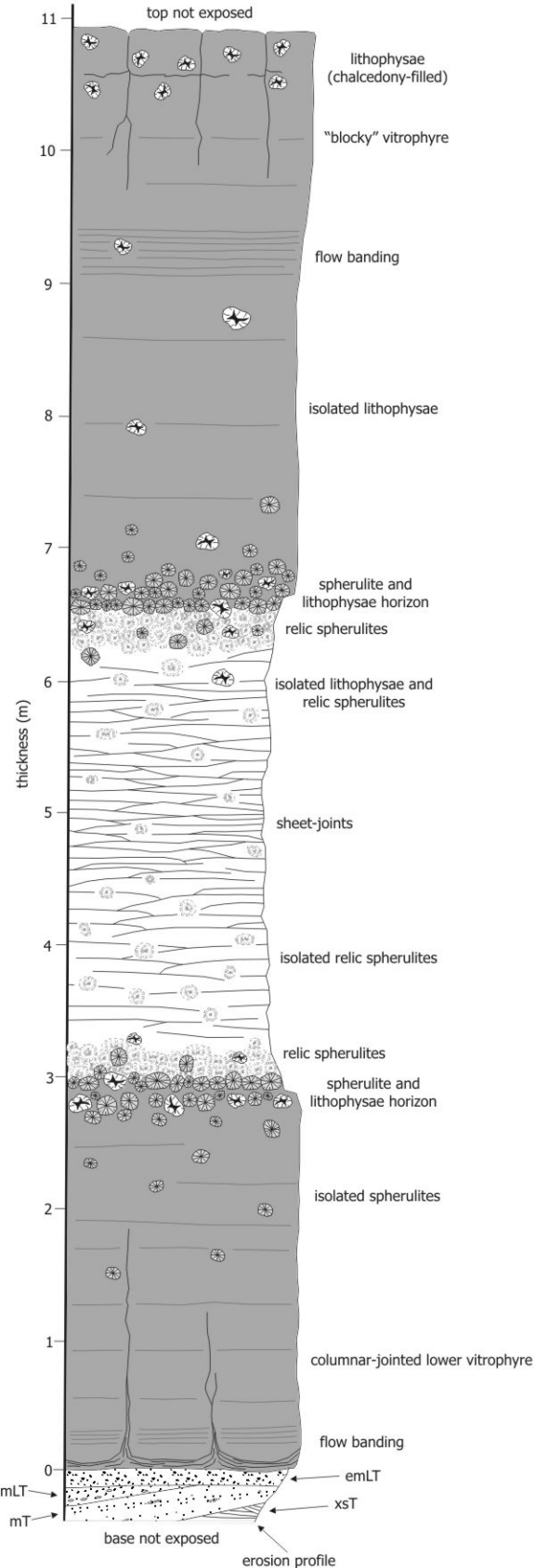
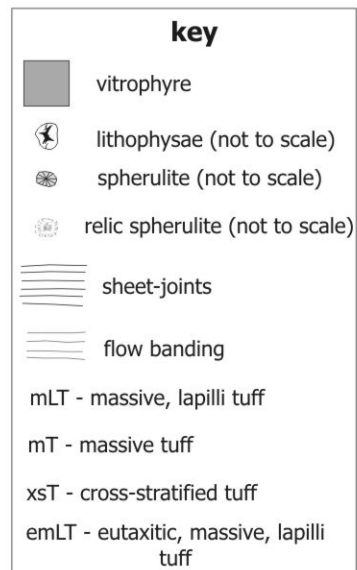


Fig. 2-9. (A) Stratigraphy approximately 5 km east of Backwaters (Fig. 1), showing units dipping gently northwards. Note the thin and uniform nature of the welded Rabbit Springs, Brown's View and Grey's Landing Members, producing prominent topographic benches. (B) Base of Rabbit Springs Member at Backwaters, showing increasing fusing intensity in originally non-welded volcaniclastic deposits (meTv = massive eutaxitic vitric tuff; sLTv = stratified vitric lapilli-tuff; mLTv = massive vitric lapilli-tuff; xsT = cross-stratified tuff; Branney and Kokelaar 2002). (C) Photomicrograph (PPL) of the Rabbit Springs Ignimbrite basal vitrophyre showing welded Y-shaped shards, strongly flattened around the corner of a plagioclase crystal. Note the axiolitic devitrification textures developed in the largest shards. (D) Photomicrograph (PPL) of Brown's View Ignimbrite basal vitrophyre, showing moderate flattening of Y-shaped shards, producing an eutaxitic fabric.



Rabbit Springs ignimbrite Member



bedded
volcaniclastic
rocks

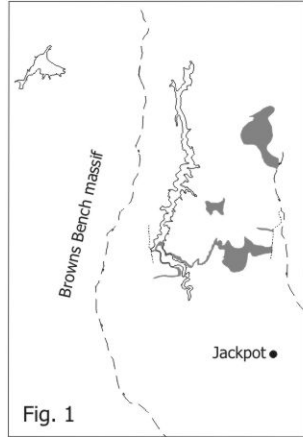


Fig. 2-10. Graphic log of the Rabbit Springs Member, from the Backwaters section. Inset shows the outcrop of the Member.

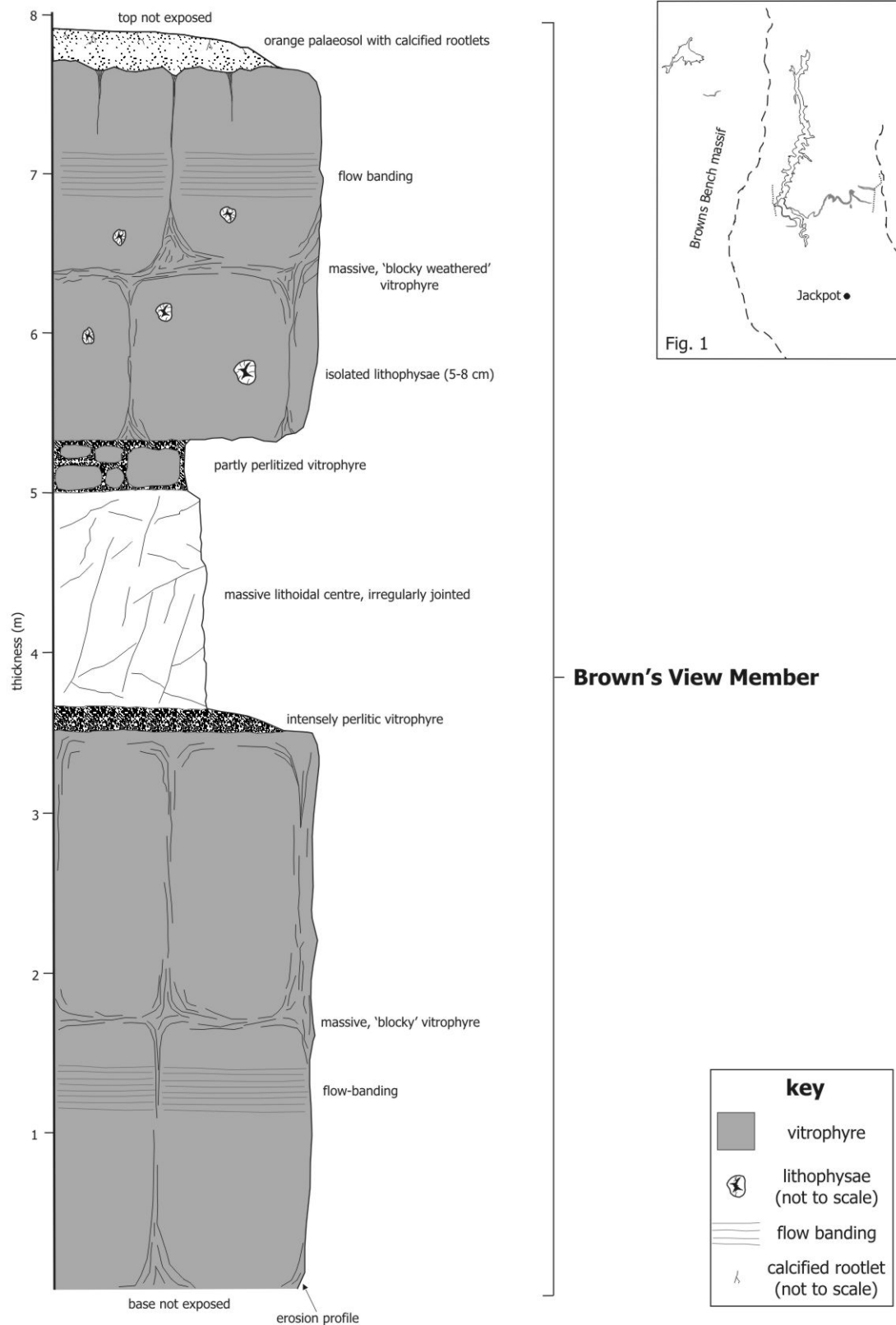


Fig. 2-11. Graphic log of the Brown's View Member from the Backwaters section. Inset shows outcrop of the Member.

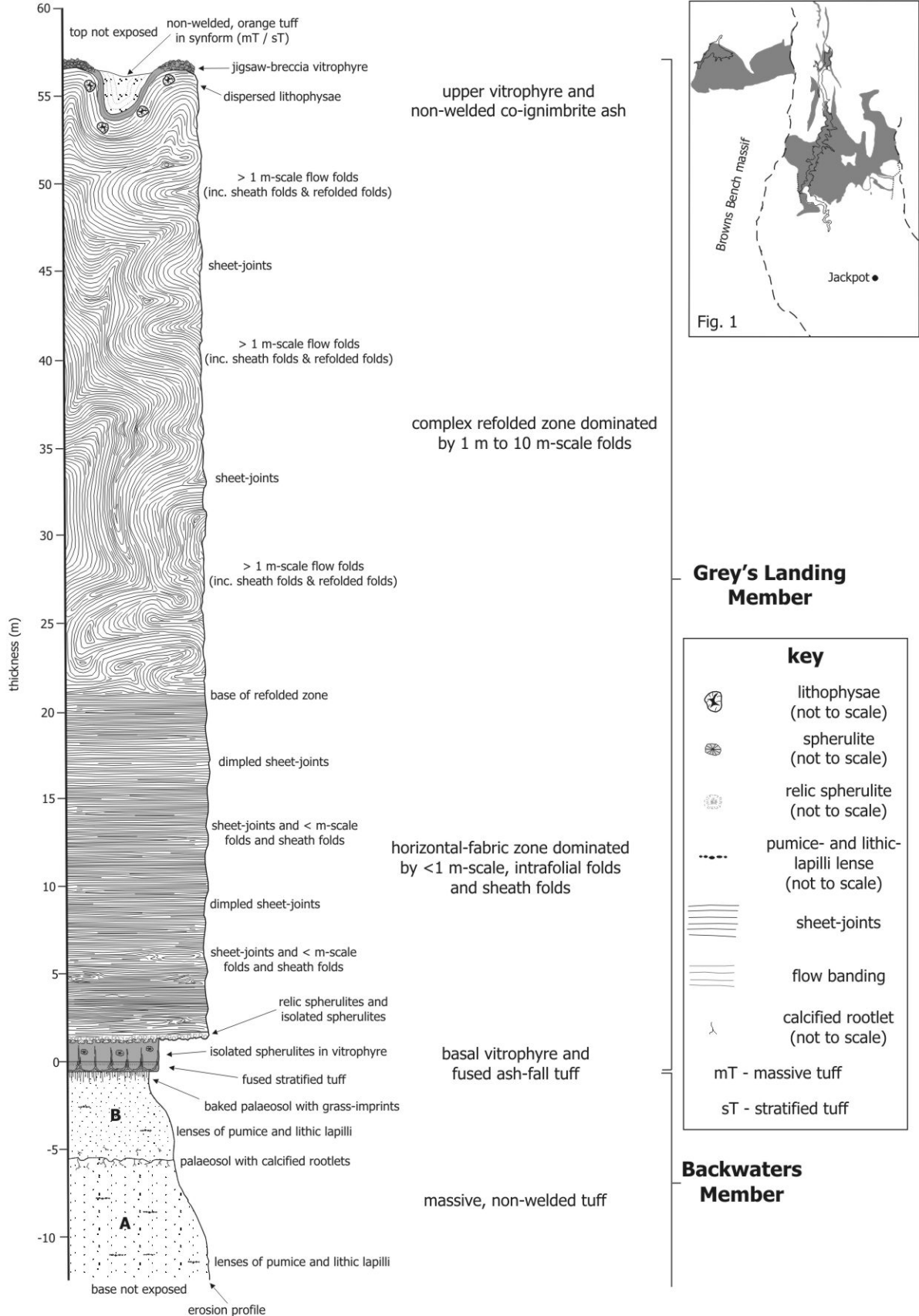


Fig. 2-12. Graphic log of the Backwaters and Grey's Landing Members based upon sections at Backwater, Grey's Landing and Salmon Dam. Inset shows the distribution of the Backwaters and Grey's Landing Members.

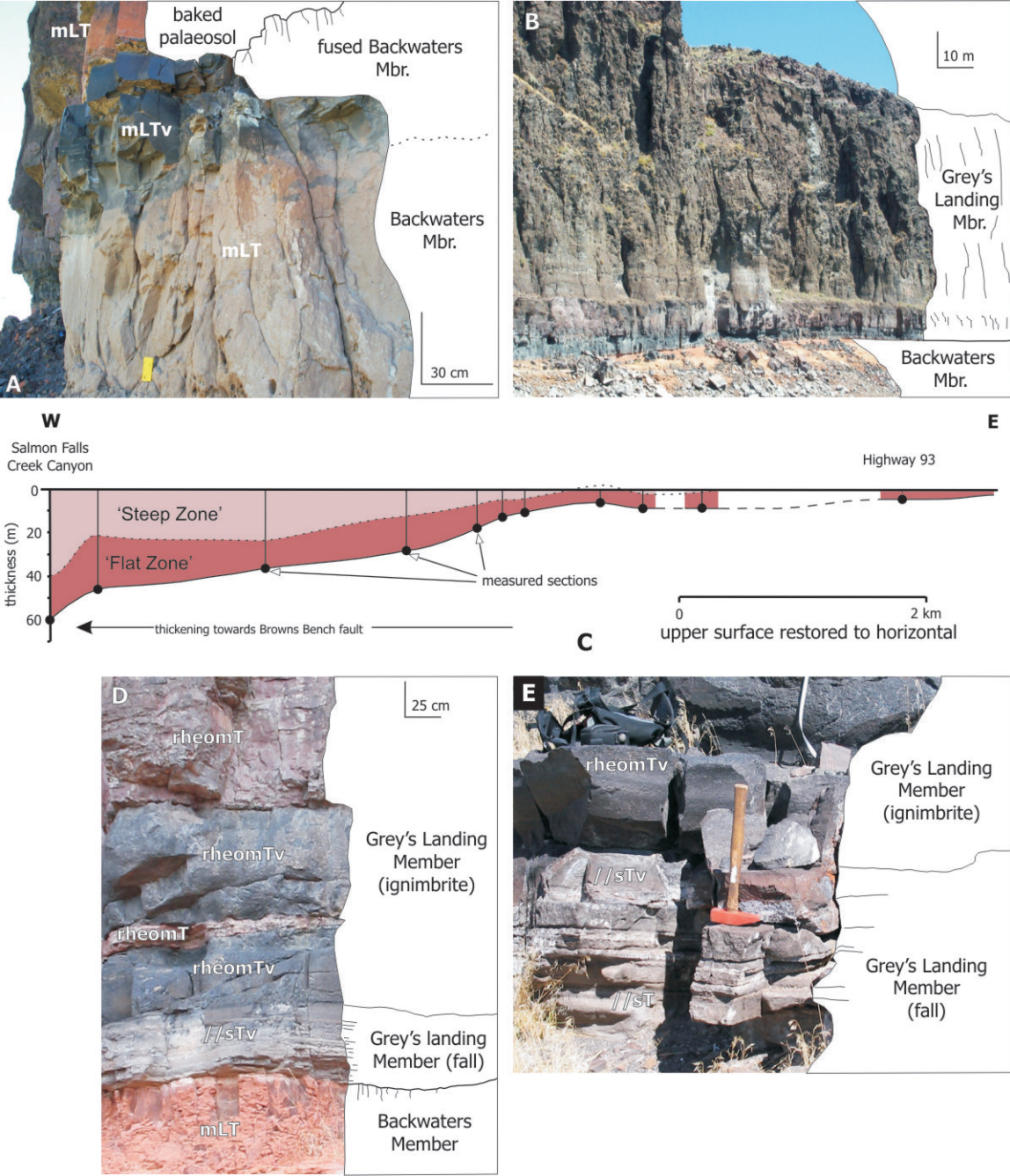


Fig. 2-13. (A) Baking and fusing zonation within the Backwaters Member, Backwaters. (B) 55 m-thick Grey's Landing Member dominated by massive, lithoidal centre, sitting on baked Backwaters Member palaeosol at Grey's Landing. (C) Cross section through the Grey's Landing ignimbrite from Salmon Falls Creek Canyon (west) to Highway 93 (east), showing wedge-shaped profile and relative thickness of the 'steep' and 'flat' zones. (D) Detail of the Grey's Landing Member base where it is ~60 m-thick, showing the basal vitrophyre lying on fused and stratified, ashfall tuff, in turn lying on baked Backwaters Member palaeosol, Backwaters. (E) Detail of the base of the Grey's Landing Member where it is ~12 m-thick, showing limited fusing of the underlying stratified tuff. Only the upper 30 cm of the stratified tuff are fused, Highway 93. mLT = massive lapilli-tuff, mLTv = massive vitric lapilli-tuff, rheomT = rheomorphic tuff, rheomTv = rheomorphic vitric tuff, //sTv = parallel stratified vitric tuff (Branney and Kokelaar 2002).

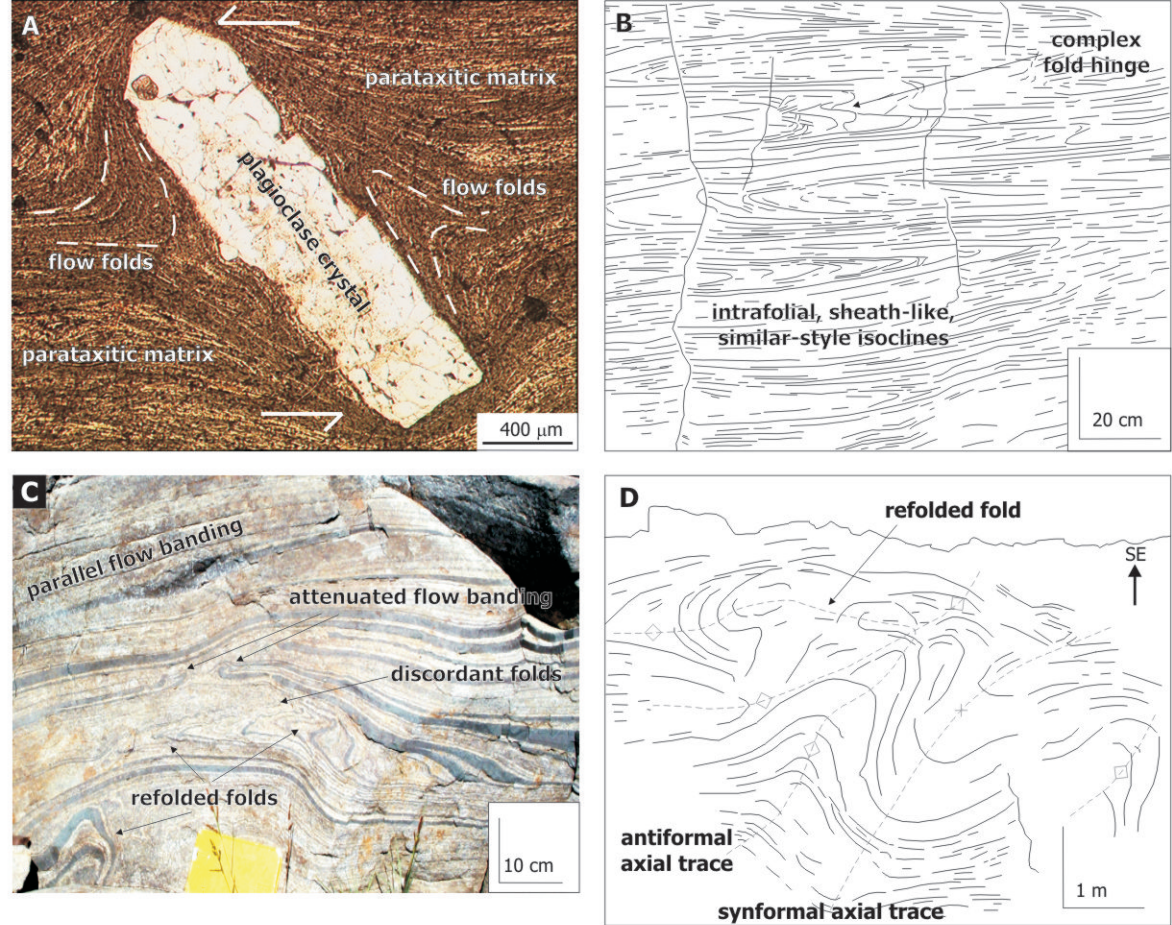


Fig. 2-14. Grey's Landing Member (A) Rotated and mantled, euhedral plagioclase crystal and associated <mm-scale folds from the basal vitrophyre, Grey's Landing, section parallel to stretching direction (PPL). Note the flow banding and 'mylonitic appearance'. (B) Sketch of dm-scale, sheath-like, intrafolial, similar-style isoclinal folds, typical of the Grey's Landing ignimbrite 'flat zone'; Grey's Landing, viewed parallel to stretching direction. (C) Complex cm-scale folding, refolding and attenuation of flow banding, Salmon Dam, oblique to stretching direction. (D) Sketch of m-scale, complexly refolded folds in the 'steep zone', Cedar Creek Reservoir, viewed perpendicular to transport direction.

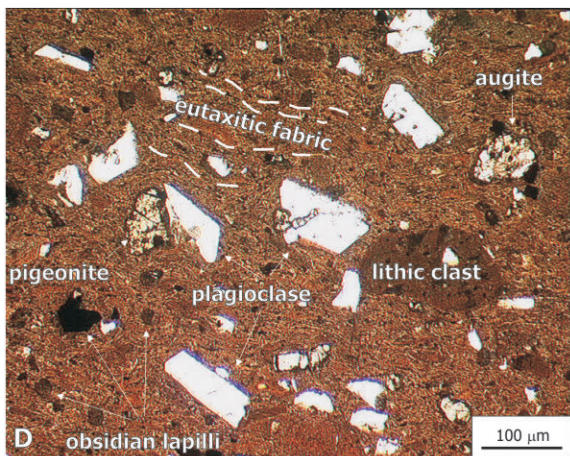
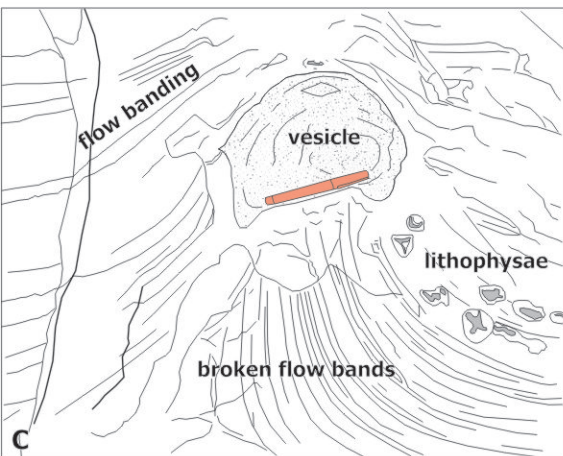


Fig. 2-15. (A) Lineation developed on sheet-joint surface, Salmon Dam (pen 12 cm). (B) Dimple-joints on surface of a loose block, Cedar Creek Reservoir (hammer shaft 40 cm). (C) Sketch of 15 cm diameter, spherical vesicle in banded, devitrified Grey's Landing ignimbrite, Cedar Creek Reservoir (pen 12 cm). Note how the vesicle has intruded upwards ('diapiric'), and broken through some banding. (D) Photomicrograph (PPL) of the Sand Springs Member showing eutaxitic, fine-tuff matrix surrounding abundant crystals and < mm-scale lithics.

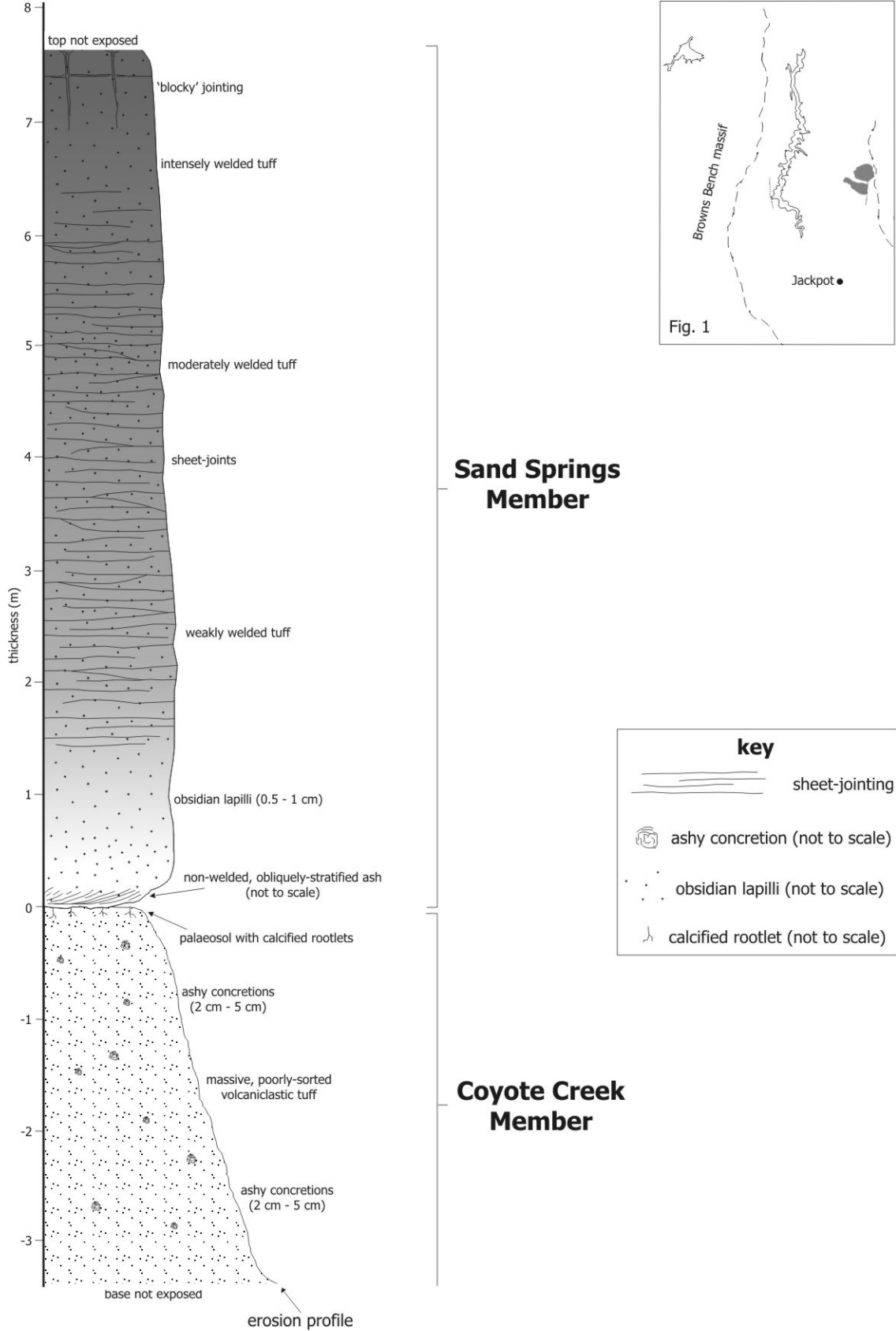


Fig. 2-16. Graphic log of the Sand Springs and Coyote Creek Members, from the Highway 93 road section. Inset shows the outcrop of the Sand Springs Member.

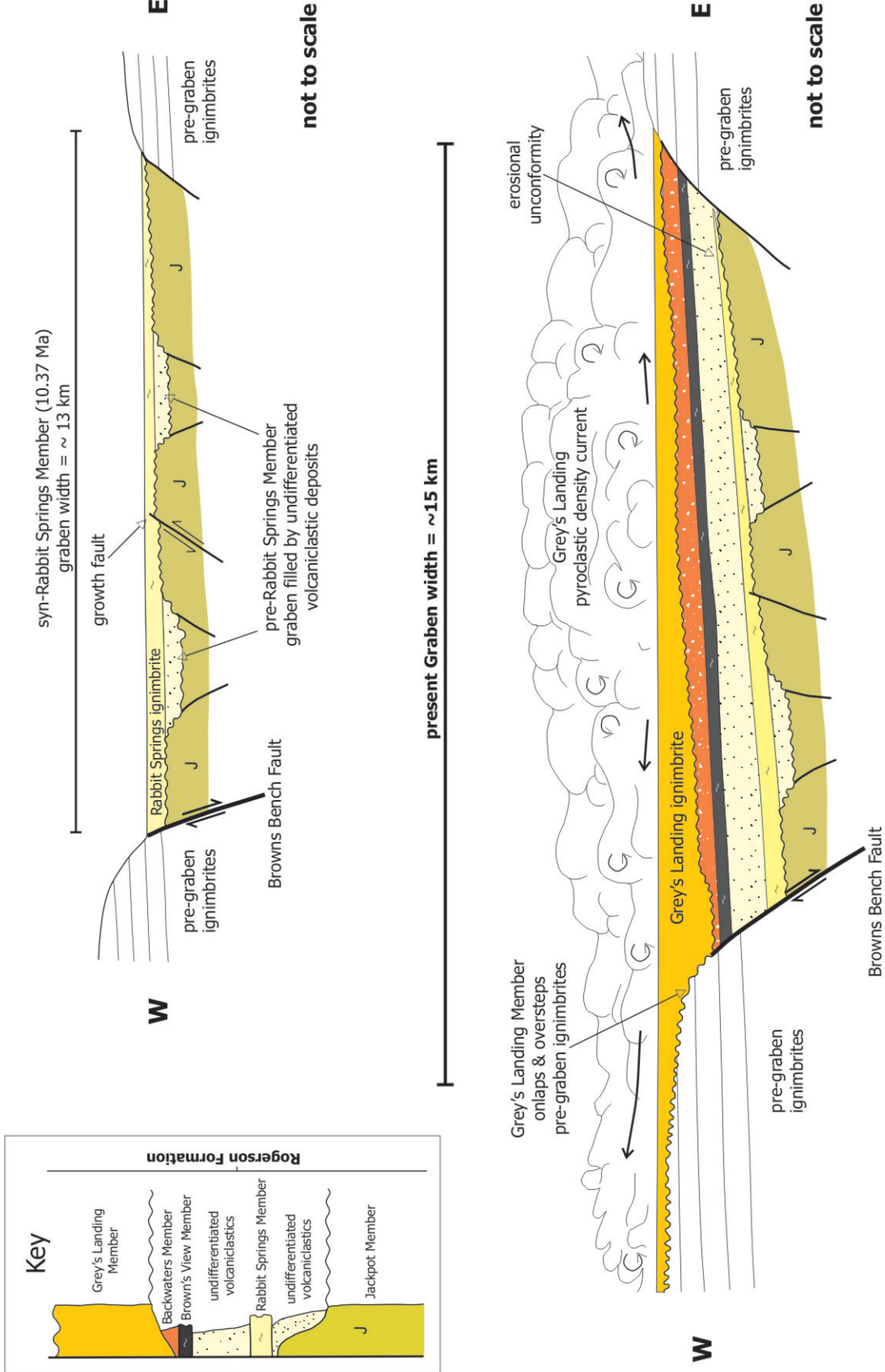


Fig. 2-17. Schematic cross-sections through the Rogerson Graben: (top) immediately after emplacement of the Rabbit Springs Member. Note growth fault and burial of earlier graben; (bottom) during emplacement of the Grey's Landing Member. Note that the Grey's Landing Member onlaps and oversteps pre-graben ignimbrites and the Brown's Bench Fault scarp.

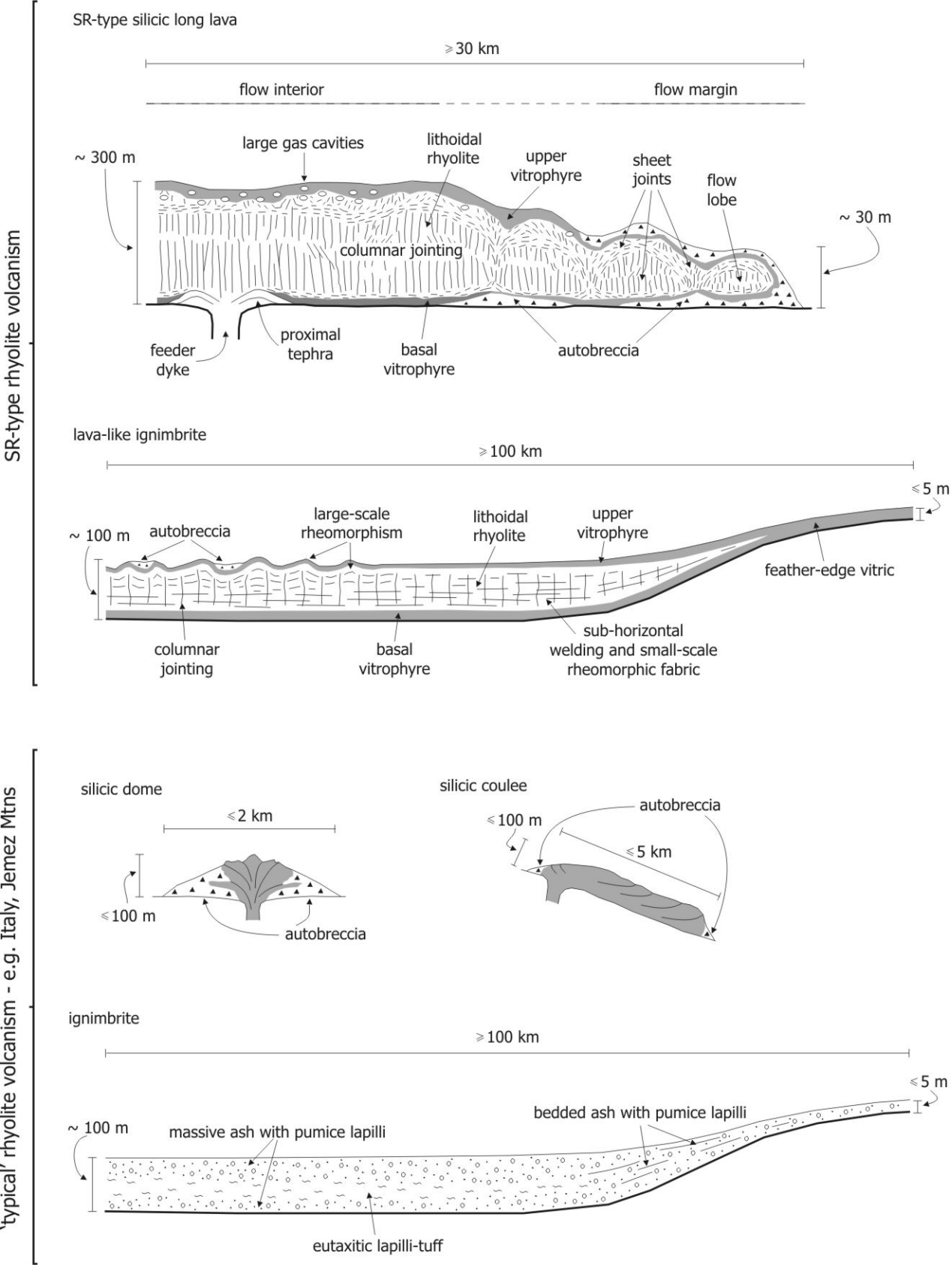


Fig. 2-18. Schematic comparison between lavas and ignimbrites typically associated with Snake River - type and 'typical' rhyolitic Plinian volcanism.

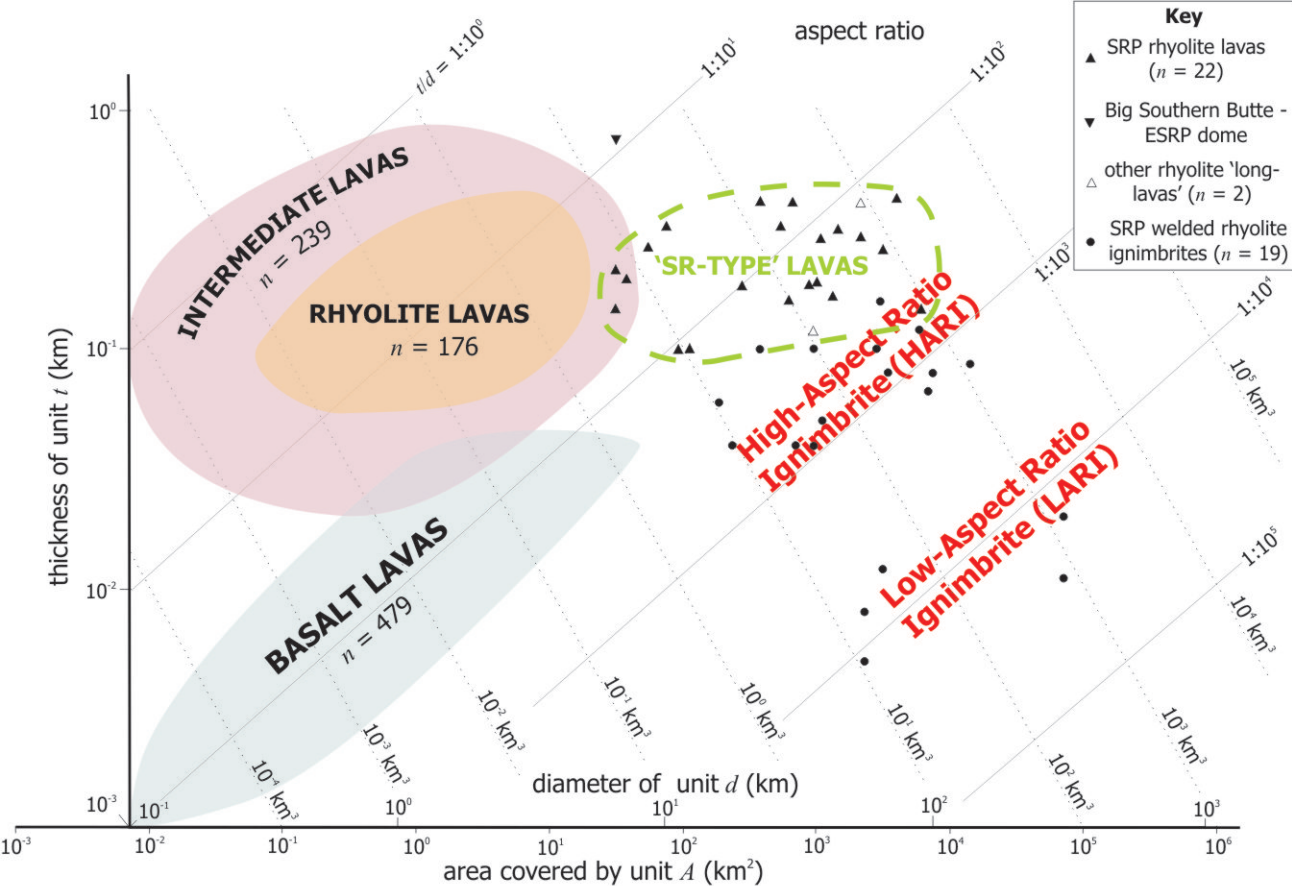
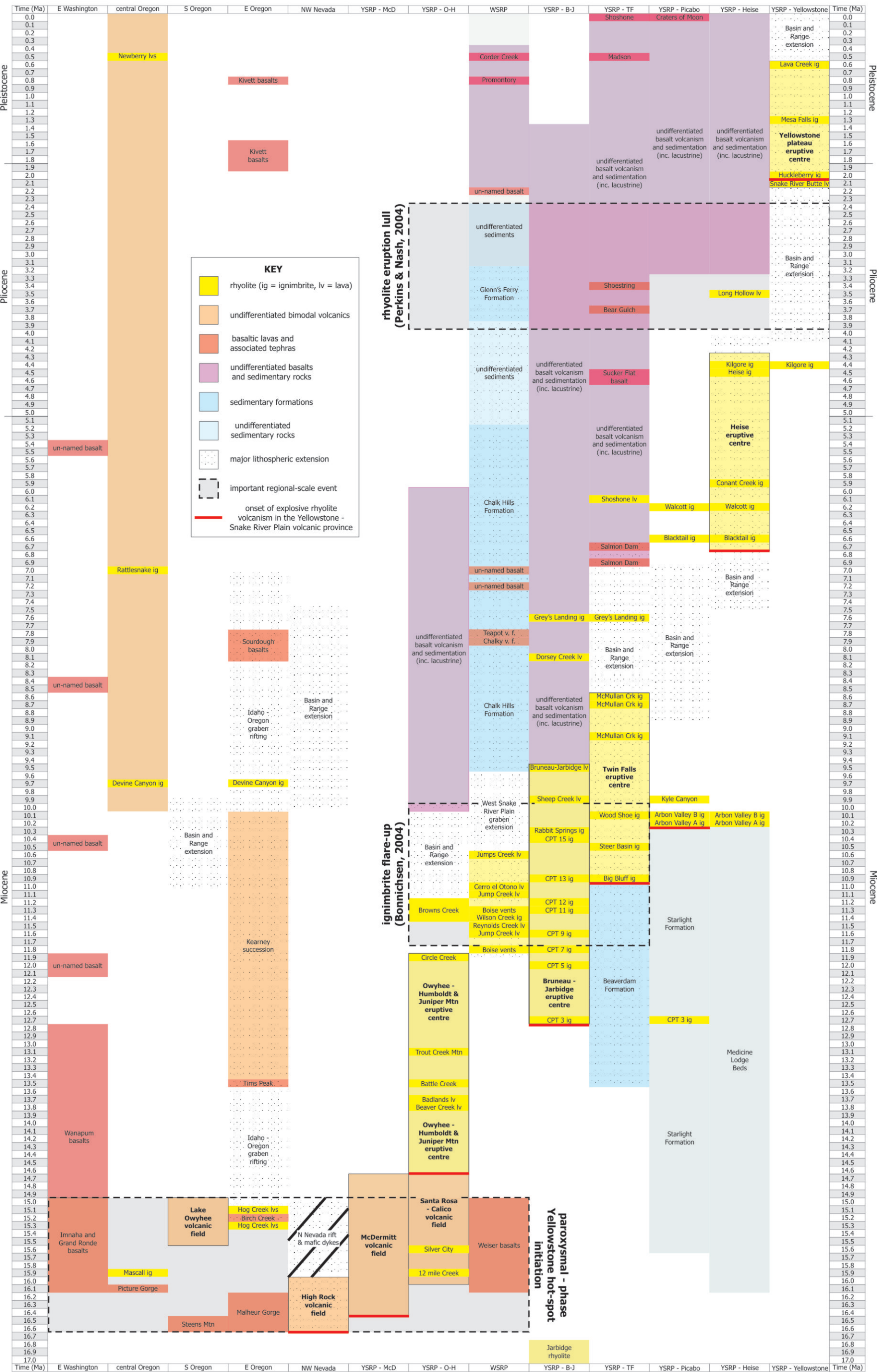


Fig. 2-19. Dimensions of rhyolite lavas and ignimbrites from the Snake River Plain volcanic province and elsewhere. Note the Snake River Plain-type rhyolite lava field (dashed line) encompassing large-volume rhyolite lavas ('long-lavas') not previously classified by Walker (1973a). The two scales on the x -axis give the area covered by the unit (A) and the diameter of a circle with that area (d). Positively sloping lines are aspect ratio (t/d), negatively sloping lines are volume (At). Modified from Walker (1973a) and Cas & Wright (1987). Ignimbrite aspect ratio fields adapted from Walker (1983).

Table 2-1. Tectono-stratigraphic range chart for the Neogene Yellowstone - Columbia River volcanic 'mega'-province



Chapter 3:

Fabrics and structures within the Grey's Landing ignimbrite

Introduction

The Grey's Landing ignimbrite is well exposed in three dimensions allowing access to many parts of the deposit. It is intensely rheomorphic throughout and makes an ideal case study for testing models of how rheomorphic ignimbrites are emplaced and how they deform (see Chapter 1). The ignimbrite hosts a diverse range of fabrics and structures, some typical of deformed rocks in mylonite zones and orogenic belts, and others unique to ignimbrites.

Chapter outline

This chapter is composed of four major sections that follow-on from each other; they are: (1) the anatomy of the Grey's Landing ignimbrite; (2) fabric elements and kinematic criteria in the Grey's Landing ignimbrite; (3) structure within 'thin' ignimbrite; and (4) structure within 'thick' ignimbrite. The first section describes the distribution of, and thickness variations within, the Grey's Landing ignimbrite that define two zones, each of which will be addressed separately. The second section describes and interprets the different fabric elements and kinematic criteria found in the ignimbrite. This is followed by description and analysis of structures in thin ignimbrite; and finally, a description and analysis of structures in thick ignimbrite. How these fabrics and structures relate to ignimbrite emplacement will be addressed in Chapter 5.

The Grey's Landing ignimbrite: general anatomy

Ignimbrite distribution and thickness variations

The Grey's Landing ignimbrite is an extensive sheet that unconformably overlies and oversteps the Backwaters Member and older ignimbrites, both within and outside the Rogerson Graben (see Chapter 2). Its known areal extent is estimated to be $\geq 20 \text{ km}^2$ (Fig. 3-1). The ignimbrite shows considerable thickness variation across the limited area over which it is exposed (Fig. 3-1); for example along Salmon Falls Creek Reservoir it reaches 65 m thick, however along Highway 93 it is approximately 5 m thick.

The Grey's Landing ignimbrite thickens to the west within the Rogerson graben and thickens to the north into the Snake River Plain (Fig. 3-1). Two arbitrary regions are established: a 'thin' region where the ignimbrite is $< 20 \text{ m}$ thick, and a 'thick' region where the ignimbrite is $> 20 \text{ m}$ thick. The approximate boundary between thin and thick ignimbrite corresponds to the inferred 20 m isopach (Fig. 3-2).

The 'thin' ignimbrite facies

The 'thin' facies (Figs 3-2 and 3-3) is characterised by thin ignimbrite ($\sim 5 \text{ m}$ to 20 m thick), that is entirely vitric or dominated by vitrophyre (basal vitrophyre is $> 5 \text{ m}$ thick). Thin ignimbrite is typically composed of a flow-banded basal vitrophyre, a flow-banded and folded lithoidal centre, and a flow-banded and sometimes folded upper vitrophyre (Fig. 3-3). Lithophysae ($\leq 8 \text{ cm}$ diameter) and spherulites ($\leq 4 \text{ cm}$ diameter) are common in vitrophyre. Thinner sections ($< 6 \text{ m}$ thick) are entirely vitric (e.g., along Highway 93; 11T 692234mE 4660906mN; Fig. 3-2) and do not exhibit folds.

The 'thick' ignimbrite facies

The 'thick' facies is characterised by thick (20 - 65 m thick) lithoidal ignimbrite with thin (≤ 2 m thick) basal and upper vitrophyres (Fig. 3-4). Examples include Grey's Landing (11T 687822mE 4666778mN) and Backwaters (11T 685154mE 4659673mN; Fig. 3-2). Within the thick facies the entire ignimbrite is pervasively flow-banded, and is folded throughout. Two structural domains are observed (Fig. 3-4). The upper surface of the ignimbrite exhibits complex textural variation, including localised autobreccias and non-welded facies (e.g., Salmon Dam; 11T 687018mE 4675787mN; Fig. 3-2).

For the purposes of a structural analysis it is useful to consider the thin and thick facies as distinct end-members. As will be shown in following sections, each facies is characterised by a different association of structures, most apparent in the scale, style, attitude, and complexity of folding.

Fabric elements and kinematic criteria in the Grey's Landing ignimbrite

Before considering the folding, this chapter considers the fabric elements present in the ignimbrite. Whereas in deformed meta-sedimentary successions the origins of fabrics are usually straightforward (planar fabric elements include sedimentary bedding, axial planar cleavage, and linear fabric elements including intersection and mineral lineations); the origins of fabrics within high-grade ignimbrites are more equivocal, and each type of fabric and structure must be examined and carefully interpreted. In this section, each type of fabric and structure is evaluated for its importance and applicability as a component in the structural analysis.

Planar fabric elements

The Grey's Landing ignimbrite exhibits pervasive planar fabric elements. Three types of planar fabric element are recognised, based on their physical characteristics, distribution, and spacing: (1) microscopic eutaxitic and parataxitic

fabrics, (2) micro- and macroscopic colour-banding, and (3) a spaced fabric defined by macroscopic partings. Each type of planar fabric will be described, interpreted, and placed in context with existing conceptual models for the formation of fabrics in welded ignimbrites.

Microscopic eutaxitic fabric

Description

A penetrative planar fabric is defined by flattened and parallel ash shards (eutaxitic fabric; Branney and Kokelaar, 2002), and is prevalent in sections throughout the upper vitrophyre of the ignimbrite (Fig. 3-5a). Ash shards (vitroclasts 0.5 mm to ≤ 3 mm in length) are well preserved in both vitric and spherulitic ignimbrite (Fig. 3-5b), and exhibit a range of colours, from dark red-brown to cream. The intensity of the fabric varies and individual shards are typically not discernible throughout the rest of the deposit. The ash shards are inferred to be deformed for three reasons: (1) flattening ratios (Peterson, 1979) of ash shards vary from 15:1 (typical of the upper vitrophyre; Figs 3-5a, 3-5b, and 3-5c) to $> 100:1$ (typical of the lower vitrophyre and centre of the deposit; Figs 3-5d, 3-5e, and 3-5f), compared to $\sim 1:1$ for typical non-flattened ash shards; (2) ash shards are seen to wrap around crystals and be less flattened in strain shadows around crystals (e.g., Fig. 3-5c); and, (3) there is a continuum between the most intense fabric, where ash shards are indiscernible from one another, and the least intense fabric where shard margins are clear.

Interpretation

Eutaxitic fabric (e.g., Figs 1-17; 3-5a; 3-5e) has been described from welded tuffs in numerous volcanic provinces (e.g., Ross and Smith, 1961; Schmincke and Swanson, 1967) and are usually interpreted as welding fabrics. The preservation of eutaxitic fabric within spherulites (e.g., Fig. 3-5b) suggests that this fabric can survive some, if not all devitrification effects. Typically eutaxitic fabric is inferred to have formed by compaction of initially non-welded tuff ('load-

welding' Freundt, 1999); however, the coalescence of molten pyroclasts or the agglutination of plastic pyroclasts may produce a similar welding fabric ('aggregation-welding' Freundt, 1999). It is not possible to reconcile which type of welding is dominant on the basis of eutaxitic fabric development alone, and I shall return to it later.

Colour-banding (lamination)

Description

A eutaxitic fabric and colour-banding exist together in many samples (e.g., Fig. 3-5d), where colour-banding is often $> 100 \mu\text{m}$ to $\leq 10 \text{ cm}$ thick. Penetrative macroscopic colour-banding is ubiquitous throughout the ignimbrite, in both vitric and devitrified welded tuff. In vitric ignimbrite, it is defined by laterally extensive alternating light and dark grey bands, 0.5 cm to $\leq 10 \text{ cm}$ thick (Fig. 3-6a), and may be cross-cut by vesicles. Typically, macroscopic colour-banding is best developed in the upper vitrophyre and weak or absent in the basal vitrophyre. Where the vitrophyre appears massive in the field, weak macroscopic lamination can be seen. Where the vitrophyre appears well banded, well-developed microscopic lamination also occurs. Colour-banding is preserved and somewhat strengthened in partly devitrified and spherulitic vitrophyre by the concentration of spherulites along certain pre-existing bands (Figs 3-6a and 3-6b). There is no discernible difference in composition between colour-bands (Fig. 3-7).

Colour-banding also occurs in devitrified, lithoidal ignimbrite as a penetrative planar fabric defined by 0.5 to 10 cm purple, brown, grey and cream bands (e.g., Figs 3-6c; 3-6d; 3-6e). Colour-bands are laterally extensive and folded. As with colour-banding in vitric ignimbrite, the colour-banding of lithoidal ignimbrite is best developed in the upper portion of the ignimbrite where there is less intense jointing.

Microscopic colour-banding is defined by light and dark (and some intermediate) colour-bands of eutaxitic tuff (Fig. 3-5d), although the contrast between light to

dark may be subtle. Colour-banding is penetrative and may be planar (e.g., Figs 3-5d; 3-5e; 3-8a) or irregular where it is deformed (e.g., Figs 3-8b; 3-8c; 3-8d; 3-8e), and the margin between light and dark is often complexly folded and inter-fingering (Fig. 3-8c). Colour-banding is deformed around porphyroclasts (Fig. 3-8f) and is sometimes deformed along with vesicles (compare Fig. 3-8c with Figs 3-8d and 3-8e). Microscopic colour-banding is only apparent in plane polarized light; in crossed polarized light the vitric tuff is isotropic. Again, there is no discernible compositional difference between colour-bands (Fig. 3-7).

Interpretation

The origin of microscopic and macroscopic colour-banding is enigmatic, but some firm interpretations and conclusions can be made. As previously described, microscopic colour-banding is concordant with adjacent eutaxitic fabric (Figs 3-5d and 3-8a) and is folded along with it (Fig. 3-8b), suggesting that they are broadly coeval. Microscopic colour-banding is best developed in macroscopically colour-banded vitrophyre, and mm-scale banding is exhibited by both; suggesting that the two are genetically linked and merely different ends of a scale-spectrum. In turn, the scale and distribution of macroscopic colour-banding in vitric and lithoidal ignimbrite is identical, suggesting that they too are genetically linked.

Devitrification is a taphanomic¹ effect acting on originally wholly vitric tuff (e.g., Ross and Smith, 1961; Lofgren, 1971a; Streck and Grunder, 1995), therefore, it is possible that the original colour variation can be inherited by the lithoidal products of devitrification. The inheritance of colour-banding from vitric to lithoidal tuff is conjectural; however, both vitric and lithoidal colour-banding, irrespective of scale, are commonly described as 'flow-banding' (e.g., Fig. 1-11) without further discussion (e.g., Smith, 2002; Gonnermann and Manga, 2005; Manga, 2005). Macro- and microscopic colour-banding in both vitric and lithoidal Grey's Landing ignimbrite can be described as flow-banding, and therefore compared with reported flow-banding from other welded tuffs (e.g.,

¹ Taphanomic – post-emplacement changes in the appearance and character of the ignimbrite, e.g., devitrification of vitric tuff.

Kobberger and Schmincke, 1999; Soriano et al., 2002). Flow-banding is a characteristic fabric of both silicic lavas (e.g., Seaman, 1995; Seaman et al., 2005) and lava-like ignimbrites (*sensu* Branney and Kokelaar, 1992).

Colour-bands are usually inferred to represent two or more mingled glass compositions (e.g., Leat and Schmincke, 1993; Seaman, 1995). However, colour is also a result of textural variation within the glass (e.g., micro-crystal concentration, micro-vesicle concentration; review by Manga, 2005). In the absence of discernible compositional variation between light and dark colour-bands (Fig. 3-7), a textural influence appears most likely.

Spaced partings – ‘sheeting joints’

Description

The lithoidal rhyolite contains abundant planar, spaced partings, that split the rock into 1 cm to 5 cm thick slabs: sheeting joints (*sensu* Bonnichsen, 1982b; Bonnichsen and Citron, 1982). Lineations occur on the parting surfaces. Where closed the partings give the appearance of laminations (Fig. 3-9a). Elsewhere void space occurs between slabs of lithoidal ignimbrite (e.g., Figs 3-9b; 3-9c). In the lithoidal centre of the ignimbrite (e.g., Fig. 3-4) the partings pick out 0.01 m to 10 m scale folds. There is a continuum of parting spacing from widely spaced (> 10 cm) in thin ignimbrite, to closely spaced (~ 2 cm) in the centre of the thick ignimbrite (Figs 3-9b and 3-9c). Sheetting joints are laterally extensive (≤ 10 m) and are seen to die out into colour-bands, and are often filled or ‘healed’ by a white vapour-phase crystallization (Fig. 3-9d). Sheetting joints are occasionally associated with highly localized and sub-parallel vesicular horizons (Fig. 3-9e).

Colour-banding and sheet joints are usually concordant (Fig. 3-10a). However, sheet joints pick out folds imperfectly; although parting surfaces closely parallel colour-banding in fold limbs, they cross-cut the colour-banding in tight hinges. As shown in Figure 3-10b, spaced partings parallel colour-banding in the fold limbs of tight and isoclinal folds, but are discordant to the colour-banding around

hinges. Many isoclinal fold hinges do not exhibit spaced partings around the hinge being picked out by colour-banding alone (e.g., Fig. 3-10b), instead sheeting joints occur only in the limbs. In contrast, open fold hinges are well defined by spaced partings with up to ≤ 10 cm spacing (e.g., Fig. 3-10c). Even where colour-banding is absent, spaced partings are discordant to the overall fabric around isoclinal fold hinges and sheath fold culminations (e.g., Fig. 3-10d). This is in contrast to eutaxitic fabric and colour-banding which pick out fold shapes especially fold hinges, perfectly (e.g., Figs 3-6a; 3-6b; 3-6e; 3-8f).

Interpretation

I interpret spaced macroscopic partings to be a post-rheomorphic mimetic fabric developed along flow-bands, probably during devitrification. This is based on three observations: (1) spaced partings are concordant with colour-banding in fold limbs and around open fold hinges, and discordant around tight and isoclinal hinges (e.g., Fig. 3-10c). Further, (2) spaced partings demonstratively post-date the formation of colour-banding, because when discordant, they brittlely deform colour-banding; and (3) spaced partings demonstratively post-date rheomorphism because discordant partings brittlely deform earlier folds and other ductile structures. Spaced partings only occur in lithoidal ignimbrite, and are least well developed in proximity to vitrophyre. Furthermore, colour-banding may give way to increasing density of spaced partings.

I conclude that spaced partings are a mimetic enhancement of the colour-banding fabric, probably due to devitrification of originally vitric and colour-banded ignimbrite. I suggest that the principal mechanism driving parting formation is dilation across colour-band boundaries in response to the $\sim 10\%$ volume loss associated with devitrification of the original glass (Fig. 3-11a; Turnbull and Cohen, 1961; Lofgren, 1971a), followed by vapour-phase crystallization along parting surfaces. This is supported by observation that partings are concordant with flow-banding on fold limbs but not around tight or isoclinal fold hinges: this stands to reason because dilation of partings can only occur in one direction due to the anisotropy of the flow-banding (i.e. perpendicular to flow-banding, and

therefore, usually vertically), and around tight or isoclinal fold hinges dilation would be required in two perpendicular directions to remain concordant (Fig. 3-11b). Dilatational strain is accommodated by brittle fracturing discordant to flow-banding when it cannot be accommodated around fold hinges (e.g., Figs 3-10b; 3-10c; 3-10e).

Such spaced partings have not been described before in high-grade ignimbrites, and therefore this interpretation and conceptual model for their formation can not be tested against existing documented examples, nor can pre-existing models be tested and applied.

Dimple joints

Description

These are irregular parting surfaces reminiscent of cratered surfaces (Figs 3-12a and 3-12b). We divide dimple-jointed surfaces into open and closed; where, the dimple is exposed or not, respectively (Fig. 3-12c). Closed dimples can be prised open to reveal an open saucer-shaped dimple (part) and discus-shaped counterpart of lithoidal ignimbrite (Fig. 3-12d). Dimple-jointed surfaces are widespread but unevenly distributed in lithoidal ignimbrite and are always parallel to adjacent planar partings.

Individual dimples are circular in plan view (5 – 20 cm in diameter) and saucer-shaped. They are asymmetric in cross-section, typically ≤ 1 cm deep with planar, rather than concave, bases (Figs 3-12a and 3-12b) and planar upper surfaces that are concordant with parting surfaces (Figs 3-12c and 3-12d). Dimples appear to be developed within sheets of lithoidal ignimbrite that are separated by vapour-phase encrusted partings. In contrast, the sides of dimples are smooth and not encrusted by vapour-phase crystals, and truncated the sheet at a high angle to the partings. Lineations are not present within dimples but are abundant on adjacent parting surfaces (Fig. 3-12b).

Interpretation

Dimple joints are enigmatic structures and have not been described before. They may reflect heterogeneous and localised cooling and initial devitrification before development of spaced partings, causing localised volume decrease. Dimple joints may, therefore, record an early stage of localised devitrification. Further volume decrease during sustained devitrification (Fig. 3-11a) is concentrated by heterogeneities including flow-banding to form parting surfaces. Subsequent exposure along spaced partings allows for the removal of the disc-shaped counter-part revealing the dimpled surface.

Conclusions: the value and use of planar fabric elements as structural components

It is likely that eutaxitic fabric and flow-banding form parallel, or very close to parallel, to the base of the ignimbrite and sub-horizontally (e.g., Ross and Smith, 1961; Schmincke, 1974; Branney and Kokelaar, 2002). Therefore, they can be considered to behave like other typically sub-horizontal, pre-tectonic planar fabrics, for example, sedimentary bedding. As I have suggested, spaced planar surfaces mimic flow-banding and, therefore are parallel to the eutaxitic fabric as well. Therefore for the purposes of this structural analysis, I will treat eutaxitic fabric, flow-banding, and spaced partings as initially planar fabric elements that are subsequently deformed. In contrast, dimple joints are of no discernible use as structural markers because of uncertainties regarding their formation and because they, themselves, are not planar. However, because they occur between and parallel to parting surfaces, dimple-jointed surfaces can be used.

Linear fabric elements

The Grey's Landing ignimbrite contains abundant linear fabric elements throughout. Two distinct types are identified: (1) stretched vesicles, and (2) linear fabrics on spaced parting surfaces. Each type of linear fabric will be described before being interpreted and placed in context with existing conceptual models for the formation of fabrics in welded ignimbrites.

Stretched vesicles

Description

Vesicles are abundant throughout the Grey's Landing ignimbrite ranging from $\leq 100 \mu\text{m}$ to $\sim 20 \text{ cm}$ in diameter. Although spherical and near-spherical vesicles exist (e.g., Fig. 2-15c), the vast majority are clearly ellipsoidal and form a prominent and measurable linear fabric wherever they occur (Fig. 3-13a). Deformed vesicles are locally abundant in the upper and lower vitrophyres and immediately adjacent devitrified ignimbrite, where they may be so common that the ignimbrite is scoriaceous (e.g., Figs 3-13b and 3-13c). Typically, they are concentrated along discrete planes (e.g., Figs 3-13a; 3-13d; 3-13e), for example spaced partings, to which they are parallel or slightly plunging ($< 5^\circ$ plunge relative to the dip of the host plane). On a single plane the density of deformed vesicles varies from high (i.e. the surface is totally covered in vesicles, some of which may overlap; Fig. 3-13a) to low (i.e. vesicles are widely scattered and not overlapping; Fig. 3-13e). The plunge of stretched vesicles, with regard to the surfaces they lie on or adjacent flow-banding, is consistent across large areas; the most impressive manifestation being the development of trains of imbricated vesicles (Figs 3-13a; 3-13b; 3-13d; 3-13e), with similar appearance to imbricated clasts in fluvial sediments. Other than where they have been folded, vesicles in particular layers all plunge in the same direction.

On any single vesiculated surface, stretched vesicles are parallel to each other (e.g., Figs. 3-13a - e), and they maintain a consistent trend over large areal extents

($\leq 100 \text{ m}^2$), except where such surfaces are folded. Two sets of vesicles, trending perpendicular to each other, are observed on adjacent parting surfaces at Monument Canyon (Fig. 3-13f), but are not seen to cross-cut one another. Spherical and near-spherical vesicles are observed to cross-cut deformed vesicles and other structures (folded flow-banding) in several locations (e.g., Monument Canyon; Fig. 2-15c). Deformed vesicles are never observed to cross-cut non-deformed vesicles. Where it is possible to examine stretched vesicles and other linear fabrics in lithoidal ignimbrite (see below), they are parallel in adjacent surfaces and across large areas. Stretched vesicles commonly have X axes plunging obliquely to the dip of flow-banding in the surrounding ignimbrite (Fig. 3-13b); this results in trains of 'imbricated' vesicles that all plunge in the same direction when viewed in the XZ plane.

Deformed vesicles are prolate (Fig. 3-14). In plan view onto a plane containing stretched vesicles (XY plane; e.g., Figs 3-13a and 3-13d), the vesicles are strongly elliptical with long axes (X) significantly greater than the short axes (Y). The X / Y ratio is observed to range from $\sim 5 : 1$ to $\leq 30 : 1$, however this is not spatially systematic. Generally the largest (by inferred volume) stretched vesicles are found in and adjacent to the lower vitrophyre (Fig. 3-13a), and the smallest are in the upper vitrophyre and adjacent devitrified ignimbrite (Figs 3-13b and 3-13c).

Interpretation

Vesicles are nearly ubiquitous in silicic volcanic rocks (Rust et al., 2003), forming repeatedly through the evolution of a volcanic unit (Navon and Lyakhovsky, 1998). Stretched vesicles are abundant in many volcanic rock types (e.g., 'tube' pumice) and volcanic units (e.g., lavas), and are usually interpreted to have formed by the deformation of originally spherical vesicles that may or may not be preserved elsewhere (Smith, 2002). The relaxation time for vesicles to recover to a non-deformed (spherical) state is typically too long in high viscosity (typical silicic units), and deformed bubbles are preserved (Toramaru, 1988). Stretched vesicles have been used widely to indicate flow directions in lavas, their long axes (X) being inferred to parallel the principal stretching direction (Coward, 1980).

The consistency of stretched vesicle trends across large areas and their concordance with lineations in lithoidal ignimbrite, suggests that they are useful and important fabrics that should be recorded as part of a structural analysis. I interpret that the long axes (X) of stretched vesicles are parallel to the principal stretching direction in the deforming ignimbrite at any one location, approximating to the flow direction. In this regard, stretched vesicles are no different from any other stretching lineation (e.g., stretched belemnites, reduction spots, or conglomerate clasts; Ramsey and Huber, 1983). Comparison with recent obsidian and basalt lava flows, where the trends of stretched vesicles parallel the observed flow directions (e.g., Smith, 2002), strongly support this interpretation. Imbricated vesicles have been used to infer the transport direction in ancient lavas (e.g., Pioli and Rosi, 2005), and I will address them in the following section on kinematic criteria.

I interpret stretched vesicles in the Grey's Landing ignimbrite to have been originally spherical, volatile-filled bubbles that were subsequently flattened and stretched during non-coaxial, prolate - plane strain (and locally ideally prolate; Fig. 3-14) deformation, and that their long axes parallel the principal stretching direction. Cross-cutting relations between deformed (Fig. 3-13a) and non-deformed vesicles (Fig. 2-15c) reveal significant post-deformation de-gassing, and suggest that parts of the ignimbrite were still ductile after the cessation of rheomorphism.

Lineations on parting surfaces in lithoidal ignimbrite

Description

Linear fabrics are almost ubiquitous throughout the lithoidal Grey's Landing ignimbrite. Not all parting surfaces are lineated, and the spacing, morphology, and dimensions of lineations are highly variable between adjacent parting surfaces. Two end-member morphologies are observed: firstly, striæform lineations; typically closely-spaced (≤ 3 mm), laterally discontinuous (≤ 5 cm), and occasionally anastomosing, lineations with low (≤ 1 mm) to moderate (≤ 5

mm) relief, resembling glacial striations (Figs 3-15a and 3-15b). Secondly, intestiniform lineations; typically widely-spaced (≤ 2 cm), laterally continuous (≥ 2 m), anastomosing lineations with moderate to high relief (≤ 1 cm), resembling stretched out intestines (Figs 3-15c and 3-15d). Neither type of lineation appears related to crystal orientation, nor do they have the typical asymmetric cleft morphology of slickenlines.

Both types of lineation may be found on adjacent parting surfaces, however, they are not seen to change from one to another on individual surfaces. They are usually parallel with each other on individual surfaces and between adjacent surfaces, and they are typically parallel to stretched vesicles (e.g., Fig. 3-15b). However, cross-cutting linear fabrics are occasionally observed on the same parting surfaces at Monument Canyon and Cedar Creek Reservoir (e.g., Fig. 3-15e), where two linear fabrics are typically $\sim 60^\circ$ oblique to each other, and $\sim 30^\circ$ either side of the stretching direction established from adjacent vesicles. Locally, lineations are affected by later, large-scale folding of the hosting planar surfaces, where the lineation is commonly reorientated (Fig. 3-15f), and occasionally folded.

Interpretation

I interpret striæform and intestiniform lineations to be stretching lineations, formed parallel to the maximum stretching direction (X), because they typically parallel stretched vesicles (Fig. 3-15b) and sheath folds hinges (see below). In the absence of a second and suitably orientated planar fabric intersecting the flow-banding, lineations on parting surfaces are unlikely to be intersection lineations (*sensu* Ramsey, 1967). Moreover, despite a passing resemblance to slickenlines, I suggest that they are not brittle fabrics, because: (1) they are intimately associated with demonstratively ductile fabrics and structures (e.g., stretched vesicles and folds); (2) they are themselves locally folded (Fig. 3-15f); (3) they are not associated with fault breccia or gouge, or brittle fracturing of parting surfaces; (4) they are exhibited on parting surfaces throughout the deposit and are not localised

to discrete shear zones; and (5) they typically taper out to nothing at each end, and do not exhibit notches at one end as is typical of slickenlines.

Descriptions of lineations in other rheomorphic ignimbrites and lavas are limited, the most common types described being stretched vesicles (e.g., Chapin and Lowell, 1979), orientated crystals (e.g., Smith, 2002; Bascou et al., 2005), boudinaged lapilli (e.g., Schmincke and Swanson, 1967), and stretched fiamme (e.g., Branney et al., 2004b). Unfortunately most instances of the use of lineations in rheomorphic ignimbrites and lavas, are restricted to their measurement (e.g., Christiansen and Lipman, 1966; Schmincke and Swanson, 1967; Kano et al., 1997) and not descriptions of their scale, distribution and morphology; and therefore I am unable to provide examples of lineations similar to these from elsewhere.

In the absence of a pre-existing explanation for the formation of lineations of parting surfaces, I infer that they are a form of stretched vesicle lineation (Fig. 3-16). Firstly, they are typically parallel to, and deformed contemporaneously with, stretched vesicles on adjacent surfaces (Figs 3-15b and 3-15f). Secondly, the scale, spacing and morphology of striæform lineations (Fig. 3-15a) are similar to strongly flattened, scoriaceous ignimbrite (e.g., Fig. 3-13b). Thirdly, the scale, spacing, and morphology of intestiniform lineations (Fig. 3-15c) are similar to strongly flattened, very large stretched vesicles in the Grey's Landing (e.g., Fig. 3-13a) and neighbouring House Creek ignimbrites (Branney et al., 2004b; Fig. 3-16). Fourthly, pairs of oblique lineations bisected by the stretched vesicle lineation (e.g., Fig. 3-15e) are probably the margins of very strongly flattened and closely-spaced vesicles. How devitrification affects, and possibly changes, the morphology of vesicles is not constrained, and therefore my interpretation is very tentative. For example, mm-scale textures associated with vesicles (e.g., walls between immediately adjacent vesicles) may be obscured or destroyed. However, there is abundant evidence from preserved vesicles (Figs 2-15c; 3-6c; 3-9e; 3-13a-f; 3-15b) that the ignimbrite was highly vesicular throughout, both during and after deformation. I tentatively suggest that there is a continuum from strongly

flattened vesicles to both striæform and intestiniform lineations, where changes in morphology because of devitrification, obscure the original vesicle margins; small, closely-spaced vesicles are preserved as striæform lineations, and large, closely-spaced vesicles are preserved as intestiniform lineations.

Kinematic criteria

Small-scale shear sense indicators are locally abundant throughout the Grey's Landing ignimbrite, especially in vitrophyre; by far the most common and widespread of these are rotated porphyroclasts (*sensu* Passchier and Trouw, 1996), usually crystals or crystal fragments that deform flow-banding. Other shear sense indicators are associated with vesicles. I will describe each type of shear sense indicator and attempt to infer their formation. Finally, each type of shear sense indicator will be evaluated as a kinematic criterion for use in a structural analysis.

Rotated crystals

Description

Discrete crystals (porphyroclasts) are ubiquitous in the Grey's Landing ignimbrite. Rotated porphyroclasts are abundant in the upper and lower vitrophyre of the Grey's Landing ignimbrite (Figs. 3-17a-f), where they are observed to have rotated during contemporaneous deformation of flow-banding and coeval vesicles (Figs 3-8d and 3-8c). Typically crystals (e.g., Fig. 3-17a) or crystal aggregates (e.g., Fig. 3-17f) have rotated (non-coaxial deformation) and deflected the surrounding flow-bands, producing characteristic flow-banding patterns around the crystals. Asymmetric structures (δ -, σ -, and Θ -objects; *sensu* Passchier and Trouw, 1996) are typical in thin sections cut parallel to an independently measured lineation.

δ -objects are the most abundant type found in the Grey's Landing ignimbrite, occurring in eutaxitic vitrophyre (e.g., Figs 3-17a-d), colour-banded vitrophyre

(e.g., Fig. 3-8f), and lithoidal ignimbrite (e.g., Fig. 3-18a). They are characterised by tight folds in diametrically opposite quarters, 'quarter folds', (Fig. 3-15a) and 'stair-stepping' fabrics (*sensu* Passchier and Trouw, 1996) where planar fabrics are vertically offset across porphyroclasts (Fig. 3-15a), making them appear asymmetric. Quarter folds are observed to often be refolded around a porphyroclast (Fig. 3-15c) as are intrafolial folds within the flow-banding fabric (Fig. 3-15d). σ -objects are very rare (never more than 1 in a single thin section) and are characterised by the development of shear band surfaces in diametrically opposite quarters, and a lack of quarter folds (Fig. 3-15e). Θ -objects are more common than σ -objects but still rare, and are characterised by the symmetrical mantling of porphyroclasts by flow-banding (e.g., Fig. 3-15f), resembling a cross-section through an onion.

Interpretation

Rotated porphyroclasts are well established as shear sense indicators (e.g., Hammer and Passchier, 1991; Passchier and Trouw, 1996; Figs 1-4; 1-6; 1-12) and have been applied successfully in many studies of mylonites and ductile shear zones, and in volcanic rocks (Christiansen and Lipman, 1966; Vernon, 1987; De Rosa et al., 1996; Ventura et al., 1996). Rotated porphyroclasts from the Grey's Landing ignimbrite are no less applicable as shear sense indicators and are very powerful kinematic criteria when combined with observed linear fabrics; giving, for the first time, unambiguous transport directions for the emplacement of an ignimbrite from an unknown source. I interpret the different types of rotated porphyroclast described to be accurate shear sense indicators suitable for application as part of a structural analysis.

Imbricated vesicles

Description

Arrays of imbricated vesicles are observed in cross-sections parallel to the maximum elongation direction (Fig. 3-18b), resembling imbricated clasts in

fluvial gravels. The plunge directions of vesicles on a single parting surface are unidirectional (e.g., Figs 3-18b and 3-18c) and the range in the degree of plunge is typically small.

Interpretation

Imbricated vesicles have been used as kinematic criteria in ancient lavas and observed forming in recent lava flows where the source is known (e.g., Walker et al., 1998; Pioli and Rosi, 2005). Imbricated crystals have been applied to rheomorphic ignimbrites (Elston and Smith, 1970). In each case, the vesicles are observed to plunge back towards the source, anti-parallel to the flow direction. This interpretation is supported by analogy with imbricated sedimentary clasts (Rust, 1972), imbricated lapilli in non-welded ignimbrites (Branney and Kokelaar, 2002), and the experimental deformation of vesicles by Rust et al. (2003) where imbricated vesicles are shown to be produced by strongly non-coaxial strain.

Shear-sense indicators within vesicles – vesicle flaps

Description

Cross-sections through some large vesicles (≥ 5 cm long, ≥ 1 cm wide) in lithoidal ignimbrite display ≤ 1 cm scale, asymmetrically folded flaps of vesicle-wall ignimbrite suspended from the inside walls of the vesicles (Fig. 3-18b). Such ‘vesicles flaps’ (new term) are uncommon but are easy to identify. Typically, they have a consistent vergence within individual vesicles, and also between adjacent vesicles. Their vergence also agrees with that established from adjacent rotated porphyroclasts and vesicle imbrication. Despite only having been observed in lithoidal ignimbrite, this does not preclude the existence of vesicle flaps in vitric ignimbrite.

Interpretation

I infer that vesicle flaps form by the deformation of planar, marginal fringes (‘flaps’) suspended from the insides of bubble walls. I tentatively suggest that

marginal flaps are the remnants of intra-vesicle walls destroyed during coalescence of vesicles. Vesicle flaps are only observed where they are asymmetrically folded, but it is conceivable that they may boudinage or deform brittly, if suitable strain and rheological conditions are prevalent.

Shear-sense indicators within vesicles – vesicle wrinkles

Description

Large vesicles exposed on parting surfaces in lithoidal ignimbrite often exhibit characteristic wrinkles towards their ends (Figs 3-18d; 3-18e). ‘Vesicle wrinkles’ (new term) are mm-scale folds exposed on both the interior lower and upper surfaces of vesicles, exposed as part and counter-part when dissected by a parting surface. They consist of alternating ridges (antiforms) and depressions (synforms) with mm-scale wavelengths and amplitudes, that characteristically close down-plunge in the lower part, and up-plunge in the upper counter-part. In each vesicle the hinge lines of the wrinkles are arcuate, symmetrical about the principal stretching axis, and merge tangentially with the margins. Vesicle wrinkles are locally common in the Grey's Landing ignimbrite and have been identified in at least one other lava-like ignimbrite outside the Rogerson Formation (the House Creek ignimbrite of Branney et al., 2004b and Bonnicksen et al., *in prep.*).

Interpretation

I infer that vesicle wrinkles form in response to competency contrasts across the vesicle-wall between the low competency volatile-filled vesicle and the high competency glassy ignimbrite. Strain is heterogeneous over the vesicle-wall, the highest strain concentrating at the vesicle tips where the vesicle tapers to nothing. The surrounding high competency glass resists the change in shape (e.g., volume change, stretching) or orientation (e.g., rotation towards the XY plane) of the vesicle, causing shortening at the vesicle tips that produces folds of the vesicle-wall (Fig. 3-19). This interpretation is tentative and based on a limited number of examples in the Grey's Landing ignimbrite.

Vesicle wrinkles appear to be similar in form and inferred formation, to the 'ropy flow structures' of the high-grade Nuraxi Tuff, Sardinia; described and interpreted by Pioli and Rosi (2005). The Grey's Landing and House Creek ignimbrites are the only other documented hosts of these structures, but it is inconceivable that they are not prevalent in many more high-grade ignimbrites. Intra-vesicle deformation structures have also been described by Chapin and Lovell (1979) and Liss et al. (2002). However, there are differences in their morphology, suggesting that these structures are different to vesicle wrinkles as described above. In the Wall Mountain Tuff, Colorado, Chapin and Lowell (1979) described "[vesicles with] streamlined internal structures formed by arcuate ridges and grooves, which toward the rear, merge tangentially with the sides", that they applied as shear sense indicators. However, it is not clear from their paper whether the internal structures were present on both the upper and lower internal surfaces of vesicles, or just on the lower. If they are indeed present on both, the Wall Mountain Tuff could be added to the list of ignimbrites displaying vesicle wrinkles. Neither Chapin and Lowell (1979) nor Pioli and Rosi (2005) offered a conceptual model for the formation of the structures they reported. In the Whin Sill, Northumberland, England, Liss et al. (2002) described cm-scale structures ('ropy flow structures') within vesicles. Their interpretation is similar to mine; that such structures formed by the buckling of the vesicle-wall in response to shear of the extraneous magma in the centre of the intrusion.

Conclusions: the value and use of kinematic criteria in rheomorphic ignimbrites

In any single locality, multiple different and independent shear sense indicators (e.g., rotated porphyroclasts and vesicle imbrication) all resolve the same shear sense direction. Though several types are not widely recognised as shear sense indicators (*cf.* Passchier and Trouw, 1996), their consistent relationship to relative shear sense direction supports their use as kinematic indicators. In conclusion, the Grey's Landing ignimbrite contains abundant shear sense indicators that are

available to be used as part of a structural analysis of the emplacement of the deposit, and to reveal the rheomorphic transport direction.

Structure within the thin ignimbrite facies

General anatomy

Thin Grey's Landing ignimbrite is characterised by a ubiquitous and penetrative, predominantly sub-horizontal rheomorphic L / S fabric (e.g., Fig. 1-22); defined by stretched and folded flow-banding and vesicles ($L \gg S$). This L / S fabric strongly resembles typical mylonitic fabric in exhumed ductile shear zones (Fig. 1-4). The upper surface of the 'mylonite-like' fabric is locally folded by later extrafolial folds.

Description of structures

Planar and linear fabric elements

The planar component of the penetrative L / S fabric is defined by flow-banding (including eutaxitic fabric, colour-banding, and parting surfaces; e.g., Figs 3-5; 3-6; 3-8; 3-9; 3-10). It typically dips $\leq 10^\circ$ and is sub-parallel to the local palaeo-slope (Fig. 3-20). Individual flow-bands are laterally extensive (≤ 30 m) and typically, maintain constant thickness (≤ 20 cm). Stretched or boudinaged flow-bands are not observed.

The linear component of the L / S fabric is defined by abundant stretched vesicles (e.g., Figs 3-13a; 3-13d; 3-13e), and uncommon striæform lineations on parting surfaces (e.g., Fig. 3-15e). All the observed stretched vesicles are prolate (Fig. 3-14). Lineation trends are consistently E - W in the eastern part of the Rogerson Graben and on the northern flank of the Browns Bench massif (Fig. 3-21). Within the graben, this trend is parallel to the inferred palaeo-slope; along the northern margin of the Browns Bench massif, this trend is perpendicular to the inferred palaeo-slope (Fig. 3-21). Lineation trends are approximately NE – SW at the

southern-most margin of the ignimbrite (Fig. 3-21). Stretched vesicles typically all plunge in the same direction at any single location because they are imbricated (e.g., Fig. 3-18b). Folded lineations have not been observed.

Kinematic criteria

Abundant kinematic criteria are preserved throughout mylonite-like ignimbrite, including rotated porphyroclasts (Figs 3-17; 3-18a), imbricated vesicles (Fig. 3-18b), vesicle flaps (Fig. 3-18b), and vesicle wrinkles (Figs 3-18d and 3-18e). In the east of the Rogerson Graben and along the southern flank of the Snake River Plain, where the lineation trend is E – W, all kinematic criteria indicate a top-to-west shear sense (Fig. 3-21). In contrast, the shear sense at the southern-most edge of the ignimbrite is top-to-southwest (Fig. 3-21). There is no observed variation in shear sense laterally or vertically through the ignimbrite at these locations.

Folds

Two different styles of folds are exhibited by thin ignimbrite: (1) small-scale, intrafolial folds that form an integral part of the mylonite-like rheomorphic fabric (above); and (2) medium-scale ($1\text{ m} \geq \lambda \leq 2\text{ m}$, and $A \leq 1\text{ m}$), extrafolial folds of the mylonite-like rheomorphic fabric. Intrafolial folds are ubiquitous throughout thin ignimbrite, whereas, the extrafolial folds occur only locally, in the uppermost 2 m of relatively thick ($\geq 8\text{ m}$) thin ignimbrite. Both fold styles are exhibited in both vitric and lithoidal ignimbrite.

Style 1: intrafolial folds

Flow-banding is pervasively deformed by small-scale, intrafolial folds that all have the same morphological characteristics (Fig. 3-22), and geometrical and spatial relations with each other, and associated structural elements, such as the stretching lineation.

All the intrafolial folds are recumbent isoclinal folds (Figs 3-22a – d), and many are sheath folds (Fig. 3-22e); and typically, their fold hinges are strongly curvilinear and parallel to the elongation direction (Fig. 3-23). They are small-scale ($\lambda \leq 1$ m, $A \geq 1$ m), and typically deform layers ≤ 50 cm thick (Fig. 3-22a). Isocline and sheath fold axial planes are characteristically planar, sub-horizontal (Fig. 3-23), and parallel to the surrounding mylonite-like rheomorphic fabric (Figs 3-20 and 3-23). The isoclinal folds and sheath folds are similar-style (class 2; Fig., 1-7b), with widely-spaced hinges (≤ 30 m) separated by apparently planar and non-folded limbs (e.g., Fig. 3-24). The style of microscopic folding of the eutaxitic fabric is the same: similar-style, intrafolial recumbent isoclinal folds (Fig. 3-22f).

Style 2: extrafolial folds

The upper 2 m of mylonite-like, thin ignimbrite is locally deformed by medium-scale, extrafolial folds that are typically upright to inclined, cylindrical or gently curvilinear antiforms and synforms (Figs 3-24; 3-25a; 3-26). This produces an undulating, folded upper surface in the thin ignimbrite. The folds are typically open (e.g., Fig. 3-25b) to tight (e.g., Fig. 3-24) and have small amplitudes ($A \leq 0.5$ m) and long wavelengths ($\lambda \geq 5$ m). They are typically periclinal with divergent gently plunging ($\leq 20^\circ$) axes (Figs 3-24 and 3-26). They exhibit a range from similar- (class 2) to, more commonly, parallel-style (class 1b; Fig. 1-7b).

Extrafolial folds fold the mylonite-like fabric and commonly refold the intrafolial folds (Fig. 3-24). Fold axes of the extrafolial folds are characteristically perpendicular to the underlying palaeo-slope (Fig. 3-26). However, their angular relationship to the trends of stretching lineations, and intrafolial fold hinges is variable: within the Graben, extrafolial fold axes are perpendicular to lineations and intrafolial fold axes (Figs 3-21; 3-23; 3-24; 3-26); whereas, along the southern margin of the Snake River Plain, extrafolial fold axes are parallel to lineations and intrafolial fold axes (Figs 3-21; 3-23; 3-26). Typically, extrafolial and intrafolial fold axial planes intersect at moderate to high angles ($\geq 40^\circ$) throughout the study area (Figs 3-23; 3-24; 3-26). Because of the spatial variation

in the geometries of superimposed extrafolial and intrafolial folds, different types of refolded fold and plan view interference patterns (*sensu* Ramsey, 1967; Figs 3-25c; 3-25d) are exhibited in different parts of the study area: type-3 refolded folds occur within the Graben (Fig. 3-24), whereas, and type-2 refolded folds are observed along the northern margin of the Browns Bench massif.

Initial interpretation

Mylonite-like ignimbrite

The structural elements observed throughout thin ignimbrite are consistent, and most compatible, with evolution in a ductile shear zone (Ramsey, 1980), that concentrated strong, heterogeneous, non-coaxial (top to west) shear. A penetrative $L / S - L > S$ fabric, intrafolial isoclinal and sheath folds, abundant kinematic criteria, and prominent prolate lineations are all characteristics of fossil ductile shear zones (e.g., Fig. 1-4; Cobbold and Quinquis, 1980; Ramsey, 1980; Simpson, 1983; Ghosh and Sengupta, 1987; Passchier and Trouw, 1996). This contrasts with, for example, a coaxial- (flattening-) dominated shear zone that would produce oblate $S > L$ fabrics, and a dearth of abundant and consistently-orientated shear sense indicators (Twiss and Moores, 1992). The association of sheath folds, inclined folds with strongly prolate linear fabric elements is commonly inferred to result from high finite strain (Cobbold and Quinquis, 1980; Skjerna, 1989; Goscombe, 1991). The ubiquity of similar-style folds, and the absence of buckle-folds, mullions, or boudinage, suggests little rheological layering existed within the deforming ductile ignimbrite. The general absence of thrust faults or tensile fractures indicates that there was no brittle strain.

The presence of rheomorphic structures throughout the full thickness of the ignimbrite, including the lower and upper margins, indicates that all of the ignimbrite has undergone ductile deformation. The consistency of structures, for example, consistent lineation trend (Fig. 3-21), limited variation in fold scale and morphology (Figs 3-22 and 3-23), suggests deformation was within a single shear zone. The thickness of folded layers and the scale of intrafolial folds provides an

upper limit to the thickness of the active shear zone (see Ramsey, 1967). The thickest folded layer observed was ~ 0.5 m, and folded by a pair of m-scale ($A \geq 2$ m; $\lambda \sim 1$ m) isoclines (e.g., Fig. 3-22c); this limits the maximum shear zone thickness to ≤ 1 m.

Later, extrafolial folding of the uppermost parts

Extrafolial folds in the uppermost 2 m thick layer of mylonite-like ignimbrite deform intrafolial folds (e.g., Fig. 3-24), and therefore are inferred to be younger, although absolute timings are not constrained (see Chapter 4). Parallel-style, upright to inclined, open to tight, folds characteristic of the uppermost parts of the thin ignimbrite are typical of layer-parallel, coaxial shortening of a layer, i.e. buckling (Ramsey, 1967), in contrast to similar-style recumbent isoclines that are characteristic of non-coaxial shear strain. The scale of the extrafolial folds ($A \leq 0.5$ m; $\lambda \geq 5$ m) is consistent with a small degree of shortening ($L > L_0$) in a ~ 2 m thick layer; the open folds indicate low strain, whereas the tighter folds correspond with higher strain (though still low compared to the strain inferred from intrafolial folds). The variation in fold style (classes 1b and 2, with intermediate shapes) within a set of deformed layer is characteristic of competency contrasts between layers (competency contrast), where stronger (more competent) layers buckle, and weaker (less competent) layers shear (see Ramsey, 1967).

Within thin ignimbrite, the extrafolial folds are typically perpendicular to the dip of the observed underlying palaeo-slope. Therefore, by analogy the orientation of the palaeo-slope can be inferred elsewhere by examining the orientation of extrafolial fold axes and the type of refolded folds present (Figs 3-25c; 3-25d; 3-26), even when it is deeply buried. Slope-perpendicular, parallel-style folds are characteristic of down-slope flows where deformation is gravity-driven (Ramsey, 1967; e.g., in lavas, Fig. 1-9, Fink, 1980; in glaciers, Fig. 1-13, Hambrey and Lawson, 2000), where they are typically curvilinear ogives.

Provisional conclusions

The thin ignimbrite facies has undergone two different phases of ductile, fold-dominated deformation. The small-scale of folds indicates that non-coaxial and high-strain deformation was concentrated in a ≤ 1 m thick, sub-horizontal zone of concentrated ductile shear. This produced a penetrative L / S fabric and intrafolial isoclinal and sheath folds, in mylonite-like ignimbrite. Transport direction during this early deformation was mostly top-to-west. Secondly, the uppermost 2 m of the ignimbrite was subsequently deformed by a coaxial and low-strain deformation phase that induced layer-parallel shortening and buckle folding, in response to gravitationally-driven, down-slope flow. This produced dip-slope perpendicular, parallel-style, extrafolial folds that refold earlier intrafolial folds, and produce type-2 and type-3 interference patterns.

Structure within the thick ignimbrite facies

General anatomy

The thick ignimbrite is arbitrarily defined by the 20 m isopach (Fig 3-2a), and ignimbrite 20 m - ≥ 60 m thick within the Rogerson Graben (e.g. Grey's Landing; Fig. 3-1), and the southern margin of the Snake River Plain (e.g., Cedar Creek Reservoir; Fig. 3-1). Within the graben, the thick facies thickens from east to west, increasing from 20 m to ≥ 60 m in a distance of ~ 4 km (Fig. 3-2b); outside the Graben, the ignimbrite region thickens northwards. The maximum thickness of the Grey's Landing ignimbrite is not known. The interior of the thick ignimbrite is best exposed within the Rogerson Graben, along the walls of Salmon Falls Creek Canyon (e.g., Grey's Landing; Fig. 3-2a). Outside the Graben, the upper surface is exposed extensively around the Cedar Creek Reservoir (Fig. 3-2a). Exposures of the ignimbrite interior outside the Graben (e.g., Monument Canyon; Fig. 3-2a), and of the upper surface within the Graben (e.g., Too Cool; Fig. 3-2a), are small and isolated.

The thick ignimbrite (Figs 3-2 and 3-4) is characterised by the presence of two distinct, sub-horizontal and laterally extensive, structural domains (Fig. 3-27): (1) the 'flat' domain - a ubiquitous, penetrative L / S rheomorphic fabric composed of intrafolial folds, a prominent lineation, and abundant kinematic criteria, that resembles a mylonite zone (e.g., Fig. 1-4); and (2) the 'steep' domain - a complexly folded zone that folds the mylonite-like ignimbrite and refolds intrafolial folds within it, restricted to the central and upper levels of the ignimbrite. Both domains form layers that thicken westward within the Rogerson Graben (Fig. 3-28a), and northwards into the Snake River Plain (Fig. 3-2a). The steep domain is always observed to be directly on top of the flat domain (Fig. 3-27), and never reaches the base of the ignimbrite.

Description of structural domains

General characteristics

The two structural domains are readily identifiable in extensive cliff sections within the Rogerson Graben (e.g., Figs 3-28b - e); where the lower 'flat' domain is characterised by relatively smooth weathered surfaces that exhibit closely-spaced, sub-horizontal parting surfaces and colour-banding (Figs 3-28b and 3-28e). In contrast, the upper 'steep' structural domain is characterized by a hackly appearance and a plethora of differently orientated parting surfaces (Figs 3-28b and 3-28d). Exposure outside the Graben is insufficient to distinguish the two domains, other than at Monument Canyon (see next section; Fig. 3-2).

Methodology

Vertical and lateral variations within the thick ignimbrite were investigated by structural analysis of ten vertical traverses through the ignimbrite, and by examining excellent natural exposures in the walls of Salmon Falls Creek Canyon (e.g., Fig. 3-28b). Each traverse is as vertical as possible given the constraints of access up the cliff-face. Structural measurements of planar fabric elements, linear fabric elements, and folds were recorded, together with their height within the

domain (Fig. 3-29). Two structural domains are present in all but one vertical traverse (lower domain only at Lucas Point), and the boundary is typically 15 – 20 m from the base of the ignimbrite. The base is not exposed at most locations, and at these, a significant thickness of the lower flat domain is not observed (Fig. 3-29).

Planar fabric elements (flow-banding and fold axial planes)

Differences in the texture and appearance of the canyon-wall surfaces (e.g., Fig. 3-28b) are manifestations of very different planar fabric attitudes between the two structural domains. Within the flat domain, flow-banding is dominantly sub-horizontal (maximum dip $\leq 30^\circ$) and sub-parallel to the base of the ignimbrite (Figs 3-28e; 3-29; 3-30a), and the fold axial planes of intrafolial folds are all recumbent (Fig. 3-30b). In contrast, flow-banding within the steep domain is typically non-parallel, and dips between horizontal and vertical (typically moderately inclined, $\leq 45^\circ$; Figs 3-28d; 3-29; 3-30a). Intrafolial folds are refolded by upright or steeply inclined extrafolial folds (typically extrafolial fold axial planes dip $\geq 60^\circ$; Fig. 3-30b).

Linear fabric elements (lineations and fold axes)

Typically lineations and fold axes are parallel to each other at individual locations (Figs 3-29; 3-31), and they vary both vertically and laterally within the thick ignimbrite. Vertical structural traverses along Salmon Falls Creek Canyon, within the Rogerson Graben, show markedly different vertical lineation trend profiles (Figs 3-29; 3-31). This is consistent with the data published by Branney et al (2004a). The predominant linear fabric trend in the Rogerson Graben is E – W (e.g., Marble Cliffs; Fig. 3-29), however, N – S (e.g., Lucas Point), NE – SW (e.g., Corral Canyon), and NW – SE (e.g., Brown's Place) trends are observed.

Five traverses exhibit unidirectional or almost unidirectional linear fabric trend profiles; Marble Cliffs, Lucas Point, Lud's Point, Corral Canyon, and Walt's Point (Figs 3-29; 3-31). In these traverses the trend of linear fabrics does not

appear to be influenced by the domain boundary or differences in the style of deformation. The five remaining traverses exhibit at least two different linear fabric trends (Figs 3-29; 3-31). Linear fabrics at Norton Bay exhibit a smooth, 70° clockwise change from 130° to 200° in 35 m vertical thickness (Fig. 3-29). Linear fabrics at Brown's Place are unidirectional except where they are off-set ~ 20° anticlockwise from 140° to 110° across a vertical distance of 1 m (Fig. 3-29) at the base of a large (≥ 10 m-scale) extrafolial sheath folds trending 100°. The vertical profile of linear fabric trends at Big Sand Bay is complex (Fig. 3-29), and divides into three parts: (1) 50° anti-clockwise off-set from 130° to 080° within 1 m vertical thickness at the domain boundary; (2) gradual clockwise change back to a 130° trend over 10 m; and (3) a unidirectional 140° trend.

The traverses at Grey's Landing and Backwaters are the most complex, exhibiting several linear fabric trends at different heights within the ignimbrite. Linear fabric trends at Backwaters are approximately 090°, however, some fold axes within the bottom 10 m of the lower domain are $\leq 90^\circ$ oblique to the 090 lineation trend (Fig. 3-29). The Backwaters linear fabrics do not appear influenced by the domain boundary. In contrast, the Grey's Landing traverse exhibits a complex vertical variation in linear fabric trend, including an apparent major off-set at the observed domain boundary (Fig. 3-29). Between 0 m and 13 m, parallel lineations and fold axes change smoothly from 090° to 150° (60° clockwise). Between 13 m and 16 m, linear fabrics appear to be off-set by ~ 120° anti-clockwise from 150° to 030°; this level corresponds with the position of the domain boundary at Grey's Landing (between 13 m and 15 m), however this is an artefact of the plotting technique, the trend change is actually less intense, from 160° to 210°. Between 16 m and 23 m, the trend of linear fabrics changes smoothly from 210° to 060°, and then is off-set to 020° (40° anti-clockwise) in a 1 m interval, corresponding with the edge of a major E – W trending sheath fold culmination. Between 25 m and 45 m, linear fabric trends change smoothly from 020° to 060° (40° clockwise), however, lineations and fold axes are up to 90° oblique to each other.

Whether linear fabric trends are unidirectional or multi-directional in a specific traverses does not appear to be spatially controlled. Adjacent traverses may show unidirectional or multi-directional profiles (e.g., Marble Cliffs and Grey's Landing; Fig. 3-31), and inflections in multi-directional profiles are not correlatable between adjacent traverses (e.g., Backwaters and Brown's View, < 500 m; Fig. 3-31).

The domain boundary: position and morphology

Typically, the domain boundary is 10 m to 20 m above the base of the ignimbrite (e.g., Grey's Landing; Figs 3-28a; 3-28b; 3-29; 3-30), however, many sections do not expose the base (e.g., Big Sand Bay; Fig. 3-30a) and the actual thickness has to be inferred from complete adjacent sections. The observed position of the domain boundary corresponds well with the change in planar fabric attitude recorded at 9 of 10 vertical traverses through graben-fill ignimbrite (inferred total thickness ≥ 30 m; Fig. 3-30a); below which planar fabrics are horizontal to sub-horizontal; and above which planar fabrics are between horizontal and vertical (Figs 3-29; 3-30). In contrast, the position of the boundary only corresponds with a significant change in the orientation of lineations at Grey's Landing and Big Sand Bay (Figs 3-29; 3-31).

The domain boundary is laterally extensive, and typically sub-horizontal and sub-parallel to the base of the ignimbrite (Figs 3-28c; 3-30a). It is not easily pinpointed in exposures because it is a subtle gradational boundary (Fig. 3-28b). Occasionally it is hidden by narrow, vegetated and regolith-covered, topographic benches where erosion has exploited the difference in planar fabric attitude (Fig. 3-28c). Extensive field observations have provided no evidence that the domain boundary is a discrete surface defined by; (1) a different lithology (e.g., an intervening vitrophyre, a palaeosol, a sedimentary rock), (2) a different texture (e.g., a breccia, a lithophysal horizon), or (3) a décollement separating an autochthonous lower domain from an allochthonous upper domain (e.g., a brittle fault or a ductile shear zone). The domain boundary is therefore most likely a rheological transition.

Structural domain 1: the flat domain

Overview

The lower structural domain (Figs 3-27; 3-28) is ≤ 20 m thick, and is characterised by a ubiquitous, penetrative, sub-horizontal L / S fabric, a prominent lineation, pervasive intrafolial isoclinal and sheath folds, and abundant kinematic criteria (Fig. 3-32). It strongly resembles a mylonite (e.g., Fig. 1-4) and is identical to mylonite-like ignimbrite of the thin facies (e.g., Fig. 3-22). Therefore, due to the dominantly horizontal nature of the structures, I will refer to this domain as the 'flat' domain.

Description: planar fabric elements

The planar component of a penetrative L / S fabric is defined by flow-banding (including eutaxitic fabric, colour-banding, and most commonly parting surfaces; e.g., Figs 3-5; 3-6; 3-8; 3-9; 3-10) deformed by intrafolial isoclinal and sheath folds (Figs 3-32a; 3-32b). Flow-banding is typically gently dipping ($\leq 10^\circ$) and sub-parallel and dip directions are variable (Fig. 3-30). Individual flow-bands are laterally extensive (≤ 30 m) and typically, maintain constant thickness (≤ 20 cm). Attenuated or boudinaged flow-bands are not observed.

Description: linear fabric elements and kinematic criteria

The linear component of the L / S fabric is defined by abundant striæform and intestiniform lineations on parting surfaces (Figs 3-15a - d), and rare stretched vesicles within the basal vitrophyre (e.g., Fig. 3-13a). Lineation trends are variable (see above, Figs 3-29; 3-31), but are dominantly E – W in the centre of the Rogerson Graben (parallel to the local palaeo-slope), and NW – SE near the southern margin where the palaeo-slope is not constrained (Fig. 3-33). At Monument Canyon on the southern flank of the Snake River Plain, lineations are perpendicular to the palaeo-slope (Fig. 3-33). Therefore, the orientation of lineations in the flat domain of thick ignimbrite, is nearly identical to that in mylonite-like, thin ignimbrite. Available kinematic criteria (rotated

porphyroclasts, imbricated vesicles) suggest a top-to-west transport direction at Grey's Landing and Backwaters (Figs 3-29 and 3-33). Once again, the down-slope transport direction within the Graben corresponds with data from the thin ignimbrite facies.

Description: folding

The flat domain is characterised by ubiquitous, intrafolial folds. Typically folds are recumbent and isoclinal (Figs 3-30b; 3-32a; 3-32b), and have axes parallel or sub-parallel (sheath-like folds) to the local elongation lineation (Fig. 3-29).

Rootless hinges and sheath folds are abundant in all sections, where they appear to 'float' within a 'sea' of L / S fabric ignimbrite (Figs 3-32c-f). Folds are typically small-scale ($\lambda \leq 1$ m, $A \geq 1$ m; Fig. 3-32), however, some sheath folds can be traced for almost 30 m along the elongation direction (e.g., at Grey's Landing; Fig. 3-32d).

The intrafolial folds are often complexly refolded by other intrafolial folds (e.g., Fig. 3-34). Type-3 interference patterns (e.g., Figs 3-25c; 3-34a; 3-34b) and complex hinges (Figs 3-34c-e) are ubiquitous. Complex intrafolial fold hinges exhibit three major forms: (1) 'club-foot' forms (e.g., Fig. 3-34c) where floating, and often rootless, type-3 refolded folds are observed in the cores of larger intrafolial folds; (2) 'rolling-pin' forms (e.g., Fig. 3-34d) where rootless, cylindrical-shaped folds are entrained in the hinge of a later, discordant intrafolial isocline; and (3) 'knotted' forms (e.g., Fig. 3-34e) where multiple cm-scale, intrafolial hinges are concentrated together within the hinge of a larger intrafolial fold. Typically the different forms of complex fold hinge are manifested as bulbous or swollen hinges, that are disproportionate to the thickness of the surrounding folded layer (e.g., Figs 3-34d; 3-34e).

Structural domain 2: the steep domain

Overview

The upper structural domain (Figs 3-27; 3-28) is typically ≥ 20 m thick, and is characterised by heterogeneous, progressive deformation of the mylonite-like ignimbrite by steeply inclined extrafolial folds (e.g., Fig 3-28d). Therefore, I will refer to this domain as the 'steep' domain. It has a lower limit ~ 10 m to 20 m from the base of the ignimbrite, below which extrafolial folding is not observed (Figs 3-27; 3-28; 3-30). The steep domain is noteworthy for the extensive exposure of folds at the upper surface that offer insights into the folding style within the interior of the deposit.

Description: planar fabric elements – primary mylonite-like fabric

A primary mylonite-like L / S fabric is similar to that in the flat domain (e.g., Fig. 3-32) and the adjacent thin ignimbrite (e.g., Fig. 3-22), and is ubiquitous throughout the steep domain. This planar, penetrative fabric, including integral intrafolial folds (e.g., Figs 3-32; 3-34), is deformed by, and defines the scale, shape and geometry of, extrafolial folds (e.g., Fig. 3-28d). Parting surfaces are the most common manifestation of flow-banding in the steep domain, except at the upper surface (e.g., Cedar Creek Reservoir; Fig. 3-2a) where lithological variations between welded and non-welded, and vitric and devitrified tuff define crude stratification (Fig. 3-27).

Description: linear fabric elements and kinematic criteria

Lineations in the steep domain are uncommon and highly localised in comparison to lineations throughout the rest of the Grey's Landing ignimbrite. The distribution of lineations is heterogeneous; they are absent from the majority of parting surfaces in the interior of the steep domain, and are only locally abundant on discrete surfaces. Where lineations are present, they are observed on relatively planar and weakly folded layers, becoming less abundant and fainter proximal to extrafolial folds. Lineations are observed in three forms: (1) locally prominent

striæform and intestiniform lineations hosted on discrete parting surfaces (e.g., Fig. 3-15a-d), these are an integral part of the L / S fabric of the thin ignimbrite facies. (2) A second set of stretched vesicles is exhibited on parting surfaces and in vitrophyre, orientated oblique or perpendicular to the dominant elongation lineation (Fig. 3-13f). These are localised on discrete surfaces at or near the upper surface, at Monument Canyon (Fig. 3-2a). (3) Localised stretched vesicles are observed around the crests of antiformal periclinal folds at the upper surface (Fig. 3-13b). These are characteristically perpendicular to the adjacent fold axis, and plunge in opposite directions either side of the axis parallel to the dip of the fold limb. Deformed lineations are observed on folded parting surfaces (e.g., Fig. 3-15f), but they are very rare (only seven examples observed).

Lination trends recorded in structural traverses within the Rogerson Graben are highly variable; trends in adjacent traverses are commonly perpendicular to each other (Figs 3-29; 3-31; 3-35). They do not exhibit a consistent orientation relative to the inferred palaeo-slope (Fig. 3-35), although limited kinematic criteria are top-to-west at Backwaters and Grey's Landing. In contrast, steep domain lineations outside the Graben (i.e. at Salmon Dam, West Bay, Monument Canyon, and Cedar Creek Reservoir) are dominantly E – W trending, and have an associated top-to-west shear sense (Fig. 3-35). These are perpendicular to the underlying palaeo-slope, and are parallel to adjacent lineations within the flat domain and the thin ignimbrite facies (Figs 3-21; 3-33). A second, stretched vesicle lineation trend at Monument Canyon (e.g., Fig. 3-13f) is perpendicular to the prominent lineation (N – S trending), and parallel to the underlying palaeo-slope (Fig. 3-35). Stretched vesicle lineations associated with periclinal fold axes at Cedar Creek Reservoir are N – S or NE – SW trending, and consistently perpendicular to the adjacent fold axis (see below).

Description: folding

Deformation in the steep domain is heterogeneous, for example, fold morphology is varied (Fig. 3-36), and the scale of folds changes vertically (Figs 3-27; 3-28). Folds in the steep domain are characteristically larger than those elsewhere in the

Grey's Landing ignimbrite ($\lambda \geq 2$ m, $A \geq 2$ m; Fig. 3-36), they are typically upright to recumbent (Figs 3-36a-d), open to tight (e.g., Figs 3-36a; 3-36b), extrafolial (Fig. 3-36a), and they refold earlier intrafolial folds (Fig. 3-36b). A spectrum of fold morphologies is observed, that can be divided into two end-members: (1) strongly-curvilinear, recumbent isoclines and sheath folds (Figs 3-36d; 3-36e), typically in the interior of the ignimbrite; and (2) upright, parallel-style folds that are non- or weakly-curvilinear (Figs 3-36a-c), observed at the upper surface of the ignimbrite.

Extrafolial curvilinear isoclines and sheath folds are only observed in the interior of the steep domain (Fig. 3-27), where the largest examples may be almost the same thickness as the domain itself (e.g., Fig. 3-37). Therefore these folds are most commonly encountered in canyon-wall sections, for example, along Salmon Falls Creek Canyon, and are not observed in shallow sections where the upper surface is preserved (Fig. 3-38). In contrast, parallel-style folds are only observed at, or immediately below (maximum depth 5 m; e.g., Fig. 3-36a), the upper surface (Fig. 27). Extensive areas of the original upper surface are not preserved or exposed where the present day erosion level is within the lithoidal interior. The original top is not observed within the Rogerson Graben (e.g., Grey's Landing), other than where down-faulted blocks have been buried by thin (≤ 10 m thick) basalt lavas (e.g., Too Cool; Fig. 3-38). Subsequent erosion through the basalt cover exposes the remaining upper surface of the ignimbrite. Outside the Graben, basalt lavas covered the original surface at Salmon Dam and West Bay (Fig. 3-38). The most extensive exposures are at and around Cedar Creek Reservoir (Fig. 3-36), where the amount of denudation has been less than within the Graben, despite the absence of any evidence for a past covering unit. There is no evidence to suggest that the heterogeneous distribution of fold morphologies is a primary phenomena, rather it appears to be an artefact related to the erosion of the upper surface within the Graben, and a lack of sufficient canyon-exposure outside the Graben.

Extrafolial folds in the interior of the thick ignimbrite are typically recumbent, isoclinal, and similar-style. Their scale is very variable, ranging through three orders of magnitude: (1) 2 to 5 m-scale isoclines (e.g., Fig. 3-36d); (2) 10 m-scale sheath folds and isoclines (e.g., Fig. 3-36e), and (3) 100 m-scale isoclines, and possibly sheath folds (e.g., Fig. 3-37). The scale of folding appears to increase with time; 2 to 5 m-scale folds are ubiquitous, folding the mylonite-like fabric and refolding intrafolial folds (e.g., Figs 3-39a; Fig. 3-39b). In turn, these folds are deformed by 10 m-scale folds producing incredibly complex interference patterns that cannot be easily resolved (e.g., Fig. 3-39c). At Grey's Landing, 10 m-scale folds are deformed by a 100 m-scale northward-closing isocline (Fig. 3-37). The axes of all sizes of isoclines and sheath folds are typically parallel or sub-parallel to the dominant lineation (E – W trending) on adjacent parting surfaces (Figs 3-35; 3-38), fold axes at a high angle to the lineation have not been observed.

Extrafolial folds at the upper surface of the thick ignimbrite vary from upright to recumbent, open to isoclinal, and similar- to buckle-style. Like folds in the interior, their scale is very variable, ranging through three orders of magnitude: (1) upright and tight 2 to 5 m-scale periclinal folds (λ and $A \leq 5$ m; e.g., Fig. 3-40a; 3-40b); (2) 10 m-scale, upright to recumbent, closed to isoclinal folds (λ and $A \leq 10$ m; e.g., Fig. 3-40c); and (3) 20 to 30 m-scale, upright and open folds ($\lambda \leq 30$ m, $A \leq 10$ m; e.g., Fig. 3-40d). Outside the Graben fold axes are perpendicular to the inferred underlying palaeo-slope, and parallel to the dominant lineation (e.g., Cedar Creek Reservoir; Figs 3-35; 3-38; 3-43). Within the Graben, surficial extrafolial folds trend N – S (Fig. 3-38) and are perpendicular to the inferred underlying palaeo-slope and the dominant lineation (Figs 3-35; 3-38). Lineations localised around the crests of antiforms at Cedar Creek Reservoir are perpendicular (N – S) to the fold axes (Fig. 3-38).

The mylonite-like fabric is folded by multiple 2 to 5 m-scale folds, that refold earlier intrafolial folds (Fig. 3-41), and often refold each other (e.g., Fig. 3-40e). In turn, 2 to 5 m-scale folds are deformed by 10 to 30 m-scale folds that are periclinal in plan view (e.g., Fig. 3-40f) and are often shaped like a convex

mushroom in cross-section (e.g., Fig. 3-40c). These are deformed by long-wavelength, 20 to 30 m-scale, buckle-style folds (e.g., Figs 3-40d; 3-43). The superposition of three scales of extrafolial folds is manifested in disharmonic, composite hinge zones of 20 to 30 m-scale folds (e.g., Figs 3-44; 3-45; 3-46) where multiple sizes and generations of fold hinges are concentrated (e.g. Fig. 3-44). Lithological layering at the upper surface is affected by all scales of extrafolial folding, for example, non-welded orange tuff is preserved in synformal periclinal folds at Cedar Creek Reservoir (Fig. 3-44) and in synforms exposed at Salmon Dam (Fig. 3-47). Folding of layering that includes the non-welded orange tuff and upper welded vitrophyre is more disharmonic (Figs 3-44; 3-47) than folding of lithoidal welded ignimbrite alone (*cf.* Figs 3-45; 3-46).

Description: brittle structures

Three distinct types of brittle structures are encountered in the steep domain of thick ignimbrite, all at the upper surface (Fig. 3-48): (1) 'chocolate-block' tensile cracks about the crests of antiformal periclinal folds (e.g., Figs 3-48a; 3-48b); (2) matrix-supported breccia between non-brecciated, welded vitrophyre and non-brecciated, orange, non-welded tuff (e.g., Figs 3-48c; 3-48d); (3) 'jig-saw fit' brecciated extrafolial folds (e.g., Fig. 3-48e). 'Chocolate-block' cracking is exhibited in discrete vesicular layers (≤ 5 cm thick), sandwiched between non-vesicular layers, and is localised (≤ 5 m² total surface area) around the crests of antiformal periclinal folds and domes (e.g., Figs 3-48a; 3-48b). Two sets of jagged, anastomosing cracks intersect at $\sim 90^\circ$, and are orientated $\sim 45^\circ$ to both axial traces of the periclinal folds. Individual cracks terminate at hairline crack tip points (Fig. 3-48b). Apparent tensile extension directions are away and down-dip from the fold axes. Vesicles within the vesicular layer trend perpendicular to the dominant NW – SW fold axes trend (e.g., Fig. 3-44), and are cut by tensile cracks.

A breccia is observed in a ≤ 30 cm thick layer at the contact between the upper vitrophyre and overlying orange, non-welded tuff (e.g., Salmon Dam; Figs 3-47; 3-48c). It is a matrix-supported breccia (maximum clast diameter ≤ 10 cm) composed of an orange, non-welded matrix and clasts of orange-red, variably

fused tuff (e.g., Fig. 3-48d). The degree of fusing within clasts increases down-section: clasts are weakly fused and not easily discernable from the matrix near the boundary with non-brecciated orange tuff; and they are fused to black glass forming *fiamme* adjacent to the vitrophyre. In the centre of the breccia layer, clasts are typically lustrous orange-red tuff. Clasts do not exhibit any preferred orientation.

Some folds within the upper vitrophyre are intensely brecciated (e.g., Fig. 3-48e) where they have been preserved at the very top of the ignimbrite (e.g., Salmon Dam; Fig. 3-47). The breccia is characteristically 'jig-saw fit'-like, preserving the original shapes and proportions of the folds. The breccia is dominantly matrix supported, and is composed of pumiceous white tuff matrix and clasts of typically pumiceous black vitrophyre. Matrix-supported 'jig-saw' breccia is common throughout the upper vitrophyre, and often forms extensive outcrops, however, identifiable folds are uncommon. Clasts do not exhibit any preferred orientation. White pumiceous tuff matrix is only observed in interstices between clasts, and other than colour-difference appear to be composed of the same material. There is no evidence to suggest that the white pumiceous tuff is an exotic tephra (e.g., different crystal assemblage, different textures, different clasts size).

Initial interpretation

Mylonite-like ignimbrite

The deformation style, E – W lineation trend, kinematic criteria, top-to-west transport direction, etc., exhibited in the flat domain of the thick ignimbrite (Figs 3-32; 3-34) are very similar to that inferred for mylonite-like fabrics in the thin ignimbrite (Fig. 3-21; 3-22; 3-23; 3-33). The mylonite-like fabric observed throughout the thick ignimbrite is consistent, and most compatible, with evolution in a ductile shear zone, with strong, heterogeneous, non-coaxial (top to west) shear. Like the mylonite-like fabric in the thin ignimbrite facies, a penetrative L / S fabric, intrafolial isoclinal and sheath folds, abundant kinematic criteria, and prominent prolate linear fabrics are all characteristics of fossilized ductile shear

zones (e.g., Fig. 1-4; Cobbold and Quinquis, 1980; Ramsey, 1980; Simpson, 1983; Ghosh and Sengupta, 1987; Passchier and Trouw, 1996). The presence of sheath folds associated with strongly prolate linear fabric elements are commonly inferred to result from high finite strain during deformation (Cobbold and Quinquis, 1980; Skjerna, 1989; Goscombe, 1991). In contrast, a coaxial- (flattening-) dominated zone of concentrated shear would be likely to produce an oblate $S > L$ fabric, and a dearth of abundant and consistently-orientated shear sense indicators (Twiss and Moores, 1992). Like the mylonite-like fabric in the thin ignimbrite facies, there is little evidence of rheological contrasts between the layers or of brittle deformation. The lack of a strain gradient is atypical of exhumed tectonic shear zones developed in initially non-strained rock; rather, the basal fall deposit is non-strained and in the base of the ignimbrite strain is effectively infinite.

The presence of ductile rheomorphic structures throughout the full thickness of the Grey's Landing ignimbrite, including the steep domain, suggests that all of the ignimbrite was deformed by ductile shear. The uniformity of intrafolial fold scale and morphology (e.g., Figs 3-32; 3-34; 3-41) suggests that the deformation occurred within a single sub-horizontal concentrated zone of shear. As with the ignimbrite in the graben-flank region, the thickest folded layer observed was ~ 0.5 m thick and the maximum fold scale (1 m-scale; Figs 3-28e; 3-32e; 3-32f), place an upper limit of ≤ 1 m for the thickness of the shear zone.

At many sites the elongation direction within the flat domain is unidirectional (e.g., Marble Cliffs, Fig. 3-29). However, variations in the trends of lineation and fold axes trend are exhibited at Grey's Landing and Backwaters (Fig. 3-29). This was interpreted by Branney et al. (2004a). It suggests a more complex shearing history, at least in those two localities, where the elongation direction has changed with height. Assuming a maximum shear zone thickness of ~ 1 m, all mylonite-like ignimbrite must have been deformed by that shear zone at some time, and assuming that an individual shear zone can only have one shearing direction at

any one point in time; I tentatively suggest that a temporal change in the stretching direction is recorded.

The trend of the elongation direction and the transport direction established from kinematic criteria are almost identical to that in adjacent graben-flank ignimbrite, both inside and outside the Rogerson Graben (E – W; *cf.* Figs 3-21; 3-23; 3-33). The division between thin and thick facies (Fig. 3-2) is not based on any observed discontinuity (e.g., a fault), rather it is an arbitrary division based on inferred thickness. Therefore, it is feasible, and almost certain, that mylonite-like in the thick ignimbrite is a thicker, lateral equivalent of the mylonite-like, thin ignimbrite.

Later, extrafolial folding of mylonite-like ignimbrite

Extrafolial folds deform intrafolial folds (e.g., Figs 3-39a; 3-41; 3-42), and therefore, are inferred to be younger, although relative timings are not constrained. Two end member styles of extrafolial fold are observed (Fig. 3-49): (1) curvilinear, similar-style isoclines and sheath folds within the interior of the extrafolial domain; and (2) parallel-style, buckle-style folds of the upper surface of the ignimbrite. This suggests two different styles of deformation operated during steep domain folding of the original mylonite-like ignimbrite.

Curvilinear folds and sheath folds in the interior

Curvilinear, similar-style folds are observed at three scales, and larger folds appear to fold smaller, earlier folds (e.g., Figs 3-37; 3-49). If the scale of a fold is controlled by the thickness of the layer it is deforming (Ramsey, 1967), then the thickness of the actively deforming layer within the Grey's Landing ignimbrite probably increased with time. The largest interior folds deform almost the full thickness of the steep domain (e.g., Fig. 3-37) suggesting that at some time, a deformation regime capable of folding a layer ≥ 30 m thick was active. Furthermore, the style of curvilinear folds in the interior of the steep domain does not change, suggesting that the same style of deformation was sustained. As in

the flat domain, the presence of recumbent, similar-style, curvilinear isoclines and sheath folds is consistent with heterogeneous non-coaxial shear in a sub-horizontal shear zone (e.g., Ramsey, 1960).

The dominant stretching direction, inferred from the trends of sheath fold axes, is typically E – W (Fig. 3-38), similar to that observed in both the mylonite-like domain (Fig. 3-33) and the graben-flank region (Fig. 3-21). Within the Rogerson Graben this trend is sub-parallel to the inferred palaeo-slope (Fig. 3-38), outside the Graben it is perpendicular to the inferred palaeo-slope (Fig. 3-38). Transport direction cannot be constrained from lineation-parallel folds (no apparent vergence); however, by analogy with the transport direction established from similar-trending linear fabrics in mylonite-like ignimbrite (Figs 3-21; 3-33), a top-to-west and down-slope transport direction can be inferred in the Graben. This inference allows for formation of interior folds by deformation within a discrete shear zone (e.g., similar to the mylonite-like ignimbrite), down-slope gravity-driven flow, or a combination of the two. However, outside the Graben the sheath fold trend is perpendicular to the inferred underlying palaeo-slope (Monument Canyon, Fig. 3-38), indicating that gravity-driven flow is unlikely to be the only, or even the major, folding mechanism throughout the ignimbrite.

Parallel-style folds at the upper surface

Parallel-style folding at the upper surface of the ignimbrite is distinctly different from folding in the interior of the steep domain (Fig. 3-49), and therefore a different style of deformation is likely. As with extrafolial folding of the upper surface of the thin ignimbrite, parallel-style, upright to inclined, open to tight, folds are typical of layer-parallel, coaxial shortening of a layer, i.e. buckling (Ramsey, 1967), in contrast to similar-style recumbent isoclines that are characteristic of non-coaxial shear strain. Balanced cross-sections can be used to constrain layer-parallel shortening of the upper surface at Cedar Creek Reservoir, where total shortening is estimated to be 70% (e.g., Fig. 3-50).

Refolding relationships suggest that the scale of folds increased through time, and hence, the thickness of the deforming layer increased at the same time (e.g., Ramsey, 1967). Firstly, 2 m to 5 m-scale folds deform fold-banding, intrafolial folds and typically only the boundary between two lithologies (e.g., orange tuff and vitrophyre; Figs 3-44; 3-47); this is typically a ≤ 5 m thick layer. In turn, these folds and the mylonite-like fabric are deformed as part of a ≤ 10 m thick layer by 10 m-scale folds (e.g., Fig. 3-45; 3-46). Finally, the largest folds ($\lambda \leq 30$ m) appear to deform a layer ≤ 15 m thick that encompasses the uppermost non-welded tuff, the upper vitrophyre, and lithoidal ignimbrite (e.g., Figs 3-40d; 3-43). Variation in fold style (classes 1b and 2, and intermediate shapes) within a set of deformed layer is characteristic of competency contrasts between layers (competency contrast), where stronger (more competent) layers buckle, and weaker (less competent) layers shear (Ramsey, 1967).

Slope-perpendicular (Fig. 3-38), parallel-style folds are characteristic of down-slope flows where deformation is gravity-driven (Ramsey, 1967), and parallel-style folds are characteristic of the deformed upper surface of gravity-driven, ductile flows (e.g., in lavas, Figs 1-9b; 1-9d, Fink, 1980; in glaciers, Fig. 1-13, Hambrey and Lawson, 2000). In lavas and glaciers upper surface folds are characteristically ogive-shaped, where they are convex-closing down-slope, with flow-parallel fold axes at the margins (e.g., Fig. 1-9b). However, folds of the upper surface of the Grey's Landing ignimbrite are not observed to be ogives, rather they are parallel to each other over an extensive area (≥ 25 km²) and typically have fold axes perpendicular to the palaeo-slope (Fig. 3-38). No ogive-closures are observed at the upper surface.

Brittle deformation at the upper surface

Brittle structures, for example, breccias and tensile cracks (Fig. 3-48) are only observed at the upper surface of the ignimbrite, and are typically localised to discrete layers. 'Chocolate-block'-like cracking is produced by two sets of mutually perpendicular tensile fractures developed in vesicular ignimbrite (Fig. 3-48a). They are only observed in vesicular layers sandwiched between non-

vesicular layers, and at the crests of antiformal periclinal folds (Fig. 3-48b). Individual cracks appear to form by propagation of hairline fractures away from the crest of the pericline, presumably away from the volume of highest strain. The vesicles trend perpendicular to the dominant fold axes trend, suggesting that they were stretched during upward propagation of the fold during ductile deformation, and were then cross-cut by later brittle fractures.

Because they are restricted to vesicular layers within otherwise non-vesicular ignimbrite, I infer that there is a first-order relationship between the presence of vesicles and development of fractures. The presence of discrete vesicular layers may have produced significant competency contrasts during folding. Exsolution of volatiles from the glass to a bubble phase increases viscosity in two ways: (1) viscosity-lowering volatiles are removed from the glass, increasing glass viscosity (Fig. 1-19c); and (2) the increase in bubble concentration increases viscosity (Fig. 1-20b). Proximity to the upper surface encourages cooling of the ignimbrite, which in turn, encourages volatile exsolution. I propose that advection of hot ignimbrite from within the deposit by folding, may lead to rapid cooling and volatile exsolution in the cores of periclinal folds. Differential exsolution and vesicle formation between layers would lead to competency contrasts during continued folding, and to localised brittle fracturing of competent layers.

I infer that the orange-tuff breccia (Figs 3-48c; 3-48d) was produced by mechanical deformation of the partly fused contact between non-welded and welded tuff, during folding of the upper surface. The orange, non-welded ash is clearly in-folded with welded ignimbrite at Salmon Dam (Fig. 3-47) and at Cedar Creek (Fig. 3-44). The breccia appears to be composed of clasts of variably fused orange tuff in a matrix of the same, non-welded tuff (Fig. 3-48d). The fused tuff clasts appear to have formed by fusing of originally non-welded orange tuff against, presumably hot, welded vitrophyre. I infer that fusing of the orange tuff created a thin layer, the thickness of which was temperature-controlled, that was more competent than both the non-welded, loosely consolidated tuff, and the hot, ductile welded vitrophyre. Disharmonic folding in welded and non-welded layers

(Figs 3-44; 3-47) suggests significant competency contrasts between the layers (Twiss and Moores, 1992). Syn- or post-fusing folding of the upper surface of the ignimbrite deformed all three layers, and competency contrasts between layers were expressed as ductile deformation in the less competent layers (non-welded tuff and vitrophyre) and brittle deformation in the more competent, intervening layer.

I infer that 'jig-saw fit' breccias (e.g., Fig. 3-48e) are not a product of brittle deformation related to emplacement of the ignimbrite, and rather that they are a taphanomic effect related to static, post-emplacement cooling. Clasts are not preferentially orientated and still preserve the general shape and proportions of original structures, suggesting that they have not been flattened (coaxial deformation) or rotated (non-coaxial deformation). Therefore, I infer that the breccia was formed *in situ*. Jig-saw breccias have been reported from the upper surfaces of several silicic lavas (McPhie and Allen, 1992; McPhie et al., 1993), where they have been interpreted to *in situ* cooling and contraction of the vitrophyre allowing the ingress of water along propagating cracks. Continued crack growth forms separate clasts separated by hydrated pumiceous tuff.

The domain boundary

It is important to consider the status of the domain boundary (e.g., Figs 3-37; 3-49). The domain boundary is a sub-planar, sub-parallel structural discontinuity separating a domain that has undergone one phase of deformation (flat domain) from a domain that has undergone two phases of deformation (the steep domain; Figs 3-27; 3-49). Therefore, it is the lower limit of later extrafolial folding deformation, and does not appear to influence the earlier, mylonite-like fabric (Fig. 3-49). This suggests that the boundary did not form before the mylonite-like fabric was formed, for example, as a depositional break or cooling break between different emplacement units (*cf.* the Jackpot Member). There is no field evidence to suggest that the boundary is a depositional break (e.g., an unconformity), for example, there is no compositional difference across it, it is not an erosion surface (e.g., a palaeosol or incised channels), nor is there any intervening tephra or

sediments. Furthermore, there is no evidence of a cooling break (e.g., inter-layered vitrophyre or lithophysal horizon).

Therefore, if the domain boundary is not a pre-existing feature, is it a décollement separating the two domains, where the upper, steep domain has undergone more shortening? If so, the domain boundary is a basal décollement to the steep domain, and both should exhibit a similar elongation direction and shearing direction. However, within most of the Rogerson Graben the elongation direction is approximately E – W throughout the ignimbrite, including the boundary (Fig. 3-29); there is no appreciable change in elongation direction across the boundary. Only at Grey's Landing and Big Sand Bay is there a $\leq 100^\circ$ anti-clockwise rotation at the domain boundary (Fig. 3-29). There is no evidence of a discrete ductile shear zone cross-cutting the mylonite-like fabric at the domain boundary (e.g., a smaller-scale (cm-scale), penetrative L / S fabric); neither is there any evidence of brittle deformation (e.g., fault gouge, cataclastite, fault breccia, slickenlines). Rather the boundary is subtle and gradual, as progressively deeper flat domain rock has become entrained in extrafolial folds (Fig. 3-49).

Provisional conclusions

I provisionally conclude that thick ignimbrite has undergone two different, and distinctive, phases of ductile, fold-dominated deformation (Fig. 3-49). Firstly, a non-coaxial and high-strain deformation phase was concentrated in a ≤ 1 m thick, sub-horizontal, ductile shear zone. This produced a penetrative L / S fabric and intrafolial isoclinal and sheath folds, in mylonite-like ignimbrite. Transport direction during this deformation was typically top-to-west (Fig. 3-51). This phase of deformation appears to be the same as that that affected mylonite-like ignimbrite in the thin ignimbrite. Secondly, the uppermost ~ 30 m of the dominant mylonite-like fabric was extensively deformed by a complex fold-dominated deformation phase (Fig. 3-49) that induced: (1) co-axial layer-parallel shortening and buckle folding at the upper surface; and (2) non-coaxial shortening within the interior of the ignimbrite associated with ≤ 100 m-scale folds. The

second phase of deformation appears to result from gravity-driven ductile flow of mylonite-like ignimbrite influenced by variable slope directions inside and outside the Rogerson Graben (Fig. 3-51).

Transitions between structural regions and domains: a case study at Monument Canyon

Overview

To investigate the lateral transition between thin and thick ignimbrite facies, and vertical changes in deformation style in each region (e.g., flat and steep domains), a case study was conducted at Monument Canyon. Monument Canyon (Fig. 3-2a) is the only locality where the transition between thin and thick ignimbrite is exposed, and it provides the best demonstration of the change from flat domain to steep domain. Furthermore, Monument Canyon provides unsurpassed exposure through extrafolial folding in thin ignimbrite, and the interior and at the upper surface of the thick ignimbrite.

Description

The Grey's Landing ignimbrite is a north-dipping ($\leq 15^\circ$) and north-thickening (0 m - ≥ 30 m) sheet in the Monument Canyon area (Fig. 3-52). The base of the sheet dips $\sim 10^\circ$ to the north; whereas the upper surface, although folded, typically dips $\sim 5^\circ$ north.

Thin ignimbrite (≤ 20 m thick)

At the southern end of Monument Canyon (Fig. 3-52), most of the ignimbrite is characterised by a ubiquitous and penetrative, sub-parallel and planar, mylonite-like fabric (e.g., Figs 3-22; 3-32a; 3-32b) hosting a prominent E – W lineation, a top-to-west transport direction, and E – W trending, recumbent intrafolial isoclines and sheath folds (Figs 3-52; 3-53). The upper surface of the thin ignimbrite (~ 15 m from base) is gently folded by a series of extrafolial, E – W

trending buckle folds and periclinal folds ($\lambda \sim 20$ m; $A \leq 5$ m; e.g., Figs 3-25a; 3-54). These folds deform the mylonite-like fabric. A second elongation lineation, N – S trending, is observed at the upper surface (Fig. 3-35), perpendicular to the dominant trend throughout the rest of the ignimbrite. This lineation has an associated top-to-north transport direction (Fig. 3-35). The base level of extrafolial folds is approximately planar, and dips north ($5^\circ - 10^\circ$; Figs 3-52; 3-53).

The thin ignimbrite is characteristically planar in cross-section (Fig. 3-53), and forms a typically 'flat' zone in contrast to the 'steep' zone formed by extrafolial folding in the thicker ignimbrite.

Thick ignimbrite (≥ 20 m thick)

The central and northern portions of Monument Canyon expose strongly folded mylonite-like ignimbrite and upper surface. The pervasive mylonite-like ignimbrite is, once again, characterised by a prominent E – W lineation, a top-to-west transport direction, and E – W trending, recumbent intrafolial isoclinal and sheath folds (Figs 3-52; 3-53). Any underlying mylonite-like ignimbrite that may be present is not exposed. It is intensely folded by upright to recumbent, open to isoclinal, extrafolial periclinal folds ($\lambda \leq 10$ m; $A \leq 10$ m - ≥ 15 m), that deform the upper surface and ≥ 30 m of ignimbrite below the upper surface (e.g., Fig. 3-49). Many of the largest fold closures are complex composite structures encompassing several discrete folds (Fig. 3-53). Composite fold closures are typically parallel-style (Fig. 3-52), and the folds within them are typically similar-style). Mushroom-shaped antiforms and recumbent antiforms are common; despite being upright at the base of the section they are typically overturned and recumbent close to the upper surface (Fig. 3-53). There is no consistent vergence direction in extrafolial folds. The 10 m-scale antiforms appear to have 'fallen-over' on their way from being upright to becoming recumbent, they resemble nappes (Fig. 3-53).

If recumbent folds that root into upright structures are returned to upright (Fig. 3-54), they are observed to form a steep zone (Figs 3-53; 3-54), and their wavelengths and amplitudes can be constrained. This techniques has the effect of splitting composite hinges apart and producing individual fold closures. The largest folds are 20 m-scale ($\lambda \leq 2$ m; $A \geq 15$ m), extrafolial folds near the boundary between graben-fill and graben-flank, and in $\sim 20 - 30$ m thick ignimbrite are 10 m-scale ($\lambda \leq 10$ m; $A \leq 10$ m). When described in this way, there is a continuum between extrafolial folds in the thin ignimbrite and those in the steep domain of the thick ignimbrite (Fig. 3-54). This continuum increases in scale and decreases in fold frequency down-slope and into progressively thicker ignimbrite (Fig. 3-54).

Interpretation

Observations at Monument Canyon support my inference that mylonite-like ignimbrite was deformed by a ductile shear zone and was only minimally influenced by the palaeo-slope, because all fabrics and folds in mylonite-like ignimbrite are transverse to the slope. In contrast, deformation that produced the steep domain was strongly influenced by the palaeo-slope because all steep domain structures suggest down-slope flow and layer-parallel shortening. I infer that down-slope flow was gravity-driven with ignimbrite being transported from 'high' ground to lower. Furthermore, I suggest that the formation of mushroom-shaped antiforms and the overturning of upright antiforms was the result of gravity, where unstable, upright folds 'fell-over'.

Summary

The Grey's Landing ignimbrite underwent two distinctive phases of rheomorphism during its emplacement. Firstly, an early, possibly syn-depositional, phase of rheomorphism in a ductile shear zone producing a pervasive mylonite-fabric. Secondly, a later phase of rheomorphism affecting a

large volume of the upper and central parts of the deposit related to gravity-driven down-slope flow.

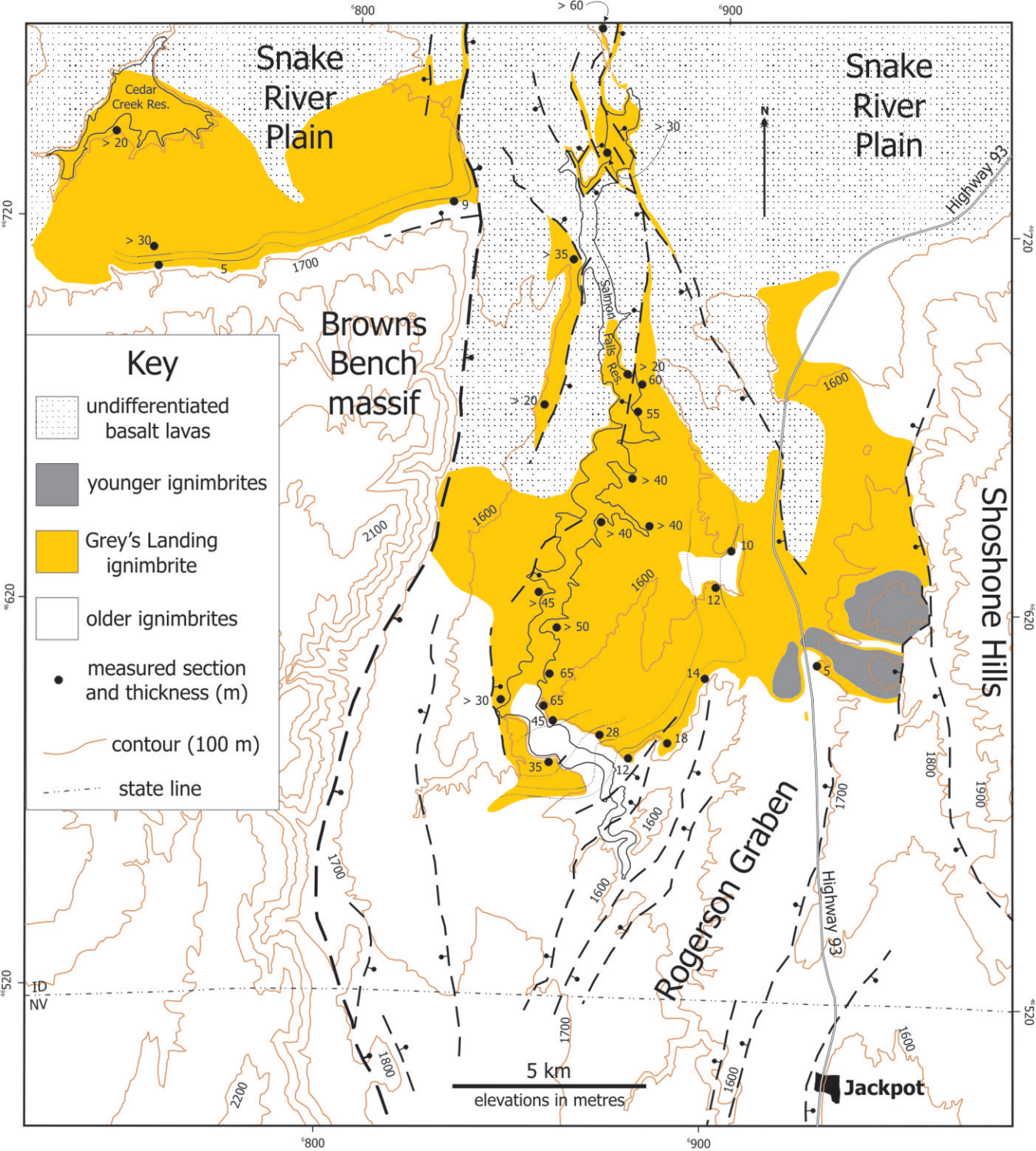


Fig. 3-1. Distribution of and thickness variation within the Grey's Landing ignimbrite (yellow) in the Rogerson Graben and surrounding area. Locations of measured sections (black dots) and thickness contours shown. Selected UTM co-ordinates for zone 11T shown.

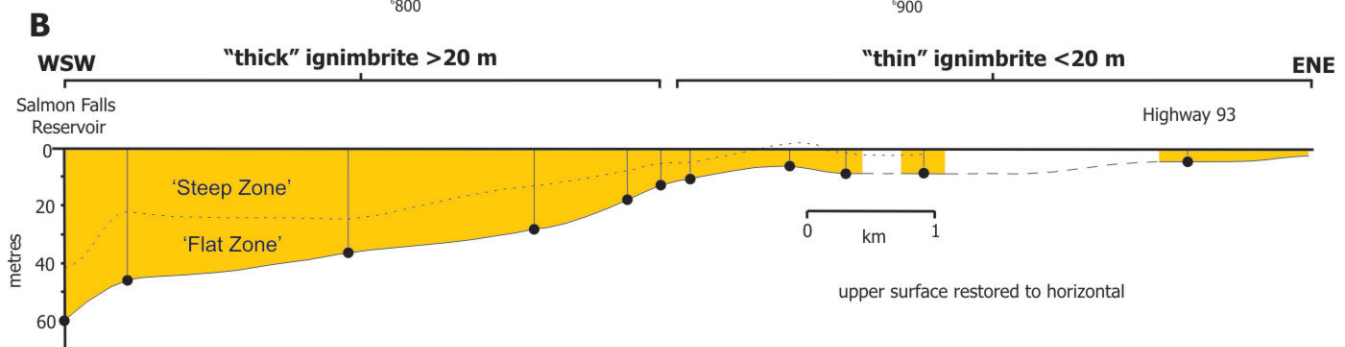
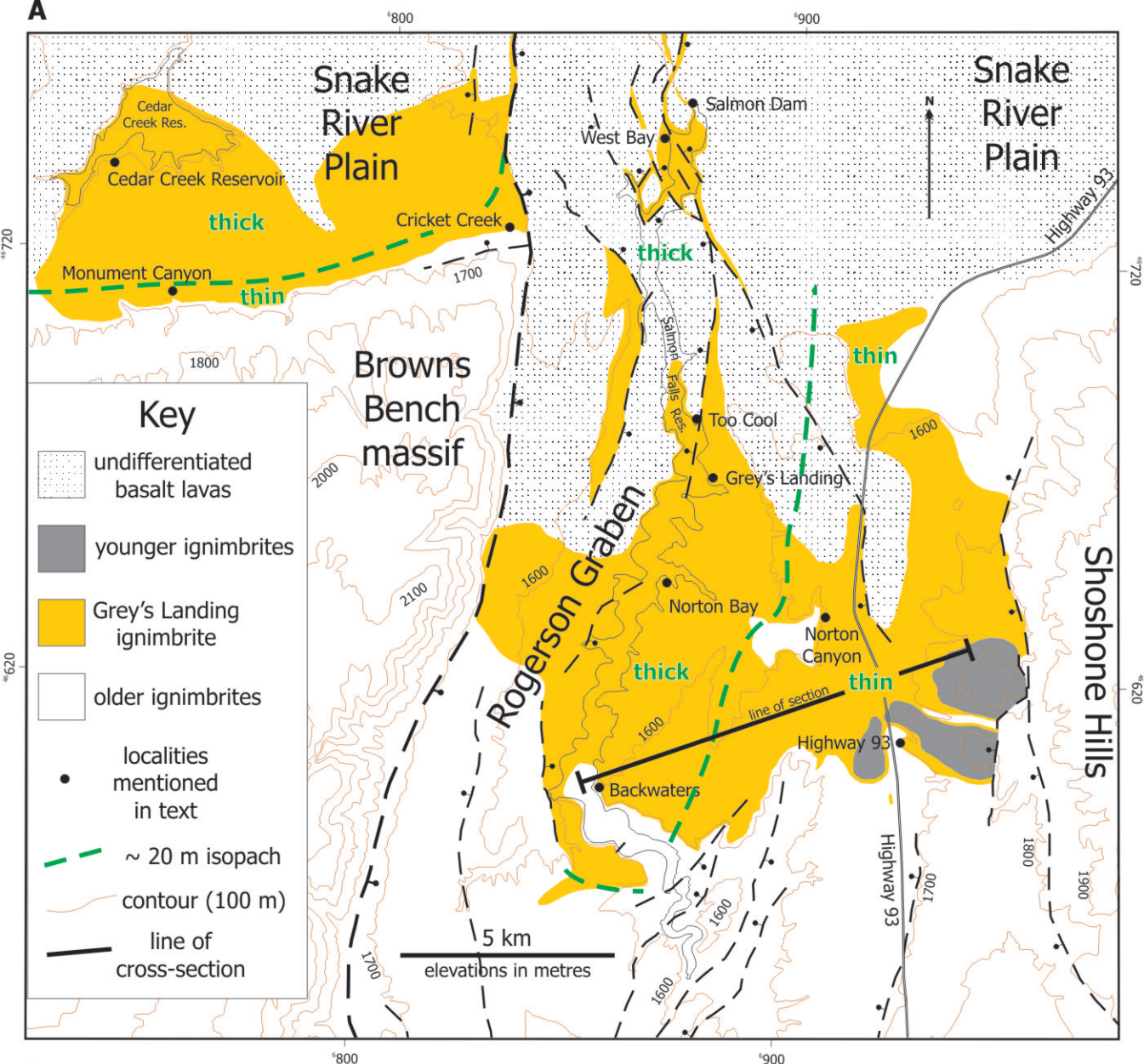


Fig. 3-2. (A) Distribution of and thickness variation within the Grey's Landing ignimbrite (yellow) in the Rogerson Graben and surrounding area. The inferred boundary between thin and thick regions is shown in green, corresponding to the ~ 20 m thickness contour. (B) WSW - ENE cross-section through the Rogerson Graben showing westward thickening ignimbrite and the relative positions and thicknesses of the two structural domains. Locations mentioned in the text shown by black dots. Selected UTM co-ordinates for zone 11T shown.

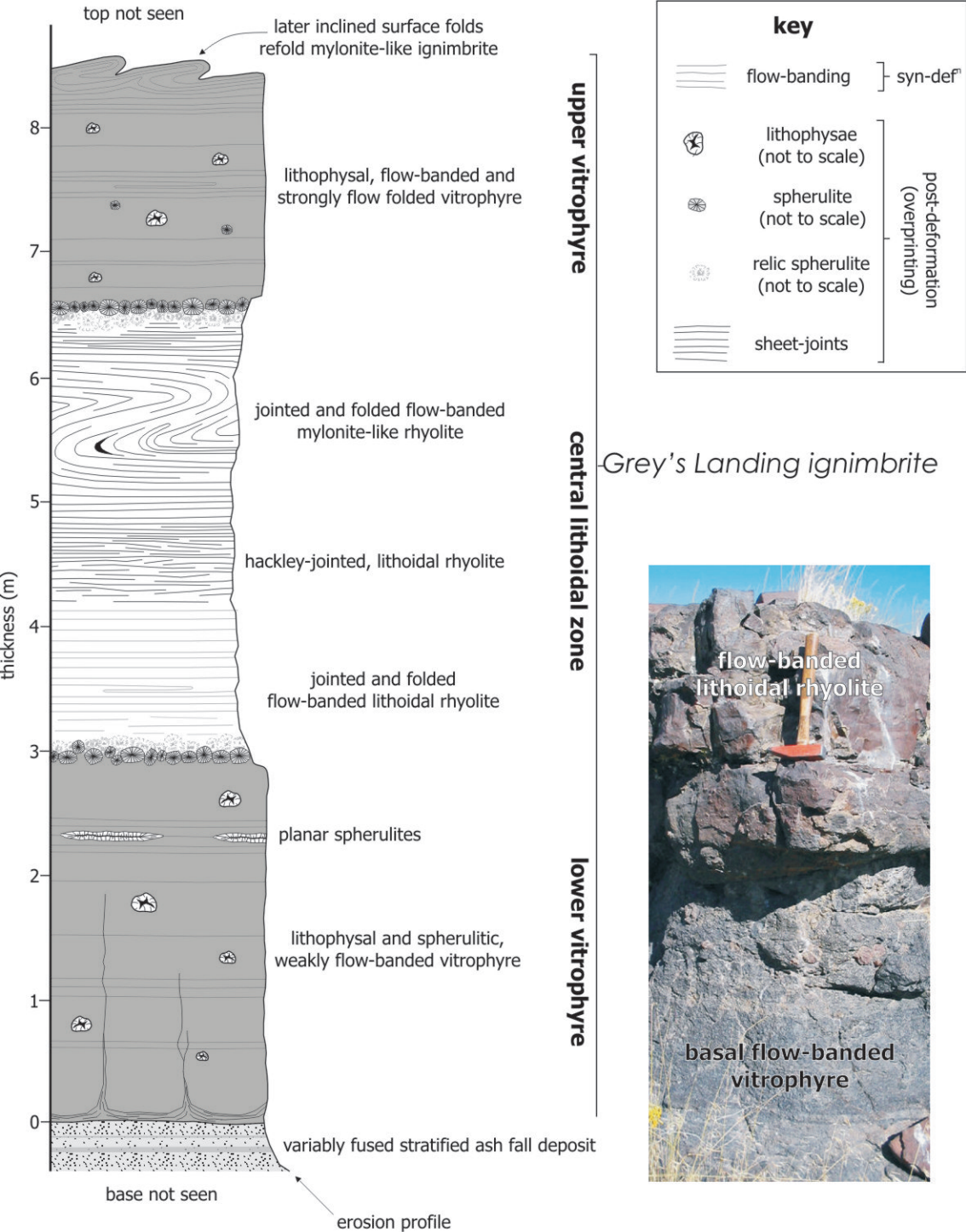


Fig. 3-3. Graphic log of typical 'thin', graben-flanking Grey's Landing ignimbrite, Norton Canyon Road, Rogerson Graben (11T 690615mE 4663972mN). Inset: typical section through the lower portion of thin ignimbrite at Norton Canyon. Sheet-joints overprint and exaggerate flow-banding in the lithoidal centre.

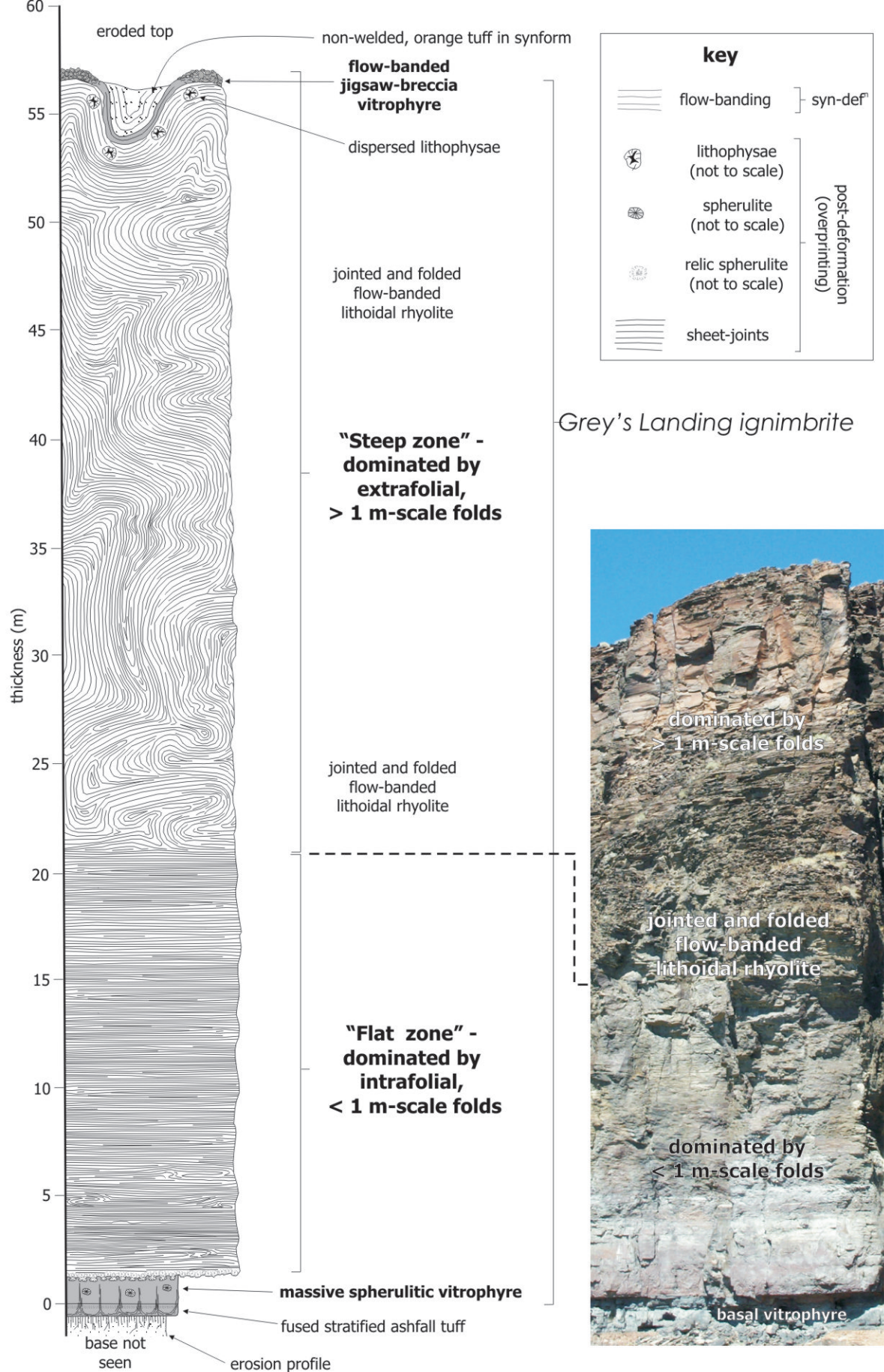


Fig. 3-4. Graphic log of typical 'thick' graben-filling Grey's Landing ignimbrite. Compiled from observations at Grey's Landing (11T 687822mE 4666778mN), Backwaters (11T 685154mE 4659673mN), and Salmon Dam (11T 687018mE 4675787mN). Inset: typical vertical section through thick ignimbrite, Grey's Landing.

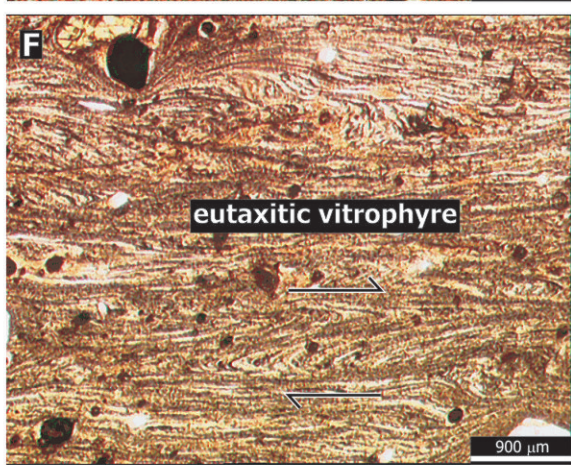
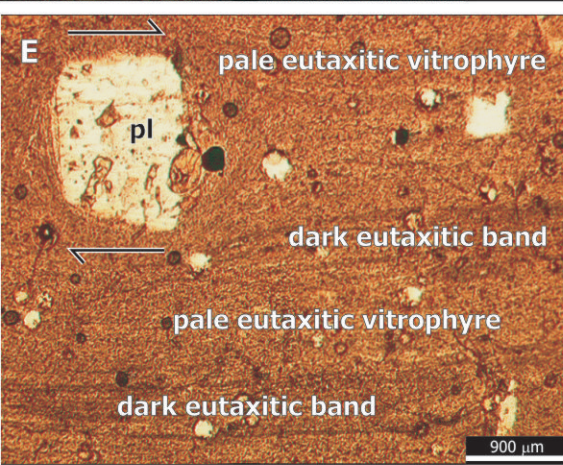
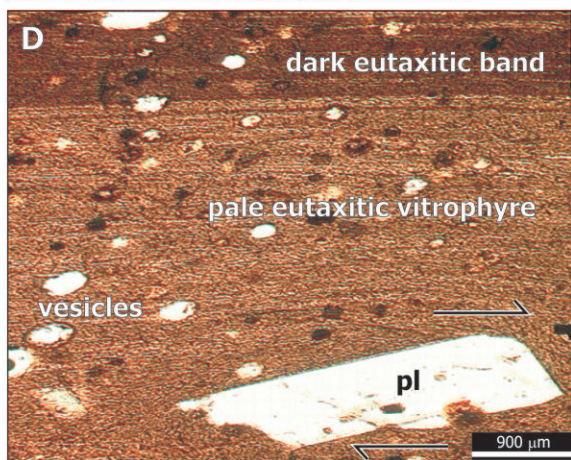
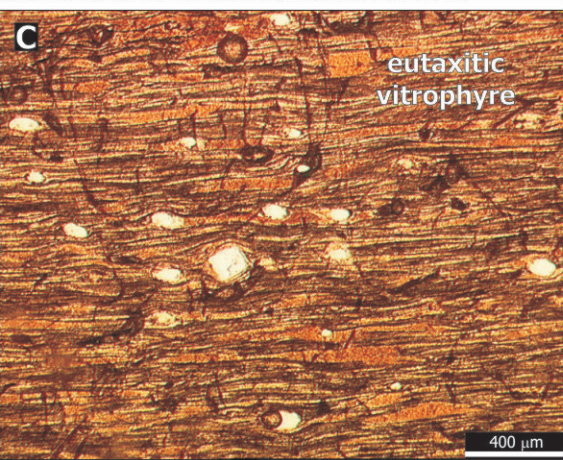
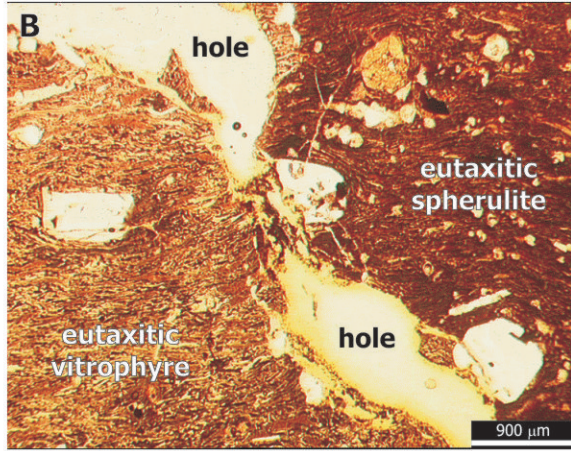
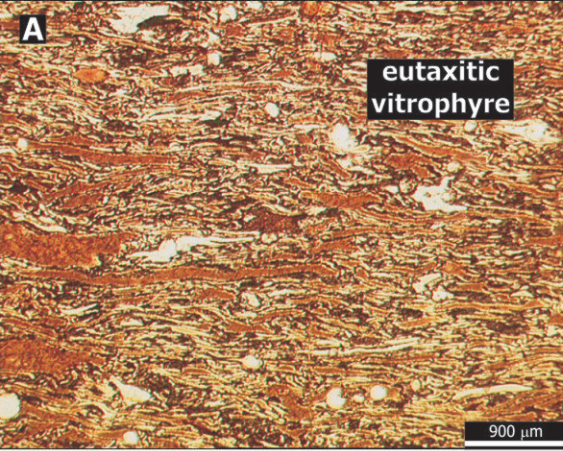


Fig. 3-5. Planar fabrics - microscopic eutaxitic fabric. (A) eutaxitic fabric of horizontal and parallel flattened ash shards (< 3 mm), 'Roadkill' (11T 692234mE 4660906mN). (B) eutaxitic fabric preserved in both vitrophyre and spherulite, Roadkill. (C) eutaxitic fabric developed in perlitic vitrophyre, Norton Canyon (11T 690615mE 4663972mN). Note how flattening is greater than in (A and B). (D) colour-banded eutaxitic fabric and dextral rotated plagioclase crystal (pl) in vesicular upper vitrophyre, 'Too Cool' (11T 687268mE 4668336mN). Note how individual vitroclasts are indiscernible. (E) colour-banded eutaxitic vitrophyre and dextral rotated plagioclase crystal (pl), Backwaters (11T 685154mE 4659673mN). (F) complex-deformed eutaxitic fabric, lower vitrophyre Grey's Landing (11T 687822mE 4666778mN). All photomicrographs are in plane polarized light.



Fig. 3-6. Planar fabrics - macroscopic colour-banding. (A) penetrative colour-banding in folded vitrophyre, Monument Canyon (11T 675840mE 4671116mN). (B) penetrative colour-banding defined by black vitrophyre and pink, densely spherulitic vitrophyre, Monument Canyon. (C) penetrative colour-banding defined by pale grey and reddish-purple bands in a vertical fold limb. Salmon Dam (11T 687018mE 4675787mN). (D) penetrative colour-banding defined by pale grey, dark grey and reddish-purple bands, Cedar Creek Reservoir (11T 673712mE 4674456mN). (E) buckle-folded penetrative colour-banding defined by pale and dark lithoidal rhyolite, 1.5 km south of Salmon Dam (11T 687207mE 4674229mN). Dark layers are more competent.

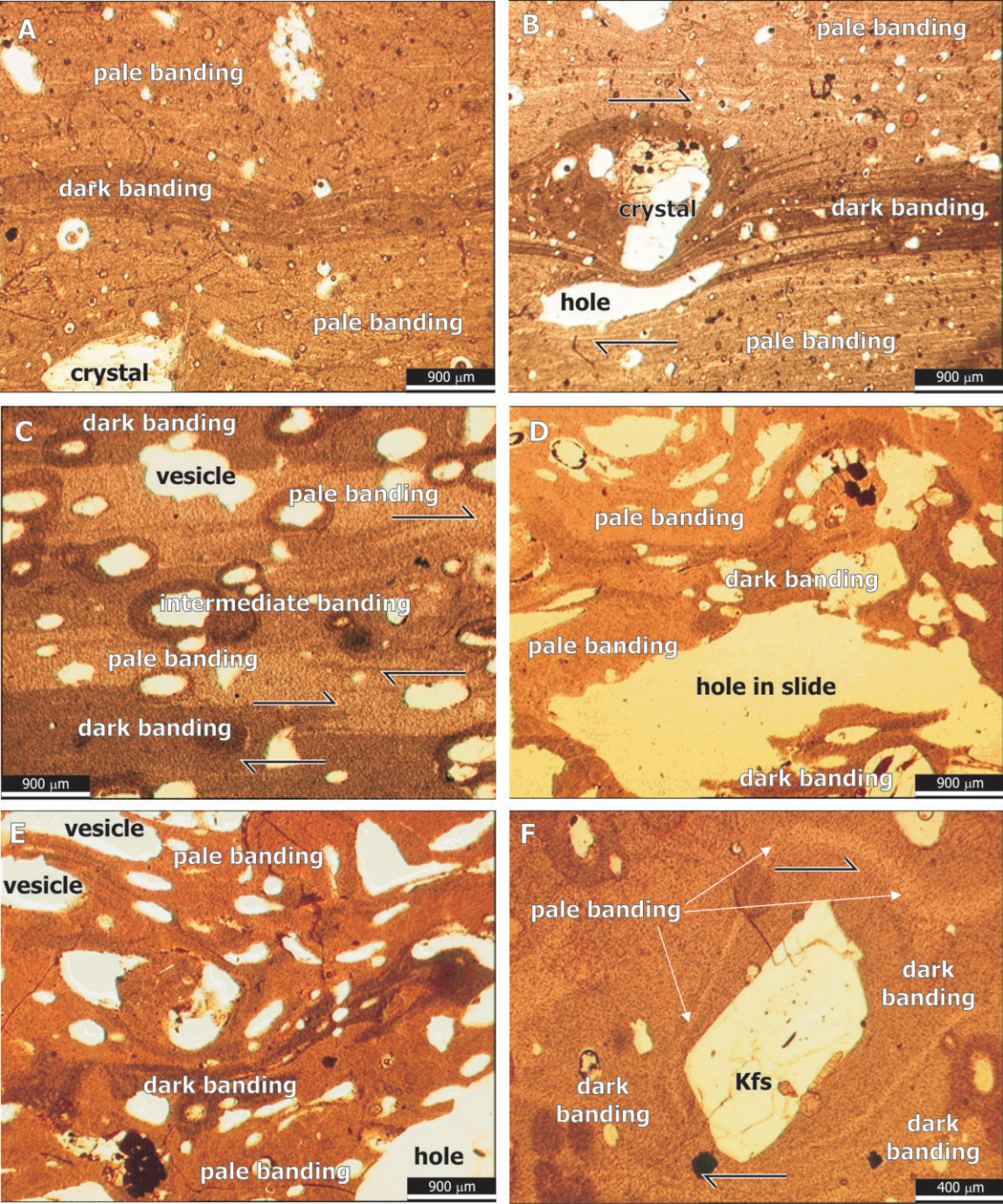


Fig. 3-8. Planar fabrics - microscopic colour-banding. (A) discrete and gently warped dark colour-band in perlitic basal vitrophyre, Norton Canyon (11T 690615mE 4663972mN). Note the fine-scale eutaxitic fabric developed in the pale vitrophyre. (B) inter-fingering pale and dark colour-banding deformed around a rotated crystal with a dextral shear sense. Partly devitrified vesicular basal vitrophyre, Norton Canyon. (C) three-tone colour-banding in vesicular and partly devitrified vitrophyre, Cedar Creek Reservoir. Note how the colour-banding is deformed by dextral non-coaxial shear. (D) uneven colour-banding in vitrophyre, Cedar Creek Reservoir (11T 673712mE 4674456mN). (E) uneven colour-banding in vesicular vitrophyre, Salmon Dam (11T 687018mE 4675787mN). (F) weak colour-banding defining dextral rotation of a sanidine crystal (Kfs) in upper vitrophyre, 1.5 km south of Salmon Dam (11T 687207mE 4674229mN). All photomicrographs are in plane polarized light.

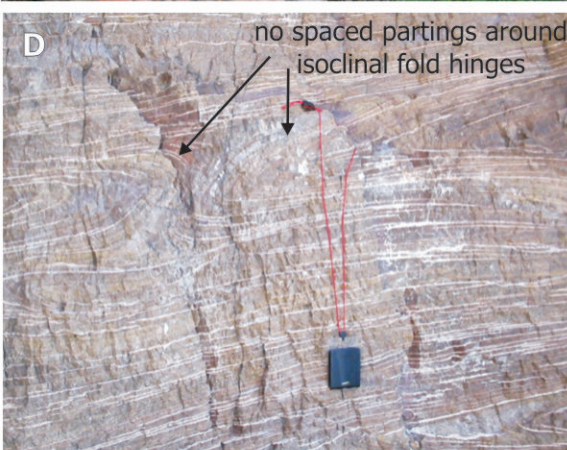


Fig. 3-9. Planar fabrics - spaced and macroscopic. (A) 3 mm spaced partings in lithoidal rhyolite, Monument Canyon (11T 675840mE 4671116mN). (B) 10 cm spaced partings in lithoidal rhyolite; some partings are lined. Norton Canyon (11T 690615mE 4663972mN). (C) 2 cm spaced partings in lithoidal rhyolite at West Bay (11T 686473mE 4675065mN). This is typical and characteristic of macroscopic planar fabric style and spacing in the Grey's Landing ignimbrite. (D) 2 cm 'healed' partings defined by colour variation in lithoidal rhyolite and white cement, probably produced by vapour-phase crystallization, Grey's Landing. (11T 687822mE 4666778mN). (E) 2 to 6 cm spaced partings associated with a localised vesicular layer in lithoidal rhyolite, Backwaters (11T 685154mE 4659673mN).

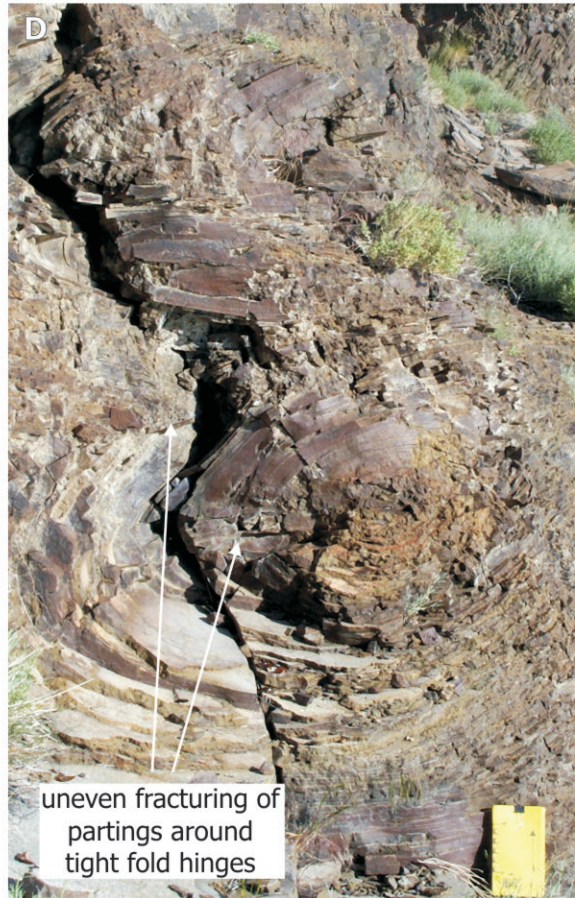


Fig. 3-10. Planar fabrics - spaced and macroscopic. (A) 1 cm spaced fabric defined by differential weathering of colour-banding in lithoidal rhyolite, Backwaters (11T 685154mE 4659673mN). (B) 5 cm spaced partings developed unevenly on 1 cm scale colour-banding, loose block Grey's Landing (11T 687822mE 4666778mN). (C) 5 cm to 10 cm spaced partings in folded lithoidal rhyolite, Cedar Creek Reservoir (11T 673712mE 4674456mN). (D) 3 cm spaced partings defining a sheath fold, note how the partings imperfectly define the tightest curves in the fold hinge, Grey's Landing.

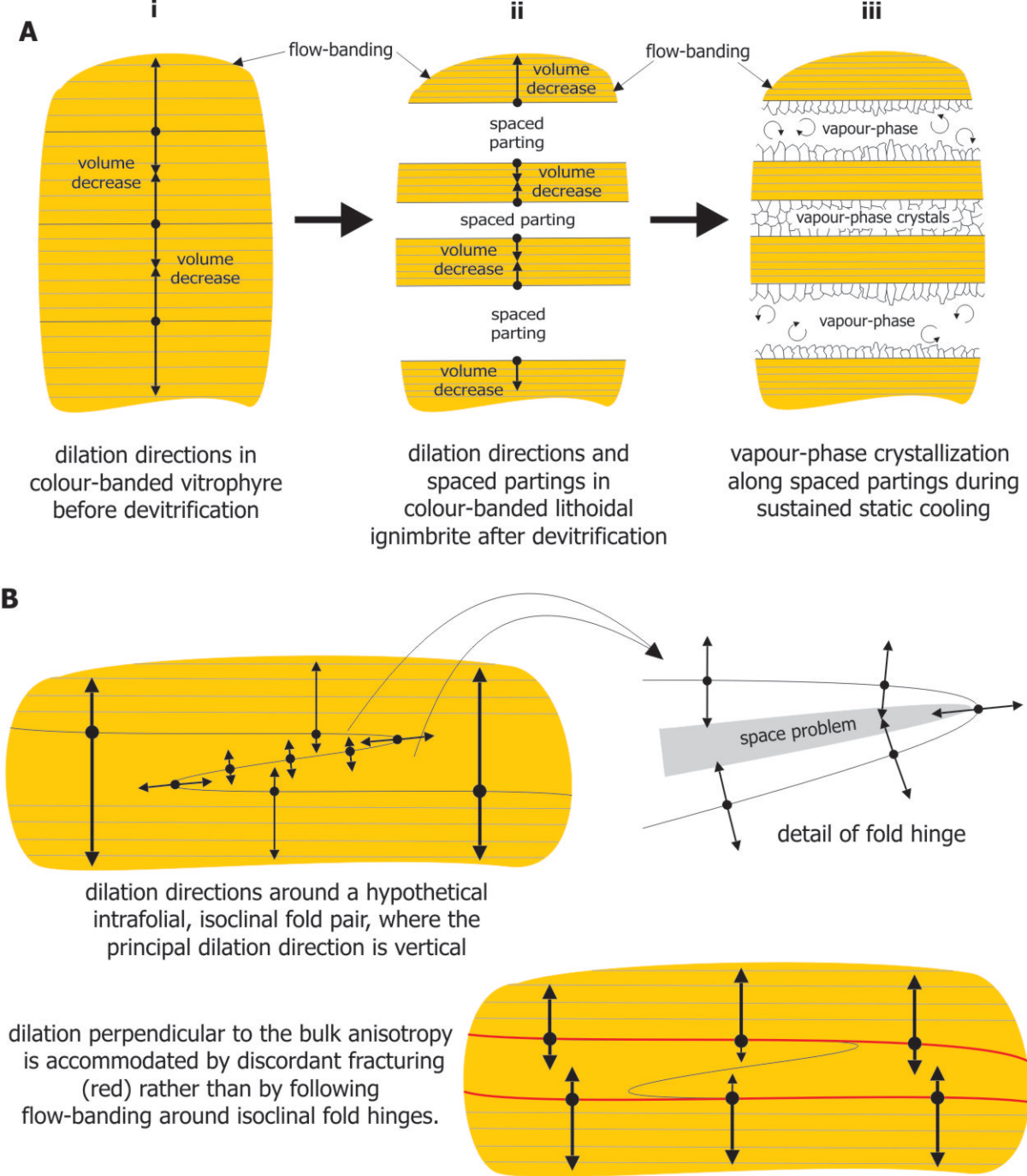


Fig. 3-11. Development of spaced partings in lithoidal ignimbrite. (A) three-stage process of spaced parting formation as inferred from the Grey's Landing ignimbrite. (i) Volume reduction due to crystallization (devitrification) encourages dilation along anisotropies (flow-banding), (ii) producing parting surfaces (exaggerated), (iii) subsequently in-filled or 'healed' by vapour-phase crystallization. (B) partings do not develop around fold hinges where local dilation would have to be perpendicular to that of the surrounding flow-banding, rather partings form near-parallel to the bulk anisotropy and discordant to folds.

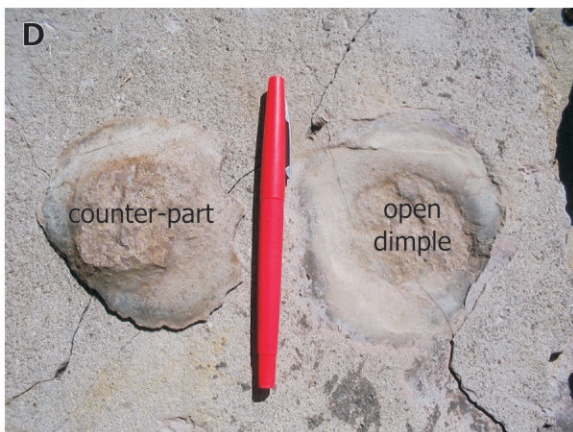
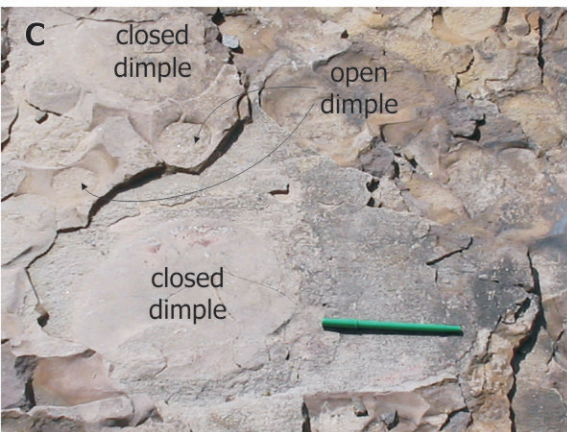


Fig. 3-12. Dimple joints. (A) open dimple joints developed between parting surfaces in lithoidal rhyolite at Monument Canyon (11T 675840mE 4671116mN). Note planar base to each dimple. (B) large open dimples, Norton Canyon (11T 690615mE 4663972mN). (C) open and closed dimple joints developed between lined parting surfaces. Note the circular outline and how the lineation (parallel to pen) is absent from each dimple, Grey's Landing (11T 687812mE 4666792mN). (D) open dimple and counter-part that has been removed. Note the planar surfaces forming the top and bottom of the dimple, in contrast to the smooth, curved sides. Grey's Landing.

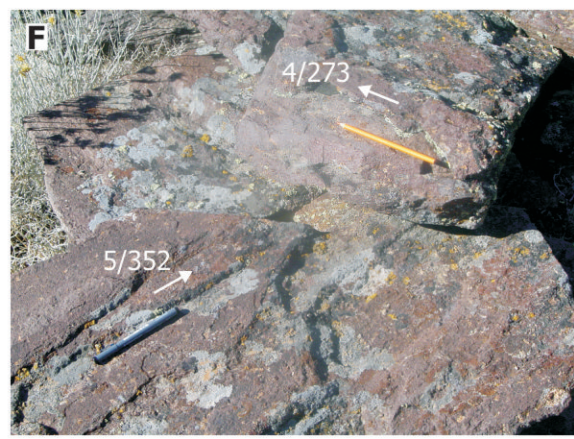
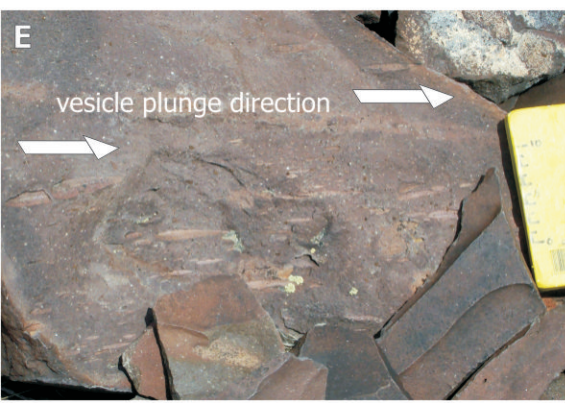
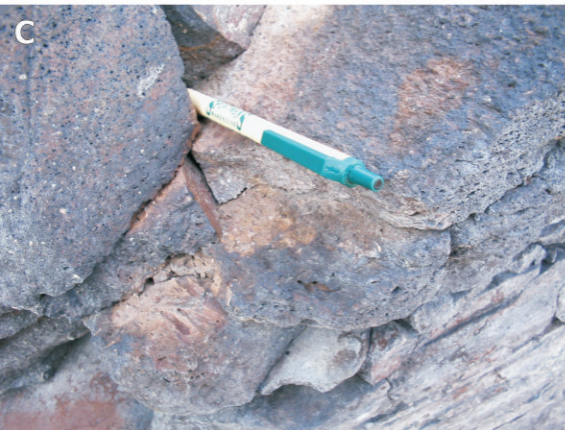
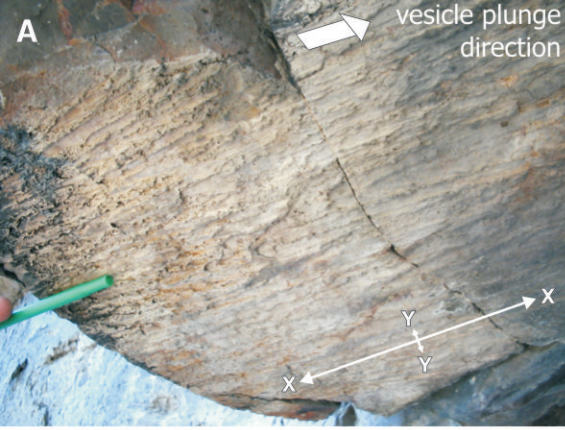


Fig. 3-13. Lineations - stretched vesicles. (A) stretched vesicles in lithoidal rhyolite, long axis (X) : short axis (Y) ratio < 18:1. Monument Canyon (11T 675840mE 4671116mN). Note how all vesicles plunge to the right. (B) steeply plunging vesicles in scoriaceous lithoidal ignimbrite, loose block from Cedar Creek Reservoir (11T 673712mE 4674456mN). Note how all the vesicles plunge to the left. (C) stretched vesicles in scoriaceous vitrophyre, X:Y ratio < 10:1, Cedar Creek Reservoir. (D) stretched vesicles in lithoidal rhyolite, X:Y ratio > 8:1, Norton Canyon (11T 690615mE 4663972mN). Note how all vesicles plunge to the right. (E) isolated stretched vesicles in lithoidal rhyolite, X:Y ratio < 6:1, Highway 93 (11T 690615mE 4663972mN). Note how all vesicles plunge to the right. (F) Two perpendicular vesicle lineations on adjacent parting surfaces, Monument Canyon. Lineations parallel to pen where appropriate.

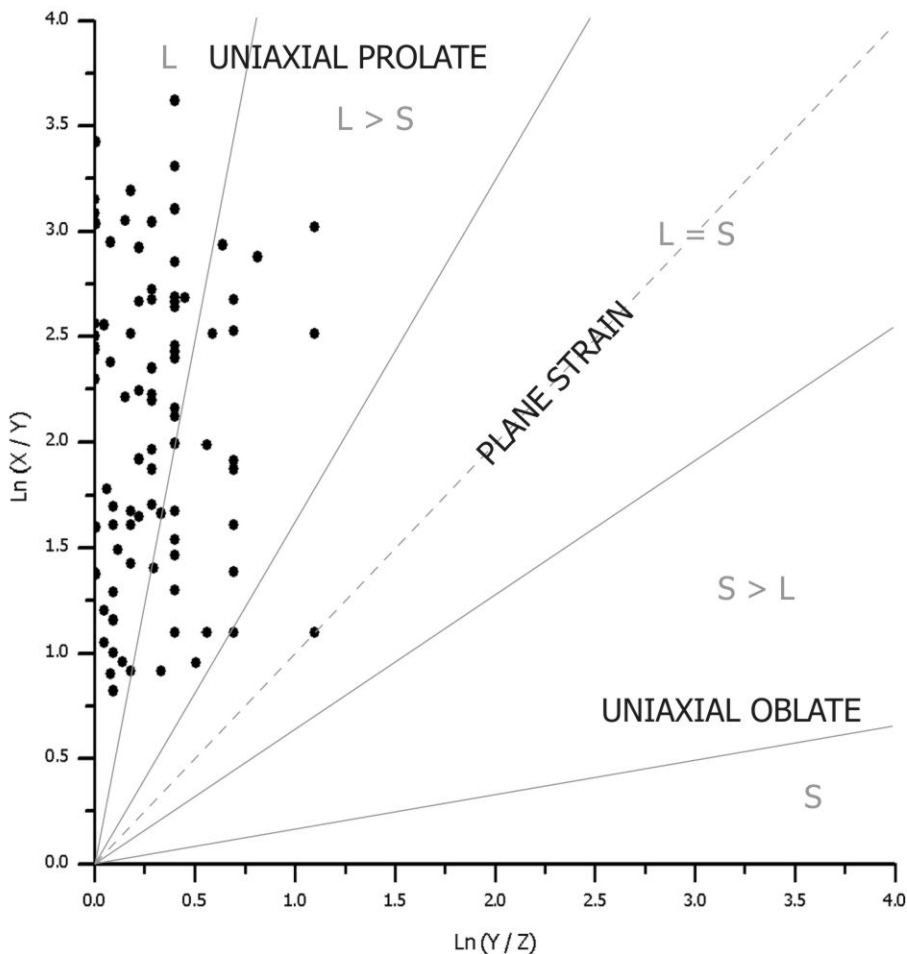


Fig. 3-14. Flinn plot of stretched vesicles from the Grey's Landing ignimbrite. Note that all the vesicles are prolate, plotting in the L-tectonite and L > S-tectonite fields, indicating stretching.

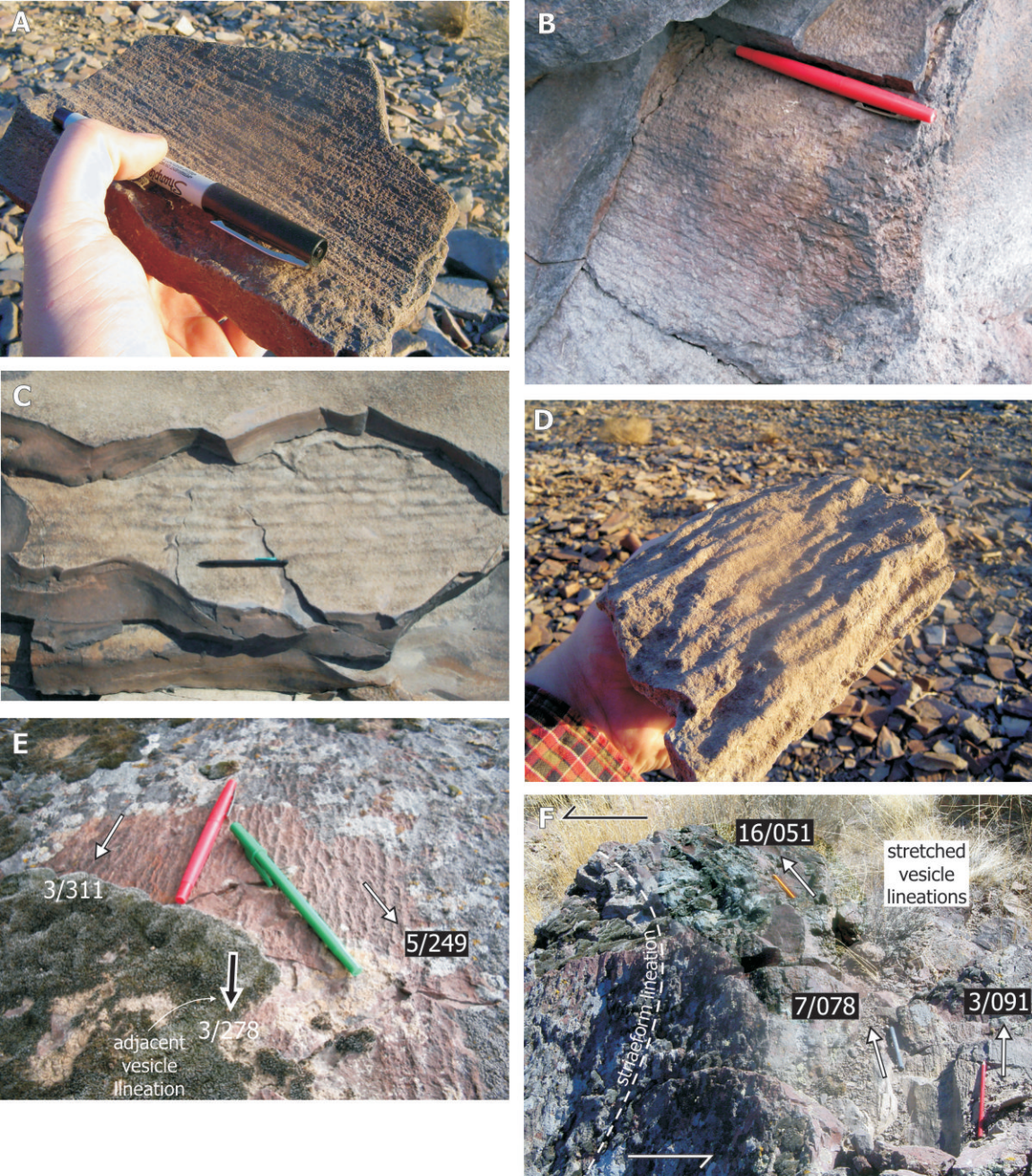


Fig. 3-15. Lineations in lithoidal rhyolite. (A) 0.2 cm spaced, striaform lination developed on a folded parting surface, loose block from Grey's Landing (11T 687822mE 4666778mN). (B) 0.2 cm spaced, striaform lination associated with parallel stretched vesicles, Cedar Creek Reservoir (11T 673712mE 4674456mN). (C) 1.5 cm spaced and anastomosing, intestinform lination developed on a parting surface, Norton Bay (11T 686902mE 4664340mN). Note how the upper adjacent parting surface does not exhibit a lination. (D) 1 cm spaced intestinform lination on a folded parting surface, loose block from Grey's Landing. (E) two cross-cutting, 1 cm spaced, striaform lineations on a parting surface, Monument Canyon (11T 675840mE 4671116mN). Note how the two lineations are bisected by the stretching lination established from adjacent vesicles. (F) Reorientated, parallel stretched vesicle and striaform lineations on a deformed parting surface, Monument Canyon. Note how the lineations are reorientated through $> 40^\circ$ with a sinistral shear sense. Lination parallel to pen.



1st stage - formation of prolate vesicles during non-coaxial deformation of vitric ignimbrite. Widely-spaced vesicles are clearly defined. Maximum elongation direction = X.



2nd stage - continued vesiculation and subsequent devitrification of highly vesicular ignimbrite. Closely-spaced stretched vesicles partly merged together. Maximum elongation direction = X.



3rd stage - sustained devitrification of highly vesicular ignimbrite. Closely-spaced stretched vesicles become indistinguishable from each other, producing striaform lineations parallel to the elongation direction (X) of the original stretched vesicles.

Fig. 3-16. Evolution of lineations on parting surfaces. (A) typical flattened and stretched vesicle in vitric ignimbrite, Roadkill (11T 692234mE 4660906mN). (B) typical closely-spaced stretched vesicles in devitrified House Creek ignimbrite (11T 666463mE 4668768mN), 5 cm bar. (C) typical closely-spaced striaform lineation on a parting surface, loose block from Grey's Landing (11T 687822mE 4666778mN).

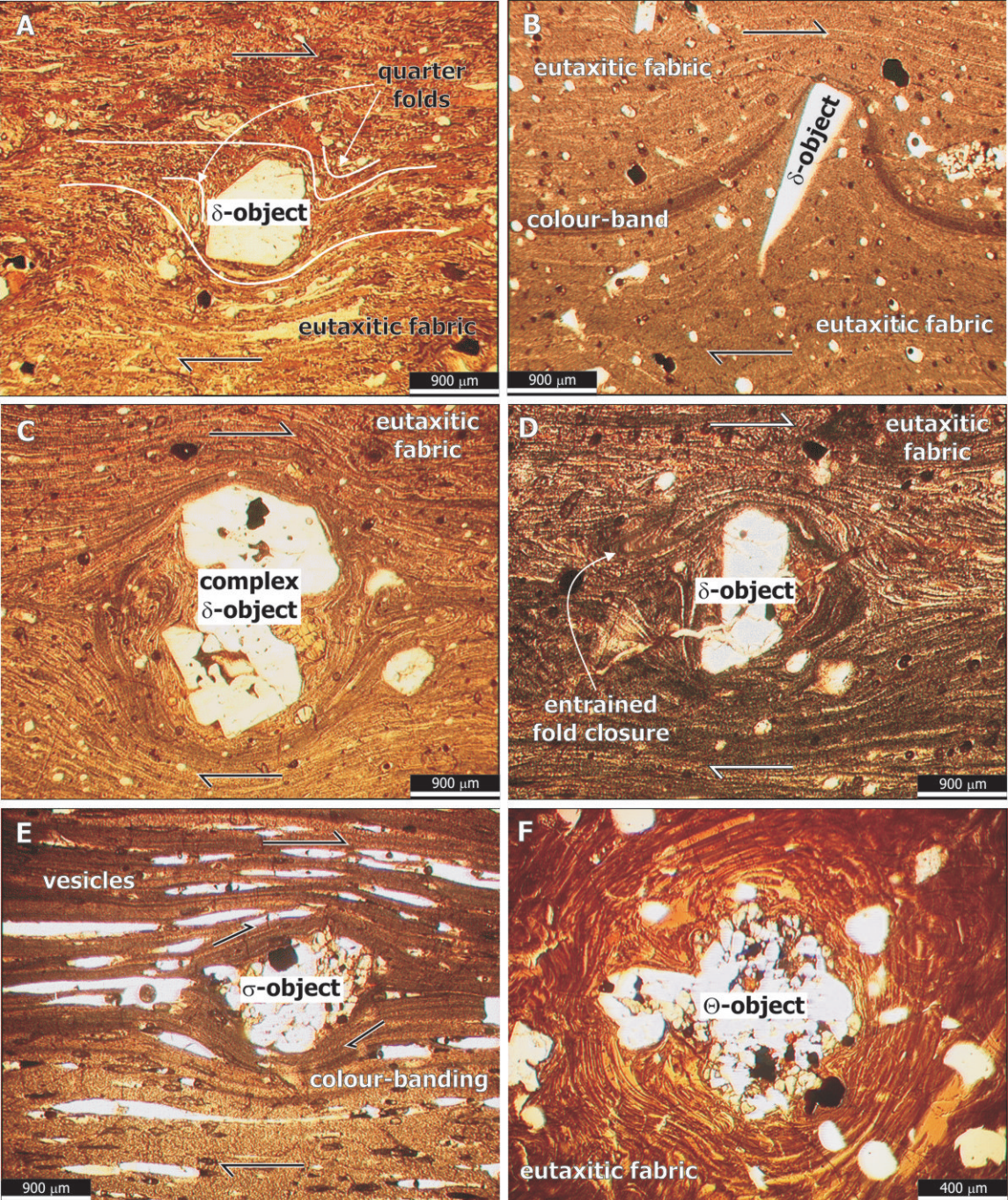


Fig. 3-17. Kinematic indicators - rotated porphyroclasts. (A) euhedral δ -object (plagioclase crystal) in eutaxitic vitrophyre, Cedar Creek Reservoir (11T 673712mE 4674456mN). (B) wedge-shaped δ -object (plagioclase lath) in colour-banded and eutaxitic vitrophyre, Grey's Landing (11T 687822mE 4666778mN). (C) complex δ -object (pair of plagioclase crystals) in eutaxitic vitrophyre, Monument Canyon (11T 675840mE 4671116mN). (D) asymmetric δ -object (plagioclase fragment) entraining an isoclinal intrafolial fold closure, Monument Canyon. (E) asymmetric σ -object (glomerocryst) in colour-banded vitrophyre, Cedar Creek Reservoir. (F) Θ -object in eutaxitic vitrophyre showing multiple rotations but no shear sense, Norton Canyon (11T 690615mE 4663972mN). All photomicrographs are in plane polarized light and viewed in the XZ plane, perpendicular to a measured lineation direction. Examples A to E display dextral shear.

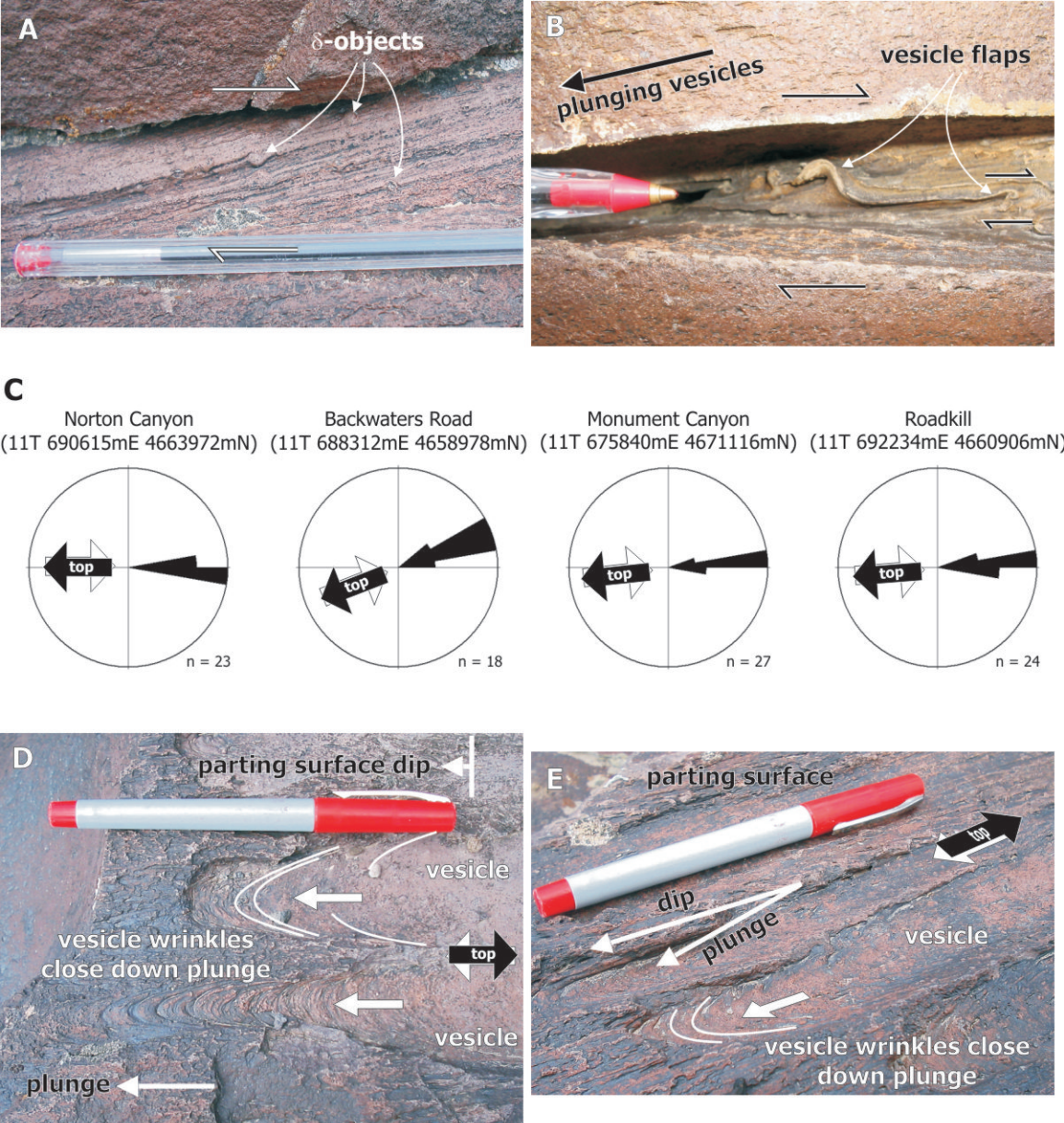


Fig. 3-18. Macroscopic kinematic indicators. (A) macroscopic δ -object (crystal) in lithoidal, flow-banded ignimbrite, Norton Canyon (11T 690615mE 4663972mN). (B) vesicle flaps within a 10 cm long, imbricated vesicle in lithoidal ignimbrite, Norton Canyon. (C) Vesicle plunge directions from four localities, and transport directions inferred from vesicle imbrication. (D) vesicle wrinkles in plan view, closing down plunge, Norton Canyon. (E) vesicle wrinkles closing down plunge in the lower half of a stretched vesicle; lithoidal ignimbrite, Norton Canyon.

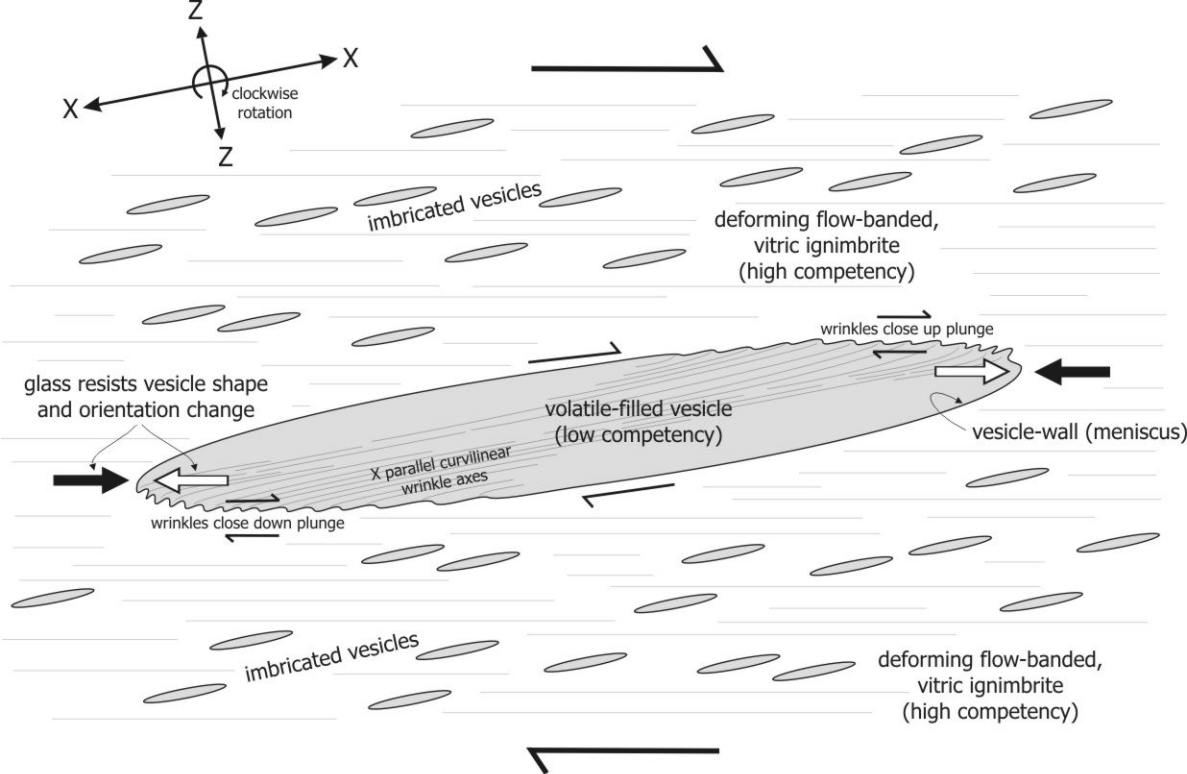


Fig. 3-19. Schematic representation of the development of vesicle wrinkles by small-scale folding of the vesicle wall. Vesicle shape and orientation change are resisted by the high competency glassy ignimbrite.

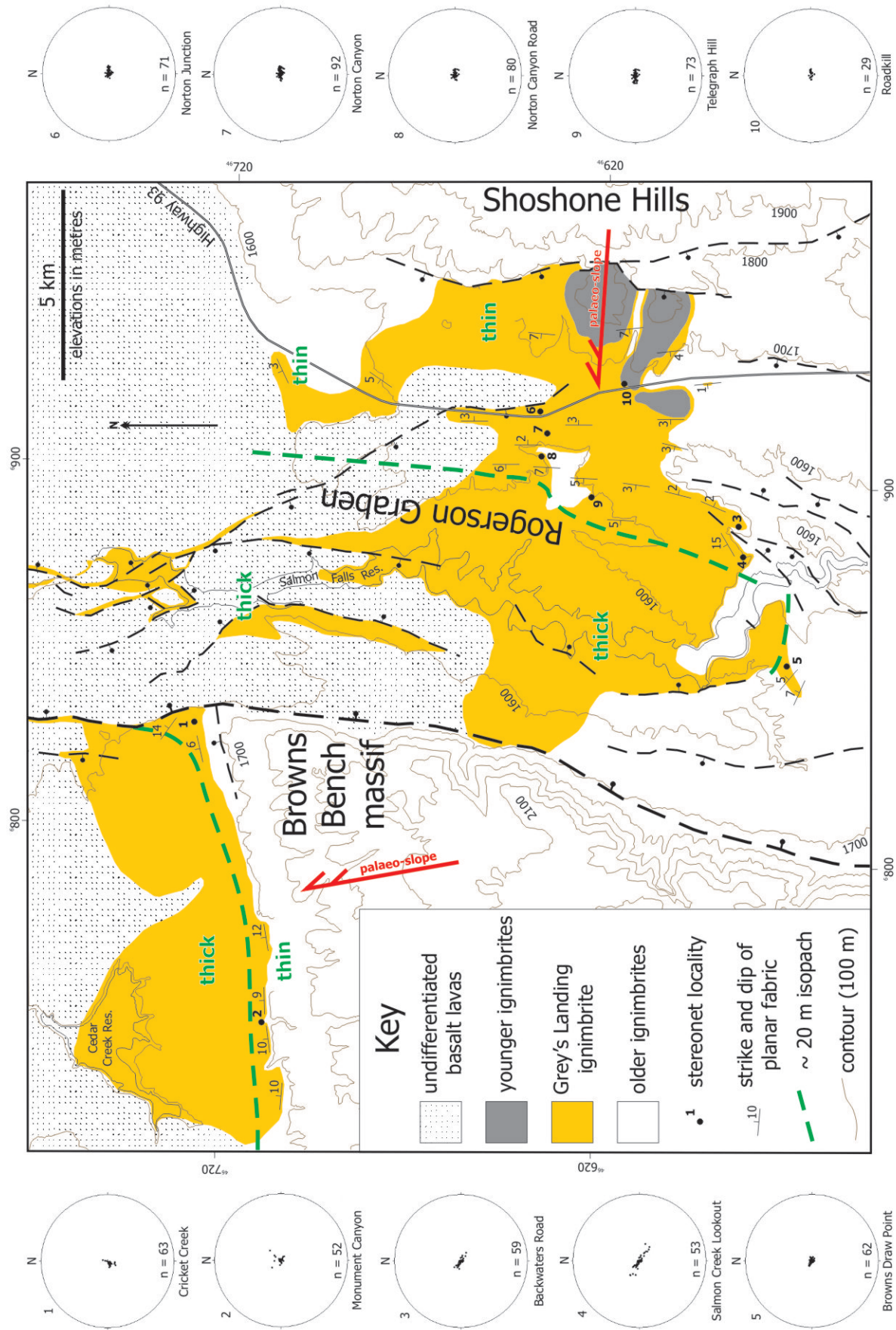


Fig. 3-20. Orientation of planar fabric elements - thin ignimbrite. Stereonets present planar fabric data (poles to planes) collected at numbered locations. Grey's Landing ignimbrite = yellow.

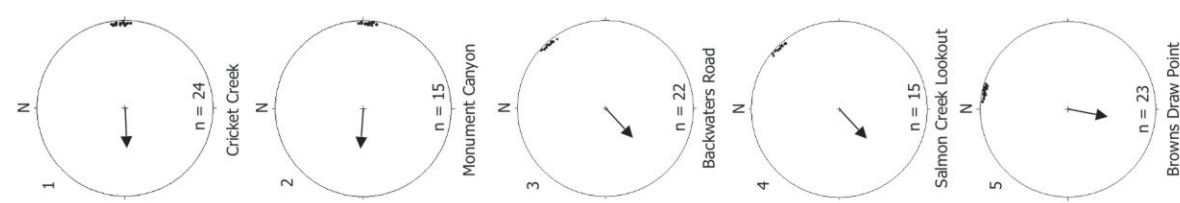
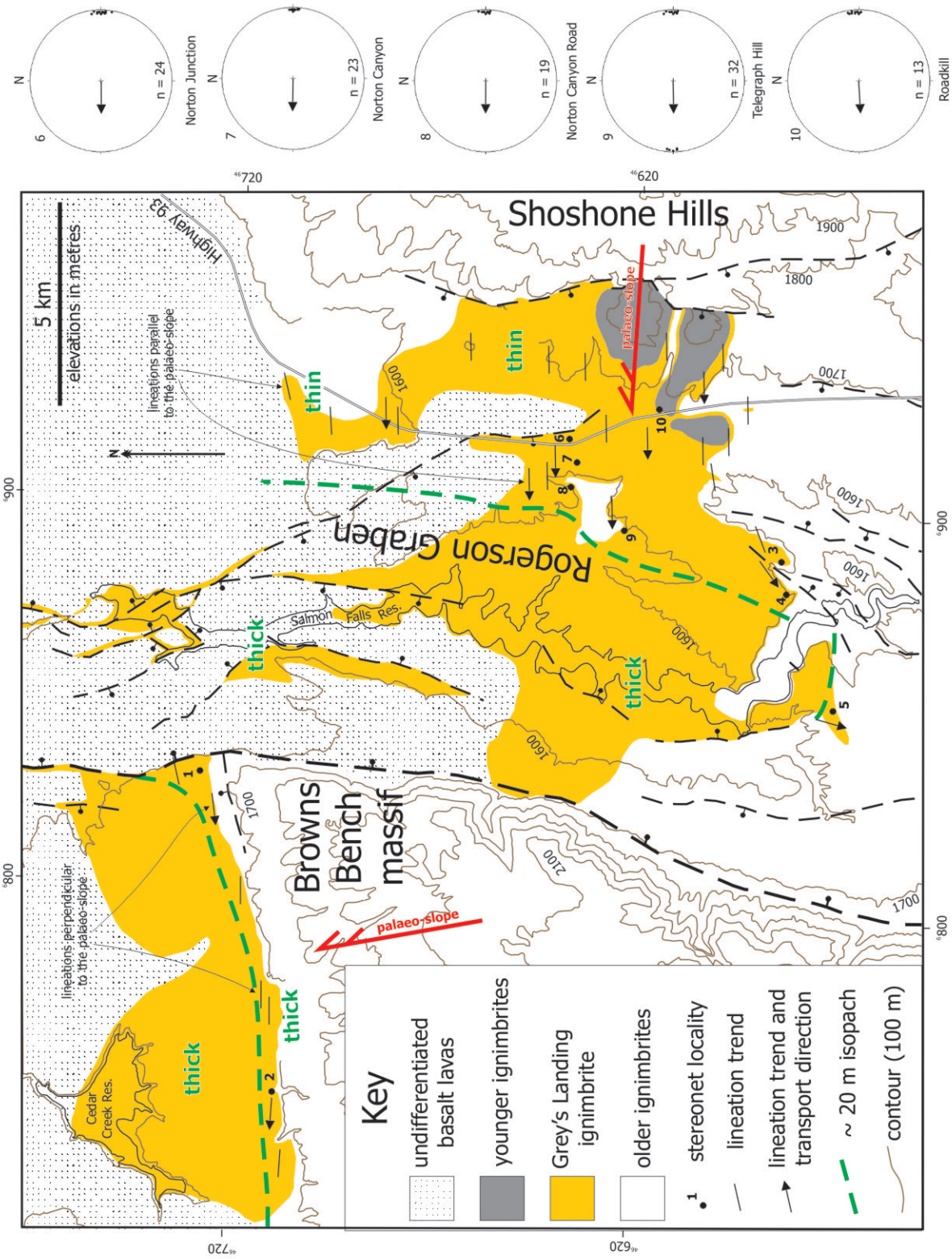


Fig. 3-21. Lineation and kinematic data from thin ignimbrite. Stereonets present linear data collected at individual locations, and the corresponding shear sense established from independent kinematic criteria (e.g., rotated porphyroclasts, vesicle imbrication, vesicle flaps, vesicles wrinkles). Grey's Landing ignimbrite (yellow). Locations of stereonets are numbered.

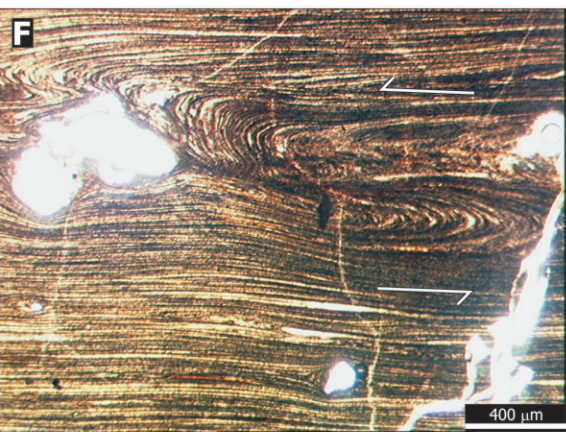
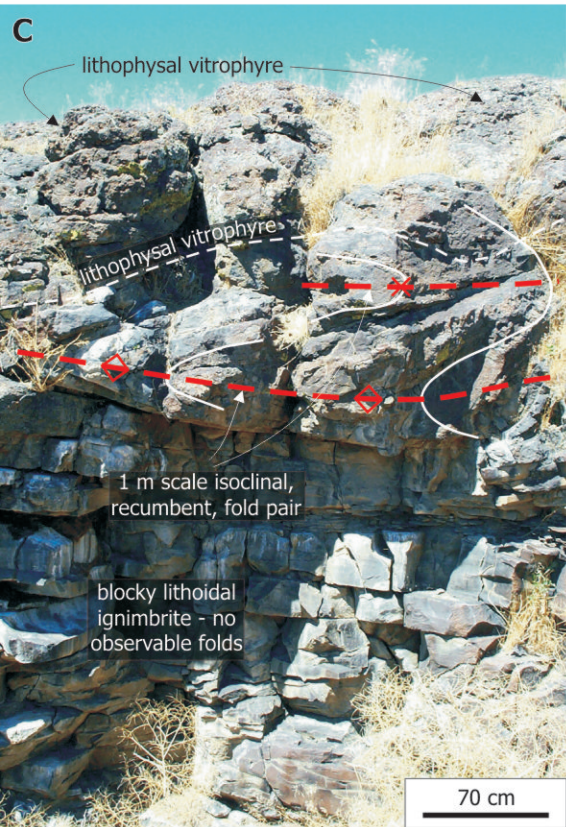
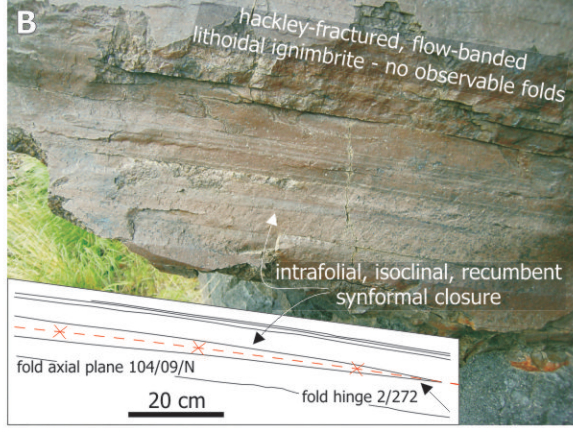
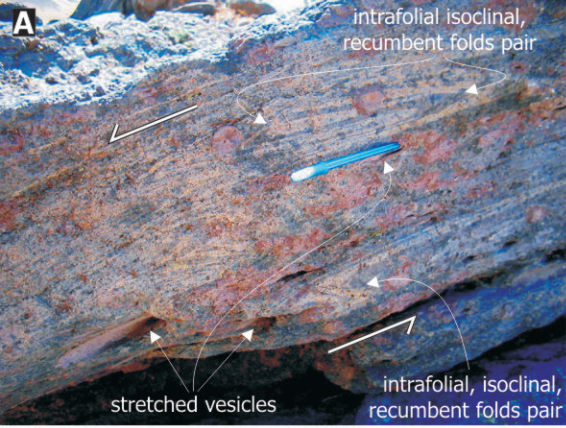


Fig. 3-22. Thin mylonite-like ignimbrite. (A) 10 cm scale, curvilinear, intrafolial fold pairs in vitrophyre; Highway 93 (11T 691940mE 4669981mN). Viewed obliquely to elongation lineation. (B) very faint intrafolial, recumbent isocline in lithoidal ignimbrite; Cricket Creek (11T 682617mE 4672934mN), viewed down plunge, parallel to elongation lineation. (C) 1 m-scale recumbent isocline pair, Backwaters Road (11T 688306mE 4658927mN). (D) complex hinge of an intrafolial, recumbent, synformal isocline in colour-banded vitrophyre. Roadkill (11T 692234mE 4660906mN), viewed perpendicular to elongation lineation. (E) 50 cm scale

sheath fold and 10 cm scale intrafolial folds, and attenuated flow-banding in lithoidal and partly devitrified ignimbrite. Viewed down plunge, parallel to elongation lineation; Cricket Creek. (F) microscopic intrafolial fold pair in eutaxitic vitrophyre, Highway 93.

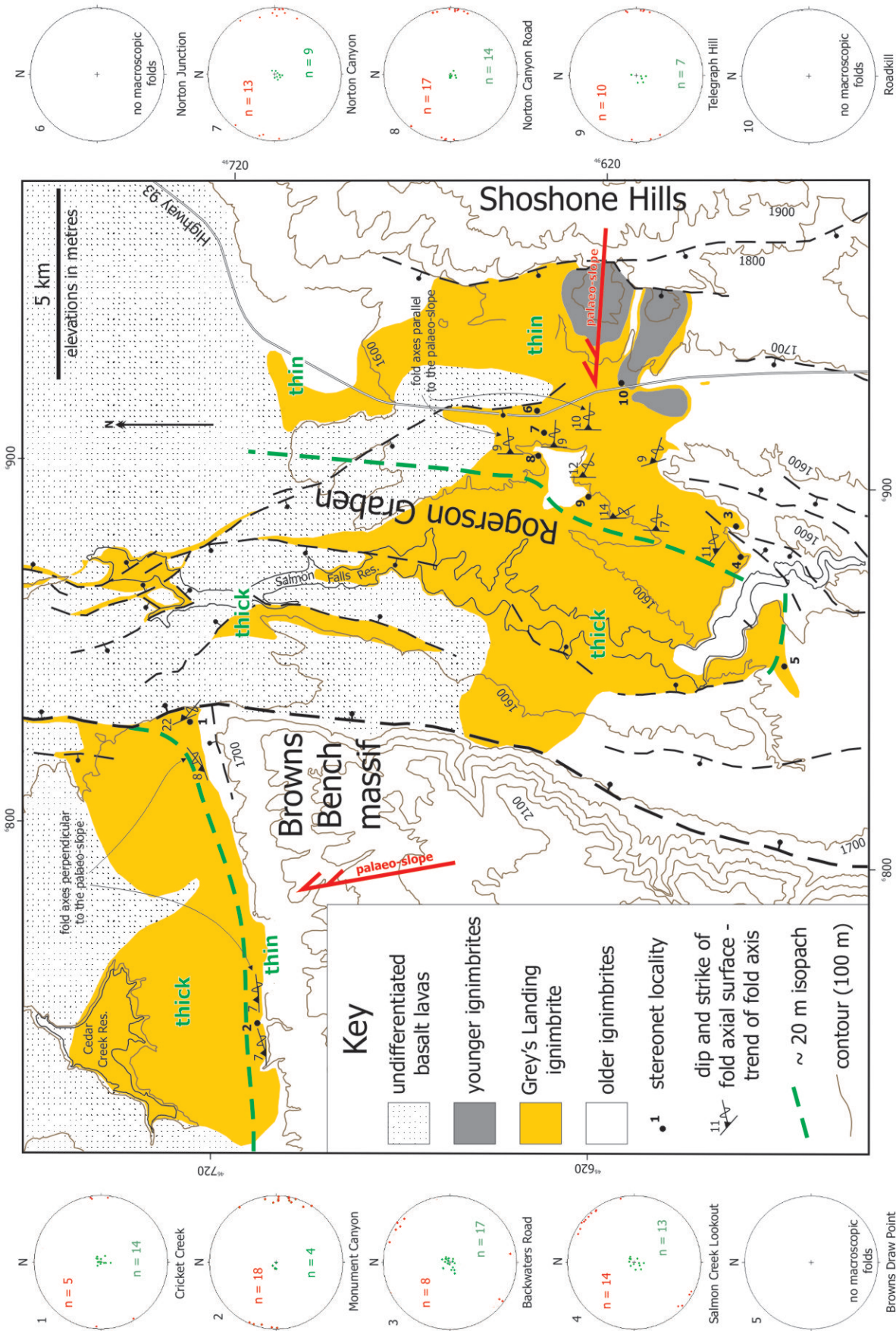


Fig. 3-23. Fold data - thin ignimbrite. Stereonets present poles to fold axial planes (green), and fold hinges (red) for folds within the sheet (filled circles), data collected at numbered locations. Grey's Landing ignimbrite (yellow). Locations of stereonets are numbered.

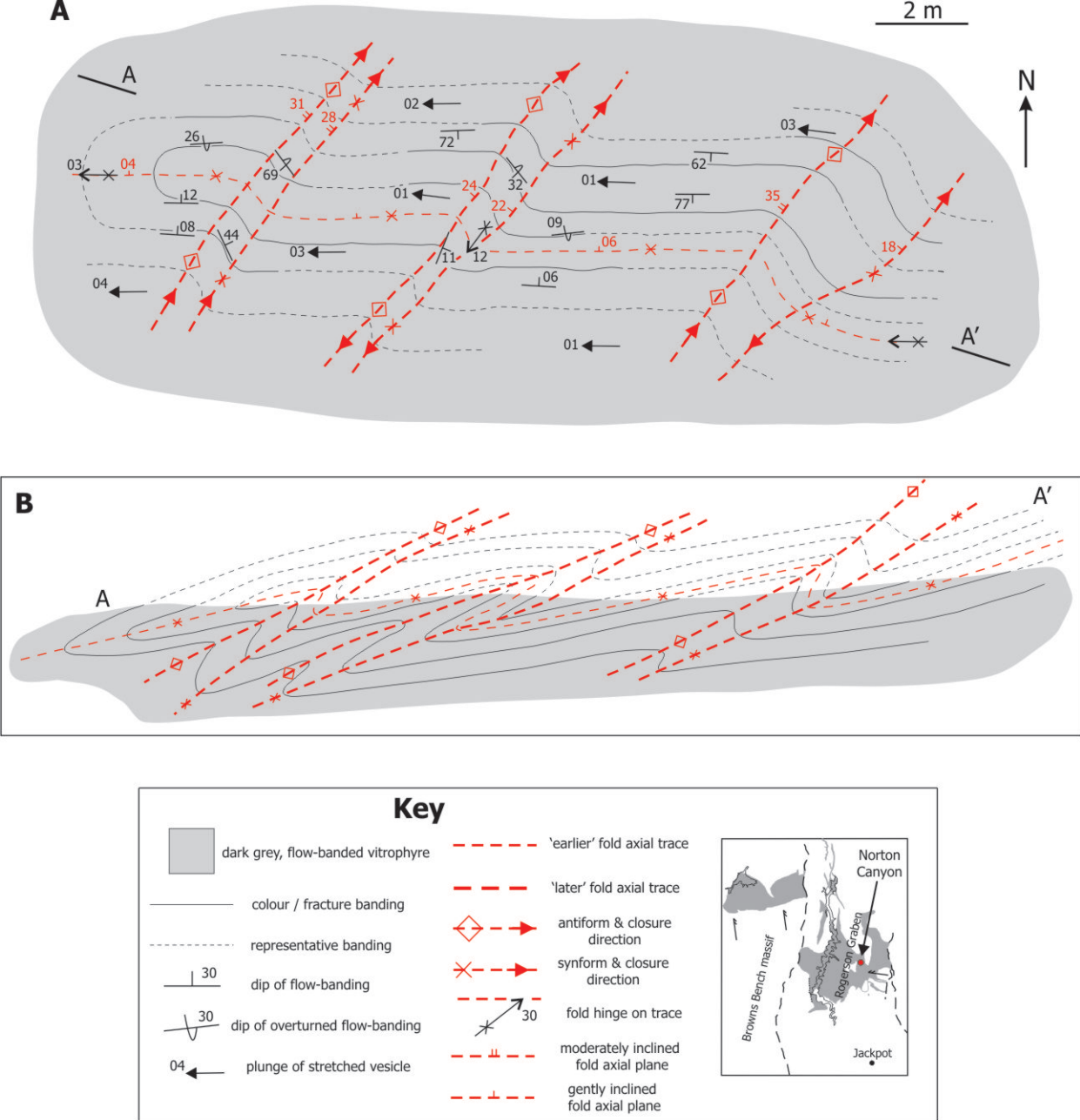


Fig. 3-24. Contrasting folding styles at the upper surface of thin ignimbrite. (A) sketch map of a recumbent isocline refolded by tight, inclined fold pairs - type-3 refolded fold (*sensu* Ramsey, 1967). Norton Canyon (11T 690615mE 4663972mN). (B) cross-section along line A - A'.

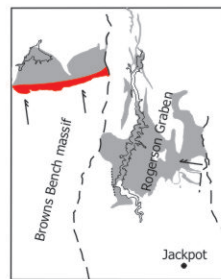
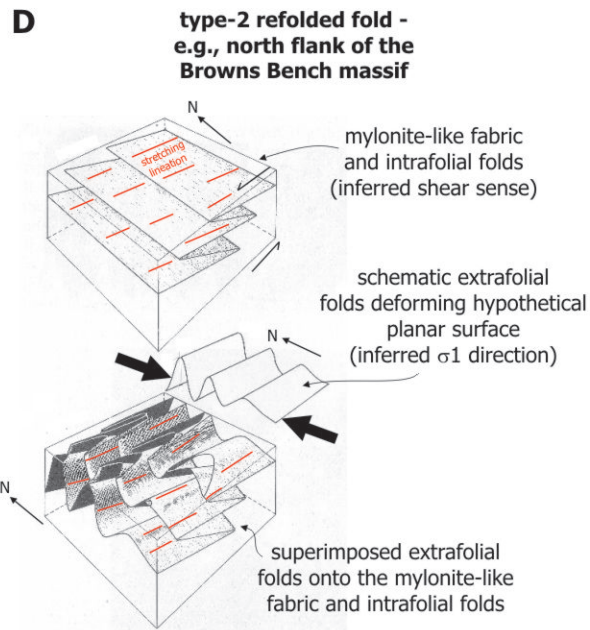
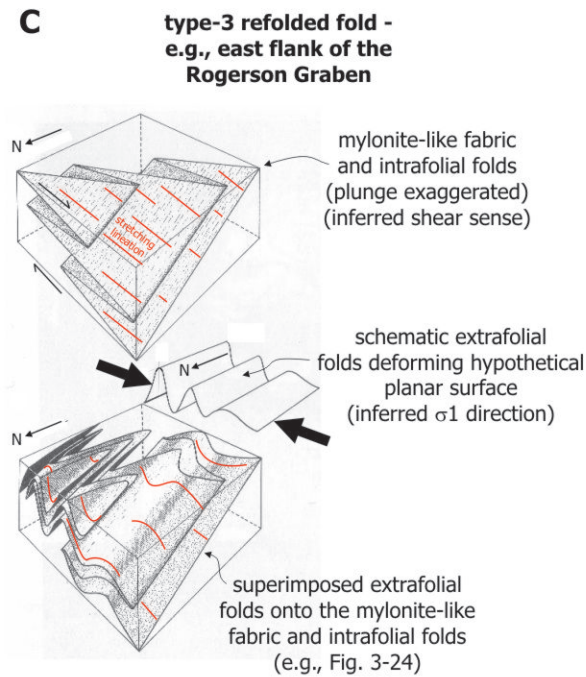
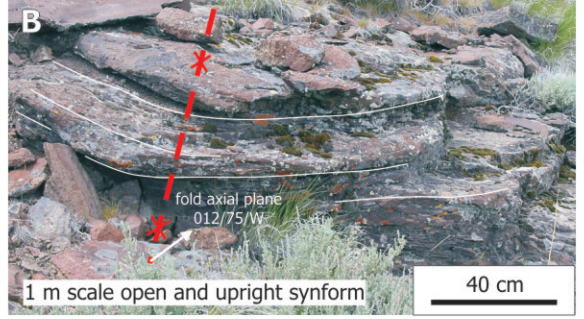
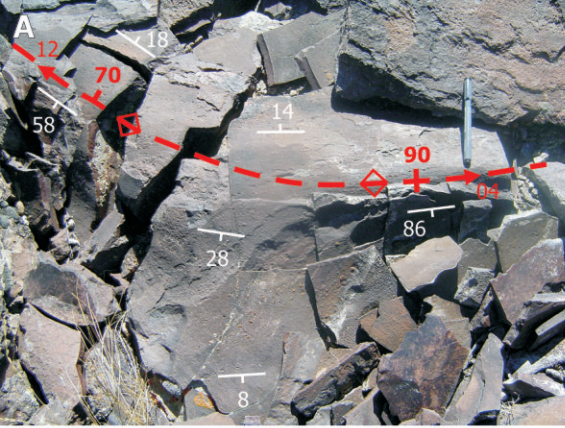


Fig. 3-25. Extrafolial folds at the upper surface of thin ignimbrite. (A) plan view of a open, upright, asymmetric, and gently curvilinear antiform at the boundary between the lithoidal zone and the upper vitrophyre. Monument Canyon (11T 675840mE 4671116mN). (B) 1 m scale open and upright synform in lithoidal ignimbrite, boundary between lithoidal ignimbrite and the upper vitrophyre. Cricket Creek (11T 682617mE 4672934mN). (C) schematic representation of the evolution of type-3 refolded folds through superimposition of extrafolial folds onto intrafolial folds in the eastern Rogerson Graben (red) Modified from Ramsey (1967). (D) schematic representation of the evolution of type-2 refolded folds along the southern flank of the Snake River Plain (red). Modified from Ramsey (1967).

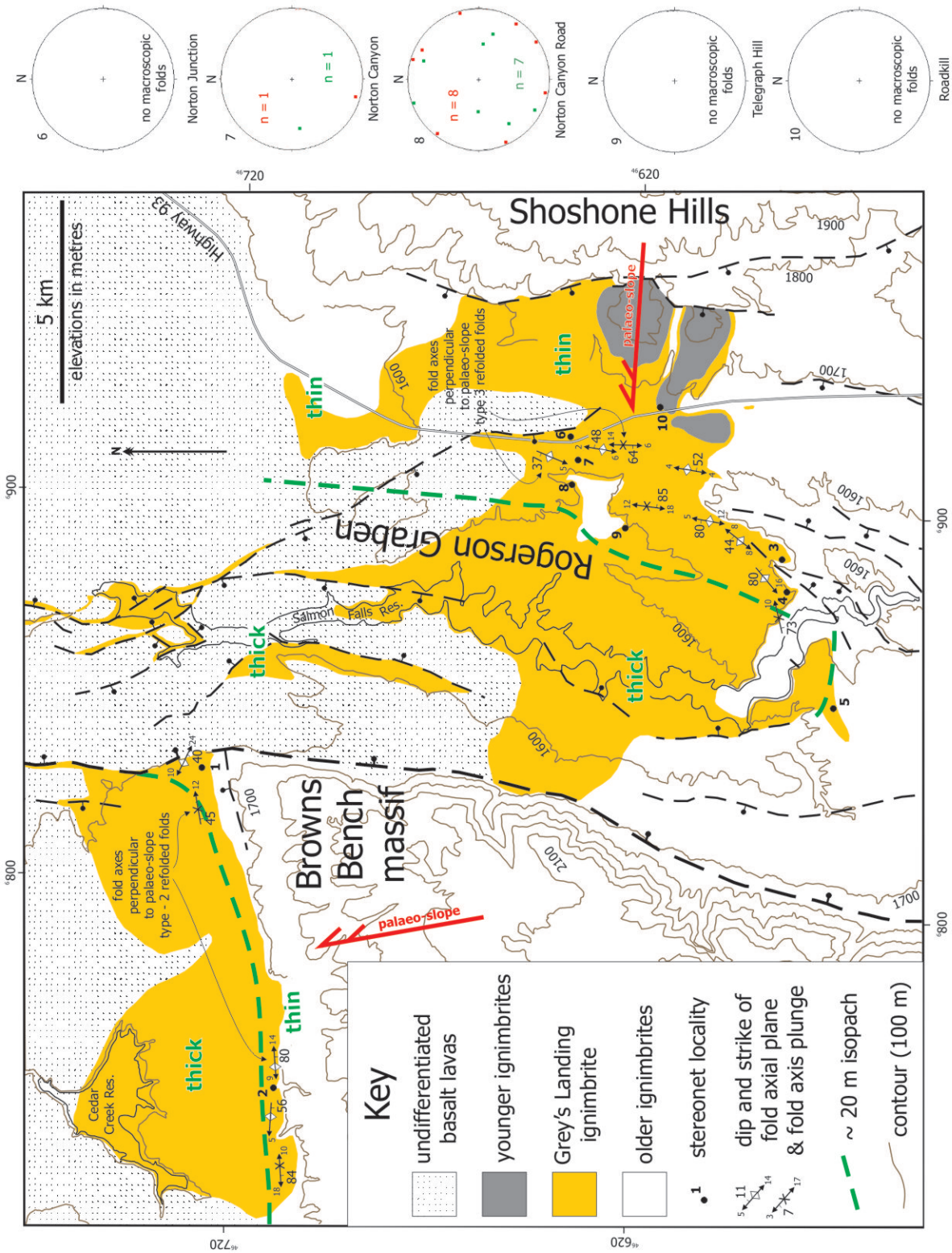


Fig. 3-26. Fold data - thin ignimbrite, upper surface. Stereonets present poles to fold axial planes (green), and fold hinges (red) for folds of the upper surface (filled squares), data collected at numbered locations. Note that fold axes are typically perpendicular to the local palaeoslope (red arrow). Grey's Landing ignimbrite (yellow). Locations of stereonet are numbered.

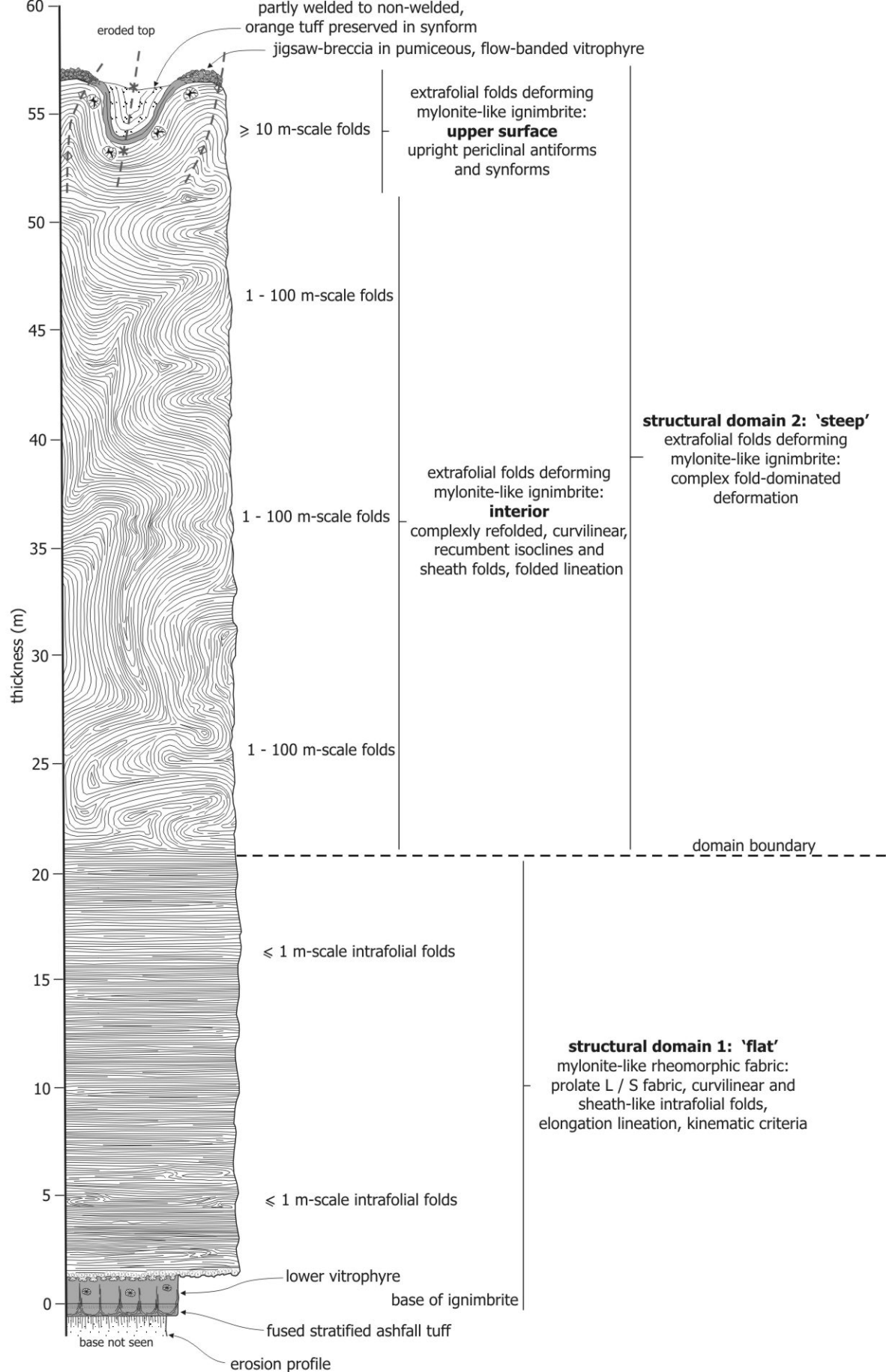


Fig. 3-27. Structural domains within thick ignimbrite. Note the vertical partitioning of distinct sub-horizontal structural domains. Note also, that fold scale increases upwards.

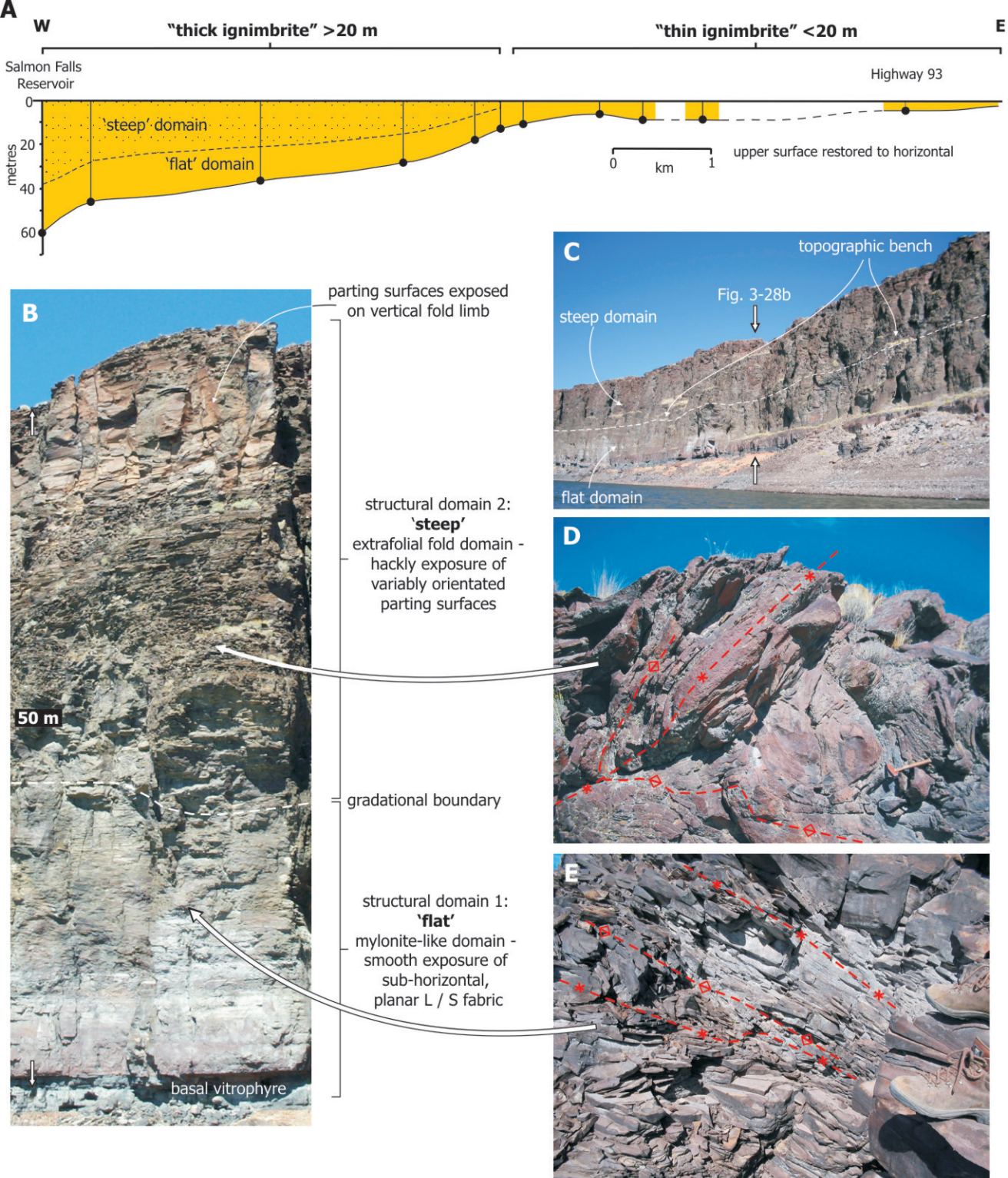
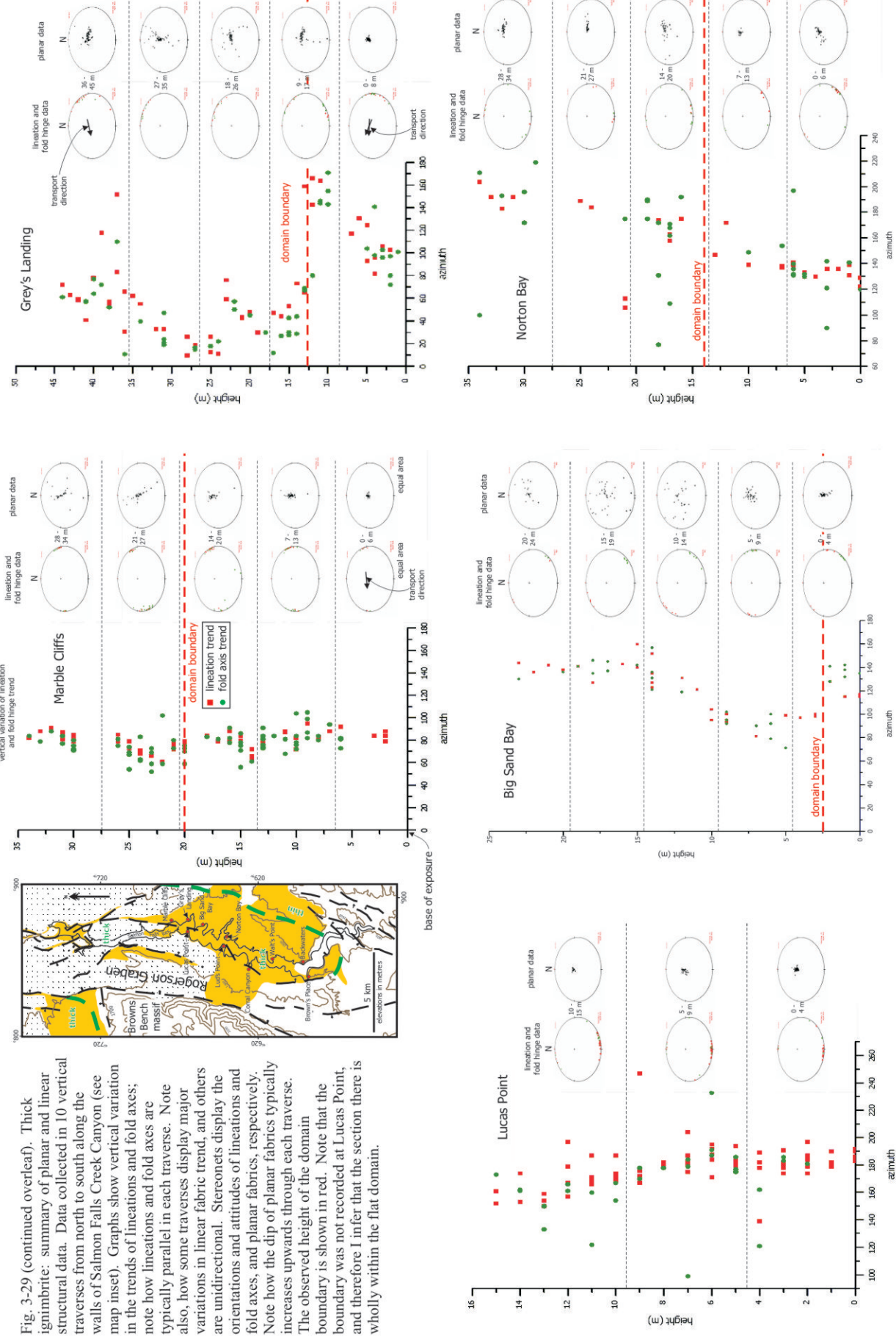


Fig. 3-28. Structural domains within thick ignimbrite. (A) schematic representation of the distributions and thicknesses of the 'flat' domain and the 'steep' domain, in thick ignimbrite. (B) typical section through thick ignimbrite where the two structural domains are readily identified by surface texture, Grey's Landing (11T 687822mE 4666778mN). (C) panoramic view of Grey's Landing showing the crude, large-scale, laterally extensive, and planar division between the two structural domains. Location of photo B is indicated. (D) an example of complex folding and interference patterns in typical steep domain, Grey's Landing. (E) typical lithoidal flat domain ignimbrite, with intrafolial folds and a penetrative L / S fabric, Backwaters (11T 685154mE 4659673mN).

Fig. 3-29 (continued overleaf). Thick ignimbrite: summary of planar and linear structural data. Data collected in 10 vertical traverses from north to south along the walls of Salmon Falls Creek Canyon (see map inset). Graphs show vertical variation in the trends of lineations and fold axes; note how lineations and fold axes are typically parallel in each traverse. Note also, how some traverses display major variations in linear fabric trend, and others are unidirectional. Stereonets display the orientations and attitudes of lineations and fold axes, and planar fabrics, respectively. Note how the dip of planar fabrics typically increases upwards through each traverse. The observed height of the domain boundary is shown in red. Note that the boundary was not recorded at Lucas Point, and therefore I infer that the section there is wholly within the flat domain.



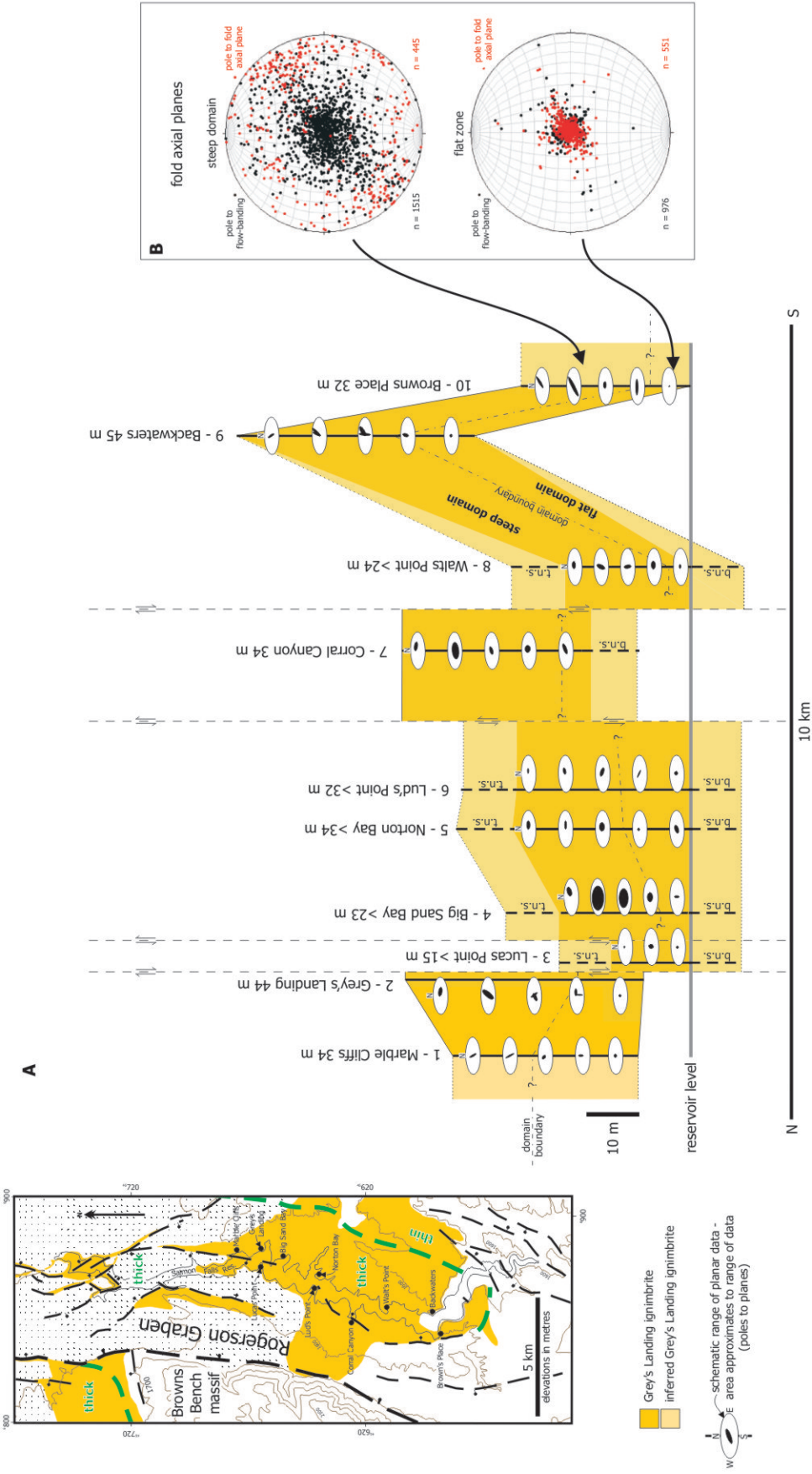


Fig. 3-30. Vertical and lateral changes (N - S) in the attitude of flow-banding (including parting surfaces) data (poles to planes, $n = 5314$) from vertical traverses 1 - 10 (Fig. 3-29), and the observed position of the boundary between lower, mylonite-like domain, and the overlying extrafolial fold domain (dashed line). The approximate range of dips measured at each interval is represented by a black disc on the surface of each small stereonet. Note that sections without preserved lower or upper margins have been extended (pale yellow). Vertical offsets within the ignimbrite are due to normal faulting oblique to the line of section. b.n.s. = base not seen; t.n.s. = top not seen. Inset: locations of traverses 1 - 10. (B) orientation and attitude of fold axial planes in the flat and steep domains, plotted with representative flow-banding data. Note that in the flat domain fold axial planes and flow-banding are parallel and sub-horizontal - intrafolial. The attitude of folds in the steep domain varies from recumbent ($< 10^\circ$) to upright ($> 80^\circ$).

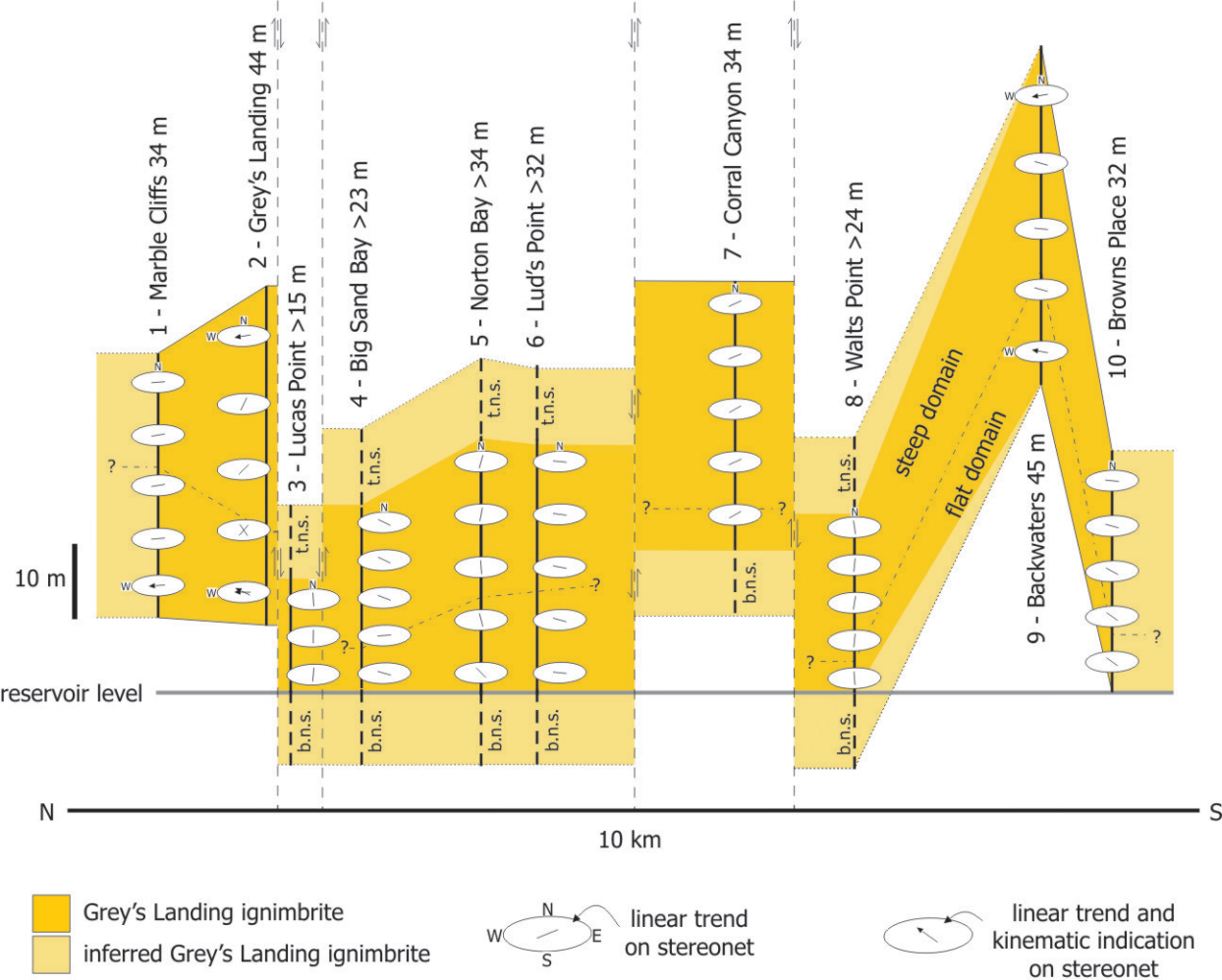


Fig. 3-31. Summary of lineation trends and kinematic criteria, where known, from vertical traverses 1 - 10. Note that the dominant lineation trend may vary by up to 90° between adjacent traverses. Note also, the relatively unidirectional lineation trends in traverses from Marble Cliffs, Lucas Point, Lud's Point, Corral Canyon, and Walt's Point. In contrast, note the multi-directional nature of lineation trends within the other traverses.

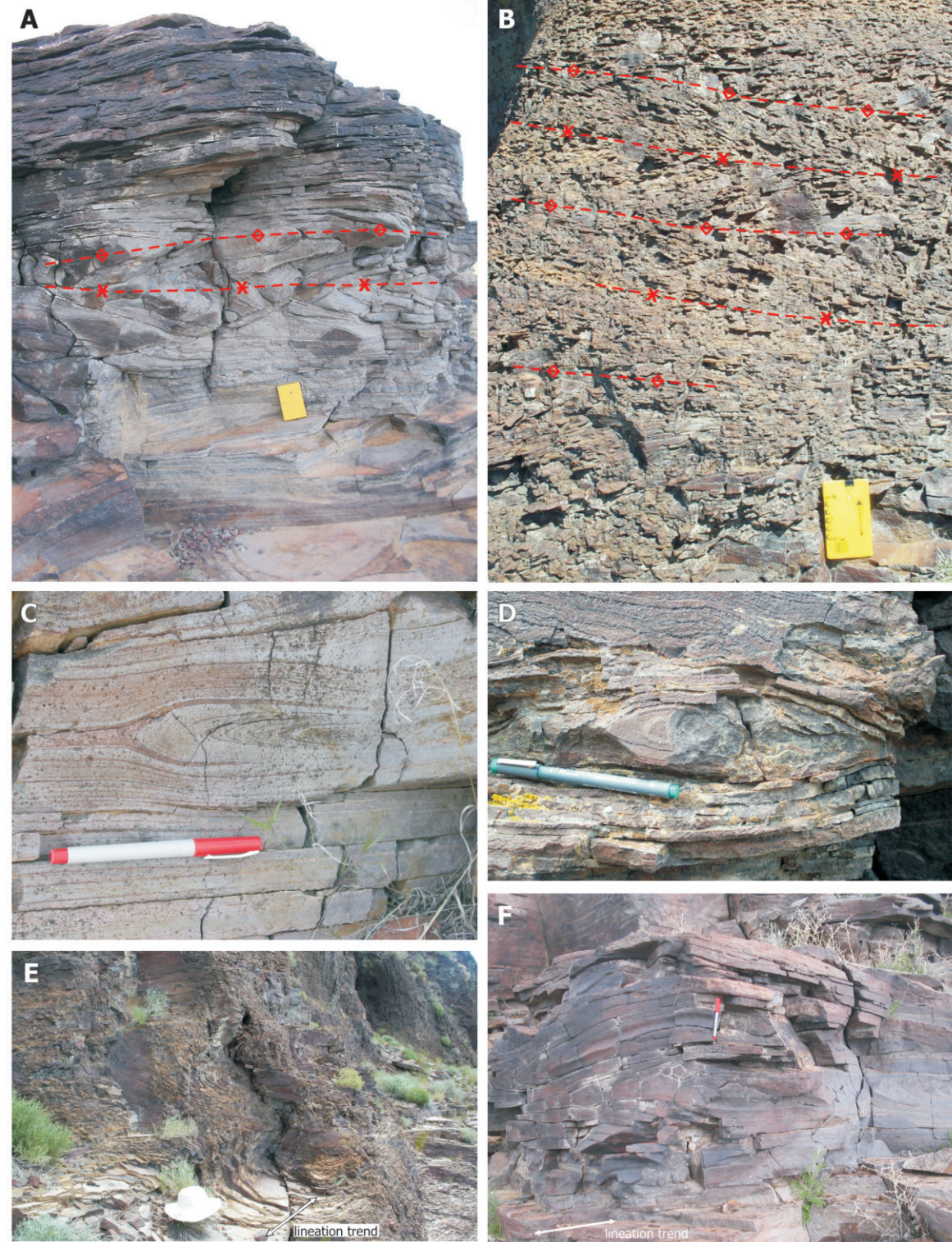


Fig. 3-32. Flat domain. (A) typical section through mylonite-like ignimbrite from West Bay (11T 686515mE 4675092mN) displaying a penetrative, sub-horizontal L / S fabric with 0.5 m-scale intrafolial folds. (B) strongly-jointed mylonite-like ignimbrite from Grey's Landing (11T 687822mE 4666778mN) displaying a penetrative, sub-horizontal L / S fabric with 1 m-scale intrafolial folds. (C) dm-scale 'floating' isoclinal hinge of a sheath-like fold, viewed parallel to elongation direction. Note major hinge thickening. West Bay (11T 686515mE 4675092mN). (D) dm-scale, 'floating' intrafolial sheath fold, Backwaters (11T 685154mE 4659673mN). (E) 1 m-scale intrafolial sheath and sheath-like folds with near-circular eye structures, Grey's Landing. (F) 1 m-scale intrafolial sheath fold with very elliptical eye-structure, West Bay.

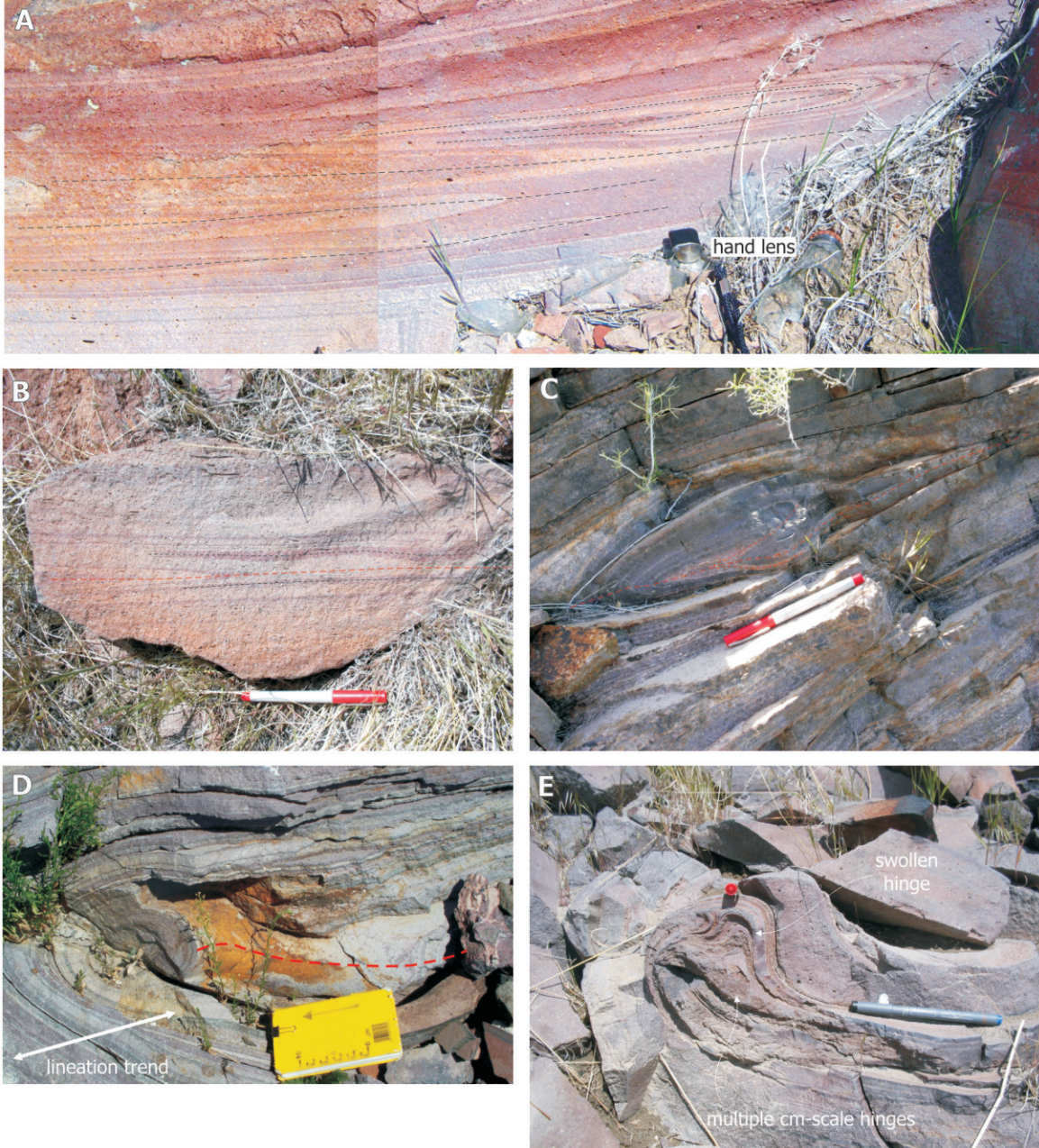


Fig. 3-34. Flat domain: refolded folds. (A) four intrafolial, similar-style isoclinal folds within a single layer, Cedar Creek Reservoir (11T 673712mE 4674456mN). Note refolded hinge (type-3; Fig. 3-25c) of the largest fold. Viewed parallel to lineation. (B) cm-scale, intrafolial refolded fold (type-3) in colour-banded ignimbrite, loose block from Marble Cliffs (11T 687503mE 4668265mN). (C) dm-scale, refolded hinge of a sheath-like isoclinal ('club-foot' form). West Bay, viewed parallel to elongation direction. (D) dm-scale, refolded sheath fold within the hinge of a sheath-like, intrafolial isoclinal ('rolling-pin' form), Backwaters (11T 685154mE 4659673mN). Viewed oblique to elongation direction. (E) complex refolded folds within the hinge of an intrafolial, sheath-like isoclinal ('knotted' form), Marble Cliffs. Viewed parallel to elongation direction.

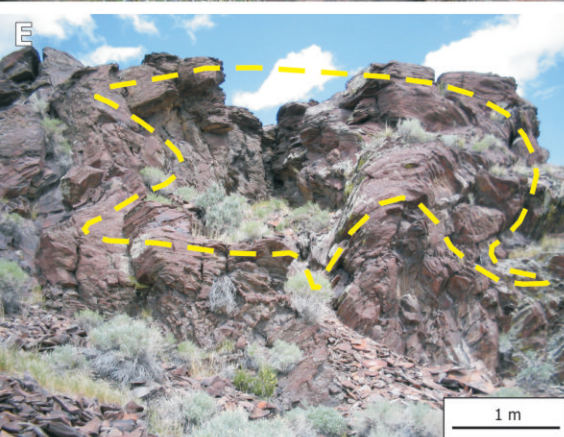


Fig. 3-36. Steep domain. (A) 10 m-scale, upright, extrafolial synform, Too Cool (11T 687260mE 4668352mN). (B) 5 m-scale, upright, extrafolial antiform refolding an intrafolial isocline, Monument Canyon (11T 675840mE 4671116mN). (C) complex antiformal hinge; 1 m-scale, upright extrafolial fold, West Bay (11T 686473mE 4675065mN). (D) 5 m-scale, recumbent, extrafolial sheath fold closure, Grey's Landing (11T 688614mE 4666624mN). (E) 10 m-scale, eye structure cross-section through a recumbent sheath fold, Grey's Landing.

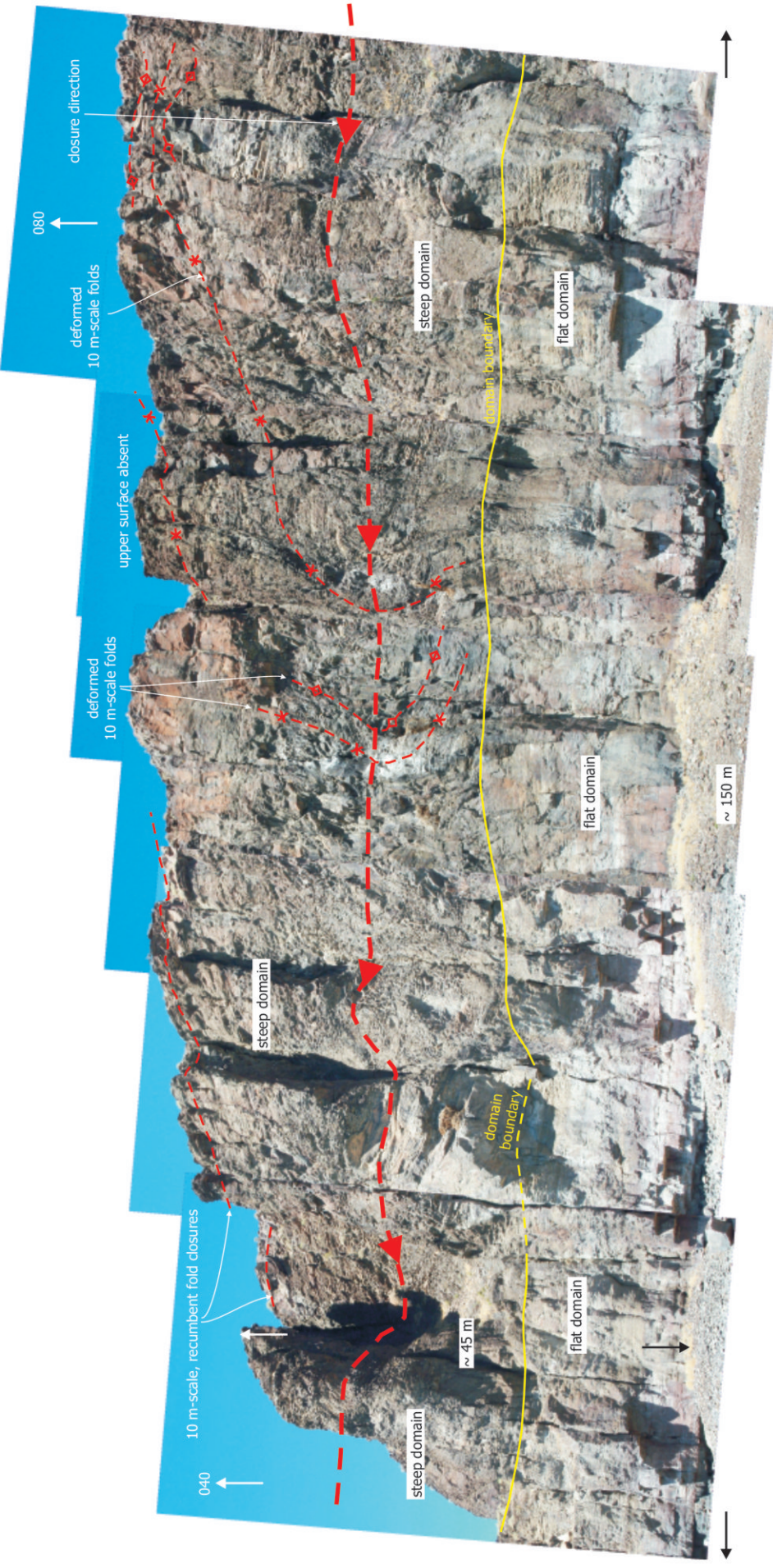


Fig. 3-37. Steep domain. Photo mosaic from Grey's Landing (11T 688614mE 4666624mN) showing a 100 m-scale recumbent fold closure in the extrafolial fold domain. Note how 10 m-scale folds are deformed by the 100 m-scale isocline.

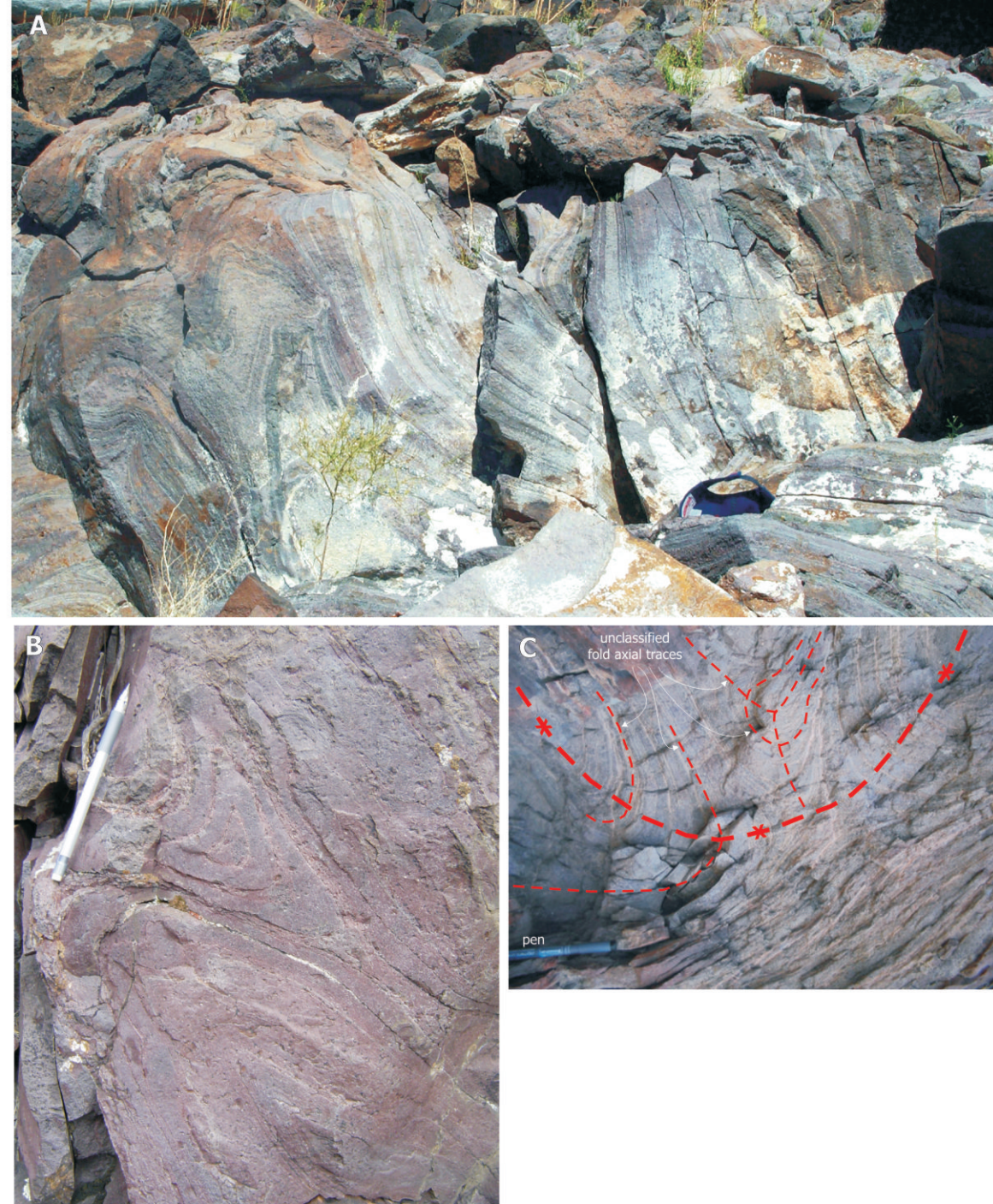


Fig. 3-39. Step domain: folding in the interior of the ignimbrite. (A) complex upright folding and refolding of colour-banded, mylonite-like ignimbrite. 3 km south of Salmon Dam (11T 685973mE 4673275mN). (B) arrow-head shaped eye structure entrained between extrafolial folds, Grey's Landing (11T 687822mE 4666787mN). (C) complex interference pattern formed by multiple intrafolial folds refolded by a strongly curvilinear, extrafolial synform, Grey's Landing.

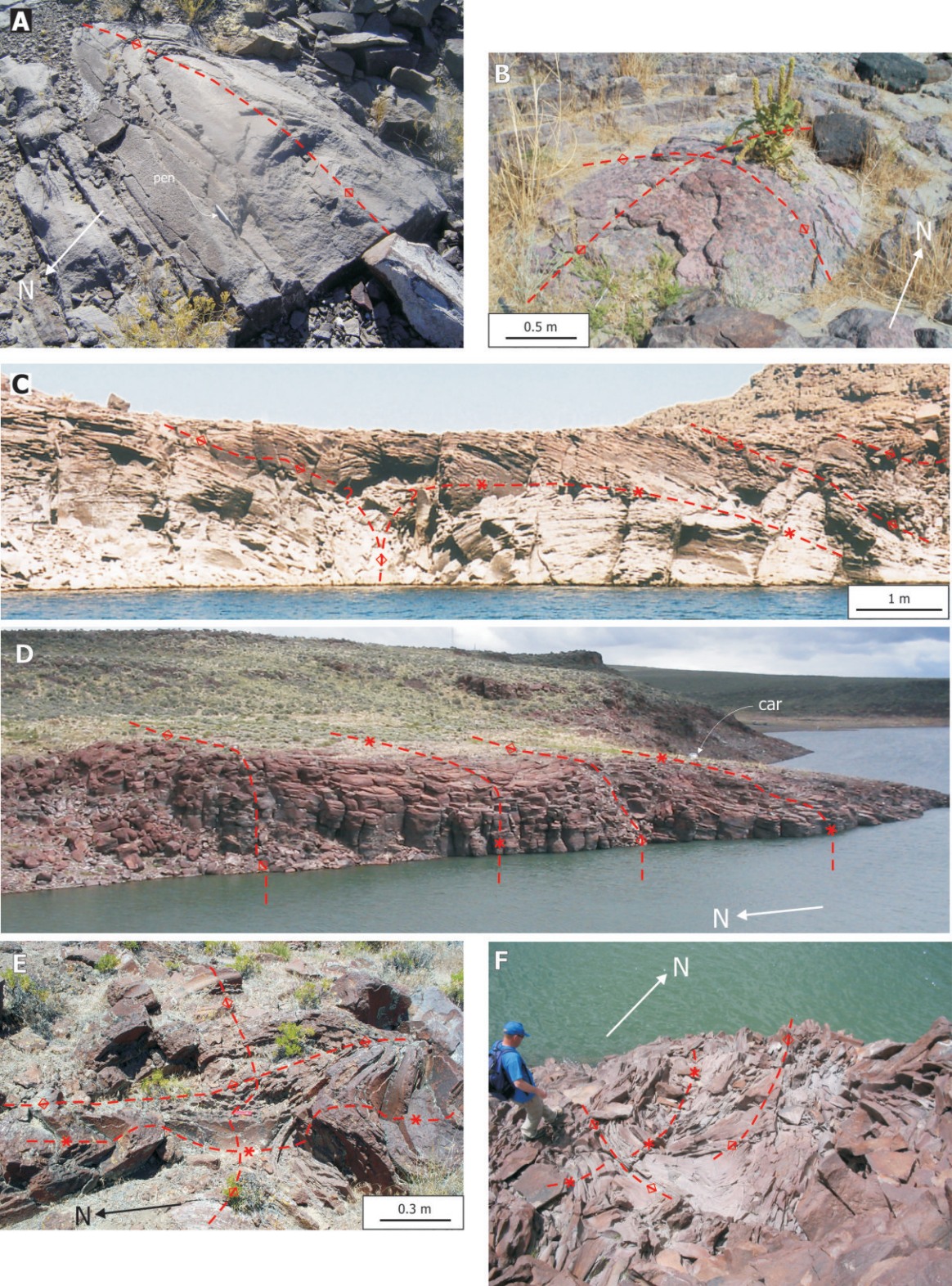
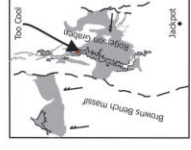
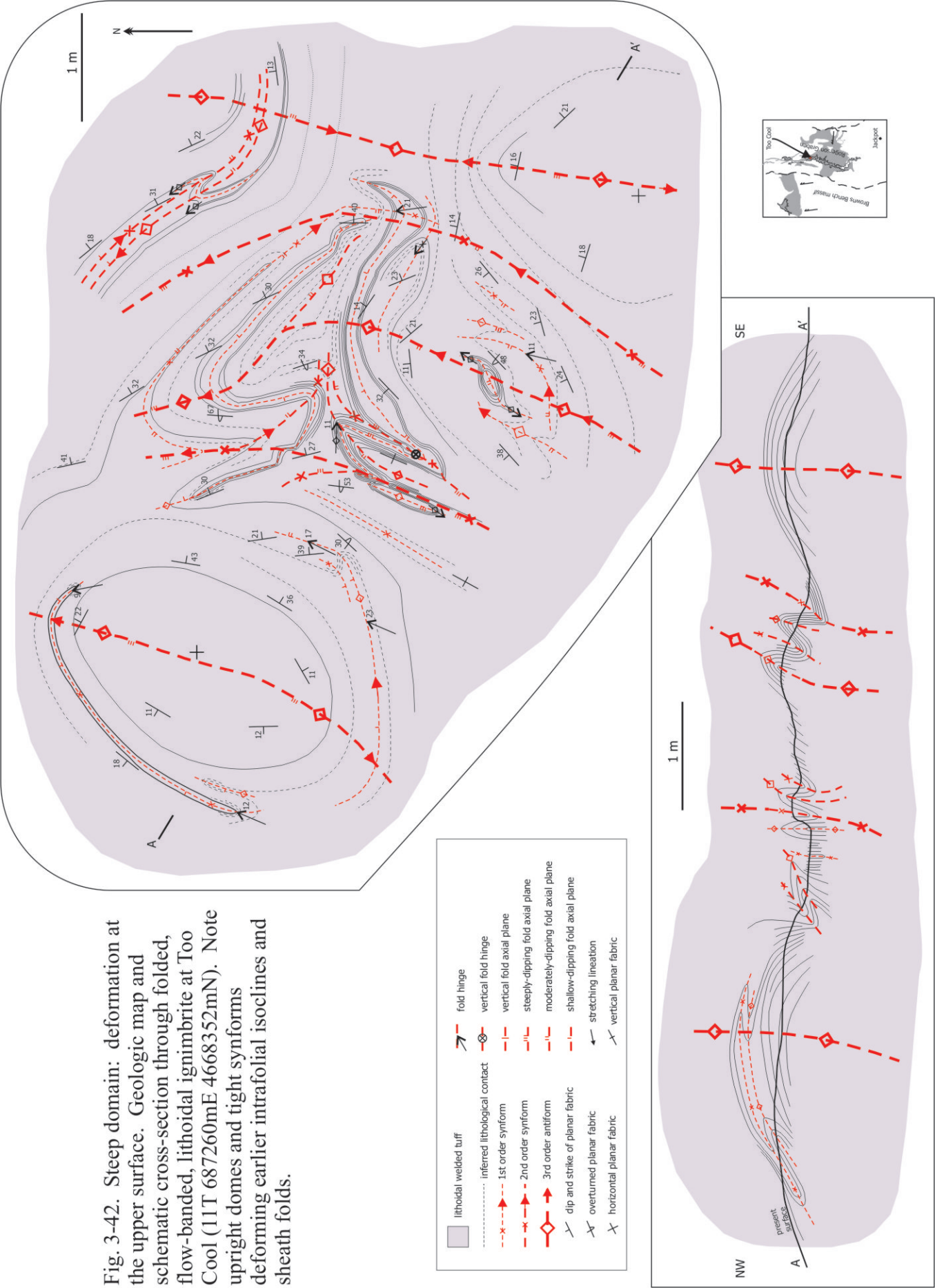


Fig. 3-40. Steep domain: deformation at the upper surface. (A) 2 m-scale, upright and tight, periclinal antiform, Cedar Creek Reservoir (11T 673712mE 4674456mN). (B) 5 m-scale, open dome, Too Cool (11T 687260mE 4668352mN). (C) 10 m-scale, mushroom-shaped, extrafolial isoclinal antiform, 1.5 km south of Salmon Dam (11T 687207mE 4674229mN). Note the antiform 'root' is upright, but the closures (antiformal and synformal) are recumbent. (D) 20 m-scale, long-wavelength, upright and open, extrafolial antiforms and synforms, West Bay (11T 686515mE 4675092mN). (E) refolded 2 m-scale domes and basins, Too Cool. (F) typical 10 m-scale domes and basins refolding 2 m-scale isoclines, Too Cool.



Fig. 3-41. Steep domain: refolded intrafolial folds at the upper surface. (A) intrafolial isocline refolded (type-3) by upright, parallel-style, extrafolial fold pair, Norton Bay (11T 686902mE 4664340mN). (B) refolded isocline, loose block, Too Cool (11T 687260mE 4668352mN). (C) complex refolded of intrafolial isoclinal folds by a gently inclined and gently curvilinear, extrafolial fold pair, West Bay (11T 686473mE 4675065mN). (D) complex interference pattern formed by refolding of intrafolial sheath folds by inclined and curvilinear, extrafolial folds, Too Cool. (E) upright and inclined, buckle-style folds in colour-banded ignimbrite, suggesting minor competency contrasts across bands. Salmon Dam (11T 686989mE 4675532mN). All *in situ* examples are viewed parallel to the local lineation trend.

Fig. 3-42. Steep domain: deformation at the upper surface. Geologic map and schematic cross-section through folded, flow-banded, lithoidal ignimbrite at Too Cool (11T 687260mE 4668352mN). Note upright domes and tight synforms deforming earlier intrafolial isoclines and sheath folds.



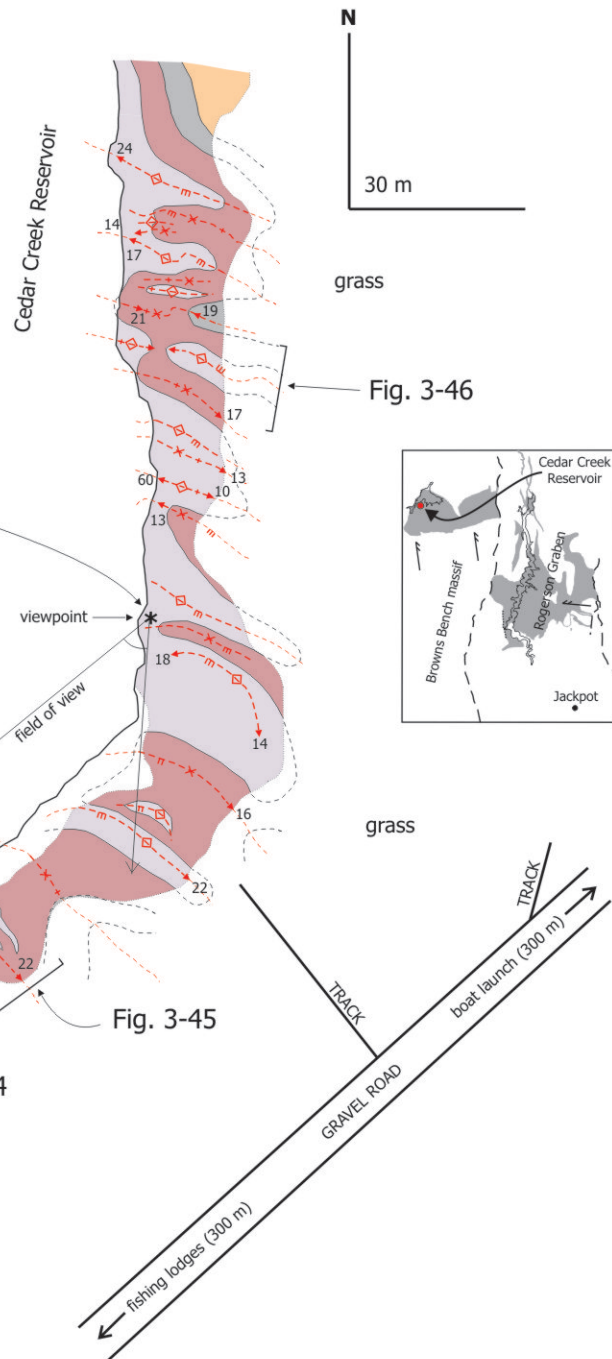
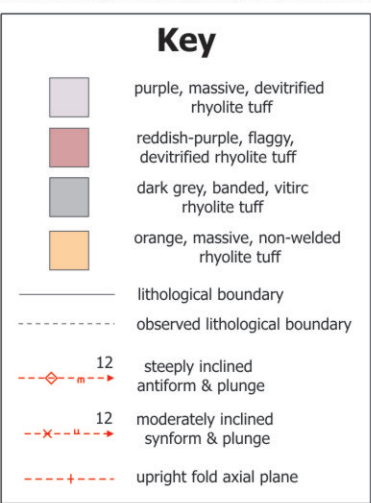
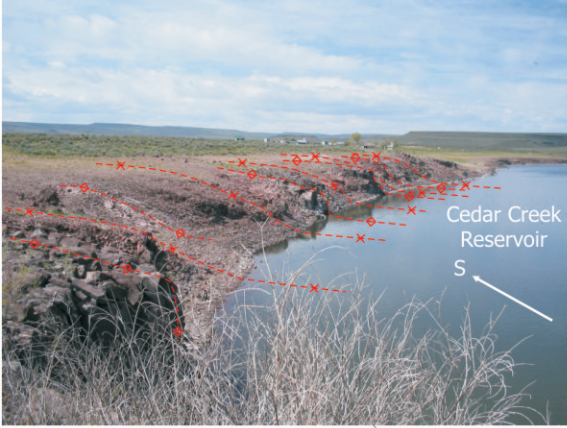


Fig. 3-43. Steep domain: deformation at the upper surface. Sketch map of long-wavelength folding at the surface of the Grey's Landing ignimbrite, Cedar Creek Reservoir (11T 673712mE 4674456mN; inset). Initially pseudo-layer-cake stratigraphy defined by lithological variation within the ignimbrite. Folds are typically upright or steeply inclined periclinal antiforms and synforms. Note the fairly regular 20 - 30 m fold wavelength, and how this is expressed in the local topography. The locations of detailed maps (Figs 3-44, 3-45, and 3-46) are shown.

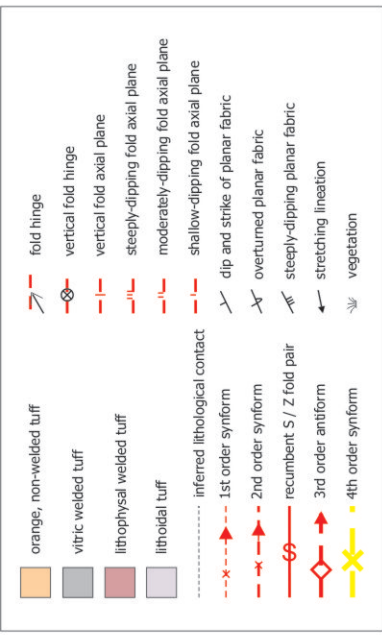


Fig. 3-44. Steep domain: deformation at the upper surface. Detailed geologic map and schematic cross-section of NW-trending, disharmonic extrafolial folds in a composite synform, deforming psuedo-layer-cake lithologies at Cedar Creek Reservoir (see inset). Note the presence of at least 4 orders of fold, progressively increasing in scale. Note also, the periclinal nature of many folds, and how their axial traces commonly merge. Folds are typically upright, open to tight, and similar- to parallel-style. Note diverging stretched vesicles perpendicular to axes of 3rd order antiforms. Line of cross-section A - A' is indicated.

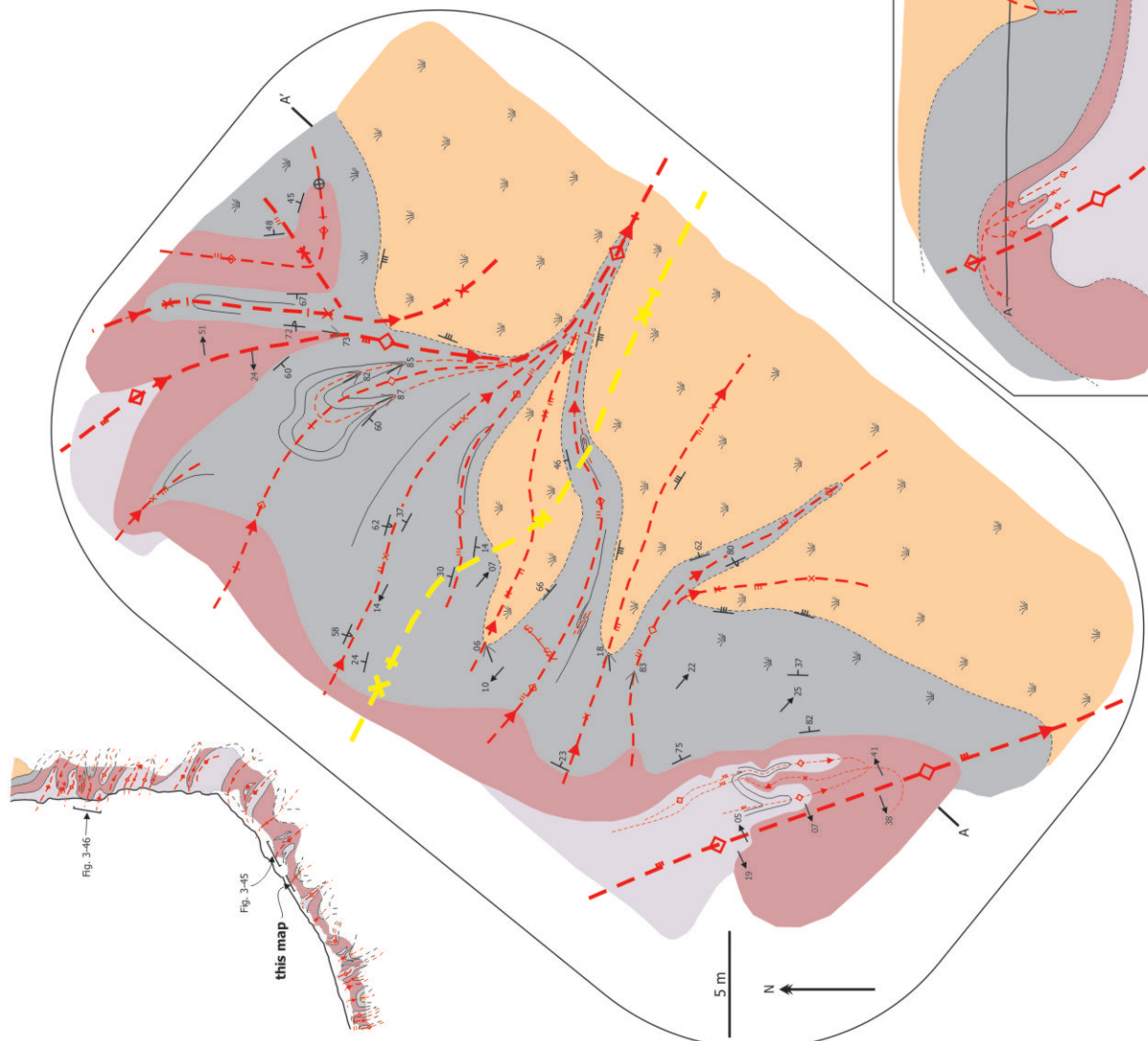


Fig. 3-46

Fig. 3-45

this map

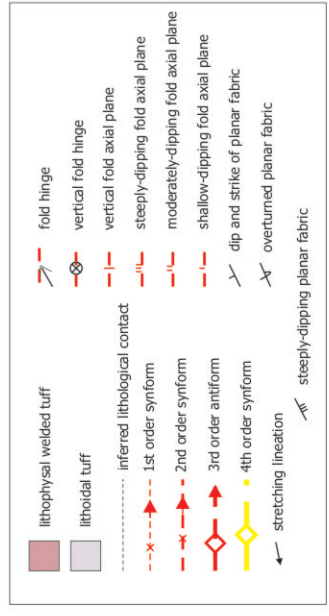
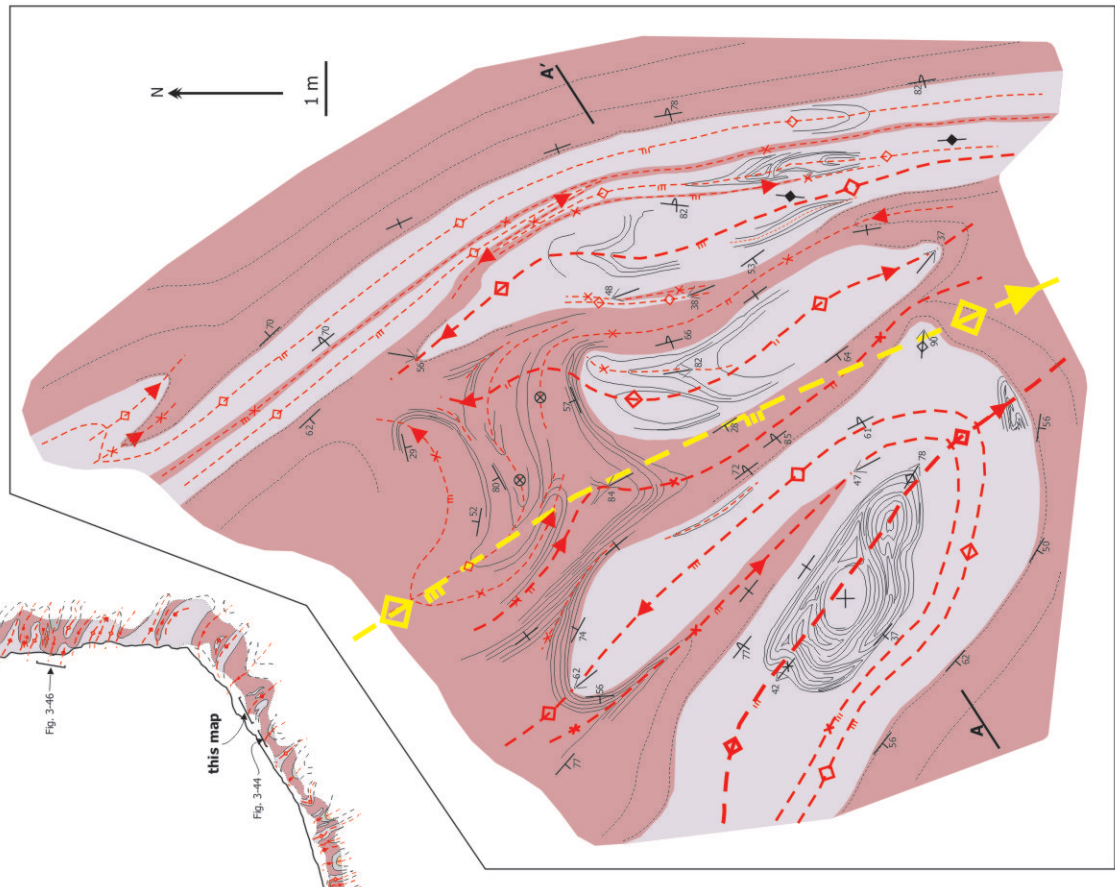
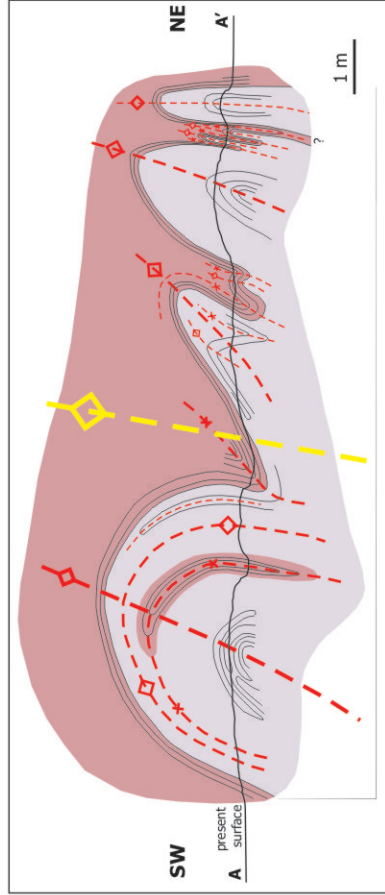


Fig. 3-45. Steep domain: deformation map and schematic cross-section of NW-trending, disharmonic extrafolial folds in a composite antiformal closure, deforming lithoidal ignimbrite, Cedar Creek Reservoir (see inset). Note the presence of at least 4 orders of fold, progressively increasing in scale. Note also, the periclinal nature of many folds, and how their axial traces are commonly folded and merge into one another. Folds are typically upright, open to tight, and similar- to parallel-style. Line of cross-section A - A' is indicated.



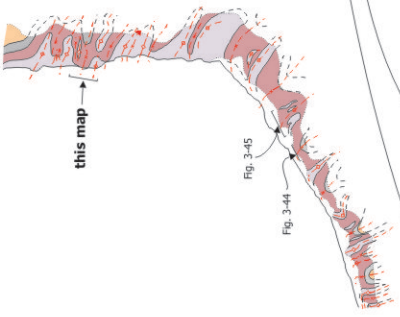
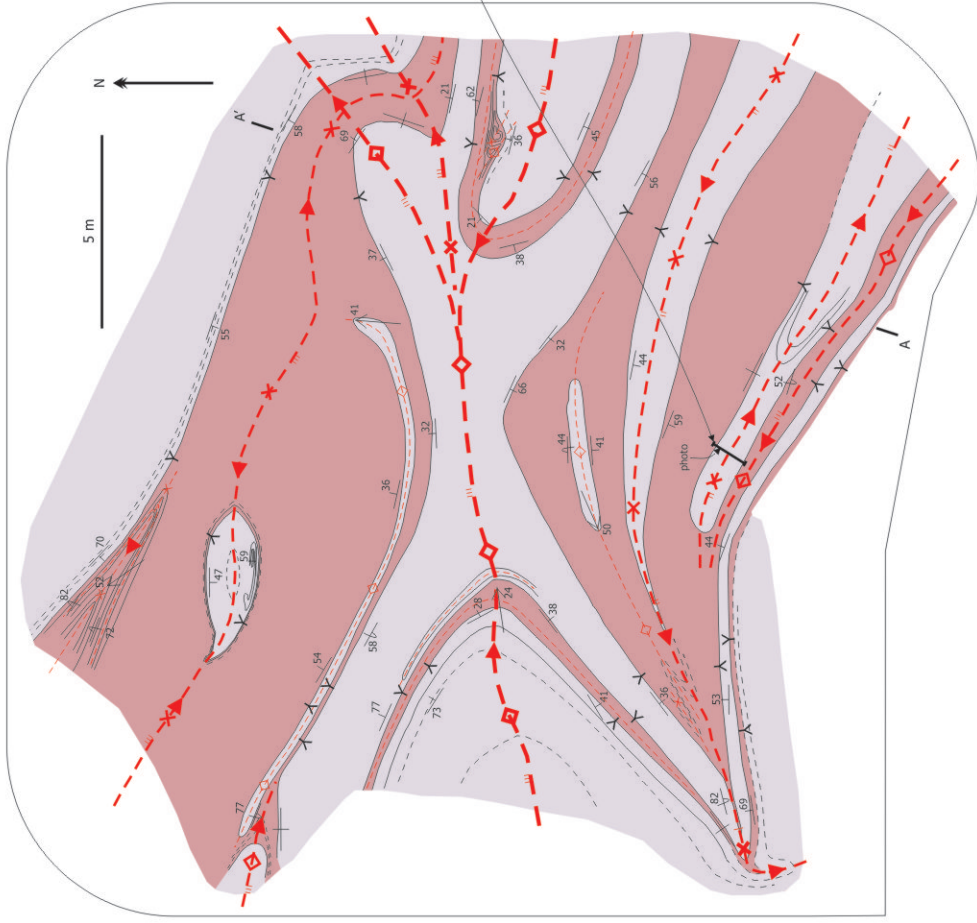
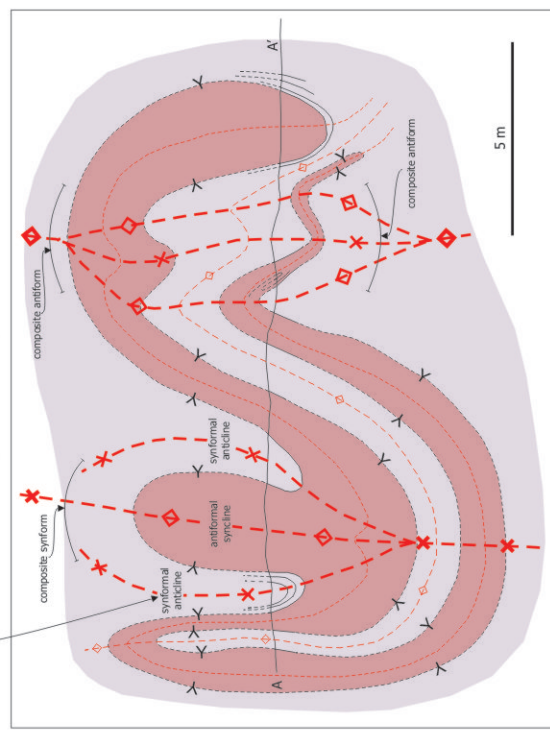


Fig. 3-46. Steep domain: deformation at the upper surface. Detailed geologic map and tentative cross-section of NW-trending, disharmonic extrafolial folds refolding an intrafolial sheath fold, Cedar Creek Reservoir (see inset). Note the presence of at least 3 orders of fold, progressively increasing in scale. Note also, the perichinal nature of many folds, and how their axial traces are commonly folded and merge into one another. Folds are upright to overturned, open to tight, and similar- to parallel-style. Line of cross-section A - A' is indicated. Photo shows a similar-style synformal anticline in detail. A tentative deformation history for this structure is presented in Fig. 3-50.



- | | | | |
|--|---------------------------------|--|-------------------------------------|
| | lithophysal welded tuff | | fold hinge |
| | lithoidal welded tuff | | vertical fold hinge |
| | inferred lithological contact | | vertical fold axial plane |
| | 1st order synform | | steeply-dipping fold axial plane |
| | 2nd order synform | | moderately-dipping fold axial plane |
| | 3rd order antiform | | stretching lineation |
| | dip and strike of planar fabric | | younging direction |
| | overturned planar fabric | | vertical planar fabric |

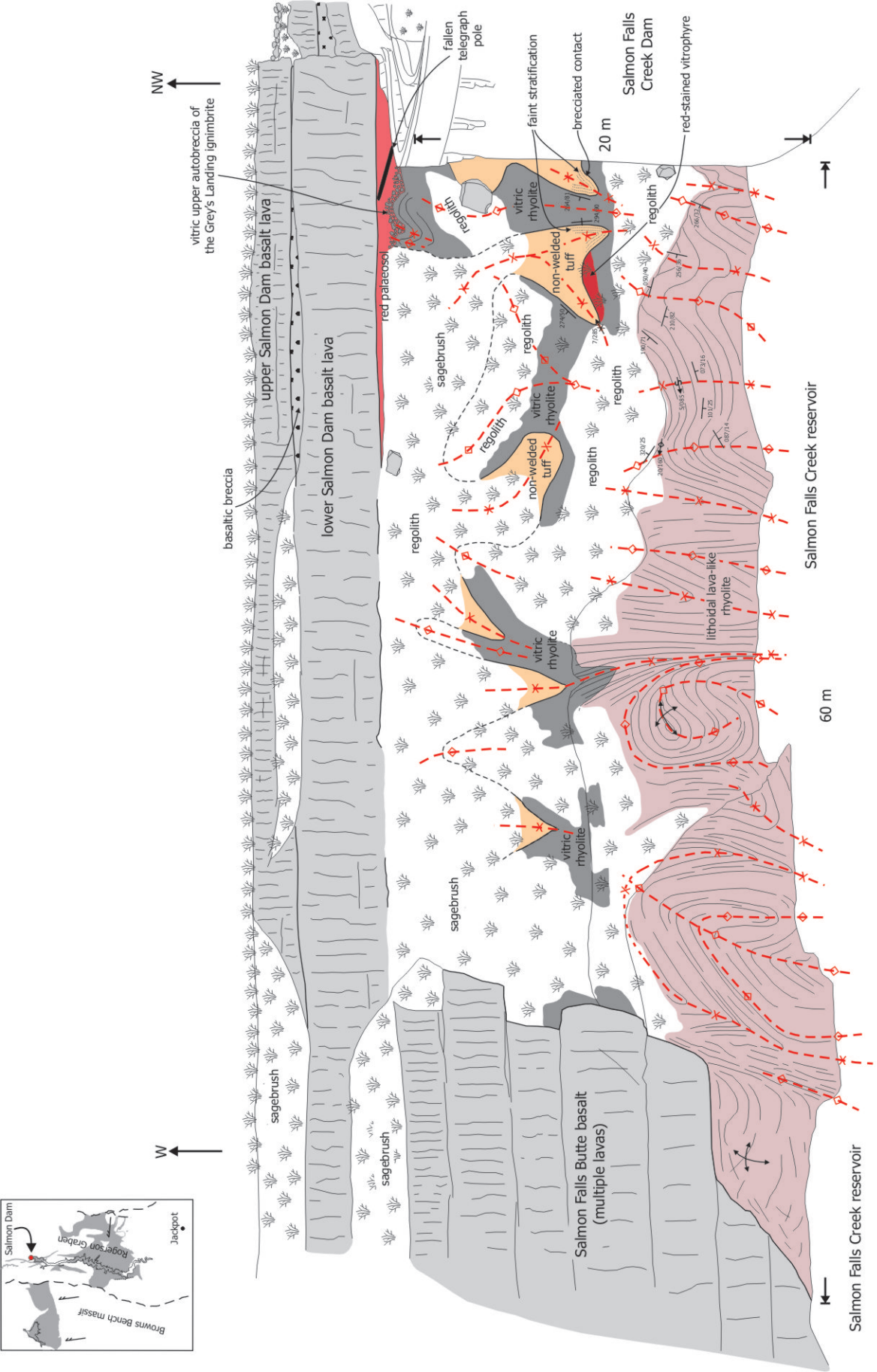


Fig. 3-47. Steep domain: deformation at the upper surface. Field-sketch of the west side of Salmon Falls Creek Canyon at Salmon Dam, showing the deformation in the upper portion of the Grey's Landing ignimbrite, and covering basalt lavas. Note that the style of folding differs between the lower lithoidal rhyolite and the upper vitrophyre - non-welded tuff contact, and that they are disharmonic. Folds within the lithoidal rhyolite are similar- and buckle-styles, and often exhibit complex interference patterns. In contrast, the folds of the vitrophyre - non-welded tuff surface are simple buckle-style folds with 5 - 10 m wavelength.

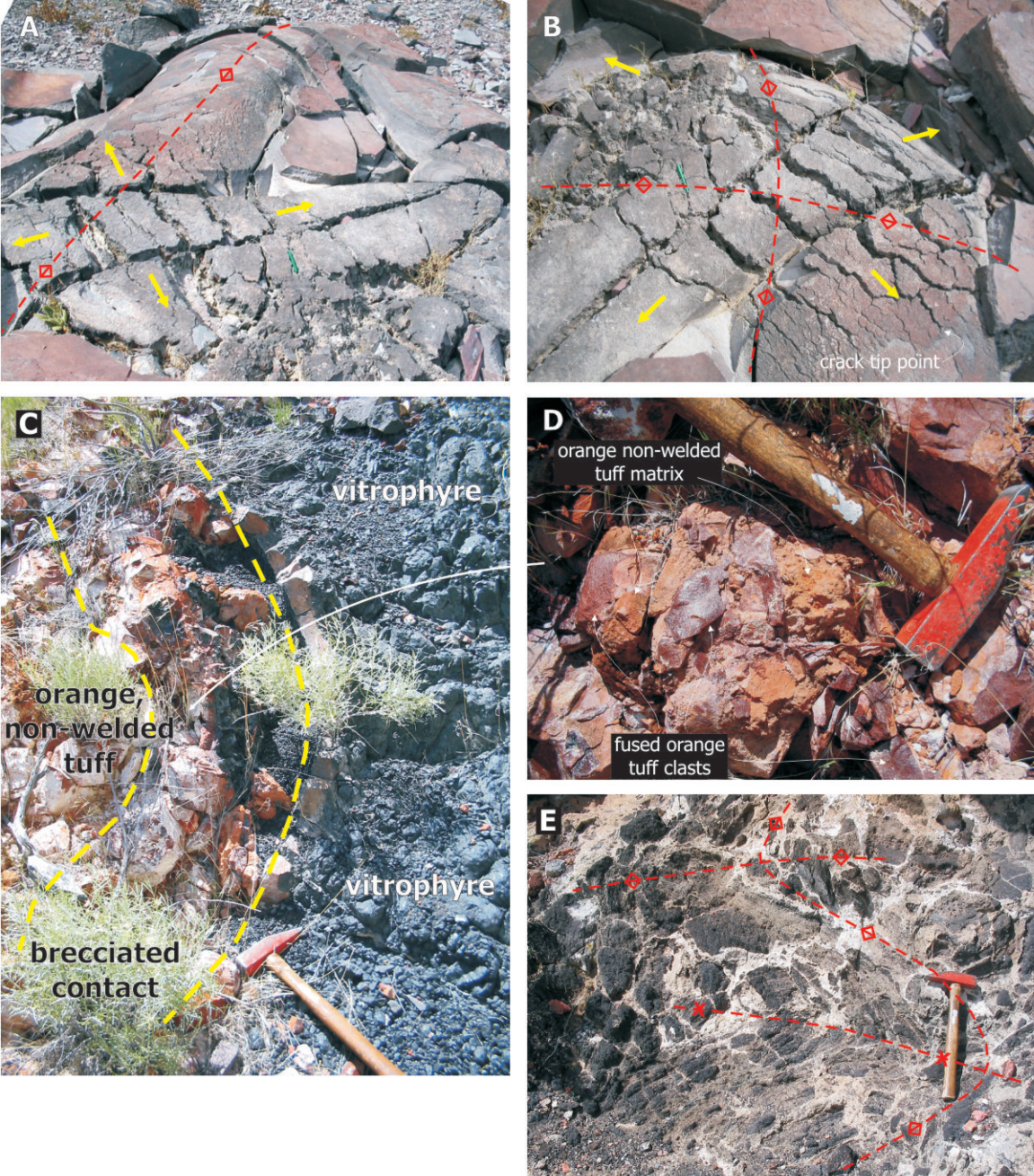


Fig. 3-48. Brittle deformation at the upper surface. (A) ‘chocolate-block’ tensile cracking of a 5 cm-thick vesicular layer, in the crest of a 10 m-scale, tight, antiformal pericline; Cedar Creek Reservoir (11T 673712mE 4674456mN). Note how brittle deformation is highly localised. Apparent extension direction indicated in yellow. (B) ‘chocolate-block’ cracking of a vesicular layer at the crest of a dome, Cedar Creek Reservoir. Note how localised brittle deformation is, and how cracks are ‘lightning fork’-shaped. Apparent extension direction indicated in yellow. (C) overturned boundary between upper vitrophyre (black) and overlying orange, non-welded tuff, Salmon Dam (11T 686997mE 4675548mN). Note that the contact is brecciated, and becomes more fused towards the vitrophyre. (D) detail of brecciated contact between the upper vitrophyre and overlying orange, non-welded tuff. Note that the clasts in the breccia are formed of partly fused, orange tuff supported by a matrix of non-welded orange tuff. (E) brecciated refolded, m-scale antiform in the upper vitrophyre, Salmon Dam. Note the ‘jig-sawfit’ of the breccia allowing the original fold shapes to be discerned.

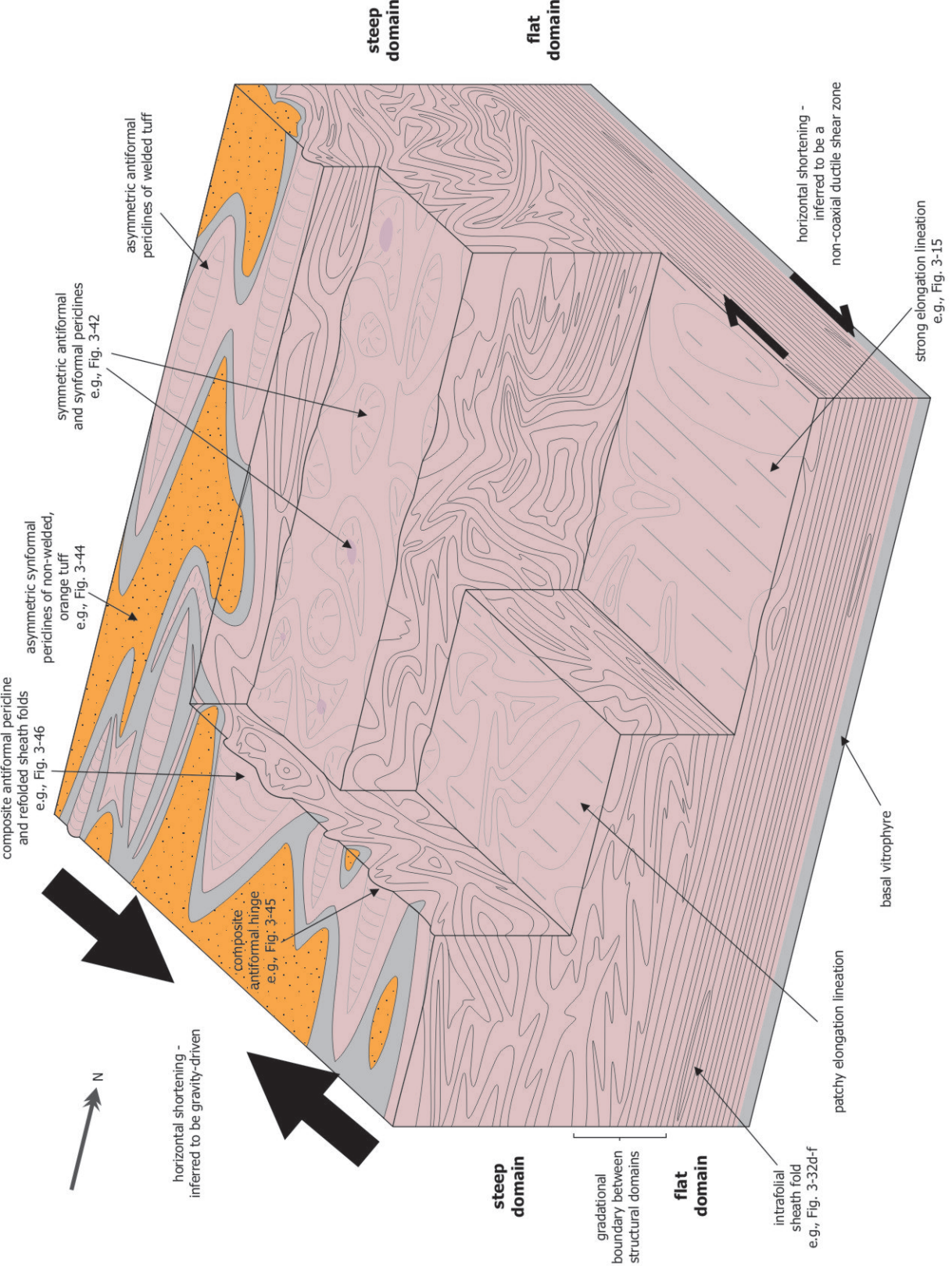
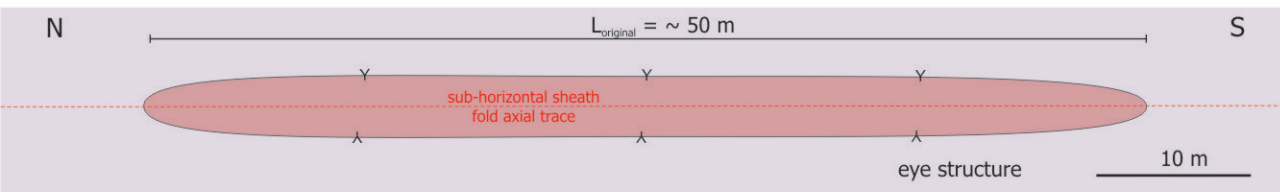


Fig. 3-49. Schematic sketch summarising the distribution of the flat and steep fold domains in thick ignimbrite, e.g., Grey's Landing. Based on field observations from throughout the field area; no single locality or vertical section displays all the features represented here.

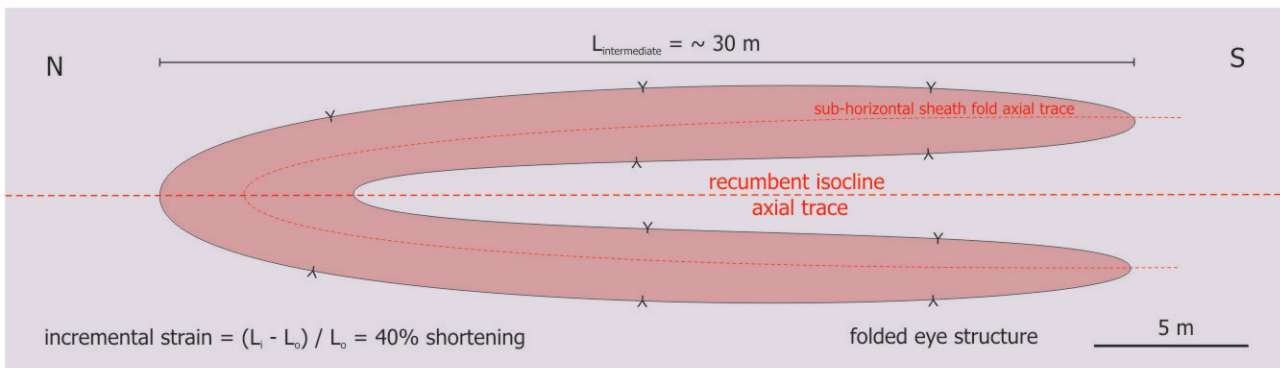
1. inferred, initially sub-horizontal lithological layering.



2. formation of intrafolial, E - W trending sheath fold.



3. sheath fold refolded into an extrafolial, recumbent isocline. Inferred fold axis trend E - W.



4. N - S trending, layer-parallel shortening forms upright antiforms and synforms.

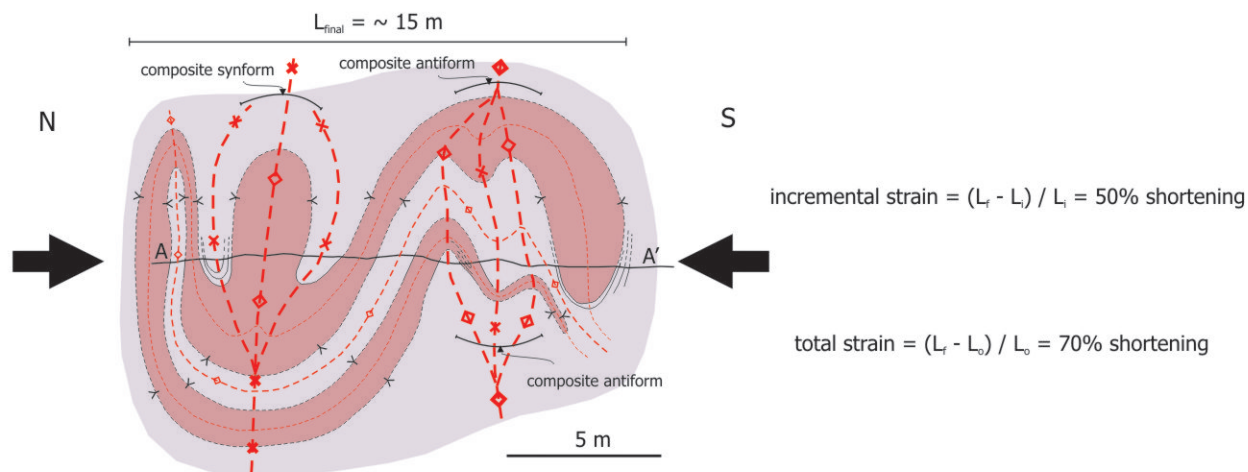


Fig. 3-50. Steep domain: deformation at the upper surface. Four stage evolution of folded tuff at Cedar Creek (detailed map 3; Fig. 3-??). 1 - inferred, initially sub-horizontal lithological layering, between massive lithoidal tuff and overlying flaggy, lithophysal tuff. 2 - formation of a large (~ 50 m), sheath fold, trending E - W parallel to local elongation lineation. 3 - sheath fold is folded into a E - W trending recumbent isocline (N closing). This may be due to continued E - W stretching, or low-angle N - S trending, non-coaxial shear. 4 - N - S trending, layer-parallel shortening produces extrafolial, upright antiforms and synforms. Totally shortening is approximately 70%.

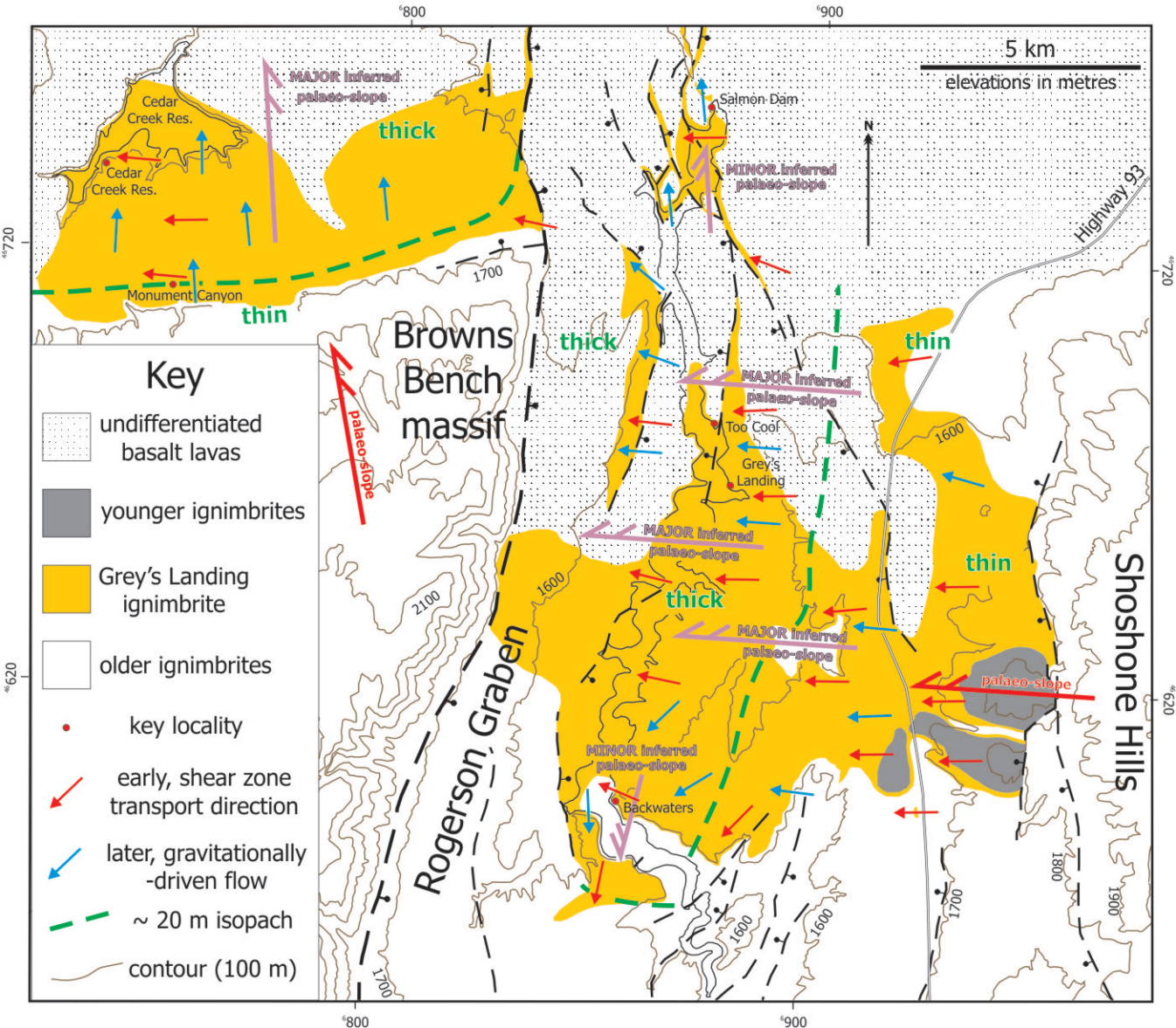


Fig. 3-51. Summary of inferred transport directions during the emplacement of the Grey's Landing ignimbrite. Transport directions related to an 'early' ductile shear zone are generally from east to west, and do not appear influenced by the inferred underlying palaeo-slope. Transport directions related to 'late', gravitationally-driven flow are typically from east to west within the Rogerson Graben, and from south to north along the northern flank of Browns Bench massif. These transport directions are parallel to the local inferred palaeo-slope.

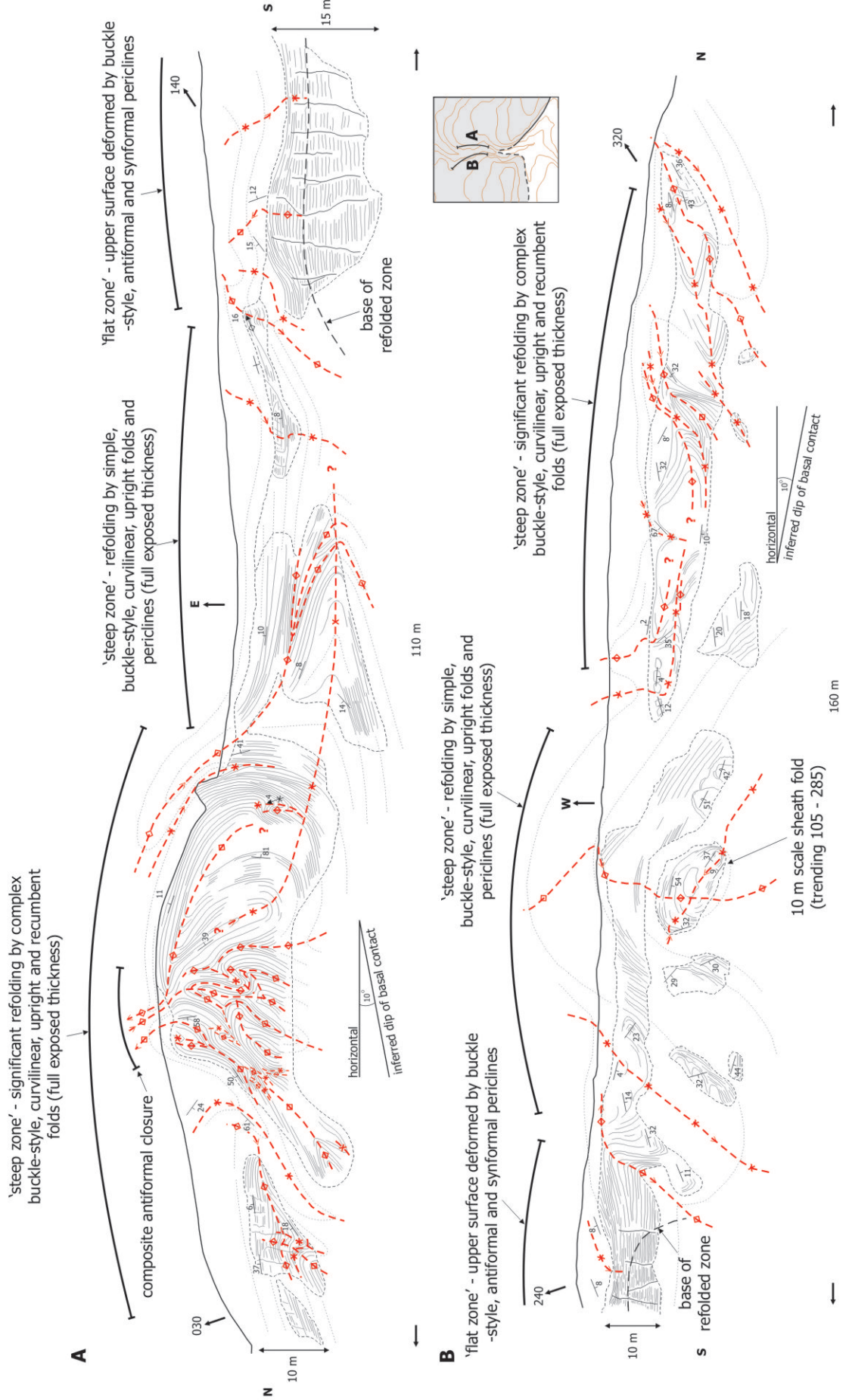


Fig. 3-53. Field-sketches of cross-sectional canyon-wall exposures in Monument Canyon (inset). (A) east wall. (B) west wall. Note the consistent change in fold wavelength and amplitude from south to north, down-slope; and the identification of flat and steep domains. Representative structural measurements and inferred traces of fold axial planes are shown.

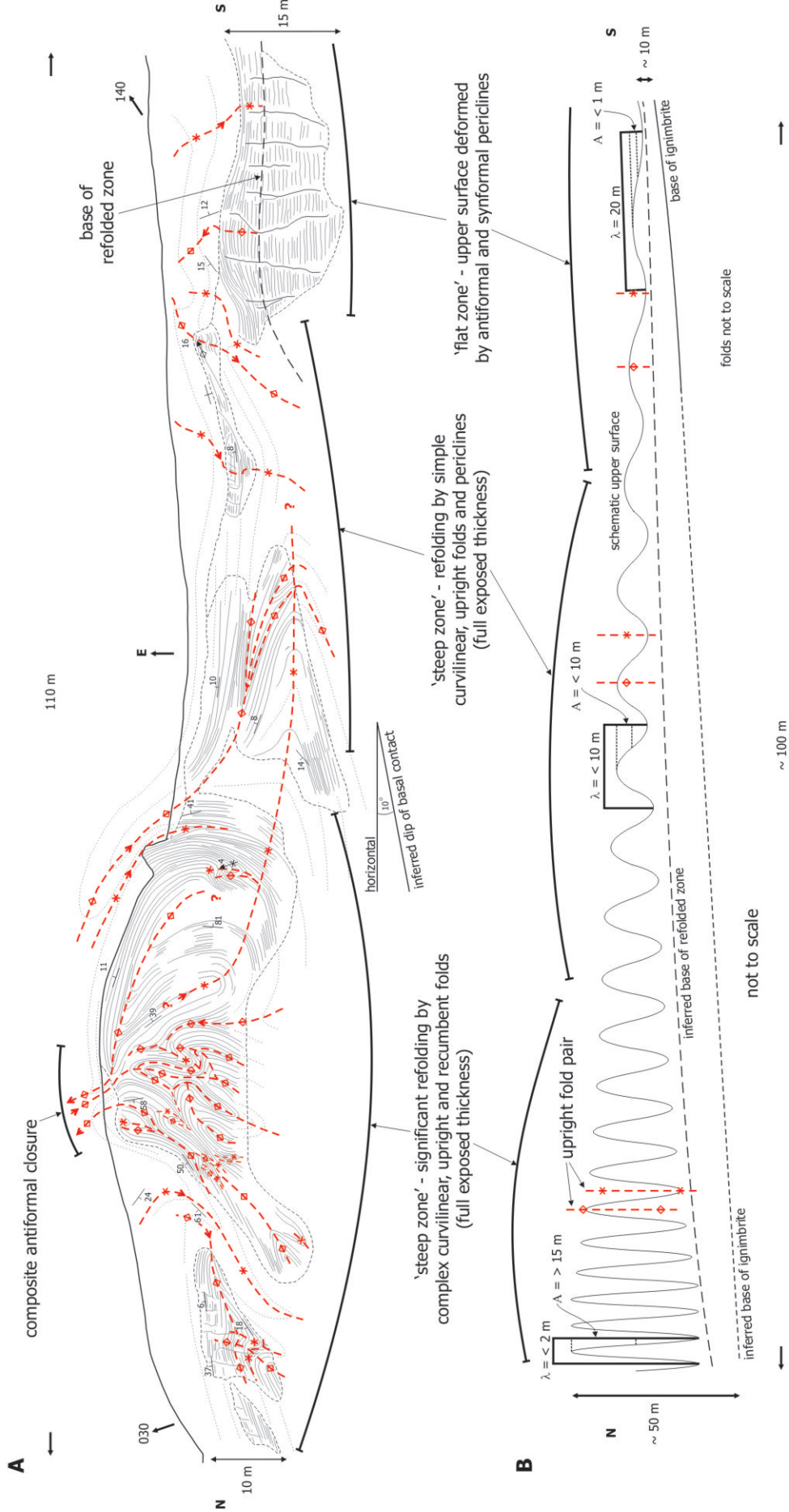


Fig. 3-54. Change in fold wavelength and amplitude down-slope. (A) field-sketch cross-section of the east wall of Monument Canyon (Fig. 3-??). (B) schematic representation of fold wavelength and amplitude in a hypothetical layer (e.g. the upper surface). Note the increasing thickness of the refolded zone ('steep zone'). All folds are assumed to be upright and symmetric, and subordinate complexity (e.g. refolding of earlier folds) is ignored.

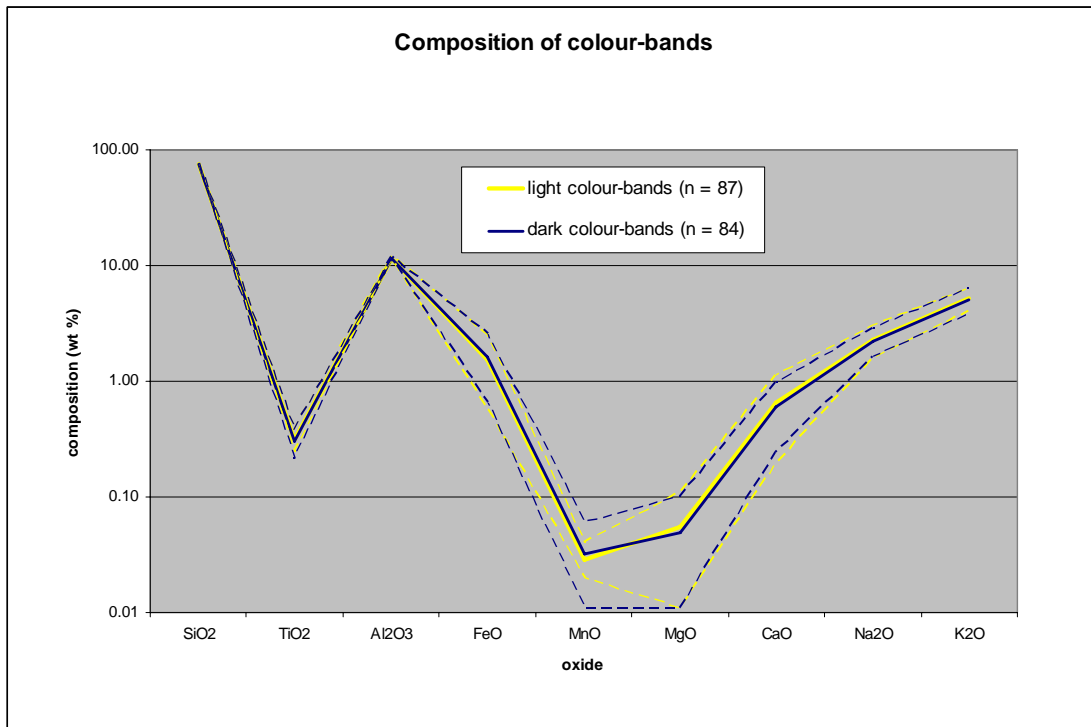


Fig. 3-7. Comparison of glass compositions in light and dark colour-banded vitrophyre samples from four localities in the Grey's Landing ignimbrite. Solid line is the mean composition, dashed lines are 1 standard deviation about that mean. Note how there is no significant difference between light and dark bands. Electron microprobe analyses.

Chapter 4:

Constraints on the rheological evolution of the Grey's Landing ignimbrite

Introduction

Objective

Chapter 3 presented evidence of two phases of ductile deformation within the Grey's Landing ignimbrite, that must have initiated, and operated largely, before the onset of a 'stiff' brittle rheology. The first phase of deformation was dominated by a widespread, sub-horizontal ductile shear zone that affected the entire unit, including the very base. Therefore it was probably present and active throughout the deposition of the ignimbrite: syn-depositional. The second deformation was a heterogeneous fold-dominated phase, and is inferred to be a gravity-driven ductile flow down the palaeo-slope after deposition of a significant proportion of the ignimbrite: post-depositional. This opens two lines of enquiry for further investigation: (1) what pre-eruptive conditions favoured the formation of the Grey's Landing ignimbrite as a lava-like rheomorphic deposit (syn-depositional deformation); and (2) how did the physical properties of the ignimbrite change after deposition and how did they control post-depositional rheomorphism?

Therefore, the purpose of this chapter is: (1) to constrain the physical parameters (e.g. viscosity, temperature, composition, volatile composition, and crystallinity) of the Grey's Landing ignimbrite from pre-eruptive to post-emplacement static cooling. (2) To constrain the rate of rheological change to provide insights into the duration of post-depositional flow; and (3) to compare and contrast the thermal and rheological evolution of an ignimbrite with a lava. This has not been attempted before for a rheomorphic ignimbrite.

Chapter outline

Because rheology is influenced by so many parameters (e.g., viscosity, strain rate) and varies so much in natural magmas (fluidal pahoehoe basalts versus ‘sticky’ rhyolite domes), it is necessary to apply a holistic method to constrain and understand rheological change within a single deposit (Fig. 4-1). I shall present new geochemical data from the Grey’s Landing ignimbrite, review field evidence described in Chapters 2 and 3, and integrate these with published volatile composition and stress estimates (Fig. 4-1). These data will be used as starting parameters for geothermometry, and petrological and thermal modelling, where appropriate (Fig. 4-1). Modelling results will be compared with field observations where possible. Finally, semi-independent estimates of viscosity (Fig. 4-1), and assessment of rheology, can be made for different stages of the ignimbrite’s emplacement: (1) pre-eruptive; (2) syn-depositional and initial rheomorphism; and (3) later, post-depositional rheomorphism.

Background: rheological control on volcanic processes

As discussed in Chapter 1 in the context of welding, rheology is the most important and variable physical characteristic affecting volcanic processes (Griffiths, 2000; Bagdassarov and Pinkerton, 2004). For example, the rheology of a melt will control whether it passively de-gases or erupts explosively, and it will control how far, and for how long, a lava can flow (Griffiths, 2000). The rheology of a material describes how it responds to an applied stress (Chapter 1); most materials will behave in either a ductile (they flow plastically) or brittle (they fracture) fashion (Webb, 1997). The rheology of a magma or lava is constantly changing in response to a plethora of changes in its physical properties (e.g., viscosity, temperature, flow-rate, composition, vesicularity, and crystallinity), and can only be analysed qualitatively. Typically lavas evolve from ductile to brittle rheologies with time and distance travelled.

Measuring ‘effective’ viscosity: a holistic methodology

Viscosity is the most important physical property controlling the rheology of a material, and is also the most variable (through 15 orders of magnitude; Rust,

2003). It is strongly influenced by other physical parameters (e.g., temperature, volatile composition and content, vesicularity, crystallinity; Chapter 1, Figs 1-19; 1-20). Because viscosity is so strongly influenced by other parameters, many of which are time variant (e.g., temperature and dissolved volatile content), viscosity itself is strongly time variant; from ‘low’ in the magma chamber to ‘high’ at the cessation of ductile flow (Fig. 4-2). Therefore, it is more useful to consider the ‘effective’ viscosity at different stages of the evolution of a lava or lava-like ignimbrite (e.g., Stevenson et al., 2001).

Several different techniques have been applied to measure viscosity directly in active lavas and lab-based experiments, and to estimate viscosity in ancient lavas. Three semi-independent methods are commonly used: (1) exploiting the relationship between viscosity, shear stress and strain rate; (2) petrological modelling and comparison with experimentally derived viscosity estimates; and (3) assessing the fluid dynamics of gravity-flows.

Viscometry – relationship with shear stress and strain rate

Viscometric studies of super-liquidus lavas and synthetic melts typically apply the relationship between viscosity, shear stress and strain rate:

$$\eta = \tau / \dot{\epsilon} \quad (1)$$

a simplification of the Bingham flow law (Shaw, 1969; Murase and McBirney, 1973; McBirney and Murase, 1984), where η is viscosity in Pa.s⁻¹, τ is shear stress in Pa, and $\dot{\epsilon}$ is strain rate in dimensionless strain per unit time (s⁻¹) (Griffiths, 2000). This relationship is linear (i.e. no yield strength has to be exceeded to induce flow), and is described as Newtonian (Webb, 1997). In contrast, sub-liquidus lavas (the majority of silicic lavas) are non-Newtonian and the above relationship is often strongly non-linear (Webb, 1997).

Field studies and laboratory experiments typically use torsion viscometers, where a paddle is rotated within a melt (e.g., Bagdassarov, 2005), and the rate of rotation (non-coaxial strain) ($\dot{\epsilon}$) and the resistance to rotation (τ) are known. Similar experiments make use of coaxial strain (e.g., Lejeune and Richet, 1995).

Experimentally-derived estimates of the viscosity of the Grey's Landing ignimbrite, across a range of temperatures, are presently being conducted at the University of Missouri.

I will apply this technique to constrain the viscosity of the ignimbrite at deposition and during syn-depositional rheomorphism. This is achieved by combining estimated strain rates, obtained from field observations and thermal modelling, with published shear stress estimates of pyroclastic density currents and lavas (Fig. 4-1; e.g., Ventura et al., 1996).

Viscometry – empirical modelling: MAGMA software

Seminal estimations of silicate melt viscosity by Bottinga and Weil (1972) and Shaw (1972) were empirically derived from experiments carried out over a range of compositions and temperatures. They, for the first time, quantitatively showed the first-order controls of temperature and composition on viscosity. Both investigations assumed an Arrhenian model for melt viscosities:

$$\log \eta = A + \frac{B}{T} \quad (2)$$

where η is viscosity in $\text{Pa}\cdot\text{s}^{-1}$, A and B are parameters determined by the composition, and T is the temperature in K (Bottinga and Weil, 1972; Shaw, 1972). Despite its age and simplicity, this relationship is still accepted as valid for super-liquidus melts, especially rhyolitic melts (Russell et al., 2003). More complex non-Arrhenian models are currently being investigated to describe a range of melt compositions at or below their liquidus (e.g., Giordano and Dingwell, 2003; 2004). These models do not consider the effects of crystal and vesicle content, or the concentration and speciation of volatiles.

The MAGMA (v. 2.48) software package (Wohletz, 2004) incorporates the empirical equations of Bottinga and Weil (1972) and Shaw (1972), and allows for the rapid and straight-forward estimation of viscosities from samples analysed for bulk rock composition (e.g., XRF analyses), or glass composition (e.g., EMP analyses). Furthermore, the effects of vesicle and crystal content are incorporated through application of the Einstein – Roscoe equation (McBirney and Murase,

1984), where volatile contents are used to infer the vesicularity. Melt densities are calculated using the technique of Bottinga and Weil (1972).

I calculate estimated viscosities for glass analyses from the Grey's Landing ignimbrite using the equations of Bottinga and Weil (1972) and Shaw (1972) through the MAGMA (v. 2.48) software package (Wohletz, 2004). Entry parameters come from observations of crystallinity and vesicularity, geothermometry, and comparison with inferred volatile contents in analogous ignimbrites and lavas.

Viscometry – fluid dynamics

The viscosity of active lava flows can be estimated by considering its fluid dynamics. The velocity of a lava of known thickness and density can be measured as it flows down a known slope, and the Jeffreys' equation applied (Jeffreys, 1925; Nichols, 1939):

$$\eta = \left(\frac{\rho g t^2}{3V} \right) * \sin(\alpha) \quad (3)$$

where η is viscosity in $\text{Pa}\cdot\text{s}^{-1}$, ρ is melt density in kg/m^3 , g is gravitational acceleration ($9.806 \text{ m}/\text{s}^2$), t is the thickness of the flowing melt in metres, 3 is a constant related to flow of a sheet-like body, V is the velocity in m/s , and α is the slope angle. The Jeffreys' equation assumes super-liquidus conditions, a Newtonian rheology, a constant flow velocity, and a constant slope. Thermal effects are incorporated in the density function (ρ). Volatile concentration and content, vesicularity and crystallinity are not considered.

This technique can be applied for ancient lavas by incorporating assumed flow velocities inferred from modern examples. Typically, application is limited to well-exposed lavas where the basal palaeo-slope can be inferred and the thickness is measured (e.g., Manley, 1992; Stevenson et al., 1994; Stevenson et al., 2001). This technique is most appropriate for assessing the viscosity of the steep domain in the Grey's Landing ignimbrite, as it is broadly analogous with a lava (Chapter 3; Fig. 3-27).

Another common fluid dynamic techniques uses Stoke's Law to measure the resistance to flow of falling spheres in synthetic melts (e.g., Scaillet et al., 1996; Manga et al., 1998).

Background: temporal trends of physical parameters

The evolution of a rheomorphic ignimbrite can be considered as a seven-stage process: process within the magma chamber, explosive eruption, particulate transport, deposition, welding, rheomorphic flow, and static cooling (Fig. 4-2). Throughout the evolution of the ignimbrite, many of the physical properties of the melt, and subsequent glass, are changing. For example, rheology, viscosity, temperature and volatile behaviour are all time variant (Fig. 4-2), and they typical display non-linear temporal changes.

Temperature evolution: cooling history

The huge range of viscosities exhibited by silicate melts (see above) is typically the result of changes in temperature and volatile behaviour. Temperature and volatile behaviour exhibit the greatest control on viscosity (see Chapter 1; Fig. 1-19). Intuitively, temperature decreases with time throughout the evolution of a lava or rheomorphic ignimbrite (Fig. 4-2); from 'high' magmatic temperatures within the magma chamber ($\geq 800^{\circ}\text{C}$; Murase and McBirney, 1973) to 'low' temperatures during static cooling ($\geq 100^{\circ}\text{C}$; Hogeweg et al., 2005), to ambient temperatures ($\leq 50^{\circ}\text{C}$). Cooling during and between different stages is likely to be strongly non-linear, for example, heat loss during explosive eruption is likely to be orders of magnitude more rapid (100s $^{\circ}\text{C}$ per second; Wilson et al., 1987; Valentine, 1998) than during static cooling ($\leq 10\text{s}$ $^{\circ}\text{C}$ per year; Manley, 1992; Wallace et al., 2003).

Estimating temperature: conceptual framework and methodology

Magmatic temperatures can be estimated for ancient lavas and ignimbrites (see below), however, the temperature evolution after eruption is not readily constrainable. Depositional temperature, deposition rate, rheomorphism, welding, porosity, permeability, crystallisation (devitrification), the thermal structure of the

substrate, and precipitation, all influence the cooling rate of an ignimbrite (Riehle et al., 1995; Bursik and Woods, 1996; Wallace et al., 2003; Wilson and Hildreth, 2003; Keating, 2005; Sheridan and Wang, 2005). However, constraints can be placed on cooling at some increments of an ignimbrite's evolution (Fig. 4-2), for example, cooling during transport in a pyroclastic density current (Bursik and Woods, 1996), and cooling after deposition (e.g., Manley, 1992). I shall incorporate estimated cooling rates during transport by pyroclastic density currents, and apply a 1D cooling model to constrain cooling rates within the deposit (Fig. 4-1).

Pre-eruptive, magmatic temperatures are typically estimated from empirical thermodynamic equations governing the diffusion of elements between pairs of adjacent or proximal minerals. Many different geothermometers exist covering a broad range of mineral compositions (e.g., feldspars and pyroxenes) and temperatures. Typically more than one geothermometer is used to constrain the pre-eruptive temperature, thereby minimising the effects of different blocking temperatures in different minerals (e.g., Honjo, 1990). I shall apply this technique to provide starting temperature parameters for thermal and petrological modelling (Fig. 4-1).

Magmatic temperature can also be constrained by estimating the liquidus temperature of volcanic glass (Sisson and Grove, 1993; Ghiorso and Sack, 1995). These complex, multi-component equations are incorporated into the MELTs (Ghiorso and Sack, 1995; Asimow and Ghiorso, 1998) and MAGMA (Wohletz, 2004) software packages. MELTs takes whole-rock compositional data and the identified crystal phases present and establishes a liquidus temperature. In contrast, MAGMA takes major element analyses of the glass matrix, inferred to best represent the original liquid.

Volatile behaviour: degassing history

Significant volatile-loss is also intuitive; typically decreasing continuously from eruption from the magma chamber to eventual static cooling (Fig. 4-2).

Typically, the removal of volatiles from the melt or glass increases its viscosity (Lange, 1994). Volatile exsolution also drives explosive eruptions (Dingwell,

1998), adds to the buoyancy of Plinian eruption columns (Valentine, 1998) and pyroclastic density currents (Bursik and Woods, 1996), and contributes to fumarolic activity in ignimbrites (e.g., Hogeweg et al., 2005). Volatile behaviour is itself strongly influenced by complex interactions between numerous physical properties; including temperature (e.g., Blank et al., 1993), crystallisation (e.g., Hort, 1998; Cashman and Blundy, 2000), lithostatic and gas pressure (e.g., Blank et al., 1993), volatile content, solubility and composition (e.g., Carroll and Webster, 1994), and melt composition (e.g., Holtz et al., 1992; 1993). Exsolution of volatiles occurs at all stages of rheomorphic ignimbrite evolution (Fig. 4-2). This is demonstrated in the Grey's Landing ignimbrite by the presence of both deformed vesicles (pre- and syn-rheomorphic; Fig. 3-13) and non-deformed vesicles (post-rheomorphism; Fig. 2-15c).

Certain volatile species significantly affect the viscosity of silicate melts, and therefore, it is important to constrain their original concentration and exsolution history from the melt or glass. Typically water and halogens (F and Cl) have the greatest influence on viscosity (Lange, 1994). Water is typically abundant in evolved silicate glasses from explosive eruptions (≤ 8 wt %; e.g., Anderson et al 1989; Bacon et al., 1992; Johnson et al., 1994), however, the solubility of water is significantly reduced by cooling, reduction in pressure, and the onset of crystallization. Therefore, the rapid exsolution of water is the most common trigger of explosive eruptions (Cashman and Blundy, 2000). Because of this, water is typically not concentrated in the degassed glass after eruption (≤ 0.2 wt %; Blank et al., 1993). In contrast, halogens have lower concentrations (typically ≤ 5 total wt %; Carroll and Webster, 1994). Chlorine readily exsolves in water-rich melts and is lost to free-fluid phases, therefore, it remains most concentrated in high-temperature, relatively anhydrous melts (Carroll and Webster, 1994). Fluorine has a higher solubility and remains in the silicate glass, even after partial crystallisation and explosive eruption (Dunbar and Kyle, 1992; Carroll and Webster, 1994). Some high-temperature (≥ 950 °C) rhyolite lavas have exceptionally high F contents (≤ 3 wt %) and low water contents (≤ 2 wt %), inferred to demonstrate F concentration in the melt during sustained degassing of water (Webster and Duffield, 1991; 1994; Manley and McIntosh, 2002).

Estimating volatile content

Silicate melts can be considered as three-phase systems composed of liquid, crystals, and gas (Cas and Wright, 1987). The relative proportions, and compositions of each phase change with time, for example, volatiles are lost to the atmosphere and liquid gradually crystallises. Melt inclusions, preserved as glass blebs, are commonly trapped within crystals, providing a ‘time-capsule’ of an earlier liquid composition and the dissolved volatile content within it (Ihinger et al., 1994; Frezzotti, 2001). Therefore, by analysing melt inclusions trapped in crystals or crystal rims inferred to have formed at or just before eruption, it is possible to estimate the melt composition and dissolved volatile content (Wallace et al., 1995). These data are important parameters in estimating the pre-eruption viscosity. Furthermore, by comparing the composition of glass in erupted tephra and that in melt inclusions, it is possible to constrain the composition and volume of volatiles released during the eruption (e.g., Bacon et al., 1992; Dunbar and Kyle, 1992). Analyses of volatile contents from glass in tephra helps to constrain the viscosity of glassy deposits, for example, high-grade ignimbrites.

The concentration and composition of volatiles within the Grey’s Landing ignimbrite glass is not well-constrained. This study has not examined melt inclusions in crystals, although this may be attempted in the future. Rather, I produce analyses of Cl concentrations within the preserved glass (vitrophyre), and anecdotal evidence of low water contents and elevated halogen contents (Fig. 4-1). There are no published volatile data for comparable high-grade ignimbrites elsewhere in the Snake River Plain volcanic province, or elsewhere in the world. Where data are available for lava-like rhyolites (e.g., Etendeka – Parana; Kirstein et al., 2001), they have not been demonstrated to be ignimbrites rather than lavas.

Physical constraints on the viscosity of the Grey’s Landing ignimbrite

Geochemical data

The Rogerson Formation is composed of five welded ignimbrites and intercalated fall and volcaniclastic deposits (see Chapter 2; Fig. 2-6). Geochemical analyses

were carried out on the welded Jackpot, Rabbit Springs, Brown's View, Grey's Landing and Sand Springs members for two reasons: (1) to characterise each member and provide a geochemical 'finger-print' to assist regional correlation; and (2) provide bulk rock, crystal and glass compositions for geothermometry, and thermal and petrological modelling (Fig. 4-1).

Analytical methods

All whole-rock samples were prepared and analysed at the University of Leicester, using a Philips PW1400 X-ray fluorescence spectrometer (XRF). Sample measurements were standardised against recognised international standards. Spot analyses of glass shard and crystal compositions (re-calculated to 100 wt. %) were analysed on a JEOL 8600 S electron microprobe (EMP) at the University of Leicester, using a 15 kV accelerating potential, 30 nA incident current, and 5 µm and 10 µm spot size respectively.

Bulk-rock data

Description

The Rogerson Formation is composed of rhyolites and rhyodacites (68.25 – 75.7 % SiO₂; Fig. 4-3a). Compositions lie on, or close to, the alkaline – tholeiitic boundary. The ignimbrites are typically metaluminous to mildly peralkaline (aluminosity index 0.9 – 1.05 (molar Al₂O₃ / Na₂O + K₂O + CaO) Rollinson, 1993; Fig. 4-3b). They all exhibit a typical A-type granitoid signature; relatively high concentrations of TiO₂, Fe₂O₃, high field strength elements (e.g., Zr, Nb, U, REEs), and relatively high Ga/Al and Fe₂O₃*/MgO ratios (Collins et al., 1982; Whalen et al., 1987; Rollinson, 1993; Appendix 1). Typically the Grey's Landing ignimbrite has higher high field strength element concentrations than the other members of the Rogerson Formation. Zr, Nb, and Ga characteristically exhibit incompatible behaviour in all members (Figs 4-4a; 4-4b).

Loss-on-ignition data shows inferred volatile contents (Rollinson, 1993) between 0.5 to 4.5 wt %, that are observed to decrease relative to incompatible elements (e.g., Zr; Fig. 4-5a). Chlorine is typically 100 – 1000 ppm, with maximum values

of ~ 25000 ppm (2 – 3 wt %) in two Grey's Landing analyses (Fig. 4-5b). Chlorine also decreases relative to incompatible elements (e.g., Zr).

Interpretation

Field evidence of volatile enrichment in the Grey's Landing ignimbrite (e.g., abundant vesicles) is supported by bulk rock data; both primary data (e.g., LOI, Cl) and anecdotal evidence (e.g., incompatible element behaviour). Loss-on-ignition data is typically interpreted to approximate to the total dissolved volatile content of the rock, for example, H₂O, CO₂, SO₂, and an unknown proportion of halogens (Rollinson, 1993). Total volatile content is moderate (≤ 4 wt %) and appears to decrease with evolution of the liquid (represented by increasing concentration of incompatible elements, e.g., Zr). This temporal decrease is typically interpreted as degassing of the magma (Fig. 4-5a), following exsolution of progressively less soluble volatile species (Carroll and Webster, 1994; Wallace et al., 1995). Degassing may be passive and sustained, or explosive.

Chlorine shows a similar decrease from initially high concentrations (≤ 3 wt %) to low concentrations (~ 100 ppm; Fig. 4-5b). I interpret this progressive decrease in dissolved Cl to be the result of Cl-degassing, either during explosive eruption or during sustained, passive degassing prior to eruption. Chlorine readily exsolves from silicate liquid when a hydrous vapour phase is present (Carroll and Webster, 1994). Because water is less soluble than Cl, it is reasonable to assume that any H₂O originally dissolved in the liquid had been liberated earlier, and was therefore available to form a hydrous vapour phase, thereby encouraging Cl exsolution.

Anecdotal evidence provides insights to the presence, concentration, and behaviour of fluorine in the liquid. Because F and Cl are both halogens, it is a reasonable assumption that F and Cl behaviour is similar: where measured Cl concentrations are high, F concentrations are likely to be high. The F / Cl ratio for silicate Earth, upper continental crust and granites is between 0.95 – 3.98 (McDonough and Sun, 1995; Wedepohl, 1995; Gao et al., 1998), therefore, for maximum Cl concentrations of ≤ 3 wt %, F is inferred to be ≤ 5 wt % (Fig. 4-5b). Moreover, F is more soluble than Cl (≤ 5 times; Carroll and Webster, 1994), and

therefore, is likely to remain in the liquid during sustained degassing of other volatiles, and explosive eruption. Elevated F contents are supported by the moderate concentrations of similarly incompatible elements, for example Zr and Nb, where they can be used as proxies for F (Fig. 4-4a; Bailey and MacDonald, 1975; Kirstein et al., 2001). Furthermore, the incompatibility of Ga may be an indicator of high F concentration (Fig. 4-4b). Usually Ga is strongly compatible with feldspar, however, it is strongly incompatible in the presence of abundant F, where F-based complexes ‘tie-down’ Ga, Zr and Nb, in the liquid (Kirstein et al., 2001).

Influence on viscosity

Bulk rock data suggest two, opposing, influences on the viscosity of the Grey’s Landing liquid / glass. The Grey’s Landing ignimbrite is close to metaluminous (Fig. 4-3b), ideal for polymerisation of the melt and a ‘high’ viscosity (McBirney and Murase, 1984; Dingwell et al., 1985; Dingwell and Hess, 1998; Giordano et al., 2004; 2005). In contrast, there is evidence of moderate to high volatile contents (possibly ≤ 10 wt %), including high concentrations of halogens. Water and halogens are significant viscosity-reducing agents in silicate melts (Shaw, 1963; Dingwell and Mysen, 1985; Persikov et al., 1990; Lange, 1992; Stevenson et al., 1998). Furthermore, elevated F concentrations are likely to remain in the liquid / glass and affect the viscosity of the glass after eruption and deposition.

Glass composition data

Description

Spot analyses of welded glass shards from the lower and upper vitrophyres of the Grey’s Landing ignimbrite are presented in Appendix 2. Analyses were only taken from the apparently least altered vitrophyre (i.e. oxidation of Fe, devitrification, perlitisation, hydration) to limit uncertainties introduced by crystallisation or hydration.

Glass in the lower vitrophyre (75 – 77 wt %) is more silicic than in the upper vitrophyre (70 – 75 wt %; Figs 4-6a; 4-6b). Two discrete compositional groups

Chapter 4 Constraints on the rheological evolution

are defined by different alkali contents: (1) a high alkali group (≥ 8 wt % Na₂O + K₂O), and (2) a low alkali group (≤ 6 wt % Na₂O + K₂O; Fig. 4-6c). There is a distinct compositional gap between the two groups. The high alkali group is observed in both lower and upper vitrophyre, in contrast, the low alkali group is only observed in the lower vitrophyre (Fig. 4-6c). The two compositional groups exhibit different aluminosity indices (Fig. 4-6d), the high alkali group is metaluminous or mildly peralkaline (0.9 – 1.0), whereas the low alkali group is strongly peraluminous (1.4 – 1.7).

Interpretation

Vertical differences in glass composition may be the consequence of compositional stratification in the original magma chamber, where an ignimbrite provides an inverted section through the original magma chamber's geochemical stratigraphy (e.g., Hildreth, 1979; 1981). Assuming straightforward tapping of a horizontally stratified magma chamber; the first magma tapped would have been at the top of the magma chamber, and would have been deposited first at the bottom of the ignimbrite. This melt would probably be less dense (more SiO₂-rich) than underlying melt. Subsequently, sustained tapping of deeper parts of the magma chamber would reach more dense (less SiO₂-rich) melt, that would be deposited later, and higher in the ignimbrite. Therefore, the Grey's Landing ignimbrite may be the product of a compositionally stratified magma chamber; this interpretation can be tested further by examining crystal compositions.

Influence on viscosity

The two compositional groups have very different aluminosity indices, possibly leading to significant differences in the viscosity of the glass between the lower and upper vitrophyres. The low alkali group is strongly peraluminous, and therefore probably had a lower viscosity than the metaluminous, high alkali group.

Crystal composition

Description

Plagioclase, pyroxene, titano-magnetite, and accessory apatite and zircon are ubiquitous in the ignimbrites of the Rogerson Formation (Fig. 4-7). This is an anhydrous crystal assemblage. They exist as single, often broken crystals (e.g., Fig. 2-15d), and as glomerocrysts of plagioclase, pyroxene, and titano-magnetite (e.g., Fig. 3-17f).

Plagioclase occurs in all units and exists in three textural forms: (1) euhedral crystals with sieve-texture (e.g., Fig. 2-14a); (2) subhedral to anhedral crystals associated with glomerocrysts; and (3) euhedral to subhedral, crystal fragments (Fig. 2-15d). All plagioclase found in Jackpot sub-units 3 and 5 is oligoclase (An 25 – 35; Figs 4-7; 4-8a), however, the plagioclase in ‘Jackpot 7’ and all other members in the Rogerson Formation is andesine (An 35 – An 50; Figs 4-7 and 4-8b). Sanidine crystals (Or 50 – Or 57; Fig. 4-8a) occur only in the Jackpot and Rabbit Springs Members. They have two forms: (1) anhedral crystals with myrmekite rims (Fig. 2-8a) and (2) subhedral crystal fragments. The former are only found in the Jackpot Member, where they are much more abundant than the latter.

Pyroxene crystals occur in all members although those in the Jackpot Member are partly oxidized and hydrated, and altered to amphibole or clay. Non-zoned Ca-rich pyroxene (augite) and Ca-poor pyroxene (pigeonite) are found in equal abundances in all units apart from the Grey’s Landing Member, in which augite is nearly absent from upper sections and minor quantities of hypersthene occur at the base (Fig. 4-7). Pyroxene crystals occur in equal measure in two forms: (1) anhedral crystals associated with glomerocrysts and (2) crystal fragments. Pyroxene compositions are presented with tie lines joining analyses from co-existing crystals (Figs 4-8c; 4-8d).

Titano-magnetite and ilmenite are present in all units other than the Grey’s Landing Member, in which ilmenite is absent (Fig. 4-7). Magnetite exists as both anhedral crystals within glomerocrysts, and as crystal fragments. Ilmenite occurs

Chapter 4 Constraints on the rheological evolution

as discrete anhedral crystals only. Subhedral and anhedral quartz crystals are only found in the Jackpot and Rabbit Springs Members (Fig. 4-7) where they exist as isolated, anhedral crystals. Anhedral apatite and zircon crystals are abundant in all units, commonly as inclusions in Fe-Ti oxides. Discrete apatites and zircons are only found associated with glomerocrysts.

Interpretation

Only the Grey's Landing Member shows any internal variation in crystal assemblage where augite decreases with increasing height and pigeonite remains uniformly abundant. I interpret this to indicate subtle, vertical compositional zonation within the Grey's Landing Member, which in turn, may indicate that it was erupted from a compositionally zoned magma chamber (e.g., Hildreth 1979, 1981), with the most evolved batch of liquid (augite = pigeonite) tapped first, followed by progressively less evolved liquid (augite \leq pigeonite), and finally, the least evolved liquid (augite \ll pigeonite). This interpretation is supported by inferences from glass composition data.

Influence on viscosity

Anhydrous crystal assemblages are characteristic of high-temperature (≥ 900 °C), water-poor (≤ 1 wt %) rhyolitic magmas (e.g., Honjo et al., 1992; Ewart et al., 1998a; 1998b; Riley et al., 2004).

Pre-eruptive temperature: estimates from geothermometry

There is anecdotal evidence that the Grey's Landing magma was 'hot' (i.e. ≥ 900 °C): (1) intense welding and rheomorphism; and (2) an anhydrous crystal assemblage. Magmatic temperature is the principal control on melt viscosity (Murase and McBirney, 1973; McBirney and Murase, 1984), and the principal control on the temperature of the deposit (Manley, 1992; Bursik and Woods, 1996; Wallace et al., 2003). Therefore, better constraints on magmatic temperature are required to allow for meaningful estimates of deposit cooling-rate and viscosity.

Geothermometry methodology

Mineral pair equilibria

Electron microprobe analyses of crystal rim pairs ($n \geq 25$) were used to calculate mean crystal compositions for individual samples referenced for stratigraphic position within each ignimbrite. Mean crystal compositions were input to appropriate Fe-Ti oxide, two-pyroxene, and two-feldspar geothermometers, depending on the different crystal populations of respective members (Fig. 4-7). The use of geothermometry assumes that crystal rims were in equilibrium with the liquid, even if crystal cores may have not re-equilibrated.

Estimates of pre-eruptive temperature from Fe-Ti oxide (magnetite – ilmenite) thermometry and fO_2 were made using (1) the model of Ghiorso and Sack (1991), and (2) the QUILF 4.1 software package (Andersen et al., 1993) applying the model of Andersen et al. (1991) and technique of Manley and Bacon (2000). All Fe-Ti oxide pairs were tested for Mg/Mn equilibrium following the method of Bacon and Hirschmann (1988) before being applied to the two geothermometers, and only samples from the Browns View Member were found to be in equilibrium. The Ghiorso and Sack (1995) model has estimated uncertainties of ± 50 °C. The QUILF software package quotes results with 2σ uncertainties.

Estimates of pre-eruptive temperature from two-pyroxene (augite – pigeonite pairs) thermometry were made in the Rabbit Springs, Browns View, Grey's Landing and Sand Springs Members, using a pressure constant of 5 kbars (e.g., Cathey and Nash 2004). First I applied the model of Andersen et al. (1991) through the QUILF 4.1 software package (Andersen et al. 1993), and secondly I applied the graphical geothermometer of Lindsley (1983) plotted onto the pyroxene quadrilateral (Figs 4-8c; 4-8d), where contours allow visual estimation of equilibrium temperature. The QUILF software package quotes results with 2σ uncertainties. The Lindsley (1983) has estimated uncertainties of ± 50 °C.

Estimates of pre-eruptive temperature from two-feldspar (plagioclase – sanidine pairs) thermometry were made in the Jackpot and Rabbit Springs Members. Using a pressure constant of 5 kbars, the geothermometers of Ghiorso (1984) and

Chapter 4 Constraints on the rheological evolution

Fuhrman and Lindsley (1988) were applied, using the SOLV CALC 1.0 software of Wen and Nekvasil (1994). Both models have uncertainties of ± 50 °C.

Liquidus temperature estimation

X-ray fluorescence whole-rock analyses were entered into the MELTs JAVA-script software package (Ghiorso and Sack, 1995; Asimow and Ghiorso, 1998), along with a list of the phases present: liquid, feldspar, clinopyroxene, oxides. Water content was estimated at 75% of the LOI value. For consistency, a pressure of 5 kbars was used.

Electron microprobe analyses of welded glass matrix were entered into the MAGMA software package (Wohletz, 2004). 1 wt % water was added as part of each data entry. A pressure of 5 kbar was used.

Geothermometry results

Mineral pair equilibria

Magmatic temperatures estimated from mineral pairs are summarised in Figure 4-9. Temperature estimates for the Rabbit Springs, Brown's View, Grey's Landing and Sand Springs Members are typically 850 °C – 1000 °C. The estimated temperature is observed to increase with height in each ignimbrite, for example, from ~ 925 °C to ~ 975 °C in the Brown's View Member, and from ~ 950 °C to ~ 1000 °C in the Grey's Landing Member (Fig. 4-9). The pre-eruptive temperature of the Jackpot Member is significantly lower (≤ 800 °C; Fig. 4-9). Oxygen fugacity estimates of – 11 to – 13 log units are reported from the Brown's View Member.

Liquidus temperatures: MELTs

Liquidus temperatures for the Grey's Landing ignimbrite, estimated from whole-rock analyses by the MELTs software package (Ghiorso and Sack, 1995; Asimow and Ghiorso, 1998), range from 896 °C to 1027 °C (Appendix 1).

Liquidus temperatures: MAGMA

Liquidus temperatures for the Grey's Landing ignimbrite, estimated from welded glass matrix analyses by the MAGMA software package (Wohletz, 2004), range from 925 °C to 993 °C (Appendix 2).

Comparison of temperature estimates

A comparison of all magmatic temperature estimates from the Grey's Landing ignimbrite shows a range between ~ 890 °C and ~ 1030 °C, centred about ~ 950 °C (Fig. 4-10a). Comparison of the mean estimated temperature by each technique (MAGMA, MELTs, QUILF, Lindsley 1983) and for different parts of the ignimbrite (lower vitrophyre, upper vitrophyre, lithoidal ignimbrite) shows good agreement (Fig. 4-10b). Mean temperatures estimated from the upper vitrophyre are typically higher (~ 961 °C) than those from the lower vitrophyre (~ 946 °C), lithoidal ignimbrite is between the two (~ 949 °C; Fig. 4-10b).

Interpretation of geothermometry data

There is a subtle increase in pre-eruptive temperature estimate with height in each member (Fig. 4-9), best displayed by estimates from the QUILF geothermometer which displays the lowest uncertainties ($\leq \pm 20$ °C). I interpret, tentatively, that this suggests compositional zoning within the Rabbit Springs, Brown's View, Grey's Landing and Sand Springs Members, where each time a 'cooler' liquid is tapped first and followed by progressively a 'hotter' liquid from deeper within the magma chamber (e.g., Hildreth 1979, 1981). This interpretation is supported by vertical differences in glass and crystal composition in the Grey's Landing ignimbrite (see above).

Temperature estimates by different techniques agree well for both the lower and upper vitrophyres of the Grey's Landing ignimbrite (Fig. 4-10). The similarity between estimates from whole-rock, glass, and crystal geothermometry within each vitrophyre gives confidence that crystals and liquid were in thermal equilibrium immediately prior to eruption (e.g., Manley and Bacon, 2000). The upper parts of the magma, tapped first and deposited, were cooler (~ 946 °C) than

deeper parts (~ 961 °C) that were tapped and deposited later. Therefore, I have two temporal (early and late) and thermal end-members for viscosity modelling (Fig. 4-1).

Viscometry

Indications of low viscosity

There is anecdotal but strong evidence that the Grey's Landing glass had a 'low' viscosity, ductile rheology during and after deposition: (1) intense welding and rheomorphism (e.g., Grunder and Russell, 2005); (2) high inferred magmatic temperatures and volatile contents (see above); and (3) post-rheomorphic vesicles (e.g., Fig. 2-15c). Magmatic temperature is the principal control on melt viscosity (Murase and McBirney, 1973; McBirney and Murase, 1984), and the principal control on the temperature of the deposit (Manley, 1992; Bursik and Woods, 1996; Wallace et al., 2003). Therefore, better constraints on magmatic temperature are required to allow for meaningful estimates of deposit cooling-rate and viscosity.

Viscometry – empirical modelling: MAGMA software

Starting parameters

Electron microprobe analyses of welded glass matrix (Appendix 2) were entered into the MAGMA software package (Wohletz, 2004). Starting conditions were as follows: (1) temperature = 946 °C for lower vitrophyre samples, and 961 °C for upper vitrophyre samples (Fig. 4-10b); (2) pressure = 5 kbar; (3) crystal and vesicle content = 5 %; (4) crystal and vesicle diameter = 0.5 mm; (5) FeO ratio = 0.61; and (6) water content = 0 wt %.

Results

Viscosity estimates for the Grey's Landing ignimbrite are between 10^6 to 10^{10} Pa.s⁻¹ (Fig. 4-11a). The lower vitrophyre has viscosities ranging from 10^6 to 10^{10} Pa.s⁻¹, in contrast the upper vitrophyre has viscosities ranging from 10^6 to 10^8 Pa.s⁻¹. These values correspond with typical dry rhyolite viscosities at ~ 950 °C

(Fig. 4-11a). Viscosity estimates by the Shaw (1972) model are consistently higher (1 – 4 log units) than those produced by the Bottinga and Weil (1972) model (Figs 4-11a; 4-11b). Estimates by the Shaw (1972) model are inversely proportional to glass liquidus temperature, in contrast, estimates by the Bottinga and Weil (1972) model are temperature insensitive (Fig. 4-11b).

Interpretation

The viscosities estimated for the lower and upper vitrophyres of the Grey's Landing ignimbrite have a limited range, the most significant source of variation is the empirical model applied (Fig. 4-11a). The Bottinga and Weil (1972) and Shaw (1972) empirical models are based on liquidus temperature and composition; they do not take volatile content or composition into account, and therefore, in a volatile-rich melt, these must be considered as maximum estimates. Furthermore, they can only be applied at liquidus and super-liquidus temperatures (Russell et al., 2003) and therefore, $10^6 \text{ Pa}\cdot\text{s}^{-1}$ can only be used to provide an absolute minimum viscosity constraint in the erupted deposit.

Viscometry - fluid dynamics

Starting parameters

The Jeffreys' equation requires the following parameters to be entered (Figs 4-1; 4-12a): (1) flow velocity; (2) slope angle; (3) the density of the flowing material; and (4) the thickness of the flowing material. The mean density of the ignimbrite is constrained at 2436 kg/m^3 by the MAGMA software package (Wohletz, 2004). This leaves flow velocity, flow thickness and slope angle to be varied. Flow velocity is estimated from published data from analogous lava flows, layer thickness is constrained by the thickness of the steep domain (Fig. 3-27), and the slope angle is inferred from field observations.

Results

Maximum flow velocity is constrained by data from Santiaguito, Guatemala, where relatively fast-flowing, dacitic, 'stealth' flows move at $\leq 12.5 \text{ m / day}$ ($1.45 \times 10^4 \text{ m/s}$; Harris et al., 2002). This is the highest observed velocity for a dacitic

or rhyolitic flow. Therefore, the viscosity of a 30 m thick layer (approximate thickness of the steep domain; Fig. 3-27) flowing down a 10° slope (e.g. at Monument Canyon; Fig. 3-52), is $\geq 10^{10}$ Pa.s⁻¹ (Fig. 4-12c).

Viscosity is inversely proportional to flow velocity, and proportional to both slope angle and layer thickness (Fig. 4-12b). Therefore, a relatively thick, slow-flowing layer on a steep slope is much higher viscosity than a thin, fast-flowing layer on a gentle slope. Furthermore, for a given layer thickness and slope angle, viscosity and flow velocity are directly inversely proportional. The minimum viscosity is constrained by the empirical liquidus viscosity ($\geq 10^6$ Pa.s⁻¹).

Interpretation

The estimated effective viscosity of $\geq 10^{10}$ Pa.s⁻¹ is similar to those proposed for other ancient rhyolite lavas, including: (1) Bruneau – Jarbidge eruptive centre, Idaho, $10^{10} - 10^{12}$ Pa.s⁻¹ (Manley, 1992); (2) Okataina volcanic centre, Taupo, $10^{10} - 10^{11}$ Pa.s⁻¹ (Stevenson et al., 1994); and (3) Ben Lomond flow, Taupo, $10^{10.5} - 10^{11.5}$ Pa.s⁻¹ (Stevenson et al., 2001). The viscosity estimated is strongly dependent on the flow velocity applied, and therefore, if a slower flow was inferred there would be a corresponding increase in viscosity.

Viscometry – relationship with shear stress and strain rate

Introduction and methodology

The relationship between viscosity, strain rate and stress (equation 1) can be constrained by understanding the temporal limit of ductile deformation within the Grey's Landing ignimbrite (Fig. 4-1). The glass transition temperature (T_g) (Chapter 1; Fig. 1-19a) is inferred to represent the ductile – brittle transition (Ryan and Sammis, 1981; Giordano et al., 2005). By modelling the cooling of the deposit it is possible to predict when different levels in the deposit will cool through T_g . The finite strain estimated from field observations (Chapter 3) can therefore be limited temporally, and a strain rate established.

Data: temporal constraints on rheomorphism

Introduction, parameters and assumptions

Two distinct phases of rheomorphism are inferred from field observations: (1) ‘early’ rheomorphism in a ductile shear zone, inferred to be synchronous with or immediately after deposition; and (2) ‘late’ rheomorphism associated with gravity-driven, down-slope flow of a large volume of the deposit. By constraining the maximum duration of ductile deformation it is possible to estimate the viscosity of the ignimbrite during syn-depositional rheomorphism, and the shear stress experienced by the ignimbrite during post-depositional rheomorphism (Fig. 4-1).

A one dimensional finite difference thermal model (Manley, 1992; Manley and Andrews, 2004) was applied to the Grey’s Landing ignimbrite. The model solves for temperature thus:

$$T[N] = \frac{K * t_s * \left(\frac{OT[N+1] - 2(OT[N]) + OT[N-1]}{D^2} \right)}{1 - \left(\frac{Lh[N]}{C_p[N] \rho[N]} \right)} + OT[N] \quad (4)$$

where T is temperature, $[N]$ specifies the vertical position (node) in the flow where T is calculated, K is thermal diffusivity ($10^{-2} \text{ cm}^2 \text{ s}^{-1}$), t_s is the length of a time increment (0.1 years), OT is temperature at the previous time increment, D is the node spacing (3 m), Lh is the latent heat evolved (7525 kJ kg^{-1}), C_p is the heat capacity ($1.3 \text{ J g}^{-1} \text{ K}^{-1}$), and ρ is the density (2436 kg/m^3). For each increment, the temperature is calculated at equally spaced nodes through the flow and 60 m into the underlying substrate. The temperature of the upper margin of the deposit is fixed at $0 \text{ }^\circ\text{C}$. At instantaneous deposition ($t = 0$) the underlying substrate is $0 \text{ }^\circ\text{C}$ and the contact is the mean of the deposit and substrate temperatures (i.e. emplacement $T / 2$).

The substrate is modelled to resemble the stratigraphy $\leq 60 \text{ m}$ below the Grey’s Landing ignimbrite; the Rabbit Springs ignimbrite (welded), the undifferentiated volcanics (non-welded), the Brown’s View ignimbrite (welded), and the

Backwaters Member (non-welded; Fig. 2-6). The overlying non-welded tuff is not included in the model because its maximum thickness is unconstrained.

The model only accounts for heat-loss by conduction to the underlying substrate and the air (i.e. no advection (rheomorphism), no convection by meteoric water, no degassing), and superheating of precipitation (~ 150 cm / year). Therefore, the cooling rate is likely to be significantly underestimated, and the time above a certain temperature overestimated.

Results: 30 m thick ignimbrite

Description of results

The thermal model was applied to 30 m thick ignimbrite (Fig. 4-13). The ignimbrite was emplaced at 1000 °C. The lower vitrophyre cools through T_g at < 1 year, the upper vitrophyre cools through T_g at ≤ 0.5 year (Table 4-1). The centre of the ignimbrite (15 m) cools through T_g at 3.5 – 4 years. The whole deposit was cooled through T_g after ~ 4 years (Fig. 4-13), at an average rate of ~ 88 °C / year (Table 4-1). The domain boundary between the flat domain and the steep domain (Figs 3-27; 3-28) corresponds with the level within the ignimbrite sustained above T_g for the longest time (Fig. 4-13a). The 30 m thick ignimbrite and 30 m thickness of heated substrate return to ambient temperature (< 50 °C) in ~ 80 years, at a cooling rate of ~ 12 °C / year (Table 4-1).

The applicability of the cooling history can be constrained by comparing the model-predicted depths of substrate fusing ($T_f \sim 350$ °C; WoldeGabriel et al., 1999) and baking ($T_b \sim 150$ °C; WoldeGabriel et al., 1999) with field observations (Fig. 4-1). These values are very poorly constrained. The depths where T_f (~ 1.5 m) and T_b (~ 8 m) are reached agree with those predicted by the cooling model (Fig. 4-13a), within the resolution of the model (3 m node spacing). Fusing of the substrate is constrained to between 2 and 6 years after ignimbrite emplacement (Table 4-1). Baking of the substrate is constrained to between 5 and 20 years after ignimbrite emplacement (Table 4-1).

Initial interpretation: 30 m thick ignimbrite

The model appears well constrained because it accurately predicts the maximum depths of fusing and baking of the substrate (Fig. 4-13a). The maximum duration of ductile behaviour ($T \geq T_g$) is 4 years; after this time cooling through T_g leads to a ductile-brittle rheological transition, and spherulite crystallisation begins (Lofgren, 1970; 1971; Manley, 1992), ceasing rheomorphism. All rheomorphism affecting the lower and upper vitrophyres must have been limited to ≤ 1 year and ≤ 0.5 year respectively. Furthermore, the base of the steep domain corresponds with the slowest cooling level within the ignimbrite (Fig. 4-13a), suggesting that the depth of extrafolial folding may be thermally controlled. Presumably thinner ignimbrite cools even faster.

Results: 60 m thick ignimbrite

Description of results

The thermal model was applied to 60 m thick ignimbrite (Fig. 4-14). The ignimbrite was emplaced at 1000 °C. The lower vitrophyre cools through T_g at < 1 year, the upper vitrophyre cools through T_g at ≤ 0.5 year (Table 4-1). The centre of the ignimbrite (30 m) cools through T_g at ~ 14 years. The whole deposit was cooled through T_g after ~ 16 years (Fig. 4-14), at an average rate of ~ 22 °C / year (Table 4-1). The domain boundary between the flat domain and the steep domain (Figs 3-27; 3-28) is close to the level within the ignimbrite sustained above T_g for the longest time (Fig. 4-14a). The 60 m thick ignimbrite and 45 m thickness of heated substrate return to ambient temperature (< 50 °C) in > 250 years, at a cooling rate of ~ 4.8 °C / year (Table 4-1).

Again, the applicability of the cooling history is constrained by comparing the model-predicted depths of substrate fusing with field observations (Fig. 4-1). The depths where T_f (~ 3 m) and T_b (~ 10 m) are reached agree with those predicted by the cooling model (Fig. 4-14a), within the resolution of the model (3 m node spacing). Fusing of the substrate is constrained to between 2 and 20 years after ignimbrite emplacement (Table 4-1). Baking of the substrate is constrained to between 3 and 80 years after ignimbrite emplacement (Table 4-1).

Initial interpretation: 60 m thick ignimbrite

Again, the model appears well constrained, accurately predicting the maximum depths of fusing and baking of the substrate (Fig. 4-14a). The maximum duration of ductile behaviour ($T \geq T_g$) is 16 years; and ≤ 1 year and ≤ 0.5 year for the lower and upper vitrophyres respectively. Furthermore, the base of the steep domain corresponds with the slowest cooling level within the ignimbrite (Fig. 4-14a), suggesting, once again, that the depth of extrafolial folding may be thermally controlled.

Strain rates and shear stresses

Possible strain rates

Mylonite-like ignimbrite in the lower and upper vitrophyres (e.g., Fig. 3-22a) must have formed in ≤ 0.5 year. Therefore, for a typical 1 m-scale, intrafolial sheath fold (e.g., Figs 3-32e; 3-32f) produced by an inferred strain of $\sim 1000\%$ (sheath fold length ten times greater than its width), requires a strain rate of $\geq 6.36 \times 10^{-5} \text{ s}^{-1}$, similar to inferred strain rates from silicic lava flows (e.g., $10^{-7} - 10^{-3} \text{ s}^{-1}$; Whittington et al., 2005; Table 4-2). This is ≥ 6 orders of magnitude greater (faster) than tectonic strain rates (e.g., $10^{-17} - 10^{-11} \text{ s}^{-1}$; Pfiffner and Ramsey, 1982; Campbell-Stone, 2002). In contrast, inferred strain rates for observed Hawaiian basalt lava flows are typically $10^{-1} - 10^{-2} \text{ s}^{-1}$ (Bagdassarov, 2005).

The final phase of deformation at the upper surface of the steep domain is characterised by 20 – 30 m wavelength folds (e.g., Fig. 3-43), with inferred strain of $\sim 50\%$ (Fig. 3-50). I interpret that all or nearly all folding of the upper surface ceased in ≤ 0.5 year (Fig. 4-14), and therefore I constrain a strain rate of $\sim 4.45 \times 10^{-6} \text{ s}^{-1}$. Again, this is consistent with strain rates inferred from silicic lavas (Whittington et al., 2005; Table 4-2).

Possible shear stresses

By applying the relationship between viscosity, shear stress and strain rate (equation 1), the shear stress (τ) applied during both the syn-depositional and post-depositional phases of rheomorphism can be estimated. Assuming a

viscosity minimum viscosity of $10^6 \text{ Pa}\cdot\text{s}^{-1}$ and an inferred strain rate of 10^{-5} s^{-1} (Table 4-2), the shear stress is $\sim 10 \text{ Pa}$ for syn-depositional rheomorphism. For a maximum viscosity ($10^{10} \text{ Pa}\cdot\text{s}^{-1}$) the shear stress is $\sim 10^5 \text{ Pa}$ (10 MPa). For post-depositional rheomorphism, the shear stress is $\sim 10^4 \text{ Pa}$ (0.01 MPa) for an estimated viscosity of $10^{10} \text{ Pa}\cdot\text{s}^{-1}$, and a strain rate of 10^{-6} s^{-1} (Table 4-2).

Discussion

The effects of volatiles

Where available, viscosity constraints are likely to be unrealistic without an appreciation of the effects of volatiles dissolved in the liquid / glass. However, these effects cannot be constrained quantitatively, and therefore, only a qualitative assessment is possible. Direct and anecdotal evidence suggests there was a relatively high volatile content in the original melt, and that F in particular was abundant. Therefore, estimates of the melt viscosity that assume a 'dry' magma are probably over-estimates, possibly by as much as 3 orders of magnitude (e.g., Fig. 1-19d). Without further, direct measurement of the volatile content of the glass and melt inclusions, this cannot be better constrained.

Moreover, F is likely to remain in the liquid phase up to and beyond eruption, and therefore, a F-rich glassy deposit will also have a lower viscosity than a 'dry' one. However, estimates of the viscosity of the deposit based on fluid dynamics and the relationship with stress and strain are independent of the volatile composition and its effects, rather they analyse the dynamics of the deposit. The only compositional parameter involved is density, that is itself not significantly altered by halogen content. Therefore, it is likely that viscosity estimates for the deposit are not under-representing the effects of volatiles, and are reasonable constraints.

Summary of the rheological evolution of the Grey's Landing ignimbrite

Intense welding and rheomorphism in the Grey's Landing ignimbrite are manifestations of its rheological evolution, where the rheology of the ignimbrite

has remained ductile for a significant length of time after deposition. The evolving rheology of the juvenile magma and the eventual deposit is as follows.

1. The juvenile magma was a hot (~ 950 °C; Fig. 4-10a), heterogeneous rhyolitic melt (Fig. 4-3a), composed of early-tapped (lower vitrophyre), peraluminous, augite-, pigeonite-, and hypersthene-phyric liquid (~ 946 °C) and a later-tapped (upper vitrophyre), metaluminous, pigeonite-phyric liquid (~ 961 °C; Figs 4-6d; 4-7). Crystal equilibration temperatures for the early-tapped liquid are ~ 950 °C and ~ 985 °C for the later-tapped liquid (Figs 4-8; 4-9; 4-10b). Both liquids had an inferred 'dry' viscosity of $\geq 10^6$ Pa.s⁻¹ (Fig. 4-11). The presence of volatiles dissolved in the liquid (e.g., ≤ 5 wt % F; Fig. 4-5) would likely have reduced the melt viscosity by 1 – 3 orders of magnitude, $\geq 10^3$ Pa.s⁻¹.
2. The duration of the ignimbrite-forming eruption was probably ≤ 1 day, based on observed paroxysmal Plinian events (Fig. 4-15). However, present-day analogues are typically an order of magnitude smaller in volume than the Grey's Landing ignimbrite (e.g., the Valley of Ten Thousand Smokes ignimbrite, Novarupta, Alaska; Fierstein and Wilson, 2005). Explosive eruption, possibly preceded by prolonged passive degassing, reduced the dissolved volatile content significantly, however F was probably preferentially withheld by the liquid. Presumably there was significant heat loss during eruption.
3. Transport of pyroclasts in a density current probably lasted hours to days following deposition of a contemporaneous fall-out ash (Figs 2-12; 4-15). It is likely that pyroclasts within the density current cooled, although how much is not constrained. Pyroclastic density currents are likely to entrain cold air during transport (Branney and Kokelaar, 2002), although highly concentrated flows may be effective at thermally insulating the juvenile pyroclasts (Bursik and Woods, 1996).
4. The scale, style and distribution of mylonite-like fabrics throughout the deposit suggest syn-depositional welding and rheomorphism (Chapter 3). The maximum duration of syn-depositional rheomorphism is approximately 6 months (Figs 4-13; 4-14; Table 4-1), however if syn-depositional rheomorphism is intrinsically linked to deposition from a

passing density current, it is limited to the duration of the current, hours to days (e.g., Bursik and Woods, 1996; Fig. 4-15). The viscosity of the newly deposited ignimbrite was $\sim 10^6 - 10^{10} \text{ Pa}\cdot\text{s}^{-1}$, at a temperature ≥ 650 °C, a strain rate of 10^{-5} s^{-1} , and a shear stress of $\geq 10 \text{ Pa}$ (Table 4-2).

5. Post-depositional rheomorphism was not possible ~ 16 years after deposition (Figs 4-13; 4-14; Table 4-1), beyond which a brittle rheology would have been dominant (≤ 650 °C). It is likely that a significant proportion of post-depositional rheomorphism occurred in the first 6 months after deposition, after which the upper vitrophyre would not have a ductile rheology (Figs 4-13; 4-14; Table 4-1). At a temperature of 650 °C, a viscosity of $\leq 10^{10} \text{ Pa}\cdot\text{s}^{-1}$, a strain rate of $\sim 10^{-6} \text{ s}^{-1}$, and a shear stress of $\leq 10000 \text{ Pa}$ are inferred (Table 4-2; Fig. 4-15).
6. Fusing and baking of the substrate probably started 2 years after deposition of the ignimbrite, and ceased ≤ 80 years later (Fig. 4-15).
7. Sustained, static cooling probably occurred for $\geq 250 - 400$ years after deposition (Fig. 4-15).

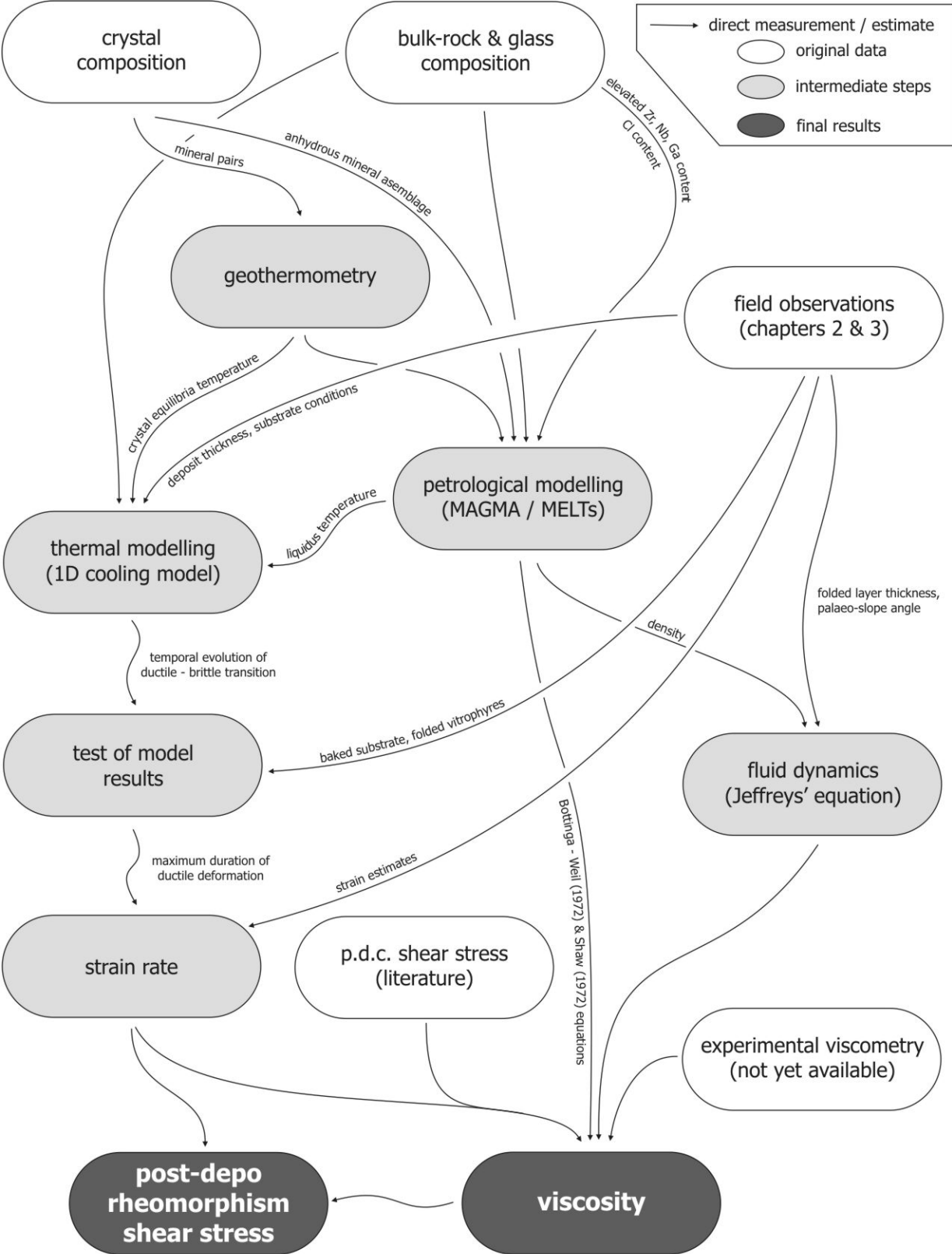


Fig. 4-1. Flow-diagram outlining the logic structure of Chapter 4, and steps required to estimate viscosity at different stages of emplacement.

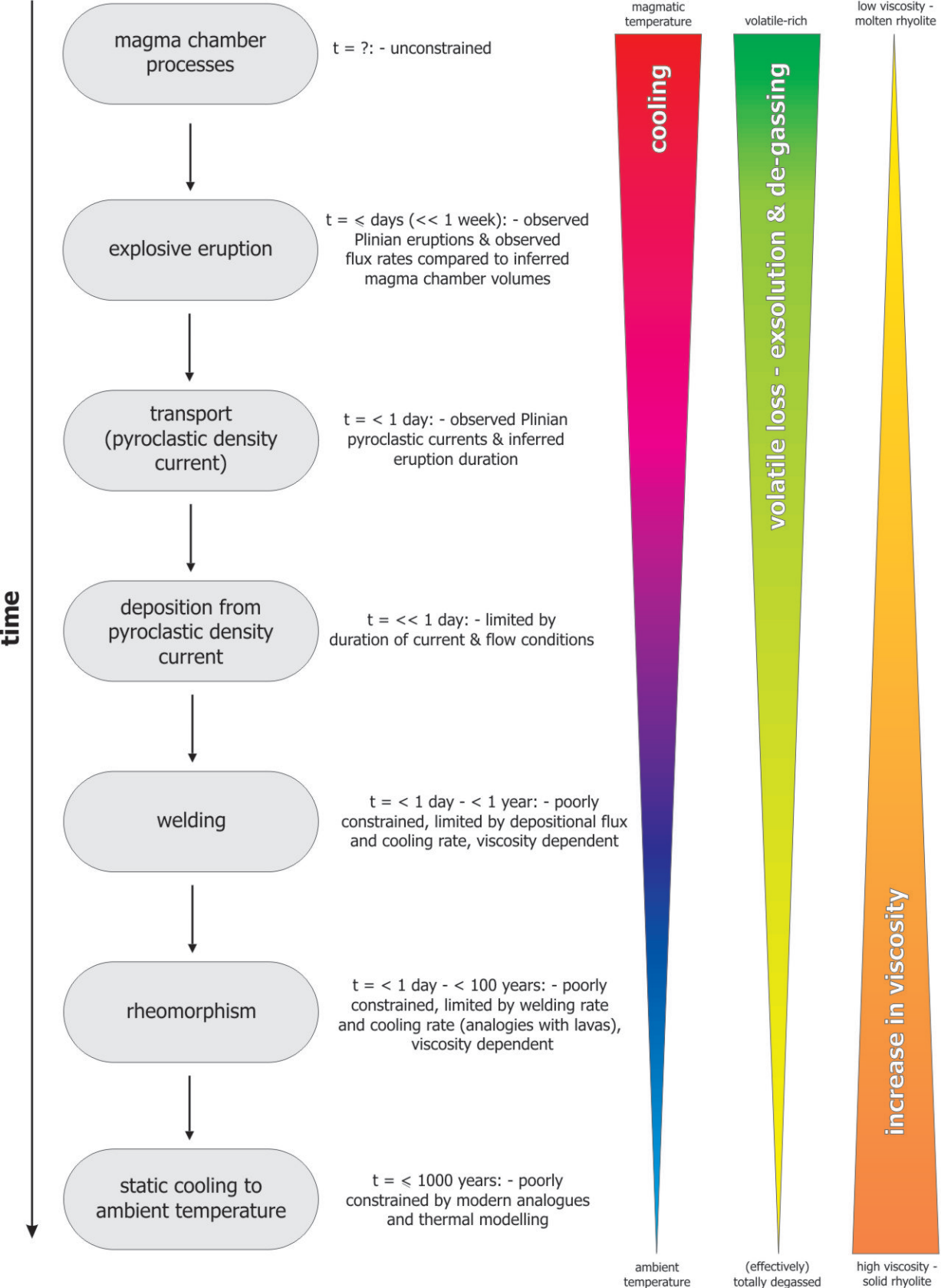


Fig. 4-2. Schematic diagram displaying the principal stages in the evolution of a rheomorphic ignimbrite and approximate timing constraints (left), and simplified summaries of selected physical parameters (right).

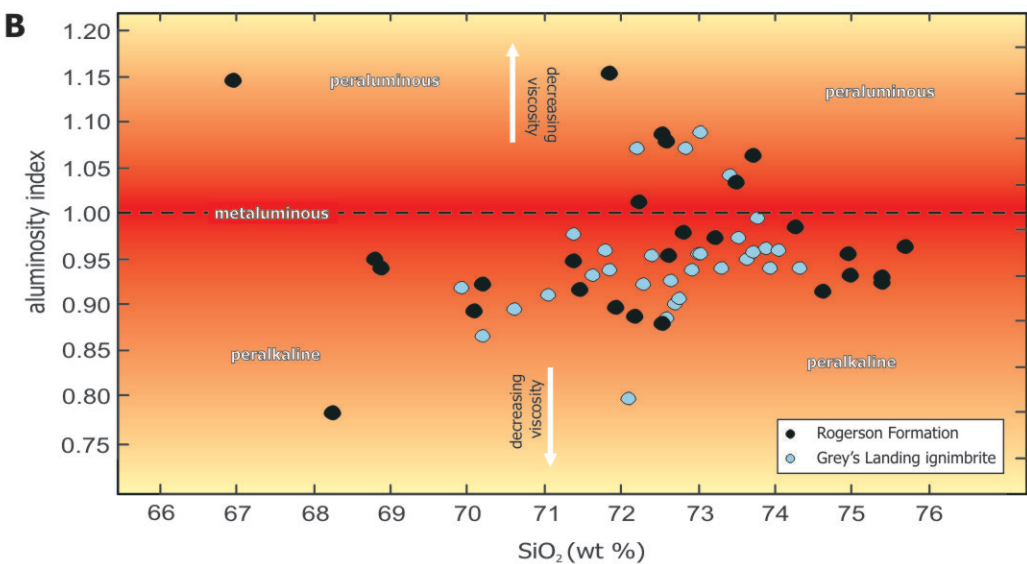
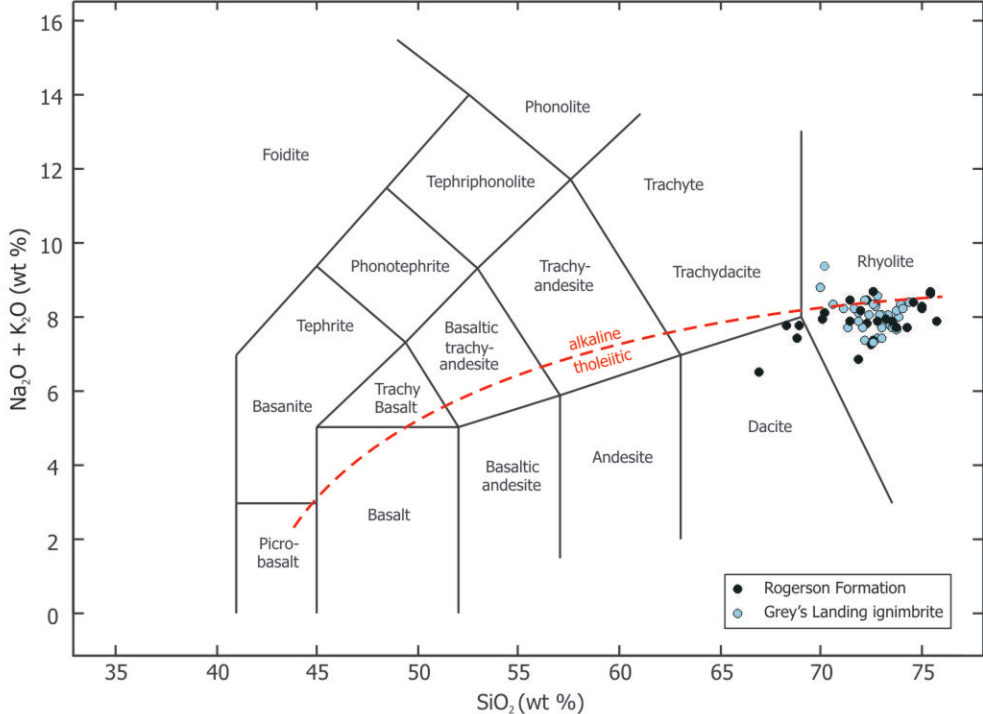


Fig. 4-3. Bulk rock composition. (A) analyses (recalculated to 100%) for ignimbrites of the Rogerson Formation, plotted on a total alkali / silica chart (Le Bas et al., 1986). (B) plot of aluminosity index (molar $\text{Al}_2\text{O}_3 / (\text{Na}_2\text{O} + \text{K}_2\text{O} + \text{CaO})$; Rollinson, 1993) against silica for ignimbrites of the Rogerson Formation. Red is relatively 'higher' viscosity, yellow is relatively 'lower' viscosity.

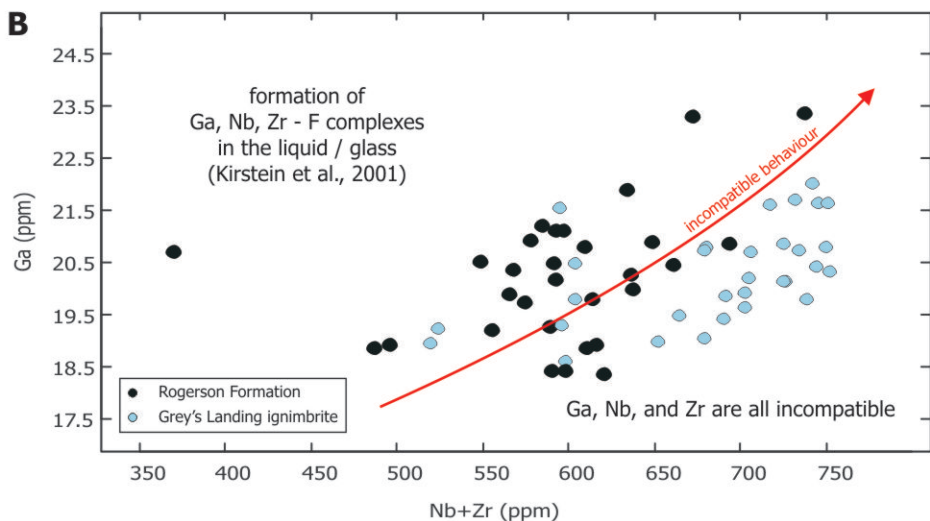
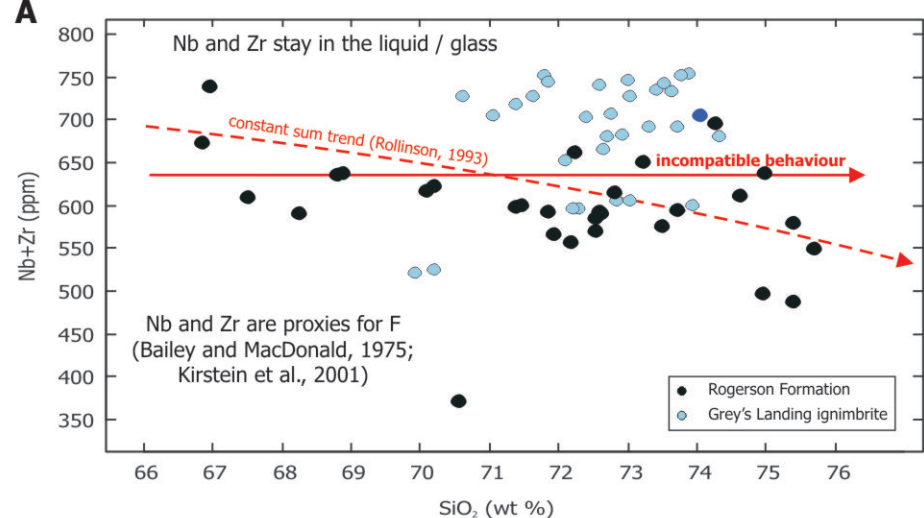


Fig. 4-4. Bulk rock composition. (A) plot of SiO₂ against Nb + Zr, showing the incompatible behaviour of Nb and Zr. The shallow negative relationship is most likely a consequence of the constant sum effect (Rollinson, 1993). Nb and Zr can be used as proxies for other highly incompatible elements (e.g., F; Kirstein et al., 2001). (B) plot of Nb + Zr against Ga, showing covariance and incompatible behaviour, suggesting that Ga is not depleted from the liquid. Ga incompatibility may result from the development of F-based complexes in the residual liquid (Kirstein et al., 2001).

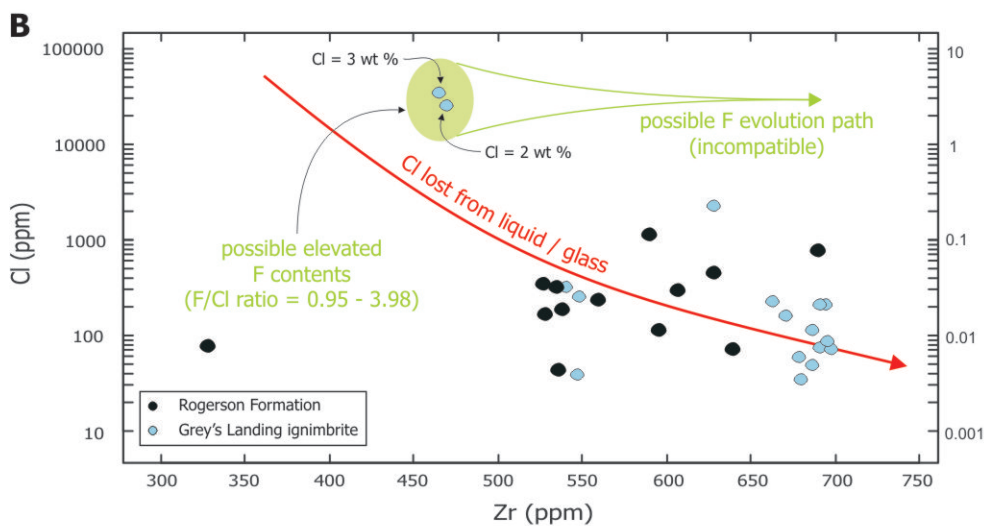
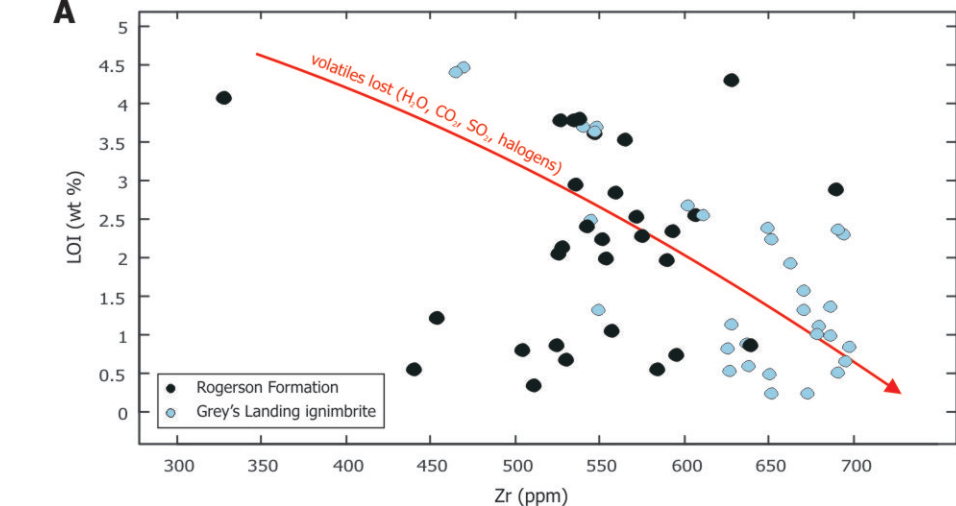


Fig. 4-5. Volatile composition: LOIs and chlorine. (A) plot of loss on ignition data (LOI) against Zr, showing a negative correlation between volatile content and incompatible elements that stay in the liquid. This may be the result of depletion of volatiles during evolution of the residual liquid. LOIs approximate to total volatile content (Rollinson, 1993). (B) plot of Zr against Cl, showing significant depletion of Cl during evolution of the residual liquid. Because Cl and F are both halogens, elevated Cl (> 1 wt %) may correspond with elevated F concentrations. However, F is less likely to become depleted in the liquid than Cl (higher solubility), and therefore, will probably follow a different evolution path. F/Cl ratio for silicate Earth (McDonough and Sun, 1995), upper continental crust (Wedepohl, 1995), and granite (Gao et al., 1998).

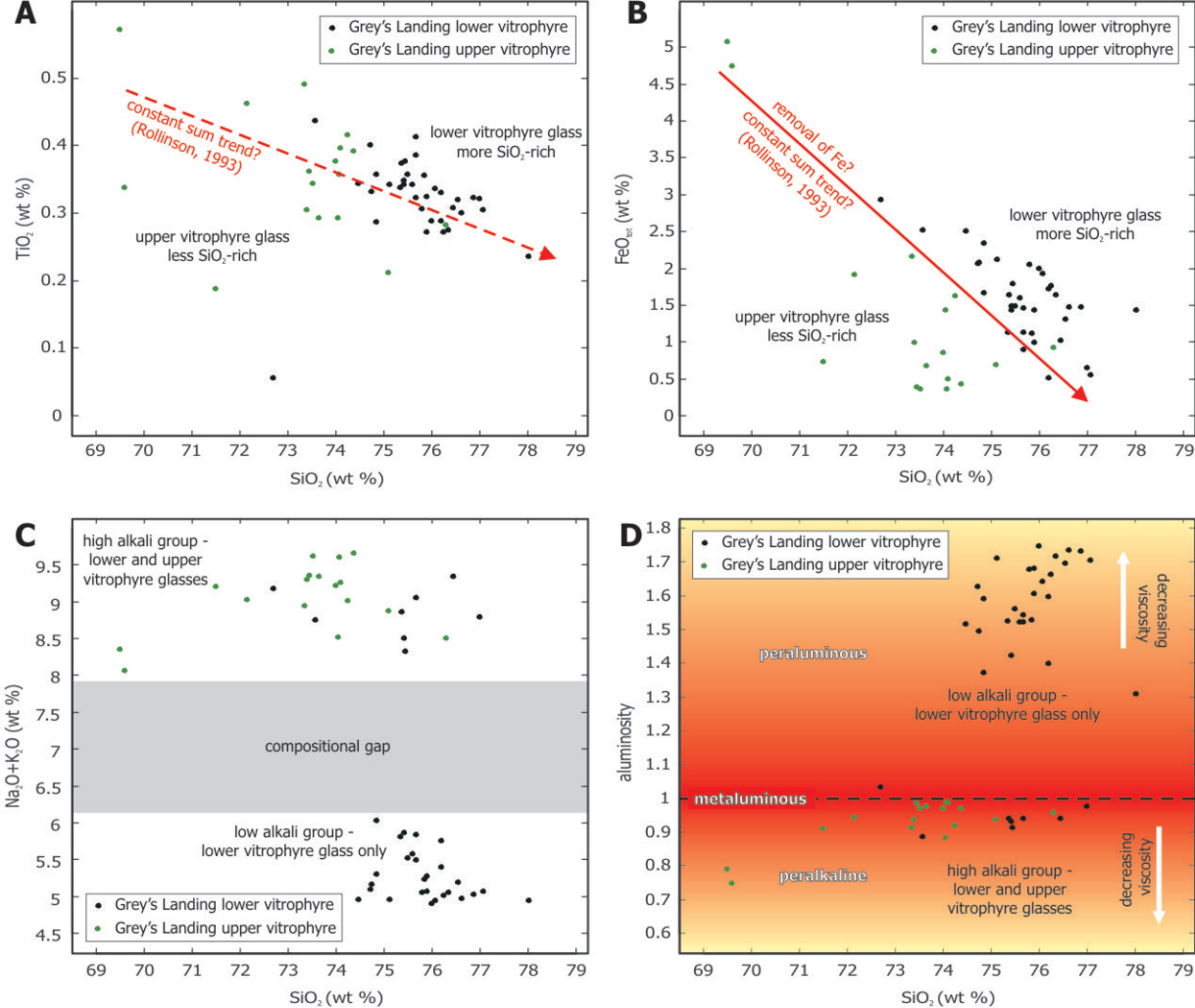


Fig. 4-6. Glass composition. (A) plot of SiO₂ against TiO₂, showing more SiO₂-rich glass in the lower vitrophyre. The apparent negative trend is probably a constant sum effect (Rollinson, 1993). (B) plot of SiO₂ against total FeO, showing more SiO₂-rich glass in the lower vitrophyre. The apparent negative trend may be a constant sum effect (Rollinson, 1993), or it may reflect depletion of FeO during evolution of the liquid / glass. (C) plot of SiO₂ against Na₂O + K₂O, showing two discrete compositional groups; a low alkali group only evident in the lower vitrophyre, and a higher alkali group evident in both the lower and upper vitrophyres. There is a broad (~ 2 wt % alkali) compositional gap between the two groups. (D) plot of aluminosity index (molar Al₂O₃ / (Na₂O + K₂O + CaO); Rollinson, 1993) against SiO₂. Red is relatively 'higher' viscosity liquid, yellow is relatively 'lower' viscosity liquid. The higher alkali group is metaluminous to mildly peralkaline, the lower alkali group is strongly peraluminous.

Crystal composition with stratigraphic height

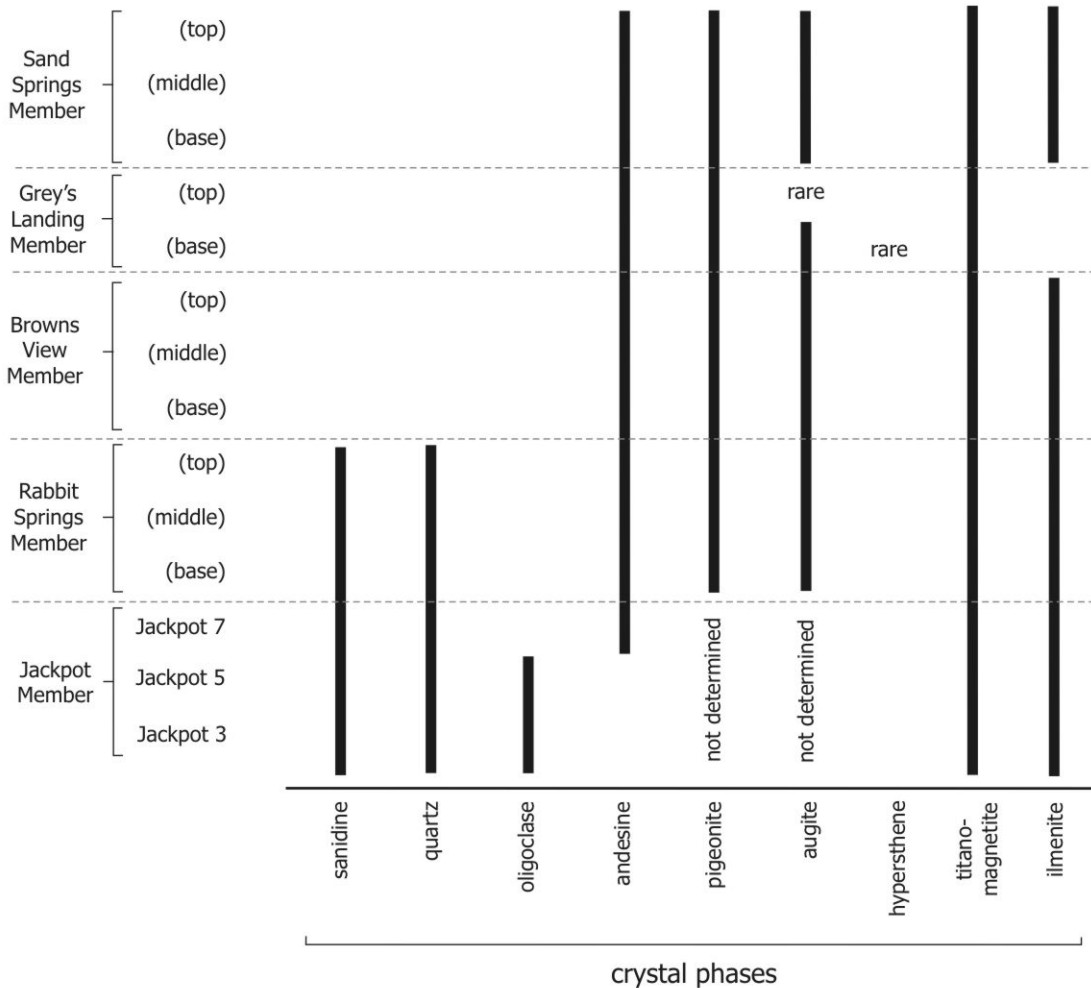


Fig. 4-7. Stratigraphic ranges of crystal assemblages within the Rogerson Formation.

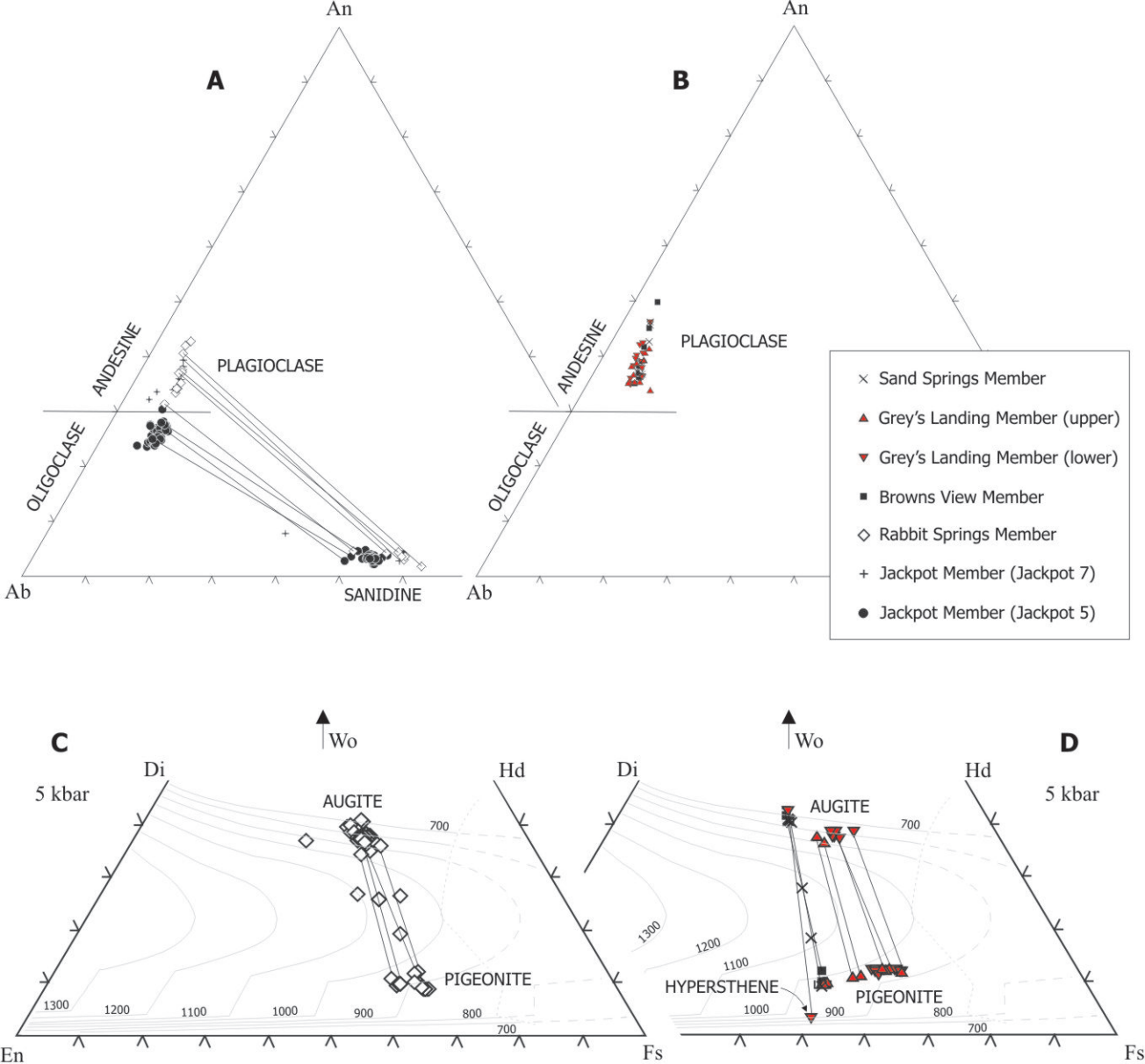


Fig. 4-8. Mineral compositions in the Rogerson Formation. (A) ternary feldspar compositions for the Jackpot and Rabbit Springs Members. Tie-lines between co-existing plagioclase and sanidine crystals. (B) ternary feldspar compositions for the Browns View, Grey's Landing and Sand Springs Members. Note the absence of sanidine. (C) pyroxene composition quadrilateral for the Rabbit Springs Member. Jackpot Member pyroxenes were oxidized and note analysed. Tie-lines between co-existing clinopyroxene and pigeonite crystals. (D) pyroxene composition quadrilateral for the Browns View, Grey's Landing and Sand Springs Members. Note the absence of augite in the upper parts of the Grey's Landing Member. Tie-lines between co-existing clinopyroxene and pigeonite crystals. Thermal contours from Lindsley (1983) at 5 kbar.

estimated magmatic temperature

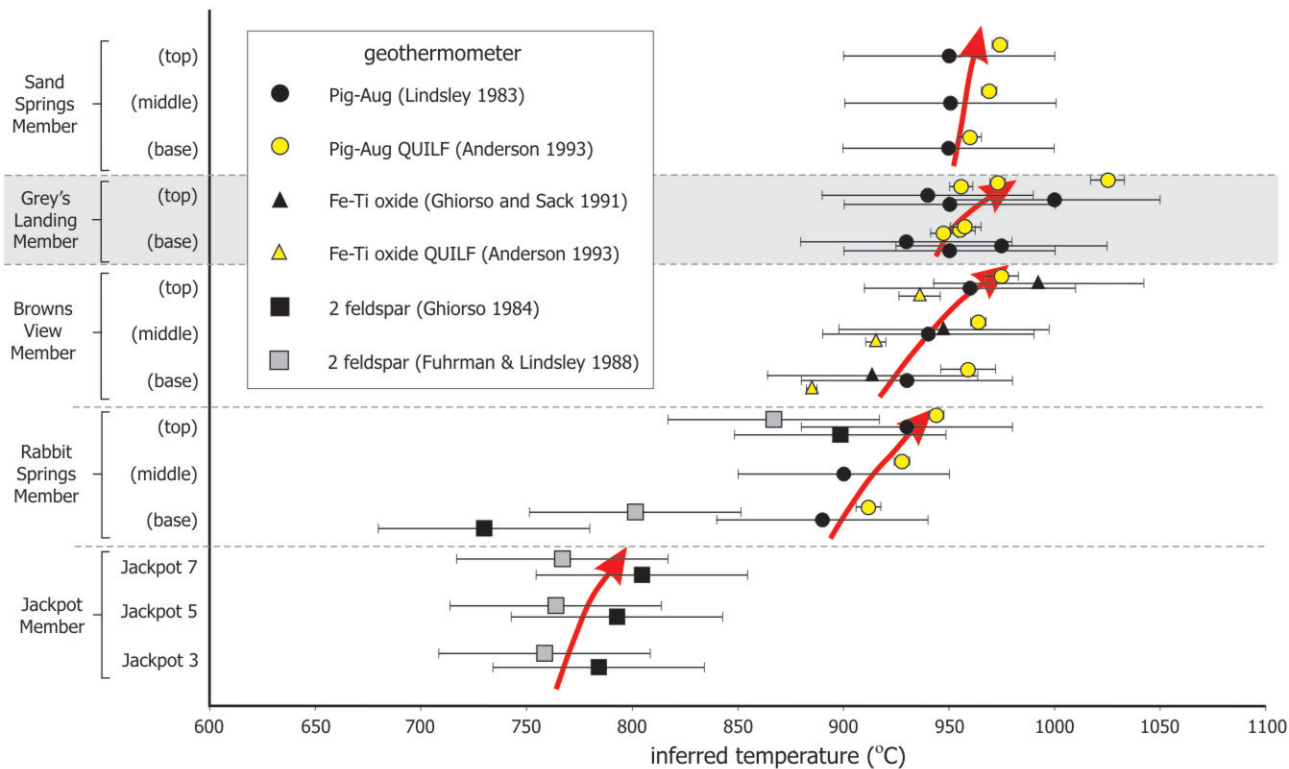


Fig. 4-9. Comparison of estimated magmatic temperature with stratigraphic height in the Rogerson Formation. Magmatic temperatures are seen to increase with height in each member (red arrows). Each data point represents the mean of 25 pairs of analyses. Error bars are $\pm 50^{\circ}\text{C}$ for the models of Fuhrman and Lindsley (1988), Ghiorso (1984), Ghiorso and Sack (1991) and Lindsley (1983). Error bars are 2σ for the model of Anderson et al. (1993).

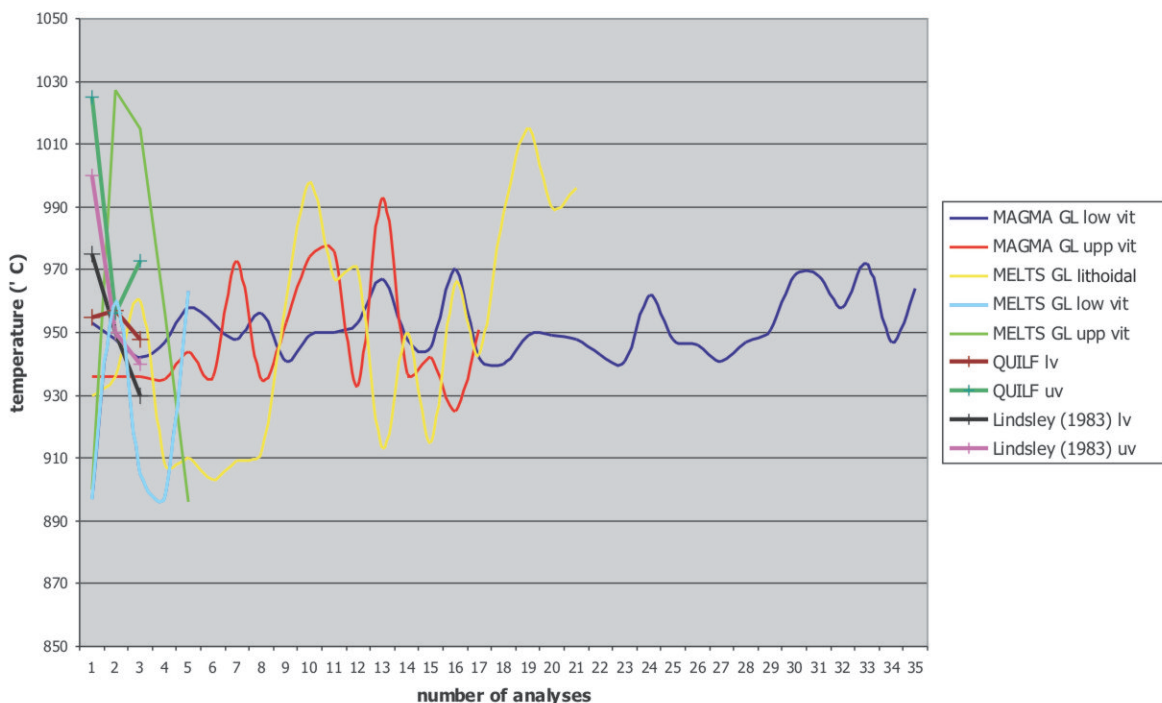
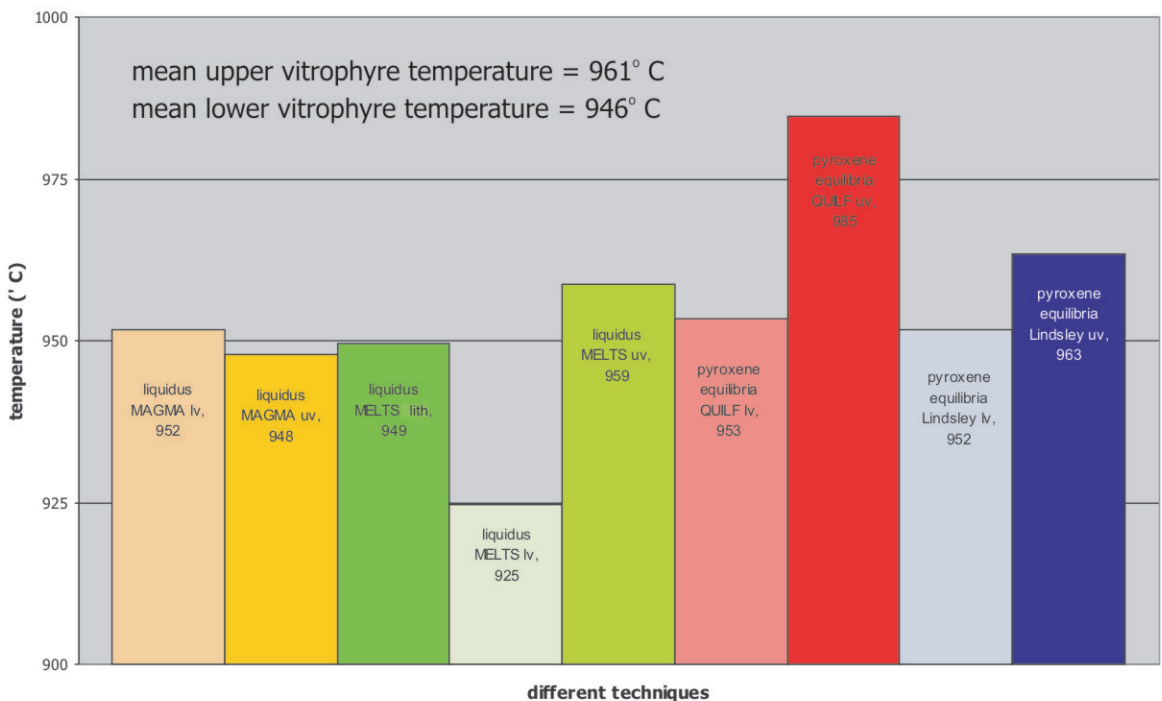
A**estimates of magmatic temperature****B****mean magmatic temperature**

Fig. 4-10. Magmatic temperature. (A) summary of liquidus and 2-pyroxene equilibria temperatures estimated from the Grey's Landing ignimbrite. (B) summary of different mean magmatic temperatures estimated by different techniques, for the lower vitrophyre (lv), upper vitrophyre (uv) and lithoidal (lith) Grey's Landing ignimbrite.

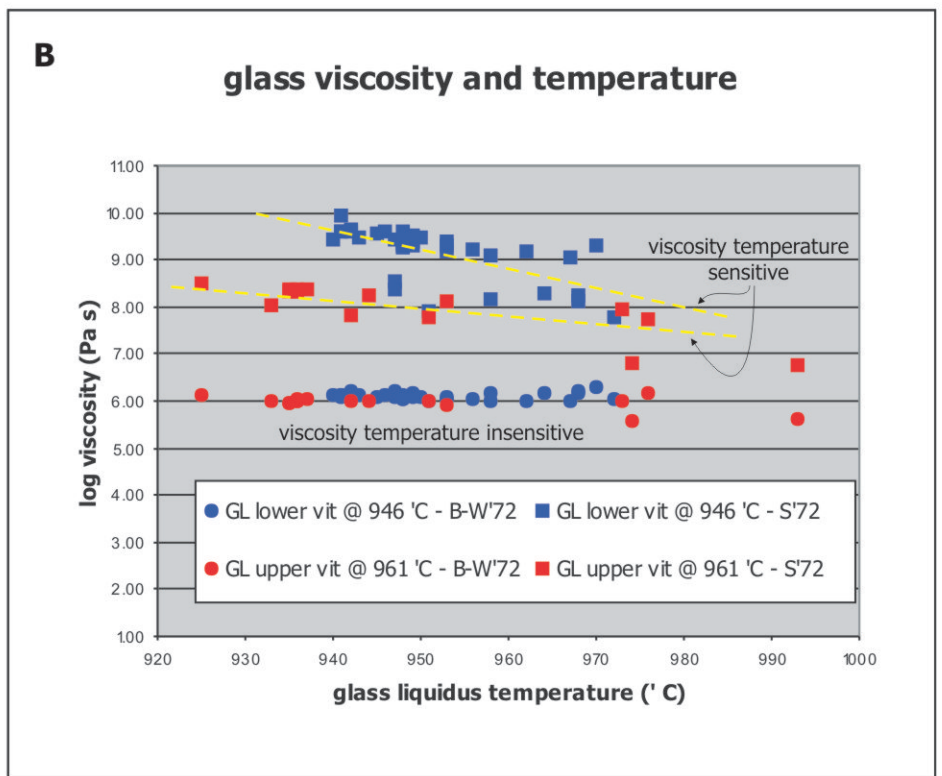
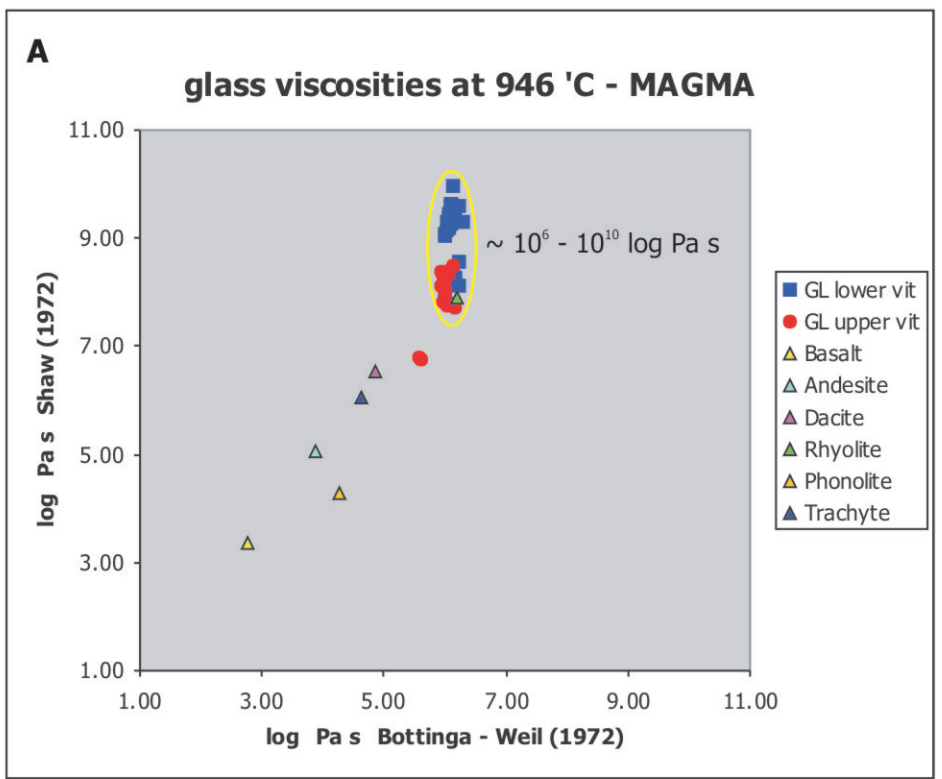


Fig. 4-11. Viscosity estimates: empirical models - MAGMA software (Wohletz, 2004). (A) comparison of viscosity estimates derived from the empirical models of Bottinga & Weil (1972) and Shaw (1972), showing data from the Grey's Landing lower and upper vitrophyres, and representative analyses from other volcanic compositions (Kilburn, 2000). Note how Shaw (1972) estimates are consistently higher (1 - 4 Pa s) than those of Bottinga & Weil (1972). (B) plot of viscosity against liquidus temperature for analyses from the Grey's Landing lower and upper vitrophyres. Note how the Shaw (1972) is temperature sensitive, in contrast Bottinga & Weil (1972) is insensitive.

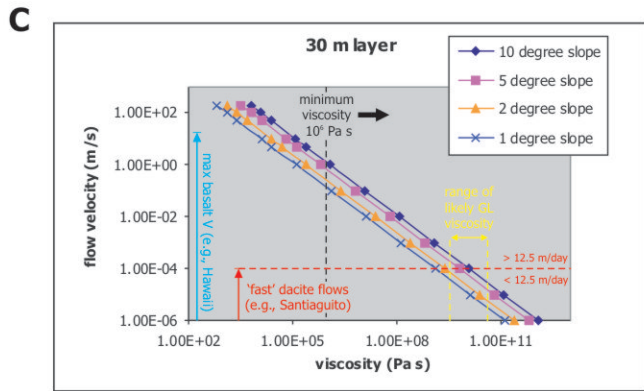
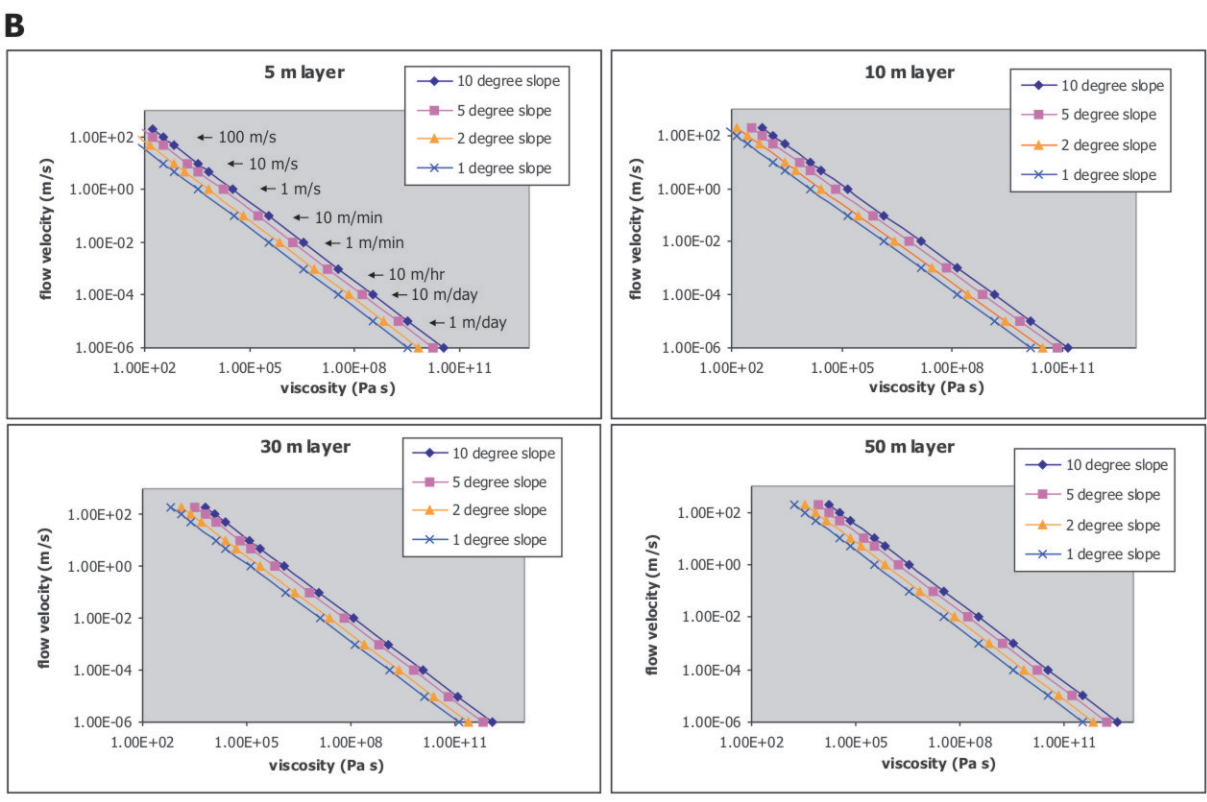
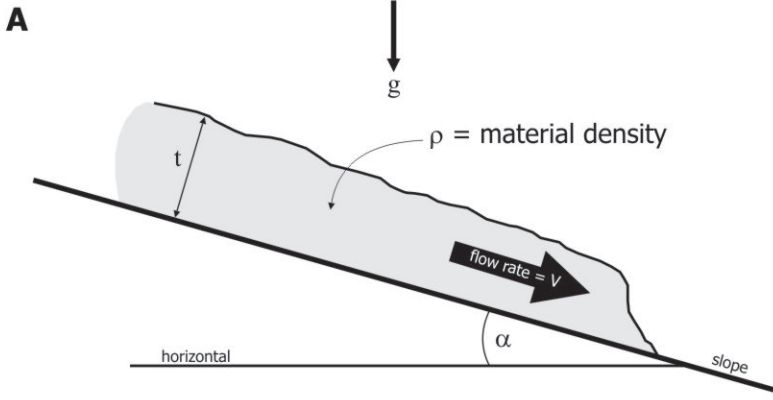
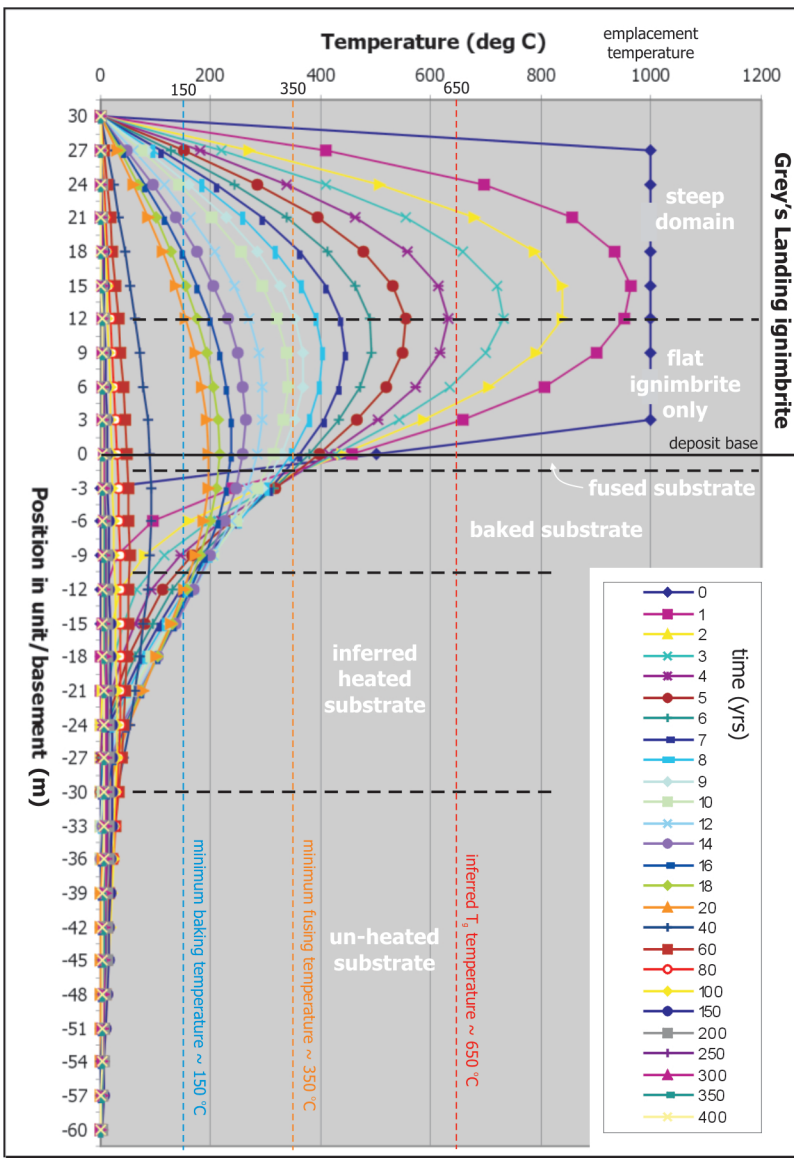


Fig. 4-12. Viscosity estimates: Jeffreys' equation. (A) schematic sketch of the components of the Jeffreys' equation. (B) plots of flow velocity and slope angle against viscosity, for 5, 10, 30 and 50 m thick flowing layers. (C) plot of flow velocity and slope angle against viscosity for a 30 m thick flowing layer, showing additional data. The likely range of viscosities for the steep domain of the Grey's Landing ignimbrite is $\sim 10^{10}$ Pa.s⁻¹. Minimum viscosity (10^6 Pa.s⁻¹) taken from empirically-derived liquidus equations (Bottinga & Weil, 1972). Santiaguito flow velocity from Harris et al. (2002). Basalt flow velocity from Harris et al. (2005).

A



B

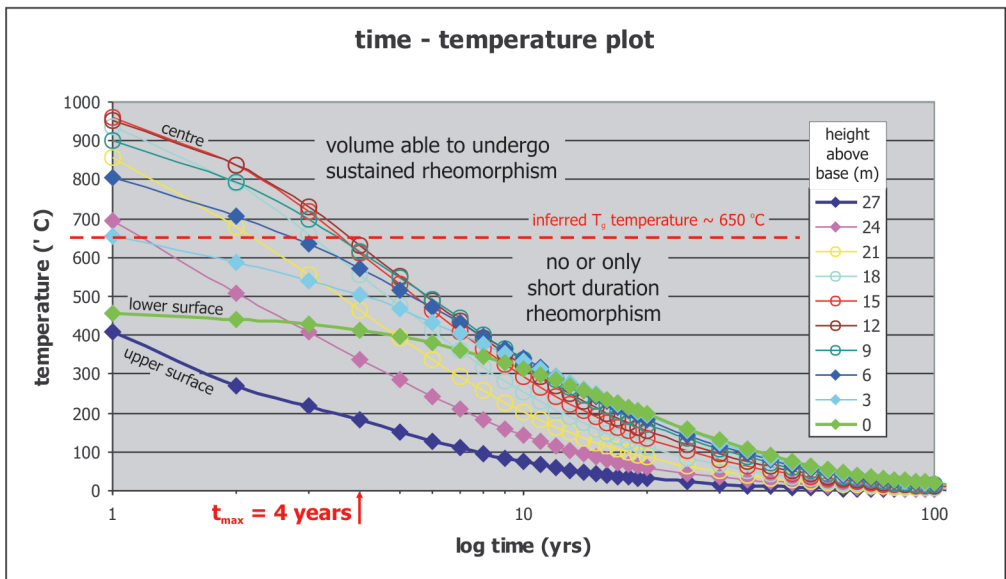
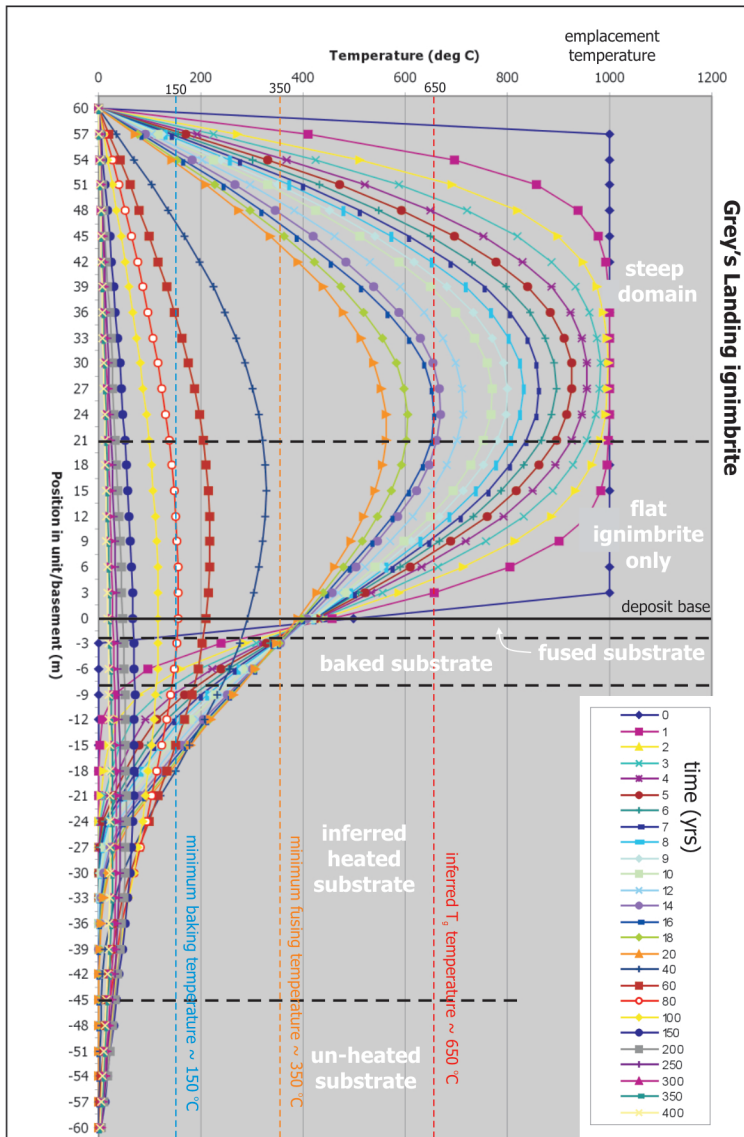


Fig. 4-13. Thermal modelling: 30 m thick ignimbrite, e.g., Monument Canyon. (A) time-specific temperature curves for a cooling ignimbrite with an emplacement temperature of 1000 °C. Note that thermal alteration horizons in the substrate (defined in the field) correspond well with the position of minimum temperatures for fusing and baking. Note also, that the base of the steep domain corresponds with the level sustained above T_g for the longest time, ~ 4 years. (B) temperature - time plot showing the cooling rates of certain depths within the deposit. Maximum duration of ductile behaviour, and therefore rheomorphism, ~ 4 years. Whole deposit reaches ambient temperature at ~ 80 years.

A



B

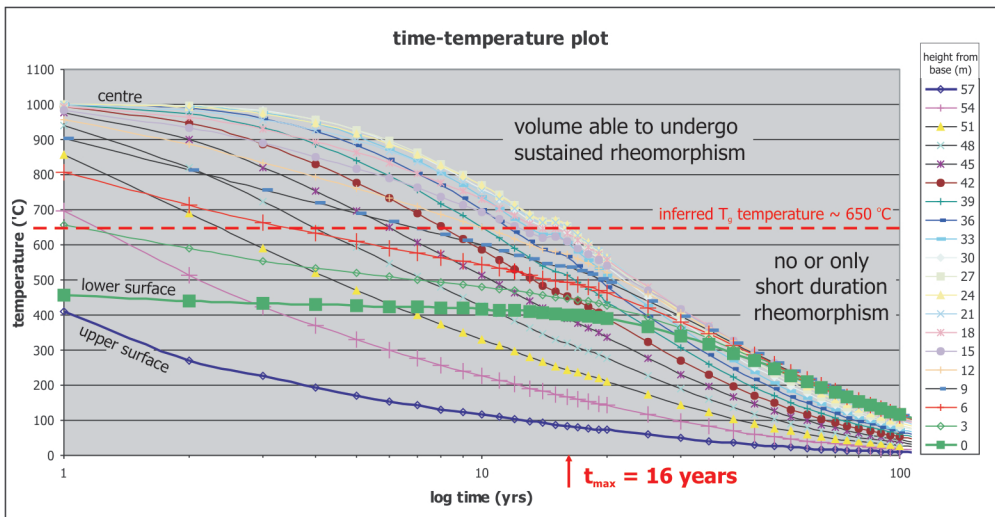


Fig. 4-14. Thermal modelling: 60 m thick ignimbrite, e.g., Backwaters. (A) time-specific temperature curves for a cooling ignimbrite with an emplacement temperature of 1000 °C. Note that thermal alteration horizons in the substrate (defined in the field) correspond well with the position of minimum temperatures for fusing and baking. Note also, that the base of the steep domain corresponds with the level sustained above T_g for the longest time, ~ 16 years. (B) temperature - time plot showing the cooling rates of certain depths within the deposit. Maximum duration of ductile behaviour, and therefore rheomorphism, ~ 16 years. Whole deposit reaches ambient temperature at > 250 years.

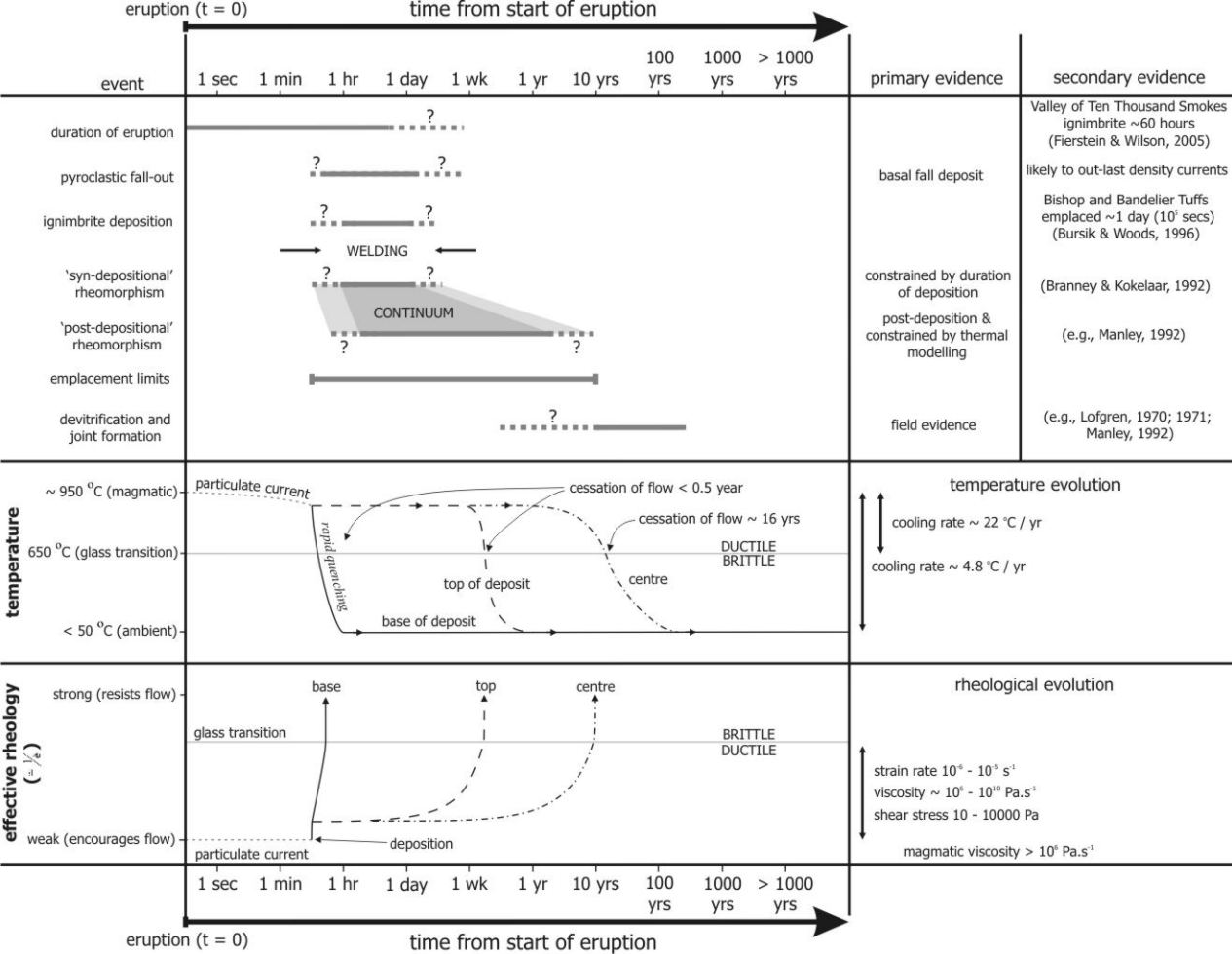


Fig. 4-15. Summary of the thermal and rheological evolution of the Grey's Landing ignimbrite, and estimated thermal and rheological parameters. The duration of different phases of the emplacement (Fig. 4-BB) are shown, along with observations from the Grey's Landing ignimbrite and data from analogous case studies. Schematic time - temperature and time - rheology paths are shown. Note that the relative timing and duration of welding are constrained by syn-depositional rheomorphism.

| thermal event | 30 m thick ignimbrite | 60 m thick ignimbrite |
|---|------------------------------|------------------------------|
| emplacement (1000 °C) | t = 0 yrs | t = 0 yrs |
| lower vitrophyre T _g (650 °C) | t = < 1 yr | t = < 1 yr |
| upper vitrophyre T _g (650 °C) | t = ≤ 0.5 yr | t = ≤ 0.5 yr |
| centre T _g (650 °C) | 15 m → t = 3.5 – 4 yrs | 30 m → t = ~ 14 yrs |
| whole deposit T_g (650 °C) | 12 m → t = ~ 4 yrs | 24 m → t = ~ 16 yrs |
| start substrate fusing (350 °C) | t = 2 yrs | t = 2 yrs |
| end substrate fusing (350 °C) | t = ~ 6 yrs | t = ~ 20 yrs |
| start substrate baking (150 °C) | t = 5 yrs | t = 3 yrs |
| end substrate baking (150 °C) | t = 20 yrs | t = 80 yrs |
| ambient (< 50 °C) | t = ~ 80 yrs | t = ≥ 250 yrs |
| cooling rate (1000 - 650 °C) | ~ 88 °C / yr | ~ 22 °C / yr |
| cooling rate (1000 - < 50 °C) | ~ 12 °C / yr | ~ 4.8 °C / yr |

Table 4-1. Summary of the cooling histories and rates for 30 m and 60 m thick Grey's Landing ignimbrite, obtained from thermal modelling (Manley, 1992). Note that the maximum duration of ductile behaviour (time above T_g) in 30 m ignimbrite is ~ 4 years, and in 60 m ignimbrite is ~ 16 years. The duration of ductile behaviour in the lower and upper vitrophyres is a lot shorter, ≤ 1 year.

| | Grey's Landing ignimbrite | | | silicic lavas | | |
|---------------------------|----------------------------------|------------------------------------|---------------------------------------|----------------------|------------------------------------|---------------------------------------|
| | T (°C) | η (Pa.s ⁻¹) | $\dot{\epsilon}$ (# s ⁻¹) | T (°C) | η (Pa.s ⁻¹) | $\dot{\epsilon}$ (# s ⁻¹) |
| magmatic | ~ 950 | 10 ⁶ - 10 ¹⁰ | n/a | ≤ 1000 | ≥ 10 ⁶ | n/a |
| syn-depo rheo | ≥ 650 | 10 ⁶ - 10 ¹⁰ | 10 ⁻⁵ | n/a | n/a | n/a |
| post-depo rheo | ≥ 650 | ≤ 10 ¹⁰ | 10 ⁻⁶ | 650 - 1000 | 10 ⁸ - 10 ¹² | 10 ⁻⁷ - 10 ⁻³ |

Table 4-2. Summary of estimated temperatures, viscosities, and strain rates at different stages of the emplacement of the Grey's Landing ignimbrite. Corresponding data from silicic lavas is provided for comparison.

Chapter 5:

Discussion: emplacement, welding, rheomorphic history of the Grey's Landing ignimbrite

Syn-depositional welding and rheomorphism

Review of evidence

Several observations suggest that deposition of the ignimbrite was accompanied by rapid welding and rheomorphism, and that rheomorphism was not, primarily, gravity-driven.

Key evidence

1. The entire thickness of the ignimbrite is welded and exhibits a rheomorphic, mylonite-like fabric.
2. Typically uniform east to west transport direction despite different palaeo-slope orientations (Fig. 3-21).
3. Localised, rapidly changing inferred transport direction in vertical sections (e.g., Grey's Landing; Fig. 3-29).

Interpretations and implications

Welding was probably dominated by aggregation-welding (*sensu* Freundt, 1999) of hot and soft pyroclasts, especially at the upper surface where there was negligible overlying deposit to support load-welding.

Small-scale rheomorphic deformation throughout the deposit, and especially at the very base and very top, indicates that a sub-horizontal, ductile shear zone was present throughout the duration of deposition. The shear zone was laterally extensive, ~ 0.5 m thick, dominated by non-coaxial strain, and affected the whole thickness of the deposit (≤ 60 m).

The typical transport direction (elongation direction) is consistently east to west, and does not appear to be affected by the dip of the underlying palaeo-slope, suggesting that momentum was provided by a mechanism other than gravity which would encourage down-slope flow. Furthermore, the inferred transport direction locally varies significantly in some sections within a short vertical thickness. This suggests local and temporal heterogeneities in the shear zone, again unlikely to be the result of gravity-driven ductile flow down the underlying palaeo-slope.

Pre-existing conceptual models for the emplacement of rheomorphic ignimbrites

Introduction

There are presently several different models for the deposition, welding and deformation of rheomorphic ignimbrites. No single model is, so far, applicable to every rheomorphic ignimbrite, and many of the aspects of each model are not mutually exclusive.

***En masse* flow of a rapidly deflated pyroclastic current**

Outline of conceptual model

In their seminal paper on rheomorphism in ignimbrite Schmincke and Swanson (1967) interpreted structures (Fig. 1-21) within Gran Canarian ignimbrites as flow structures produced by laminar, lava-like flow of welded ignimbrite during the final stages of emplacement. This model was conceptually tied to the plug-flow model of ignimbrite deposition where an expanded pyroclastic density current deflates, decelerates and welds *en masse*. The sequence of events described by this model is represented in Figure 5-1a. Two critical observations are: (1) there is a basal imbricated fiamme and pumice fabric, which suggests that the ignimbrite plug was still moving during initial welding; and (2) the fiamme-defined welding fabric is folded and stretched. Therefore, rheomorphism cannot

be pre-welding, and is interpreted to be dominantly post-welding. Schmincke and Swanson (1967) described structures traditionally associated with plane strain and non-coaxial shear, for example; a stretched fiamme lineation, rotated porphyroclasts, asymmetrically boudinaged fiamme, and asymmetric folds (Fig. 1-21). Schmincke and Swanson (1967) noted that both buckle-style and similar-style folds occur, with isoclinal similar-style folds and sheath folds concentrated towards the base (Fig. 1-21). They associate some folding in the upper half of each ignimbrite with ramp structures similar to those in silicic lavas (e.g., Fig. 1-10). They attribute ramping to layer-parallel buckling and thrusting of the upper portion of each unit, with the ductile interior acting as a ductile shear zone. However, Ragan and Sheridan (1972) interpreted these structures to be formed during coaxial flattening, in line with their ideas of *in situ*, static welding. Schmincke (1974) subsequently identified that welding could be very rapid in their Gran Canarian examples due to low pyroclast viscosity, and that therefore, prolonged *in situ* compaction-driven welding as proposed by Ragan and Sheridan (1972) was not necessary.

Predicted features

Predicted features include: (1) basal imbricated fiamme and eutaxitic fabric; (2) a lower, sub-horizontal ductile shear zone ‘carrying’ the overlying majority of the deposit; (3) cylindrical, flow-perpendicular folds; and (4) down-slope parallel elongation lineation and kinematic criteria (Fig. 5-1a; Table 5-1).

Comparison with features observed in the Grey’s Landing ignimbrite

The Schmincke and Swanson (1967) model does not account for the ubiquitous mylonite-like rheomorphic fabric developed in the Grey’s Landing ignimbrite, rather mylonite-like fabric can only be formed within the ductile shear zone near the base of the deposit (Fig. 5-1a; Table 5-1). There is no conceivable way for a mylonite-like fabric formed in this fixed shear zone to be ubiquitous. However, it does account for the sheared base. Nor can it explain slope-perpendicular transport directions (Table 5-1); because the majority of rheomorphism is inferred

to be post-deposition. Elongation directions should reflect gravity-driven, down-slope flow.

Remobilization of a static welded layer

Outline of conceptual model

Wolff and Wright (1981b) developed Ragan and Sheridan's (1972) and Sheridan's (1979) concept of *in situ* welding of static ignimbrite after deposition, followed by later rheomorphism by remobilization and slumping of the ignimbrite down slope. Their work was the first truly structural geology study. Wolff and Wright's (1981b) model was based on their (contentious) interpretation of the Green Tuff on Pantelleria, Italy, as a rheomorphic welded fall deposit (Wright, 1980; Wolff and Wright, 1981a), and therefore, they assumed that because lateral transport was not involved during deposition, all non-coaxial flow structures had to be post-welding. Crucially they did not report a basal imbricate fabric, a feature they would have interpreted as characteristic of ignimbrite deposition and welding (e.g., Schmincke and Swanson, 1967). Figure 5-1b summarises the deposition, welding and remobilization of ignimbrite as proposed by Wolff and Wright (1981b). Wolff and Wright (1981b) do not present a conceptual framework for the style of deformation produced during rheomorphism of remobilized ignimbrite, other than to describe the variety of structures present. They describe a range of fold styles and orientations, and refolded folds, consistent with progressive, heterogeneous deformation in the interior, and flattening of upper surface buckle-style folds. Circumferential folds (ogives) and ramp structure are not reported. They make an analogy with soft-sediment slumping based on the range of fold styles present, though this may be equally valid for silicic lavas; and therefore the best analogue.

Subsequent studies suggest that the Green Tuff is an ignimbrite, and that it does exhibit a basal imbricated fabric (e.g., Orsi and Sheridan, 1984; Mahood and Hildreth, 1986; Branney et al., 2004a), and that rapid, simultaneous welding and rheomorphism can occur in fall deposits (e.g., Furukawa and Kamata, 2004;

Capaccioni and Cuccoli, 2005). Furthermore, structures that Wolff and Wright (1981b) cite as diagnostic of remobilized ductile flow (e.g. lineations, rotated porphyroclasts and asymmetric folds) have been inferred to have formed during syn-depositional in other units (e.g., Pioli and Rosi, 2005). On balance, this conceptual model is not widely favoured in the light of modern field and laboratory studies concerning the relative timing and durations of deposition, welding and rheomorphism (e.g., Branney and Kokelaar, 1992; Branney et al., 1992; 2004a; Freundt, 1998; 1999; Sumner and Branney, 2002; Gimeno et al., 2003; Pioli and Rosi, 2005).

Predicted features

Predicted features include: (1) a horizontal basal eutaxitic fabric; (2) a lower, sub-horizontal ductile shear zone ‘carrying’ the overlying majority of the deposit; (3) cylindrical, flow-perpendicular folds; and (4) down-slope parallel elongation lineation and kinematic criteria (Fig. 5-1b; Table 5-1).

Comparison with features observed in the Grey’s Landing ignimbrite

Again, the Wolff and Wright (1981b) model does not account for the ubiquitous mylonite-like rheomorphic fabric developed in the Grey’s Landing ignimbrite. Like the Schmincke and Swanson (1967) model a mylonite-like fabric can only be formed within the ductile shear zone near the base of the deposit (Fig. 5-1b; Table 5-1). There is no conceivable way for a mylonite-like fabric formed in this fixed shear zone to be ubiquitous. It cannot account for the intensely sheared nature of the base of the Grey’s Landing ignimbrite (Table 5-1), in contrast to their prediction of a flattening-dominated layer (e.g., Fig. 5-1b); nor can it explain slope-perpendicular transport directions (Table 5-1); because the majority of rheomorphism is inferred to be post-deposition elongation directions should reflect gravity-driven, down-slope flow.

Deposition from a rapidly deflating and shearing pyroclastic density current

Outline of conceptual model

The valley-confined Wall Mountain Tuff, Colorado, was interpreted to have been deposited and deformed during initial emplacement (Chapin and Lowell, 1979). They interpreted the dominant flow-banding fabric to be have formed during welding and non-coaxial deformation within a thin shear zone at the base of a plug-flow (Fig. 5-2a) because it was lineated and commonly steeply dipping throughout, and was therefore incompatible with *in situ* compaction as envisaged by Ragan and Sheridan (1972). Chapin and Lowell (1979) suggested the presence of a thin ductile shear zone based on the generally small-scale of similar-style folds compared to the total deposit thickness. Of critical importance was their interpretation that folds were perpendicular to the palaeo-valley margins and the transport direction (Fig. 5-3, F₁). They conceived of a plug-flow shearing along the valley axis and margins, gradually transferring pyroclastic material through a transient and upward-migrating, bounding shear zone to be accreted to the valley floor and walls (Figs 5-2a t₃ – t₄; 5-3). Gradually the palaeo-valley filled with accreted ignimbrite with a pervasive fabric of flow-banding folded by small-scale, similar-style isoclinal folds and with a strong valley-parallel lineation (Fig. 5-3, L₁). Chapin and Lowell (1979) termed this phase of syn-emplacement rheomorphism as primary deformation (D₁) and considered it as separate and distinct from later, *en masse* rheomorphic deformation (D₂). Valley-margin parallel folds (Fig. 5-3, F₂) were interpreted to record hot ignimbrite slumping down the palaeo-valley sides after the original pyroclastic plug-flow had dissipated. However this poses conceptual problems: (1) there is no second, slope-parallel lineation (L₂); and (2) progressive deformation and the formation of curvilinear folds was not considered. Moreover, their D₂ rheomorphism is limited to valley-confined ignimbrites, and therefore cannot be readily applied to non-confined sheets.

Predicted features

Predicted features include: (1) a ubiquitous mylonite-like fabric; (2) ‘early’ valley-axis perpendicular, cylindrical folds, and ‘late’ valley-axis parallel, cylindrical folds; (3) a sheared basal eutaxitic fabric; and (4) down-slope transport direction and kinematic criteria (Figs 5-2a; 5-3; Table 5-1).

Comparison with features observed in the Grey’s Landing ignimbrite

The Chapin and Lovell (1979) model is the first to account for the ubiquitous mylonite-like rheomorphic fabric developed in the Grey’s Landing ignimbrite. Furthermore, it accounts for the intensely sheared nature of the base of the Grey’s Landing ignimbrite (Table 5-1). Mutually perpendicular fold phases are observed outside the Rogerson Graben (e.g., Monument Canyon; Fig. 3-52), however, it does not account for the widespread occurrence of curvilinear folds and sheath folds, both in mylonite-like ignimbrite and in the steep domain. Moreover, this model again depends on gravity-driven, down-slope ductile flow.

Progressive aggradation and deformation at the base of a sustained pyroclastic density current

Outline of conceptual model

Branney and Kokelaar (1992; 2002) radically re-interpreted the emplacement of rheomorphic ignimbrites with the concept of progressive aggradation as the principal mode of ignimbrite deposition. They proposed a model where hot pyroclasts are progressively aggraded from the base of a sustained pyroclastic density current, and that these weld and deform in a transient and upward-migrating, non-coaxial shearing boundary layer at the current – deposit interface (Figs 5-2b, $t_1 - t_4$; and 5-4). Progressive aggradation has become the most widely accepted depositional mechanism for all ignimbrites (e.g., Branney and Kokelaar, 2002). Welding and initial deformation within this thin shear zone produce a eutaxitic fabric or flow-banding, and an imbricated basal fabric. Folds formed within this shear zone are expected to be curvilinear or sheath folds, and limited in

scale by the thickness of the shear zone. The momentum driving-rheomorphism is envisaged as a combination of three forces: (1) momentum transferred from the particulate current through pyroclast aggradation; (2) momentum transferred by shear-coupling across the current-deposit boundary, analogous with the fetch of the prevailing wind creating waves on the upper surface of a body of water; and (3) flow down any suitably orientated slope. Progressive deformation is expected to continue within the freshly deposited ignimbrite, leading to progressive modification of early-formed structures and fabrics, to a depth controlled by the rheology of the deposit. Syn-emplacement welding and rheomorphism as envisaged by Branney and Kokelaar (1992) is dependent on very rapid welding as supported by Freundt (1998; 1999) rather than prolonged compaction-driven welding (Ross and Sheridan, 1972). Structures consistent with syn-emplacement rheomorphism as proposed by Branney and Kokelaar (1992) have now been reported from numerous examples (e.g. Branney et al., 1992; Smith and Cole, 1997; Kokelaar and Königer, 2000; Mukhopadhyay et al., 2001; Sumner and Branney, 2002; Branney et al., 2004b; Pioli and Rosi, 2005). Furthermore, Branney and Kokelaar's (1992) model allows for large-scale deformation, up to whole deposit-scale, after the pyroclastic density current has dissipated; this allows for the a range of structures characteristic of non-particulate gravity currents (e.g. ramps, ogives, and large-scale refolding) to develop.

Predicted features

Predicted features include: (1) a ubiquitous mylonite-like fabric; (2) curvilinear folds and sheath folds; (3) a sheared basal eutaxitic fabric; (4) transport direction independent of local topography; and (5) local, rapid vertical variation in transport direction (Figs 5-2b; 5-4; Table 5-1).

Comparison with features observed in the Grey's Landing ignimbrite

The Branney and Kokelaar (1992) model, and studies following-on from it, account for the ubiquitous mylonite-like fabric and incorporated curvilinear folds and sheath folds. Furthermore, it accounts for transport directions both parallel

and perpendicular to the underlying palaeo-topography, and for localised, vertical changes in the transport direction. It allows for a both syn- and post-depositional rheomorphism.

Applicability of different models

Only the Branney and Kokelaar (1992) model is consistent with the structures observed in the Grey's Landing ignimbrite (Table 5-1). It accounts for the pervasive mylonite-like fabric, variation in transport direction in relation to the palaeo-slope, and rapid localised variations in transport direction. In contrast, the Schmincke and Swanson (1967) and Wolff and Wright (1981b) models cannot explain the pervasive mylonite-like fabric because they envisage a 'fixed' ductile shear zone at the base of the deposit. This criteria alone is enough to discount them. Moreover, the Wolff and Wright (1981b) model does not allow for syn-depositional welding or rheomorphism. The Chapin and Lovell (1979) model, although it accounts for a pervasive mylonite-like fabric, does not incorporate ideas of progressive deformation, and therefore requires two phases of rheomorphism to produce sheath folds and curvilinear folds in the mylonite-like fabric.

Syn-depositional welding and rheomorphism in the Grey's Landing ignimbrite

I propose a model of syn-depositional welding and rheomorphism similar to that of Branney and Kokelaar (1992). A ubiquitous mylonite-fabric is consistent with formation in a transient, upward migrating, sub-horizontal ductile shear zone where deposition, welding, and the first increments of rheomorphism are contemporaneous (Fig. 5-5). The shear zone is approximately 0.5 m thick, and deformation within it is strongly non-coaxial and prolate, producing a strong elongation lineation, kinematic criteria, and curvilinear folds and sheath folds (Fig. 5-5). The top of the shear zone corresponds with the boundary between the fast-moving, over-riding particulate current (low concentration) and the slow-moving, non-particulate deposit (high concentration); this boundary has a strong

rheological contrast across it (Fig. 5-5). As the deposit aggrades and the shear zone migrates upwards, deformed ignimbrite passes out of the base of the active shear zone, and no longer undergoes significant rheomorphism. This lower boundary is likely to be gradational.

Curvilinear folds and sheath folds formed within the shear zone likely developed in one or more of three ways: (1) progressive stretching and hinge rotation of originally flow-perpendicular folds into parallelism (Figs 1-8a; Fig. 5-5; e.g., at Cedar Creek Reservoir, Fig. 3-44 recumbent S / Z fold pairs); (2) nucleation around flow perturbations (e.g., porphyroclasts, Fig. 1-8b; flow cells, Fig. 1-8c); and (3) as originally obliquely-nucleated folds.

The momentum driving deformation is likely to come from the same mechanisms as proposed by Branney and Kokelaar (1992): (1) momentum transferred from the particulate current through pyroclast aggradation (Fig. 5-5); (2) momentum transferred by shear-coupling across the current-deposit boundary, analogous with the fetch of the prevailing wind creating waves on the upper surface of a body of water; and (3) gravity-driven flow down any suitably orientated slope. The final mechanism cannot be the most important, as the mylonite-like fabric is equally well developed in ignimbrite deposited on slopes of differing orientations.

Post-depositional rheomorphism

Review of evidence

Key evidence

1. Parallel-style folds deforming the earlier mylonite-like rheomorphic fabric.
2. Folds are typically perpendicular to the underlying palaeo-slope.
3. Post-depositional folds are not pervasive, rather they are concentrated in the central and upper parts of thick ignimbrite.

Interpretations and implications

Therefore, there is clearly a second, discrete phase of rheomorphism that appears to be localised in the thickest, and best insulated, parts of the ignimbrite. Gravity-driven down-slope ductile flow appears to be the principal cause of shortening.

Conceptual models for post-depositional rheomorphism

Different mechanisms have been proposed for post-depositional rheomorphism, many drawing on inferences from silicic lavas.

Ductile flow like a lava

Presumably the freshly deposited hot and ductile ignimbrite behaved more or less like a rhyolite lava, the most significant difference being the imposition of a pre-existing mylonite-like fabric. The ignimbrite was deposited across uneven palaeo-topography, and therefore, it is intuitive that post-depositional flow to achieve gravitational stability. This phase of ductile flow would have continued until either: (1) the deposit became gravitationally stable; or (2) ductile flow was no longer possible.

The ignimbrite emplacement models of Schmincke and Swanson (1967), Chapin and Lowell (1979), and Wolff and Wright (1981b) envisage deposit-scale rheomorphism driven by gravity, like deformation in lavas (e.g., Fink, 1983; Smith, 2002; Cioni and Funedda, 2005). Predicted structures include: (1) slope perpendicular surface folds including distal, down-slope closing ogives (e.g., Fig. 1-9; Fink, 1980); (2) thrust faults and ramping at the distal end (Fig. 1-10); (3) down-slope parallel elongation lineations and kinematic criteria (Smith, 2002; Cioni and Funedda, 2005); (4) multiple fold generations reflecting gradual increase in the thickness of the folded layer due to cooling (e.g., Gregg et al., 1998); and (5) thick autobreccias. Typically the proximal parts of lavas extend by shear-thinning as the flow progresses.

Comparison with features observed in the Grey's Landing ignimbrite

Ogive folds, ramping and significant thicknesses of autobreccia are typical of the distal ends of lavas, where the viscosity of lava increases with distance from the vent due to cooling and degassing. However, these structures are not observed in the Grey's Landing ignimbrite, probably because post-depositional rheomorphism did not lead to significant transport from the original starting position (where it was deposited) and the thickest ignimbrite was well insulated and had a lower viscosity for longer. Down-slope parallel lineations (Fig. 3-52), slope perpendicular folds (Fig. 3-43), and multiple fold generations (Figs 3-44; 3-45) are typical of the proximal and medial parts of large silicic lavas, and these are observed.

Deposit-scale sliding on ductile substrate

Rheomorphic deformation has also been recorded from deposit-scale slides (akin to sedimentary slides, e.g., Stow, 1986) where weak and ductile substrate has accommodated motion. Embree and Hoggan (1999) described folding of the Huckleberry Ridge Tuff in Eastern Idaho, caused by loading-induced failure and horizontal movement of unconsolidated alluvial and lacustrine sediments. The base of the ignimbrite and the internal eutaxitic fabric are folded around 100 m-scale, upright to overturned, buckle-style monoclines that strike perpendicular to the sliding direction. They reported a localized transition from ductile to brittle deformation and concluded that deformation occurred post-welding but before the ignimbrite had cooled sufficiently to behave as a wholly brittle sheet. The upper surface of the ignimbrite was planar and not folded suggesting that shear thinning occurred within the ductile centre of the deposit. Kokelaar and Königer (2000) described the submarine emplacement of a high-grade ignimbrite and localized sliding-related rheomorphism in the Pitts Head Tuff of North Wales. They described sediment-filled shear zones that allowed allochthonous ignimbrite sheets (nappes) to pile-up (nappe-stacking), and sediment-filled rootless diapirs. They concluded that rapidly emplaced, hot ignimbrite boiled pore water in

unconsolidated sediment, in turn fluidizing the sediment and allowing it to buoyantly inject the ignimbrite.

Comparison with features observed in the Grey's Landing ignimbrite

There is no evidence of rheomorphism related to foundering of the substrate beneath the Grey's Landing ignimbrite.

Post-depositional rheomorphism in the Grey's Landing ignimbrite

I conclude that post-depositional rheomorphism was the result of gravity-driven, down-slope flow of the recently deposited ignimbrite. It extended by shear-thinning on the flanks of the Rogerson Graben and the Snake River Plain, and shortened by layer-parallel buckling. The upper surface of the ignimbrite is pervasively folded, with an apparent increase in fold-scale through time suggesting cooling and downward increasing thickness and competency of the folded layer. Folding of the upper surface was of short duration compared to the interior. Not all of the deposit experienced post-depositional rheomorphism, the base of the steep zone corresponding with the depth in the unit that remained ductile for the longest time. Therefore, it is possible that a certain amount of post-depositional flow was effectively 'intrusive', and continued to deform the interior but not the upper surface. Where the syn- and post-depositional rheomorphism flow directions were similar (e.g., within the Graben) curvilinear folds and sheath folds dominate, and it is not possible to separate the end of syn-depositional rheomorphism from the start of post-depositional rheomorphism; rather there is probably continuous deformation of the deposit over a short period of time.

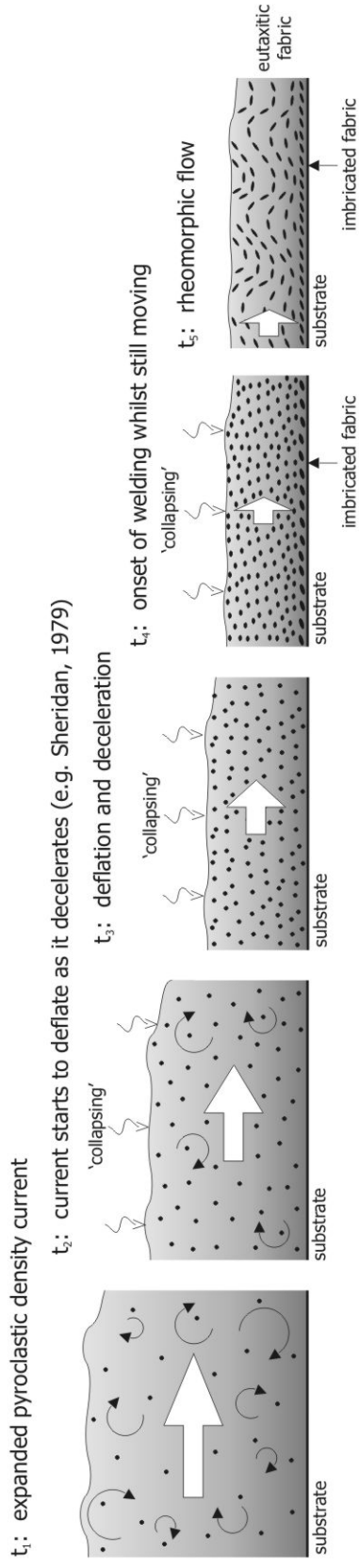
Summary

The Grey's Landing ignimbrite underwent two distinct phases of rheomorphism, that may have been broadly contemporaneous. Syn-depositional welding and rheomorphism was influenced by a 0.5 m thick shear zone at the boundary

between the pyroclastic density current and the deposit, and produced a characteristic 'flat zone' of penetrative mylonite-like fabric. Later, gravity-driven rheomorphism folded the mylonite-like fabric into the 'steep' zone characterised by extrafolial buckle folds and sheath folds. The presence of an early mylonite-like fabric deformed by late folding is characteristic of rheomorphic ignimbrites, and therefore, distinguishes lava-like ignimbrites from lavas.

A *En masse* flow of a rapidly deflated pyroclastic current (Schmincke & Swanson, 1967).

Expanded current deflates and agglutinates, gradually transforming into a rheomorphic ignimbrite.



B *Remobilization* of a static welded layer (*sensu* Wolff & Wright, 1981)

Expanded current deflates, and agglutinates on becoming stationary; followed by rheomorphic flow of remobilized welded ignimbrite.

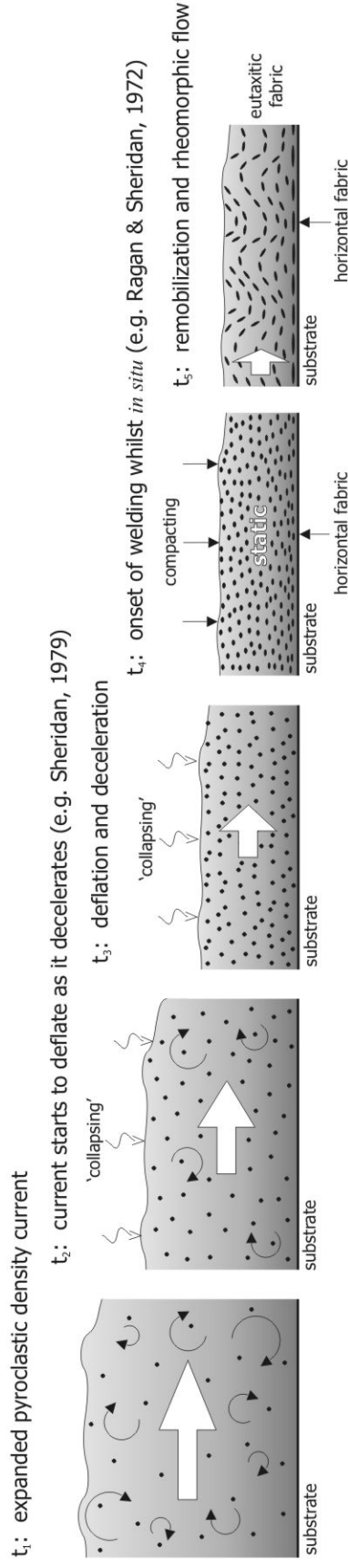
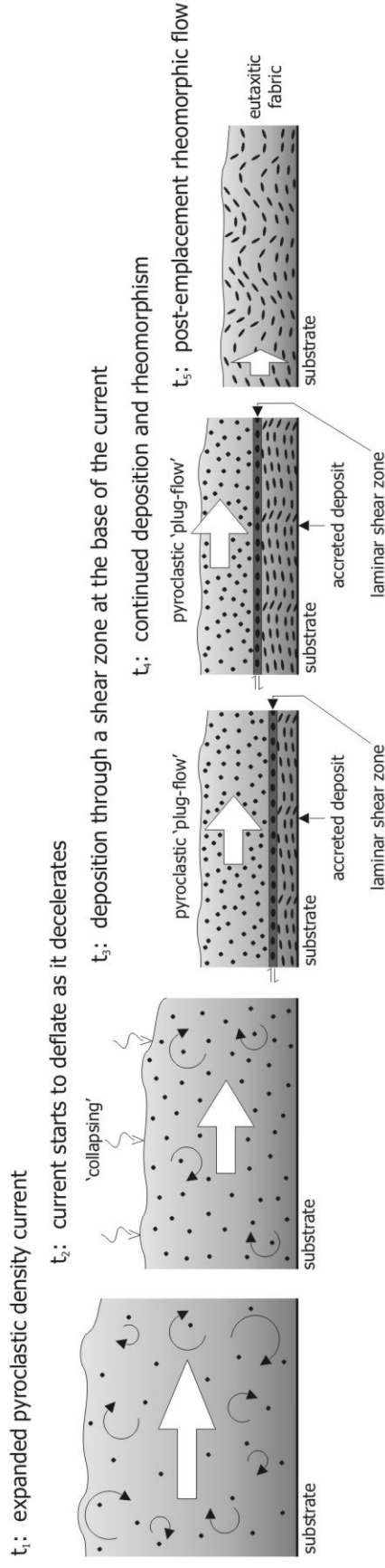


Fig. 5-1. Emplacement of rheomorphic ignimbrite - post-welding models. (A) cartoon showing stages of deposition, welding and rheorphism in a rheomorphic ignimbrite after Schmincke & Swanson (1967). Note how there is gradual deceleration and deflation of the current from particulate to non-particulate. In this scheme welding is followed seamlessly by rheorphism ($t_4 - t_5$). Note the presence of a characteristic basal fabric of imbricated framme. (B) cartoon showing stages of deposition, welding and rheorphism in a rheomorphic ignimbrite after Wolff & Wright (1981). Note how there is a break between deposition and deflation ($t_1 - t_2$), and welding (t_3), when transport has ceased. Welding proceeds *in situ*; rheorphism occurs by the remobilization of the welded mass (t_5). Note that there is no basal imbricated fabric in this model as welding does not occur during transport.

A Deposition from a rapidly deflating and shearing pyroclastic current (*sensu* Chapin & Lowell, 1979).

Expanded current deflates and gradually agglutinates at a laminar shear zone.



B Progressive aggradation and deformation at the base of a sustained pyroclastic density current (*sensu* Branney & Kokelaar, 1992).

Agglutination and deformation at, and within, the base of sustained current.

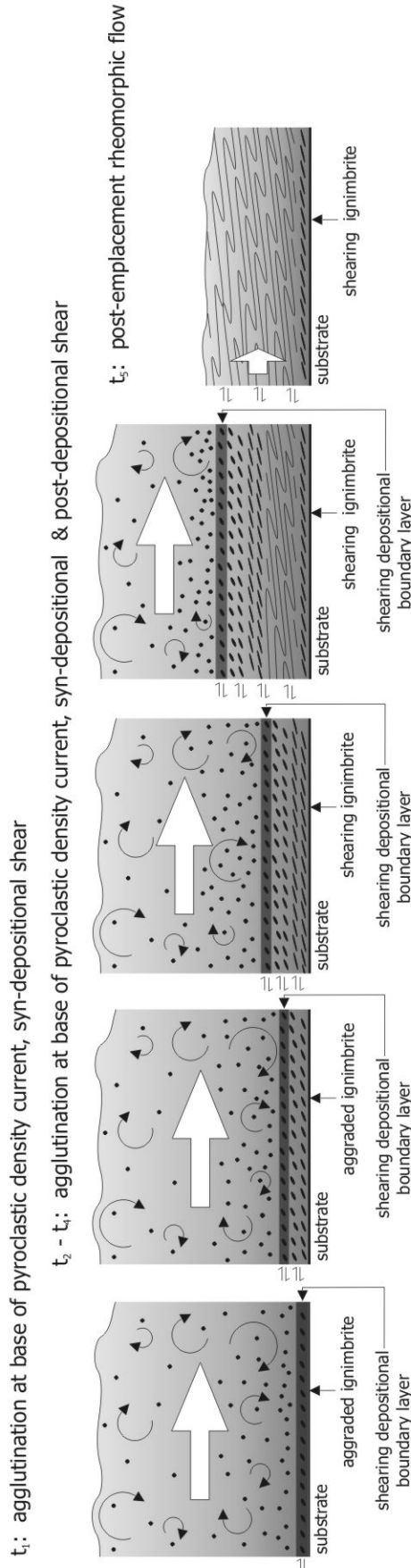
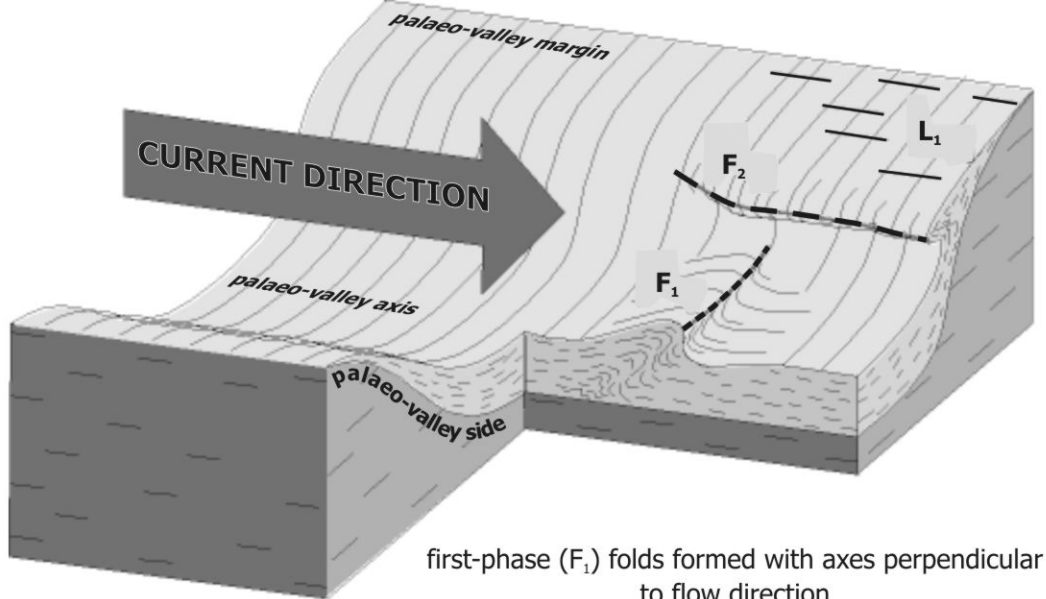


Fig. 5-2. Emplacement of rheomorphic ignimbrite - syn-welding models. (A) cartoon showing stages of deposition, welding and rheomorphism after Chapin & Lowell (1979). Note how as the expanded current collapses (t₂), ignimbrite is accreted from the base of the plug-flow, rapidly welds, and is deformed (t₃ - t₄) in a boundary-layer regime of plane strain and non-coaxial shear. The ignimbrite may continue to deform after the plug-flow has dissipated (t₅). (B) cartoon showing stages of deposition, welding and rheomorphism after Branney & Kokelaar (1992). Note how aggradation from a sustained, inflated current, and shearing at a boundary layer is progressive (t₁ - t₄), and that deformation within the deposit is also progressive and may continue after the current has dissipated (t₄ - t₅).



first-phase (F_1) folds formed with axes perpendicular to flow direction

second-phase (F_2) folds formed with axes parallel to valley sides, and formed by slumping of hot ignimbrite towards valley axis

Fig. 5-3. Schematic block diagram showing 2-phase rheomorphism as inferred by Chapin & Lowell (1979) from the Wall Mountain Tuff, Colorado. Modified from Branney et al. (2004a).

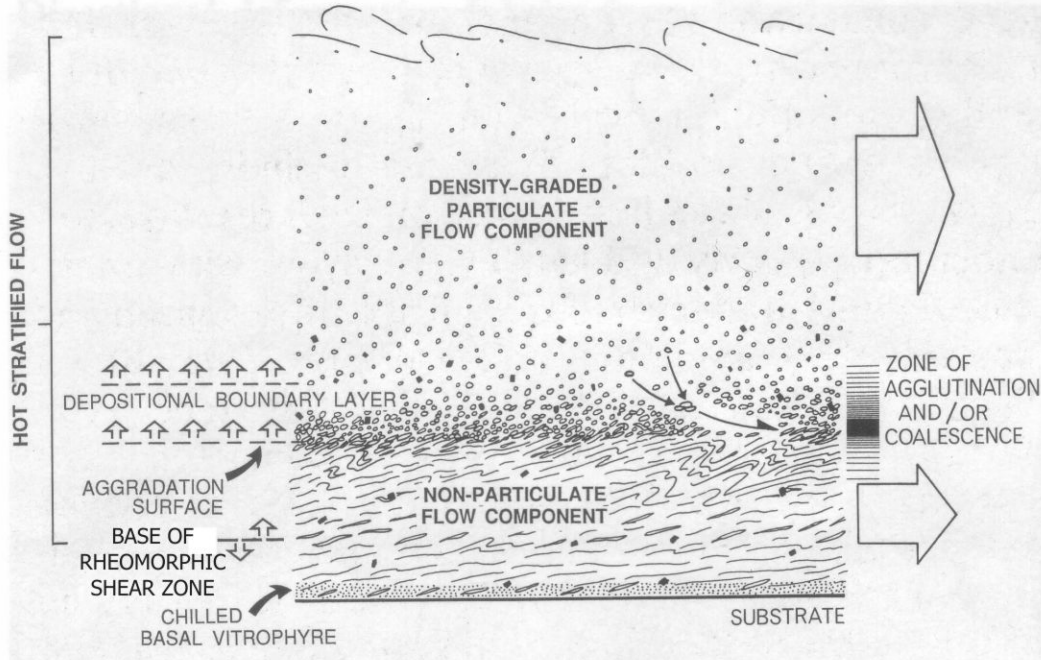


Fig. 5-4. Schematic cross-section showing emplacement and progressive aggradation of an extremely high-grade ignimbrite. Not to scale. Modified from Branney & Kokelaar (1992).

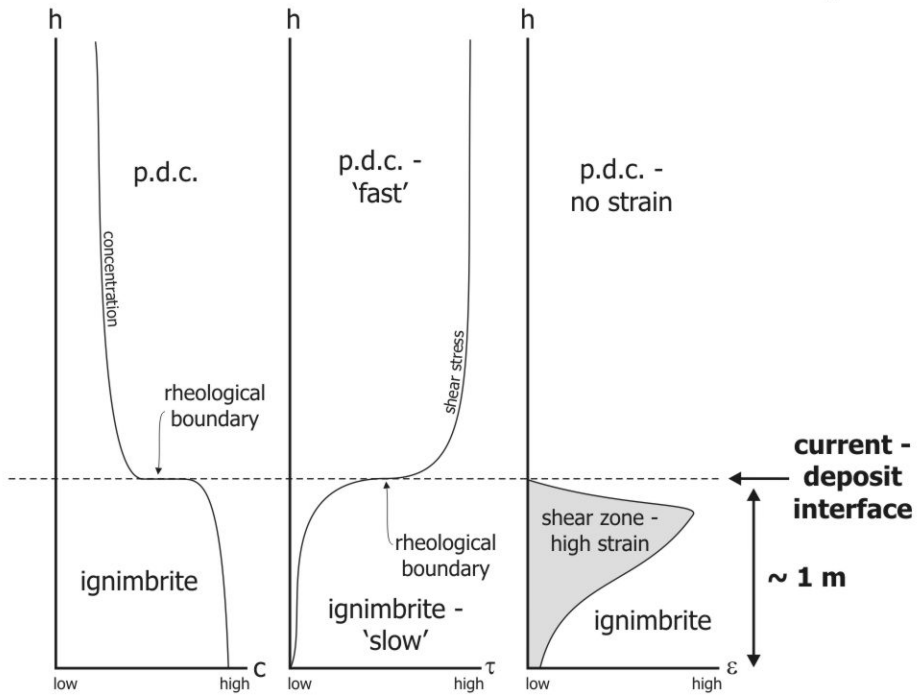
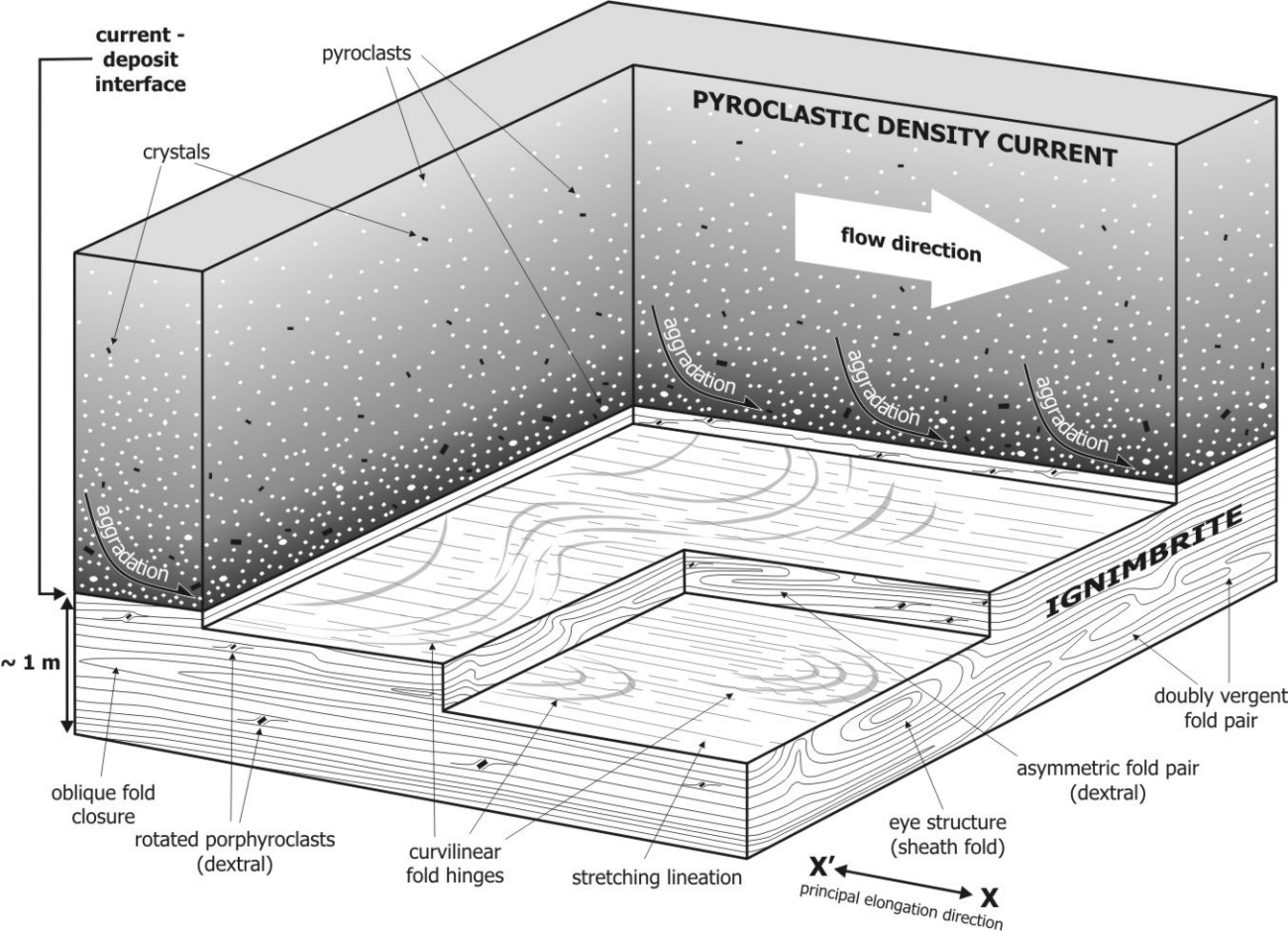


Fig. 5-5. Schematic cut-away block diagram showing the development of curvilinear folds, sheath folds, and other structures in a syn-emplacement ductile shear zone at the base of a sustained pyroclastic density current. This is a development from models of ignimbrite deposition proposed by Branney and Kokelaar (1992).

| <i>features</i> | Schmincke & Swanson, 1967 (Fig. 5-1a) | Wolff & Wright, 1981b (Fig. 5-1b) | Chapin & Lowell, 1979 (Fig. 5-2a) | Branney & Kokelaar, 1992; Branney et al., 2004a (Fig. 5-2b) | Grey's Landing ignimbrite (this study) |
|---|--|--|--|--|--|
| <i>ubiquitous, penetrative, rheomorphic fabric</i> | no – base only | no – base only | yes | yes | yes – mylonite-like ignimbrite, present throughout the deposit including both vitrophyres |
| <i>sheared (non-coaxial) basal eutaxitic fabric</i> | yes – imbricated fiamme | no | yes | yes – imbricated and sheared fiamme | yes – intensely sheared fiamme and eutaxitic fabric (Fig. 3-22) |
| <i>flattened (coaxial) basal eutaxitic fabric</i> | no | yes – horizontal fiamme | no | no | no |
| <i>rapidly changing transport direction</i> | no – parallel to slope | no – parallel to slope | no – parallel to valley axis and slopes | yes – meandering current | yes – rapid elongation direction changes at Grey's Landing and Backwaters (Fig. 3-29) |
| <i>down-slope transport direction</i> | yes - exclusively | yes - exclusively | yes - exclusively | not exclusively | no – early rheomorphism is slope independent, later rheomorphism is slope-controlled (Fig. 3-51) |
| <i>curvilinear folds and sheath folds</i> | not described | not described | no – 2 phase of perpendicular folds | yes | yes – ubiquitous in mylonite-like ignimbrite (Fig. 3-10d) |
| <i>inferred processes</i> | | | | | |
| <i>syn-depositional welding</i> | yes – during density current collapse | no – <i>in situ</i> welding of the deposit | yes | yes - agglutination | yes – must precede syn-depositional rheomorphism |
| <i>load-driven welding</i> | yes | yes | yes | yes - not necessary | possibly – does not account for intensely welded upper surface |
| <i>aggregation-driven welding</i> | possible | no | yes | yes - agglutination | yes – intensely welded upper surface |
| <i>syn-depositional rheomorphism</i> | yes - at base only | no | yes – shear zone at base of current | yes – shear zone at base of current | yes – pervasive, early, mylonite-like fabric throughout |
| <i>post-depositional rheomorphism</i> | yes - throughout | yes - throughout | yes – local modification only | yes – not necessary | yes – localised, later, deformation of the earlier, mylonite-like fabric |

Table 5-1. Summary of the observed features, and inferred processes, predicted by the four most important conceptual models for the emplacement of rheomorphic ignimbrite, and how they compare and contrast with observations and interpretations from the Grey's Landing ignimbrite.

References

- Allen SR, McPhie J (2003) Phenocryst fragments in rhyolitic lavas and lava domes. *J Volcanol Geotherm Res* 126:263-283
- Alsop GI (1992) Progressive deformation and the rotation of contemporary fold axes in the Ballybofey Nappe, northwest Ireland. *Geological Journal* 27:271-283
- Alsop GI, Holdsworth RE (2002) The geometry and kinematics of flow perturbation folds. *Tectonophysics* 350:99-125
- Anders MH, Geissman JW, Piety LA, Sullivan JT (1989) Parabolic distribution of circum-eastern Snake River Plain seismicity and latest Quaternary faulting: migratory pattern and association with the Yellowstone hotspot. *J Geophys Res* 94:1589-1621
- Anders MH (2004) Constant silicic eruption and migration rates of Yellowstone – Snake River Plain volcanism: evidence for a classical hot-spot model? *Geol Soc Am Abs w/Prog* 36:96
- Andersen DJ, Bishop FC, Lindsley DH (1991) Internally consistent solution models for Fe-Mg-Mn-Ti oxides: Part II Fe-Mg-Ti oxides and olivine. *Am Mineral* 76:427-444
- Andersen DJ, Lindsley DH, Davidson PM (1993) QUILF: a Pascal program to assess equilibria among Fe-Mg-Mn-Ti oxides, pyroxenes, olivine, and quartz. *Comp Geosci* 19:1333-1350
- Anderson AT, Newman S, Williams SN, Druitt TH, Skirius C, Stolper E (1989) H₂O, CO₂, Cl, and gas in Plinian and ash-flow Bishop rhyolite. *Geology* 17:221-225
- Anderson SW, Stofan ER, Plaut JJ, Crown DA (1998) Block size distributions on silicic lava flow surfaces: implications for emplacement conditions. *Geol Soc Am Bull* 110:1258-1267
- Andrews GDM, Branney MJ, Bonnicksen B, McCurry M (*in press*) Rhyolite ignimbrites in the Rogerson Graben, southern Snake River Plain volcanic

References

- province: volcanic stratigraphy, eruption history and basin evolution. *Bull Volcanol* xx:xxx-xxx
- Asimow PD, Ghiorso MS (1998) Algorithmic modifications extending MELTs to calculate sub-solidus phase relations. *Am Mineral* 83:1127-1131
- Bacon CR, Hirschmann MM (1988) Mg/Mn partitioning as a test for equilibrium between coexisting Fe-Ti oxides. *Am Mineral* 73:57-61
- Bacon CR, Newman S, Stolper E (1992) Water, CO₂, Cl, and F in melt inclusions in phenocrysts from three Holocene explosive eruptions, Crater Lake, Oregon. *Am Mineral* 77:1021-1030
- Bagdassarov NSh (2005) Non-Newtonian and viscoelastic properties of lava flows. *Am Geophys Union Abs w/Prog*, xx:xxx-xxx
- Bagdassarov NSh, Dingwell DB (1992) A rheological investigation of vesicular rhyolite. *J Volcanol Geotherm Res* 50:307-322
- Bagdassarov NSh, Dingwell DB (1993) Deformation of foamed rhyolites under internal and external stresses: an experimental investigation. *Bull Volcanol* 55:147-154
- Bagdassarov NSh, Pinkerton H (2004) Transient phenomena in vesicular lava flows based on laboratory experiments with analogue materials. *J Volcanol Geotherm Res* 132:115-136
- Bailey DK, MacDonald R (1975) Fluorine and chlorine in peralkaline liquids and the need for magma generation in an open system. *Mineral Mag* 40:405-414
- Bascou J, Camps P, Dautria JM (2005) Magnetic versus crystallographic fabrics in a basaltic lava flow. *J Volcanol Geotherm Res* 145:119-135
- Bellieni G, Brotzu P, Comin-Chiaramonti P, Ernesto M, Melfi A, Pacca IG, Piccirillo EM (1984) Flood basalt to rhyolite suites in the southern Parana Plateau (Brazil): palaeomagnetism, petrogenesis and geodynamic implications. *J Petrol* 25:579-618
- Best MG, Christiansen EH (1997) Origin of broken phenocrysts in ash-flow tuffs. *Geol Soc Am Bull* 109:63-73
- Best MG, Christiansen EH, Blank RH (1989) Oligocene caldera complex and calc-alkaline tuffs and lavas of the Indian Peak volcanic field, Nevada and Utah. *Geol Soc Am Bull* 101:1076-1090

References

- Beucler E, Chevrot S, Montagner JP (1999) The Snake River Plain experiment revisited: relations between a Farallon plate fragment and the transition zone. *Geophys Res Lett* 26:2673-2676
- Bindeman IN, Valley JW (2003) Rapid generation of both high- and low- $\delta^{18}\text{O}$, large-volume silicic magmas at the Timber Mountain / Oasis Valley caldera complex, Nevada. *Geol Soc Am Bull* 115:581-595
- Blake S, Ivey GN (1986) Magma-mixing and the dynamics of withdrawal from stratified reservoirs. *J Volcanol Geotherm Res* 27:153-178
- Blank JG, Stolper EM, Carroll MR (1993) Solubilities of carbon dioxide and water in rhyolitic melt at 850°C and 750 bars. *Earth Planet Sci Lett* 119:27-36
- Bonnichsen B (1982a) The Bruneau-Jarbridge Eruptive Center, southwestern Idaho. In: Bonnichsen B, Breckinridge RM (eds) *Cenozoic Geology of Idaho*. Idaho Bur Min Geol Bull 26:237-254
- Bonnichsen B (1982b) Rhyolite lava flows in the Bruneau-Jarbridge Eruptive Center, southwestern Idaho. In: Bonnichsen B, Breckinridge RM (eds) *Cenozoic Geology of Idaho*. Idaho Bur Min Geol Bull 26:283-320
- Bonnichsen B (2004) The Snake River Plain 11.7 – 10.0 Ma ignimbrite flare-up. *Geol Soc Am Abs w/Prog* 36:24
- Bonnichsen B, Christiansen RL, Morgan LA, Moye FJ, Hackett WR, Leeman WP, Honjo N, Jenks MD, Godchaux MM (1989) Excursion 4A: Silicic volcanic rocks in the Snake River Plain – Yellowstone Plateau province. In: Chapin CE, Zidek J (eds) *Field excursions to volcanic terranes in the western United States; Volume II, Cascades and Intermountain West*. New Mex Bur Mines Min Res 47:135-182
- Bonnichsen B, Citron GP (1982) The Cougar Point Tuff, southwestern Idaho. In: Bonnichsen B, Breckinridge RM (eds) *Cenozoic Geology of Idaho*. Idaho Bur Min Geol Bull 26:255-281
- Bonnichsen B, Godchaux MM (2002) Late Miocene, Pliocene, and Pleistocene geology of southwestern Idaho with emphasis on basalts in the Bruneau-Jarbridge, Twin Falls, and Western Snake River Plain regions. In: Bonnichsen B, White CM, McCurry, M (eds) *Tectonic and Magmatic*

References

- Evolution of the Snake River Plain Volcanic Province. Idaho Geol Surv Bull 30:233-312
- Bonnichsen B, Kauffman DF (1987) Physical features of rhyolite lava flows in the Snake River Plain volcanic province, Southwestern Idaho. In: Fink JH (ed.) The emplacement of silicic domes and lava flows. Geol Soc Am Spec Pap 212:119-145
- Bonnichsen B, Leeman WP, McIntosh WC, Godchaux M (*in press*) Miocene rhyolitic volcanism in southwestern Idaho, with an emphasis on the geochronology and geochemistry of the central Snake River Plain. Bull Volcanol xx:xxx-xxx
- Bonnichsen B, McCurry M, Godchaux MM (2004) Miocene Snake River Plain rhyolites of the Owyhee Front, Owyhee County, Idaho. In: Haller KM, Wood SH (eds) Geological field trips in Southern Idaho, Eastern Oregon, and northern Nevada. Boise, Dept Geosci, Boise State Univ, pages 155-173
- Boroughs S, Wolff J, Bonnichsen B, Godchaux M, Larson P (2005) Large-volume, low- $\delta^{18}\text{O}$ rhyolites of the central Snake River Plain, Idaho, USA. Geology 33:821-824
- Bottinga Y (1994) Rheology and rupture of homogeneous silicate liquids at magmatic temperatures. J Geophys Res 99:9415-9422
- Bottinga Y, Weil DF (1972) Viscosities of magmatic silicate liquids: an empirical method of prediction. Am Jour Sci 272:870-893
- Brandon AD, Goles GG (1988) A Miocene subcontinental plume in the Pacific Northwest: geochemical evidence. Earth Planet Sci Lett 88:273-283
- Branney MJ, Barry TL, Andrews GDM (2004a) Ductile flow in welded ignimbrites: a structural analysis. (abs) IAVCEI General Assembly, Pucón, Chile
- Branney MJ, Barry TL, Godchaux MM (2004b) Sheath folds in rheomorphic ignimbrites. Bull Volcanol 66:485-491
- Branney MJ, Kokelaar BP (1992) A reappraisal of ignimbrite emplacement: progressive aggradation and changes from particulate to non-particulate flow during emplacement of high-grade ignimbrite. Bull Volcanol 54:504-520

References

- Branney MJ, Kokelaar BP (1997) Giant bed from a sustained catastrophic density current flowing over topography: Acatlàn ignimbrite, Mexico. *Geology* 25:115-118
- Branney MJ, Kokelaar, BP (2002) Pyroclastic density currents and the sedimentation of ignimbrites. *Geol Soc Mem* 27
- Branney MJ, Kokelaar BP, McConnell BJ (1992) The Bad Step Tuff: a lava-like rheomorphic ignimbrite in a calc-alkaline piecemeal caldera, English Lake District. *Bull Volcanol* 53:187-199
- Brott CA, Blackwell DD, Ziagos JP (1981) Thermal and tectonic implications of heat flow in the eastern Snake River Plain, Idaho. *J Geophys Res* 86:11709-11734
- Brown RJ, Branney MJ (2003) Event-stratigraphy of a caldera-forming ignimbrite eruption on Tenerife: the 273 ka Poris Formation. *Bull Volcanol* 66:392-416
- Brown RJ, Branney MJ (2004) Bypassing and diachronous deposition from density currents: evidence from a giant regressive bedform in the Poris ignimbrite, Tenerife. *Geology* 32:445-448
- Brown RJ, Barry TL, Branney MJ, Pringle MS, Bryan SE (2003) The Quaternary pyroclastic succession of southern Tenerife, Canary Islands: explosive eruptions, related caldera subsidence, and sector collapse. *Geol Mag* 140:265-288
- Brueseke ME, Hart WK, Heizler MT (*in prep.*) Diverse mid-Miocene silicic volcanism associated with the Yellowstone – Newberry thermal anomaly. *Bull Volcanol* xx:xxx-xxx
- Brueseke ME, Hart WK, Shoemaker KA (2004) Re-evaluating the “Owyhee – Humboldt” eruptive centre: relationships between voluminous middle Miocene silicic volcanism and the Owyhee plateau. *Geol Soc Am Abs w/Prog* 36:97
- Bryan SE, Ewart A, Stephens CJ, Parianos J, Downes PJ (2000) The Whitsunday volcanic province, central Queensland, Australia: lithological and stratigraphic investigations of a silicic-dominated large igneous province. *J Volcanol Geotherm Res* 99:55-78

References

- Bursik MI, Woods AW (1996) The dynamics and thermodynamics of large ash flows. *Bull Volcanol* 58:175-193
- Camp VE, Ross ME (2004) Mantle dynamics and genesis of mafic magmatism in the intermontane Pacific Northwest. *J Geophys Res* 109, 14 pages, doi: 10.1029/2003JB002838
- Camp VE, Ross ME, Hanson WE (2003) Genesis of flood basalts and Basin and Range volcanic rocks from Steens Mountain to the Malheur River Gorge, Oregon. *Geol Soc Am Bull* 115:105-128
- Campbell-Stone E (2002) Realistic geologic strain rates. *Geol Soc Am Abs w/Prog* 34:374
- Capaccioni B, Cuccoli F (2005) Spatter and welded air fall deposits generated by fire-fountaining eruptions: cooling of pyroclasts during transport and deposition. *J Volcanol Geotherm Res* 145:263-280
- Carlson RW, Hart WK (1987) Crustal genesis on the Oregon plateau. *J Geophys Res* 92:6191-6206
- Carlson RW, James DE, Fouch MJ, Grove TL, Hart WK, Grunder AL, Duncan RA, Keller GR, Harder SH, Kincaid CR (2005) On the causes of voluminous magmatism in the northwestern United States. *Geol Soc Am Abs w/Prog* 37:125
- Carrasco-Nunez G, Branney MJ (2005) Progressive assembly of a double-zoned massive ignimbrite: the Zaragoza ignimbrite, Mexico. *Bull Volcanol* 68:3-20
- Carreras J, Druguet E, Grier A (2005) Shear zone-related folds. *Struct Geol* 27:1229-1251
- Carroll MR, Webster JD (1994) Solubilities of S, noble gases, N, Cl, and F in magmas. *Am Mineral Soc Rev Min* 24 231-279
- Cas RAF, Wright JV (1987) Volcanic successions: modern and ancient. Allen and Unwin, London, 529 pages.
- Cashman KV, Blundy J (2000) Degassing and crystallization of ascending andesite and dacite. *Phil Trans R Soc Lond* 358:1487-1513

References

- Cashman KV, Thornber C, Kauahikaua JP (1999) Cooling and crystallization of lava in open channels, and the transition of pāhoehoe lava to 'a'ā. *Bull Volcanol* 61:306-323
- Castro J, Cashman KV (1999) Constraints on rheology of obsidian lavas based on mesoscopic folds. *J Struct Geol* 21:807-819
- Castro J, Cashman KV, Joslin N, Olmsted B (2002) Structural origin of large cavities in the Big Obsidian Flow, Newberry Volcano. *J Volcanol Geotherm Res* 114:313-330
- Cathey HE (2005) Compositional relationships among the multiple rhyolite lavas and the Cougar Point Tuff of the Miocene Bruneau – Jarbidge eruptive centre, Yellowstone hotspot. *Geol Soc Am Abs w/Prog* 37:289
- Cathey HE, Nash BP (2004) The Cougar Point Tuff: implications for thermochemical zonation and longevity of high-temperature, large-volume silicic magmas of the Miocene Yellowstone hotspot. *J Petrol* 45:27-58
- Chapin CE, Lowell GR (1979) Primary and secondary flow structures in ash-flow tuffs of the Gribbles Run palaeovalley, central Colorado. In: Chapin CE, Elston WE (eds) *Ash-flow tuffs*. *Geol Soc Am Sp Pap* 180:137-154
- Childs C, Nicol A, Walsh JJ, Watterson J (2003) The growth and propagation of synsedimentary faults. *J Struct Geol* 25:633-648
- Christiansen RL (2001) The Quaternary and Pliocene Yellowstone Plateau volcanic field of Wyoming, Idaho and Montana. *US Geol Surv Prof Pap* 729-G
- Christiansen RL, Foulger GR, Evans JR (2002) Upper mantle origin of the Yellowstone hotspot. *Bull Geol Soc Am* 114:1245-1256
- Christiansen RL, Lipman PW (1966) Emplacement and thermal history of a rhyolite lava flow near Forty-mile Canyon, southern Nevada. *Geol Soc Am Bull* 77:671-684
- Cioni R, Funedda A (2005) Structural geology of crystal-rich silicic lava flows: a case study from San Pietro Island (Sardinia, Italy). In: Manga M, Ventura G (eds) *Kinematics and dynamics of lava flows*. *Geol Soc Am Spec Pub* 396:1-14

References

- Cloos E (1957) Lineation: a critical review and annotated bibliography. *Geol Soc Am Mem* 18, 136 pages
- Cobbold PR, Quinquis H (1980) Development of sheath folds in shear regimes. *J Struct Geol* 2:119-126
- Colgan JP, Dumitru TA, Miller EL (2004) Diachroneity of Basin and Range extension and Yellowstone hotspot volcanism in northwestern Nevada. *Geology* 32:121-124
- Collins WJ, Beams SD, White AJ, Chappell BW, (1982) Nature and origin of A-type granites with particular reference to southeastern Australia. *Cont Mineral Petrol* 80:189–200
- Coward MP (1980) The analysis of flow profiles in a basaltic dyke using strained vesicles. *J Geol Soc Lon* 137:605-615
- Creaser RA, White AJR (1991) Yardea Dacite – large-volume, high-temperature Felsic volcanism from the Middle Proterozoic of South Australia. *Geology* 19:48-51
- Cummings, D (1964) Bodies as indicators of local flow direction in rhyolite. *US Geol Surv Prof Pap* 475:-D:70-72
- Cummings ML, Evans JG, Ferns ML, Lees KR (2000) Stratigraphic and structural evolution of the middle Miocene syn-volcanic Oregon – Idaho graben. *Geol Soc Am Bull* 112:668-682
- Dadd KA (1992) Structures within large volume rhyolite lava flows of the Devonian Comerong Volcanics, southeastern Australia, and the Pleistocene Ngongotaha lava dome, New Zealand. *J Volcanol Geotherm Res* 54:33-51
- De Rosa R, Mazzuoli G, Ventura G (1996) Relationships between deformation and mixing processes in lava flows: a case study from Salina (Aeolian Islands, Tyrrhenian Sea). *Bull Volcanol* 58:286-297
- Dickinson WR (2002) The Basin and Range province as a composite extensional domain. *Int Geol Rev* 44:1-38
- Dingwell DB (1987) Melt viscosities in the system NaAlSi₃O₈-H₂O-Fe₂O₃. In: Mysen BO (ed) *Magmatic processes: physiochemical principles*. *Geochem Soc Spec Pub* 1:423-431

References

- Dingwell DB (1989) Effect of fluorine on the viscosity of diopside liquid. *Am Mineral* 74:333-338
- Dingwell DB (1998a) Recent experimental progress in the physical description of silicic magma relevant to explosive volcanism. In: Gilbert JS, Sparks RSJ (eds) *The physics of explosive volcanic eruptions*. *Geol Soc Lon Spec Pub* 145:9-26
- Dingwell DB (1998b) Magma degassing and fragmentation: recent experimental advances. *Developments in volcanology*, Elsevier, Amsterdam, 4:1-23
- Dingwell DB, Hess KU (1998) Melt viscosities in the system Na-Fe-Si-O-F-Cl: contrasting effects of F and Cl in alkaline melts. *Am Mineral* 83:1016-1021
- Dingwell DB, Mysen BO (1985) Effects of water and fluorine on the viscosity of albite melt at high-pressure: a preliminary investigation. *Earth Planet Sci Lett* 74:266-274
- Dingwell DB, Scarfe CM, Cronin DJ (1985) The effect of fluorine on viscosities in the system Na₂O-Al₂O₃-SiO₂: implications for phonolites, trachytes and rhyolites. *Am Mineral* 70:80-87
- Dingwell DB, Webb SL (1990) Relaxations in silicate melts. *Eur J Mineral* 2:427-449
- Dobran F (1992) Non-equilibrium flow in volcanic conduits and application to eruptions of Mt St Helens on May 18, 1980, and Vesuvius in AD 79. *J Volcanol Geotherm Res* 49:285-311
- Dunbar NW, Kyle PR (1992) Volatile contents of obsidian clasts in tephra from the Taupo Volcanic Zone, New Zealand: implications to eruptive processes. *J Volcanol Geotherm Res* 49:127-145
- Ebinger CJ, Sleep NH (1998) Cenozoic magmatism throughout east Africa resulting from impact of a single plume. *Nature* 395:788-791
- Ekren EB, McIntyre DH, Bennett EH (1984) High-temperature, large-volume, lavalike ash-flow tuffs without calderas in southwestern Idaho. *US Geol Surv Prof Pap* 1272
- Elliott CG, Williams PF (1988) Sediment slump structures: a review of diagnostic criteria and application to an example from Newfoundland. *J Struct Geol* 10:171-182

References

- Elston WE, Smith EI (1970) Determination of flow direction of rhyolitic ash-flow tuffs from fluidal textures. *Geol Soc Am Bull* 81:3393-3406
- Embree GF, Hoggan RD (1999) Secondary deformation within the Huckleberry Ridge Tuff and subjacent Pliocene units near the Teton Dam: road log to the regional geology of the eastern margin of the Snake River Plain, Idaho. In: Hughes SS, Thackray GD (eds) *Guidebook to the geology of Eastern Idaho*. Pocatello, Idaho Mus Nat Hist: 181-203
- Ewart A, Milner SC, Armstrong RA, Duncan AR (1998a) Etendeka volcanism of the Goboboseb Mountains and Messum igneous complex, Namibia. Part I: geochemical evidence of early Cretaceous Tristan plume melts and the role of crustal contamination in the Parana – Etendeka CFB. *J Petrol* 39:191-225
- Ewart A, Milner SC, Armstrong RA, Duncan AR (1998b) Etendeka volcanism of the Goboboseb Mountains and Messum igneous complex, Namibia. Part II: voluminous quartz latite volcanism of the Awahab magma system. *J Petrol* 39:227-253
- Ez V (2000) When shearing is a cause of folding. *Earth Sci Rev* 51:155-172
- Fackler-Adams BN, Busby CJ (1998) Structural and stratigraphic evolution of extensional oceanic arcs. *Geology* 26:735-738
- Farrell SG (1984) A dislocation model applied to slump structures, Ainsa Basin, south central Pyrenees. *J Struct Geol* 6:727-736
- Fierstein J, Wilson CJN (2005) Assembling an ignimbrite: compositionally defined eruptive packages in the 1912 Valley of Ten Thousand Smokes ignimbrite, Alaska. *Geol Soc Am Bull* 117:1094-1107
- Fink JH (1980) Surface folding and viscosity of rhyolite flows. *Geology* 8:250-254
- Fink JH (1983) Structure and emplacement of a rhyolite obsidian flow: Little Glass Mountain, Medicine Lake Highland, northern California. *Geol Soc Am Bull* 94:362-380
- Fisher RV (1966) Mechanism of deposition from pyroclastic flows. *Am J Sci* 264:350-363
- Fisher RV, Schminke H-U (1984) *Pyroclastic rocks*. New York, Springer-Verlag p.472

References

- Fleck RJ, Theodore TG, Sarna-Wojcicki A, Meyer CE (1998) Age and possible source of air-fall tuffs of the Miocene Carlin Formation, northern Carlin trend. In: Tosdal RM (ed.) Contributions to the gold metallogeny of northern Nevada. US Geol Surv Open File Report 98-338:176-192
- Fleuty MJ (1964) The description of folds. Proc Geol Assoc Lon 75:461-492.
- Forbes CJ, Betts PG, Lister GS (2004) Synchronous development of Type 2 and Type 3 fold interference patterns: evidence for recumbent sheath folds in the Allendale Area, Broken Hill, NSW, Australia. J Struct Geol 26:113-126
- Freundt A (1998) The formation of high-grade ignimbrites; 1: Experiments on high- and low-concentration transport systems containing sticky particles. Bull Volc 59:414-435
- Freundt A (1999) Formation of high-grade ignimbrites; 2: A pyroclastic suspension current model with implications also for low-grade ignimbrites. Bull Volc 60:545-567
- Freundt A, Schminke H-U (1995) Eruption and emplacement of a basaltic welded ignimbrite during caldera formation on Gran Canaria. Bull Volc 56:640-659
- Frezzotti M-L (2001) Silicate-melt inclusions in magmatic rocks: applications to petrology. Lithos 55:273-299
- Friedman I, Long W, Smith RL (1963) Viscosity and water content of rhyolitic glass. J Geophys Res 68:6523-6535
- Fuhrman ML, Lindsley DL (1988) Ternary-feldspar modelling and thermometry. Am Mineral 73:201-215
- Furukawa K, Kamata H (2004) Eruption and emplacement of the Yamakogawa rhyolite in central Kyushu, Japan: a model for emplacement of rhyolitic spatter. Earth Planet Space 56:517-524
- Gao S, Luo T-C, Zhang B-R, Zhang H-F, Han Y-W, Zhao Z-D, Hu Y-K (1998) Chemical composition of the continental crust as revealed by studies in East China. Geochim Cosmochim Acta 62:1959-1975
- Ghiorso MS (1984) Activity/composition relations in the ternary feldspars. Contrib Mineral Petrol 87:282-296

References

- Ghiorso MS, Sack RO (1991) Fe-Ti oxide geothermometry; thermodynamic formulation and the estimation of intensive variables in silicic magmas. *Contrib Mineral Petrol* 108:485-510
- Ghiorso MS, Sack RO (1995) Chemical mass transfer in magmatic processes IV: a revised and internally consistent thermodynamic model for the interpretation and extrapolation of liquid – solid equilibria in magmatic systems at elevated temperatures and pressures. *Contrib Mineral Petrol* 119:197-212. <http://melts.ofm-research.org/>
- Ghosh SK, Sengupta S (1987) Progressive development of structures in a ductile shear zone. *J Struct Geol* 9:277-287
- Ghosh SK, Hazra S, Sengupta S (1999) Planar, non-planar and refolded sheath folds in the Phulad Shear Zone, Rajasthan, India. *J Struct Geol* 21:1715-1729
- Gifkins CC, Allen RL, McPhie J (2005) Apparent welding textures in altered pumice-rich rocks. *J Volcanol Geotherm Res* 142:29-47
- Gill WD (1979) Syn-depositional sliding and slumping in the West Clare Namurian Basin, Ireland. *Geol Soc Ir Spec Pub* 4
- Gimeno D (2003) Devitrification of natural obsidian glasses: petrographic and microstructural study (SEM + EDS) of recent (Lipari Island) and ancient (Sarrabus, SE Sardinia) samples. *J Non-Crystal Solid* 323:84-90
- Gimeno D, Diaz N, García-Vallés M, Martínez-Manent S (2003) Genesis of bottom vitrophyre facies in rhyolitic pyroclastic flows: a case study of syneruptive glass welding (Nuraxi unit, Sulcis, SW Sardinia, Italy). *J Non-Crystal Solid* 323:91-96
- Giordano D, Dingwell DB (2003) Non-Arrhenian multicomponent melt viscosity: a model. *Earth Planet Sci Lett* 208:337-349
- Giordano D, Dingwell DB (2004) Erratum to ‘Non-Arrhenian multicomponent melt viscosity: a model’. *Earth Planet Sci Lett* 221:449
- Giordano D, Dingwell DB, Romano C (2000) Viscosity of a Teide phonolite in the welding interval. *J Volcanol Geotherm Res* 103:239-245

References

- Giordano D, Nichols ARL, Dingwell DB (2005) Glass transition temperatures of natural hydrous melts: a relationship with shear viscosity and implications for the welding process. *J Volcanol Geotherm Res* 142:105-118
- Giordano D, Romano C, Dingwell DB, Poe B, Behrens H (2004) The combined effects of water and fluorine on the viscosity of silicic magmas. *Geochim Cosmochim Acta* 68:5159-5168
- Godchaux MM, Bonnicksen B (2002) Syn-eruptive magma – water and post-eruptive lava – water interactions in the western Snake River Plain, Idaho, during the past 12 million years. In: Bonnicksen B, White CM, McCurry, M (eds) *Tectonic and Magmatic Evolution of the Snake River Plain Volcanic Province*. Idaho Geol Surv Bull 30:387-434
- Gonnermann HM, Manga M (2003) Explosive volcanism may not be an inevitable consequence of magma fragmentation. *Nature* 426:432–435
- Gonnermann HM, Manga M (2005) Flow banding in volcanic rocks: a record of multiplicative magma deformation. *Earth Planet Sci Lett* 236:135-147
- Goodsell B, Hambrey MJ, Glasser NF (2002) Formation of band ogives and associated structures at Bas Glacier d'Arolla, Valais, Switzerland. *J Glaciol* 48:287-300
- Goodsell B, Hambrey MJ, Glasser NF, Nienow P, Mair D (2005) The structural glaciology of a temperate valley glacier: Haut Glacier d'Arolla, Valais, Switzerland. *Arct Antarct Alp Res* 37:218-232
- Goscombe B (1991) Intense non-coaxial shear and the development of mega-scale sheath folds in the Arunta Block, central Australia. *J Struct Geol* 13:299-318
- Goscombe BD, Passchier CW (2003) Asymmetric boudins as shear sense indicators – an assessment from field data. *J Struct Geol* 25:575-589
- Gottsmann J, Dingwell DB (2001) Cooling dynamics of spatter-fed phonolite obsidian flows on Tenerife, Canary Islands. *J Volcanol Geotherm Res* 105:323-342
- Grasemann B, Wiesmayr G, Dragantis E, Füsseis F (2004) Classification of re-fold structures. *J Geol* 112:119-125

References

- Green JC (1989) Physical volcanology of mid-Proterozoic plateau lavas: the Keweenaw North Shore Volcanic Group, Minnesota. *Geol Soc Am Bull* 101:486-500
- Green JC, Fitz III TJ (1993) Extensive Felsic lavas and rheoignimbrites in the Keweenaw Mid-continent Rift plateau volcanics, Minnesota: petrographic and field recognition. *J Volcanol Geotherm Res* 54:177-196
- Greene RC (1973) Petrology of the welded tuff of Devine Canyon, southeastern Oregon. *US Geol Surv Prof Pap* 792, 26 pages
- Gregg TKP, Fink JH, Griffiths RW (1998) Formation of multiple fold generations on lava flow surfaces: influence of strain rate, cooling rate, and lava composition. *J Volcanol Geotherm Res* 80:281-292
- Griffiths RW (2000) The dynamics of lava flows. *Annu Rev Fluid Mech* 32:477-518
- Griffiths RW, Fink JH (1993) Effects of surface cooling on the spreading of lava flows and domes. *J Fluid Mech* 252:667-702
- Grunder AL, Laporte D, Druitt TH (2005) Experimental and textural investigation of welding: effects of compaction, sintering, and vapour-phase crystallization in the rhyolitic Rattlesnake Tuff. *J Volcanol Geotherm Res* 142:89-104
- Grunder AL, Russell JK (2005) Welding processes in volcanology: insights from the field, experimental, and modelling studies. *J Volcanol Geotherm Res* 142:1-9
- Hall A (1996) *Igneous petrology*. Longman, Harlow, 551 pages
- Ham AP, Bell TH (2004) Recycling of foliations during folding. *J Struct Geol* 26:1989-2009
- Hambrey MJ, Glasser NF (2003) The role of folding and foliation development in the genesis of medial moraines: examples from Svalbard glaciers. *J Geol* 111:471-485
- Hambrey MJ, Lawson W (2000) Structural styles and deformation fields in glaciers: a review. In: Maltman AJ, Hubbard B, Hambrey MJ (eds) *Deformation of glacial materials*. *Geol Soc Lon Spec Pub* 176:59-83

References

- Hambrey MJ, Murray T, Glasser NF, Hubbard A, Hubbard B, Stuart G, Hansen S, Kohler J (2005) Structure and changing dynamics of a polythermal valley on a centennial timescale: Midre Lovénbreen, Svalbard. *J Geophys Res Earth Sur* 110
- Hammer S, Passchier CW (1991) Shear-sense indicators: a review. *Geol Surv Can Pap* 90-17
- Harris AJL, Flynn LP, Matías O, Rose WI (2002) The thermal stealth flows of Santiaguito dome, Guatemala: implications for the cooling and emplacement of dacite block-lava flows. *Geol Soc Am Bull* 114:533-546
- Harris AJL, Dehn J, Patrick M, Calvari S, Ripepe M, Lodato L (2005) Lava effusion rates from hand-held thermal infrared imagery: an example from the June 2003 effusive activity at Stromboli. *Bull Volcanol* 68:107-117
- Hart WK, Aronson JJ (1983) K – Ar ages of rhyolites from the western Snake River Plain area, Oregon, Idaho, and Nevada. *Isochron West* 36:17-19
- Hatcher RD (1995) *Structural geology: principles, concepts, and problems*. Prentice Hall, New Jersey, 525 pages
- Hausback BP (1987) An extensive, hot, vapour-charged rhyodacite flow, Baja California, Mexico. In: Fink JH (ed) *The emplacement of silicic domes and lava flows*. *Geol Soc Am Spec Pub* 212:111-118
- Hay RL, Hildreth W, Lambe RN (1979) Globule ignimbrite of Mount Suswa, Kenya. In: Chapin CE, Elston WE (eds) *Ash-flow tuffs*. *Geol Soc Am Sp Pap* 180:167-175
- Head JW, Wilson L (1989) Basaltic pyroclastic eruptions: Influence of gas-release patterns and volume fluxes on fountain structure, and the formation of cinder cones, spatter cones, rootless flows, lava ponds and lava flows. *J Volcanol Geotherm Res* 37:261-271
- Henry CD, Price JG, Rubin JN, Laubach SE (1990) Case study of an extensive silicic lava: the Bracks Rhyolite, Trans-Pecos Texas. *J Volcanol Geotherm Res* 43:113-132
- Henry CD, Price JG, Rubin JN, Parker DF, Wolff JA, Self S, Franklin R, Barker DS (1988) Widespread, lava-like silicic volcanic rocks of Trans-Pecos Texas. *Geology* 16:509-512

References

- Henry CD, Wolff JA (1992) Distinguishing strongly rheomorphic tuffs from extensive silicic lavas. *Bull Volcanol* 54:171-186
- Hildreth W (1979) The Bishop Tuff: evidence for the origin of compositional zonation in silicic magma chambers. *Geol Soc Am Spec Pap* 180:43-75
- Hildreth W (1981) Gradients in silicic magma chambers: implications for lithospheric magmatism. *J Geophys Res* 86:10153-10192
- Hildreth W, Halliday AN, Christiansen RL (1991) Isotopic and chemical evidence concerning the genesis and contamination of basaltic and rhyolitic magma beneath the Yellowstone Plateau volcanic field. *J Geol* 32:63-138
- Hirt WH (2002) Transition from ash-flow to voluminous lava-flow activity, Bruneau-Jarbridge Eruptive Center, Southwestern Idaho. In: Bonnicksen B, White CM, McCurry, M (eds) *Tectonic and Magmatic Evolution of the Snake River Plain Volcanic Province*. *Idaho Geol Surv Bull* 30:195-204
- Hogeweg N, Keith TEC, Colvard EM, Ingebritsen SE (2005) Ongoing hydrothermal heat loss from the 1912 ash-flow sheet, Valley of Ten Thousand Smokes, Alaska. *J Volcanol Geotherm Res* 143:279-291
- Holtz F, Behrens H, Dingwell DB, Taylor RP (1992) Water solubility in aluminosilicate melts of haplogranite composition at 2 kbar. *Chem Geol* 96:289-302
- Holtz F, Dingwell DB, Behrens H (1993) Effects of F, B₂O₃ and P₂O₅ on the solubility of water in haplogranite melts compared to natural silicate melts. *Contrib Mineral Petrol* 113:492-501
- Honjo N (1990) Geology and stratigraphy of the Mount Bennett Hills, and the origin of west-central Snake River Plain rhyolites. PhD thesis, Rice University, Houston, TX, pp 57-148
- Honjo N, Bonnicksen B, Leeman WP, Stormer Jr. JC (1992) Mineralogy and geothermometry of high-temperature rhyolites from the central and western Snake River Plain. *Bull Volcanol* 54:220-237
- Hooper PR, Binger GB, Lees KR (2002) Ages of the Steens and Columbia River basalts and their relationship to extension-related calc-alkaline volcanism in eastern Oregon. *Geol Soc Am Bull* 114:43-50

References

- Hooper P, Johnson J, Hawkesworth C (2002) A model for the origin of the western Snake River Plain as an extensional strike-slip duplex, Idaho and Oregon. In: Bonnicksen B, White CM, McCurry, M (eds) Tectonic and Magmatic Evolution of the Snake River Plain Volcanic Province. Idaho Geol Surv Bull 30:59-67
- Hort M (1998) Abrupt change in magma liquidus temperature because of volatile loss or magma mixing: effects on nucleation, crystal growth and thermal history of the magma. J Petrol 39:1063-1076
- Hughes SS, McCurry M (2002) Bulk major and trace element evidence for a time-space evolution of Snake River Plain rhyolites, Idaho. In: Bonnicksen B, White CM, McCurry, M (eds) Tectonic and Magmatic Evolution of the Snake River Plain Volcanic Province. Idaho Geol Surv Bull 30:161-176
- Humphreys ED, Deuker KG, Schutt DL, Smith RB (2000) Beneath Yellowstone: evaluating plume and non-plume models using teleseismic images of the upper mantle. GSA Today 10:1-7
- Ihinger PD, Hervig RL, McMillan PF (1994) Analytical methods for volatiles in glasses. Am Mineral Soc Rev Min 30:67-121
- Jeffreys H (1925) The flow of water in an inclined channel of rectangular section. Phil Mag 49:793-807
- Johnson MC, Anderson AT, Rutherford MJ (1994) Pre-eruptive volatile contents of magmas. Am Mineral Soc Rev Min 30:281-330
- Jordan BT (2005) Age-progressive volcanism of the Oregon High Lava Plains: overview and evaluation of tectonic models. In: Foulger GR, Natland JH, Presnall DC, Anderson DL (eds) Plates, plumes, and paradigms. Geol Soc Am Spec Pap 388:503-515
- Jordan BT, Grunder AL, Duncan RA, Deino AL (2004) Geochronology of age-progressive volcanism of the Oregon High Lava Plains: implications for the plume interpretation of Yellowstone. J Geophys Res 109, 19 pages, doi 10.1029/2003JB002776
- Jourdan F, Féraud G, Bertrand H, Watkeys MK, Kampunzu AB, Le Gall B (2006) Basement control on dyke distribution in Large Igneous Provinces: case study of the Karoo triple junction. Earth Planet Sci Lett 241:307-322

References

- Kano K, Matsuura H, Yamauchi S (1997) Miocene rhyolitic welded tuff infilling a funnel-shaped eruption conduit Shiotani, southeast of Matse, SW Japan. *Bull Volcanol* 59:125-135
- Keating GN (2005) The role of water in cooling ignimbrites. *J Volcanol Geotherm Res* 142:145-171
- Kilburn CRJ (2000) Lava flows and flow fields. In: Sigurdsson H (ed) *Encyclopedia of Volcanoes*. Academic Press, San Diego, pages 291-305
- Kirstein LA, Hawkesworth CJ, Garland FG (2001) Felsic lavas or rheomorphic ignimbrites: is there a chemical distinction? *Cont Mineral Petrol* 142:309-322.
- Knight MD, Walker GPL (1988) Magma flow directions in dikes of the Koolau complex, determined from magnetic fabric studies. *J Geophys Res* 93:4301-4319
- Kobberger G, Schminke HU (1999) Deposition of rheomorphic ignimbrite D (Mogán Formation), Gran Canaria, Canary Islands, Spain. *Bull Volcanol* 60:465-485
- Kokelaar BP, Königer S (2000) Marine emplacement of welded ignimbrite: the Ordovician Pitts Head Tuff, North Wales. *J Geol Soc Lon* 157:517-536
- Kuntz MA, Owen DE, Champion DE, Gans PB, Smith SC, Brossy C (2004) Geology of the Craters of the Moon 30' x 60' map area and new perspectives on basaltic volcanism of the eastern Snake River Plain, Idaho. In: Haller KM, Wood SH (eds) *Geological field trips in Southern Idaho, Eastern Oregon, and northern Nevada*. Boise, Dept Geosci, Boise State Univ, pages 135-153
- Lange RL (1994) The effect of H₂O, CO₂ and F on the density and viscosity of silicate melts. *Am Mineral Soc Rev Min* 24:331-369
- Lange RL, Carmichael ISE (1991) Thermodynamic properties of silicate liquids with emphasis on density, thermal expansion and compressibility. *Am Mineral Soc Rev Min* 23:25-66
- Leat PT, Schminke H-U (1993) Large-scale rheomorphic shear deformation in Miocene peralkaline ignimbrite E, Gran Canaria. *Bull Volcanol* 55:155-165

References

- Le Bas MJ, Le Maitre RW, Streckeisen A, Zanettin B (1986) A chemical classification of volcanic rocks based on the total alkali – silica diagram. *J Petrol* 27:745-750
- Leeman WP (1982a) Development of the Snake River Plain-Yellowstone Plateau province, Idaho and Wyoming: an overview and petrologic model. In: Bonnicksen B, Breckinridge RM (eds) *Cenozoic Geology of Idaho*. Idaho Bur Min Geol Bull 26:155-177
- Leeman WP, Menzies MA, Matty DJ, Embree GF (1985) Strontium, neodymium and lead isotopic compositions of deep crustal xenoliths from the Snake River Plain: evidence for Archean basement. *Earth Planet Sci Lett* 75:354-368
- Lejeune A-M, Richet P (1995) Rheology of crystal-bearing silicate melts: an experimental study at high viscosities. *J Geophys Res* 100:4215-4229
- Lindsley DH (1983) Pyroxene thermometry. *Am Mineral* 68:477-493
- Link PK, McDonald HG, Fanning CM, Godfrey AE (2002) Detrital zircon evidence for Pleistocene drainage reversal at Hagerman Fossil Beds National Monument, central Snake River Plain, Idaho. In: Bonnicksen B, White CM, McCurry, M (eds) *Tectonic and Magmatic Evolution of the Snake River Plain Volcanic Province*. Idaho Geol Surv Bull 30:105-120
- Liss D, Hutton DHW, Owens WH (2002) Ropy flow structures: a neglected indicator of magma-flow direction in sills and dikes. *Geology* 30:715-718
- Lofgren G (1970) Experimental devitrification rate of rhyolite glass. *Geol Soc Am Bull* 81:553-560
- Lofgren G (1971) Experimentally produced devitrification textures in natural rhyolitic glass. *Geol Soc Am Bull* 82:111-124
- McBirney AR, Murase T (1984) Rheological properties of magmas. *Annu Rev Earth Planet Sci* 12:337-357
- McCurry M, Watkins AM, Parker JL, Wright K, Hughes SS (1996) Preliminary volcanological constraints for sources of high-grade, rheomorphic ignimbrites of the Cassia Mountains, Idaho: implications for the evolution of the Twin Falls Volcanic Center. *Northwest Geol* 26:81-91

References

- McDonough WF, Sun S-S (1995) Composition of the Earth. *Chem Geol* 120:223-253
- McPhie J, Allen RL (1992) Facies architecture of mineralised submarine volcanic sequences: Cambrian Mount Read Volcanics, western Tasmania. *Econ Geol* 87:587-596
- McPhie J, Doyle M, Allen RL (1993) Volcanic textures. CODES, Univ Tas, 196 pages.
- McQuarrie N, Rodgers DW (1998) Subsidence of a volcanic basin by flexure and lower crustal flow: the eastern Snake River Plain, Idaho. *Tectonics* 17:203-220
- Mahood GA (1984) Pyroclastic rocks and calderas associated with strongly peralkaline volcanic rocks. *J Geophys Res* 89:8540-8552
- Mahood GA, Hildreth W (1986) Geology of the peralkaline volcano at Pantelleria, Strait of Sicily. *Bull Volcanol* 48:143-172
- Malde HE, Powers HA (1962) Upper Cenozoic stratigraphy of the western Snake River Plain, Idaho. *Geol Soc Am Bull* 73:1197-1210
- Manga M (2005) Deformation of flow bands by bubbles and crystals. In: Manga M, Ventura G (eds) Kinematics and dynamics of lava flows. *Geol Soc Am Spec Pub* 396:47-53
- Manga M, Castro J, Cashman KV, Loewenberg M (1998) Rheology of bubble-bearing magmas. *J Volcanol Geotherm Res* 87:15-28
- Manga M, Loewenberg M (2001) Viscosity of magmas containing highly deformable bubbles. *J Volcanol Geotherm Res* 105:19-24
- Manley CR (1992) Extended cooling and viscous flow of large, hot rhyolite lavas: implications of numerical modelling results. *J Volcanol Geotherm Res* 53:27-46
- Manley CR (1996a) Physical volcanology of a voluminous rhyolite lava flow: the Badlands lava, Owyhee plateau, SW Idaho. *J Volcanol Geotherm Res* 71:129-153
- Manley CR (1996b) *In situ* formation of welded tuff-like textures in the carapace of a voluminous silicic lava flow, Owyhee County, SW Idaho. *Bull Volcanol* 57:672-686

References

- Manley CR, Andrews GDM (2004) A numerical modelling investigation of the duration of post-emplacement rheomorphism in a high-grade ignimbrite: Grey's Landing, Idaho. *Geol Soc Am Abs w/Prog* 36:12
- Manley CR, Bacon CR (2000) Rhyolite thermobarometry and the shallowing of the magma reservoir, Coso Volcanic Field, California. *J Petrol* 41:149-174
- Manley CR, Fink JH (1987) Internal textures of rhyolite flows as revealed by research drilling. *Geology* 15:549-552
- Manley CR, McIntosh WC (2002) The Juniper Mountain Volcanic Center, Owyhee County, Southwestern Idaho: age relations and physical volcanology. In: Bonnichsen B, White CM, McCurry, M (eds) *Tectonic and Magmatic Evolution of the Snake River Plain Volcanic Province*. Idaho Geol Surv Bull 30:205-227
- Marques FG, Cobbold PR (1995) Development of highly non-cylindrical folds around rigid ellipsoidal inclusions in bulk simple shear regimes: natural examples and experimental modelling. *J Struct Geol* 17:589-602
- Martin BS (1989) The Roza Member, Columbia River Basalt Group; chemical stratigraphy and flow distribution. In: Reidel SP, Hooper PR (eds) *Volcanism and tectonism in the Columbia River flood-basalt province*. *Geol Soc Am Spec Pap* 239:85-104
- Martinsen OJ (1994) Mass movements. In: Maltman A (ed) *The geological deformation of sediments*. Chapman & Hall, London, 362 pages
- Martinsen OJ, Bakken B (1990) Extensional and compressional zones in slumps and slides in the Namurian of County Clare, Ireland. *J Geol Soc Lon* 147:153-164
- Matthews V, Anderson CW (1973) Yellowstone convection plume and breakup of the western United States. *Nature* 243:158-159
- Mies JW (1991) Planar dispersion of folds in ductile shear zones and kinematic interpretation of fold-hinge girdles. *J Struct Geol* 13:281-297
- Milner SC, Duncan AR, Ewart A (1992) Quartz latite rheoignimbrite flows of the Etendeka Formation, northwestern Namibia. *Bull Volcanol* 54:200-219

References

- Morgan LA, Doherty DJ, Leeman WP (1984) Ignimbrites of the eastern Snake River Plain: evidence for major caldera-forming eruptions. *J Geophys Res* 89:8665-8678
- Morgan LA, McIntosh WC (2005) Timing and development of the Heise volcanic field, Snake River Plain, Idaho, western USA. *Geol Soc Am Bull* 117:288-306
- Morgan WJ (1971) Convection plumes in the lower mantle. *Nature* 230:42-43
- Mues-Schumacher U, Schumacher R, Viereck-Götte, LG, Lepetit P (2004) Areal distribution and bulk rock density variations of the welded İncesu ignimbrite, Central Anatolia, Turkey. *Turk J Earth Sci* 13:249-267
- Mukhopadhyay J, Ray A, Ghosh G, Medda RA, Bandyopadhyay PP (2001) Recognition, characterization and implications of high-grade silicic ignimbrite facies from the Palaeoproterozoic Bijli rhyolites, Dongargarh Supergroup, central India. *Gondwana Res* 4:519-527
- Murase T, McBirney AR (1973) Properties of some common igneous rocks and their melts at high temperatures. *Geol Soc Am Bull* 84:3563-3592
- Nakayama K, Yoshikawa S (1997) Depositional processes of primary to reworked volcanoclastics on an alluvial plain; an example from the Lower Pliocene Ohta tephra bed of the Tokai Group, central Japan. *Sed Geol* 107:211-229
- Navon O, Lyakhovskiy V (1998) Vesiculation processes in silicic magmas. In: Gilbert JS, Sparks RSJ (eds) *The physics of explosive eruptions*. *Geol Soc Lon Spec Pub* 145:27-50
- Nichols BL (1939) Viscosity of lava. *J Geol* 47:290-302
- Orsi G, Sheridan MF (1984) The Green Tuff of Pantelleria: rheoignimbrite or rheomorphic fall? *Bull Volcanol* 47:611-626
- Palmer BA, Walton AW (1990) Accumulation of volcanoclastic aprons in the Mount Dutton Formation (Oligocene-Miocene), Marysvale volcanic field, Utah. *Geol Soc Am Bull* 102:734-748
- Park RG (1989) *Foundations of structural geology*, 2nd edition. Blackie, Glasgow, 148 pages
- Passchier CW, Simpson C (1986) Porphyroclast systems as kinematic indicators. *J Struct Geol* 8 831-844

References

- Passchier CW, Trouw RAJ (1996) *Microtectonics*. Springer Verlag, Berlin, 290 pages
- Paterson SR, Tobisch OT (1993) Pre-lithification structures, deformation mechanisms, and fabric ellipsoids in slumped turbidites from the Pigeon point Formation, California. *Tectonophys* 222:135-149
- Perkins ME, Nash BP (2002) Explosive silicic volcanism of the Yellowstone hotspot: the ash fall tuff record. *Geol Soc Am Bull* 114:367-381
- Perkins ME, Nash WP, Brown FH, Fleck RJ (1995) Fallout tuffs of Trapper Creek Idaho – a record of Miocene explosive volcanism in the Snake River Plains volcanic province. *Geol Soc Am Bull* 107:1484-1506
- Persikov ES, Zharikov VA, Bukhtiyarov PG, Pol'skoy SF (1990) The effects of volatiles on the properties of magmatic melts. *Eur J Mineral* 2:621-642
- Perugini D, Ventura G, Petrelli A, Poli G (2004) Kinematic significance of morphological structures generated by mixing of magmas: a case study from Salina Island (southern Italy). *Earth Planet Sci Lett* 222:1051-1066
- Peterson DW (1979) Significance of the flattening of pumice fragments in ash-flow tuffs. In: Chapin CE, Elston WE (eds) *Ash-flow tuffs*. *Geol Soc Am Sp Pap* 180:195-204
- Pfiffner OA, Ramsey JG (1982) Constraints on geological strain rates: arguments from finite strain rates of naturally deformed rocks. *J Geophys Res* 87:311–321
- Pierce KL, Morgan LA (1992) The track of the Yellowstone hotspot: volcanism, faulting, and uplift. In: Link PK, Kuntz MA, Platt LP (eds) *Regional Geology of Eastern Idaho and Western Wyoming*. *Geol Soc Am Mem* 179:1-53
- Pierce KL, Morgan LA, Saltus RW (2000) Yellowstone plume head: postulated tectonic relations to the Vancouver slab, continental boundaries, and climate. *US Geol Surv Open File Report (on-line edition)* 00-498, 39 pages
- Pierce KL, Morgan LA, Saltus RW (2002) Yellowstone plume head: postulated tectonic relations to the Vancouver slab, continental boundaries, and climate. In: Bonnichsen B, White CM, McCurry, M (eds) *Tectonic and*

References

- Magmatic Evolution of the Snake River Plain Volcanic Province. Idaho Geol Surv Bull 30:5-33
- Pioli L, Rosi M (2005) Rheomorphic structures in a high-grade ignimbrite: the Nuraxi Tuff, Sulcis volcanic district (SW Sardinia, Italy). J Volcanol Geotherm Res 142:11-28
- Piper DJW, Cochonat P, Morrison ML (1999) The sequence of events around the epicentre of the 1929 Grand Banks earthquake: initiation of debris flows and turbidity current inferred from sidescan sonar. Sedimentology 46:79-97
- Ponce DA, Glen JMG (2002) Relationship of epithermal gold deposits to large-scale fractures in northern Nevada. Econ Geol 97:3-9
- Quane SL, Russell JK (2003) Rock strength as a metric of welding intensity in pyroclastic deposits. Eur J Mineral 15:855-864
- Quane SL, Russell JK (2005a) Ranking welding intensity in pyroclastic deposits. Bull Volcanol 67:129-143
- Quane SL, Russell JK (2005b) Welding: insights from high-temperature analogue experiments. J Volcanol Geotherm Res 142:67-87
- Rahl JM, McGrew AJ, Foland KA (2002) Transition from contraction to extension in the northeastern Basin and Range: new evidence from the Copper Mountains, Nevada. J Geol 110:179-194
- Ragan DM, Sheridan MF (1972) Compaction of the Bishop Tuff, California. Geol Soc Am Bull 83:95-106
- Ramsey JG (1962) Interference patterns produced by the superposition of folds of similar types. J Geol 70:466-481
- Ramsey JG (1967) Folding and fracturing in rocks. McGraw-Hill, New York, 568 pages
- Ramsey JG (1980) Shear zone geometry: a review. J Struct Geol 2:83-99
- Ramsey JG, Huber MI (1983) The techniques of modern structural geology, volume 1: strain analysis. Academic Press, London, 307 pages
- Ramsey JG, Huber MI (1987) The techniques of modern structural geology, volume 2: folds and fractures. Academic Press, London, 390 pages
- Reidel SP, Tolani TL, Hooper PR, Beeson MH, Fecht KR, Bentley RD, Anderson JL (1989) The Grande Ronde basalt, Columbia River basalt group;

References

- stratigraphic descriptions and correlations in Washington, Oregon, and Idaho. In: Reidel SP, Hooper PR (eds) *Volcanism and tectonism in the Columbia River flood-basalt province*. Geol Soc Am Spec Pap 239:21-54
- Ridley J (1986) Parallel stretching lineations and fold axes oblique to a shear displacement direction – a model and observations. *J Struct Geol* 8:647-653
- Riehle JR (1973) Calculated compaction profiles of rhyolitic ash-flow tuffs: computational model. *Bull Volcanol* 57:319-336
- Riehle JR, Miller TF, Bailey RA (1995) Cooling, degassing, and compaction of rhyolitic ash-flow tuffs: a computational model. *Bull Volcanol* 57:319-336
- Rodgers DW, Hackett WR, Ore HT (1990) Extension of the Yellowstone plateau, eastern Snake River Plain, and Owyhee plateau. *Geology* 18:1138-1141
- Rodgers DW, Ore HT, Bobo RT, McQuarrie N, Zentner N (2002) Extension and subsidence of the Eastern Snake River Plain, Idaho. In: Bonnicksen B, White CM, McCurry, M (eds) *Tectonic and Magmatic Evolution of the Snake River Plain Volcanic Province*. Idaho Geol Surv Bull 30:121-155
- Rollinson HR (1993) *Using geochemical data: evaluation, presentation, interpretation*. Prentice Hall, Harlow, England, 352 pages
- Rosas F, Marques FG, Luz A, Coelho S (2002) Sheath folds formed by drag induced by rotation of rigid inclusions in viscous simple shear flow: nature and experiment. *J Struct Geol* 24:45-55
- Ross CS, Smith RL (1961) Ash-flow tuffs: their origin, geologic relations and identification. *US Geol Surv Prof Pap* 366:1-81. In: *New Mex Geol Soc Spec Pub* (1980) 9
- Russell JK, Giordano D, Dingwell DB (2003) High-temperature limits on viscosity of non-Arrhenian silicate melts. *Am Mineral* 88:1390-1394
- Russell JK, Quane SL (2005) Rheology of welding: inversion of field constraints. *J Volcanol Geotherm Res* 142:173-191
- Rust AC (2003) How bubbles affect the viscosity and flow of magma. MAC Len Berry Summer School, Univ Brit Columb, Sept 2003
- Rust AC, Manga M, Cashman KV (2003) Determining flow type, shear rate and shear stress in magmas from bubble shapes and orientations. *J Volcanol Geotherm Res* 122:111-132

References

- Rust AC, Russell JK (2000) Detection of welding in pyroclastic flows with ground penetrating radar: insights from field and forward modelling data. *J Volcanol Geotherm Res* 95:23-34
- Rust AC, Russell JK (2001) Mapping porosity variation in a welded pyroclastic deposit with a signal and velocity patterns from ground-penetrating radar surveys. *Bull Volcanol* 62:457-463
- Rust BR (1972) Pebble orientation in fluvial sediments. *J Sed Petrol* 42:384-388
- Ryan MP, Sammis CG (1981) The glass transition in basalt. *J Geophys Res* 86:9519-9535
- Rytuba JJ, McKee EH (1984) Peralkaline ash flow tuffs and calderas of the McDermitt volcanic field, southeast Oregon and north central Nevada. *J Geophys Res* 89:8616-8628
- Samanta SK, Mandal N, Chakraborty C (2002) Development of structures under the influence of heterogeneous flow field around rigid inclusions: insights from theoretical and numerical models. *Earth Sci Rev* 58:85-119
- Sarna-Wojcicki AM, Reheis MC, Pringle MS, Fleck RJ, Burbank D, Meyer CE, Slate JL, Wan E, Budahn JR, Troxel B, Walker JP (2005) Tephra layers of Blind Spring Valley and related Upper Pliocene and Pleistocene tephra layers, California, Nevada, and Utah: isotopic ages, correlation, and magnetostratigraphy. *US Geol Surv Prof Pap* 1701, 63 pages
- Scaillet B, Holtz F, Pichavant M (1998) Phase equilibrium constraints on the viscosity of silicic magmas: 1 volcanic-plutonic comparison. *J Geophys Res* 103:27257-27266
- Scaillet B, Holtz F, Pichavant M, Schmidt MO (1996) The viscosity of Himalayan leucogranite: implications for mechanisms of granitic magma ascent. *J Geophys Res* 101:27691-27699
- Schnellmann M, Anselmetti FS, Giardini D, McKenzie JA (2005) Mass movement-induced fold-and-thrust belt structures in unconsolidated sediments in Lake Lucerne (Switzerland). *Sedimentology* 52:271-289
- Schultz-Ela, DD (2001) Excursus on gravity gliding and gravity spreading. *J Struct Geol* 23:725-731

References

- Schmincke H-U (1974) Volcanological aspects of peralkaline silicic welded ash-flow tuffs. *Bull Volcanol* 38:594-636
- Schmincke H-U, Swanson DA (1967) Laminar viscous flowage structures in ash-flow tuffs from Gran Canaria, Canary Islands. *J Geol* 75:641-664
- Seaman SJ (1995) Multi-stage magma mixing and mingling and the origin of flow banding in the Aliso Lava Dome, Tumacacori Mountains, southern Arizona. *J Geophys Res* 100:8381-8398
- Seaman SJ, Dyar D, Marinkovic N (2005) Flow banding in rhyolite: a manifestation of water concentration heterogeneity in the melt? *Am Geophys Union Abs w/Prog*, xx:xxx-xxx
- Self S, Thordarson T, Keszthelyi L, Walker GPL, Hon K, Murphy MT, Long P, Finnemore S (1996) A new model for the emplacement of Columbia River basalts as large, inflated pahoehoe lava flow fields. *Geophys Res Lett* 23:2689-2692
- Sharp TG, Stevenson RJ, Dingwell DB (1996) Microlites and "nanolites" in rhyolitic glass: microstructural and chemical characterization. *Bull Volcanol* 57:631-640
- Shaw HR (1963) Obsidian-H₂O viscosities at 1000 and 2000 bars in the temperature range 700° to 900°C. *J Geophys Res* 68:6337-6343
- Shaw HR (1972) Viscosities of magmatic silicate liquids: an empirical model of prediction. *Am J Sci* 272:438-475
- Sheridan MF, Wang Y (2005) Cooling and welding history of the Bishop Tuff in Adobe Valley and Chidago Canyon, California. *J Volcanol Geotherm Res* 142:119-144
- Shervais JW, Shroff G, Vetter SK, Matthews S, Hanan BB, McGee JJ (2002) Origin and evolution of the western Snake River Plain: implications from stratigraphy, faulting, and the geochemistry of basalts near Mountain Home, Idaho. In: Bonnicksen B, White CM, McCurry, M (eds) *Tectonic and Magmatic Evolution of the Snake River Plain Volcanic Province*. *Idaho Geol Surv Bull* 30:343-361
- Simpson C (1980) Strain and shape fabric variation associated with ductile shear zones. *J Struct Geol* 5:61-72

References

- Sisson TW, Grove TL (1993) Experimental investigations of the role of H₂O in calc-alkaline differentiation and subduction zone magmatism. *Contrib Mineral Petrol* 113:143-166
- Skjervaa L (1989) Tubular folds and sheath folds: definitions and conceptual models for their development, with examples from the Grapesvare area, northern Sweden. *J Struct Geol* 11:689-703
- Smith GA (1986) Coarse-grained non-marine volcanoclastic sediment: terminology and depositional process. *Geol Soc Am Bull* 97:1-10
- Smith JV (1996) Ductile-brittle transition structures in the basal shear zone of a rhyolite lava flow, eastern Australia. *J Volcanol Geotherm Res* 72:217-223
- Smith JV (1997) Shear thickening dilatancy in crystal-rich flows. *J Volcanol Geotherm Res* 79:1-8
- Smith JV (2000a) Textural evidence for dilatant (shear thickening) rheology of magma at high crystal concentrations. *J Volcanol Geotherm Res* 99:1-7
- Smith JV (2000b) Flow pattern within a Permian submarine slump recorded by oblique folds and deformed fossils, Ulladulla, south-eastern Australia. *Sedimentology* 47:357-366
- Smith JV (2002) Structural analysis of flow-related textures in lavas. *Earth Sci Rev* 57:279-297
- Smith JV, Houston EC (1994) Folds produced by gravity spreading of a banded rhyolite lava flow. *J Volcanol Geotherm Res* 63:89-94
- Smith RB, Shuey RT, Freidline RO, Otis RM, Alley LB (1974) Yellowstone hot spot: new magnetic and seismic evidence. *Geology* 2:451-455
- Smith RB, Shuey RT, Pelton JP, Bailey JP (1977) Yellowstone hot spot: contemporary tectonics and crustal properties from earthquake and aeromagnetic data. *J Geophys Res* 82:3665-3676
- Smith RL (1960a) Ash flows. *Geol Soc Am Bull* 71:795-841
- Smith RL (1960b) Zones and zonal variations in welded ash-flows. *US Geol Surv Prof Pap* 354-F: 149-158. In: *New Mex Geol Soc Spec Pub* (1980) 9
- Smith RL, Bailey RA (1966) The Bandelier Tuff – A study of ash-flow eruptive cycles from zoned magma chambers. *Bull Volcanol* 29:83-104

References

- Soriano C, Zafrilla S, Martí J, Bryan S, Cas R, Ablay G (2002) Welding and rheomorphism of phonolitic fallout deposits from the Las Canadas caldera, Tenerife, Canary Islands. *Geol Soc Am Bull* 114:883-895
- Sparks RSJ, Self, S, Walker GPL (1973) Products of ignimbrite eruptions. *Geology* 1:115-118
- Sparks RSJ, Tait SR, Yanev Y (1999) Dense welding caused by volatile resorption. *J Geol Soc Lon* 156:217-225
- Sparks RSJ, Wright JV (1979) Welded air-fall tuffs. In: Chapin CE, Elston WE (eds) *Ash-flow tuffs*. *Geol Soc Am Spec Pap* 180:155-166
- Stein DJ, Spera FJ (1992) Rheology and microstructure of magmatic emulsions – theory and experiments. *J Volcanol Geotherm Res* 49:157-174
- Stevenson DS, Bagdassarov NS, Dingwell DB, Romano C (1998) The influence of trace amounts of water on the viscosity of rhyolites. *Bull Volcanol* 60:89-97
- Stevenson RJ, Dingwell DB, Bagdassarov NS, Manley CR (2001) Measurement and implication of “effective” viscosity for rhyolite flow emplacement. *Bull Volcanol* 63:227-237
- Stevenson RJ, Dingwell DB, Webb SL, Sharp TG (1996) Viscosity of microlite-bearing rhyolitic obsidians: an experimental study. *Bull Volcanol* 58:298-309
- Stevenson RJ, Hodder APW, Briggs RM (1994) Rheological estimates of rhyolite flows from the Okataina volcanic centre, New Zealand. *NZ J Geol Geophys* 37:211-221
- Stow DAV (1986) Deep clastic seas. In: Reading HG (ed) *Sedimentary environments and facies*. Blackwell, Oxford, 399-444
- Strachan LJ (2002) Slump-initiated and controlled syn-depositional sandstone remobilization: an example from the Namurian of County Clare, Ireland. *Sedimentology* 49:25-41
- Streck MJ, Ferns M (2004) The Rattlesnake Tuff and other Miocene silicic volcanism in eastern Oregon. In: Haller KM, Wood SH (eds) *Geological field trips in Southern Idaho, Eastern Oregon, and northern Nevada*. Boise, Dept Geosci, Boise State Univ, pages 2-17

References

- Streck MJ, Grunder AL (1995) Crystallization and welding variations in a widespread ignimbrite sheet - the Rattlesnake Tuff, Eastern Oregon, USA. *Bull Volcanol* 57:151-169
- Sumner JM, Branney MJ (2002) The emplacement history of a remarkable heterogeneous, chemically zoned, rheomorphic and locally lava-like ignimbrite: 'TL' on Gran Canaria. *J Volcanol Geotherm Res* 115:109-138
- Sumner JM, Blake S, Matela RJ, Wolff JA (2005) Spatter. *J Volcanol Geotherm Res* 142:49-65
- Talbot CJ, Aftabi P (2004) Geology and models of salt extrusion at Qum Kuh, central Iran. *J Geol Soc Lon* 161:321-334
- Talbot CJ, Jarvis RJ (1984) Age, budget and dynamics of an active salt extrusion in Iran. *J Struct Geol* 6:521-533
- Talbot CJ, Medvedev S, Alavi M, Shahrivar H, Heidari E (2000) Salt extrusion rates at Kuh-e-Jahani, Iran: June 1994 to November 1997. In: Vendeville BC, Mart Y, Vigneresse JL (eds) *Salt, shale and igneous diapirs in and around Europe*. *Geol Soc Spec Pub* 174:93-110
- Thomas RME, Sparks RSJ (1992) Cooling of tephra during fallout from eruption columns. *Bull Volcanol* 54:542-553
- Thordarson T, Self S (1993) The Laki (Skaftár Fires) and Grímsvötn eruptions in 1793 – 1795. *Bull Volcanol* 55:233-263
- Tobisch OT (1984) Development of foliation and fold interference patterns produced by sedimentary processes. *Geology* 12:441-444
- Toramaru A (1988) Formation of propagation pattern in two-phase flow systems with application to volcanic eruptions. *Geophys J Roy Astr Soc* 95:613-623
- Tuffen H, Dingwell DB, Pinkerton H (2003) Repeated fracture and healing of silicic magma generate flow banding and earthquakes? *Geology* 31:1089-1092
- Turnbull D, Cohen MH (1961) Free-volume model of the amorphous phase: glass transition. *J Chem Phys* 34:120-125
- Twiss RJ, Moores EM (1992) *Structural geology*. Freeman Press, New York, 532 pages

References

- Urbain G, Bottinga Y, Richet P (1982) Viscosity of liquid silica, silicates and aluminosilicates. *Geochim Cosmochim Acta* 46:1061-1072
- Valentine GA (1998) Eruption column physics. In: Freundt A, Rosi M (eds) *From magma to tephra. Developments in volcanology*, Elsevier, Amsterdam, 4:91-138
- Ventura G (1998) Kinematic significance of mingling-rolling structures in lava flows: a case study from Porri Volcano (Salina, Southern Tyrrhenian Sea). *Bull Volcanol* 59:394-403
- Ventura G, De Rosa R, Colletta E, Mazzuoli R (1996) Deformation patterns in high-viscosity lava flow inferred from the crystal preferred orientation and imbrication structures: an example from Salina (Aeolian Islands, southern Tyrrhenian Sea, Italy). *Bull Volcanol* 57:555-562
- Vernon RH (1987) A microstructural indicator of shear sense in volcanic rocks and its relationship to porphyroblast rotation in metamorphic rocks. *J Geol* 95:127-133
- Voight B, Davis MJ (2000) Emplacement temperatures of the November 22, 1994 *nuée ardente* deposits, Merapi volcano, Java. *J Volcanol Geotherm Res* 100:371-377
- Wada Y (1992) Magma flow directions inferred from preferred orientations of phenocrysts in a composite feeder dyke, Miyake-Jima, Japan. *J Volcanol Geotherm Res* 49:119-126
- Walker GPL (1973) Lengths of lava flows. *Philos Trans Roy Soc Lon Series A* 274:107-118
- Walker GPL (1983) Ignimbrite types and ignimbrite problems. *J Volcanol Geotherm Res* 17:65-88
- Walker GPL (1985) Origin of coarse lithic breccias near ignimbrite source vents. *J Volcanol Geotherm Res* 25:157-171
- Walker GPL, Canon-Tapia E, Herrero-Bervera E (1998) Origin of vesicle layering and double imbrication by endogenous growth in the Birkett basalt flow (Columbia River Plateau). *J Volcanol Geotherm Res* 88:15-28
- Wallace PJ, Anderson AT, Davis AM (1995) Quantification of pre-eruptive exsolved gas contents in silicic magmas. *Nature* 377:612-616

References

- Wallace PJ, Dufek J, Anderson AT, Zhang Y (2003) Cooling rates of Plinian-fall and pyroclastic-flow deposits in the Bishop Tuff: inferences from water speciation in quartz-hosted glass inclusions. *Bull Volcanol* 65:105-123
- Webb SL (1997) Silicate melts: relaxation, rheology, and the glass transition. *Rev Geophys* 35:191-218
- Webb SL, Dingwell DB (1990) Non-Newtonian rheology of igneous melts at high stresses and strain rates: experimental results for rhyolite, andesite, basalt, and nephelinite. *J Geophys Res* 95:15695-15701
- Webster JD, Duffield WA (1991) Volatiles and lithophile elements in Taylor Creek Rhyolite: constraints from glass inclusion analysis. *Am Mineral* 76:1628-1645
- Webster JD, Duffield WA (1994) Extreme halogen abundances in tin-rich magma of the Taylor Creek Rhyolite, New Mexico. *Econ Geol* 89:840-850
- Wedepohl KH (1995) The composition of the continental crust. *Geochim Cosmochim Acta* 59:1217-1239
- Wen S, Nekvasil H (1994) SOLV CALC: An interactive graphics program package for calculating the ternary feldspar solvus and for two-feldspar geothermometry. *Comp Geosci* 20:1025-1040
- Whalen JB, Currie KL, Chappell BW (1987) A-type granite: geochemical characteristics, discrimination and petrogenesis. *Cont Mineral Petrol* 95:407-419
- Whittington AG, Hellwig, BM, Getson JM, Behrens H (2005) Domes versus flows: dacite liquid viscosity and magma rheology. *Geol Soc Am Abs w/Prog* 37:530
- Williams GD, Chapman TJ (1979) The geometrical classification of non-cylindrical folds. *J Struct Geol* 1:181-185
- Williams PL, Mytton JA, Morgan WA (1999) Geologic map of the Stricker 3 quadrangle, Twin Falls and Cassia counties, Idaho. *US Geol Surv Misc Invest Map* I-2633, 1:48,000
- Wilson CJN (1997) Emplacement of the Taupo ignimbrite. *Nature* 385:306-307
- Wilson CJN, Hildreth W (1997) The Bishop Tuff: new insights from eruptive stratigraphy. *J Geol* 105:407-439

References

- Wilson CJN, Hildreth W (2003) Assembling an ignimbrite: mechanical and thermal building blocks in the Bishop Tuff, California. *J Geol* 111:653-670
- Wilson L, Pinkerton H, Macdonald R (1987) Physical processes in volcanic eruptions. *Ann Rev Earth Planet Sci* 15:73-95
- Wohletz K (2004) MAGMA v. 2.48 software package. KWare - Los Alamos Natl Lab, NM. <http://www.ees1.lanl.gov/Wohletz/Magma.htm>
- WoldeGabriel G, Keating GN, Valentine GA (1999) Effects of shallow basaltic intrusion pyroclastic deposits, Grants Ridge, New Mexico, USA. *J Volcanol Geotherm Res* 92:389-411
- Wolff JA, Wright JV (1981a) Formation of the Green Tuff of Pantelleria. *Bull Volcanol* 44:681-690
- Wolff JA, Wright JV (1981b) Rheomorphism of welded tuffs. *J Volcanol Geotherm Res* 10:13-34
- Wood SH, Clemens DM (2002) Geologic and tectonic history of the western Snake River Plain, Idaho and Oregon. In: Bonnichsen B, White CM, McCurry, M (eds) *Tectonic and Magmatic Evolution of the Snake River Plain Volcanic Province*. Idaho Geol Surv Bull 30:69-103
- Wright JV (1980) Stratigraphy and geology of the welded air-fall tuffs of Pantelleria, Italy. *Geol Rundsch* 69:26-91
- Wright KE, McCurry M, Hughes SS (2002) Petrology and geochemistry of the Miocene Tuff of McMullen Creek, central Snake River Plain, Idaho. In: Bonnichsen B, White CM, McCurry, M (eds) *Tectonic and Magmatic Evolution of the Snake River Plain Volcanic Province*. Idaho Geol Surv Bull 30:177-194
- Ximenis L, Calvet J, Garcia D, Casas JM, Sabat F (2000) Folding in the Johnsons Glacier, Livingston Island, Antarctica. In: Maltman AJ, Hubbard B, Hambrey MJ (eds) *Deformation of glacial materials*. Geol Soc Lon Spec Pub 176:147-157
- Zoback ML, McKee EH, Blakely RJ, Thompson GA (1994) The northern Nevada rift: regional tectono-magmatic relations and middle Miocene stress direction. *Geol Soc Am Bull* 106:371-382

| Sample # | 85 | GA02/14/8/2 | GA02/12/8/6 | GA02/14/8/1 | GA02/27/6/1 | GA02/27/6/3 | GA02/8/8/1 | GA02/28/8/1 | GA02/30/7/3 |
|--------------|--------------|---------------|---------------|--------------|---------------|---------------|--------------|---------------|--------------|
| Member | Sand Spr | Sand Spr | Sand Spr | Coyote | GL vit | GL vit | GL vit | GL vit | GL vit |
| SiO2 | 72.24 | 70.10 | 68.25 | 67.51 | 72.10 | 72.31 | 71.07 | 73.94 | 73.30 |
| TiO2 | 0.50 | 0.69 | 0.68 | 0.81 | 0.47 | 0.62 | 0.53 | 0.39 | 0.49 |
| Al2O3 | 12.13 | 12.08 | 12.00 | 13.02 | 11.36 | 12.09 | 12.06 | 11.54 | 12.00 |
| Fe2O3 | 3.13 | 4.12 | 4.05 | 4.91 | 3.48 | 3.65 | 3.86 | 2.87 | 3.65 |
| MnO | 0.05 | 0.06 | 0.06 | 0.08 | 0.08 | 0.06 | 0.07 | 0.05 | 0.07 |
| MgO | 0.25 | 0.54 | 0.64 | 0.60 | 0.35 | 0.36 | 0.21 | 0.08 | 0.21 |
| CaO | 1.12 | 1.86 | 2.99 | 1.58 | 2.39 | 1.29 | 1.46 | 0.91 | 1.20 |
| Na2O | 2.69 | 2.83 | 2.78 | 2.62 | 2.84 | 2.87 | 3.10 | 2.85 | 3.31 |
| K2O | 5.12 | 5.10 | 4.98 | 4.57 | 4.88 | 5.60 | 5.11 | 5.51 | 4.77 |
| P2O5 | 0.13 | 0.13 | 0.65 | 0.07 | 0.10 | 0.10 | 0.08 | 0.04 | 0.08 |
| LOI | 2.55 | 2.53 | 3.61 | 3.53 | 2.67 | 1.30 | 2.22 | 2.49 | 0.88 |
| As | 5.55 | n/a | n/a | n/a | n/a | n/a | n/a | n/a | n/a |
| Ba | 1210.96 | 1131.15 | 1091.69 | 1004.94 | 1248.80 | 1142.61 | 1196.38 | 1168.30 | 1239.06 |
| Ce | 157.06 | 149.98 | 146.07 | 144.56 | 145.07 | 153.47 | 156.02 | 157.07 | 162.89 |
| Co | 4.31 | 8.28 | 7.76 | 10.55 | 6.74 | 7.87 | 8.54 | 4.29 | 7.08 |
| Cr | 6.74 | 0.98 | 7.69 | 34.59 | 2.91 | 12.36 | 4.56 | 2.13 | 2.80 |
| Cs | 0.52 | 7.87 | 4.68 | 6.40 | 2.87 | 6.98 | 3.86 | 2.41 | 5.53 |
| Cu | 5.36 | 13.50 | 18.29 | 10.04 | 8.01 | 10.47 | 9.13 | 1.46 | 13.42 |
| Ga | 20.43 | 18.90 | 19.26 | 20.79 | 18.98 | 19.29 | 19.92 | 18.60 | 19.40 |
| La | 79.77 | 78.35 | 74.41 | 69.78 | 79.08 | 80.69 | 81.75 | 80.37 | 85.40 |
| Mo | 2.23 | 3.52 | 3.39 | 2.83 | 3.32 | 2.83 | 3.13 | 3.36 | 2.31 |
| Nb | 54.43 | 44.62 | 42.05 | 44.16 | 49.79 | 47.12 | 51.91 | 53.56 | 53.27 |
| Nd | 63.99 | 61.54 | 58.02 | 56.79 | 65.73 | 62.20 | 65.97 | 64.49 | 70.64 |
| Ni | -0.01 | -0.39 | 1.84 | 1.98 | 0.71 | -0.35 | 0.85 | 2.53 | 1.01 |
| Pb | 25.46 | 26.19 | 26.24 | 28.66 | 25.32 | 26.54 | 24.63 | 26.88 | 26.68 |
| Rb | 172.48 | 169.27 | 154.49 | 160.92 | 138.99 | 184.02 | 153.50 | 168.46 | 156.98 |
| Sc | 2.92 | 7.66 | 8.08 | 8.67 | 6.03 | 8.08 | 6.57 | 5.01 | 4.95 |
| Sn | -0.20 | n/a | n/a | n/a | n/a | n/a | n/a | n/a | n/a |
| Sr | 75.44 | 95.32 | 116.99 | 127.36 | 107.39 | 69.94 | 98.78 | 58.00 | 90.41 |
| Th | 28.82 | 27.67 | 26.90 | 26.98 | 26.02 | 31.30 | 26.46 | 28.10 | 27.41 |
| U | 6.76 | 6.75 | 5.99 | 6.78 | 6.41 | 7.41 | 5.76 | 5.86 | 6.31 |
| V | 8.46 | 20.31 | 20.87 | 35.32 | 6.89 | 20.19 | 9.38 | 5.34 | 7.63 |
| Y | 75.15 | 61.45 | 58.65 | 55.66 | 69.00 | 61.34 | 73.52 | 71.81 | 77.95 |
| Zn | 62.74 | 54.36 | 55.13 | 68.89 | 64.78 | 51.95 | 72.04 | 60.06 | 68.70 |
| Zr | 607.45 | 571.76 | 548.03 | 565.51 | 602.83 | 549.28 | 651.78 | 545.36 | 637.92 |
| Cl | 290.02 | n/a | n/a | n/a | n/a | n/a | n/a | n/a | n/a |
| ASI | 1.01 | 0.89 | 0.78 | 1.07 | 0.79 | 0.92 | 0.91 | 0.94 | 0.94 |
| Total | 99.91 | 100.03 | 100.70 | 99.30 | 100.70 | 100.25 | 99.77 | 100.65 | 99.95 |
| Bead-mj | LF22411 | LF20985 | LF20988 | LF20976 | LF20964 | LF20980 | LF20990 | LF20992 | LF20993 |
| Pellet-tr | L42167 | L41103 | L41106 | L41094 | L41082 | L41098 | L41108 | L41110 | L41111 |
| Liquidus T | n/a | n/a | n/a | n/a | 897 | 960 | 905 | 898 | 963 |

Appendix 1: XRF bulk rock analyses from the Rogerson Formation.

ASI = aluminosity index

Liquidus temperature (° C) estimated from whole-rock composition
MELTS software (Ghiorso & Sack, 1995; Asimow & Ghiorso, 1998)

| Sample # | 57 | 64 | 62 | 100 | 103 | 104 | 7(a) | X | 35 |
|-------------------|--------------|--------------|--------------|--------------|---------------|---------------|---------------|--------------|---------------|
| Member | GL | GL | GL | GL | GL | GL | GL | GL | GL |
| SiO2 | 71.38 | 73.41 | 73.54 | 72.20 | 72.84 | 73.05 | 70.20 | 69.92 | 73.66 |
| TiO2 | 0.49 | 0.48 | 0.49 | 0.37 | 0.36 | 0.37 | 0.32 | 0.32 | 0.50 |
| Al2O3 | 12.15 | 11.97 | 12.03 | 11.87 | 12.06 | 12.03 | 11.99 | 11.95 | 12.08 |
| Fe2O3 | 3.73 | 3.67 | 3.21 | 2.73 | 2.77 | 2.77 | 2.49 | 2.46 | 3.63 |
| MnO | 0.07 | 0.02 | 0.02 | 0.05 | 0.05 | 0.05 | 0.04 | 0.04 | 0.07 |
| MgO | 0.33 | 0.09 | 0.21 | 0.41 | 0.42 | 0.38 | 0.59 | 0.60 | 0.34 |
| CaO | 1.43 | 0.75 | 1.22 | 1.00 | 1.04 | 0.95 | 0.82 | 0.79 | 1.34 |
| Na2O | 2.69 | 3.12 | 3.25 | 2.36 | 2.41 | 2.35 | 4.03 | 3.73 | 3.39 |
| K2O | 5.03 | 4.64 | 4.47 | 5.00 | 5.02 | 5.05 | 5.32 | 5.06 | 4.38 |
| P2O5 | 0.07 | 0.38 | 0.08 | 0.03 | 0.03 | 0.03 | 0.03 | 0.03 | 0.10 |
| LOI | 1.91 | 1.09 | 0.98 | 3.69 | 3.68 | 3.63 | 4.46 | 4.40 | 1.00 |
| As | 4.01 | 7.79 | 7.70 | 4.08 | 2.12 | 5.60 | 12.64 | 14.96 | 6.62 |
| Ba | 1208.89 | 1262.59 | 1264.45 | 1159.29 | 1335.65 | 1330.33 | 1018.51 | 940.90 | 1402.42 |
| Ce | 156.26 | 129.42 | 139.10 | 158.42 | 152.67 | 160.02 | 146.03 | 142.25 | 158.51 |
| Co | 5.34 | 5.74 | 5.46 | 3.35 | 3.93 | 4.67 | 3.50 | 2.11 | 6.40 |
| Cr | 1.39 | 7.66 | 0.59 | 1.40 | 2.71 | -0.19 | 0.25 | 6.16 | 7.74 |
| Cs | 2.00 | 5.53 | 5.21 | 2.62 | 5.31 | 2.36 | 5.62 | 1.21 | 0.89 |
| Cu | 4.39 | 5.94 | 3.00 | 4.68 | 2.58 | 2.33 | 2.75 | 4.63 | 5.94 |
| Ga | 21.60 | 20.71 | 22.01 | 21.52 | 19.79 | 20.46 | 19.22 | 18.94 | 21.68 |
| La | 80.69 | 76.23 | 77.22 | 85.18 | 87.36 | 88.06 | 75.23 | 75.91 | 89.44 |
| Mo | 2.27 | 4.76 | 3.28 | 2.62 | 2.99 | 2.61 | 3.20 | 4.38 | 0.72 |
| Nb | 53.69 | 54.17 | 55.01 | 54.85 | 56.08 | 57.60 | 54.05 | 54.90 | 53.79 |
| Nd | 66.49 | 58.90 | 64.66 | 67.36 | 68.37 | 71.52 | 59.75 | 59.41 | 70.13 |
| Ni | 2.09 | 2.05 | 1.37 | 0.75 | 1.17 | 1.05 | 0.56 | 1.28 | -0.80 |
| Pb | 25.33 | 35.66 | 22.54 | 31.59 | 32.00 | 28.20 | 31.27 | 27.28 | 26.93 |
| Rb | 165.54 | 170.45 | 170.96 | 172.45 | 172.87 | 174.25 | 163.74 | 162.59 | 169.80 |
| Sc | 4.48 | 5.50 | 7.31 | -0.32 | 5.26 | 3.58 | 2.44 | 3.52 | 6.34 |
| Sn | 0.05 | 3.47 | 6.70 | 8.29 | 1.81 | 6.85 | 7.54 | 7.55 | 3.10 |
| Sr | 89.93 | 79.78 | 91.00 | 58.06 | 81.06 | 72.18 | 44.85 | 43.28 | 95.78 |
| Th | 27.47 | 25.32 | 33.81 | 25.92 | 31.50 | 33.06 | 33.42 | 34.22 | 31.04 |
| U | 6.93 | 6.43 | 4.68 | 6.38 | 5.40 | 6.01 | 6.95 | 8.98 | 4.38 |
| V | 8.30 | 16.06 | 16.28 | 4.76 | 8.00 | 10.28 | 36.10 | 34.72 | 12.30 |
| Y | 79.87 | 59.51 | 66.67 | 81.73 | 83.61 | 79.49 | 71.62 | 73.38 | 82.20 |
| Zn | 74.75 | 65.17 | 68.42 | 60.87 | 52.67 | 55.25 | 50.01 | 52.40 | 69.84 |
| Zr | 663.78 | 680.55 | 687.15 | 540.22 | 548.43 | 547.00 | 469.88 | 465.08 | 678.69 |
| Cl | 228.14 | 33.81 | 47.35 | 311.86 | 249.69 | 37.86 | 25256.77 | 34473.42 | 58.22 |
| ASI | 0.97 | 1.04 | 0.97 | 1.07 | 1.07 | 1.08 | 0.86 | 0.91 | 0.95 |
| Total | 99.29 | 99.63 | 99.49 | 99.70 | 100.68 | 100.65 | 100.30 | 99.29 | 100.47 |
| Bead-mj | LF22388 | LF22393 | LF22395 | LF22396 | LF22397 | LF22398 | LF22399 | LF22400 | LF22414 |
| Pellet-tr | L42144 | L42149 | L42151 | L42152 | L42153 | L42154 | L42155 | L42156 | L42170 |
| Liquidus T | 930 | 936 | 960 | 908 | 910 | 903 | 909 | 912 | 960 |

Appendix 1 continued: XRF bulk rock analyses from the Rogerson Formation.

ASI = aluminosity index

Liquidus temperature (° C) estimated from whole-rock composition
MELTS software (Ghiorso & Sack, 1995; Asimow & Ghiorso, 1998)

| Sample # | 34 | 39(a) | 67 | 30 | 40 | 38 | 9 | 32 | GA02/31/7/1 |
|-------------------|--------------|---------------|--------------|---------------|--------------|---------------|---------------|---------------|--------------|
| Member | GL | GL | GL | GL | GL | GL | GL | GL | GL |
| SiO2 | 73.02 | 73.90 | 73.77 | 71.81 | 72.60 | 71.85 | 72.92 | 73.04 | 72.71 |
| TiO2 | 0.49 | 0.51 | 0.50 | 0.51 | 0.48 | 0.53 | 0.48 | 0.51 | 0.45 |
| Al2O3 | 12.01 | 12.01 | 11.94 | 12.13 | 11.79 | 12.08 | 12.14 | 12.00 | 11.60 |
| Fe2O3 | 3.77 | 3.72 | 3.72 | 3.80 | 3.71 | 3.92 | 3.68 | 3.79 | 3.42 |
| MnO | 0.05 | 0.05 | 0.05 | 0.06 | 0.07 | 0.07 | 0.03 | 0.04 | 0.10 |
| MgO | 0.31 | 0.36 | 0.36 | 0.31 | 0.43 | 0.30 | 0.21 | 0.30 | 0.23 |
| CaO | 1.10 | 1.05 | 1.03 | 1.32 | 1.97 | 1.35 | 1.29 | 1.30 | 1.09 |
| Na2O | 3.38 | 3.42 | 3.29 | 3.07 | 3.18 | 2.93 | 3.42 | 3.29 | 3.38 |
| K2O | 4.65 | 4.60 | 4.39 | 4.83 | 4.19 | 5.21 | 4.64 | 4.45 | 4.96 |
| P2O5 | 0.10 | 0.08 | 0.09 | 0.08 | 0.14 | 0.08 | 0.07 | 0.17 | 0.21 |
| LOI | 0.50 | 0.84 | 0.64 | 2.30 | 1.35 | 2.36 | 1.13 | 1.30 | 0.81 |
| As | 7.23 | 10.53 | 9.29 | 4.92 | 5.43 | 5.77 | 3.93 | 13.81 | n/a |
| Ba | 1361.39 | 1313.47 | 1319.95 | 1183.36 | 1702.97 | 1214.24 | 1216.76 | 1329.00 | 1459.84 |
| Ce | 160.16 | 159.22 | 156.06 | 148.25 | 150.91 | 157.13 | 141.80 | 119.07 | 160.75 |
| Co | 7.74 | 7.54 | 7.50 | 6.13 | 7.59 | 6.01 | 7.02 | 6.66 | 6.64 |
| Cr | 6.23 | 4.47 | 10.12 | 11.41 | 1.23 | -0.19 | 7.92 | -1.28 | 2.38 |
| Cs | 2.60 | 4.37 | 2.67 | 7.87 | 2.14 | 1.41 | 7.78 | 0.20 | 0.44 |
| Cu | 9.80 | 6.04 | 4.72 | 2.20 | 5.95 | 2.86 | 4.25 | 5.41 | 12.38 |
| Ga | 21.61 | 20.30 | 20.78 | 21.61 | 19.79 | 20.42 | 20.79 | 20.13 | 19.03 |
| La | 85.06 | 87.17 | 89.16 | 81.49 | 81.12 | 85.13 | 80.65 | 65.52 | 81.89 |
| Mo | 1.52 | 3.06 | 2.55 | 2.67 | 3.81 | 4.39 | 3.27 | 2.87 | 2.97 |
| Nb | 54.97 | 54.44 | 54.51 | 56.93 | 52.72 | 53.42 | 52.77 | 54.74 | 52.90 |
| Nd | 69.93 | 71.90 | 69.84 | 65.44 | 65.56 | 66.55 | 64.89 | 55.74 | 65.80 |
| Ni | -0.65 | -0.52 | -1.74 | 3.24 | 0.86 | -0.08 | 3.13 | -1.86 | 0.46 |
| Pb | 31.33 | 27.37 | 29.09 | 26.23 | 31.07 | 23.78 | 28.45 | 25.37 | 28.29 |
| Rb | 165.69 | 167.28 | 168.74 | 163.14 | 167.23 | 169.38 | 168.34 | 165.59 | 164.06 |
| Sc | 3.40 | 6.83 | 5.02 | 6.04 | 6.77 | 2.14 | 2.26 | 5.74 | 4.43 |
| Sn | 5.97 | 2.39 | 0.33 | 7.43 | 3.82 | 3.94 | 3.89 | 4.58 | n/a |
| Sr | 86.53 | 88.37 | 89.06 | 81.58 | 118.63 | 86.47 | 123.82 | 96.34 | 90.11 |
| Th | 32.13 | 27.25 | 31.31 | 34.27 | 29.55 | 27.12 | 29.88 | 32.14 | 28.32 |
| U | 8.25 | 5.50 | 6.13 | 8.03 | 7.80 | 6.76 | 6.51 | 6.18 | 6.18 |
| V | 26.10 | 17.88 | 19.06 | 4.97 | 16.19 | 1.68 | 10.46 | 27.71 | 25.52 |
| Y | 83.37 | 86.98 | 88.08 | 81.51 | 77.78 | 82.53 | 65.55 | 58.86 | 76.15 |
| Zn | 76.36 | 73.07 | 72.68 | 73.63 | 69.85 | 73.84 | 60.97 | 66.92 | 70.47 |
| Zr | 691.32 | 698.58 | 696.05 | 694.49 | 686.47 | 690.99 | 628.23 | 671.72 | 626.55 |
| Cl | 74.63 | 69.99 | 84.62 | 208.17 | 110.61 | 204.22 | 2214.66 | 161.12 | n/a |
| ASI | 0.95 | 0.96 | 0.99 | 0.96 | 0.88 | 0.93 | 0.93 | 0.95 | 0.90 |
| Total | 99.38 | 100.54 | 99.78 | 100.22 | 99.92 | 100.67 | 100.01 | 100.19 | 98.97 |
| Bead-mj | LF22415 | LF22416 | LF22417 | LF22418 | LF22419 | LF22422 | LF22423 | LF22424 | LF20965 |
| Pellet-tr | L42171 | L42172 | L42173 | L42174 | L42175 | L42178 | L42179 | L42180 | L41083 |
| Liquidus T | 998 | 967 | 970 | 913 | 950 | 915 | 966 | 943 | 988 |

Appendix 1 continued: XRF bulk rock analyses from the Rogerson Formation.

ASI = aluminosity index

Liquidus temperature (° C) estimated from whole-rock composition
MELTS software (Ghiorso & Sack, 1995; Asimow & Ghiorso, 1998)

| Sample # | GA02/9/8/8 | GA02/31/7/2 | GA02/31/7/5 | GA02/9/8/10 | GA02/9/8/2 | GA02/9/8/9 | GA02/27/6/1 | GA02/9/8/1 | 47 |
|-------------------|--------------|--------------|---------------|---------------|--------------|---------------|--------------|---------------|---------------|
| Member | GL | GL | GL | GL vit | GL vit | GL vit | GL vit | GL vit | GL (ash) |
| SiO2 | 72.77 | 73.73 | 74.33 | 72.65 | 70.61 | 74.06 | 71.65 | 72.40 | 73.73 |
| TiO2 | 0.57 | 0.50 | 0.50 | 0.47 | 0.53 | 0.50 | 0.47 | 0.49 | 0.35 |
| Al2O3 | 11.88 | 11.92 | 12.19 | 11.76 | 11.74 | 12.17 | 12.02 | 12.06 | 11.89 |
| Fe2O3 | 4.01 | 3.66 | 3.65 | 3.33 | 3.90 | 3.79 | 3.66 | 3.65 | 2.68 |
| MnO | 0.06 | 0.05 | 0.06 | 0.06 | 0.06 | 0.06 | 0.07 | 0.06 | 0.05 |
| MgO | 0.22 | 0.17 | 0.15 | 0.19 | 0.21 | 0.19 | 0.30 | 0.23 | 0.23 |
| CaO | 1.01 | 0.94 | 1.03 | 1.12 | 1.17 | 1.05 | 1.36 | 1.23 | 0.91 |
| Na2O | 3.69 | 3.38 | 3.54 | 3.00 | 3.58 | 3.46 | 2.79 | 3.11 | 2.12 |
| K2O | 4.85 | 4.80 | 4.89 | 5.31 | 4.76 | 4.74 | 5.42 | 4.92 | 5.61 |
| P2O5 | 0.08 | 0.10 | 0.07 | 0.05 | 0.08 | 0.08 | 0.14 | 0.06 | 0.07 |
| LOI | 0.48 | 0.59 | 0.52 | 2.54 | 0.22 | 0.23 | 1.56 | 2.39 | 2.94 |
| As | n/a | n/a | n/a | n/a | n/a | n/a | n/a | n/a | 3.36 |
| Ba | 1195.76 | 1252.15 | 1238.60 | 1160.68 | 1261.16 | 1210.36 | 1330.22 | 1169.40 | 1193.04 |
| Ce | 162.58 | 151.39 | 157.80 | 160.05 | 161.41 | 153.50 | 171.08 | 162.94 | 155.63 |
| Co | 7.95 | 7.39 | 8.22 | 6.31 | 7.43 | 8.21 | 7.46 | 6.43 | 3.75 |
| Cr | 144.36 | -0.68 | 161.51 | 7.74 | 2.54 | 3.42 | 2.73 | 1.99 | 5.54 |
| Cs | 4.60 | 3.66 | 5.24 | 7.17 | 6.52 | 3.44 | 2.91 | 3.97 | 3.32 |
| Cu | 13.09 | 8.95 | 12.38 | 4.29 | 9.37 | 6.58 | 15.27 | 3.35 | 4.70 |
| Ga | 20.69 | 19.84 | 20.72 | 19.47 | 20.13 | 20.19 | 20.83 | 19.64 | 20.16 |
| La | 92.25 | 83.48 | 85.62 | 81.08 | 85.12 | 81.00 | 87.49 | 82.11 | 84.02 |
| Mo | 1.98 | 2.41 | 2.72 | 2.98 | 3.25 | 3.39 | 3.57 | 3.44 | 2.21 |
| Nb | 55.46 | 53.41 | 52.83 | 53.86 | 52.94 | 52.99 | 55.06 | 52.75 | 56.67 |
| Nd | 72.50 | 65.82 | 68.70 | 66.85 | 70.34 | 65.71 | 69.93 | 67.60 | 66.47 |
| Ni | 1.41 | 1.55 | 0.09 | 0.26 | 1.11 | 0.83 | 0.88 | 1.12 | 1.30 |
| Pb | 27.85 | 27.75 | 24.25 | 25.64 | 25.71 | 26.87 | 28.80 | 25.26 | 33.00 |
| Rb | 156.77 | 157.55 | 164.04 | 161.45 | 156.64 | 158.37 | 151.82 | 156.56 | 178.12 |
| Sc | 5.86 | 7.25 | 4.79 | 5.27 | 7.08 | 5.97 | 6.56 | 4.89 | 5.74 |
| Sn | n/a | n/a | n/a | n/a | n/a | n/a | n/a | n/a | 3.95 |
| Sr | 78.34 | 86.06 | 90.10 | 72.46 | 96.28 | 89.43 | 92.77 | 82.47 | 52.44 |
| Th | 28.21 | 28.23 | 27.82 | 28.15 | 27.29 | 26.10 | 29.27 | 27.05 | 36.68 |
| U | 6.53 | 6.37 | 6.28 | 7.35 | 5.76 | 4.82 | 6.53 | 5.97 | 7.05 |
| V | 10.80 | 24.40 | 8.50 | 7.49 | 9.39 | 10.14 | 8.61 | 5.15 | 1.87 |
| Y | 75.79 | 69.31 | 70.35 | 74.34 | 71.45 | 69.30 | 77.73 | 73.40 | 78.53 |
| Zn | 63.19 | 65.86 | 67.03 | 66.64 | 70.11 | 67.39 | 73.95 | 71.57 | 62.23 |
| Zr | 651.03 | 638.15 | 627.03 | 611.58 | 673.08 | 652.28 | 671.06 | 650.30 | 536.16 |
| Cl | n/a | n/a | n/a | n/a | n/a | n/a | n/a | n/a | 42.51 |
| ASI | 0.90 | 0.95 | 0.94 | 0.92 | 0.89 | 0.96 | 0.93 | 0.95 | 1.06 |
| Total | 99.61 | 99.84 | 100.92 | 100.50 | 96.86 | 100.33 | 99.43 | 100.60 | 100.60 |
| Bead-mj | LF20978 | LF20979 | LF20986 | LF20968 | LF20971 | LF20973 | LF20981 | LF20991 | LF22389 |
| Pellet-tr | L41096 | L41097 | L41104 | L41086 | L41089 | L41091 | L41099 | L41109 | L42145 |
| Liquidus T | 1015 | 990 | 996 | 900 | 1027 | 1015 | 956 | 896 | n/a |

Appendix 1 continued: XRF bulk rock analyses from the Rogerson Formation.

ASI = aluminosity index

Liquidus temperature (° C) estimated from whole-rock composition
MELTS software (Ghiorso & Sack, 1995; Asimow & Ghiorso, 1998)

| Sample # | 102(a) | 167 | 59 | 22 | GA3 | GA4 | GA02/3/8/4 | GA02/3/8/5 | GA02/3/8/3 |
|--------------|---------------|---------------|--------------|--------------|---------------|--------------|---------------|---------------|---------------|
| Member | GL (ash) | GL (ash) | GL (ash) | GL (ash) | Backwaters | Backwaters | Browns | Browns | Browns |
| SiO2 | 72.54 | 72.59 | 72.81 | 71.87 | 66.85 | 70.56 | 70.22 | 71.47 | 72.64 |
| TiO2 | 0.36 | 0.35 | 0.38 | 0.37 | 0.89 | 0.37 | 0.64 | 0.61 | 0.57 |
| Al2O3 | 11.96 | 11.96 | 11.61 | 12.19 | 12.88 | 13.29 | 12.24 | 12.04 | 11.91 |
| Fe2O3 | 2.68 | 2.71 | 2.82 | 2.83 | 5.63 | 2.67 | 4.13 | 3.59 | 3.16 |
| MnO | 0.04 | 0.05 | 0.05 | 0.05 | 0.08 | 0.05 | 0.05 | 0.05 | 0.04 |
| MgO | 0.38 | 0.38 | 0.19 | 0.59 | 0.87 | 1.40 | 0.50 | 0.42 | 0.30 |
| CaO | 1.04 | 1.05 | 0.93 | 1.08 | 2.18 | 1.45 | 1.68 | 1.42 | 1.18 |
| Na2O | 2.26 | 2.30 | 2.93 | 2.13 | 2.46 | 1.74 | 2.57 | 2.62 | 2.39 |
| K2O | 5.01 | 5.00 | 4.95 | 4.74 | 3.94 | 3.73 | 5.57 | 5.81 | 5.95 |
| P2O5 | 0.03 | 0.03 | 0.04 | 0.06 | 0.09 | 0.03 | 0.13 | 0.11 | 0.09 |
| LOI | 3.76 | 3.78 | 2.84 | 3.80 | 4.28 | 4.05 | 2.27 | 2.23 | 2.40 |
| As | 4.56 | 3.59 | 3.14 | 5.73 | 4.54 | 2.90 | n/a | n/a | n/a |
| Ba | 1140.74 | 1127.64 | 1222.30 | 1137.73 | 1202.89 | 841.87 | 1088.42 | 1231.63 | 1109.92 |
| Ce | 157.01 | 154.76 | 149.00 | 161.31 | 147.29 | 138.63 | 150.89 | 147.67 | 148.68 |
| Co | 4.83 | 4.06 | 2.96 | 4.81 | 13.98 | 4.12 | 8.12 | 7.21 | 6.00 |
| Cr | 0.87 | 2.48 | 4.69 | 5.76 | 13.63 | 11.94 | 3.34 | 1.88 | 9.38 |
| Cs | 8.73 | 5.97 | 7.06 | 5.03 | 3.98 | 8.17 | 9.68 | 4.85 | 1.19 |
| Cu | 1.10 | 0.67 | -0.86 | 7.18 | 6.64 | 6.75 | 13.14 | 9.45 | 6.01 |
| Ga | 21.20 | 20.47 | 19.77 | 21.10 | 23.28 | 20.68 | 18.33 | 18.41 | 18.42 |
| La | 82.97 | 83.24 | 82.83 | 80.54 | 74.88 | 74.83 | 77.35 | 76.42 | 77.85 |
| Mo | 2.03 | 2.12 | 3.05 | 2.31 | 1.89 | 1.76 | 3.01 | 3.56 | 3.59 |
| Nb | 57.92 | 56.44 | 54.34 | 54.42 | 44.61 | 42.51 | 45.45 | 46.12 | 46.98 |
| Nd | 67.61 | 64.39 | 64.68 | 64.90 | 58.18 | 58.60 | 60.58 | 61.00 | 59.74 |
| Ni | 0.95 | 0.18 | 2.73 | 0.99 | 1.55 | 2.65 | 0.79 | -0.12 | 1.66 |
| Pb | 28.51 | 31.92 | 26.62 | 27.22 | 27.00 | 25.71 | 25.34 | 26.63 | 26.81 |
| Rb | 174.69 | 174.07 | 173.46 | 163.58 | 162.21 | 162.22 | 175.97 | 181.69 | 190.23 |
| Sc | 3.10 | 3.46 | 3.70 | 3.88 | 8.87 | 4.72 | 7.65 | 5.69 | 5.51 |
| Sn | 3.30 | 2.89 | 4.58 | 2.49 | 7.93 | 4.90 | n/a | n/a | n/a |
| Sr | 54.12 | 53.71 | 56.74 | 64.77 | 130.84 | 114.28 | 95.43 | 75.88 | 63.24 |
| Th | 31.18 | 26.16 | 26.61 | 27.36 | 28.56 | 44.35 | 29.13 | 31.60 | 32.03 |
| U | 9.61 | 7.48 | 6.68 | 7.86 | 4.62 | 7.51 | 5.97 | 6.58 | 6.27 |
| V | 7.96 | 3.65 | 5.57 | 9.01 | 34.85 | 26.77 | 17.73 | 15.67 | 13.45 |
| Y | 78.76 | 77.48 | 78.62 | 77.27 | 55.55 | 64.97 | 61.89 | 61.83 | 61.30 |
| Zn | 58.50 | 58.94 | 58.35 | 63.52 | 76.15 | 53.70 | 50.74 | 48.35 | 44.61 |
| Zr | 527.33 | 535.13 | 559.86 | 538.37 | 628.74 | 328.12 | 575.83 | 552.39 | 543.34 |
| Cl | 344.09 | 321.16 | 230.91 | 188.11 | 444.62 | 77.50 | n/a | n/a | n/a |
| ASI | 1.08 | 1.08 | 0.98 | 1.15 | 1.05 | 1.39 | 0.92 | 0.91 | 0.95 |
| Total | 100.05 | 100.19 | 99.56 | 99.69 | 100.16 | 99.35 | 100.00 | 100.37 | 100.63 |
| Bead-mj | LF22390 | LF22391 | LF22392 | LF22421 | LF22386 | LF22387 | LF20963 | LF20977 | LF20982 |
| Pellet-tr | L42146 | L42147 | L42148 | L42177 | L42142 | L42143 | L41081 | L41095 | L41100 |
| Liquidus T | n/a | n/a | n/a | n/a | n/a | n/a | n/a | n/a | n/a |

Appendix 1 continued: XRF bulk rock analyses from the Rogerson Formation.

ASI = aluminosity index

Liquidus temperature (° C) estimated from whole-rock composition
MELTS software (Ghiorso & Sack, 1995; Asimow & Ghiorso, 1998)

| Sample # | GA02/3/8/2 | GA02/12/8/10 | GA02/3/8/6 | 7 | 11 | GA02/12/8/7 | GA02/12/8/9 | 78 | 81 |
|--------------|--------------|---------------|--------------|---------------|--------------|--------------|---------------|---------------|---------------|
| Member | Browns | Rabbit Spr | Rabbit Spr | Jackpot 7 | Jackpot 7 | Jackpot 7 | Jackpot 7 | Jackpot 6 | Jackpot 6 |
| SiO2 | 68.89 | 75.42 | 72.19 | 74.29 | 73.24 | 72.55 | 74.96 | 73.50 | 66.97 |
| TiO2 | 0.75 | 0.40 | 0.54 | 0.45 | 0.48 | 0.50 | 0.37 | 0.42 | 0.91 |
| Al2O3 | 12.59 | 11.61 | 11.88 | 12.05 | 12.31 | 12.07 | 11.67 | 12.14 | 14.26 |
| Fe2O3 | 4.51 | 2.56 | 3.63 | 3.17 | 3.48 | 2.28 | 2.45 | 2.83 | 5.41 |
| MnO | 0.05 | 0.03 | 0.04 | 0.04 | 0.08 | 0.01 | 0.01 | 0.03 | 0.06 |
| MgO | 0.66 | 0.15 | 0.26 | 0.26 | 0.24 | 0.15 | 0.14 | 0.23 | 0.98 |
| CaO | 1.94 | 0.84 | 1.32 | 1.13 | 1.17 | 1.30 | 0.93 | 1.03 | 2.08 |
| Na2O | 2.64 | 3.12 | 3.33 | 3.32 | 3.44 | 3.54 | 2.89 | 2.38 | 2.99 |
| K2O | 5.13 | 5.49 | 5.13 | 4.38 | 4.50 | 5.15 | 5.34 | 5.52 | 3.49 |
| P2O5 | 0.15 | 0.05 | 0.09 | 0.09 | 0.07 | 0.08 | 0.09 | 0.05 | 0.15 |
| LOI | 2.33 | 0.55 | 0.33 | 0.85 | 0.72 | 2.05 | 1.20 | 2.13 | 2.87 |
| As | n/a | n/a | n/a | 16.29 | 6.11 | n/a | n/a | 4.86 | 3.59 |
| Ba | 1073.54 | 1022.62 | 1317.12 | 1310.28 | 1502.87 | 1167.52 | 1080.41 | 1200.64 | 1137.24 |
| Ce | 155.12 | 143.01 | 138.25 | 147.40 | 165.93 | 157.61 | 142.40 | 140.61 | 168.37 |
| Co | 9.21 | 3.09 | 6.56 | 5.17 | 6.26 | 2.94 | 2.78 | 3.52 | 12.37 |
| Cr | 102.41 | 2.47 | 0.40 | 2.09 | 5.55 | 104.26 | 18.43 | 3.93 | 9.32 |
| Cs | 9.03 | 3.11 | 9.43 | 2.15 | 5.32 | 2.91 | 7.62 | 0.39 | 4.30 |
| Cu | 18.62 | 2.04 | 5.08 | 7.13 | 7.39 | 6.86 | 6.33 | 1.20 | 13.15 |
| Ga | 20.24 | 18.85 | 19.19 | 20.85 | 20.87 | 20.33 | 18.92 | 19.71 | 23.34 |
| La | 80.14 | 79.27 | 76.76 | 83.31 | 88.60 | 89.72 | 79.19 | 76.74 | 86.09 |
| Mo | 3.27 | 3.03 | 2.34 | 3.37 | 1.78 | 2.13 | 1.47 | 2.23 | 1.79 |
| Nb | 43.34 | 46.19 | 43.49 | 54.26 | 54.28 | 42.88 | 41.83 | 47.23 | 47.70 |
| Nd | 61.18 | 59.25 | 56.88 | 68.38 | 73.43 | 68.47 | 64.45 | 58.93 | 67.50 |
| Ni | 0.44 | 2.51 | 1.40 | -0.86 | 7.07 | 0.76 | -0.47 | 3.06 | 0.41 |
| Pb | 26.36 | 30.08 | 25.60 | 35.16 | 30.28 | 27.37 | 30.19 | 29.11 | 38.46 |
| Rb | 165.39 | 201.55 | 177.20 | 174.95 | 169.11 | 185.73 | 194.75 | 198.13 | 136.98 |
| Sc | 9.69 | 4.61 | 6.02 | 2.50 | 7.31 | 5.45 | 4.83 | -1.70 | 10.55 |
| Sn | n/a | n/a | n/a | 7.50 | 0.55 | n/a | n/a | 6.87 | 5.18 |
| Sr | 120.39 | 54.58 | 89.85 | 84.23 | 102.85 | 98.30 | 88.31 | 60.39 | 146.40 |
| Th | 29.27 | 33.52 | 30.48 | 35.61 | 29.89 | 29.27 | 31.91 | 39.79 | 36.34 |
| U | 6.92 | 7.08 | 7.02 | 7.23 | 10.68 | 5.49 | 7.25 | 11.37 | 5.92 |
| V | 23.89 | 12.59 | 18.64 | 36.93 | 17.84 | 18.78 | 8.80 | 3.64 | 37.33 |
| Y | 64.81 | 60.22 | 64.43 | 77.86 | 89.35 | 59.85 | 60.25 | 67.43 | 73.44 |
| Zn | 58.03 | 43.72 | 54.34 | 65.78 | 53.28 | 55.98 | 38.66 | 49.05 | 134.59 |
| Zr | 593.35 | 440.96 | 512.03 | 640.21 | 595.41 | 525.83 | 454.52 | 527.95 | 690.01 |
| Cl | n/a | n/a | n/a | 69.49 | 113.08 | n/a | n/a | 161.72 | 771.30 |
| ASI | 0.94 | 0.92 | 0.88 | 0.98 | 0.97 | 0.88 | 0.95 | 1.03 | 1.14 |
| Total | 99.65 | 100.21 | 98.74 | 100.01 | 99.74 | 99.67 | 100.04 | 100.26 | 100.18 |
| Bead-mj | LF20984 | LF20972 | LF20974 | LF22412 | LF22413 | LF20967 | LF20987 | LF22385 | LF22406 |
| Pellet-tr | L41102 | L41090 | L41092 | L42168 | L42169 | L41085 | L41105 | L42141 | L42162 |
| Liquidus T | n/a | n/a | n/a | n/a | n/a | n/a | n/a | n/a | n/a |

Appendix 1 continued: XRF bulk rock analyses from the Rogerson Formation.

ASI = aluminosity index

Liquidus temperature (° C) estimated from whole-rock composition
MELTS software (Ghiorso & Sack, 1995; Asimow & Ghiorso, 1998)

| Sample # | 79 | GA02/24/6/3 | GA02/5/8/4 | GA02/12/8/1 | GA02/6/8/1 | GA02/6/8/2 | GA02/12/8/2 |
|-------------------|--------------|---------------|---------------|---------------|--------------|--------------|--------------|
| Member | Jackpot 6 | Jackpot 5 | Jackpot 5 | Jackpot 5 | Jackpot 5 | Jackpot 5 | Jackpot 5 |
| SiO2 | 68.81 | 74.98 | 74.63 | 71.39 | 75.41 | 75.70 | 71.94 |
| TiO2 | 0.63 | 0.49 | 0.39 | 0.59 | 0.36 | 0.33 | 0.56 |
| Al2O3 | 12.90 | 11.85 | 11.59 | 12.46 | 11.91 | 11.12 | 11.96 |
| Fe2O3 | 4.60 | 3.41 | 3.02 | 4.18 | 1.78 | 2.65 | 3.95 |
| MnO | 0.07 | 0.04 | 0.04 | 0.06 | 0.06 | 0.04 | 0.06 |
| MgO | 0.55 | 0.17 | 0.06 | 0.46 | 0.02 | 0.01 | 0.16 |
| CaO | 2.13 | 1.03 | 0.96 | 1.72 | 0.86 | 0.72 | 1.49 |
| Na2O | 3.09 | 3.39 | 3.38 | 2.70 | 3.30 | 3.05 | 3.23 |
| K2O | 4.32 | 4.89 | 4.99 | 5.19 | 5.39 | 4.84 | 4.93 |
| P2O5 | 0.11 | 0.07 | 0.05 | 0.16 | 0.14 | 0.16 | 0.12 |
| LOI | 1.97 | 0.55 | 1.04 | 1.98 | 0.67 | 0.80 | 0.85 |
| As | 2.06 | n/a | n/a | n/a | n/a | n/a | n/a |
| Ba | 2519.08 | 1321.10 | 1246.62 | 1298.44 | 1538.25 | 1792.50 | 1196.14 |
| Ce | 141.36 | 154.34 | 143.76 | 153.66 | 139.91 | 145.02 | 146.30 |
| Co | 10.99 | 5.89 | 5.02 | 9.61 | 1.68 | 4.56 | 8.49 |
| Cr | 4.16 | 4.97 | -0.31 | 6.17 | 7.92 | 236.42 | 36.18 |
| Cs | 4.58 | 7.27 | 2.39 | 3.37 | 7.99 | 4.39 | 4.86 |
| Cu | 4.43 | 9.10 | 5.31 | 12.09 | 2.38 | 10.90 | 13.29 |
| Ga | 21.86 | 19.98 | 18.83 | 21.09 | 20.92 | 20.50 | 19.89 |
| La | 83.51 | 86.04 | 76.82 | 81.99 | 86.27 | 84.12 | 76.15 |
| Mo | 1.67 | 2.84 | 2.33 | 3.11 | 2.36 | 2.27 | 2.80 |
| Nb | 44.45 | 52.96 | 53.40 | 43.17 | 48.23 | 44.13 | 41.48 |
| Nd | 61.29 | 66.71 | 63.46 | 63.60 | 62.77 | 64.87 | 61.17 |
| Ni | 3.56 | -0.25 | 1.80 | 0.88 | 0.93 | 0.84 | 0.66 |
| Pb | 29.79 | 26.00 | 26.56 | 26.66 | 29.71 | 25.33 | 25.42 |
| Rb | 155.15 | 161.13 | 167.51 | 171.94 | 189.69 | 175.13 | 175.64 |
| Sc | 8.15 | 4.04 | 3.46 | 6.67 | 4.43 | 4.18 | 6.12 |
| Sn | 3.47 | n/a | n/a | n/a | n/a | n/a | n/a |
| Sr | 196.01 | 87.54 | 73.42 | 110.30 | 78.10 | 82.95 | 94.30 |
| Th | 25.57 | 27.76 | 27.48 | 31.78 | 29.38 | 28.20 | 28.43 |
| U | 6.21 | 5.85 | 5.85 | 7.26 | 4.49 | 5.78 | 5.98 |
| V | 22.31 | 16.96 | 8.92 | 16.14 | 27.24 | 16.19 | 22.93 |
| Y | 68.17 | 72.94 | 66.20 | 68.48 | 56.88 | 67.48 | 57.58 |
| Zn | 78.21 | 61.47 | 60.04 | 65.84 | 74.66 | 68.79 | 58.99 |
| Zr | 589.69 | 584.83 | 558.02 | 554.27 | 530.54 | 505.09 | 524.85 |
| Cl | 1120.53 | n/a | n/a | n/a | n/a | n/a | n/a |
| ASI | 0.95 | 0.93 | 0.91 | 0.94 | 0.93 | 0.96 | 0.89 |
| Total | 99.16 | 100.86 | 100.14 | 100.88 | 99.89 | 99.40 | 99.23 |
| Bead-mj | LF22410 | LF20966 | LF20969 | LF20970 | LF20975 | LF20983 | LF20989 |
| Pellet-tr | L42166 | L41084 | L41087 | L41088 | L41093 | L41101 | L41107 |
| Liquidus T | n/a | n/a | n/a | n/a | n/a | n/a | n/a |

Appendix 1 continued: XRF bulk rock analyses from the Rogerson Formation.

ASI = aluminosity index

Liquidus temperature (° C) estimated from whole-rock composition
MELTS software (Ghiorso & Sack, 1995; Asimow & Ghiorso, 1998)

Geological Society of America
Field Guide 6
2005

Folds, fabrics, and kinematic criteria in rheomorphic ignimbrites of the Snake River Plain, Idaho: Insights into emplacement and flow

Graham D.M. Andrews
Michael J. Branney

Department of Geology, University of Leicester, Leicester LE1 7RH, UK

ABSTRACT

Recent structural analysis of the Grey's Landing ignimbrite offers new insights into the emplacement of rheomorphic ignimbrites. We present several key localities, where volcanological and structural features reveal the emplacement history of a lava-like ignimbrite and the evolution of ductile deformation structures during and after deposition across complex topography. Excellent three-dimensional exposure allows us to interpret structural features of the Grey's Landing ignimbrite in the context of diverse emplacement models for rheomorphic ignimbrites elsewhere and to consider field criteria to distinguish between lava-like ignimbrites and extensive silicic lavas.

Keywords: rheomorphic tuff, ignimbrite, shear zone, rhyolite, sheath fold.

OBJECTIVES

This excursion is intended to stimulate discussion about ductile deformation processes in rheomorphic ignimbrites. The Grey's Landing ignimbrite provides an unrivalled opportunity to examine abundant rheomorphic structures and fabrics that reveal something of its emplacement and deformation history. We will discuss field criteria that may be used to discern a variety of emplacement and deformation models. This trip is aimed toward both physical volcanologists and structural geologists with interests in rheology, ductile deformation, and the flow of materials such as lavas, glaciers, and crustal shear zones.

INTRODUCTION

Ignimbrites and Rheomorphism: A History of Ideas

Ignimbrites (or ash-flow tuffs) are deposits of pyroclastic density currents (Branney and Kokelaar, 2002). They typically contain various proportions of pumice and lithic lapilli in a poorly sorted matrix of ash shards. In some hot eruptions,

the pyroclasts weld together and, if sufficiently hot, the welded deposit may flow as a coherent ductile mass, a process known as rheomorphism. Rheomorphic ignimbrites typically contain a penetrative welding fabric, flow folds, and an elongation lineation, such as stretched vesicles and prolate fiamme (Fig. 1). They typically exhibit microscopic to 10-m-scale folds and, in some cases, upper autobreccias. A variety of kinematic indicators include an oblique foliation (sometimes described as imbrication of fiamme), rotated porphyroclasts, boudinaged fiamme, and inclined tension cracks (e.g., Schmincke and Swanson, 1967; Wolff and Wright, 1981; Branney and Kokelaar, 1992).

Various models have been proposed for the emplacement and ductile deformation of rheomorphic ignimbrite (Fig. 2); these are not mutually exclusive, and different rheomorphic ignimbrites may have different deformation histories. Current research is aimed at constraining (1) what causes the rheomorphic deformation, (2) its timing relative to deposition, and (3) the duration and style of deformation, as these differ between the existing models.

Welding in ignimbrites has commonly been inferred to postdate emplacement so that the vertical welding profile reflects

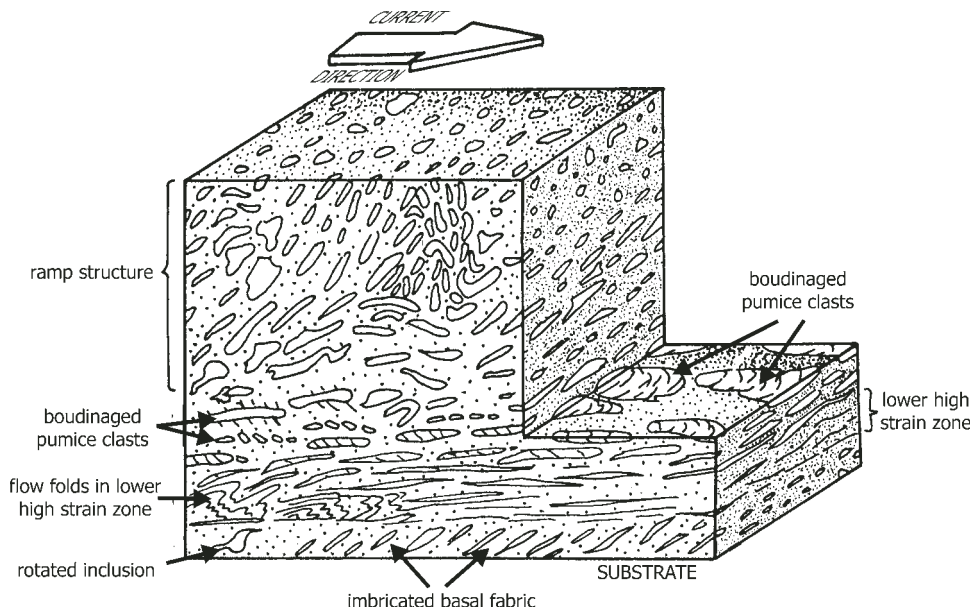
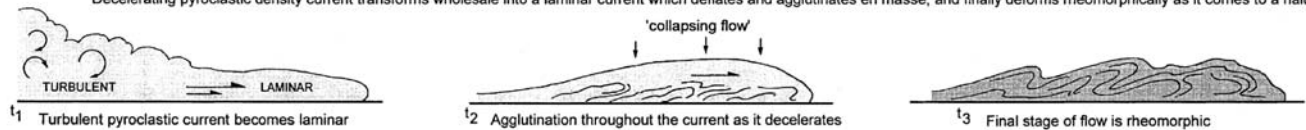


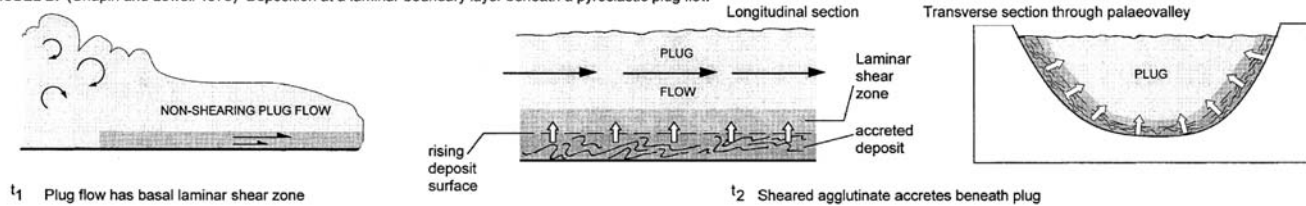
Figure 1. Schematic block diagram showing structures formed by rheomorphism in ignimbrites of the Mogán Formation, Gran Canaria (after Schmincke and Swanson, 1967).

MODEL A. (Schmincke and Swanson 1967)

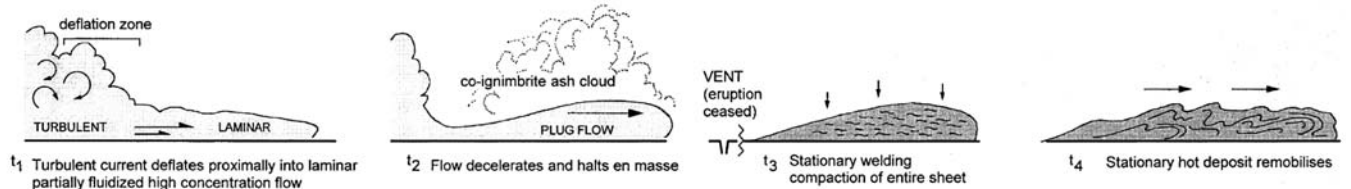
Decelerating pyroclastic density current transforms wholesale into a laminar current which deflates and agglutinates en masse, and finally deforms rheomorphically as it comes to a halt



MODEL B. (Chapin and Lowell 1979) Deposition at a laminar boundary layer beneath a pyroclastic plug flow



MODEL C: (Walker 1983; Sparks 1976; Wright and Walker 1981; Wolff and Wright) En masse deflation followed by hot state remobilisation of stationary ignimbrite



MODEL D. (Branney and Kokelaar 1992) Agglutination and deformation at, and within the base of, a sustained hot pyroclastic density current

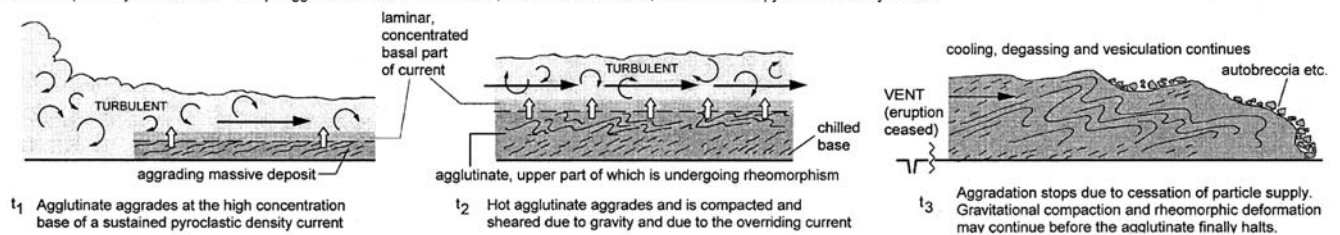


Figure 2. Schematic diagrams summarizing the emplacement of a rheomorphic ignimbrite as inferred from the four most readily accepted models. From Sumner and Branney (2002).

the thermal and compaction profiles through the ignimbrite after emplacement (Ross and Smith, 1961). However, Schmincke and Swanson (1967) interpreted rheomorphic deformation in peralkaline ignimbrites to occur while a hot pyroclastic current decelerates, gradually deflates, agglutinates, and comes to a halt en masse (Fig. 2A). In this conceptual model, the welding and rheomorphism starts prior to, and independently of, any post-emplacement cooling and welding. Chapin and Lowell (1979) invoked progressive agglutination, accretion and shear within a laminar boundary layer at the base and sides of a valley-filling plug-like pyroclastic current that behaved as a Bingham fluid (Fig. 2B), forming L_1 and F_1 structures, before slumping in a hot state toward the valley axis (perpendicular to the earlier flow direction) producing F_2 folds (Fig. 3).

In contrast, Wolff and Wright (1981) proposed that welding and rheomorphism begin only after the pyroclastic density current has ceased transport and deposition (Fig. 2C); the stationary deposit welds in situ due to internal heat and loading and then is able to *remobilize* and flow down-slope en masse. Branney and Kokelaar (1992) proposed that ignimbrites deposit by rapid, progressive aggradation from the base of a sustained pyroclastic density current and that in some cases welding and rheomorphism may start *during* deposition (Figs. 2D and 4); in this scenario, rheomorphic deformation may initially be partitioned in a subhorizontal ductile shear zone near the top of the deposit, and this migrates upward as the deposit continues to aggrade (Fig. 4). The rheomorphism may then continue after the pyroclastic current has dissipated (t_3 of Fig. 2D). An implication of this model is that one cannot assume the ignimbrite sheet was initially isother-

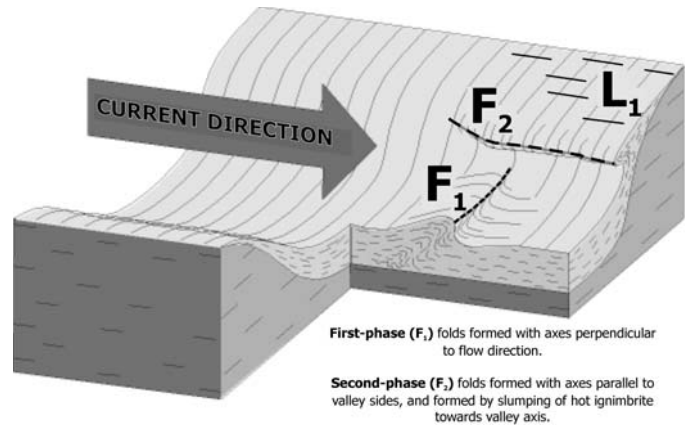


Figure 3. Schematic block diagram showing two-phase rheomorphism as inferred by Chapin and Lowell (1979) from the Wall Mountain Tuff, Colorado. L_1 —elongation lineation formed by stretched pumice lapilli and vesicles.

mal, and some ignimbrite welding profiles may reflect in part the differing rheologies of successive pyroclast populations supplied by the current to the site of deposition with time.

Sheath folds (Fig. 5) with axes subparallel to elongation lineations have been discovered in many rheomorphic ignimbrites (Branney et al., 2004). This discovery means that the two-phase deformation of Chapin and Lowell (1979) and Schmincke (1990) is more readily interpreted as recording a single sustained, progressive deformation event. Ideas thus have paralleled those

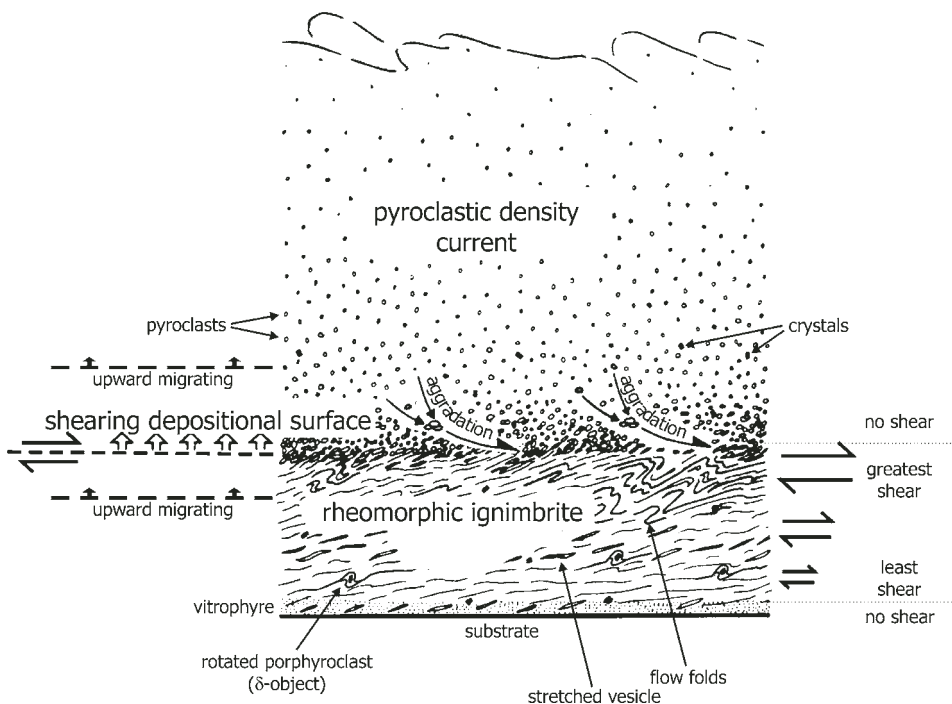


Figure 4. Schematic diagram showing the development of rheomorphic structures in a syndepositional shear zone at the current-deposit interface during progressive aggradation of ignimbrite (modified from Branney and Kokelaar, 1992).

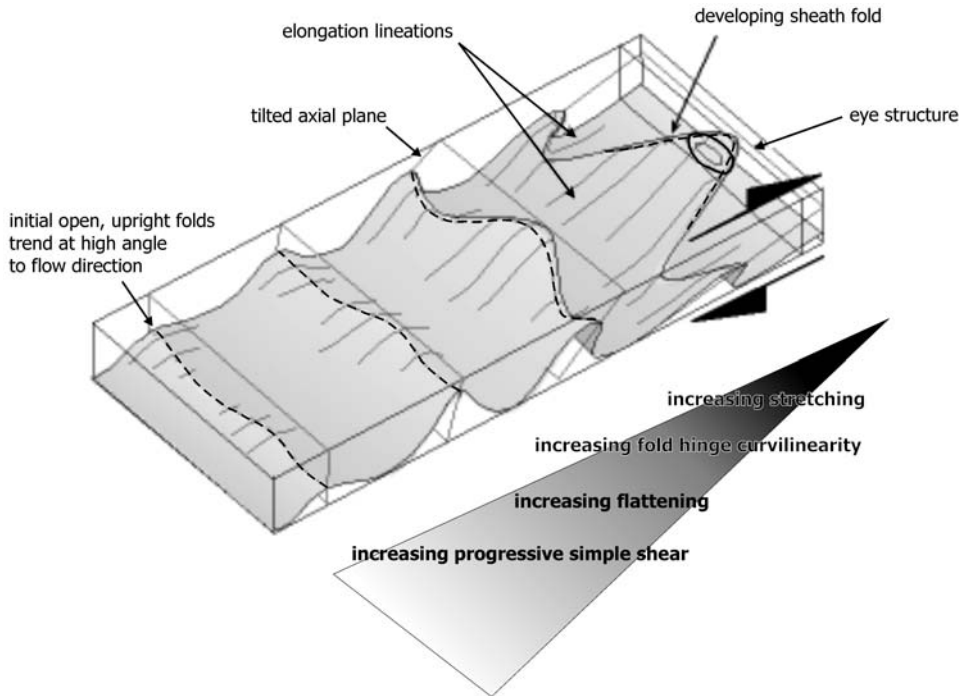


Figure 5. Schematic block diagram showing the development of a sheath fold during progressive simple shear.

developed for tectonic shear zones. Critical evidence in support of this is that most ignimbrites have only one elongation lineation and that in some (e.g., the Grey's Landing ignimbrite), the azimuth orientation of this lineation and the sheath fold axes change with height in the ignimbrite, which may reflect changing shear directions during deposition.

Terminology

Welding in Tuffs

Welding is the adhesion, plastic deformation, and compaction of hot pyroclasts (Ross and Smith, 1961). According to pyroclast rheology, welding may vary from rapid agglutination and even coalescence during deposition to slower loading-compaction during cooling of a thick ignimbrite sheet (e.g., Freundt, 1998).

High- and Extremely High-Grade Ignimbrite

Grade refers to the intensity of welding exhibited by ignimbrite sheets (Walker, 1983; Branney and Kokelaar, 1992). The grade continuum may be divided into four intergradational categories: (1) Low-grade ignimbrites are predominantly non-welded and may be emplaced at temperatures down to ambient. (2) Moderate-grade ignimbrites have both welded and nonwelded zones with little intense welding and generally no rheomorphism. (3) High-grade ignimbrites are predominantly welded, with intensely welded zones, and commonly exhibit local rheomorphism. (4) Extremely high-grade ignimbrites are intensely welded even to their upper surfaces. They typically exhibit rheomorphic structures and include lava-like lithofacies (e.g., the Grey's Landing ignimbrite).

Agglutination and Coalescence

Agglutination is the very rapid welding of depositing hot pyroclasts prior to burial compaction (e.g., in some basaltic spatter deposits). Coalescence is the homogenization of hot pyroclasts back to a coherent viscous fluid on deposition, so that the original clast outlines disappear (Branney and Kokelaar, 1992) (e.g., in the Grey's Landing ignimbrite, and in some clastogenic lavas [Furukawa and Kamata, 2004]).

Lava-Like

"Lava-like" is a purely descriptive term referring to a lithofacies that resembles a lava in that it lacks visible vitroclastic textures. It may be massive or flow-banded. This term can be used for parts of extremely high-grade ignimbrites, where pyroclasts are inferred to have coalesced. It does not imply any particular origin or emplacement mechanism.

Rheomorphism

Rheomorphism is the ductile deformation of hot, welded pyroclastic material during and/or just after deposition; this is separate and distinct from tectonic deformation. Ignimbrites undergoing rheomorphism develop a variety of ductile deformation structures, including flow-banding, flow-folds, folded and attenuated pumices, vesicles, and welding fabrics (Schmincke and Swanson, 1967; Wolff and Wright, 1981, Branney et al., 2004). These features develop in the viscous welded mass while it is still hot and degassing. For rheomorphism to occur, pyroclasts must be sufficiently fluidal at the time of welding to readily deform. This condition is favored by high emplacement temperatures, high eruptive mass-flux, minimal ingestion of atmospheric

air into the density current during transport, rapid deposition, strongly peralkaline chemistries, and/or high dissolved volatile (e.g., H₂O, Cl, F) contents (Mahood, 1984).

Progressive Aggradation

Progressive aggradation is the incremental increase in the thickness of a deposit with time because of deposition. Fisher (1966) and Branney and Kokelaar (1992, 1997) proposed that deposits of most pyroclastic density currents, including massive layers in ignimbrites, deposit incrementally beneath a sustained current (Fig. 4). This is in contrast to the conceptual model in which a pyroclastic density current progressively deflates during runout causing it to decelerate and ultimately halt en masse. Rates of aggradation may vary (unsteadiness), and this may impart layering within an ignimbrite.

Sheath Fold

“Sheath fold” is a purely descriptive term for strongly curvilinear folds where the measured fold hinge is parallel or subparallel to the stretching lineation. Sheath folds are interpreted to be produced by high finite, inhomogeneous strain. They characteristically appear as eye-structures when viewed parallel to the stretching direction (Fig. 5) and commonly occur associated with oblique folds. Branney et al. (2004) have shown that sheath folds and oblique folds are common in rheomorphic ignimbrites from diverse volcanic settings (e.g., Gran Canaria, Colorado, Pantelleria).

Themes for Discussion throughout the Field Trip

Is There Any Link between Rheomorphism and Pyroclastic Emplacement?

Is rheomorphism affected by pyroclastic transport and deposition, or is it entirely “secondary” and thus independent of the emplacement mechanisms? For example, if rheomorphic shear accompanies transport and deposition (Fig. 2), evidence of these processes may be “frozen” into the ignimbrite and be used to provide insights into pyroclastic emplacement processes.

Rates of Welding and Rheomorphism

Welding has traditionally been considered to occur on timescales of weeks to years (e.g., Riehle et al., 1995). However, high- and extremely high-grade ignimbrites are now commonly interpreted to undergo syndepositional and rapid welding in just seconds to minutes (Mahood, 1984; Branney and Kokelaar, 1992; Freundt, 1998). Welding rate is principally controlled by the pyroclast viscosity and the exerted stress. It may be that ignimbrites interpreted to have undergone load-welding were cooler (e.g., ≤ 750 °C) than those interpreted to have undergone agglutination and rheomorphism (e.g., 750–1050 °C). What evidence can be used to constrain rates of welding and rheomorphic deformation?

The Deformation History

How can the deformation history be unraveled from rheomorphic structures and fabrics? Was the deformation polyphase

and/or progressive? Was the strain partitioned spatially, and did this change with time?

Distinguishing Extremely High-Grade Ignimbrites from Lavas

Given the very different eruption and emplacement mechanisms (e.g., explosive versus extrusive), what criteria can be used to decide whether a unit is a lava-like ignimbrite or a true lava? Criteria proposed include the presence or absence of remnant pyroclastic layering, vitroclastic textures, autobreccias, crystal breakage, lithic concentrations, and overall morphology with respect to substrate topography (e.g., Ekren et al., 1984; Bonnichsen and Kauffmann, 1987; Branney et al., 1992; Henry and Wolff, 1992; Sumner and Branney, 2002). Some of these criteria are not reliable and some can be obscured by deformation and devitrification. As with lavas, extremely high-grade ignimbrites tend to exhibit scarce lithic clasts and lower crystal breakage relative to lower grade ignimbrites (Branney and Kokelaar, 1992). Conversely, lavas commonly develop local vitroclastic textures (fiamme and welded shards) by hot shearing of pumiceous autobreccia (Pichler, 1981; Manley, 1995). Amongst the best criteria are the presence of widespread *basal* autobreccia (Henry and Wolff, 1992), only known to occur in lavas, and topography-draping veneer-like, thin (<10 m), sheet-like morphologies with tapering margins, which are characteristic of ignimbrites. However, such features may not be exposed, so can structural analysis be used? Lavas can, for example, inherit folds and fabrics from conduit walls, whereas ignimbrites must develop their folds and fabrics develop after eruption.

Similarities and Differences to Tectonic Shear Zones

The structures in the Grey’s Landing ignimbrite are similar to those commonly found in exhumed ductile shear zones. Both typically are characterized by strong, noncoaxial plane strain, and have a strong, subhorizontal L = S fabric with intrafolial folds, and sheath folds. Cleavage, however, does not develop in rheomorphic ignimbrites, which are largely noncrystalline at the time of deformation. This can hinder structural analysis. Tectonic shear zones are confined—bound on either side by nondeforming rock mass—whereas rheomorphic ignimbrites have a free upper surface. Tectonic shear zones tend not to migrate, whereas rheomorphic shear zones may migrate during aggradation. Crustal shear zones often intersect layered sequences (e.g., bedded sediments) with an inherent mechanical anisotropy, which strongly influences the deformation (e.g., a thick quartzite will deform differently from a sequences of interbedded, thin shales and sandstones). In contrast, the Grey’s Landing ignimbrite may have been almost mechanically isotropic during deformation, and the deformation is more akin to deformation within glaciers and lavas.

REGIONAL SETTING AND STRATIGRAPHY

The Yellowstone–Snake River Plain volcanic province (Fig. 6) is dominated by large-volume (>10 km³) rhyolite lavas and ignimbrites, erupted from a series of major eruptive centers

that show an age progression from McDermitt caldera (ca. 16 Ma) in the southwest to the Yellowstone Plateau (ca. 2–0.6 Ma) in the northeast (Pierce and Morgan, 1992). The systematic age progression appears to be related to the southwestward movement of the North American plate over a fixed thermal anomaly, or hot spot. Presently, there is renewed debate as to the nature of this hot spot, with two opinions: (1) it represents a deep-rooted “mantle plume-tail” related to the mantle plume that produced the Columbia River Basalts (e.g., Pierce and Morgan, 1992); and (2) it represents an upper mantle convection anomaly at the base of the lithosphere (e.g., Humphreys et al., 2000).

The Yellowstone–Snake River Plain volcanic province is one of the most important regions for the study of large volume rhyolite eruptions (Bonnichsen, 1982; Christiansen, 2001; Ekren et al., 1984; Bonnichsen and Kauffman, 1987; Manley, 1996). Canyons and escarpments across southwestern and southern Idaho expose voluminous (<1000 km³) rhyolite sheets that include long lavas and extensive ignimbrites erupted from inferred eruptive centers (Owyhee-Humboldt, Bruneau-Jarbridge, and Twin Falls, between ca. 15 and ca. 8 Ma; Fig. 6). Mid- to late-Miocene rhyolites of southern Idaho and northern Nevada have been consigned to the Idavada Group (Malde and Powers, 1962). This includes the Cougar Point Tuff Formation (Bonnichsen and Citron, 1982), thought to be derived from the Bruneau-Jarbridge eruptive center; the Cassia Mountains succession, thought to be derived from the Twin Falls eruptive center (McCurry et al., 1996); and the Rogerson Formation, which occupies the intervening region between Twin Falls, Idaho, and Jackpot, Nevada (Andrews et al., 2006; Fig. 6).

The Rogerson Formation (Fig. 7) comprises seven ignimbrite members intercalated with volcanoclastic sediments and paleosols (Andrews et al., 2006). It records at least eight large explosive eruptions with intervening repose periods. The ignimbrites are predominantly fine-grained and intensely welded. Most are welded and two are rheomorphic and lava-like, although nonwelded rhyolitic pyroclastic layers also occur. They are typical Snake River Plain high-silica rhyolites (e.g., Hughes and McCurry, 2002), with sparse anhydrous plagioclase and 2-pyroxene glomerocrysts and Fe-Ti oxides. No vents have been identified, and the Rogerson Formation eruptions may have been located at the Bruneau-Jarbridge and Twin Falls eruptive centers, or in the intervening area (Fig. 6).

The Grey’s Landing ignimbrite Member (type locality: Grey’s Landing Recreation Ground, Idaho; Fig. 8) is a 5–65-m-thick rhyolite sheet. It comprises a stratified ashfall deposit, overlain by a largely lava-like ignimbrite with a lower vitrophyre, a thick lithoidal center, and a thin upper vitrophyre, locally overlain by a nonwelded top (Figs. 9 and 10). The ignimbrite is intensely rheomorphic; it is compositionally zoned with vertical variations in glass and pyroxene crystal chemistry (Andrews et al., 2006). Eruption temperature is estimated at 950 °C–1050 °C (Andrews et al., 2006). No source vent has been identified, nor has a reliable radiometric age been confirmed; however, the ignimbrite is demonstrably younger than the 10.54 Ma Rabbit Springs ignimbrite (Bill Bonnichsen, 2004, personal commun.).

FIELD TRIP

This field trip will visit the Grey’s Landing ignimbrite of the Rogerson Formation (Fig. 7) and, if time allows, the neighboring House Creek ignimbrite. We will examine a small number of key localities around the Rogerson Graben. The itinerary has been ordered so as to begin by introducing participants to the graben and its rhyolite stratigraphy before examining the range of rheomorphic structures, starting with the simplest structures and then building up to a more complex and complete picture. This requires some backtracking each day; this is not a “linear” road-log based trip.

Logistics

All localities are (at the time of writing) on publicly owned open land and most are easily accessible by a combination of short walks and vehicles. Most localities are accessible to two-wheel drive/low clearance vehicles provided care is taken. Relevant topographic maps: 1:100,000—Rogerson; 1:24,000—Cedar Creek, Browns Bench North, Meteor, Salmon Butte. There are several hotel-casinos in Jackpot, Nevada, together with a general store and gas station. There is a gas station and small store in Rogerson, Idaho. As with all desert fieldwork, remember to bring sufficient water and sunblock. This excursion does not require strenuous effort; however, care should be taken: local hazards include fast traffic, steep and loose talus slopes, snakes, and hunters (late August–January). *Please refrain from hammering at the outcrops*—the exposed surfaces are often more informative than fresh alternatives, and the rocks are visually stunning—some offer genuine aesthetic pleasure; they make much better photographs. The talus slopes contain abundant fresh, hand-specimen-sized fold closures and lineated foliation surfaces.

Day 1

Introduction to the succession and to welding and fusing in tephra. Syndepositional rheomorphic folds, elongation lineations, and kinematic indicators. Depart Jackpot, Nevada, heading north on U.S. Highway 93 (U.S. 93).

Stop 1.1—Backwaters: stratigraphic context, welding and fusing of tephra;

Stop 1.2—Roadkill (U.S. 93): thin ignimbrite on stratified ashfall deposit;

Stop 1.3—Norton Canyon Road: intermediate-thickness ignimbrite with rheomorphic folds;

Stop 1.4—Grey’s Landing: thick ignimbrite with abundant small-scale sheath folds.

Directions to Stop 1.1

Drive north from Jackpot, Nevada, on U.S. 93 for ~7 mi (11 km), and turn left for Backwaters Recreation Area (signposted). Continue along a gravel track to the parking area at the base of the large cliffs on the right (north).

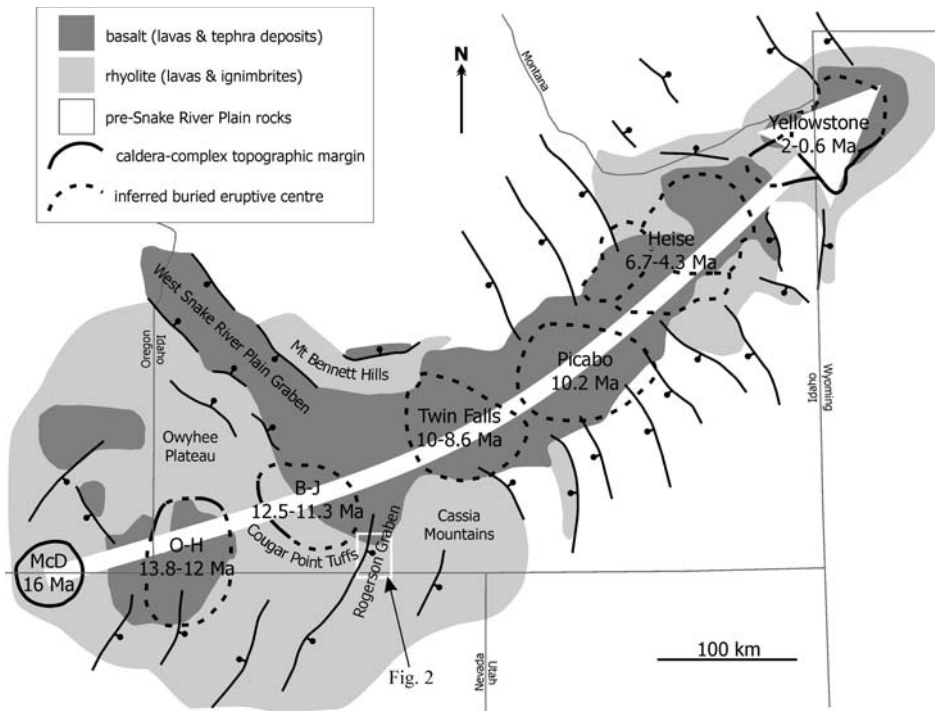


Figure 6. Simplified geologic map of the Yellowstone-Snake River Plain volcanic province. Modified from Pierce and Morgan (1992); Hughes and McCurry (2002); and Rodgers et al. (2002). Age data taken from Hughes and McCurry (2002).

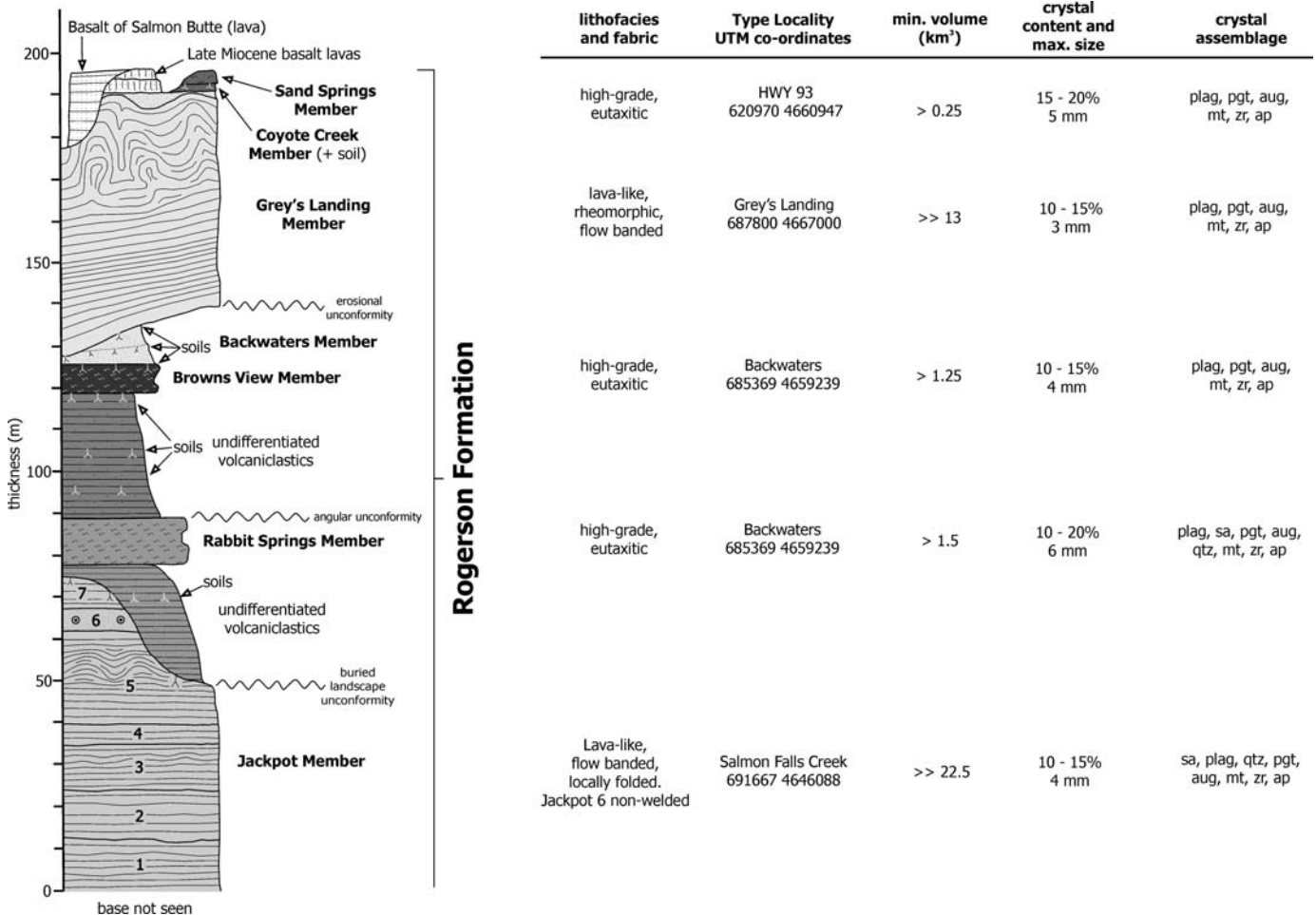


Figure 7. General vertical section through the Rogerson Formation in the Rogerson Graben. Soils, erosion surfaces, and unconformities are marked. Details of lithofacies, welding grade, type locality, minimum volume, and crystal assemblage are given on the right.

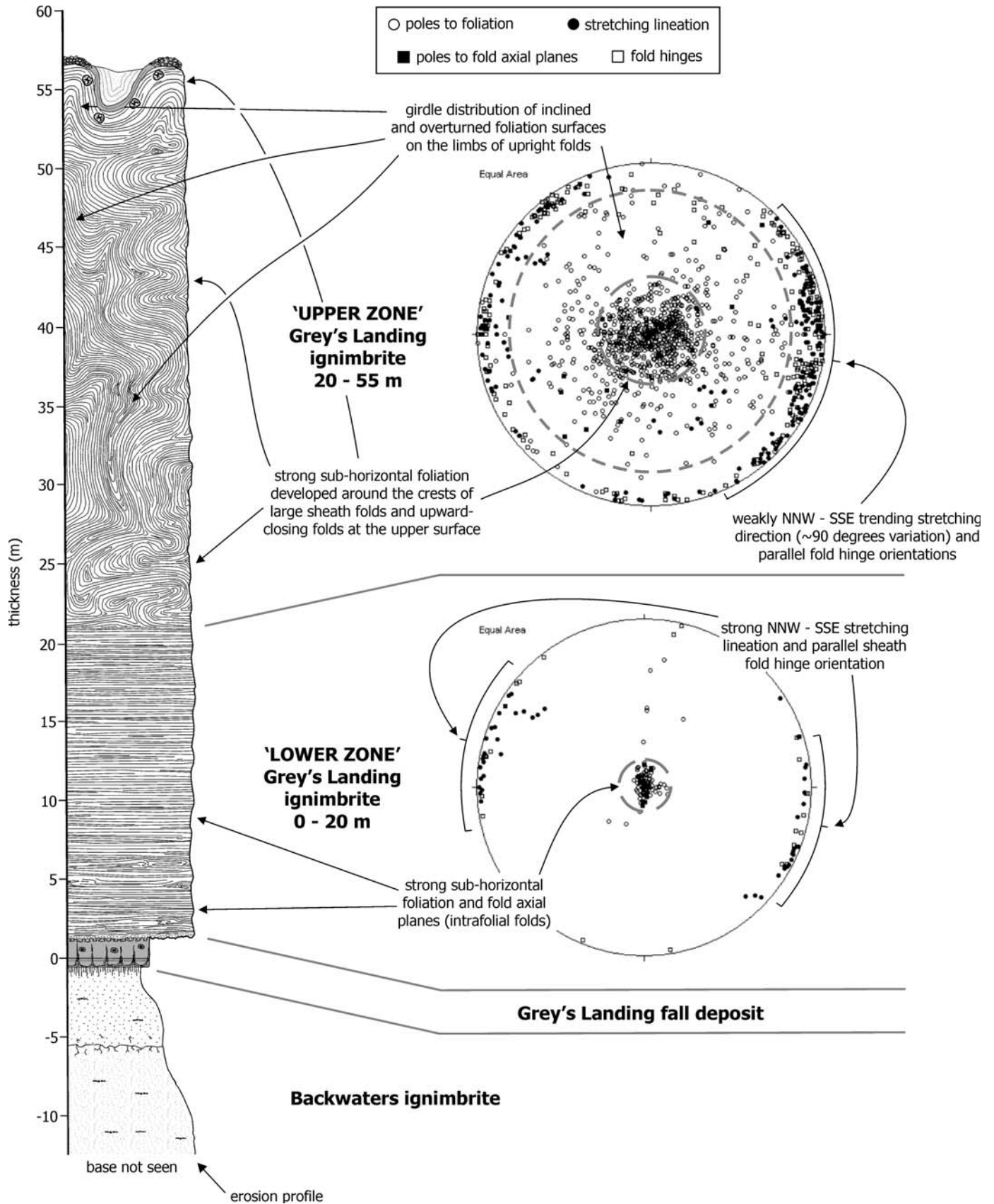


Figure 9. Vertical division into two structural zones at Grey's Landing (stops 1.1, 1.4, 2.1, 2.2, and 2.3). The lower zone (0–20 m) is predominantly a penetrative, subhorizontal foliation with intrafolial folds and sheath folds. The upper zone (20–55 m) is dominated by meter-scale to 10-m-scale complex folding and refolding of an earlier penetrative and intrafolial fabric. We interpret the earlier fabric to be the same as that which dominates the lower zone.

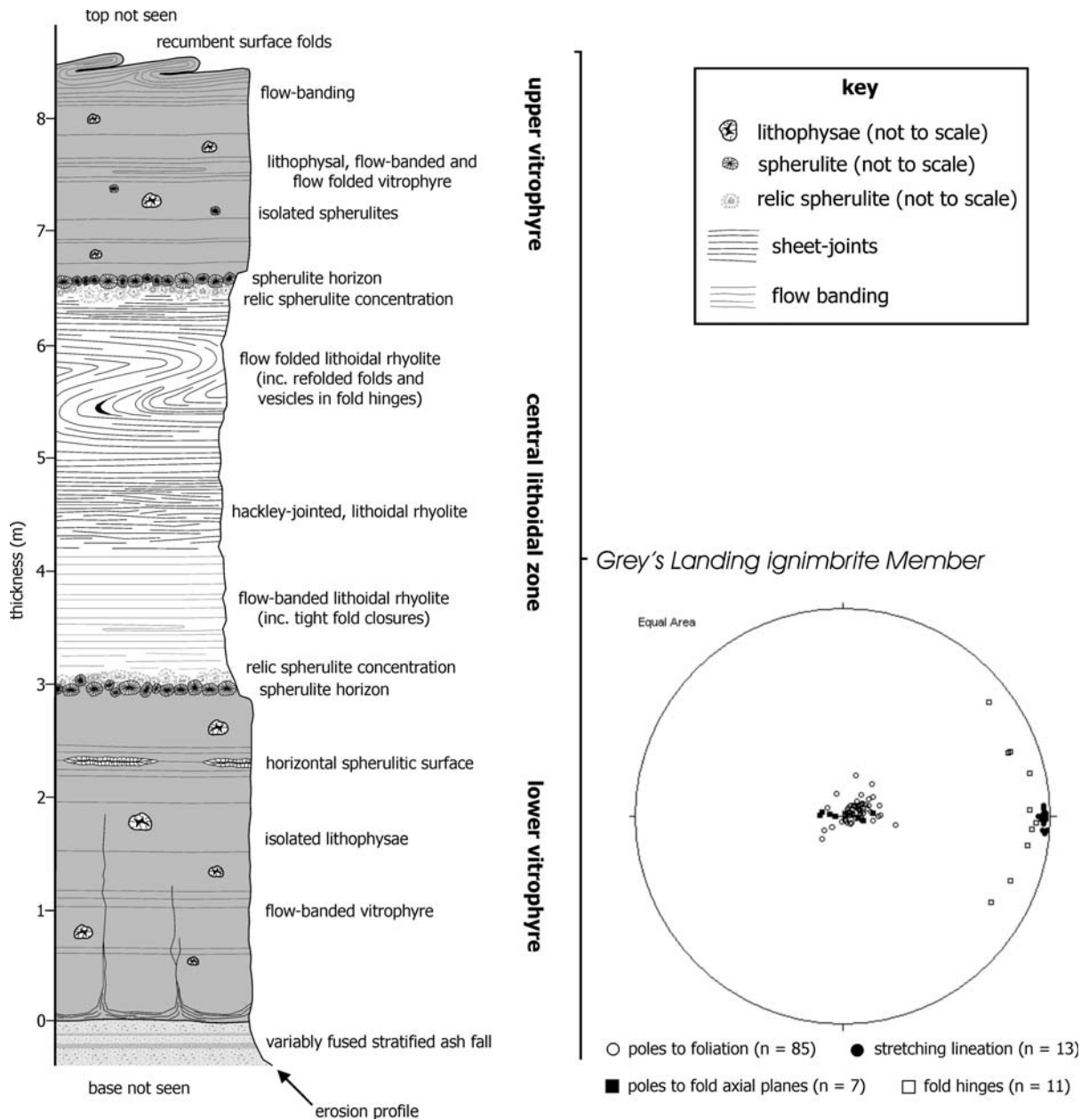


Figure 10. Graphic log of the Grey's Landing ignimbrite in the area around Stop 1.3.

Stop 1.1: Backwaters (UTM Zone 11: 685154E 4659673N)

This locality provides an introduction to the Rogerson Formation (Fig. 7) and the Rogerson Graben (Fig. 8) and is a good place to consider the geological context for the remainder of the excursion. The Rogerson Graben is a NNE-SSW-trending half-graben that deepens westward toward the Browns Bench Fault. The footwall of the fault has uplifted a thick succession of extensive rhyolitic ignimbrites that comprise the Browns Bench escarpment on the western horizon. The ignimbrites are high-grade and may derive from the Bruneau-Jarbidge eruptive

center (Bonnichsen and Citron, 1982; see Fig. 6) 30 km to the west. The Rogerson Graben is one of at least 10 similarly trending half-graben on the southern side of the Snake River Plain. They are thought to relate to Basin and Range extension, and the volcanism seems to have accompanied the extension.

The Rogerson Formation (Andrews et al., 2006) occupies the Rogerson Graben and postdates the ignimbrites exposed in the escarpment. It includes seven ignimbrites and associated tephra (Fig. 7) erupted from the Snake River Plain to the north. Unconformities and variations in ignimbrite thickness

indicate that eruption and deposition were contemporaneous with graben extension.

The lowest exposed unit in the formation, the Jackpot rhyolite (Fig. 7), is best observed on the track in and out of the Backwaters recreation area. It forms the cliffs and rolling surface to the south. It is overlain by poorly exposed bedded volcanoclastic sediments, the Rabbit Springs ignimbrite (a vitric layer at road level), some younger, poorly exposed volcanoclastic sediments, and the Browns View ignimbrite, which forms a discontinuous ledge at base of cliffs to the east. The overlying buff-colored and poorly exposed Backwaters ignimbrite is partly fused by the overlying Grey's Landing ignimbrite, which is the main cliff-forming unit on either side of the small canyon.

Examine accessible parts of the Rabbit Springs and Browns View ignimbrites on the approach the base of the Grey's Landing ignimbrite. The basal contact relations of the Grey's Landing ignimbrite reveals that the massive vitrophyre overlies a stratified, crystal-rich vitrophyre that, in turn, rests on a baked paleosol (Fig. 9). There is no autobreccia at the base of the ignimbrite. Examine the underlying Backwaters ignimbrite, noting how parts are fused to black glass.

Themes to consider: How do these deposits compare to less welded ignimbrites? Why are fiamme and lithic clasts absent? How might the deposits be distinguished from lavas? Does the stratified vitrophyre represent a fused ashfall deposit? Exactly where, within the vitrophyre, is the base of the Grey's Landing ignimbrite? Why is the underlying paleosol baked rather than fused?

Directions to Stop 1.2

Return to U.S. 93, noting how the Grey's Landing ignimbrite (the topmost exposed unit) thins dramatically toward the east. Turn right (south) and drive ~1 mi (1.6 km) and stop in the large pull-off on the right (west) side of U.S. 93. Cross the road to examine the exposure in the road-cut. Take care; the exposure is named Roadkill for a reason!

Stop 1.2: Roadkill (UTM Zone 11: 692234E 4660906N)

Along U.S. 93, the Grey's Landing ignimbrite is an entirely vitric sheet, ≤ 5 m thick. It sits on a sequence of stratified ash and pumice-rich layers that overlie a paleosol. The upper 0.5–1 m of the stratified ash is interpreted as an ash-fall deposit from the Grey's landing eruption (Andrews et al., 2006). It correlates with the stratified, crystal-rich vitrophyre at Stop 1.1. Examine the basal contact of the ignimbrite and note how the stratified ash deposits become increasingly fused toward the base of the ignimbrite. The ignimbrite does not have a basal autobreccia, and the underlying ash deposit is not deformed. The ignimbrite is massive glass, and neither bedding nor rheomorphic structures are discernible within it. Next, note the stretched vesicles (E-W) at the top surface of the outcrop (best seen along the very edge). Orientated thin sections from this locality show that the entire ignimbrite is intensely sheared, top to the west, even at the base.

Themes to consider: What criteria distinguish between lava-like ignimbrites and lavas? What is the significance of the

absence of autobreccia? Can rhyolite lavas be emplaced as very thin sheets?

Directions to Stop 1.3

Return north on U.S. 93 and turn on to the Norton Canyon road (signposted). Pull up on the right after ~250 m, on reaching the first set of low crags on the right. Here the Grey's Landing ignimbrite is 6–10 m thick (Fig. 10) and forms the local topographic surface. It overlies the same partly fused ashfall deposit as at Stops 1.1 and 1.2 (poorly exposed here) and, again, the base of the ignimbrite lacks an autobreccia and the underlying fused ash is not deformed.

Stop 1.3: Norton Canyon Road (UTM Zone 11: 690615E 4663972N)

This locality introduces the effects of devitrification as well as some macroscopic rheomorphic structures. The ignimbrite comprises three subhorizontal and subparallel zones defined by differences in devitrification: (A) a basal vitrophyre, (B) a central lithoidal zone, and (C) an upper vitrophyre (see Fig. 10). The basal and upper vitrophyres represent the original glassy state of the unit during deposition (as at Stop 1.2). The jointed, red-brown central lithoidal zone represents the devitrified center of what was probably originally a glassy hot deposit. Devitrification is the static crystallization of volcanic glass during prolonged cooling from high initial emplacement temperature. It is associated with volume loss that encourages the formation of joints, and it can obscure vitroclastic textures.

Abundant deformation structures occur within the central lithoidal zone and upper vitrophyre but are absent in the basal vitrophyre. Note, within the lithoidal zone, a strong stretching lineation, curvilinear flow folds (picked out by the pervasive jointing), rotated porphyroclasts (probably crystals), and sheared and oblique vesicles. Meter-scale, recumbent isoclines on the top surface of the upper vitrophyre have hinge lines parallel to the vesicle stretching direction (E-W). Structural data collected at this and adjacent localities are presented in Figure 10; note the dominant subhorizontal foliation and intrafolial nature of the fold axial planes and the girdle-like distribution of fold hinges parallel to oblique to the lineation.

Themes to consider: What is the structural style? How does this compare to styles seen at tectonic shear zones and/or mylonite zones? What of folds on the upper surface? How much of the deposit has undergone rheomorphism? Is there any evidence that mechanical layering has influenced the rheomorphism? Can existing emplacement models account for structures such as these? Given how thin the deposit is, how long could deposition and/or deformation have continued? What role, if any, might devitrification exert on deformation? Why are the clearest structures found in the devitrified material?

Directions to Stop 1.4

Return to U.S. 93 and turn left (north), then turn left (west) for Grey's Landing Recreation Ground (signposted). Proceed to Grey's Landing and park near the slipway.

Stop 1.4: Grey's Landing (UTM Zone 11: 687822E 4666778N)

First walk along the lake shore at the base of the northern cliffs and examine the base of the Grey's Landing ignimbrite; take care crossing the extensive talus slopes. Note that the stratified ashfall tuff at the base is totally fused here, and the underlying paleosol is baked (similar to Stop 1.1; Fig. 9). Fossil grass imprints are preserved on the top surface of the paleosol. The basal part of the ignimbrite is massive vitrophyre that lacks macroscopic rheomorphic structures such as folds and autobreccia. Examine the base of the much thicker, central lithoidal zone (cf. Stop 1.3); a "devitrification front" is made up of spherulites that protrude downward into the vitrophyre.

Where within the basal vitrophyre is the contact between ignimbrite and fall deposit? What is the origin of the boundary between vitric and devitrified rhyolite?

Walk south along the base of the cliffs (beware of loose talus) and onto the prominent bench developed in devitrified ignimbrite. The ignimbrite immediately below the bench is thoroughly penetrated by closely spaced, anastomosing joints and exhibits no macroscopic folds. The lowest macroscopic folds, including excellent sheath folds, occur at the top of the bench, where the jointing is more hackley and traces out abundant intrafolial fold closures on vertical surfaces. Subhorizontal foliation surfaces have a strong lineation parallel to fold hinges. Many surfaces exhibit scallop-shaped "dimple joints" on which the lineation is absent. Stretching lineations and fold hinges are consistently parallel and trend E-W at this level within the ignimbrite (lower stereonet Fig. 9).

We shall see that with increasing height in the ignimbrite, this orientation gradually changes, first in a counter-clockwise sense and then, above 33 m, in a clockwise sense. This has been interpreted as recording gradual changes in the rheomorphic transport direction with time, while the ignimbrite progressively aggraded (Branney et al., 2004).

Themes to consider: Is the style of folding here similar to Stop 1.3? What is the origin of the diverse forms of jointing? Has the jointing been folded, or did it mimic (develop along) already folded flow-banding? When did it form relative to rheomorphism? Why does the lowermost lithoidal rhyolite lack rheomorphic structures?

Summary

Day 1 familiarized participants with the stratigraphy and structure of the Rogerson Graben and gave an impression of the intensity of welding and rheomorphic deformation in the Greys Landing ignimbrite, along with its devitrification history. We have examined the ubiquitous subhorizontal fabric in lower parts of the ignimbrite, and have seen that lowermost folds include intrafolial sheath folds. We have observed that at a given height in the ignimbrite, the orientation of fold axes is subparallel to the elongation lineations.

Day 2

Nature of "late" rheomorphism in thick ignimbrite.

Stop 2.1—Upper part of Grey's Landing ignimbrite: large-scale folding of the earlier fabric;

Stop 2.2—"Too Cool": later, large-scale folding in 3D;

Stop 2.3—Cedar Creek Reservoir: later folding at the upper surface.

Directions to Stop 2.1

Depart Jackpot, Nevada, heading north on U.S. 93. Return to Grey's Landing Recreation Ground and park at the slipway (originally Stop 1.4).

Stop 2.1: Upper Parts of Grey's Landing Ignimbrite (UTM Zone 11: 688087E 4666732N)

Examine the exposures above the talus slope on the north side, immediately adjacent to and above the slipway. Ascend a narrow gully near the corner of the cliff; climb out of the gully on to the flat promontory on the left. Examine the curved cliff face behind the promontory, noting the complex folding of the earlier intrafolial, subhorizontal fabric that we saw yesterday. Large-scale folds are not intrafolial; they are upright to recumbent and tight to isoclinal.

Descend out of the gully, and then walk east along the base of the cliffs, examining the large-scale folds and refolding of the earlier intrafolial structures. Note that the large-scale folds are curvilinear and trend ~E-W. Gradually ascend the slope, and pause where the cliffs turn north into a small side-canyon. Look east across the side-canyon at the opposite face and appreciate the large-scale eye-structures developed near the top of the cliff. Cross the side-canyon and ascend to examine the complex refolding patterns produced around the large sheath fold. While descending the slope and returning to the slipway, note how the dominant fabric is intrafolial away from the effects of refolding by later, large-scale folds.

Structural data collected within the complexly refolded zone at this locality is presented in Figure 9. Note the spread of foliation and fold axial plane data around the horizontal and the preferred trend of lineation and fold hinges E-W. This supports observations that the later folds are curvilinear to sheath-like and commonly recumbent.

Themes to consider: What is the style of folding? How do these folds relate to the earlier, intrafolial and smaller folds? Does an increase in fold scale indicate a change in rheological conditions? What form has the transition between levels dominated by initial folding and those dominated by subsequent folding?

Directions to Stop 2.2

Drive back out from Grey's Landing and turn left (north) through the prominent iron gate at the junction of four tracks. Drive along a rough track ~1.5 mi (3.1 km), then descend the prominent fault scarp to the shore in a small N-S-trending cove (not suitable for 2WD or low-clearance vehicles).

Stop 2.2: Too Cool (UTM Zone 11: 687268E 4668336N)

Examine the low, subhorizontal surface immediately west of the beach. This surface is the eroded remnant of the original upper

surface of the Grey's Landing deposit. Different colored layers (due to variations in devitrification) are folded into a series of 2-m-scale domes and basins, complex refolded folds, and sheath folds. Explore this area and, if possible, descend to the base of the low cliffs it examine these features in three dimensions.

Themes to consider: What is the style of folding? How do the folds relate to structures seen at lower levels in the ignimbrite, e.g., at Stops 1.4 and 2.1? Can any effect of proximity to the original surface be discerned? Did the differently colored layers exhibit different mechanical properties during the deformation?

Directions to Stop 2.3

Return to U.S. 93 and turn left (north) and then turn left (northwest) on to unnamed road immediately after milepost 13. Turn left (west) onto the Murphy Hot Springs Road and cross Salmon Dam; continue west to Cedar Creek Reservoir (signposted). Pass around the north side of the outbuildings and turn right (north) toward the slipway (signposted). Pull off the track to the left and stop on the broad, flat area overlooking the reservoir, after ~1 mi (1.6 km).

Stop 2.3: Cedar Creek Reservoir (UTM Zone 11 673712E 4674456N)

Walk west to where the wire fence reaches the cliff line. Then follow the cliff line toward the northeast, noting the folded internal layering within the ignimbrite (Fig. 11). This layering is produced by different devitrification and welding intensities within the Grey's Landing ignimbrite. Although thicknesses of the layers vary, their stratigraphic order remains consistent. The uppermost layer is a nonwelded, orange tuff that will be seen again at Stop 3.4 (Salmon Dam) resting upon the upper vitrophyre. The layering is folded into upright, 10-m-scale anticlines and synclines with hinges trending NW-SE (Fig. 11). Many folds are strongly curvilinear, and axes plunge steeply to both the NW and SE. Several of the anticlinal closures are composite and include more than one generation of earlier fold closure within them. This produces re-fold interference patterns in which more than three generations of folds interact. Continue for ~400 m to the northeast until the cliff line peters out.

If the reservoir level is sufficiently low (typically in August–November), descend to the lake bed and walk southwest along the base of the cliffs. Excellent sheath folds and refolded folds can be seen along the cliffs and in loose blocks on the lake bed. Some surfaces preserve dilational fractures of vesiculated ignimbrite around fold closures.

Themes to consider: What is the style of folding? Does the scale and wavelength of the folds inform us about rheology of the unit? How are these folds produced: are they buckle folds produced by coaxial shortening, or are they similar-style flow folds produced by continued flow during emplacement and modified by gravity?

Summary

At the end of Day 2, participants should have learned something of the nature and style of post-emplacement rheomorphism

as demonstrated by the complex refolding of the earlier ubiquitous subhorizontal fabric. We can draw two major conclusions today: (1) there has been a second generation of folds (phase of rheomorphism) in the Grey's Landing ignimbrite; and (2) we can characterize this second (generation) phase of rheomorphism. The duration of this rheomorphism can be constrained using cooling models.

The second phase of rheomorphism remains enigmatic. The fold axes trend east-west, similar to that of the early folds. Could the later folds have developed as buckle-style, coaxial shortening folds during a phase of downslope creep perpendicular to the initial emplacement direction, or could they simply have been generated by continued flow in the same direction as the initial emplacement? Critical to this interpretation is that there is no second set of stretching lineations perpendicular to the late fold axes and at high angles to the initial stretching lineation. Participants are encouraged to consider the alternatives and look for supporting evidence.

The cooling history of the ignimbrite affects its rheological evolution, and hence, its deformation history. Viscosity within silicic glasses is inversely proportional to temperature for a given composition and volatile content. This relationship is strongly nonlinear; at the glass transition temperature (~650 °C–725 °C for anhydrous rhyolite), viscosity increases by several orders of magnitude. At low temperatures and short timescales, below the glass transition, the glass responds to strain as a brittle solid (Webb, 1997). At high temperatures and short timescales, above the glass transition, it behaves as a non-Newtonian fluid and will flow. Therefore, cooling is an important limiting factor on the duration and style of deformation.

Thermal profiles can be established by adapting cooling models (e.g., Manley, 1992) for magmatic temperature estimates obtained from crystal analyses and geothermometry. This has been done for the 60-m-thick, intensely welded (low porosity) Grey's Landing ignimbrite, emplaced at 1000 °C on to porous substrate and then buried by a thin, porous ash deposit. This model deals with conduction of heat to the air and the substrate, and does not account for convection of fluids and/or volatiles, advection of hot material due to rheomorphic folding. It predicts rapid (<1 yr) cooling of the upper and lower parts (now vitrophyres) and more gradual cooling of the interior of the ignimbrite. By incorporating the glass transition, the duration of ductile behavior at different depths can be estimated. The maximum duration of ductile behavior in the center is ~15 yr; however, given the exclusion of heat loss by convection and advection, this is probably a considerable overestimate.

Day 3 (Half Day)

Stop 3.1—Monument Canyon: transition from a domain preserving dominantly effects of “early” rheomorphism to a domain recording early deformation modified by “late” rheomorphism;

Stop 3.2 (optional)—House Creek: rheomorphism in an incredibly thin ignimbrite;

Stop 3.3 (optional)—West Bay: intrafolial sheath folds and spaced zones of “late” rheomorphism;

Stop 2-3 - Cedar Creek Reservoir

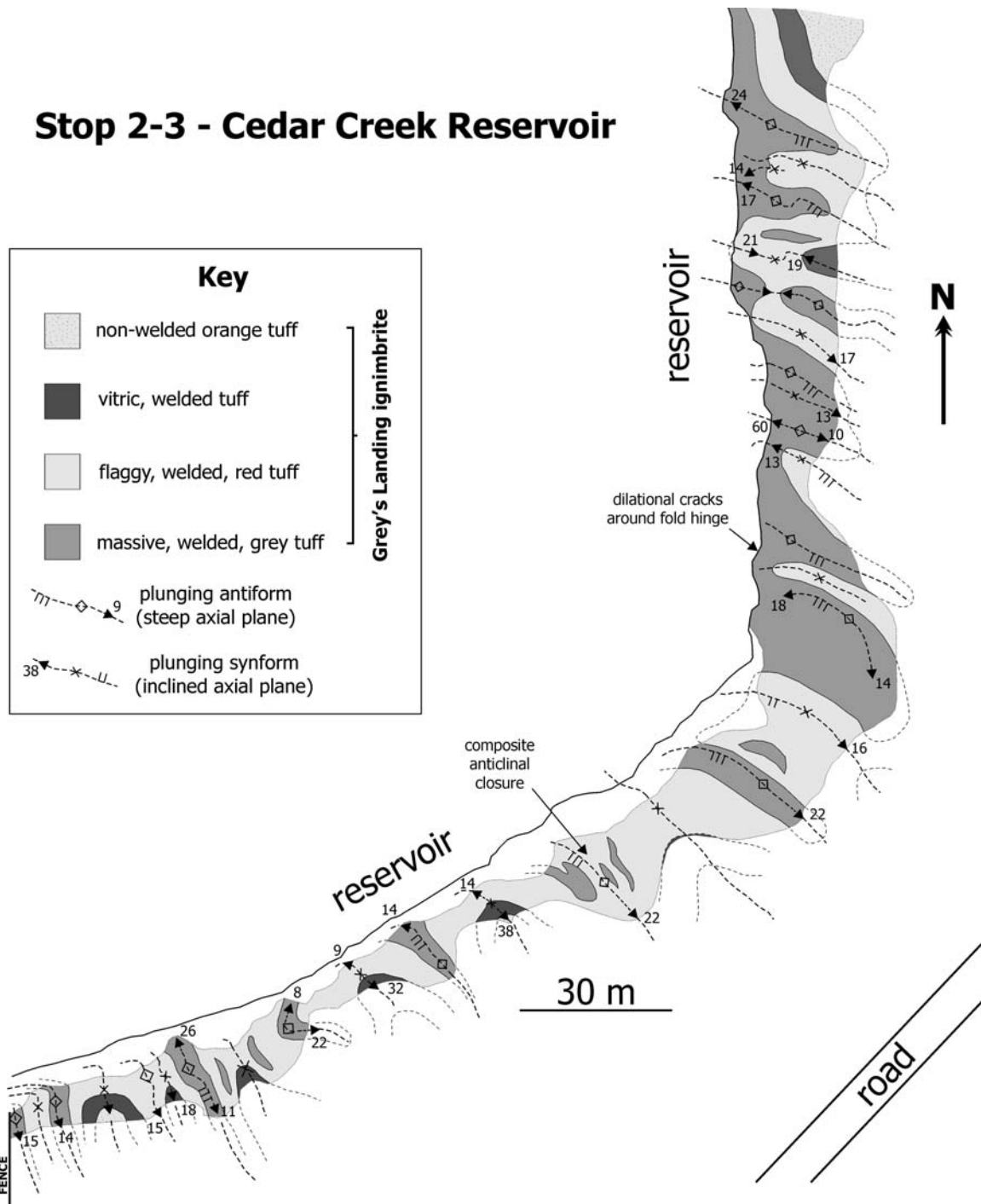


Figure 11. Simplified geologic map of Stop 2.3, Cedar Creek Reservoir, showing the location of fold axial traces within the Grey's Landing ignimbrite.

Stop 3.4 (optional)—Salmon Dam: large-scale synforms at the upper surface with infolded orange tuff.

Directions to Stop 3.1

Depart Jackpot, Nevada, heading north on U.S. 93. Follow the route for Day 2 across Salmon Dam, and turn right (south) on to a gated track ~300 m east of the junction for Cedar Creek Reservoir. Proceed along this rough track (not suitable for low ground-clearance vehicles) until you reach a large water tank and corral.

Stop 3.1: Monument Canyon (UTM Zone 11 675840E 4671116N)

This stop involves a short walk to consider how rheomorphism was influenced by substrate topography. It provides the opportunity to draw together understanding of rheomorphic features seen in the previous two days. Walk south along the track and onto the ridge to the immediate right. Gradually walk westward, examining the low crags at the top of the ridge to look for fold closures in the central lithoidal zone. The Grey's Landing ignimbrite in this vicinity forms a thin feather-edge. Is there any rheomorphism at this location? Has devitrification and/or jointing obscured any macro-structures?

Over the next 400 m, the ignimbrite thickens to >15 m at the southern entrance to Monument Canyon. Meter-scale stretched vesicles are exposed in overhangs at head height; they parallel the local stretching direction (E-W) and give a top-to-the-west shear sense. Curvilinear, recumbent isoclines are abundant at the entrance to Monument Canyon, and the strong, subhorizontal fabric is obvious in cliffs on the opposite side.

The ignimbrite continues to thicken over the next 200 m to the north before undergoing a dramatic change. The attitude and nature of the subhorizontal, intrafolial fabric changes abruptly across a steep ~E-W trending boundary (parallel to stretching direction and edge of the deposit). To the north of this boundary, the subhorizontal fabric is folded and refolded at different scales (meter scale to ten meter scale). The later folds are characteristically upright to inclined, open through to isoclinal, and plunge gently to steeply. Participants should range across the canyon flanks, making sure to look back across the canyon at the opposite flank.

Themes to consider: How is the earlier, subhorizontal fabric affected by later folding? Is there evidence of a time break between early and later folding? How do these structures relate to the two alternative explanations given for the "late" rheomorphism (see Summary, Day 2)?

Directions to Stop 3.2

Return to the Murphy Hot Springs Road and turn left toward Salmon Dam. Continue west ~8 mi (12 km) and pull off to the left opposite a large sand pit. Walk northeast ~250 m to a small abandoned quarry.

Stop 3.2: House Creek Quarry (UTM Zone 11 666463E 4668768N)

The line of low (1–2 m) crags forming the edge of the quarry is the House Creek ignimbrite (Bonnichsen et al., 1989). Note

how thin the ignimbrite is (~5 m original thickness) and the development of sheath folds and a strong stretched vesicle lineation (Branney et al., 2004). No autobreccia has been observed in this deposit.

Themes to consider: What is the structural style? Are there any kinematic indicators that can be used to determine the transport direction of ductile shear? How can rheomorphism occur within such a thin unit? What is the significance of the apparent absence of autobreccia?

Directions to Stop 3.3

Drive eastward, past the turnoffs for Stops 2.3 and 3.1. Turn right (south) onto a rough track running down to a flat area on top of a low slope above West Bay. Note the rotation of fault blocks on west-dipping, listric, normal faults in the middle distance.

Stop 3.3: West Bay (UTM Zone 11 686473E 4675065N)

Examine the low crags and exposed surfaces at the top of the slope, gradually tracking south. Here the deposit is at least 50 m thick; subhorizontal L = S fabrics have been gently warped by open, upright folds, which are most clearly seen across West Bay in the foreground. Sheath folds are well exposed throughout this section. Walk slowly along the cliff line southward, noting that the foliation reveals narrow "steep belts" of intensely refolded deposit, spaced ~50 m apart.

Themes to consider: Can the L = S tectonites (including sheath folds and strong stretching lineation) at this location be accounted for in the same way as those at Stops 1.2, 1.3, and 1.4? How does the style of later folding here relate to that seen at Stops 2.2–3.1?

Directions to Stop 3.4

Return to the road and turn right; drive ~100 m and pull off onto the open ground on the left at the top of the grade. Park vehicles and walk back to the dam. Beware traffic appearing around the corner.

Stop 3.4: Salmon Dam (UTM Zone 11 687018E 4675787N)

To the north of the dam, the Salmon Falls Creek canyon can be seen cutting through Pliocene basalts erupted from Salmon Butte (multiple dark gray flows on right side; Bonnichsen and Godchaux, 2002) and the Grey's Landing ignimbrite (red-brown exposures on the left). The Grey's Landing ignimbrite is exposed below two basalt lavas where the dam meets the west side of the canyon. Observe the variation in color and structure in the steep face, from the dam and the far side of the canyon. A large, upright syncline within the upper part of the Grey's Landing ignimbrite has preserved a partly enclosed remnant of massive, orange tuff, which varies from nonwelded to slightly fused near the contact with the ignimbrite upper vitrophyre. Take extreme care on these slopes. Close examination of the contact relations reveals that the tuff was deposited when the ignimbrite was hot, ductile, and still deforming. Please do not hammer.

Themes to consider: Is the orange tuff an upper nonwelded part of the ignimbrite (note the Grey's Landing ignimbrite generally lacks pumice lapilli), or is it an ashfall deposit (e.g., of co-ignimbrite origin)? What is the effect of continued deposition of nonwelded tephra? What is the nature of the contact between welded and nonwelded tephra?

CONCLUDING REMARKS

We leave it for individuals to decide which (if any) of the various preexisting models for rheomorphism best accounts for the deformation features in the Grey's Landing ignimbrite. A structural analysis (authors' work in preparation) suggests that the ubiquitous small-scale intrafolial folds and associated strong lineation, initiated within in a narrow shear zone (~0.5–1 m thick) during pyroclastic deposition and agglutination. With time, this shear zone migrated upward along with the rising aggradation surface (Fig. 4) so that, by the time the entire thickness of ignimbrite had aggraded, all levels had been subjected to intense shear. The layer of orange ash from the same eruption was then deposited on top (Stop 3.4). Below this, ductile, gravity-driven shear continued, probably at decreasing strain rates but affecting an increased thickness of the ignimbrite. The larger scale of the later sheath folds and oblique folds reflects the greater thickness of the shearing layer. The steeper attitudes of some of these folds reflects the presence, during the deformation, of an upper free surface, which has no direct analogy in crustal shear zones. The later deformation affected the upper orange ash and so must have developed after pyroclastic emplacement had ceased. We infer that at this time the shear rate was decreasing as cooling and degassing caused changes in rheology. The last stages of deformation were partly brittle, with the formation of tension cracks in upper parts of the ignimbrite. Overall, the deformation history was probably progressive (rather than comprising two entirely separate fold phases), and the style of deformation evolved in response to the evolving stresses and rheologies.

Analysis of the Grey's Landing ignimbrite is continuing, in order to characterize the deformation and develop a model for the ignimbrite emplacement and rheomorphism.

ACKNOWLEDGMENTS

Many thanks to Bill Bonnichsen, Marty Godchaux, and Mike McCurry for introducing us to some of these wonderful localities and their continued discussion, advice, and encouragement. Curtis Manley kindly allowed us to apply his cooling model to the Grey's Landing ignimbrite, and Craig White kindly provided equipment support. Nancy Riggs, Jocelyn McPhie, John Stix, Guillermo Labarthe-Hernandez, Gerardo Aguirre-Diaz, and Jorge Aranda-Gomez provided much-needed practice for GDMA's viva examination on different occasions during the fieldwork. GDMA was supported by Natural Environment Research Council (NERC) studentship NER/S/A/2001/06292 and the University of Leicester.

REFERENCES CITED

- Andrews, G.D.M., Branney, M.J., Bonnichsen, B., and McCurry, M., 2006, Rhyolitic ignimbrites in the Rogerson Graben, southern Snake River Plain volcanic province: volcanic stratigraphy, eruption history and basin evolution: *Bulletin of Volcanology* (in press).
- Bonnichsen, B., 1982, Rhyolite lava flows in the Bruneau-Jarbridge Eruptive Center, southwestern Idaho, *in* Bonnichsen, B., and Breckinridge R.M., eds., *Cenozoic Geology of Idaho: Idaho Bureau Mines and Geology Bulletin*, v. 26, p. 283–320.
- Bonnichsen, B., and Citron, G.P., 1982, The Cougar Point Tuff, southwestern Idaho, *in* Bonnichsen, B., and Breckinridge, R.M., eds., *Cenozoic Geology of Idaho: Idaho Bureau Mines and Geology Bulletin*, v. 26, p. 255–281.
- Bonnichsen, B., and Godchaux, M.M., 2002, Late Miocene and Pliocene, and Pleistocene geology of southwestern Idaho with emphasis on basalts in the Bruneau-Jarbridge, Twin Falls, and Western Snake River Plain regions, *in* Bonnichsen, B., White, C.M., and McCurry, M., eds., *Tectonic and magmatic evolution of the Snake River Plain volcanic province: Idaho Geological Survey Bulletin*, v. 30, p. 233–312.
- Bonnichsen, B., and Kauffman, D.F., 1987, Physical features of rhyolite lava flows in the Snake River Plain volcanic province, southwestern Idaho, *in* Fink, J.H., ed., *The emplacement of silicic domes and lava flows: Geological Society of America Special Paper 212*, p. 119–145.
- Bonnichsen, B., Christiansen, R.L., Morgan, L.A., Moye, F.J., Hackett, W.R., Leeman, W.P., Honjo, N., Jenks, M.D., and Godchaux, M.M., 1989, Excursion 4A: Silicic volcanic rocks in the Snake River Plain—Yellowstone Plateau province, *in* Chapin, C.E., and Zidek, J., eds., *Field excursions to volcanic terranes in the western United States; Volume II, Cascades and Intermountain West: New Mexico Bureau of Mines and Mineral Resources*, v. 47, p. 135–182.
- Branney, M.J., and Kokelaar, P., 1992, A reappraisal of ignimbrite emplacement: progressive aggradation and changes from particulate to non-particulate flow during emplacement of high-grade ignimbrite: *Bulletin of Volcanology*, v. 54, p. 504–520, doi: 10.1007/BF00301396.
- Branney, M.J., and Kokelaar, B.P., 1997, Giant bed from a sustained catastrophic density current flowing over topography: Acatlán ignimbrite, Mexico: *Geology*, v. 25, p. 115–118, doi: 10.1130/0091-7613(1997)025<0115:GBFASC>2.3.CO;2.
- Branney, M.J., and Kokelaar, P., 2002, *Pyroclastic density currents and the sedimentation of ignimbrites*: London, The Geological Society Memoir 27, 143 p.
- Branney, M.J., Kokelaar, P., and McConnell, B.J., 1992, The Bad Step Tuff: a lava-like ignimbrite in a calc-alkaline piecemeal caldera, English Lake District: *Bulletin of Volcanology*, v. 54, p. 187–199.
- Branney, M.J., Barry, T.L., and Godchaux, M., 2004, Sheathfolds in rheomorphic ignimbrites: *Bulletin of Volcanology*, v. 66, p. 485–491, doi: 10.1007/s00445-003-0332-8.
- Chapin, C.E., and Lowell, G.R., 1979, Primary and secondary flow structures in ash-flow tuffs of the Gribbles Run paleovalley, central Colorado, *in* Chapin, C.E., and Elston, W.E., eds., *Ash-flow tuffs: Geological Society of America Special Paper 180*, p. 137–154.
- Christiansen, R.L., 2001, The Quaternary and Pliocene Yellowstone Plateau volcanic field of Wyoming, Idaho, and Montana: *U.S. Geological Survey Professional Paper 729-G*, 145 p.
- Ekren, E.B., McIntyre, D.H., and Bennett, E.H., 1984, High-temperature, large-volume, lavalike ash-flow tuffs without calderas in southwestern Idaho: *U.S. Geological Survey Professional Paper 1272*, 73 p.
- Fisher, R.V., 1966, Mechanism of deposition from pyroclastic flows: *American Journal of Science*, v. 264, p. 350–363.
- Freundt, A., 1998, The formation of high-grade ignimbrites; 1: Experiments on high- and low-concentration transport systems containing sticky particles: *Bulletin of Volcanology*, v. 59, p. 414–435, doi: 10.1007/s004450050201.
- Furukawa, K., and Kamata, H., 2004, Eruption and emplacement of the Yamakogawa rhyolite in central Kyushu, Japan: A model for emplacement of rhyolitic spatter: *Earth Planet Space*, v. 56, p. 517–524.
- Henry, C.D., and Wolff, J.A., 1992, Distinguishing strongly rheomorphic tuffs from extensive silicic lavas: *Bulletin of Volcanology*, v. 54, p. 171–186.
- Hughes, S.S., and McCurry, M., 2002, Bulk major and trace element evidence for a time-space evolution of Snake River Plain rhyolites, Idaho, *in* Bonnichsen, B., White, C.M., and McCurry, M., eds., *Tectonic and magmatic evolution of the Snake River Plain Volcanic province: Idaho Geological Survey Bulletin*, v. 30, p. 161–176.

- Humphreys, E.D., Dueker, K.G., Schutt, D.L., and Smith, R.B., 2000, Beneath Yellowstone; evaluating plume and non-plume models using Teleseismic images of the upper mantle: *GSA Today*, v. 10, no. 12, p. 1–7.
- McCurry, M., Watkins, A.M., Parker, J.L., Wright, K., and Hughes, S.S., 1996, Preliminary volcanological constraints for sources of high-grade, rheomorphic ignimbrites of the Cassia Mountains, Idaho: Implications for the evolution of the Twin Falls Volcanic Center: *Northwest Geology*, v. 26, p. 81–91.
- Mahood, G.A., 1984, Pyroclastic rocks and calderas associated with strongly peralkaline volcanic rocks: *Journal of Geophysical Research*, v. 89, p. 8540–8552.
- Malde, H.E., and Powers, H.A., 1962, Upper Cenozoic stratigraphy of the western Snake River Plain, Idaho: *Geological Society of America Bulletin*, v. 73, p. 1197–1210.
- Manley, C.R., 1992, Extended cooling and viscous flow of large, hot rhyolite lavas: implications of numerical modelling results: *Journal of Volcanology and Geothermal Research*, v. 53, p. 27–46, doi: 10.1016/0377-0273(92)90072-L.
- Manley, C.R., 1995, How voluminous rhyolite lavas mimic rheomorphic ignimbrites: eruptive style, emplacement conditions, and formation of tuff-like features: *Geology*, v. 23, p. 349–352, doi: 10.1130/0091-7613(1995)023<0349:HVRLMR>2.3.CO;2.
- Manley, C.R., 1996, Physical volcanology of a voluminous rhyolite lava flow: the Badlands lava, Owyhee plateau, SW Idaho: *Journal of Volcanology and Geothermal Research*, v. 71, p. 129–153, doi: 10.1016/0377-0273(95)00066-6.
- Pichler, H., 1981, *Italienische Vulkan-Gebeite III: Lipari, Vulcano, Stromboli, Tyrrhenisches Meer: Sammlung Geologische Führer*, v. 69, p. 1–233.
- Pierce, K.L., and Morgan, L.A., 1992, The track of the Yellowstone hotspot: volcanism, faulting, and uplift, *in* Link, P.K., Kuntz, M.A., and Platt, L.P., eds., *Regional geology of eastern Idaho and western Wyoming: Geological Society of America Memoir 179*, p. 1–53.
- Riehle, J.R., Miller, T.F., and Bailey, R.A., 1995, Cooling, degassing, and compaction of rhyolitic ash-flow tuffs: a computational model: *Bulletin of Volcanology*, v. 57, p. 319–336.
- Rodgers, D.W., Ore, H.T., Bobo, R.T., McQuarrie, N., and Zentner, N., 2002, Extension and subsidence of the Eastern Snake River Plain, Idaho, *in* Bonnicksen, B., White, C.M., and McCurry, M., eds., *Tectonic and magmatic evolution of the Snake River Plain volcanic province: Idaho Geological Survey Bulletin*, v. 30, p. 121–155.
- Ross, C.S., and Smith, R.L., 1961, Ash-flow tuffs: their origin, geologic relations and identification: *U.S. Geological Survey Professional Paper 366*, p. 1–81.
- Schmincke, H.-U., and Swanson, D.A., 1967, Laminar viscous flowage structures in ash-flow tuffs from Gran Canaria, Canary Islands: *Journal of Geology*, v. 75, p. 641–664.
- Schmincke, H.-U., with contributions by Freundt, A., Ferriz, H., Kobberger, G., Leat, P., 1990, *Geological Field Guide: Gran Canaria: Witten, Germany*, Pluto Press, 202 p.
- Sumner, J.M., and Branney, M.J., 2002, The emplacement history of a remarkable heterogeneous, chemically zoned, rheomorphic and locally lava-like ignimbrite: “TL” on Gran Canaria: *Journal of Volcanology and Geothermal Research*, v. 115, p. 109–138, doi: 10.1016/S0377-0273(01)00311-0.
- Walker, G.P.L., 1983, Ignimbrite types and ignimbrite problems: *Journal of Volcanology and Geothermal Research*, v. 17, p. 65–88, doi: 10.1016/0377-0273(83)90062-8.
- Webb, S.L., 1997, Rheology, relaxation and the glass transition in silicate melts: *Reviews of Geophysics*, v. 35, p. 191–218, doi: 10.1029/96RG03263.
- Wolff, J.A., and Wright, J.V., 1981, Rheomorphism of welded tuffs: *Journal of Volcanology and Geothermal Research*, v. 10, p. 13–34, doi: 10.1016/0377-0273(81)90052-4.

